Examination of stress-induced transformations within multicomponent pharmaceutical crystals

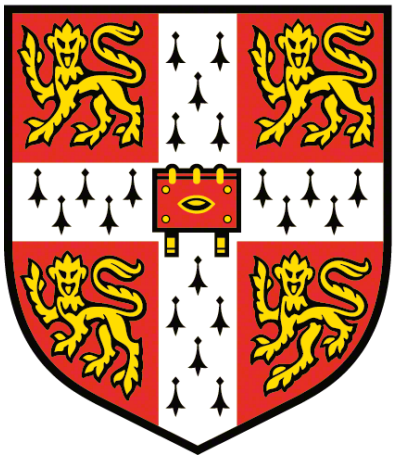

Gabriela Schneider Rauber

Department of Chemistry

University of Cambridge

A dissertation submitted for the degree of

Doctor of Philosophy

Sidney Sussex College

May 2018

Abstract

Title: "Examination of stress-induced transformations within multicomponent pharmaceutical crystals"

Author: Gabriela Schneider Rauber

Crystal engineering has advanced the strategies of design and synthesis of organic solids with the main focus being on improving the properties of the developed materials. Research in this area has a significant impact on large-scale manufacturing as industrial processes may give rise, at various stages, to stress-induced transformations and product modification. This thesis investigates the solid-state properties at play in the case of the surface and structural reorganization which results from the stress within a crystal during the drying of labile multicomponent organic solids.

Chapter 1 introduces various concepts in solid-state chemistry and explores their application in the manufacture of solid pharmaceuticals. The significance of stress-induced transformations during the drying process is illustrated by reactions associated with crystal decomposition processes such as dehydration, desolvation and sublimation. The chapter also introduces carbamazepine (CBZ) multicomponent materials as models for the studies of stress-induced transformations.

Chapter 2 presents the experimental section of the work and describes the materials, methods and equipment used for the study.

Chapter 3 presents the analysis of the various crystal structures of CBZ. The crystal forms are classified with an emphasis on a comparison of intermolecular interactions, coformer arrangement, crystal packing and the geometric parameters of slip/cleavage planes within the crystals.

Chapter 4 details the experimental methods for preparation of the samples. Cooling solution crystallization was the standard method which has been selected, and crystal habit and surface variations have been studied as a function of the solution concentration and the crystallization environment. Attention is given, in particular, to the preparation of carbamazepine dihydrate and the specific cocrystals carbamazepine cocrystals formed with benzoquinone and oxalic acid.

Chapter 5 is devoted to the dehydration of carbamazepine dihydrate for samples prepared and examined in approximate 1-gram laboratory scale quantities. It explores the effect of vacuum, temperature, humidity and seeding on the surface and bulk properties of the products.

Chapter 6 presents the solid-state characterization results obtained for samples crystallized at a much larger scale (ca. kilogram quantities) with a particular emphasis placed on their mechanical properties. It explores the comparison of large scaled batches with laboratory scale samples in order to obtain a greater understanding of how small-scale laboratory studies may be extrapolated to more commercial processes.

Chapter 7 present results on the stress-induced transformations of carbamazepine solvates and cocrystals. It details the effect of thermal decomposition on the surface and bulk properties of the products, possible seeding effects, and the interconversion between carbamazepine dihydrate and carbamazepine benzoquinone cocrystal.

Chapter 8 combines the research findings concerning the structural analyses of the materials in the context of current literature. Limitations related to the use of carbamazepine as a model and to the experimental set-up are also explored.

In the final chapter conclusions are presented which correlate observations made on the crystallization and decomposition of multicomponent materials operating at small-scale to effects appropriate to manufacturing of pharmaceuticals at large scale.

Declaration

I hereby declare that except where specific reference is made to the work of others, the contents of this dissertation are original and have not been submitted in whole or in part for consideration for any other degree or qualification in this, or any other university. This dissertation is my own work and contains nothing which is the outcome of work done in collaboration with others, except as specified in the text and Acknowledgements.
It does not exceed the 60000-word limit prescribed by the Degree Committee for the Faculty of Physics and Chemistry.

Gabriela Schneider Rauber
May 2018

Acknowledgments

The author is greatly appreciative of life.

I dedicate this thesis to my parents, Noeli Teresinha Schneider Rauber and Celso Rauber. They have raised me with a combination of love, support and freedom that I could only fully appreciate during the last few years. They showed me the wonders of life in this planet and were my first science educators. Dad taught me to observe Nature and the environment surrounding myself in such a way that I realised I was only a small part of something much bigger. He had names for trees, knew fruits that could be eaten, the effect of the moon in the crops, showed me the interpretation of the sky by means of its clouds and colours, the wind and the sound of the animals in the forest. Mom showed me the principle of relatedness. She taught me to observe my own body and introduced me to medicinal plants, spirituality and scientific books. Mom showed me that there were theories and phenomena explaining what I could observe in Nature and we were particularly enchanted by menstrual cycle diagrams and the Giants Causeway in Northern Ireland. Mom and dad encouraged me on my excursions into the wild to pick crystals and collect plants to prepare exsiccates and extracts at home. They unconsciously put chemistry lessons together and were the first enthusiasts of my curiosity and talents, even before I could dream using them in a professional environment.

I am grateful to my sister, *mana* Dulci Noeli Rauber Bacca. She has introduced me to literature books and I am especially grateful for her influence on my Paulo Freire's readings. From her I have learnt that I could dream and express my feelings, and that it was fine to think different from my parents. She used to try on me everything she was learning at the University as a pedagogy student. Every conference she went was a book to my "library", even before I knew how to read. The very first time I have heard about a PhD degree was during *mana*'s graduation as a teacher. I remember I found it interesting and told my parents I wanted to get a PhD; they laughed on me – I was 6 years-old.

I would also like to acknowledge the influence I had from all the other women in my family (even the ones I have not met in this life). My grandmas, aunties, cousins and my sister-in-law had touched my heart and influenced myself in such a way I could not put in words.

I would like to mention my Godmother *madi* Celei Ana Schneider, who helped raising me on my first years and is one of the most courageous women I have ever met.

And we also learn so much from the children in the family… I thank my nieces and nephew, Maria Helena Rauber Bacca, Maria Vitória Ertel Rauber and Lucas Ertel Rauber. They taught me detachment from material world as they destroyed the books I had in the abovementioned library (I think I am still grieving *Charalina*). But more than that, they opened and offered their pure and naïve hearts to me. All the experiences we had together still remind me to listen to my inner child. I do believe this can make us adults that feel and relate in a more constructive way.

I feel very grateful to all the teachers I had so far. Undoubtedly, I must mention my previous supervisors in Brazil. They kept supporting me during the PhD time. Prof Simone Gonçalves Cardoso introduced me to the quality control of pharmaceutical materials, while Prof Silvia Lucia Cuffini introduced me to solid-state chemistry. Thank you very much for the friendship, the trust, the opportunities and the laughs in the lab.

I also thank my friends back in Brazil and the ones I have met in these years abroad. Sharing with them makes life spicy and soothes the challenges. I would like to specially mention the ones who were closer and inspired me during this PhD experience, Aline Ferreira, Ana Carol Miranda, Anna Dankova (*and soon little Hanna*), Annelise Smit de Carvalho and Pieter Smit, Andrea Granada, Arathi Ramachandran, Cheryl Pittas, Cinira Fandaruff, Debora Rosa, Diego Calza, Gelson Pasetti, Juliana Gonçalves, Maggie Green, Myrtes Magagnin, Natalia Oliveira, Rachel Anne, Rodrigo Ferreira Velasco, Solomon Kweku Sagoe Amoah, Viviane Nart and Wilson Ricardo Leal.

And there is that one special friend who became a partner! From our discussions on milling, grain size and fracture mechanics, to hand in hand walking and adventurous backpack trips, I thank Pablo *fofis* Lia Fook. Nothing that I can verbalize could ever illustrate how grateful I am for sharing life with him. He has mirrored me when it was time to face inwards. He has grounded me when butterfly-Gabi was winging around lost in her own unknown skies. He has been helping me to open the cage and fly free as it is time to expand and grow. And he has seen myself. Pablo taught me that silence, stillness and surrender are courageous acts, and that life is very simple… So simple that I can lay down my questions and just observe it manifesting in front of my silent eyes. *Fofis*, you are in my heart.

I was particularly fortunate to work with such bright and helpful colleagues and friends in our research group! I would like to mention Abida Wassen, Andrea Araya, David Hughes (*and Susan*), Davide Scaramuzza, Debora Zanolla, Dinesh Ramesh Mirpuri Vatvani, Dritan Hasa (*and Andjola Pacaj*), Ernest Chow, Eugenia Miniussi, Hugh Thompson, Ilona

Materek, Joey Howard, Johnathan Hooke, Kathleen Toussaint (*and Miguel Acosta*), Liliana Mazur, Mariana Pastore, Marina Marosa, Mark Eddleston (*Magdalene and little Liliana*), Massimo Galletti, Mihails Arhangelskis, Nadeesh Adassooriya (*and Gihani Ranasinghe*), Ryan Rienze, Samuel Stratford (*Cara and little Matthew*), Stefan Diez, and Wenju Liu. Thank you very much! Our discussions have always been fruitful, and I had a lot of fun by your side.

Specific (and special!) thanks go to: Dr Ernest Chow for the time he dedicated teaching me on using the atomic force microscope. Dr Mark Eddleston for introducing me to transmission electron microscopy experiments and for providing me with a zone axis finder program that was used to analyse the diffraction patterns collected during cryo-transmission electron microscopy experiments. Dr Dinesh Ramesh Mirpuri Vatvani for the permission to reproduce Figure 299, which was taken from his PhD thesis. Dr Mihails Arhanguelskis for the calculation of the decomposition enthalpies of the carbamazepine multicomponent materials, for refining the dihydrate structure against powder data collected in capillary, for creating and refining two models of a theoretical carbamazepine monohydrate, and for valuable and friendly discussions. Dr Dritan Hasa for the insights and very much appreciated scientific discussions. Dr Ana Belenguer for the encouragement, discussions and the support on safety matters and translations. Matthew Brooker for his efforts on solving a wide range of issues in the lab. Dr Michael Casford for teaching me on using the scanning electron microscope. Dr John Davies and Dr Andrew Bond for the single crystal X-ray diffraction data collection and structure solution. Ms Clair M. Castle MCLIP for her support on searching Databases and old scientific papers. Dr Giulio Lampronti (Department of Earth Sciences) for trials on using the scanning electron microscope coupled with electron backscatter diffraction. Dr Dejan-Krešimir Bučar and Dr Mérina Corpinot (Department of Chemistry, University College, UK) for collecting capillary powder X-ray diffraction data. Eftychios Hadjittofis (Department of Chemical Engineering, Imperial College, UK) for his support on searching activity coefficients on Databases. Prof Mojtaba Ghadiri and Wei Pin Goh (School of Chemical and Process Engineering, University of Leeds, UK) for nanoindentration and breakage experiments, and for valuable discussions on mechanical properties of solids. Prof Rik Drummond-Brydson, Dr Nicole Hondow, James Cattle and Mark S'ari (School of Chemical and Process Engineering, University of Leeds, UK) for discussions and the transmission electron microscopy experiments (conventional and under cryogenic conditions). Dr Gislaine Kuminek (University of Michigan, Ann Arbour, USA), Juliana Rosa and Tatiane Cogo Machado (Federal University of Santa Catarina, Florianópolis, Brazil) for fruitful discussions on the solubility diagrams of cocrystals. Dr Raimundo Ho (AbbVie Inc., Chicago, Illinois, USA) for the attachment energy calculations. Dr Kushal Sinha (AbbVie Inc., Chicago, Illinois, USA) for the development of one

crystallization method which was applied in the preparation of carbamazepine dihydrate in kilogram-scale and for permission on reproducing a summary of his work in Chapter 6.

AbbVie Inc. (Chicago, Illinois, USA) is acknowledged for the financial support given to this project and for the opportunity of a summer internship in 2015. I would also like to thank the scientific members of the AbbVie project, Dr Ahmad Sheikh, Dr Geoff Zhang, Dr Nandkishor Nere, Dr Raimundo Ho, and Dr Shailendra Bordawekar from the AbbVie team; Dr Jerry Heng, Eftychios Hadjittofis and Mark Antonin Isbell from the Imperial College team; and Prof Mojtaba Ghadiri and Wei Pin Goh from the University of Leeds. I am humbled beyond words by everything that I have learnt from them. Not only from the honour of discussing science with such skilled people, but also by the chance of seeing them beyond their degrees and professional achievements. The diversity of perspectives, backgrounds and attitudes was undoubtedly a very rich environment for me as a student and observer. Once more, I am very grateful.

I wish to thank CAPES – *Coordenação de Aperfeiçoamento de Nível Superior* (Science Without Borders Program, Brazil) and Cambridge Overseas Trust (United Kingdom) for personal financial support and student fellowship (CsF BEX 9530/13-4).

I have been particularly fortunate to come to Cambridge for studying. I must certainly acknowledge the teachings received from this Land. I have learnt so much from the warmth of silent wintery days and the autumn colouring! I thank that old mulberry tree on Cloister Court at Sidney Sussex College, the giant Cedar around the corner of Perbenton Terrace with Brookside Road, the Willow trees along (with) river Cam, the cherry trees in the Botanic Garden, the woods surrounding Byron's pool, the Castle Hill, Rosie (the cat) and all the Cantabrigian countryside fields, daffodils, squirrels and robins.

Another lovely contribution to this Cambridge experience was Sidney Sussex College. I have received a lot of support from the staff and fellows, who made me feel very welcomed and happy. I would like to mention Angela Parr-Burman and Gillian Johnstone (former and present PA to the Graduate Tutors), Alan Stevens (Librarian), David Graves (Finance Manager), Colin Maxted and the other Porters, Karolyn Duke and the others in the housekeeping team.

I also thank all the staff in the Department of Chemistry, whose efforts on building a more inclusive, supportive and friendly environment are remarkable. I am grateful for everything I have learnt and the people I have met while in the Athena Swan and the Graduate Networking & Social Committees. I especially thank the staff from the departmental workshops, the stores, the reception, the accounts' office, the cleaners' team, the librarians, the reprographics and photography offices, the IT officers and the safety officer. I am afraid I

cannot add all the names, but I would like to particularly mention a few people. Glenda Harden and Julie Lee for all the support and friendliness; and Dr Deborah Longbottom, Prof Melinda Duer and Dr Rachel MacDonald for listening to me with kindness, and providing helpful advices, encouragement and guidance.

Finally, Bill Jones. I would like to express the deepest feelings of gratitude to my supervisor, Professor William Jones. I have learnt so much from observing him and his way of leading us with ethics, wisdom, patience and humility. I have been particularly fortunate to dream about my early career having his retirement in the background and questioning, "What journey will make my heart shine when I retire? What journey do I want to share with others?" The lessons I have learnt from Bill remind me about a documentary I have watched a few years ago. It had the story of a young guitar player describing a great lesson he had learnt from a senior accordion artist and singer in Brazil. The young man told they finished a concert with an improvisation set, which he played using several notes and techniques to impress his colleague. Instead, when the senior player had his turn, he beautifully mastered it with only four notes. That experience had a major effect in the youngster's career as he said "*In that exact moment I learnt the meaning of playing with my heart. Those four minutes completely changed myself"* (Yamandu Costa referring to Dominguinhos' teaching). Can you imagine four years of such experiences? To you, Bill, I dedicate a free translation of Eduardo Galeano's words (I wish you could read and feel them in Spanish): *"…contemplating human life from high in the sky, he says 'This is the world, lots of people, we are a sea of little fires.' No two fires are the same. Each person shines with their own light amidst all others. There are large fires and tiny fires, and there are fires of all the colours. There are people of serene fire who do not notice the wind. And there are people of crazy fire that charges the air with sparks. Some fires, silly fires, neither light nor burn. But others… Others burn with such power that it is not possible to look at them without being dazzled and those who get close enough, kindle."* Thank you, Bill, for illuminating and inspiring us.

To my parents, Noeli and Celso

“Me pongo el sol al hombro y el mundo es amarillo”

- Fecundo Cabral, In: “No soy de aquí, ni soy de allá” (1992)

Table of contents

Abbreviations and symbols

AFM	Atomic force microscopy
API	Active pharmaceutical ingredient
ATR-FTIR	Attenuated total reflection Fourier transform infrared spectroscopy
BFDH	Bravais-Friedel-Donnay-Harker model of morphology prediction
CBZ	Carbamazepine
CBZ:ACA	Carbamazepine:acetic acid 1:1 solvate
CBZ:ACE	Carbamazepine:acetone 1:1 solvate
CBZ:BZQ	Carbamazepine:benzoquinone 1:1 cocrystal
2CBZ:BZQ	Carbamazepine:benzoquinone 2:1 cocrystal
2CBZ:DIOX	Carbamazepine:dioxane 2:1 solvate
CBZ:DMA	Carbamazepine:dimethyl acetamide 1:1 solvate
CBZ:DMF	Carbamazepine:dimethyl formamide 1:1 solvate
CBZ:DMSO	Carbamazepine:dimethyl sulfoxide 1:1 solvate
CBZ:FA	Carbamazepine:formic acid 1:1 solvate
CBZ:FORM	Carbamazepine:formamide 1:1 solvate
CBZ:NIT	Carbamazepine:nitromethane 1:1 solvate
2CBZ:OXA	Carbamazepine:oxalic acid 2:1 cocrystal
CBZ:TFA	Carbamazepine:trifluoroacetic acid 1:1 solvate
CBZ:TFE	Carbamazepine:trifluoroethanol 1:1 solvate
2CBZ:TFE	Carbamazepine:trifluoroethanol 2:1 solvate
CSD	Cambridge Structural Database
D	Distance between hydrogen bond donor and acceptor (in HB)
d	Distance between hydrogen and hydrogen acceptor (in HB)
DFT	Density functional theory
DSC	Differential scanning calorimetry
$\mathbf{E^{AB}}$	Energy of intermolecular interaction between molecules “A” and “B”
G	Gibbs free energy
GRAS	Generally recognized as safe
H	Enthalpy
HB	Hydrogen bond
HPLC	High performance liquid chromatography
IR	Infrared

IUCr	International Union of Crystallography
K_2SO_4	Potassium sulphate
LiCl	Lithium chloride
MW	Molecular weight
OM	Optical microscopy
p	Pressure
PDF	Pair distribution function
PXRD	Powder X-ray diffraction
P_2O_5	Phosphorous pentoxide
RH	Relative humidity
RPM	Rotations per minute
S	Entropy
SEM	Scanning electron microscopy
T	Temperature
T_t	Temperature of transition
t_r	Retention time
TEM	Transmission electron microscopy
Tg	Glass transition temperature
TGA	Thermogravimetric analysis
THF	Tetrahydrofuran
UV	Ultraviolet
V	Volume
Z	Number of formula units in the unit cell
Z'	Number of formula units in the asymmetric unit
Ø	Diameter
θ	Angle between hydrogen donor, hydrogen and hydrogen acceptor (in HB)
ρ	Density

CHAPTER 1 – Literature review

1.1 Solid-state chemistry – introductory remarks

1.1.1. Discussion on nomenclature and some working definitions

Nomenclature in chemistry has long considered an important issue and the situation becomes even more complicated when it is necessary also to consider nomenclature as defined by governments, regulatory agencies and patent law.[1,2] In an attempt to avoid confusion with regard to the work described in this thesis the names and definitions which will be used are given below.

Traditionally, a *solid* is classified as a material with fixed volume and shape, a *liquid* has a fixed volume but the shape of its container and a *gas* has variable volume and shape. The condensed state can be elaborated further in terms of viscosity and its response to shear stress. In this case, solids do not present fluidic characteristics, although liquids show insignificant initial elastic behaviour but deform continuously after shear.[34] These concepts, however, cannot fully explain the wide variety of materials existing in Nature. For example, regarding structural terms, solids can be classified as *amorphous* (glassy) or *crystalline*. While the former possesses only local atomic arrangement and short-range order, the latter is characterised by repeated atomic patterns with pronounced long-range order – which can also tolerate some *disorder* within its structure (e.g. rotational disorder and thermal motion). When the periodic and repetitive arrangement of the atoms is perfect or extended throughout the whole sample without interruption, the result is a perfect *single crystal*. On the other hand, *polycrystalline materials* are made of single-crystal units arranged in random crystallographic orientations (as crystalline *domains* or *crystallites*). The surrounding regions of these domains also may present disorder, with free atoms/molecules, voids/vacancies and impurities (Figure 1).[3,5–7]

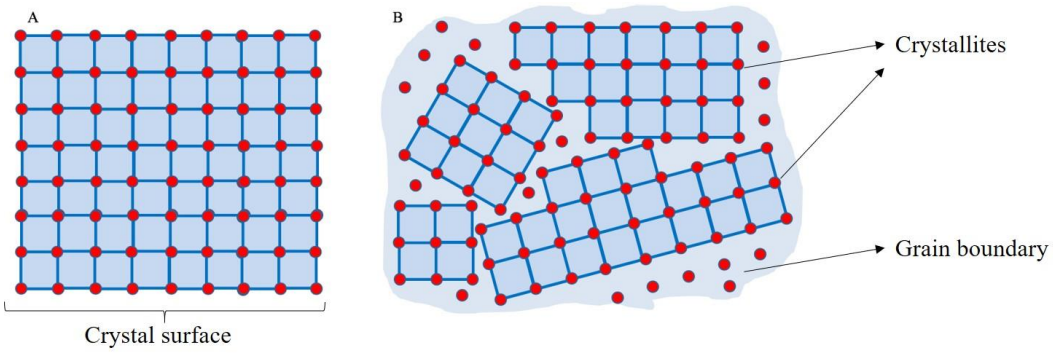

Figure 1 - Scheme of the lattice arrangement in a perfect single crystal (A) and polycrystalline sample (B) (adapted from Mittemeijer & Scardi, 2004;[7] Callister & Rethwish, 2012[6]).

Additional factors can be introduced using Figure 1: (i) the size of the crystallites may vary and affect the sample properties; (ii) the repetition of the three-dimensional array is not infinite but is limited by the existence of surfaces of the crystal or crystallites; and (iii) the "junction" of the different surfaces in a crystal can create different morphologies (crystal habit).

Surfaces are considered the major imperfection of a crystal and, in fact, the atoms on a solid surface have a higher free energy and an environment that differs markedly from that of the atoms in the bulk.[7–10] During crystallization, a surface tends to minimize its free energy (or tension) by means of relatively small atom movements needed to break up the surface into small sections (terraces), one or more of which have an orientation of lower energy (Figure 2).[8–11] As a consequence, surfaces present other *structural defects*, such as steps, kinks and vacancies, which may also affect the observed bulk properties. [10,12] Within the actual bulk of the material the types of defects which may be found are point defects (vacancies/interstitials), line and planar defects (dislocations, stacking faults, twin boundaries) and volume defects (clusters, cracks, rods, tubes or precipitates).[13,14]

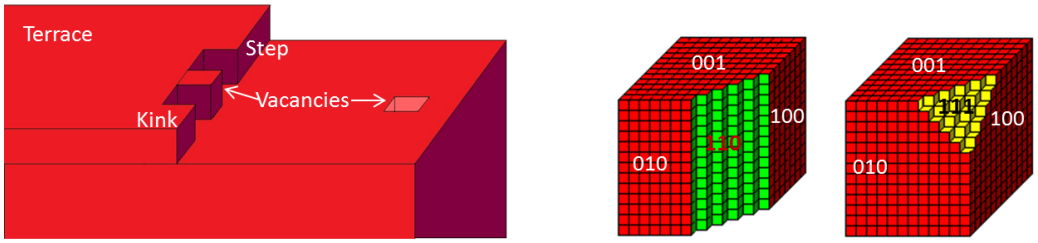

Figure 2 - Terrace identifying steps, kinks and vacancies on the surface (left) and faced crystals (right) (adapted from Samorjai & Li;[10] Giacovazzo et al.[15]).

Another source of diversity in solids is the composition and the type of packing. Materials with the same composition and different crystalline structures are related by the concept of *polymorphism*. Multicomponent materials, i.e. *cocrystals*, *solvates* and *salts*, may also have some chemical similarity but may exist in different polymorphic forms.[2,5,16,17] In this thesis, in multicomponent solids I refer to one component as the "target" or "host" molecule/ion (corresponding to the drug or the "main" molecule), and the other(s) as the "coformer" or "guest" molecule/ion.[18] To avoid misinterpretations, I have selected purely academic definitions of multicomponent materials, as follows:

(i) solvates are solids containing in their structure at least one type of molecule which forms in its own state a liquid at room temperature;

(ii) hydrates are a subset of solvates with water molecules in the structure;

(iii) cocrystals are stoichiometric multicomponent systems connected by non-covalent interactions where all the individual components are solids under ambient conditions;

(iv) salts are solids where two or more of the components are charged i.e. excluding zwitterions.

1.1.2. Crystal engineering and the design of solids

A wide variety of characteristics need to be considered in order to have a better understanding of the properties of solids: crystallinity, nature of any disorder, defect content, polymorphism, morphology, surface chemistry, particle size, composition and the nature of any supramolecular interactions. While these characteristics are well recognised in inorganic chemistry, the study of organic materials have been relatively neglected in the past owing to experimental difficulties (*e.g.* sample stability, molecular size, etc) and lack of technological/commercial interest. These materials, however, have recently found application in many different areas, *e.g.* organic solid state synthesis, pharmaceutical dosage forms, electrically conducting polymers, organic superconductors, thermotropic liquid crystals, optoelectronic devices.[19,20]

In the *pharmaceutical field*, solid-state chemistry has proved to be important on drug product development, manufacture and commercialization. Historically, a frequently cited example, with significant economic and health consequences, was the recall in 1998 of the medicine Ritonavir (Norvir®, Abott Laboratories) after the appearance of an unknown polymorph in commercial products. Other cases include the Ranitidine hydrochloride patent litigation, in which Glaxo SmithKline and other pharmaceutical companies went to trial due to non-agreement on of patents involving two polymorphic forms of the drug.[2]

In practical terms, solid-state characteristics will impact the active pharmaceutical ingredient (API) density, hardness, cleavage, solubility and dissolution, water uptake, optical and electrical properties, thermal behaviour, reactivity, physical and chemical stability.[5] As a result, these characteristics make APIs good candidates for crystal engineering strategies. *Crystal engineering* is an interdisciplinary subject involved with the design, synthesis, and development of new solid materials with targeted chemical/physical properties. It includes the study of marketed and known materials, their properties, and their structure-property and energy relationships.[21–27]

Although the recent past has shown an academic community divided in its opinion about the actual capabilities of crystal engineering,[28–30] several studies have been successful in designing the mechanical properties of molecular solids.[31,32] One interesting case involved the use of cocrystallization to improve the compressibility of crystalline paracetamol.[33] It was observed among the paracetamol polymorphs that the sheet-like layered arrangement of

molecules in Form 2 resulted in better compressibility compared to Form 1 (which contains molecules linked by hydrogen bonding to create corrugated sheets). The use of paracetamol Form 2, however, was limited due to its metastability and rapid conversion to polymorph 1. In this case, a screening of cocrystalline forms of paracetamol was performed and an appropriate planar arrangement was generated which was stable at room temperature and had good compressibility.[33]

Another interesting aspect of mechanical properties involves the ability to bend or break crystals, *i.e.* elastic versus plastic deformation respectively. Both characteristics play a role in the tableting and grinding properties of a material and have been attributed to the anisotropic nature (or not) of a crystal.[31,34] According to Reddy and coworkers,[35] a material is prone to undergo elastic deformation when it has anisotropy within its structure and interactions (Figure 3). The effect of the strength and the number of the intermolecular interactions on the Young's modulus has also been observed in the literature. For example, the comparison of the effect of temperature on anisotropy has shown an interesting correlation of structure and mechanical property in saccharin and L-alanine.[36]

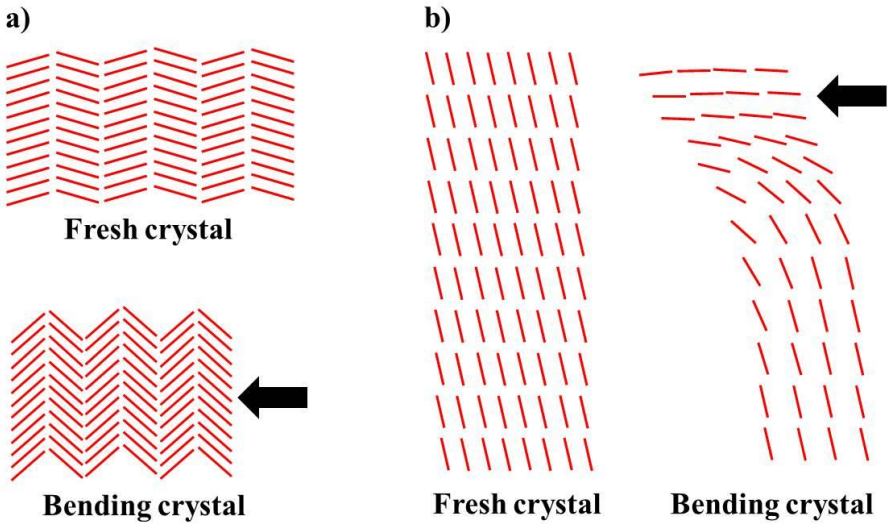

Figure 3 - Scheme illustrating the structural changes occurring during bending tests reported in the literature (adapted from *(a)* Ghosh *et al.*[34], and *(b)* Reddy *et al.*[35]). The anisotropy of interactions and the stacking have shown to affect the mechanical properties of organic materials.

Day and co-workers[37] have recently published one of the first studies that followed the principle of "crystal-to-structure-to-property". They reported a crystal structure prediction study of covalent organic frameworks and ranked the methane storage capacity and guest-molecule selectivity based on their computationally predicted structures. Subsequent experimental work on synthesised materials confirmed the predictions. While this is a milestone,

the literature is in general agreement that each organic solid represents a new system with new characteristics which still makes the engineering of solid materials a difficult task.

1.1.3. Molecular interactions and crystal forms

Molecules are not only special because of their empirical structure *per se*, but because of the nature of their interactions with the surrounding environment. In this regard, a crystal can be considered as one type of environment containing the drug molecule. The intermolecular interactions in the crystal follow a compromise between efficient packing and connectivity/topology.[26] The importance of this balance can be illustrated by the fact that molecular flexibility or size alone has shown no correlation with the ability of a compound to be polymorphic, while the synthon approach itself is not always robust in the design of supramolecular networks.[38]

In a crystal, the molecules are generally efficiently packed and show optimised density by using short range interactions, which can present a non-directional isotropic character or weak directionality. These weak interactions are exemplified by dispersion-repulsion forces, by weak hydrogen bonds and by such van der Waals interactions as π stacking. If analysed in isolation, each of these interactions will not provide a significant contribution to the overall lattice energy of the crystal. It is the sum of these interactions which gives rise to a stable crystal.[26,27]

While the debate about the effect and the collective contribution of weak hydrogen bonds to organic solids have been recently discussed, the concept of dispersion forces dominating the packing was introduced almost 50 years ago. Kitaigorodskii stated that shape and size were critical to the formation of a lattice network.[39] In his close-packing description, a stable low energy structure would be achieved by the molecules packing as efficiently as possible, with the largest amount of near-neighbour molecules and contacts. In fact, the scientific community has agreed that molecules tend to close-pack, although deviations are observed when the molecules are subjected to directional electrostatic interactions, such as strong hydrogen bonds.[1,40]

The hydrogen-bonds are characterized as attractive non-covalent interactions between a hydrogen atom and an electronegative atom. This interaction is possible because the hydrogen has a partial positive charge since it is covalently bonded to an electronegative atom. Consequently, the unshielded portion of the hydrogen is attracted to the partial negative charge of an atom's electron lone pair. A hydrogen bond is schematically represented as X-H···Y-Z, and is characterized by its length (D=X↔Y≈2.6-3.1Å, and d=H↔Y≈1.6-2.5Å) and by

frequently an approximately linear angle (Figure 4). The shortest the distance between the hydrogen and the electron lone pair, and the closest the geometry between the atoms is to linearity, the strongest the hydrogen bond.

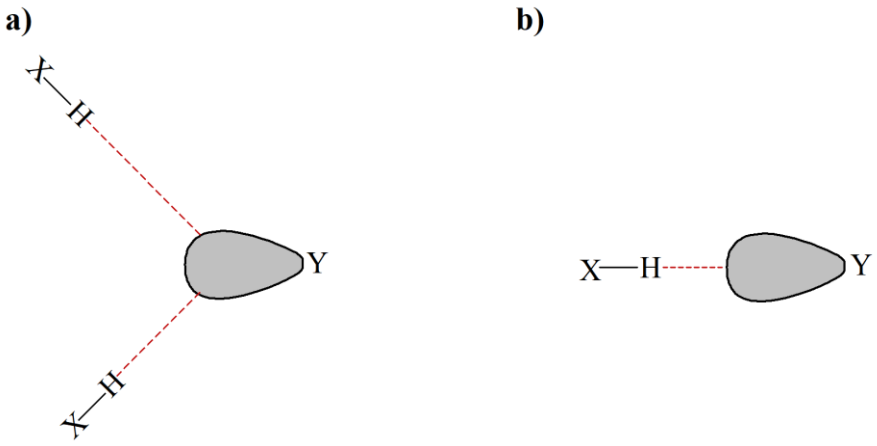

Figure 4 - Hydrogen bonds scheme (red dashed lines) illustrating the differences on distance, directionality and, consequently, strength of interactions: (a) and (b) represent the geometry of weak and strong interactions, respectively. The present notation will be used through the text.

One major consequence of the properties of the hydrogen bond in solid-state chemistry is that it operates at long distance and can form different types of networks. Another aspect is that hydrogen bonds may show an orienting effect on molecules prior to nucleation.[41] This factor affects the crystallization in solution, but may also influence the recrystallization from polyamorphous materials. In this case, the residual or persistent interactions in amorphous solids can be influenced by the environment and can result in unexpected and unwanted crystallization. Thi, Rademann & Emmerling[42] have used this hypothesis to explain the different polymorphs of paracetamol obtained from its crystallization in different solvents. The authors coupled *in situ* X-ray synchrotron analysis with Raman spectroscopy to characterise the crystallization profile, while PDF analyses provided structural information about two different amorphous intermediates. The intermediates were solvent-specific and showed pronounced resemblance to the respective polymorphs to which they were precursors.

Perhaps the difference in hydrogen bond orientation may be related to the difference of stability in a bulk crystal *versus* the stability of a nucleus in the ongoing crystallization. For example, a recent study by Belenguer *et al.*[43] showed that the lattice energy of two different polymorphs changed substantially with particle size. The authors showed a crossing point in the diagram of lattice energy with particle size, and predicted that the stability relationship between polymorphs was different when considering large or small crystals. These theoretical considerations were also seen experimentally. The authors attributed this effect to the balance

of surface area and bulk volume, but they did not explore the effect of hydrogen bond directionality on the properties of such small particles.

Surface effects and hydrogen bonding issues can be exemplified by the templating effect of specific interactions and conformations on the outcome of a crystallization process. A successful demonstration of this is the crystallization of carbamazepine Form V, which could only be crystallised on the surface of a crystal of 9,10-dihydrocarbamazepine Form II which acted as a template with the required surface hydrogen bond pattern.[44] This strategy allowed the crystallization of a polymorph previously predicted in theoretical calculations to be among the most stable forms of carbamazepine but not previously experimentally obtained.[45,46] These examples illustrate how intermolecular interactions can dictate the polymorphic form during crystallization, in solution and in the solid-state.

1.1.4. Nucleation, crystal growth and morphology

Crystallization from solution is the classical method of preparation of organic solids and allows many variables with regard to the way of achieving supersaturation, *e.g.* solvent evaporation, cooling or antisolvent addition. However, other techniques are also available, such as solid-solid transformations mediated by heat or vapour, gas-solid processes by sublimation and freeze drying, slurrying, melting, crystallization using pressure and supercritical fluids, laser-induced crystallization and grinding.[18,47–53] Regardless of the variety of these methodologies, the crystallization process follows the same steps of nucleation and growth. Classical nucleation theory requires that the nuclei form by random collisions of the dissolved constituents (Figure 5). The balance between the bulk and surface energy determine a critical size for the nuclei to become stable and grow. Some authors propose a theory for nucleation that adds the concept of a pre-nucleus cluster to the classical theory. They preserve the competition between surface and volume free energy and introduce an excess free energy for the primary particles (terms shown in Figure 5). This approach can be applied whether particle aggregation first nucleates an amorphous or metastable phase (positive free energy) or directly forms the crystalline phase (negative free energy).[54–59,54,55,57,58]

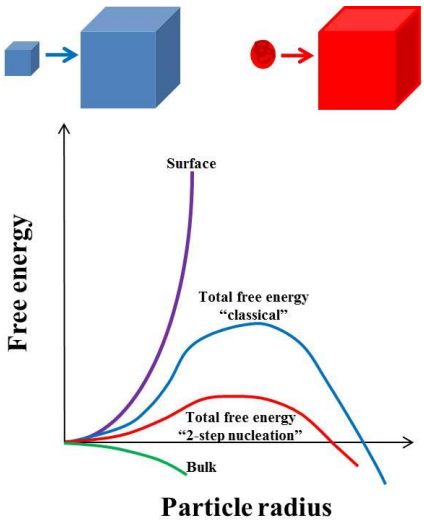

Figure 5 - Gibbs free energy *versus* particle radius plots for the classical nucleation theory (blue line A) and for the proposed 2-step nucleation theory which accounts for the existence of amorphous nuclei or primary clusters (red line B) (adapted from Baumgartner et al, 2013; De Yoreo, 2013; Gebauer et al, 2014).

These small particles, or nuclei, grow and form the crystal as an entity morphologically defined by its edges, surfaces and angles. The crystal habit is affected by the balance between the internal structure symmetry (thermodynamics) and the relative growth rates of the crystalline faces (kinetics).[11,60,61]

The morphology has been predicted by a variety of models with the BFDH (Bravais-Friedel-Donnay-Harker) being the simplest one. The BFDH model takes into account only the geometrical parameters of space group and the unit cell dimensions. As a result, this approach ignores the chemical particularities involved, such as the strength of interactions between molecules in the crystal and between crystal and solvent molecules during crystallization. Another modelling approach is the energy based Hartman-Perdok theory, which adds the attachment energy of a crystal surface to the bulk in the morphology calculations.[11,60,61] This energy approach was modified by Docherty *et al.* and Roberts *et al.* as a modified attachment energy model which accounts for solvent effects as it introduces a surface solvation energy into the model.[62–65] Vatvani[60] developed another method based on a 2D nucleation model of crystal growth. The method did not account for solvent effects but presents a better agreement to experimental data in comparison to the other models. Alternatively, Ramkrishna *et al.* developed a morphology population based model that determines the morphology domains of a crystalline form. This method groups families of faces with similar molecular arrangement and combines them to lattice parameters illustrated by the vector of perpendicular distance of faces to the centre of the crystal.[66,67]

Experimentally, different studies have reported variations in crystal habit as a function of the intermolecular interactions within the crystal and with the surrounding growth

medium. The crystallization of needles with high aspect ratios (a:b:c of 1:1:≥100) is of interest as they present poor mechanical properties and introduce challenges to manufacturing processes, *e.g.* filtration.[68] The case of urea and biuret is a classic example of surface "docking" promoting crystal growth of preferred faces.[11,61,69,70] Additionally, Shailendra et al (2013) have shown the effect of small quantities of a polymeric impurity on the morphology of a fenofibrate salt. The authors further added temperature and supersaturation effects to their studies as the surface-specific growth rate can also be modified by these variables. They showed strong evidence in support of the fact that the changes in morphology resulting from different supersaturation levels was in fact due to a change in the mechanism of crystal growth (from spiral growth to 2D nucleation).[71] From another perspective, Camacho et al (2016) evaluated the kinetics of growth of methyl stearate in different solvents. The authors attributed the differences observed in crystal morphology to the growth rates of the crystal faces in the solvents and could fit the influence of supersaturation to different kinetic models of growth mechanism.[72]

Interestingly, the crystallization environment might affect not only the crystal habit, but also the dominant or preferred face of the crystal, named *tracht* in German (Figure 6). *Tracht* is applied to describe the variation of forms due to the degree of development of faces within the same category of *habitus*.[61] In this case, although the volume of crystals presenting different *tracht* is the same, the area of the respective surfaces is different. The contribution of different faces in a crystal might also change during growth leading to the differences existing in equilibrium and growth morphologies. Once again, it is observed that the balance between thermodynamics and kinetics are crucial in solid state chemistry.

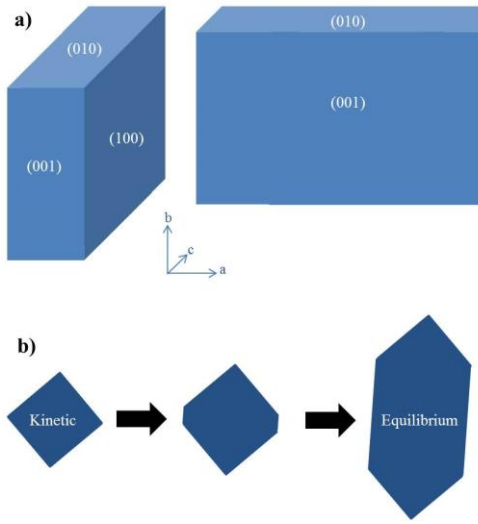

Figure 6 - Morphology variations due to kinetic effects. *a)* displays two plate crystals with distinct dominant faces as an example of same crystal habit, but different *tracht*. b) shows the evolution of a hypothetical crystal during growth. The first developing faces exhibit fast growth rate and have their significance diminished over time. Consequently, conditions of crystal growth far from equilibrium (i.e. fast cooling) tend to generate kinetic morphologies. The slower growth faces dominate the equilibrium morphology. Adapted from Davey & Garside[11] and Sunagawa[61].

1.1.5. Thermodynamic and kinetics

Energy is the driving force behind all processes in Nature, including the ones described above. The formation of chemical bonds, the existence of chemical structures, how they interact in solution, how and when they crystallise, the morphology of the crystals adopted and how they transform into a different crystal form - all these events can be described by changes tending to minimise the total energy (Gibbs free energy, G) of a system (Equation 1). As a consequence, a process which releases energy will happen spontaneously ($\Delta G<0$), while a process which absorbs energy ($\Delta G>0$) is not favourable and will not happen unless an external driving force is applied (i.e. changes in temperature and pressure). The relationship obtained from the energy of initial and final states of a process is characterised by thermodynamics.[73]

(Equation 1) $G = H - TS$

where G corresponds to the Gibbs free energy, H to the enthalpy, T to the absolute temperature and S to entropy.

Part of the driving force towards thermodynamic equilibrium comes from a combination of entropy and temperature, while another part comes from enthalpy. The entropy contribution derives from the fact that molecules are constantly moving, changing configuration, twisting and vibrating. In other words, entropy accounts for the disorder in a system and is positively related to temperature. On the other hand, enthalpy corresponds to the internal energy or heat, which could be correlated to the lattice energy of a solid.[73]

An important situation occurs when the Gibbs free energy difference is equivalent to zero. In solid-state chemistry this thermodynamic point of equilibrium between different states represents a point in the phase diagram in which both states are in equilibrium and can coexist. This phenomenon is generally known as a transition point. From this transition point, the variation of a given parameter will qualitatively change the dynamics of the system and energetically drive the outcome of a process.[74] Figure 7 illustrates two types of thermodynamic transitions. They are exemplified by the solvent activities in solubility diagrams of solvates, and by the temperature transition points (T_t) between polymorphs.

Considering a pair of polymorphs, if the transition occurs above the melting point, the polymorphic relationship is said to be monotropic and both melting events are experimentally observable. On the other hand, if the T_t takes place before the melting, the polymorphs are enantiotropically related and the transition is (energetically if not kinetically) reversible in the solid state. This means that there will be one phase stable at low temperatures (below T_t) and another phase stable at high temperatures (above T_t). The observed melting event

then corresponds to the melting of the high temperature form, which is metastable at lower temperature.[2,5,16]

The lifetime and the crystallization of a metastable form is determined by its thermodynamic driving force, G, and more specifically the driving force difference between the polymorph pair. This means that lattice energy and molecular mobility play a role, but also the interface free energy and kinetics may contribute to the course of a transformation.

Kinetics accounts for the relationship among all the steps and intermediates in the reaction coordinate taking into consideration the transition activation energies (Figure 8). Thus, a solid-state process is kinetically affected by surface chemistry and roughness, particle morphology, crystal size, presence of seeds (and other templating surfaces), the crystallization environment and the experimental conditions.

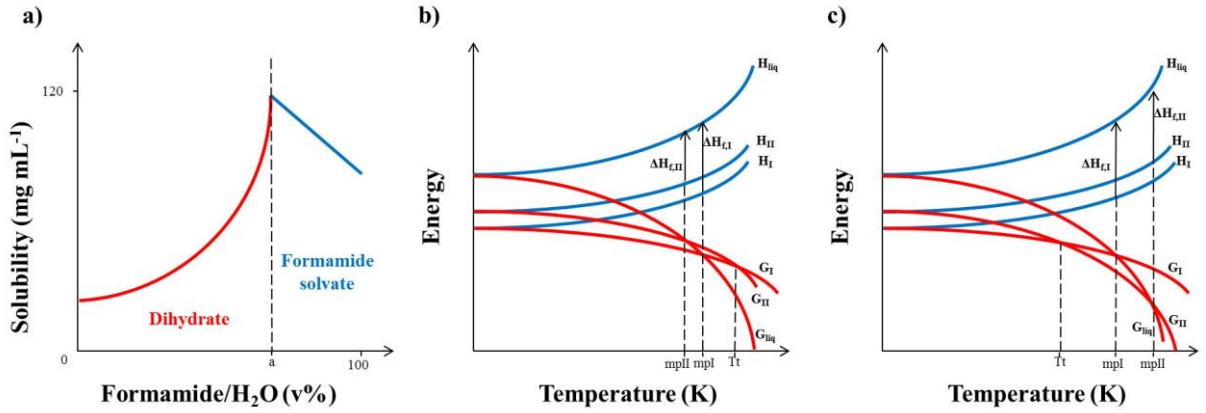

Figure 7 – Graphs illustrating different phase transition points. Graph *a* shows the crossing point in the solubility curves of two solvates, which is usually named as solvent activity (adapted from Byrn, Pfeiffer & Stowel[5]). Graph *b* shows the energy diagram of two hypothetical monotropic polymorphs, and graph *c* shows an energy diagram of two hypothetical enantiotropic polymorphs (adapted from Bernstein[2]).

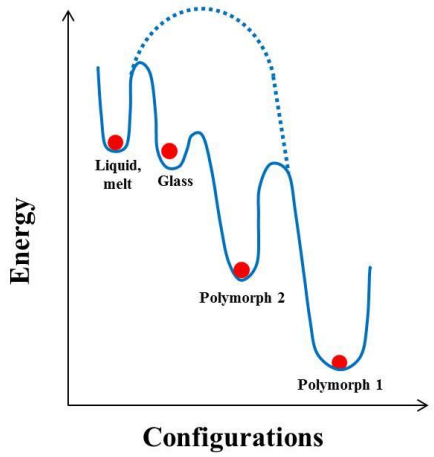

Figure 8 – Graph comparing the free energies of different coordinates in a hypothetical crystallization, from the liquid phase to the most stable solid form. The graph also shows the energetic barriers to the change of configuration and illustrates the basics of Ostwald's rule of stages. It is worth mentioning that, amorphous materials do not strictly need to be higher in energy than the crystalline forms. This scenario has been illustrated in the MOFs literature.[75]

Kinetics is sometimes misunderstood and frequently blamed when experiments misbehave. Kinetic phenomena have been recognised, however, for a long time. In the 19th century, for example, Ostwald stated a rule of stages acknowledging that a system preferably crystallises into the nearest metastable form in the energy diagram. This pathway of crystallization is favourable as less molecular organization (less energy release) is required to reach the nearest potential well. The practical implication of this is the often observed crystallization of metastable forms in the first instants of a process.[2,76]

Again, one might conclude that balance and compromise among different characteristics and forces are key aspects in what concerns solid-state materials and their interactions with the environment. Yet, what is the balance in the relationship of thermodynamics and kinetics?

1.1.6. Analytical techniques for bulk and surface characterization of organic solids

The previous sections have addressed the diversity of phenomena which may affect the bulk and surface properties of a material. The factors suggest that each system of study is a unique experience. The conventional strategy adopted to develop an understanding of such systems combines a wide range of characterization techniques. As a result, extensive and varied data have the potential to make evident the properties of a material and process limitations and challenges that are experienced during manufacture.

X-ray techniques are crucial, with single crystal X-ray diffraction providing detailed information about identity, crystal packing, molecular conformation, bond lengths and intermolecular interactions. X-ray charge density measurement is a powerful method to study the chemical bonding as a function of charge distribution in space. Powder X-ray diffraction (PXRD), in turn, is useful for the identification of different polycrystalline samples and is comparatively easy to use as a screening technique. However, isostructural materials can be difficult to differentiate and may be distinguished by using other techniques.[15,77]

Solid-state nuclear magnetic resonance provides structural information, mainly about molecular conformation but also the number of species in the asymmetric unit. Vibrational spectroscopies, *i.e.* Raman and infrared (IR), can be also used to characterize materials with different chemical environments, whether they are salts, cocrystals, solvates and/or amorphous .[78]

Other important tools are the thermoanalytical techniques. The presence of endothermic and exothermic events and baseline shifts in the heat flow curve obtained by differential scanning calorimetry (DSC) provides evidence of melting, desolvation, solid-state

transitions, crystallization and even degradation. Thermogravimetric analysis (TGA) complements this information providing a weight loss profile upon heating of the sample. These are complementary techniques useful for a deeper understanding of the material properties when used with other methods. For example, a heating source can be coupled with an X-ray diffractometer, spectrometer or microscopes (hot stage microscope).[5,16,79]

Many types of microscopes are available. Regarding optical microscopy (OM), the technique shows particularly the external morphology of the particles, shape, size and state of agglomeration. While the optical microscope is limited in magnification range, polarizing optics are useful tools to analyse the quality and integrity of a crystal. On the other hand, the scanning electron microscope (SEM) provides images with higher magnification and shows the topography of the sample surface based on the scanning of an electron beam. Depending on the available technology and the resolution of the analysis, crystalline domains can be identified by SEM, especially in instruments coupled to an electron backscattering diffraction device.[5,16,79] Also based on an electron beam technology, but now transmitted through thin samples, is transmission electron microscopy (TEM). This represents an alternative to the study of systems providing, under appropriate conditions, atomic level resolution. The combination of image, diffraction and spectroscopic data from the same sample has the potential for analyzing the unit cell as well as crystallographic defects.

Unfortunately, organic samples do not tolerate extreme conditions of analysis. For example, they usually sublime or collapse (if for example a hydrate) under high vacuum and, in these cases, are not suitable for SEM and TEM experiments. A few strategies may be used to overcome these limitations. In SEM, because organic materials are also poor electron conductors, coating the sample (with gold or graphite) helps improving the quality of the images. Additionally, the coating may protect the sample from sublimation, although the process of coating itself is carried out in a vacuum environment. The strategy used in TEM of organic materials is the same methodology which awarded the 2017 chemistry Nobel Prize to Dubochet, Frank & Henderson ("*for developing cryo-electron microscopy for the high-resolution structure determination of biomolecules in solution*"). The use of cryo-cooled samples increases their stability in regard to the ultra-high vacuum and to beam damage, although the sample can undergo phase transition during the process of cooling.[80,81]

Additional microscopy techniques are used to overcome the limitations of characterizing organic samples, such as confocal and scanning probe microscopy. [80–83] SPM images are obtained by scanning across a surface with a sharp probe that generates an image as a response to tip–sample interactions. Scanning tunneling microscopy monitors the surface applying an electric current from the tip through the sample, which is usually not successfully

possible for organic crystals. In turn, atomic force microscope (AFM) provides an image by using the mechanical displacement of the tip because of its interactions with the surface. The usual AFM mode of operation used in organic materials is tapping (intermittent) mode as it causes less damage to fragile surfaces. AFM is useful for both amorphous and crystalline materials, and can provide information on a wide range of physicochemical phenomena, such as crystal growth and nucleation, structure-property relationships, surface reactivity, adhesion forces on processed samples, local dissolution behavior, solid-state transitions, molecular movements, mechanical, thermal and electronic properties analysis.[83–86]

1.2 The manufacturing of pharmaceutical materials

The challenge of characterizing organic solids and understanding the balance of thermodynamics and kinetics, is illustrated by the challenges involved in the manufacture of pharmaceutical materials. A key aspect in this case appears to be the scale-up from laboratory sized preparations, to pilot and production-scale batches. During this process, variables such as the equipment used, the surface of the containers, the manner of energy dissipation, the rate and homogeneity of heat diffusion, the homogeneity of the materials, particle-particle attrition, mechanical stress and storage will be affected by the size of the batch being made. As a result, industrial processes may give rise, at various stages, to stress-induced transformations and product modification, especially in the case of labile multicomponent organic solids such as solvates. In this section, drying is introduced as a common operation in pharmaceutical manufacturing and a source of stress-induced transformations when applied to the processing of solvates.

1.2.1. The drying process

The drying process consists of removing the excess liquid associated with a specific material, such as the wet cake of an API obtained from filtration or granules prepared prior to tablet compaction. The importance of removing the residual solvents is based on the prevention of chemical instability, solid transformations, particle coarsening and surface roughness, which may affect particle flow, surface energy and compaction. Excessive drying of a material, however, may also be disadvantageous – for example increasing the particle static charge.[87,88]

It is critical, therefore, to know the intrinsic properties of the material and to identify the residual liquid that will be removed and how it is bound to the solid. There are essentially two types of liquid states subjected to drying in a solid: unbound and bound liquids. The

unbound liquid is adsorbed on the outer surface of the particles and is the first liquid to be removed.[87,89] The bound liquid, in turn, consists of structural or capillary solvent entrapped within particles, defects and/or cavities.[16,87,89] Both types show a different loss profile upon drying and are affected by thermodynamic and kinetic characteristics. While the release of capillary liquid is mainly influenced by kinetics and is removed through less robust and reproducible reactions, the release of periodic lattice liquid accounts for a combination of factors further discussed in the next section.

1.2.2. Solvates and stress-induced transformations

1.2.2.1. Background

Solvates are studied and screened by pharmaceutical companies as a result of their characteristics and applications and can be manufactured as excipients or as the final API in a product. The selection of a precursor solvent, however, is not trivial. In terms of safety, it is necessary that the components of the final product meet the appropriate Generally Recognised As Safe (GRAS) classification, from which water is the most acceptable. In fact, the Pharmacopoeias show a great majority of monographs of APIs and excipients commercialized as hydrates, while only a few are solvates (for example cefatrizin propylenglycol, doxyclin hemiethanolate hemihydrate and warfarin 2-propanol are reported in the European Pharmacopoeia). It has also been demonstrated that the greater number of pharmacopeical monographs describe hydrates of salts. This predominance is attributed to the intrinsically strong electrostatic interactions of ions with water and other dipolar solvates.[89,90]

The likelihood of hydrate formation as a result of intermolecular interactions has been the aim of many studies. Desiraju et al.[91] have suggested that water molecules balance the hydrogen bond donor-acceptor capabilities of an organic molecule which has, for example, more donor than acceptor groups. This idea was corroborated by Jeffrey & Maluszinska,[92] whose studies have showed that water is a stronger hydrogen bond acceptor than a donor. More recently it has been suggested that this characteristic is only true for linear hydrogen bonds. Gillon et al.[93] have showed that bifurcated hydrogen bonds with the water oxygen as the acceptor provides equivalent strength to the counter-part of the donor water molecule. In addition, Steiner & Saenger[94] have showed that C-H···O hydrogen bonds are frequently used to stabilise the arrangement of water bonds. Alternatively, Infantes et al.[95] have analysed a set of structures reported in the CSD and found no correlation of specific number of donors and acceptors with hydrate formation. They found, however, a positive correlation between hydrate

formation with an increase in the total polar surface of the molecule and the sum of the average donor and acceptor counts for functional groups. One recent study has statistically analysed the CSD and developed a method to predict the hydrate and solvate formation only based on the number of polar H atoms, the molecular size and the branching.[96] Although the proposed method does not account for hydrogen bond strength and polar groups which are hindered and not accessible, the authors have successfully predicted 80% of the hydrates/solvates reported in the dataset.

1.2.2.2. Classification and properties

The most common classification of solvates is based on the arrangement of the solvent molecules in the host lattice.[16] The solvent molecules may be isolated and form pocket sites and are then classified as zero-dimensional assemblies. On the other hand, solvent arrangements in channels usually form one-dimensional superstructures which may be combined along different crystal axes leading to two-dimensional interpenetrated channels. Another type of 2D framework involves the arrangement of solvent molecules in layers, commonly seen in salts and ceramics. The literature usually classifies in a separated group the metal-ion coordinated solvates.

Considering the host molecules as rigid molecular building blocks strongly connected in very specific orientations, it is clear that different solvent molecules can assemble in similar crystal structures (Figure 9). Consequently, isostructurality is considered more common in multicomponent than unicomponent materials. This characteristic has been used as a mean of assessing the stability of a lattice on the basis of persistence of host-host interactions in solvates, or of testing the equivalence of hydrogen/halogen bonds and other functional groups in cocrystals.[97–101]

According to the IUCr Dictionary of Crystallography, "*two crystals are said to be isostructural if they have the same structure, but not necessarily the same cell dimensions nor the same chemical composition, and with a 'comparable' variability in the atomic coordinates to that of the cell dimensions and chemical composition*.".[102] In this case, it is understandable that the properties of isostructural multicomponent materials are dependent on the properties and arrangements of the guest molecule. Galcera & Molins[103] have studied the solubility of isostructural lamotriguine salts of dicarboxylic acids and saccharin. The authors showed that the water solubility of these salts was directly related to the solubility of the precursor acid. Csoregh and coworkers[104] have showed significant differences in the IR spectra of isostructural inclusion compounds which presented varied host guest ratios and the presence of bound water

molecules. This difference of the interaction between host and guest, regardless of the host matrix, may affect the thermal behaviour of the material. Nassimbeni, Su & Weber[105] have studied isostructural compounds of two guests in different structures: pyridine:morpholine, pyridine:benzene and pyridine:morpholine:benzene. The authors attributed the higher temperature for pyridine release observed in the pyridine:morpholine complex to the high boiling point of its precursors. On the other hand, both complexes containing benzene showed a pyridine release at lower temperature due to the lower temperature of benzene release and to the formation of fine particles with higher surface area and increased reactivity.

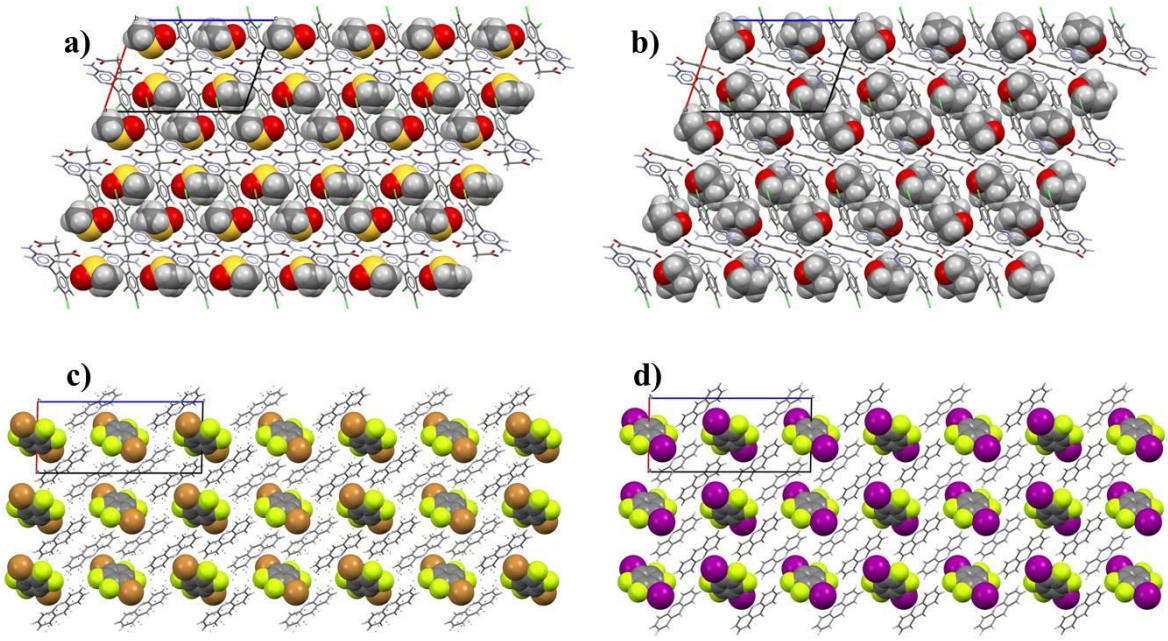

Figure 9 – Examples of isostructural materials. *a)* is lamotriguine succinate DMSO solvate and *b)* is lamotriguine acetylenedicarboxylate THF solvate from Galcera et al.;[98] *c)* is (acridine)$_2$-tetrafluroiodobenzene cocrystal and *d)* is (acridine)$_2$-tetrabromoiodobenzene cocrystal from Cincic, Frisic & Jones[100].

1.2.2.3. Stress-induced transformations

Stress-induced transformations in organic solids using transmission electron microscopy was first observed by Jones, Thomas & Williams[106] in a study of 1,8-dichloro-10-methylanthracene who observed crystallites with faulted areas resulting from the stress of rapidly cooling the specimen. The diffraction patterns of the resulting domains showed an ordered and coherent lattice rearrangement, which was reversible with an increase of temperature and relaxation of the stress.

Prior to the 1,8-dichloro-10-methylanthracene work, the accepted idea was that no structure correlation necessarily existed between the substrate crystal and the product crystal.[39,107,108] This hypothesis is still alive in the scientific community and reshaped into the statement that phase transitions are not homogeneous and only occur via 3D nucleation with

further growth.[109] Following this basic rule, Mnyukh has suggested that there are two activation energies involved in phase transitions: one for nucleation and one for the molecular migration at the interfaces. The author acknowledges the existence of an orientation effect (epitaxy), but suggests this is the result of oriented nucleation and not a direct relationship. For Mnyukh, only free energy determines which polymorph is stable under a particular condition, which is true if thermodynamics alone is considered.

> *"At this point it should be emphasized that this "similarity" of structures is in no way equivalent to a certain cooperative course of a polymorphic change. Mnyukh has convincingly demonstrated that the growth of one crystal from another crystal follows the same laws as does the growth of a crystal from melt, regardless of whether the polymorphic modifications are similar.*
> *No special significance should be assigned to the similarity of structures. It is evident that the free energies of two structures at a certain p,T may be equal both in "similar" and "unlike" structures." – A.I. Kitaigorodskii, In "Molecular Crystals and Molecules", 74p. (1973)*

The current most accepted approach for the analysis of solid transformations, including desolvation, takes into account the structure of the parent and daughter phases and the analysis of varied mechanistic aspects. In practical terms, the outcome of a desolvation process may vary from an amorphous product to a crystalline product that may or may not resemble the solvated structures.[5] The interest in understanding and trying to stablish a structural correlation between reactants and products is, however, attractive because desolvation can provide a final product with the improved morphology, enantiomer identity, particle size distribution and polymorphic form.[110–113]

Petit & Coquerel[114] have proposed a unified model for the dehydration of molecular crystals which may be expanded to the overall class of solvates (Figure 10). This model is based on the existence of planes or channels in the structure, whether these are crystallographic features present in the parent phase or develop during the first stages of reaction. In cases where this requirement is met and the crystal lattice energy from the host molecules is greater than the energy contribution from the bonds with the solvent, the processes are classified as cooperative. A cooperative release mechanism can lead to desolvated materials with no structural reorganization or to the cooperative rearrangement of the molecules. The later process shows a structural filiation relationship and only occurs if the domains formed upon desolvation are above a critical size and there is sufficient long range order. In cases where the critical size and

the order are not sufficient, the structures tend to collapse into an amorphous phase or crystallize into a new phase via nucleation and growth. Both possibilities can also happen if the reaction follows a destructive mechanism in which no planes or channels are present in the structure and the energy from the interactions with solvent molecules overcome the lattice energy contribution from the host.

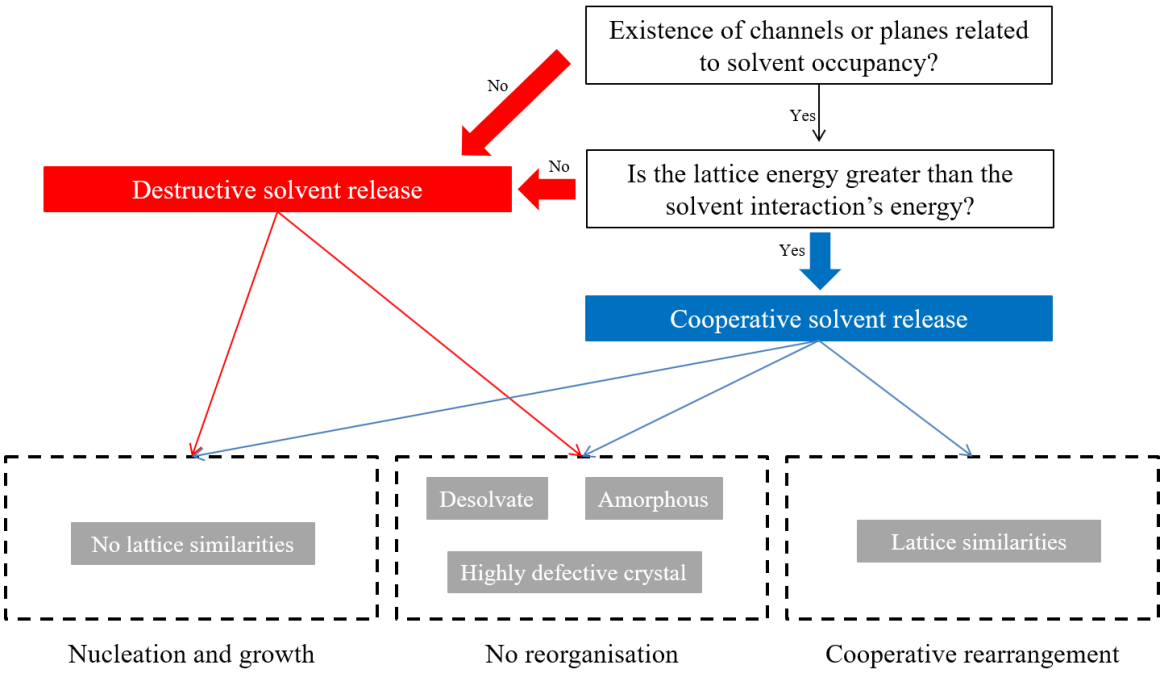

Figure 10 - Scheme summarizing the unified model of desolvation proposed by Petit & Coquerel.[114]

Kaupp has also considered the modulation of reactivity and the polymorphic outcome in solid reactions as being highly influenced by the cleavage planes in the structure.[115] Cleavage planes allow molecules to slip and migrate, which may affect the release of solvent and the recrystallization. According to Kaupp, the ability of a cleavage plane to move are influenced by the tilt angle of the molecular axis with respect to the plane, the interaction distances of molecules on the plane, and the interlocking characteristics of the molecules between layers/cleavage planes.

Galwey has also discussed the mechanistic aspects of desolvation reactions, which the author classified as crystolisis.[116] He suggested that diffusion takes place in structures presenting solvent molecules in channels and layers, in which case the gradient of concentration along the channel is the driving force towards desolvation. The energy released during the diffusion of one molecule can also be transferred directly to its neighbour in a chain reaction. This chain-type reaction may be catalysed by charge effects and the presence of strain and defects. The most common defects in these reactions are cracks and newly created polycrystalline domains, which expose clean surfaces for the reaction to propagate.

In the case of defects, rougher surfaces containing a lot of steps, kinks, vacancies and domains, present an entropic contribution that is significant for the increase of atom transport along the surface of the material.[10,12] Bulk diffusion through a perfect single crystal is dominated by point defects, while diffusion along two- and three-dimensional imperfections is seen for dislocations and channel-like defects. When a solid state reaction takes place at defect sites of crystal structures or surfaces, the increased mobility and displacement of molecules can lead either to an increase of the reaction rate but also to different mechanisms and products.[10,12,117,118]

Byrn, Pfeiffer & Stowel[5] have suggested that the desolvation outcome of a channelled structure is likely to be mainly influenced by the packing surrounding the channels. The authors also highlight other characteristics which may affect the reaction in a system-specific way: the channel size, the number of channels per unit area, the density of host molecules, the number and strength of hydrogen bonds to the solvent molecule, the coordination in the case of salts, the direction of the solvent chain relative to weak planes in the structure, the position of the channel related to the host molecule and the tortuosity of the channel. All these characteristics seem to be correlated to the strain generation from molecular movements and to an increase in local pressure. In this case, chemical environments subjected to desolvation may be compared to the concept of "reaction cavities". These cavities provide specific environments in which the bonds within molecules contribute to the stress around the leaving site, while lattice flexibility avoids the disintegration of the crystal as a result of stress. One example of the effect of strain on desolvation is given by Perrier & Byrn[119]. They predicted and confirmed that the dehydration threshold for different compounds was related to channel area and the hydrogen bond strength.

Mechanistic explanations fill the literature with descriptions of desolvation reactions and successful structure correlations between parent and daughter phases. The contrary situation is, however, also frequent. An interesting illustration is the desolvation of furosemide solvates. Minkov et al.[112] investigated different systems in which none of the results could be explained by crystal structure analysis. The authors showed that the desolvation of the THF solvate always resulted in furosemide Form III, regardless of the particle size. In turn, desolvation of the dioxane, DMF and DMSO solvates consistently lead to Form III in the case of large particles, and Form I in the case of powders.

This example illustrates the influence of kinetic variables during desolvation. It is expected, therefore, that the rate of desolvation, particle size, surface contacts and other seeds may change the resulting product. At this stage, one may conclude that the current state-of-art in the area does not translate into "crystal-to-structure-to-property", although it does provide

plenty of food for thought as "*the constraint imposed upon organic molecules as a result of being placed in the perfect and repeated environment of the crystalline phase"* keeps raising *"many interesting questions for the organic solid-state chemist*".[120]

1.3 Carbamazepine crystal forms: a model of examination of stress-induced transformations

Carbamazepine (CBZ), 5H-dibenzo[b,f]azepine-5-carboxamide (Tegretol®, [298-46-4], $C_{15}H_{12}N_2O$, 236.3g.mol^{-1}) (Figure 11), was first reported in 1960 in US patent 2,948,718 as one of a series of N-substituted azepines.[121] It was initially used as an anticonvulsant, but later clinical trials demonstrated its effectiveness in the treatment of neuralgia.[122] The mechanism(s) of action of currently marketed anticonvulsant drugs, including CBZ, is not fully understood and might involve several molecular targets. It is, however, believed that the modulation of voltage-dependent sodium channels plays a major role in their pharmacological activity.[123,124]

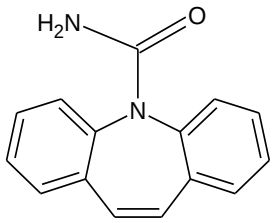

Figure 11 - Molecular structure of carbamazepine

The robustness of CBZ treatment over the years is noteworthy. The British Medical Journal reported in 1964 an initial daily dose of 200 mg, which is the same preferred dosage described in Remington's classic textbook more than 50 years later. The dosage and, more specifically, the maintenance of sustained blood levels, are crucial in the treatment of epilepsy.[122,124] Historically, in 1988 one CBZ marketed product was the subject of a major recall after patients reported relapse and unexpected seizures.[125,126] It is believed that the failure in the dissolution test observed for such batches was related to the hydration of CBZ in the tablets. Further analyses showed that the bioequivalence tests performed on the recalled generic product exhibited large differences in bioavailability and dissolution rates. While additional studies suggested that storage and humidity may have affected the dissolution of CBZ tablets, the manufacturer attributed the failure to differences in the particle size of the raw materials, possibly related to a change in supplier.[127,128]

CBZ has been extensively studied in the field of solid-state chemistry. This API presents a large number of crystalline forms reported in the CSD: five polymorphs, 18 solvates,

38 cocrystals (4 of which are solvated) and 6 salts (3 of which are solvated). The literature shows the use of CBZ as a model material for numerous types of studies, *i.e.* polymorphic transformations, amorphous characterization, the effect of processing and formulation components on the product performance, dissolution and biopharmaceutical studies. Although numerous, the studies are not consistent and sometimes contradict each other (Appendix 1).[44,45,136–145,46,146–155,129,156–165,130,166–175,131–135] The fact that there are disagreements in the literature is not in itself surprising. After all, these studies have been performed over the last 40 years and used a wide range of analytical approaches (even the nomenclature of CBZ polymorphs has varied).

1.3.1 The polymorphs of carbamazepine

According to previous studies, the energy landscape was used to order the stability of the CBZ polymorphs, from the more stable to the least stable one, as being: III=IV>I>II. A later obtained polymorph (Form V), was also located among the lowest energy predicted structures as described in Figure 12.[45,46]

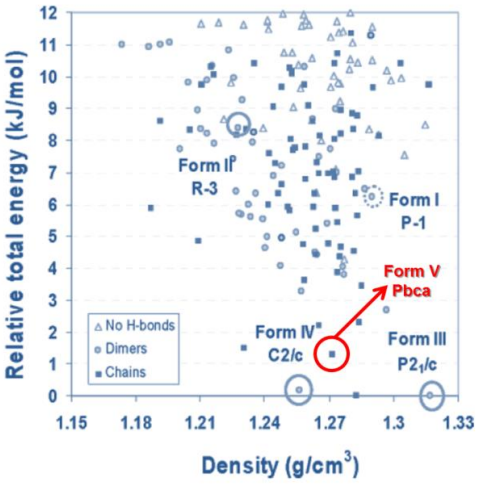

Figure 12 - CBZ energy landscape from crystal structure prediction classified by hydrogen-bonding motifs (adapted from Cruz-Cabeza *et al.*[45,46]).

The literature shows that CBZ Form I is the most stable form at high temperature, while CBZ Form III is the most stable form at room temperature.[137,174] The polymorphs are enantiotropically related, which means that the transition temperature between both occurs below melting. Different studies, however, have reported different T_t. For instance, stability studies involving solvent mediated experiments have shown a CBZ(III)→CBZ(I) transition temperature of 73 ºC which is in good agreement with the 71 ºC value previously calculated from thermal data (heat of fusion and melting temperature).[137,174] Krahn & Mielck,[136] in turn,

have shown that Form I converts to Form III when stored at 72 ºC for 200 days. They suggested that the transition occurs above 100 ºC, a conclusion also supported by Griesser *et al.*,[173] who report 120 ºC and 115±5 ºC as values of T_t calculated in separate studies. These values were determined from thermal data and published only as posters and internal reports, thereby limiting a comparison of the experimental details. It is noteworthy, that the studies conducted by Krahn & Mielck[136] were set out to evaluate the physical and chemical stability of CBZ mixtures (40%, w/w) with silicon dioxide. The mixtures were prepared using glass beads and the samples were stored under different humidity conditions (41, 60 and 75% RH). In other words, the CBZ(I)→CBZ(III) conversion was not observed in pure samples only containing the API. The experiments, in turn, involved quite complex systems, which also combined with degradants (iminostilbene, 9-methylacridine, acridine-9-carboxylic acid, acridine and acridone) as the reaction developed.

The DSC curves of CBZ polymorphs I and III reported in the literature have shown that Form I melts at approximately 190 ºC, while Form III melts at about 176 ºC.[137,174] The melting of polymorph III, however, is not always detectable because of the CBZ(III)→CBZ(I) solid-state conversion which is observed around 150 ºC.[137,139,145,153]

Although particle size, heating rate and sublimation of CBZ may affect the thermal profiles reported in the literature as well as the enantiotropic conversion between the polymorphs, it is also possible that the templating effect of surfaces on the crystallization of CBZ plays a role. Heng and his group have studied the selective surface-induced nucleation of CBZ on chemically modified glass vials and on foreign surfaces (which resembles the well-known case of CBZ Form V being only obtained from sublimation over 10,11-dihydrocarbamazepine crystal surfaces).[167,168,172] O'Mahony and coworkers have also suggest that the surfaces of CBZ crystals could act as a template for other forms. They have shown that CBZ molecules on the surface of polymorph I have a similar molecular arrangement as found in polymorph III. Due to this characteristic, the authors state that polymorph I can act as a template for Form III in solvent mediated reactions.[165,166]

Regarding the other polymorphs of CBZ, the metastable polymorph II is reportedly formed with the aid of inclusion solvents, such as toluene, tridecane and tetrahydrofuran. The solvent molecules, in this case, are located in the cavities formed by CBZ molecules and are said to help stabilizing the crystal form. Additionally, it is also suggested that highly concentrated solutions and high cooling rates - in other words conditions of crystallization far from equilibrium - are favourable for the crystallization of polymorph II.[45,157,158,176,177] CBZ Form IV, in turn, presents a similar lattice energy as Form III and was first crystallized from methanolic solutions containing hydroxypropylcellulose (Mw=60,000).[148]

1.3.2 The dihydrate of carbamazepine and its dehydration studies in the literature

Perhaps the most generally accepted assumption in the literature is that CBZ dihydrate (CBZ:2H_2O) will crystallize in water. The morphology of the CBZ crystals has shown a larger effect on the kinetics of hydration than the polymorphic form of the parent crystal. The limiting step appears to be the nucleation of the dihydrate on the surface of the CBZ polymorph. In contrast, under solution mediated experiments, some recent studies in the area of process engineering have shown that the rate of crystallization of the dihydrate is limited by the dissolution of the corresponding CBZ polymorph.[160,164]

With respect to the various crystallization conditions which are described in the literature, the dihydrate is most frequently obtained from mixtures of ethanol and water. A careful analysis reveals that different types of CBZ:2H_2O particles were crystallised depending on the ethanol:water solution composition (Figure 13), although the studies in the literature have not investigated this characteristic.[150,163,175,178] Additionaly, Khoo *et al.*[163] suggested that the (100) face might develop cracks along the main axis of the needle-particles at early stages of dehydration, and correlated these cracks with the (020) cleavage plane. On the other hand, Kachrimanis & Griesser[162] showed intersecting cracks on the (020) face and attributed these to lattice shrinkage after dehydration of twinned crystals. None of these cracks were observed in the SEM images of crystals obtained from a systematic study involving the use of additives to control the morphology of CBZ:2H_2O.[179] In this study, Rodriguez-Hornedo & Murphy have observed that sodium taurocholate changed the morphology of the dihydrate crystals from acicular to lath and prismatic, depending on the surfactant concentration.

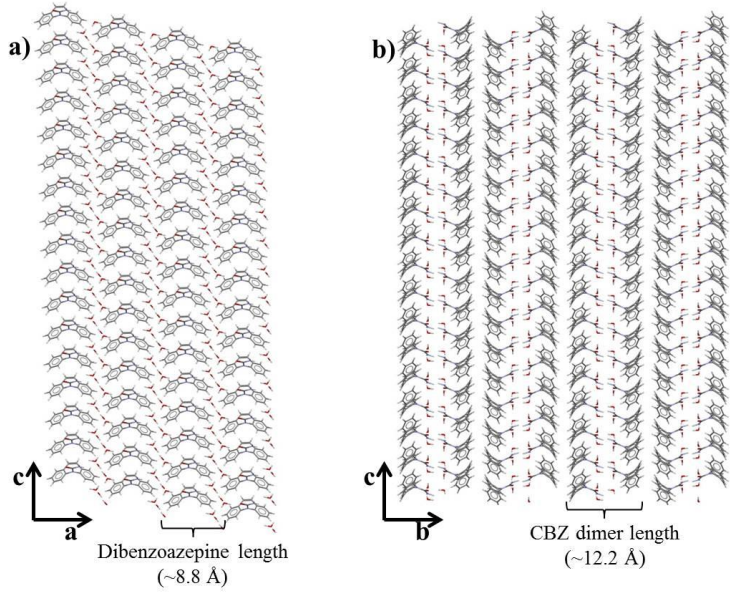

Figure 13 - Scheme representing the molecular arrangement on different surfaces of CBZ:2H_2O crystals. *a)* illustrates the first layer of molecules on the (020) surface reported as the dominant face in crystals obtained by Kachrimanis & Griesser[162]; *b)* shows the (100) surface reported as the dominant face by Khoo *et al.*[163].

Regarding the dehydration behaviour of CBZ, this is an example of an extensively studied reaction for which no clear mechanistic picture emerges. Literature reports dehydration using a variety of methods including heating, heating under modulated relative humidity, high pressure with different temperatures, under various organic vapours at different temperatures and under vacuum (Appendix 1). Some authors suggest that the dehydration is influenced by the particular experimental method being evaluated, but in some cases, no agreement was observed despite similar experiments being performed. These differences were attributed to possible seeds on the starting materials or due to in-process seeds being created. The complex outcome of numerous studies is summarized in Figure 14.

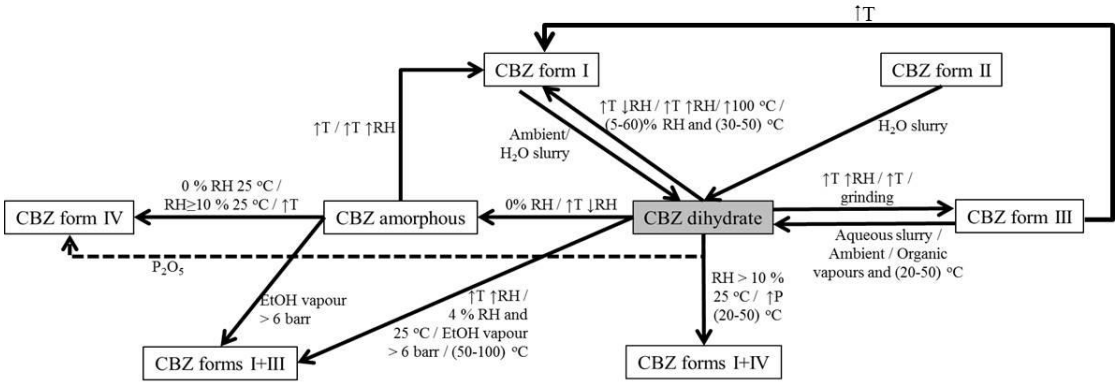

Figure 14 - Flow chart summarizing the experimental conditions evaluated in studies of CBZ dihydrate and the polymorphic outcome (reviewed by the present author from the literature; the articles are listed in Appendix 1).

A further hypothesis concerning the different dehydration outcomes which have been obtained is that they result from the existence of different forms of the hydrate.[139,144,151] McMahon and coworkers were unable to provide evidence of true polymorphs of CBZ dihydrate using PXRD and spectroscopy techniques, while others have claimed that CBZ:2H_2O may exist in two different forms: one monoclinic and one orthorhombic.[180–182] The difference of these two crystalline structures essentially involves two different models which concern the existence of disorder (or not) of the carboxamide portion in the CBZ molecule within the crystal. Sovago *et al.*[182] have summarised the situation by stating that "there are simply two different, but almost equally valid descriptions of the same averaged structure".

It is clear from Figure 15 that the packing in both proposed structures is very similar and therefore gives rise to comparable calculated PXRD patterns with systematic absences and intensities fitting the two models. As a result, it is questionable how powder X-ray diffraction might be used to distinguish these two forms or the existence of a mixture. A few papers also mention that the degree of disorder may be specimen preparation dependent, in which case different crystallization conditions (or even different crystals in the same batch) could lead to different forms and/or mixtures.

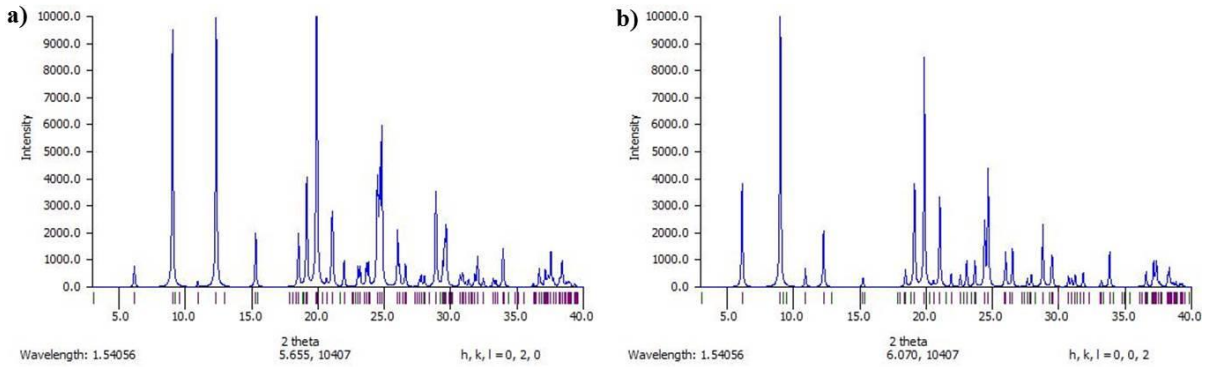

Figure 15 - Comparison of the monoclinic (*a*, FEFNOT02) versus orthorhombic (*b*, FEFNOT10) calculated PXRD patterns of CBZ:2H_2O (from Mercury®, CSD).

At this point one could debate, therefore, if the difference between these two structures is significant in terms of properties of the dihydrate crystals. A first argument towards suggesting it may be important is that having the carboxamide group disordered implies that the two molecules of water in the orthorhombic structure are equivalent while in the (ordered) monoclinic form two different molecules of water will exist (Figure 16). In the orthorhombic case, the water molecules all face similar environments and would be expected to move along the channel in a similar fashion. In theory, non-equivalent water molecules in the monoclinic structure, however, exist in different hydrogen bonding networks, which could lead to different dehydration behaviours and/or forms with intermediate stoichiometry (*i.e.* a monohydrate). In practice, the structure analysis suggests that the general chemical environment of the independent water molecules in the monoclinic model is very similar. Both molecules are next to the carboxamide group and form an intricate network with other molecules in the channel. This means that the behaviour of the water in the orthorhombic and monoclinic models may not differ. Particularly in the case of disorder and defects, these characteristics can be averaged and mixed in one same single crystal.

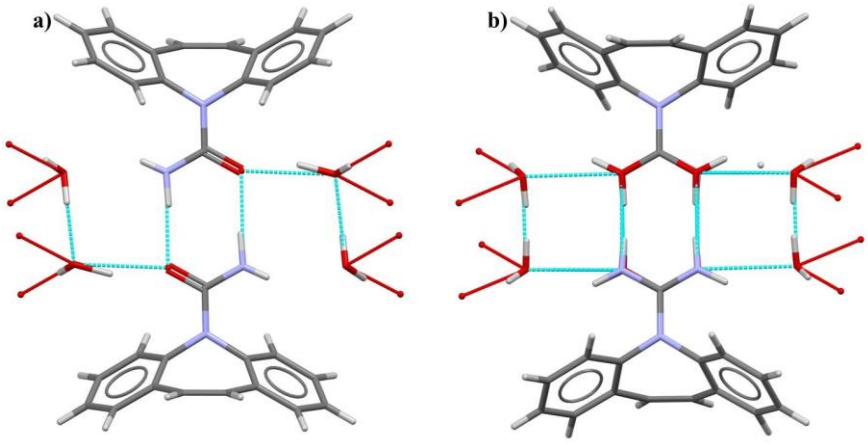

Figure 16 - Comparison of the hydrogen bonding network of water molecules in the monoclinic *(a)* and the orthorhombic *(b)* models of CBZ:2H_2O. In *a)* the two water molecules are not equivalent.

The formation of an intermediate during dehydration has also been suggested, although only a dihydrate is reported on the CSD.[139,151,175] Kachrimanis & Griesser[162] reported dehydration occurring in two distinguishable steps not related to a monohydrate but representing the kinetics of the reaction. They have used thermal analysis and moisture sorption experiments to fit a variety of kinetic models. According to the authors, the dehydration is mediated by diffusion at temperatures below the glass transition ($T_g \approx 53$ °C), while the interface formed between CBZ:2H_2O and the crystalline product is dominant above the T_g. The biphasic character of the dehydration was more pronounced on large crystals, while smaller crystals showed better correlation to a single diffusion model. The authors have also suggested dehydration was controlled by three-dimensional nucleation of the anhydrous phase regardless of the environmental humidity (0-98%), though different CBZ crystalline forms could crystallise depending on humidity.

Another interesting point raised from the monoclinic *versus* orthorhombic dilemma is the mechanical properties of both forms. It is possible to infer that the state of order/disorder of the carboxamide group may change the stress within the crystal. The twinning of these structures could also influence the mechanical strength of the dihydrate. The monoclinic dihydrate studied by Harris et al.[180] was reported to present twinning by pseudo-merohedry in the proportion 5:1. It was suggested that this twinning could be a domain-type disorder (with domain sizes of tens to hundreds of Å) or could occur on a microscopic level (multiple micro-twinning or penetration twinning). But no conclusive data was provided in that study. Following the twinning hypothesis, twinned CBZ dihydrate would potentially exist as a highly ordered lattice. The twinned structure could be characterized with a smaller unit cell and the planes intersecting the *b* axis could potentially show different electron densities compared to the non-twinned packing. In any case, these remain as hypotheses and, to the best of my knowledge, the mechanical properties of CBZ dihydrate have still to be assessed.

1.3.3 The crystallographic analysis of carbamazepine crystal forms reported in the literature

In general, the crystallographic analyses of CBZ crystal structures in the literature oscillate between the analysis of the hydrogen bonding and the analysis of the packing. While screening studies have been focused on the search for preferred strong synthons for the carboxamide moiety, it is clear that the diversity of CBZ crystal structures is highly influenced by the effect of stacking and weak hydrogen bonds on the energetically favourable crystal.[25,45,46,181,183]

The crystal packing within different CBZ forms involves two basic modes of stacking of the CBZ molecules either related by translation or inversion (Figure 17).[45,46,183] The translation of CBZ molecules leads to structures showing π-π stacking, while molecules related by an inversion centre about the azepine group show herringbone motifs (also referred to as inversed-cups). The crystal forms also show aromatic interactions and other contacts which are beneficial to the overall stabilization of the lattice. In general, however, the herringbone structures are energetically more stable than pairs of molecules related by translational stacking.

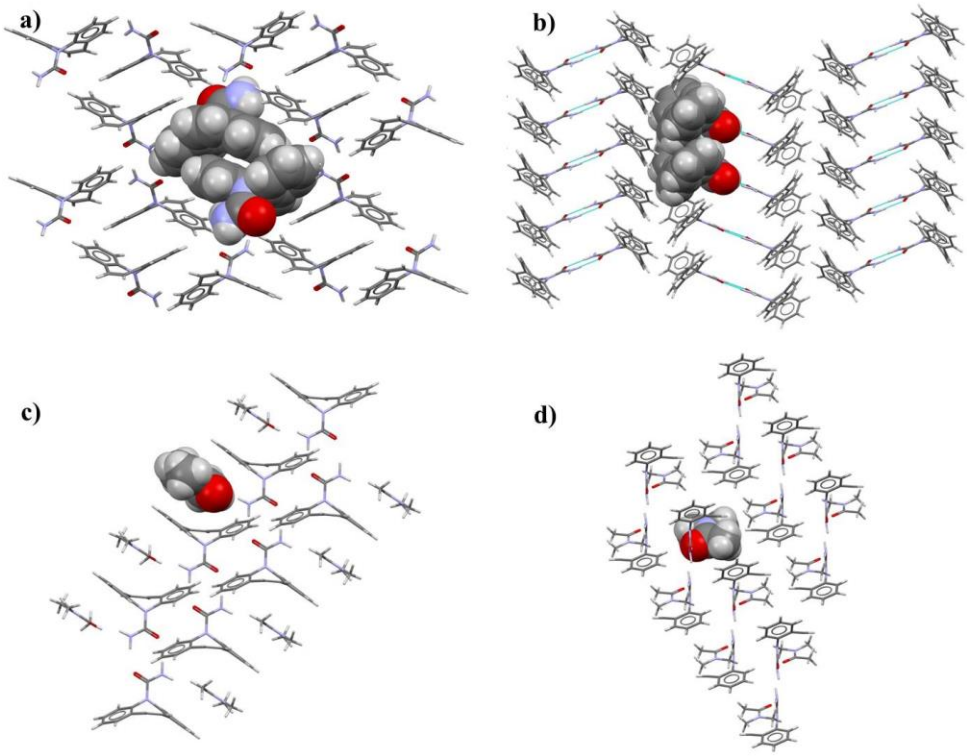

Figure 17 - Basic packing arrangements observed in CBZ structures. *a)* shows the herringbone (inversed-cup) motifs, and *b)* shows the translational stacking interaction. Variations of these modes are also observed and classified as coformer-pairing (*c, d*), for example. Details include pairs of molecules in spacefill (CBZ in *a* and *b*; guest molecule in *c* and *d*).

An aspect deriving from crystal packing and intermolecular interactions is the coplanarity of the CBZ molecules within a dimer. Cruz-Cabeza *et al.*[45] have shown that the isolated amide groups prefer a planar dimer conformation, while deformations are observed in real structures. The amide groups of the CBZ molecule in the dimer are coplanar in the thermodynamically most stable Form III, while an offset is observed in the metastable polymorphs I and II. The authors attributed the deformation to additional C-H···N interactions with surrounding molecules. In another work, Childs *et al.*[183] also attributes significance to these extra interactions in the screening of multicomponent forms. The authors suggest that the N-H proximity to the dibenzoazepine causes steric hindrance which blocks the access of additional acceptor groups to the amine donor.

Another interesting characteristic accounts for the dimeric molecular units of CBZ. Cruz-Cabeza and co-workers[46] stated that single-component crystals exhibiting CBZ molecules in chains and dimers are energetically comparable. The bonding within the CBZ chain is strained, however, because of the packing and the molecular shape of the azepine ring. This could be the reason why the great majority of experimentally obtained CBZ crystal forms exhibit the dimer motif.

In the presence of competing molecules, *i.e.* cocrystals and solvates, the CBZ homodimer is not easily disrupted with the CBZ molecules tending to retain the carboxamide homodimer. [25,183] The exception to this is in the case of competing carboxylic acids. Similarly, competing molecules, depending on their size, shape and donor/acceptor functionalities, change the arrangement of the stacks of CBZ dimers. The CBZ scaffolding in these structures also leads to different arrangements of the coformer molecule, *i.e.* pockets, channels and layers, an observation which is interesting with regard to the studies reported in this thesis.

1.4 Thesis aim and project outline

The main objective of the present thesis is to investigate the solid-state properties at play in the surface and structural reorganizations that result from the stress within a crystal of labile multicomponent organic solids during drying. The motivation was a collaborative project between a pharmaceutical company and two other academic institutions. The mutual target of this collaboration was to achieve a better understanding of crystal breakage upon drying and characterize particle breakage of dried particles as a result of applied mechanical stress. My role in the project was to bring basic concepts of solid-state chemistry to the study and to propose an investigative framework to assess labile materials in studies of drying. The study of desolvation, dehydration and sublimation reactions upon thermal treatment (mainly) was selected as a type of stress-induced transformation representative of what happens during drying. Strategies of particle design and crystallization studies are also described in the thesis as part of the crystal engineering process.

A literature review and scope studies were initially performed to select a material that could serve as a model for all the parts involved in the project. The preliminary list of materials contained acetaminophen, aspirin, carbamazepine, furosemide, ibuprofen, naproxen, theophylline and thiamine. Carbamazepine, and specifically CBZ:$2H_2O$, was finally selected.

From the perspective of the present work, the study of CBZ stress-induced transformations was undertaken for several reasons. First, many different crystal forms were already reported in the literature providing us with a large library of different packing, hydrogen

bonding arrangements, classes of coformer and the existence of isostructural materials. Importantly, since the CBZ molecule is rigid and does not show intramolecular hydrogen bonding, the system offers less stress from sources deriving from complex torsions within the host molecule during desolvation and sublimation reactions.

Studies in the literature suggest that the CBZ crystals are not difficult to obtain in reasonable sizes, *e.g.* which would be suitable for AFM analysis. Interestingly, the surface properties of CBZ materials have received very little study. As was discussed earlier, the literature has shown distinct morphologies of CBZ:2H_2O and suggested different surface features upon dehydration. The authors, however, presented no comparison of each other's results and the structural meaning of the different findings was not fully explored.

Lastly, several of the CBZ structures have already been crystallographically analysed and carefully compared, while crystal structure prediction studies are also available to support the interpretation of the results obtained in the present work. The results can also be associated with the previous studies on CBZ:2H_2O dehydration giving special attention to the impact of solid-solid transformations on subsequent properties of the materials.

CHAPTER 2* – *Experimental section

2.1 Materials

All solvents were supplied by Sigma-Aldrich Company Ltd and used without further purification. Other chemicals used are the following: carbamazepine and benzoquinone (Alfa Aesar, Thermo Fisher Scientific), and oxalic acid dihydrate (Sigma-Aldrich Company Ltd). The solids were analysed by PXRD to confirm their identity (*e.g.* polymorphic form and phase purity) prior to use.

2.2 Equilibrium solubility experiments

The solubility was assessed in saturated solutions generated by slurrying CBZ in different ethanol:coformer proportions. The slurries were typically equilibrated for at least 24 hours. After the system reached equilibrium, the solid phase was separated from the mother liquor and analysed by PXRD (Section 2.8), while the amount of CBZ remaining in solution was quantified by UV spectrometry or LC analyses (Section 2.2.1). The CBZ concentration of the solution phase at each ethanol:conformer proportion was combined with the PXRD analysis of the solids to determine the equilibrium solubility of the respective solid. This procedure was repeated for all the CBZ multicomponent systems under study, except the CBZ/OXA system.

2.2.1. Quantification of species in solution

The quantification of carbamazepine in solution was performed by UV spectrometry, while solutions containing carbamazepine and benzoquinone required analysis by high performance liquid chromatography (HPLC). The methods were adapted from the procedures reported in the Brazilian Pharmacopoeia (5^{th} Edition)[184] and from an HPLC method which was already being used by members of the group to quantify carbamazepine.

A LKB Ultrospec 4050 UV/Vis spectrophotometer and a 10 mm quartz cell were used to collect the absorbance measurements at 285 nm. The HPLC experiments were performed on an Agilent 1100 series equipped composed of a quaternary pump (G1311A), a degasser module (G1379A), a variable wavelength detector (G1314B), an autosampler (G1329A) with cooling station (G1330B), and a C_{18} column (250 x 4.6 mm, 5 µm particle size, Agilent Zorbax Eclipse XDB) held in a thermostatted column compartment (G1316A). Data

was acquired and processed in the ChemStation software. The elution mode was isocratic and the mobile phase consisted of 0.1% formic acid water:acetonitrile (60:40, v/v) at a flow rate of 1.0 mL min^{-1}. The injection volume was 20 µL and the detection wavelength was 284 nm for carbamazepine (T_r=6.0 minutes) and 244 nm for benzoquinone (T_r=3.9 minutes).

Preparation of standard solutions: accurately weighed amounts of the respective analyte were diluted in ethanol 96% (UV) or in acetonitrile (HPLC) to prepare a stock solution of 500 µg.mL^{-1}. Aliquots of the corresponding stock solution were diluted in ethanol 96% for UV studies (final concentration of 25 µg.mL^{-1}) or acetonitrile:water (50:50, v:v) for LC analyses (final concentration of 10 µg.mL^{-1}).

Preparation of sample solutions: as the methods of quantification were mainly used to measure the dissolved material in slurries, a prior step of separation of solids and mother liquor was necessary. Slurries in ethanol:water solutions were filtered by syringe filters (polyethersulfone membrane, Millex®, 0.22 µm of pore size) because the experiments were performed at different temperatures and the separation had to be quick in order to avoid cooling and precipitation. The slurries in different solvent compositions were aliquoted and centrifuged in a mini centrifuge (5000 RPM) for 10 minutes. The solutions analysed by UV were appropriately diluted in ethanol 96% to concentrations limited to the range 2-40 µg.mL^{-1}, while the solutions measured by HPLC were diluted in acetonitrile:water (50:50, v:v) to concentrations within the range 2-40 µg.mL^{-1}. The content of the analyte was calculated from the comparison of the average absorbance (UV) or the average area under the curve (HPLC) recorded for the samples to the respective standard solutions.

2.3 Sample preparation

2.3.1 Slurrying

Slurries of CBZ in the appropriate solvent were typically equilibrated for at least 24 hours at room temperature. The solid phase was filtered and analysed by PXRD. Eventually, slurries of CBZ at different temperatures and ethanol:conformer proportions were also prepared. Slurrying was used in the preparation of CBZ:$2H_2O$, 2CBZ:BZQ, CBZ:FORM and CBZ:ACA samples using different CBZ polymorphs with the intention to test the effect of seeds on the outcome of thermal treatment.

2.3.2 Solution crystallization

Solution-based crystallisation used the cooling technique in order to preserve the activity of the solvents throughout the crystallization period. The solutions were typically prepared by solubilizing CBZ upon heating and stirring in the respective solvent, and cooling the system to precipitate spontaneously, *i.e.* without the addition of seeds. The cooling rate was set to 5 $^{o}C.h^{-1}$ (until room temperature) and no agitation was used during the process to avoid particle breakage. The crystals were harvested by vacuum filtration and, when necessary, dried under room conditions.

Following this general method, different crystallization experiments were performed by varying the solution concentration and, in the case of needle-like crystals, the crystallization environment. In order to change the crystallization environment, distinct binary solvent mixtures of ethanol and the respective multicomponent coformer were assessed. The concentration of the crystallization solutions was defined in relation to the solubility of the solid phase in the respective solvent mixture (as determined from the equilibrium solubility experiments in Section 2.2). In general, the concentrations ranged from twofold (2xS), to fourfold (4xS) and sixfold (6xS) of the solubility values, when applicable. In the case of the cocrystals of carbamazepine with benzoquinone and oxalic acid, the preparation involved solution crystallization in the same solvents reported in the literature (ethanol and ethyl acetate, respectively).[25,183] Also, the cocrystals of CBZ with BZQ were screened in different coformer concentrations (similarly to the case of the CBZ solvates). 2CBZ:OXA, in turn, was only crystallized in solutions containing stoichiometric proportions of CBZ and OXA. Table 1 shows the summary of the crystallization conditions used in the present work.

A few modifications in the general crystallization method were made in order to expand the understanding of the factors affecting the crystallization of CBZ:2H_2O:

(i) Crystallization at different cooling rates: similar to the general method of crystallization, but at cooling rates of 1 ^{o}C/day or without cooling control.

(ii) Crystallization in isopropanol:water: similar to the general method of crystallization, but replacing ethanol for isopropanol. Two solvent compositions (75:25 and 25:75 isopropanol:water, v:v) were tested and the initial concentration of CBZ corresponded to 2xS.

(iii) Crystallization with seeding: supersaturated ethanolic solutions of carbamazepine were prepared at 80 ^{o}C and slowly cooled until 40 ^{o}C (5 $^{o}C.h^{-1}$). The solutions were carefully examined in order to identify early nucleation. Only clear solutions at 40 ^{o}C were seeded (with seeds of CBZ:2H_2O prepared by slurrying and ground with mortar and pestle, 0.5%

wt). The seeded solutions were allowed to settle overnight at 40 ºC and the crystals harvested by filtration. Different degrees of supersaturation (1.2, 1.4, 1.7 and 2.0 with regard to the equilibrium solubility of CBZ:2H_2O) and two solvent compositions (75:25 and 25:75 ethanol:water, v:v) were tested.

Table 1 - Summary of the cooling crystallization conditions tested in the present work.

Crystal form	Solution composition (volume proportion)	Solubility ($mg.mL^{-1}$)	Initial concentration (in regards to equilibrium solubility)	Solubilizing temperature (ºC)
CBZ:ACE	100% ACE	12.0	2xS, 4xS and 6xS	55
CBZ:DMSO	100% DMSO	94.6	6xS	80
CBZ:DMF	100% DMF	105.7	6xS	80
CBZ:DMA	100% DMA	99.9	4xS, 6xS	80
CBZ:BZQ	100% ethanol	3.3 / 24.4 (CBZ/BZQ)	4xS, 6xS[1]	70
2CBZ:BZQ	100% ethanol	11.6 / 2.4 (CBZ/BZQ)	2xS, 4xS, 6xS[1]	70
2CBZ:OXA[2]	100% ethyl acetate	-	-	70
CBZ:2H_2O[3]	75% H_2O, 25% ethanol	1.2	1.2xS, 1.4xS, 1.7xS, 2xS, 4xS and 6xS	70
	60% H_2O, 40% ethanol	5.0	1.2xS, 1.4xS, 1.7xS, 2xS and 6xS	
	50% H_2O, 50% ethanol	10.4	1.2xS, 1.4xS, 1.7xS, 2xS and 6xS	
	40% H_2O, 60% ethanol	18.3	1.2xS, 1.4xS, 1.7xS, 2xS and 6xS	
	25% H_2O, 75% ethanol	34.6	1.2xS, 1.4xS, 1.7xS, 2xS, 4xS and 6xS	
CBZ:FORM	100% FORM	5.6	2xS, 4xS and 6xS	80
	18.5% FORM,75% ethanol	42.5	2xS, 4xS and 6xS	
2CBZ:DIOX	100% DIOX	41.9	2xS, 4xS and 6xS	80
	33% DIOX, 75% ethanol	75.5	2xS, 4xS and 6xS	
CBZ:TFE	100% TFE	231.3	4xS	70
2CBZ:TFE	50% TFE, 50% ethanol	78.9	4xS	
CBZ:TFA	100% TFA	354.6	2xS	70
	50% TFA, 50% ethanol	26.6	2xS, 4xS	
CBZ:ACA	100% ACA	20.2	2xS, 4xS and 6xS	80
	25% ACA, 75% ethanol	18.6	2xS, 4xS and 6xS	
CBZ:FA	100% FA	106.0	2xS, 4xS and 6xS	80
	25% FA, 75% ethanol	66.9	2xS, 4xS and 6xS	

[1] Solutions prepared with variable amounts of CBZ and BZQ, according to the equilibrium phase diagram.
[2] Solution prepared with 27.0 $mg.mL^{-1}$ of 2CBZ:OXA prepared from grinding.
[3] The method of preparation of CBZ:2H_2O which used ethanol:water (75:25, v:v) and initial CBZ concentration of 2xS resulted in the crystallization of crystals with (h00) dominant face; this sample has been named (h00) sample. In turn, the method of preparation of CBZ:2H_2O which used ethanol:water (25:75, v:v) and initial CBZ concentration of 6xS resulted in the crystallization of crystals with (0k0) dominant face; this sample has been called (0k0) sample.

(iv) Crystallization by antisolvent addition with seeding: undersaturated ethanolic solutions of carbamazepine were prepared at 40 ºC and 25 ºC with stirring. Two different initial solution composition were tested: 85:15 and 40:60 (ethanol:water, v:v). Supersaturation was

subsequently generated by the slow addition of water until the final ethanol:water proportion was reached (respectively 60:40 and 25:75 ethanol:water, v:v). Different degrees of supersaturation were tested (1.2, 1.4, 1.7 and 2.0 with regard to the equilibrium solubility of CBZ:2H_2O). The solutions were carefully examined in order to identify early nucleation. Only clear solutions were seeded (seeds of CBZ dihydrate prepared by slurrying and ground with mortar and pestle, 0.5% wt). The seeded solutions were allowed to settle and the crystals were harvested by filtration.

(v) Crystallization with additives (after Rodriguez-Hornedo & Murphy, 2004)[150]: ethanolic solutions of carbamazepine with sodium taurocholate (5 and 9 mM) were prepared at 70 ^oC and slowly cooled until 25 ^oC (5 $^oC.h^{-1}$) without agitation or seeding. The initial amount of carbamazepine dissolved was dependent on the ethanol:water v:v proportions (75:25=6.5 $mg.mL^{-1}$; 25:75=13 $mg.mL.^{-1}$).

Kilogram-scale crystallizations of CBZ:2H_2O were performed by Dr Kushal Sinha (Abbvie Inc., Chicago, Illinois, USA). The samples were prepared in crystallization reactors of 10 L and 170 L, and used Ultra-Turrax® dispersers for wet milling (IKA-T10 and IKA-T25, respectively).

2.3.3 Grinding

The grinding experiments were performed using a Retch MM200 grinder (30 Hz, 30 minutes) using steel jars and two steel balls per jar (7 mm Ø). The studied molar proportions CBZ:coformer varied, but the overall amount of material was maintained at approximately 200 mg. In liquid assisted grinding, the standard procedure used 70 µL of acetonitrile as the added liquid. Cocrystals of carbamazepine with benzoquinone and oxalic acid were prepared by grinding.

2.3.4 Sublimation

Sublimation experiments were performed under vacuum using a sublimation apparatus placed inside an oil bath at 100 ^oC. The starting material was placed on the hot surface of the apparatus and allowed to sublime onto a cold glass surface approximately 2 cm above. Carbamazepine polymorph I and benzoquinone were prepared by this method.

2.3.5 Storage in humidity chambers

Samples of CBZ:2H_2O and 2CBZ:BZQ were stored under controlled humidity and temperature conditions. Environments of 0% RH were generated in desiccators containing P_2O_5, while saturated solutions of LiCl and K_2SO_4 were used to generate approximately 11% and 98% RH, respectively. The desiccators were stored at 22, 25, 30 and 40 ^oC and their temperature and humidity monitored with a thermohygrometer (Testo 608 H2).

2.3.6 Interconversion studies of carbamazepine dihydrate and carbamazepine benzoquinone cocrystal

The possibility of exchanging the molecules of water for benzoquinone (and vice versa) in single crystals of CBZ:2H_2O (and 2CBZ:BZQ) was tested by different methods: (i) in solution; (ii) from the vapour; and (iii) from the vapour with the aid of ethanol. The process started by preparing CBZ:2H_2O (the (0k0) and the (h00) samples) and 2CBZ:BZQ by cooling crystallization as described in Section 2.2.2. Crystals and the mother-liquor were subsequently separated by filtration. Both, crystals and solution, were used in the interconversion experiments in solution (i). The method involved the storage of CBZ:2H_2O crystals in the mother-liquor resulting from 2CBZ:BZQ crystallization, and 2CBZ:BZQ crystals in the mother-liquor of CBZ:2H_2O crystallization. The crystals were gently submerged in these solutions in a proportion of about 30 $mg.mL^{-1}$, and the samples were examined after various times. The interconversion experiments in the vapour phase (ii) were performed in sealed desiccators containing water vapour (conversion from the cocrystal to the dihydrate) or benzoquinone vapour (conversion from the dihydrate to the cocrystal). The 98% water vapour environment was generated as described in Section 2.2.5, while the benzoquinone vapour environment was created from a ‘bed’ of solid benzoquinone at the bottom of the desiccator. The interconversion experiments in (iii) involved the storage of CBZ:2H_2O crystals on the top of a saturated solution of benzoquinone in ethanol. All the experiments were performed at room temperature.

2.4 The use of the Cambridge Structural Database (CSD)

Conquest was used to search for deposited crystal structures. Mercury was used for general structural analysis and visualization as well as obtaining crystal packing similarities between structures, predicted crystal morphologies using the Bravais-Friedel-Donnay-Harker

(BFDH) geometric method, simulated PXRD patterns, values of intermolecular energy calculated using the UNI force-field potentials, and maps of preferential interaction sites around the molecules in the crystal structures.[185–187]

2.5 Calculation of attachment energy

The attachment energy calculations of 2CBZ:BZQ, 2CBZ:OXA, CBZ:2H_2O, CBZ:FORM and, 2CBZ:DIOX were performed by Dr Raimundo Ho using Materials Studio 5.5 (Morphology Module) using the COMPASS forcefield. Prior to the calculations, the crystal structures were geometry optimized.

2.6 Calculation of desolvation enthalpy

The enthalpies of crystal decomposition of CBZ:ACE, CBZ:DMSO, CBZ:DMF, CBZ:DMA, CBZ:BZQ, 2CBZ:BZQ, 2CBZ:OXA, CBZ:2H_2O, CBZ:FORM, CBZ:NIT, CBZ:TFA, CBZ:ACA and CBZ:FA were calculated by Dr Mihails Arhangelskis. The calculations combined the lattice energies of the CBZ polymorphs to the energy of the guest molecule in the gas phase, and subtracting this value from the calculated lattice energies of the respective multicomponent form. The energies were calculated with periodic DFT code CASTEP.[188] Prior to the calculations, the crystal structures were geometry optimized.

2.7 Single crystal X-ray diffraction

The single crystal X-ray diffraction data was collected by Dr Andrew Bond, University of Cambridge. Two different diffractometers were used: (i) Nonius Kappa CCD diffractometer with MoKα radiation (0.71073 Å) at 180 K, 50 kV and 30 mA; (ii) Bruker D8-Quest Ploton-100 with CuKα radiation (1.54178 Å) at 180 K, 50 kV and 30 mA. Structure solution and refinement were also performed by Dr Andrew Bond using SHELXT.[189]

2.8 Powder X-ray diffraction (PXRD)

PXRD measurements were performed at room temperature on a PanAnalytical X'pert PRO Multi-Purpose Diffractometer using Kα copper radiation (λ=1.5418 Å) and a Real Time Multiple Strip (RTMS) detector. The X-ray generator was set at a voltage of 40 kV and

current of 40 mA. Samples were placed onto a flat glass slide and scanned from 3° to 40° 2θ using a scanning time of 5 minutes.

Experiments with modulated temperatures used an Anton Paar TTK 450 temperature chamber. Samples were evaluated with different temperature gradients: non-isothermal runs at heating rate of 10 $^{o}C.min^{-1}$ (one 2 minutes scan every 10^{o}C), non-isothermal runs at heating rate of 1 $^{o}C.min^{-1}$ (one 2 minutes scan every 5 ^{o}C).

2.9 Attenuated total reflection Fourier transform infrared spectroscopy (ATR-FTIR)

Spectra were collected on a ThermoNicolet Nexus FT-IR spectrometer with a Smart Golden Gate Single Reflection ATR accessory. Samples were measured from (500-4000) cm^{-1} at a resolution of 4 cm^{-1} and 32 scans.

2.10 Differential scanning calorimetry (DSC) and thermogravimetric analysis (TGA)

DSC analyses were carried out using a Mettler Toledo DSC822 instrument. Typically, samples weighing 1.0-4.0 mg were heated in 40 µL pin-holed closed pans and scanned at heating rate of 10 $K.min^{-1}$, under nitrogen air atmosphere (80 $mL.min^{-1}$).

The mass loss of the samples as a function of temperature was determined using a Mettler Toledo TGA/SDTA851e/SF/1100 instrument. Typically, 2-10 mg were placed in open 100 µL aluminum crucibles at a heating rate of 10 $K.min^{-1}$, under nitrogen atmosphere (80 mL.min−1). The obtained thermal data were processed using Metler STARe software.

2.11 Optical microscopy (OM)

Micrographs and videos were recorded with a Leica DM1000 LED transmission optical microscope (polarizing filter) equipped with a JVC colour video camera. The microscope was also used for recording images during hot stage experiments. The heating programs were made in a Metler Toledo FP90 Central Processor connected to a FP84HT TA Microscopy Cell. The samples were prepared in 7mm Ø opened glass pans and scanned at heating rate of 10 $K.min^{-1}$, under open atmosphere. The data was processed using Studio software.

A Dino-Lite Handheld Digital Microscope was also used to collect reflectance mode micrographs.

2.12 Scanning electron microscopy (SEM)

SEM images were taken using a JEOL JSM-5510LV Scanning Electron Microscope. The samples were mounted with adhesive tape over an aluminium holder and sputtered with gold for 3 minutes (Agar Sputter Coater).

2.13 Transmission electron microscopy (TEM)

The TEM data was collected in collaboration to Prof Rik Drummond-Brydson's group (School of Chemical and Process Engineering, University of Leeds, UK). Conventional TEM analyses were performed at room temperature on a FEI Tecnai instrument operating at 200 kV. Data was directly collected as digital images by a CCD camera. The diffraction patterns had the position of the reflections and the angles between them measured in Image J software. Three d-spacing values per diffractogram and their respective angles were combined and matched to the reported structures in order to check the identity of the crystals characterized by TEM. As a final step, Crystal Maker Single Crystal v1.3 was used in order to compare the experimental diffraction pattern to the simulated diffraction pattern of the indicated zone axis, which was obtained from the reported structures retrieved from CSD.

Samples were directly prepared onto lacey-carbon films supported on 300 mesh copper grids. The sample preparation of CBZ:$2H_2O$ typically consisted of evaporating ethanol:water solutions of carbamazepine directly onto the TEM grid. The preparation of 2CBZ:BZQ samples typically consisted of evaporating acetonitrile solutions containing carbamazepine and benzoquinone directly onto the TEM grid. Samples for cryoTEM analyses were prepared by Dr Nicole Hondow by plunge-freezing the TEM grids in liquid ethane. The samples were transferred in a cryo-holder under temperature control, and were maintained at 170 K during the analyses. In certain cases, the temperature was then allowed to increase in order to perform conventional TEM analyses using the same grid and investigate the effect of temperature. The rate of warming of the sample was, however, uncontrolled.

2.14 Atomic force microscopy (AFM)

AFM images were recorded using a MultiMode atomic force microscope (NanoScope IIIa controller; Veeco). The stage was equipped with a video microscope to position the sample on the *J* scanner base. All images were recorded in tapping mode using TESP 15 series (HQ:NSC15/Al BS) sharpened silicon probes with nominal spring constant of

40 N/m and nominal resonance frequency of 325 kHz (μmasch). The scan rate was changed according to the size of the scan area and the features observed on the surface. The scans were analysed using NanoScope software version 6.13 (Veeco). Each height image was processed using the plane-fitting third-order and the flatten zero-order commands in the software. For the amplitude images, the plane-fitting zero-order command was performed.

The samples were fixed to glass coverslips using sticky tabs over stainless steel sample holders. Before AFM analysis, the samples were observed on the metallic discs using a binocular GX reflective optical microscope equipped with a Motticam 2000 microscope digital camera

2.15 Impact tests

Breakage experiments were performed by Wei Pin Goh, from Prof Mojtaba Ghadiri's group (School of Chemical and Process Engineering, University of Leeds, UK). The methods used the Scirocco disperser of the Malvern Mastersizer 2000 and the Morphologi G3 apparatus from Malvern.[190,191] Different dispersion pressures were tested per equipment. Although an increase in the dispersion pressure affects the particle acceleration, the magnitude of the dispersion pressures and in the impact velocity were not comparable.

CHAPTER 3 – Crystallographic analysis of carbamazepine crystal forms used in the present study

3.1. Introduction

The first assortment of CBZ forms within the reported multicomponent materials took into account all the solvates, hydrates and cocrystals with coformers amenable to sublimation. Classical salts of CBZ were purposely not considered, although one salt will be found in the discussion of later chapters on a comparative basis. The list of multicomponent structures was then analysed according to the solvent/coformer arrangement and four motifs identified: pocket, channel, intersecting-channel and layer-like structures. Further classifications considered the packing (inversion-cup/herringbone *versus* translational stacking) and the type of hydrogen bonding (dimer *versus* catemer) of the CBZ molecules. Finally, 13 solvates (including one hydrate) and two cocrystals were initially selected. The number of structures was later expanded to 14 solvates and three cocrystals as new structures with different stoichiometry were obtained during the crystallization studies of the benzoquinone cocrystal and the trifluoroethanol solvate in this project.

Unless specified, the cif files were retrieved from the CSD. Table 2 displays the crystallographic data of the known CBZ forms, including additional structures reported in the thesis. The structures were mainly analysed in Mercury® and the results are shown in the following Section 3.2. The structural comparison of the materials and additional classifications are considered at the end of the chapter, in the Section 3.3. The molecular structures of coformer molecules is given in Figure 18.

N.B. Crystal planes related by translation of the lattice along one of the crystal directions were identified in one general set of planes indicated by *h*, *k* and/or *l*. In other words, planes passing through the origin and planes passing through fractional lattice spacings are characterized in the same group. For example, the (010) and (020) planes in CBZ:2H_2O are identified as (0k0). This notation was adopted because it facilitates the comparison of equivalent planes in different crystal forms and it simplifies the comparison of structural features to the desolvation/sublimation outcome that will be considered in further experimental chapters.

Table 2 - Crystallographic data of the studied CBZ materials

Material	CBZ I	CBZ II	CBZ III	CBZ IV	CBZ V
Formula	$C_{15}H_{12}N_2O$	$C_{15}H_{12}N_2O$	$C_{15}H_{12}N_2O$	$C_{15}H_{12}N_2O$	$C_{15}H_{12}N_2O$
MW/g.mol^{-1}	236.27	236.27	236.27	236.27	236.27
T/K	158	298	298	158	123
Crystal system	Triclinic	Trigonal	Monoclinic	Monoclinic	Orthorhombic
Space group	*P*-1	*R*-3	$P2_1/c$	*C*2/*c*	*Pbca*
a/Å	5.1705(6)	35.454(3)	7.529(1)	26.609(4)	9.1245(5)
b/Å	20.574(2)	35.454(3)	11.148(2)	6.9269(10)	10.4518(5)
c/Å	22.245(2)	5.253(1)	15.470(2)	13.957(2)	24.8224(11)
α/º	84.124(4)	90	90	90	90
β/º	88.008(4)	90	116.17(1)	109.702(2)	90
γ/º	85.187(4)	120	90	90	90
V/Å^3	2344.82	5718.32	1165.34	2421.93	2367.25
Z/Z’	8/4	18/1	4/1	8/1	8/1
ρ/g.cm^{-3}	1.339	1.235	1.347	1.296	1.326
R-factor/%	5.06	6.9	3.5	3.57	4.5
CSD refcode	CBMZPN11	CBMZPN03	CBMZPN01	CBMZPN12	CBMZPN16
Reference	Grzesiak *et al.* (2003)[149]	Lowes *et al.* (1987)[135]	Reboul *et al.* (1981)[192]	Lang *et al.* (2002)[148]	Arlin *et al.* (2011)[44]

Material	10CBZ:THF[a]	CBZ:ACE	CBZ:DMSO[a/b]	CBZ:DMSO[a/c]	CBZ:DMF
Formula	$(C_{15}H_{12}N_2O)_{10}$ (C_4H_8O)	$(C_{15}H_{12}N_2O)$ (C_3H_6O)	$(C_{15}H_{12}N_2O)$ (C_2H_6OS)	$(C_{15}H_{12}N_2O)$ (C_2H_6OS)	$(C_{15}H_{12}N_2O)$ (C_3H_7NO)
MW/g.mol^{-1}	2434.80	294.35	314.40	314.40	309.36
T/K	100	100	110	280	123
Crystal system	Trigonal	Triclinic	Triclinic	Triclinic	Triclinic
Space group	*R*-3	*P*-1	*P*-1	*P*-1	*P*-1
a/Å	35.243(5)	7.3985(15)	8.8708(2)	7.4105(3)	7.7118(4)
b/Å	35.243(5)	8.9054(18)	12.1901(3)	8.9753(3)	9.1503(4)
c/Å	5.1853(10)	11.873(2)	14.6128(4)	12.2407(4)	11.6969(6)
α/º	90	95.809(3)	94.9700(10)	94.259(2)	100.192(3)
β/º	90	93.401(4)	100.2170(10)	94.526(3)	95.379(2)
γ/º	120	101.362(3)	95.0360(10)	100.200(2)	101.908(3)
V/Å^3	5577.64	760.479	1540.67	795.544	787.584
Z/Z’	18/1	2/1	4/2	2/1	2/1
ρ/g.cm^{-3}	1.305	1.285	1.355	1.313	1.305
R-factor/%	5.12	7.68	4.75	4.86	4.77
CSD refcode	MIMQIJ	CRBMZA01	UNEYIV04	UNEYIV01	QANQUS
Reference	Fabbiani *et al.* (2007)[158]	Fleischman *et al.* (2003)[25]	Cruz-Cabeza *et al.* (2011)[193]	Cruz-Cabeza *et al.* (2011)[193]	Johnston *et al.* (2005)[194]

Material	CBZ:DMA[a]	CBZ:BZQ	2CBZ:BZQ	2CBZ:OXA[d]	CBZ:OXA
Formula	$(C_{15}H_{12}N_2O)$ (C_4H_9NO)	$(C_{15}H_{12}N_2O)$ $(C_6H_4O_2)$	$(C_{15}H_{12}N_2O)_2$ $(C_6H_4O_2)$	$(C_{15}H_{12}N_2O)_2$ $(C_2H_2O_4)$	$(C_{15}H_{12}N_2O)$ $(C_2H_2O_4)$
MW/g.mol^{-1}	323.39	344.36	580.63	562.57	326.30
T/K	123	180	100	180	173
Crystal system	Monoclinic	Triclinic	Monoclinic	Monoclinic	Monoclinic
Space group	$P2_1/c$	P-1	$P2_1/c$	$P2_1$	$P2_1/c$
a/Å	7.5046(7)	7.0891(2)	10.3335(18)	10.3940	10.330(14)
b/Å	19.506(2)	10.2587(3)	27.611(5)	25.6938	26.24(3)
c/Å	11.7808(13)	12.6557(3)	4.9960(9)	5.0900	5.110(6)
α/°	90	80.435(2)	90	90	90
β/°	96.597(8)	86.6170(10)	102.275(3)	103.5037	104.21(3)
γ/°	90	71.0080(10)	90	90	90
V/Å^3	1713.11	858.172	1392.86	-	1342.73
Z/Z’	4/1	2/1	4/1	4/1	4/1
ρ/g.cm^{-3}	1.254	1.333	1.384	-	1.614
R-factor/%	6.76	3.58	5.45	-	14.08
CSD refcode	KIWBEY	-	UNEYOB	-	MOXWUS
Reference	Johnston *et al.* (2008)[195]	This work	Fleischman *et al.* (2003)[25]	This work	Childs *et al.* (2009)[196]

Material	CBZ:2H$_2$O	CBZ:2H$_2$O[a]	CBZ:FORM	2CBZ:DIOX[a]	CBZ:NIT
Formula	$(C_{15}H_{12}N_2O)$ $(H_2O)_2$	$(C_{15}H_{12}N_2O)$ $(H_2O)_2$	$(C_{15}H_{12}N_2O)$ (CH_3NO)	$(C_{15}H_{12}N_2O)_2$ (C_4H_8O)	$(C_{15}H_{12}N_2O)$ (CH_3NO_2)
MW/g.mol^{-1}	272.30	272.30	281.31	560.79	297.33
T/K	120	100	100	180	123
Crystal system	Monoclinic	Orthorhombic	Triclinic	Monoclinic	Monoclinic
Space group	$P2_1/c$	*Cmca*	P-1	$P2_1/n$	$P2_1/n$
a/Å	10.066(2)	19.638(6)	5.1077(11)	16.7756(18)	10.9242(11)
b/Å	28.719(5)	4.8378(16)	16.057(3)	4.9169(6)	5.1617(5)
c/Å	4.831(1)	28.856(8)	17.752(4)	17.9988(19)	26.309(3)
α/°	90	90	73.711(3)	90	90
β/°	103.45(1)	90	89.350(3)	107.826(6)	100.104(2)
γ/°	90	90	88.636(3)	90	90
V/Å^3	1358.27	2741.46	1397.06	1413.34	1460.49
Z/Z’	4/1	8/0.5	4/2	4/1	4/1
ρ/g.cm^{-3}	1.332	1.319	1.337	1.317	1.352
R-factor/%	7.29	6.46	7.66	6.57	5.16
CSD refcode	FEFNOT02	FEFNOT10	UNIBOI	-	KIWBOI
Reference	Harris *et al.* (2005)[180]	Sovago *et al.* (2016)[182]	Fleischman *et al.* (2003)[25]	This work	Johnston *et al.* (2008)[195]

Material	CBZ:TFE	2CBZ:TFE[a]	CBZ:TFA[a]	CBZ:ACA	CBZ:FA
Formula	$(C_{15}H_{12}N_2O)$	$(C_{15}H_{12}N_2O)_2$	$(C_{15}H_{12}N_2O)$	$(C_{15}H_{12}N_2O)$	$(C_{15}H_{12}N_2O)$
	$(C_2H_3F_3O)$	$(C_2H_3F_3O)$	$(C_2HF_3O_2)$	$(C_2H_4O_2)$	(CH_2O_2)
MW/g.mol^{-1}	336.31	572.58	350.29	296.32	282.32
T/K	173	180	150	100	100
Crystal system	Triclinic	Triclinic	Monoclinic	Monoclinic	Monoclinic
Space group	*P*-1	*P*-1	$P2_1/n$	$P2_1/c$	$P2_1/c$
a/Å	10.236(2)	5.2419(2)	15.0142(4)	5.1206(4)	5.2031(9)
b/Å	12.937(2)	15.0825(5)	5.28710(10)	15.7136(13)	14.741(2)
c/Å	13.614(2)	18.4638(6)	20.2489(6)	18.4986(15)	17.882(3)
α/º	62.419(2)	103.874(2)	90	90	90
β/º	88.218(2)	93.756(2)	101.735(3)	96.5460(10)	98.132(3)
γ/º	84.286(2)	97.404(2)	90	90	90
V/Å^3	1589.76	1398.3	1573.79	1478.75	1357.74
Z/Z'	4/2	4/2	4/1	4/1	4/1
ρ/g.cm^{-3}	1.405	1.360	1.478	1.331	1.381
R-factor/%	4.64	8.18	3.86	4.92	5.33
CSD refcode	SAPDUJ	-	GINFOZ	UNEZIW	UNEZOC
Reference	Lohani *et al.* (2005)[197]	This work	Fernandes *et al.* (2007)[198]	Fleischman *et al.* (2003)[25]	Fleischman *et al.* (2003)[25]

[a] Structure presents disorder
[b] Low temperature form
[c] High temperature form
[d] A final refinement of the structure is still needed. The study is in progress.

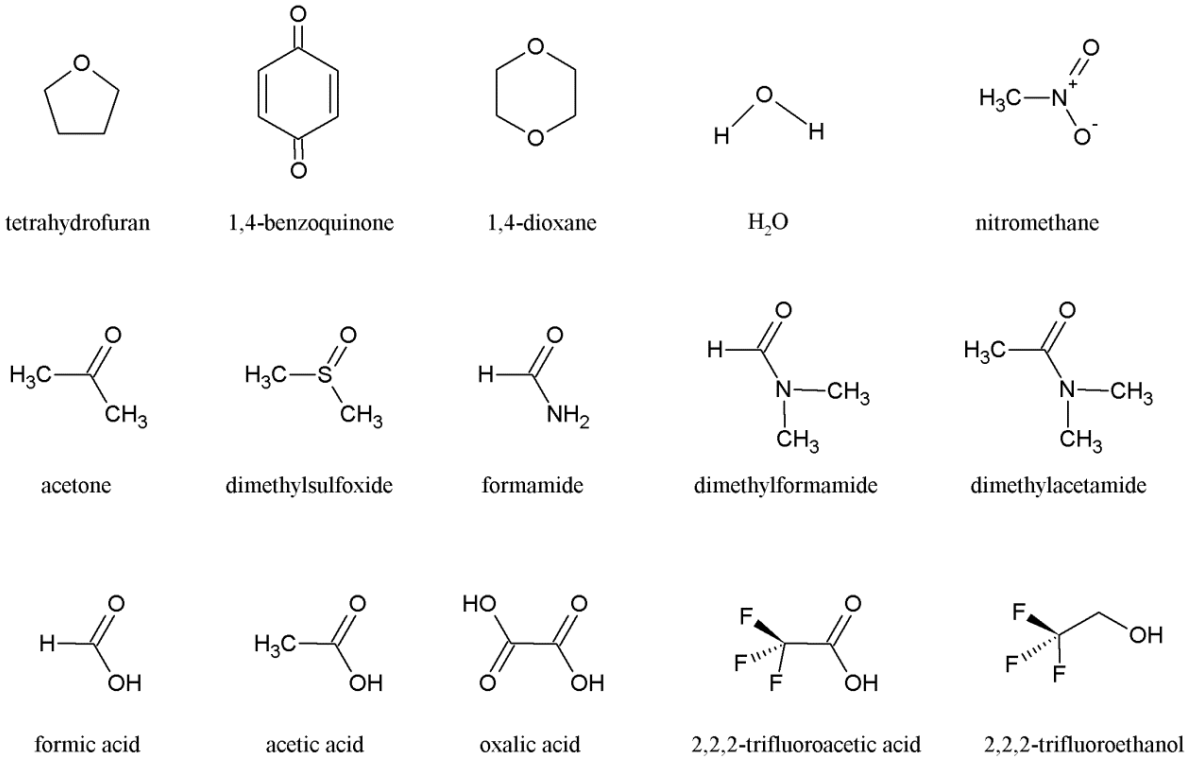

Figure 18 - Molecular structure of the coformers of the CBZ multicomponent materials discussed in this chapter.

3.2. Structure analysis

3.2.1 Carbamazepine polymorph I

CBZ polymorph I has a triclinic structure and with four molecules in the asymmetric unit (the notation of the independent CBZ molecules is shown in Figure 19). The crystal structure consists of three different types of $R^2_2(8)$ carboxamide dimers: one formed only by CBZ 2, one formed only by CBZ 3 and another formed by CBZ 1 and 4 molecules. The dimers 2 and 3 have very similar dimensions and the same N–H···O bond length in the dimer (D_2=2.894 Å, d_2=2.035 Å, θ_2=178.38º; and D_3=2.884 Å, d_3=1.978 Å, θ_3=176.93º). The dimer 1+4 is composed of non-equivalent molecules and the dimensions of the hydrogen bonds within the $R^2_2(8)$ is slightly different (N–H_1···O_4: D=2.919 Å, d=2.086 Å, θ=172.37º; and N–H_4···O_1: D=2.831 Å, d=1.762 Å, θ=171.78º). As expected, different hydrogen bond lengths result in a 16.95º tilt of the carboxamide groups and therefore dimers 1+4 show not only a planar displacement of the CBZ molecules but also the hydrogen bonding in the dimer is not coplanar (Figure 19). In the case of dimers 2 and 3, no tilt is observed and the coplanarity offset, θ^{AB}, between the two molecules in the dimers is 9.45º and 8.99º, respectively.

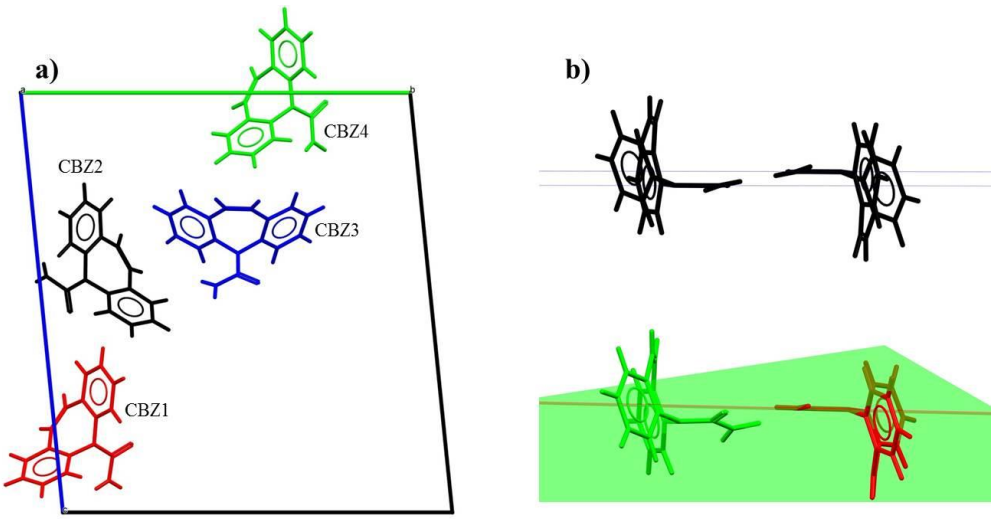

Figure 19 –Asymmetric unit of CBZ polymorph I down the *a* axis (a). The independent molecules have been identified and the notation will be used in the text. Comparison of dimers composed of offset molecules 2 and molecules 1+4 dimers exhibiting coplanarity offset and tilt (b).

Additional weak interactions exist between the benzene portions and the carboxamide groups of neighbouring molecules. In fact, the interaction maps in Figure 20 show that favourable regions of interaction around the amide groups are occupied by aromatic C–H groups. This characteristic can be suggested to result from the lack of additional stronger synthons in the molecule of CBZ. It also confirms how important weak interactions and

stacking are within the CBZ polymorphic forms and raises questions about the behaviour of hydrates, solvates and cocrystals of CBZ. In the case of multicomponent materials, extra synthons are available and may change the energetic contribution and the balance between connectivity and packing in the structures.

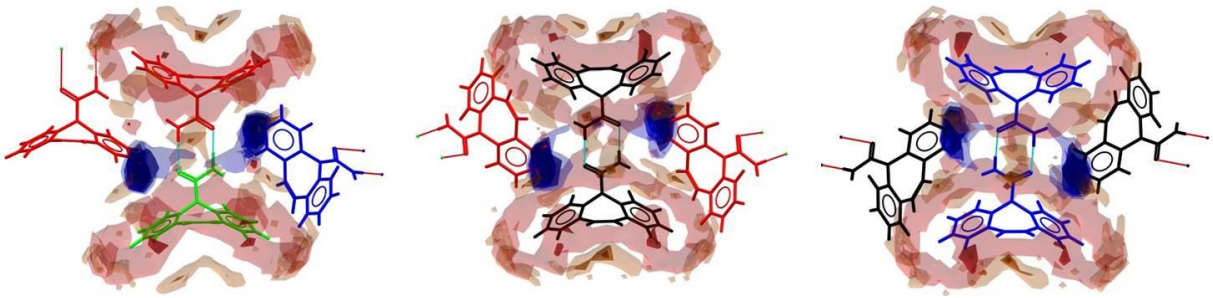

Figure 20 - Interaction maps comparing the statistically preferred interactions in the CSD to the interactions and the packing adopted by the CBZ dimers in the structure of CBZ Form I.

Returning to the CBZ Form I analysis, a translational mode of stacking is observed along the *a* axis in the crystal, which also shows additional weak interactions. The different types of dimers, however, are stacked in the structure arrange in two different intercalating layers along *c* (Figure 21). One layer has the CBZ 2 and CBZ 3 dimers, while another has the CBZ 1+4 dimers. The molecules have similar types of benzene-carboxamide interactions, as mentioned before. One distinct type of contact, however, is seen between CBZ 4 molecules, as they show near dibenzoazepine groups.

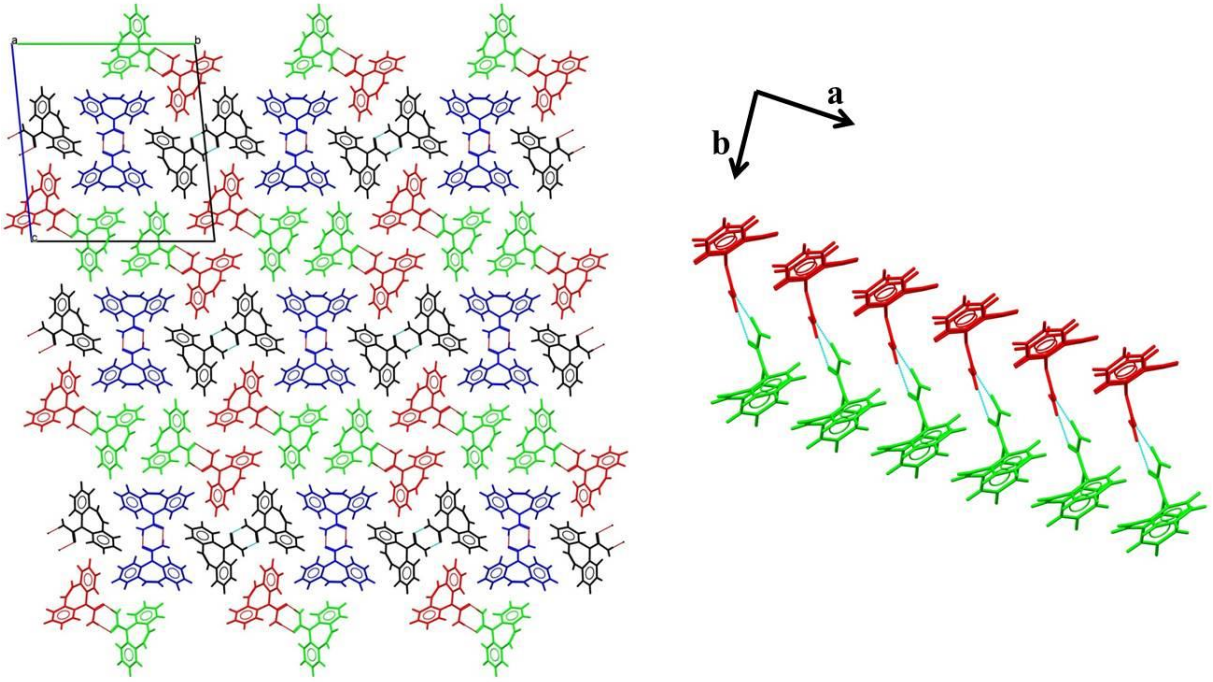

Figure 21 - Packing of carbamazepine polymorph I on the (h00) plane *(left)*. Two types of layers of CBZ dimers are observed along *c*. All the CBZ independent molecules are stacked along the *a* axis (the figure shows the example of CBZ dimers 1+4 stacking on the *right*).

Interaction energies, expressed herein as E^{AB}, suggest that pairs of molecules related by stacking along the *a* axis interact very strongly: 42.9 kJ mol^{-1}, 42.4 kJ mol^{-1}, 43.1 kJ mol^{-1}, and 42.6 kJ mol^{-1} for molecules 1, 2, 3 and 4, respectively. The $R^2_2(6)$ hydrogen bonded molecules show energies of interaction: 34.2 kJ mol^{-1}, 36.2 kJ mol^{-1} and 35.5 kJ mol^{-1} for CBZ 1+4, CBZ 2 and CBZ 3 dimers, respectively. Additionally, two CBZ 4 molecules in contact via their dibenzoazepine portions show intermolecular energy of 25.6 kJ mol^{-1}.

Dimers and stacks are the strongest interactions in Form I crystals. With regard to crystal growth, it is proposed that the formation of a CBZ:CBZ stack contributes to the formation of a CBZ dimer, and vice versa, as these events occur along the same axis. In this case, the packing of CBZ in the crystal and the energetic relationship between pairs of molecules suggest this is a highly anisotropic structure. The predicted BFDH morphology is indeed a needle with the main axis along *a*. Experimental data from the literature also agree to the needle-shaped crystals of polymorph I.[140]

3.2.2 Carbamazepine polymorph II and carbamazepine tetrahydrofuran solvate (10CBZ:THF)

The crystal structure of CBZ polymorph II consists of dimers of CBZ ($R^2_2(8)$, N–H···O: D=2.890 Å, d=1.907 Å, θ=162.40º, θ^{AB}=9.04º, E^{AB}=-38.5 kJ mol^{-1}) organised in three-fold symmetric sets forming channels along the *c* axis (Figure 22). The volume associated with these channels corresponds to 522.70 $Å^3$ and is equivalent to 9.1% of the unit cell.

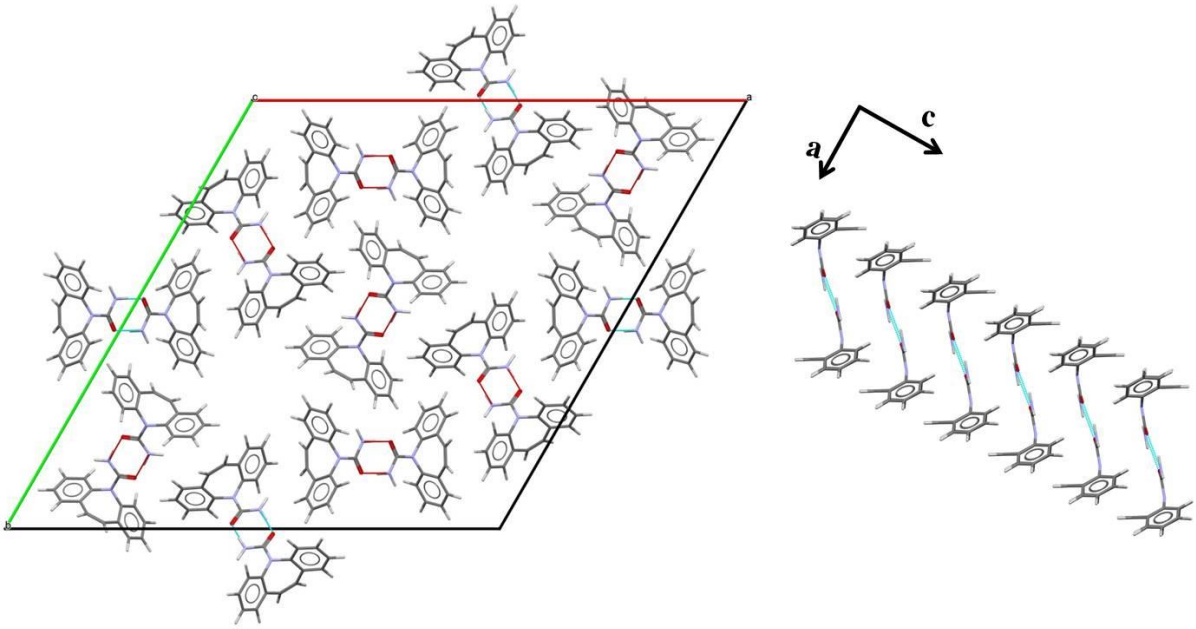

Figure 22 - Unit cell of carbamazepine polymorph II illustrating the molecular arrangement on the (00l) plane *(left)*. The stacking of CBZ molecules down the c axis is shown on the *right*.

This trigonal cell is nearly identical to that within the reported THF solvate and the characteristics of the dimers are also very similar ($R^2_2(8)$, N–H···O: D=2.891 Å, d=2.004 Å, θ=170.13°, θ^{AB}=8.83°, E^{AB}=-34.2 kJ mol^{-1}). In fact, CBZ polymorph II is a highly metastable form principally obtained by using solvent molecules which can be included to stabilise the channels within the structure. It is suggested that both structures are to be considered the same, as the solvent molecules act as accessory agents which, eventually, leave the lattice but are initially responsible for the stabilization during growth.[182]

The CBZ molecules in Form II are stacked along *c* and also present additional intermolecular interactions between the carboxamide and benzene groups of neighbouring molecules (Figure 23). The translational stacking corresponds to the stronger intermolecular interactions in the structure (-40.8 kJ mol^{-1}). The stacking along the *c* axis and the dimer formation also follow the main axis of the BFDH predicted needle-*like* crystals.[157]

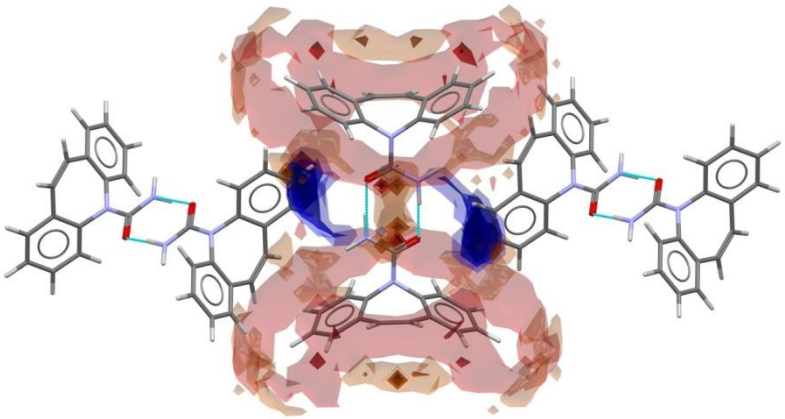

Figure 23 – Interaction maps comparing the statistically preferred interactions in the CSD to the interactions and the packing adopted by the CBZ dimers in the structure of CBZ Form II.

3.2.3 Carbamazepine polymorph III

The crystal structure of CBZ polymorph III consists of dimers of CBZ ($R^2_2(8)$, N–H···O: D=2.929 Å, d=2.111 Å, θ=173.96°, θ^{AB}=n/a, E^{AB}=-28.8 kJ mol^{-1}) organised in a *P*-monoclinic cell (Figure 24). Along the *b* axis, the CBZ molecules are stacked in two distinct fashions according to the crystal symmetry. Dimers related by a centre of inversion through the dibenzoazepine portion interact via inversion-cup stacking and show parallel benzene rings distanced by 3.791 Å and 6.677 Å. Dimers related by a screw axis along *b*, in turn, present stacking of tilted benzene rings angled by 20.87°.

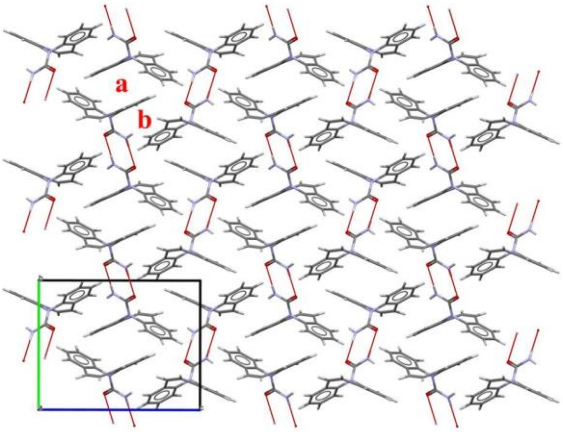

Figure 24 – Packing of carbamazepine polymorph III. It illustrates the molecular arrangement on the (h00) plane and shows the stacking modes in CBZ Form III (a: inversion-cup; b: tilted benzene).

Additional interactions are observed from the azepine and benzene portions to the carbonyl groups along the *a* and the *c* axes. In the case of CBZ Forms I and II, the C–H interactions originate instead from the benzene portion. This difference is attributed to the packing of CBZ molecules observed in Form III (Figure 25). The interaction map illustrates how the combination of all these factors might contribute to packing stabilization by filling favourable regions of interaction around the CBZ molecule.

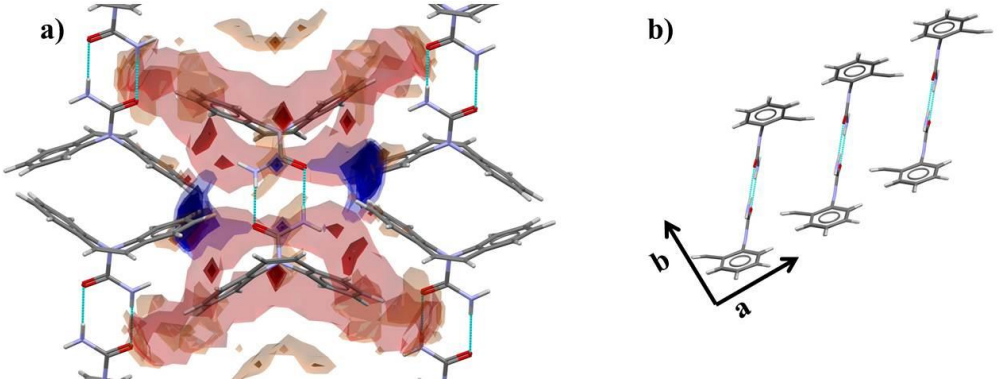

Figure 25 - Interaction maps comparing the statistically preferred interactions in the CSD to the interactions and the packing adopted by the CBZ dimers in the structure of CBZ Form II (a). Aromatic groups occupy the regions around the dimer along the *c* axis, while (b) azepine portions form contacts along *a*.

The intermolecular energy values show that the interaction between the molecules related by inversion-cup stacking is the stronger interaction in the crystal (-43.4 kJ mol^{-1}), while the CBZ dimer and the molecules related by tilted stacking results in weaker contacts (-28.8 kJ mol^{-1} and -27.3 kJ mol^{-1}, respectively). It is interesting to note that the formation of stacks along *a*, favours the formation of dimers along *b*. This may dissipate the connectivity contribution within the lattice axes, resulting in a more isotropic material. In practice, the BFDH morphology of CBZ form III is characterised by blocks, which is also experimentally reported in the literature.[149]

3.2.4 Carbamazepine polymorph IV

The crystal structure of CBZ polymorph IV consists of dimers of CBZ ($R^2_2(8)$, N–H···O: D=2.874 Å, d=1.949 Å, θ=177.55º, θ^{AB}=6.53º, E^{AB}=-36.4 kJ mol^{-1}) organised in a *C*-centred monoclinic cell (Figure 26). CBZ molecules again stack in two different modes, as seen in the polymorph III. The inversion-cup stacking shows benzene rings distanced by 3.445 Å and 6.571 Å, and corresponds to the strongest contact in the structure (-40.9 kJ mol^{-1}). Different sets of dimers related by a 2-fold axis, in turn, give rise to interactions between the azepine C–H and the carboxamide group, and between stacked benzene rings. This stack is tilted by 39.95º and hence characterises a weaker interaction of -31.3 kJ mol^{-1}. The interaction map in Figure 26 illustrates how these contacts satisfy favourable interaction regions around the CBZ molecules in the dimers.

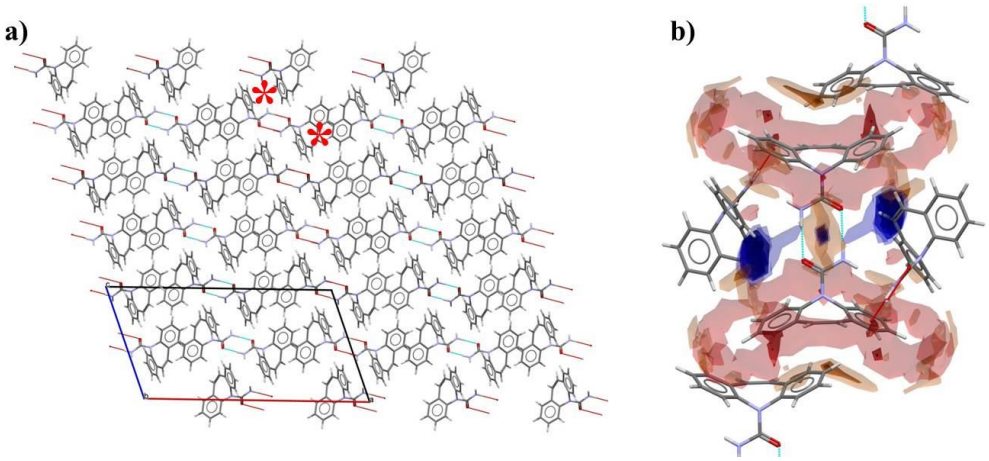

Figure 26 – *(a)* Packing of carbamazepine polymorph IV illustrating the molecular arrangement on the (0k0) plane. *(b)* Interaction map comparing the statistically preferred interactions in the CSD to the interactions and the packing adopted by the CBZ dimers in the structure of CBZ Form III. The two stacking modes of CBZ are shown by asterisks.

The stacking axis in CBZ Form IV is *c*, while the dimer axis runs along *a*. This packing arrangement leads to a more isotropic lattice than CBZ I and results in lath (BFDH) and plate crystals (literature).[148]

3.2.5 Carbamazepine polymorph V

The crystal structure of CBZ polymorph V consists of chains of CBZ held via N–H···O hydrogen bonds (C(4), D=2.877 Å, d=2.158 Å, θ=135.23º, E^{AB}=-23.3 kJ mol^{-1}) along the *a* axis of the orthorhombic cell (Figure 27). The interaction between two C(4) hydrogen bonded molecules accounts for -23.3 kJ mol^{-1}, a much weaker interaction when compared to the CBZ dimers analysed in the previous structures. This result agrees with the hypothesis of Cruz-

Cabeza *et al.*,[46] in which CBZ chain bonding is not experimentally favourable because of its strained character. It was also suggested in the literature that the packing helps stabilize CBZ polymorph V. The interaction map also illustrates how aromatic portions of the CBZ molecules are found at favourable interaction regions around a CBZ molecules in the chain and, therefore, help stabilizing the structure. CBZ Form V shows plate-like morphology (BFDH and literature).[44]

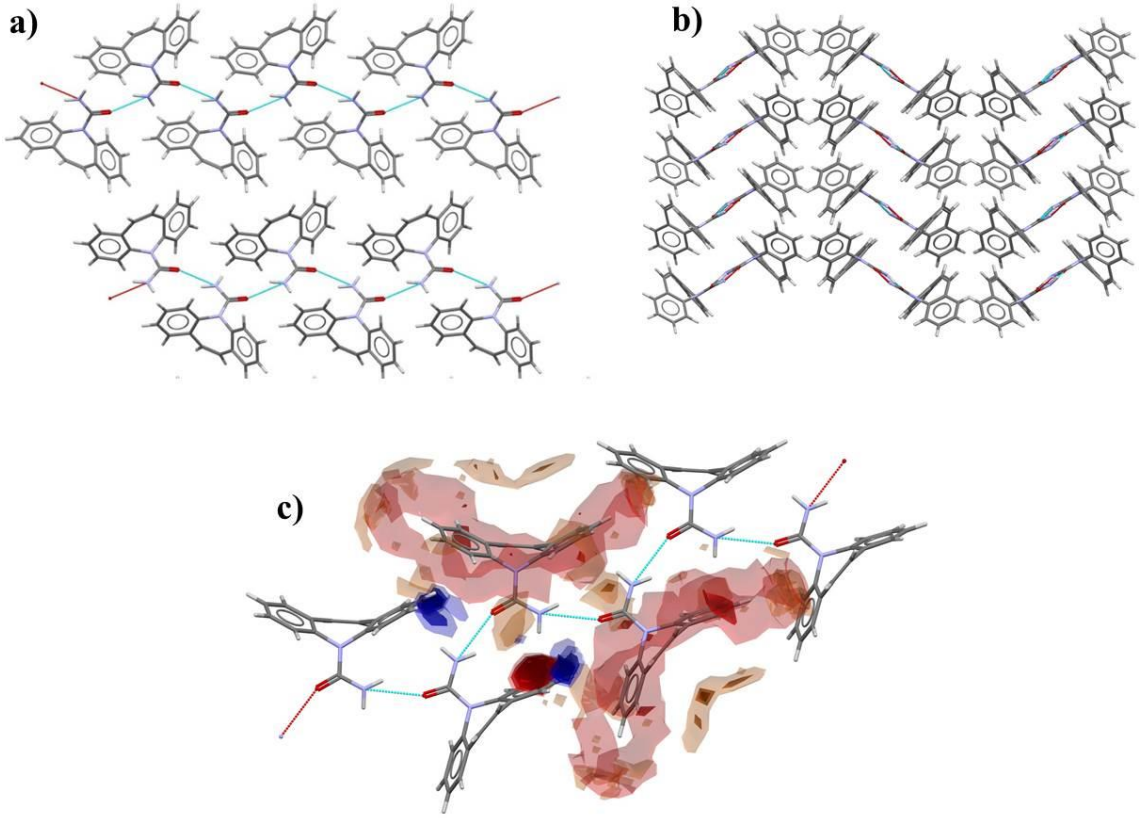

Figure 27 - *(a)* Packing of carbamazepine polymorph V illustrating the CBZ chains along the *a* axis and *(b)* how these layers of chains interact along *b*. The interaction map in (c) shows the fulfilment of favourable regions of interaction around the CBZ molecules.

3.2.6 CBZ acetone solvate (CBZ:ACE)

The crystal structure consists of dimers of CBZ ($R^2_2(8)$, N–H···O: D=2.928 Å, d=2.095 Å, θ=157.22º, θ^{AB}=11.68º). The dimers are linked to two molecules of acetone through N–H···O hydrogen bond between the amine group of CBZ and the carbonyl of acetone (D=3.018 Å, d=2.275 Å, θ=142.09º) (Figure 28). The interaction map also suggests that weaker contacts contribute to the packing stabilization. While the CBZ carbonyl interacts with the methyl groups of neighbouring acetone molecules, the acetone carbonyl is close to the azepine and benzene groups of CBZ. It is also shown in Figure 28 that the CBZ:acetone N–H···O hydrogen bonds

geometry almost falls out of the preferred region of interaction, while the proximity of the benzoazepine portion occupies the remaining favourable region in the crystal.

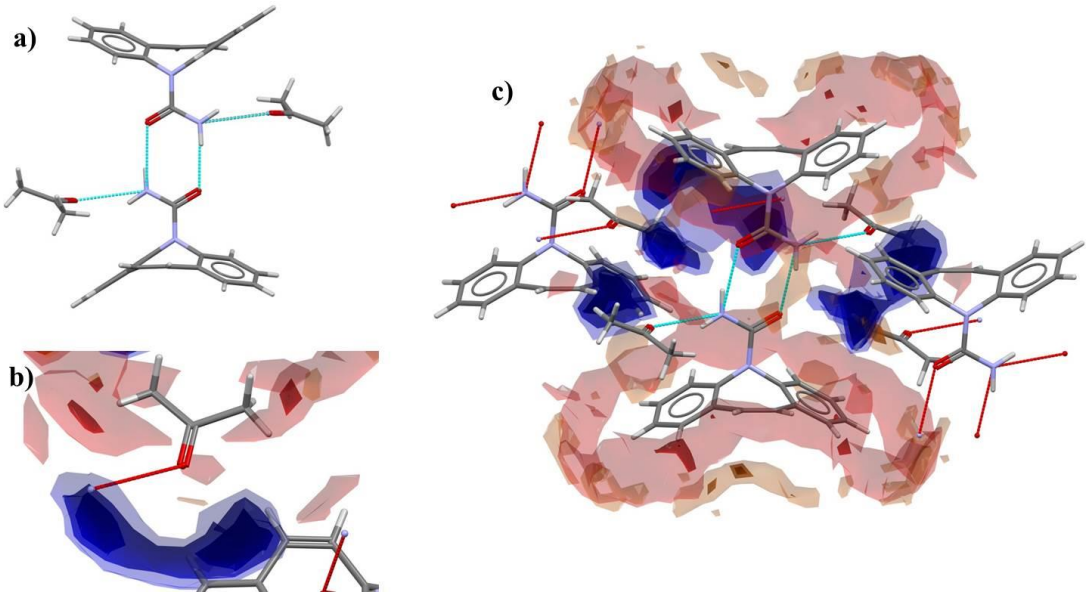

Figure 28 - Main hydrogen bonds observed in the CBZ:ACE solvate (a). The interaction map shows that the N–H···O hydrogen bond between CBZ and acetone presents an offset configuration in the map contour (b). Additional C–H groups occupy these favourable regions and stabilise the packing (c).

Similar to the structure of CBZ Form III, the inversed-cup type of stacking also shows the strongest intermolecular energy in the structure of CBZ:ACE (-44.5 kJ mol^{-1}), as CBZ dimers and CBZ:solvent give values of -30.5 kJ mol^{-1} and -23.9 kJ mol^{-1}. The distance between stacked benzene rings along *a* is 3.756 Å and 6.619 Å along *a* (Figure 29).

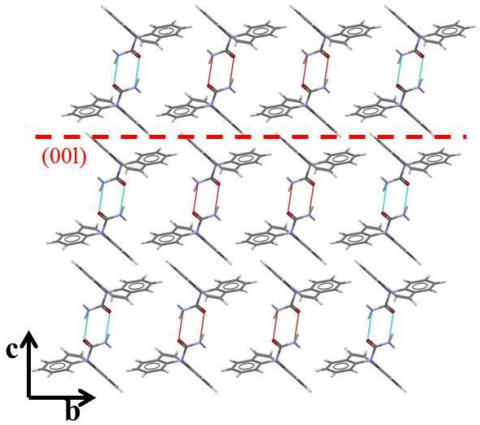

Figure 29 - Packing of CBZ molecules in CBZ:ACE detailing the (00l) plane (acetone molecules are omitted).

The acetone molecules arrange in channels along the *a* and *b* axes resulting in "crossing-channels" as a result of interpenetration. It is evident from Figure 30 that the channels do not present a smooth surface and the acetone molecules forms almost layers crossing to the *c* axis. The surface of the channel is composed of aromatic portions of CBZ and polar

carboxamide fragments in the $R^2_2(8)$ motif. The volume related to this solvent arrangement corresponds to 152.35 $Å^3$ and is equivalent to 20.0% of the unit cell. The calculated BFDH morphology corresponds to blocks.

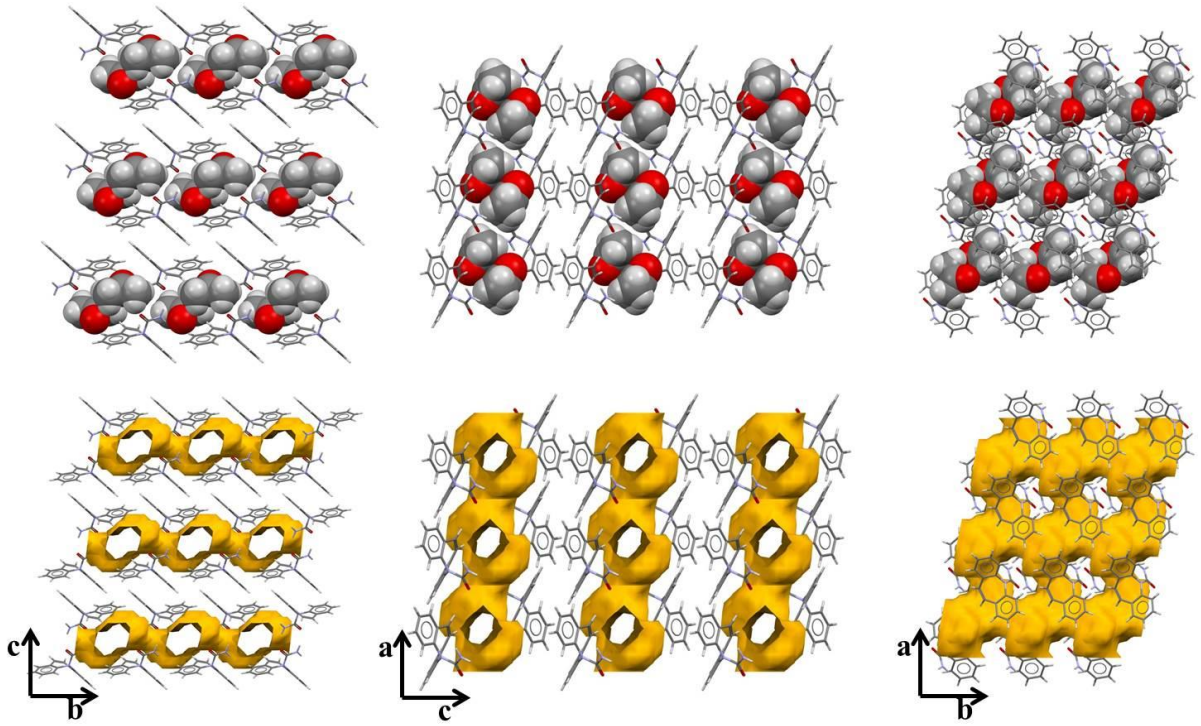

Figure 30 - Organization of acetone molecules in the CBZ:ACE solvate. The solvent molecules are highlighted in spacefill (top row) and the virtual voids are also shown (bottom row).

3.2.7 CBZ dimethylsulfoxide solvates (CBZ:DMSO)

The CBZ:DMSO system is known to exist in two different structures, one stable at room temperature and another stable at lower temperature.[193] The polymorphs are, however, very similar and show differences only in the disorder of the DMSO molecules. While the room temperature form has dynamic disorder and interchangeable DMSO configurations, the low temperature form contains static disorder. The structure selected for analysis in this section represents the form stable at room temperature (UNEYIV01), as it is more appropriate to the experimental discussion. The crystallographic data for the low temperature form is, however, presented in Table 2.

UNEYIV01 crystal structure consists of dimers of CBZ ($R^2_2(8)$, N–H···O: D=2.986 Å, d=2.150 Å, θ=163.94º, θ^{AB}=7.63º) linked to two molecules of DMSO (Figure 31). The CBZ-DMSO hydrogen bond parameters are not displayed as the solvent molecules are disordered. In this case, the static measurements of bond lengths do not represent the reality in the crystal. The same observation is accounted throughout the chapter where structures present dynamic disorder.

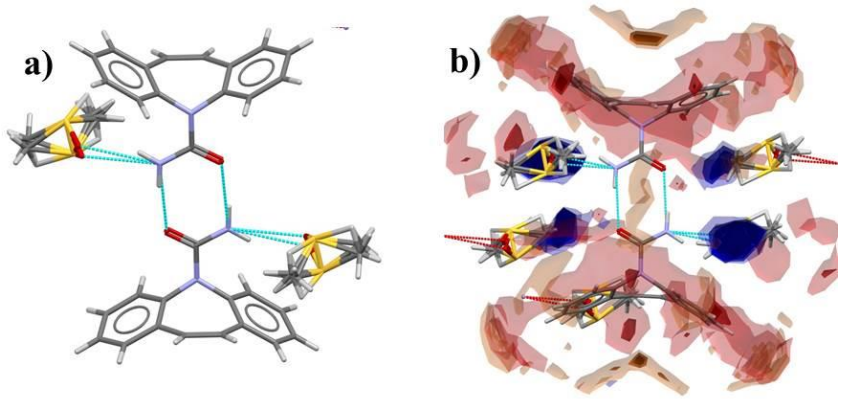

Figure 31 - Main hydrogen bonds observed in the CBZ:DMSO solvate (a). The interaction map of the CBZ dimer bonded to DMSO molecules shows missing regions of favourable interactions which are filled by additional interactions with other DMSO molecules (b).

Additional interactions are also observed between the benzene groups and the neighbouring sulfoxide groups. The packing of CBZ:DMSO is characterised by the inverse-cup motif along *a* with stacking of benzene rings distanced by 3.756 Å and 6.787 Å (Figure 32). The intermolecular energy between these stacked molecules corresponds to -44.4 kJ mol^{-1}, while the CBZ dimer and the CBZ:solvent molecule interaction resulted in -28.3 kJ mol^{-1} and -27.8 kJ mol^{-1}.

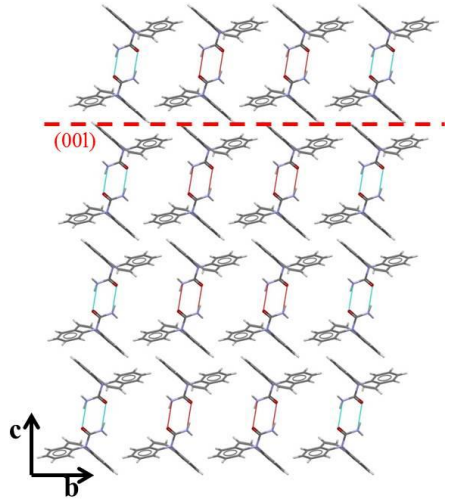

Figure 32 - Packing of CBZ molecules in CBZ:DMSO detailing the (00l) plane (DMSO molecules are omitted).

The DMSO molecules are arranged in crossing-channels along the *a* and *b* axes (Figure 33). The channels do not have a smooth surface and the DMSO molecules may be considered to almost form layers perpendicular to the *c* axis. The surface of the channel is composed of the aromatic portions of CBZ and the polar fragments of amine and carbonyl in $R^2_2(8)$ motis. The volume related to the solvent arrangement corresponds to 204.60 $Å^3$ and is equivalent to 25.7% of the unit cell. The calculated BFDH morphology corresponds to blocks.

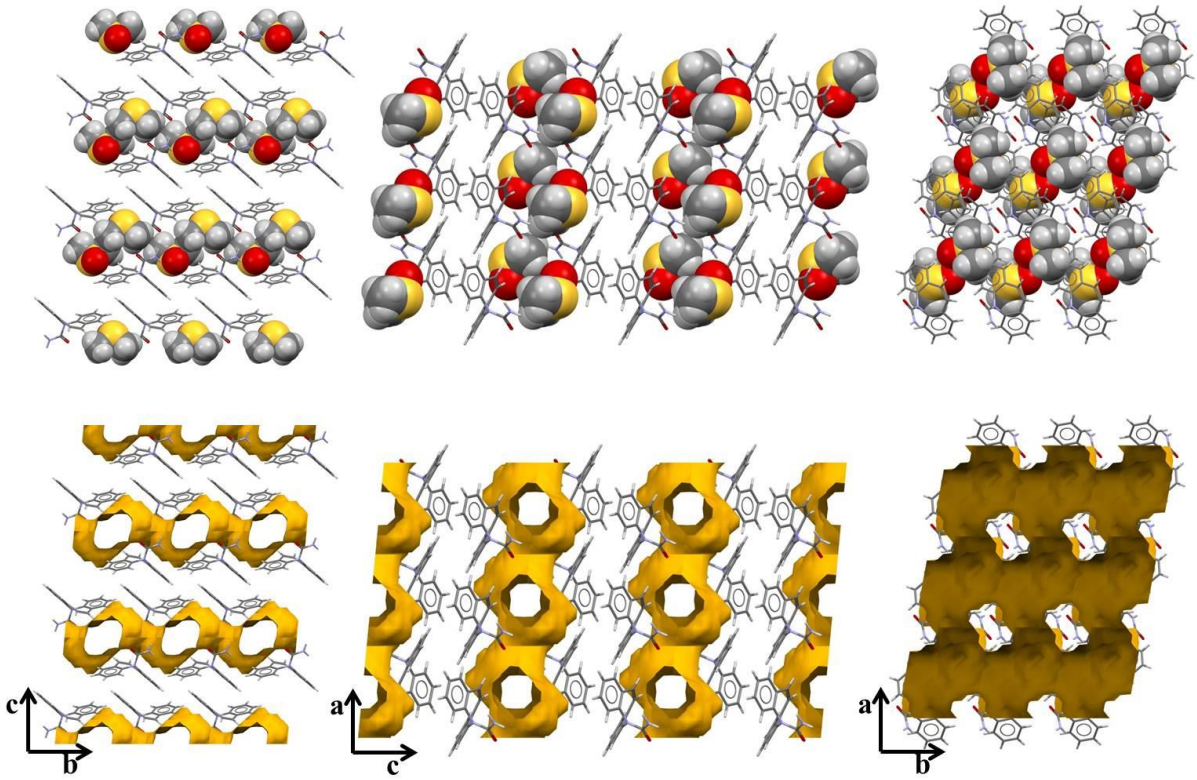

Figure 33 - Organization of DMSO molecules in the CBZ:DMSO solvate. The solvent molecules are highlighted in spacefill (top row) and the virtual voids are also shown (bottom row).

3.2.8 CBZ dimethylformamide solvate (CBZ:DMF)

The crystal structure of the DMF solvate is very similar to the acetone and DMSO forms. It consists of dimers of CBZ ($R^2_2(8)$, N–H···O: D=2.972 Å, d=2.103 Å, θ=167.40º, θ^{AB}=15.55º) linked to two molecules of DMF through N–H···O hydrogen bond between the amine group of CBZ and the carbonyl from DMF (D=2.822 Å, d=1.963 Å, θ=154.47º) (Figure 34). In contrast to the earlier solvates, DMF molecules form dimers and additional $R^2_4(8)$ motifs from methyl groups of DMF to the neighbouring carbonyl groups of DMF and CBZ. These characteristics are evident in the interaction map as extra DMF molecules occupy the favourable regions of hydrogen bond donors in the structure.

DMF presents a larger molecule in which the methyl groups are more separated from the carbonyl than DMSO and acetone. In fact, to accommodate these changes into a similar CBZ scaffolding as observed in the CBZ:ACE solvate, for example, the DMF molecules has to rearrange. Figure 35 shows the differences in orientation of the solvent molecules for both structures along the *a* and *b* axes. While in the CBZ:ACE solvate the hydrogen bonds between CBZ and solvent are stablished along the *a* axis, in CBZ:DMF, these interactions run along *b*.

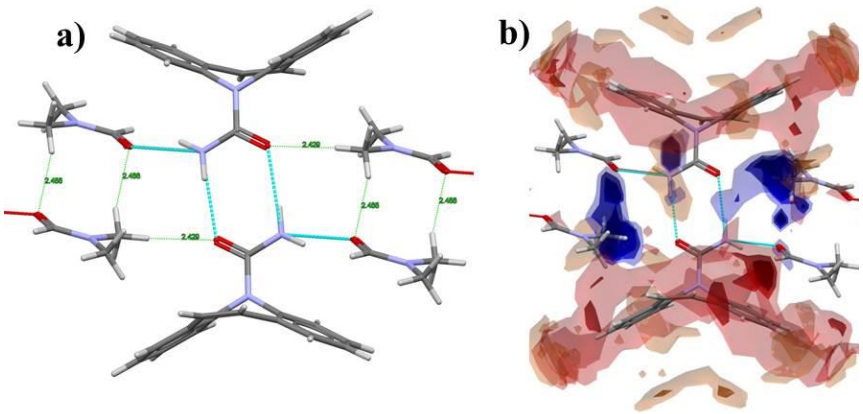

Figure 34 - Main hydrogen bonds observed in the CBZ:DMF solvate and additional DMF dimer and $R^2_4(8)$ motif with two CBZ and two DMF molecules (a). The interaction maps of the CBZ dimer bonded to DMF molecules show missing regions of favourable interactions that are filled by additional C–H···O interactions with other DMF molecules (b).

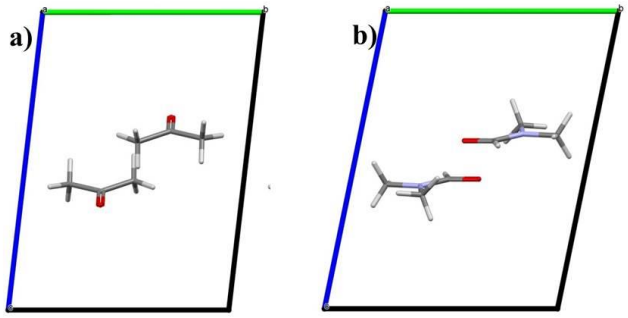

Figure 35 - Comparison of the solvent molecules of CBZ:ACE (a) and CBZ:DMF (b) oriented down the *a* axis.

The changes in the solvent orientation, however, do not change the lattice arrangement. The packing of CBZ:DMF is characterised by the inversed-sup motif, which leads to the stacking of benzene rings distanced by 3.671 Å and 6.717 Å along *a* (Figure 36). The intermolecular energy between these stacked molecules correspond to -45.2 kJ mol^{-1}, while the CBZ dimer and the CBZ:solvent molecule energy resulted in -30.6 kJ mol^{-1} and -32.4 kJ mol^{-1}.

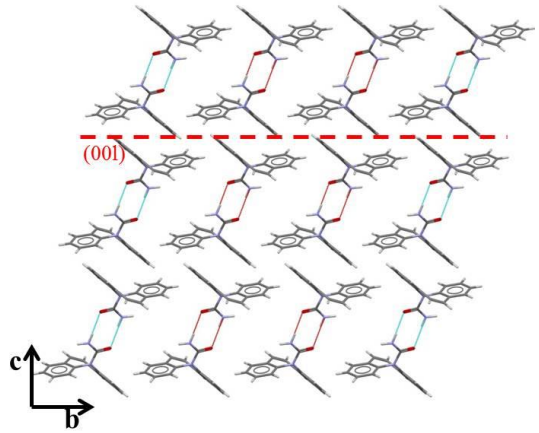

Figure 36 - Packing of CBZ molecules in CBZ:DMF detailing the (00l) plane (DMF molecules are omitted).

The DMF molecules arrangein crossing-channels along *a* and *b* axes (Figure 37). The channels in CBZ:DMF are not smooth and the DMF molecules almost form layers perpendicular to the *c* axis (although the connection between the channels is clearly smaller than the previous solvates). The surface of the channel is composed of the aromatic portions of CBZ and the polar fragments of amine and carbonyl in $R^2_2(8)$ motifs. The volume related to the solvent arrangement corresponds to 153.88 $Å^3$ and is equivalent to 19.5% of the unit cell. The calculated BFDH morphology corresponds to blocks.

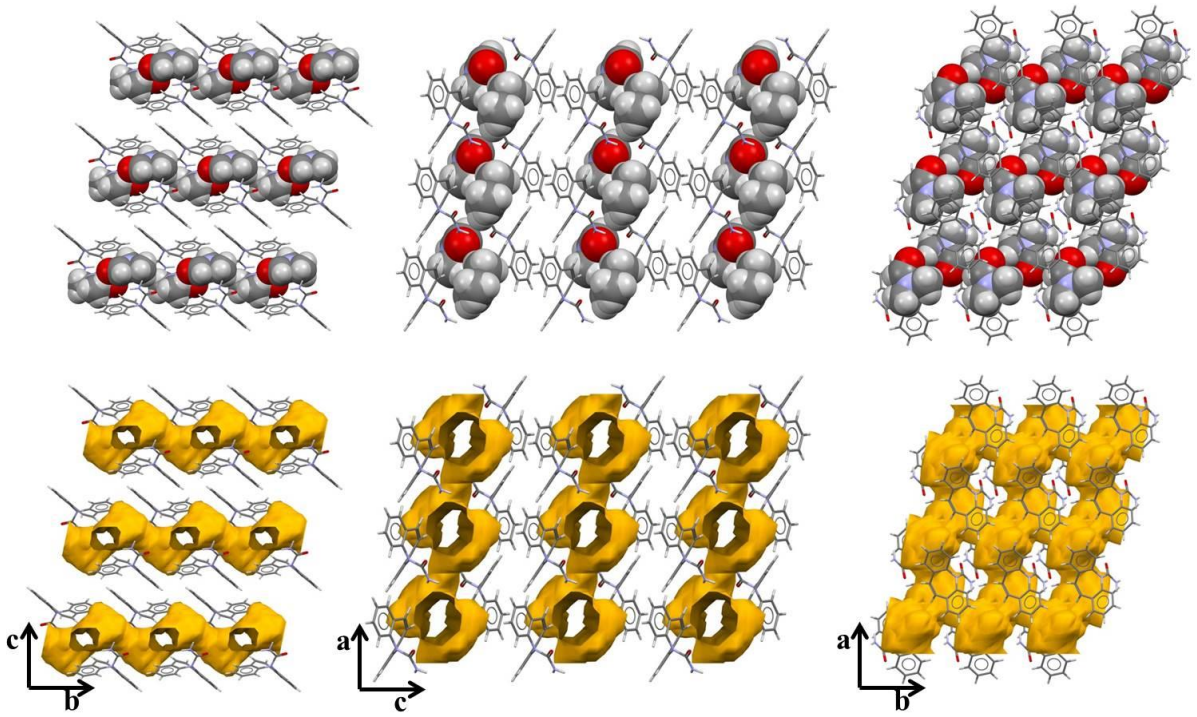

Figure 37 - Organization of DMF molecules in the CBZ:DMF solvate. The solvent molecules are highlighted in spacefill (top row) and the virtual voids are also shown (bottom row).

3.2.9 CBZ dimethylacetamide solvate (CBZ:DMA)

The crystal structure consists of dimers of CBZ ($R^2_2(8)$, N–H···O: D=2.944 Å, d=2.036 Å, θ=163.60º, θ^{AB}=n/a) linked to two disordered molecules of DMA (Figure 38). Similar to the DMF solvate, additional $R^2_4(8)$ motifs are formed from methyl groups of DMA to neighbouring DMA and CBZ carbonyls. While the proximity of benzene C–H groups is also observed, the interaction map illustrates how important the DMA molecules are in the stabilization of the structure.

Although the interaction motif of is very similar in comparison to the CBZ:DMF solvate, CBZ:DMA presents a somewhat distinct packing arrangement (Figure 39). The structure analysis of CBZ:DMF suggests that one additional carbon in the chain (as observed

in DMA) would hinder the main hydrogen bonding between solvent and CBZ. This might be the cause for such a substantial change of CBZ arrangement in the DMA solvate.

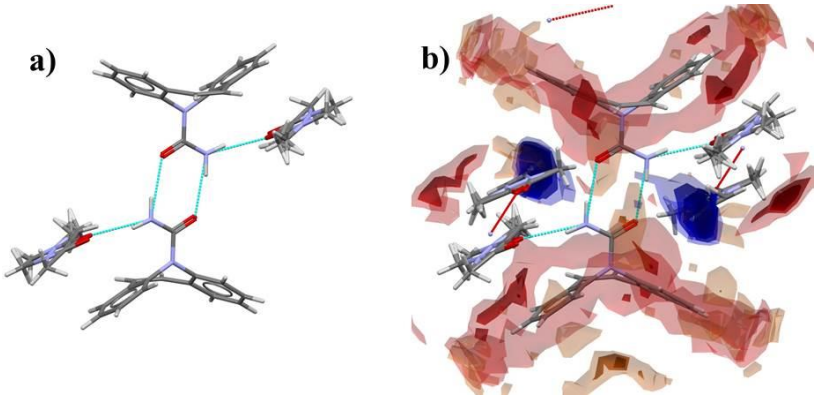

Figure 38 - Main hydrogen bonds observed in the CBZ:DMA solvate showing the disorder in DMA (a). The interaction maps of the CBZ dimer bonded to DMA molecules show missing regions of favourable contacts that are filled by additional interactions with other DMA molecules (b).

The CBZ:DMA lattice is a subtype of the translational stacking mode (coformer-pairing) in which the coformer molecules intercalate the CBZ dimers along *a*. In this case, it is expected that the energetic relationship between different "stacked" molecules is less significant due to the interweaving solvent molecules. In fact, these "stacked" CBZ molecules show only -13.7 kJ mol^{-1} of intermolecular energy, while the CBZ dimer, the CBZ:solvent hydrogen bonded molecules and the "stacked" CBZ:solvent are characterised by -33.0 kJ mol^{-1}, -39,3 kJ mol^{-1} and -24.5 kJ mol^{-1}, respectively.

The "stacked" dimers along *a* are organised in layers of the same orientation along the *c* axis in which their azepine C-H face each other. Along *b*, these layers change orientation and the combination of all these characteristics creates a curious three-dimensional honeycomb-like structure (Figure 40). The DMA molecules are arranged in large and smooth channels corresponding to 445.62 $Å^3$ and equivalent to 26.0% of the unit cell. The surface of the channel is again composed of the dibenzoazepine portions of CBZ and the polar fragments of amine and carbonyl in $R^2_2(8)$ motis. The calculated BFDH morphology corresponds to blocks.

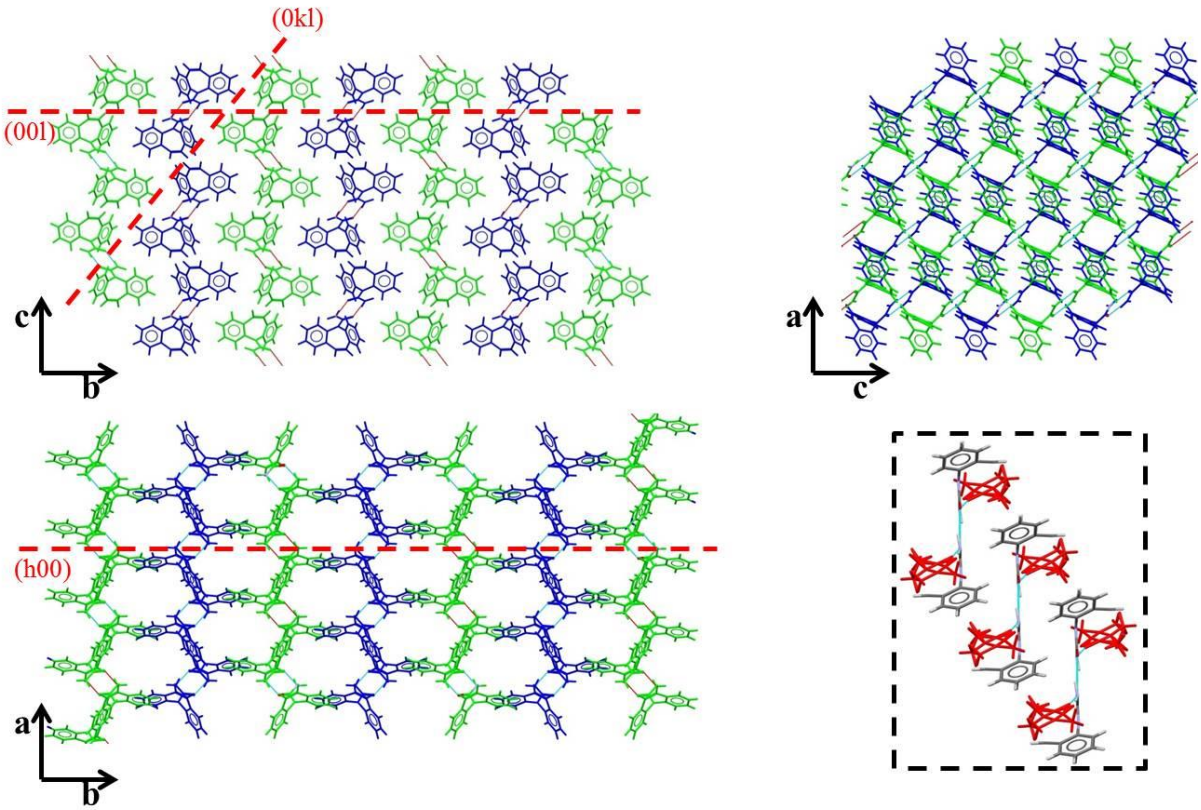

Figure 39 - Packing of CBZ molecules in CBZ:DMA solvate (DMA molecules are omitted). The colours of the molecules (green and blue) distinguish layers of dimers with different orientations down *a*. Details include: the clipping illustrating the translational stacking of the dimers paired with DMA molecules (in red), and the (00l), (0kl) and (h00) planes.

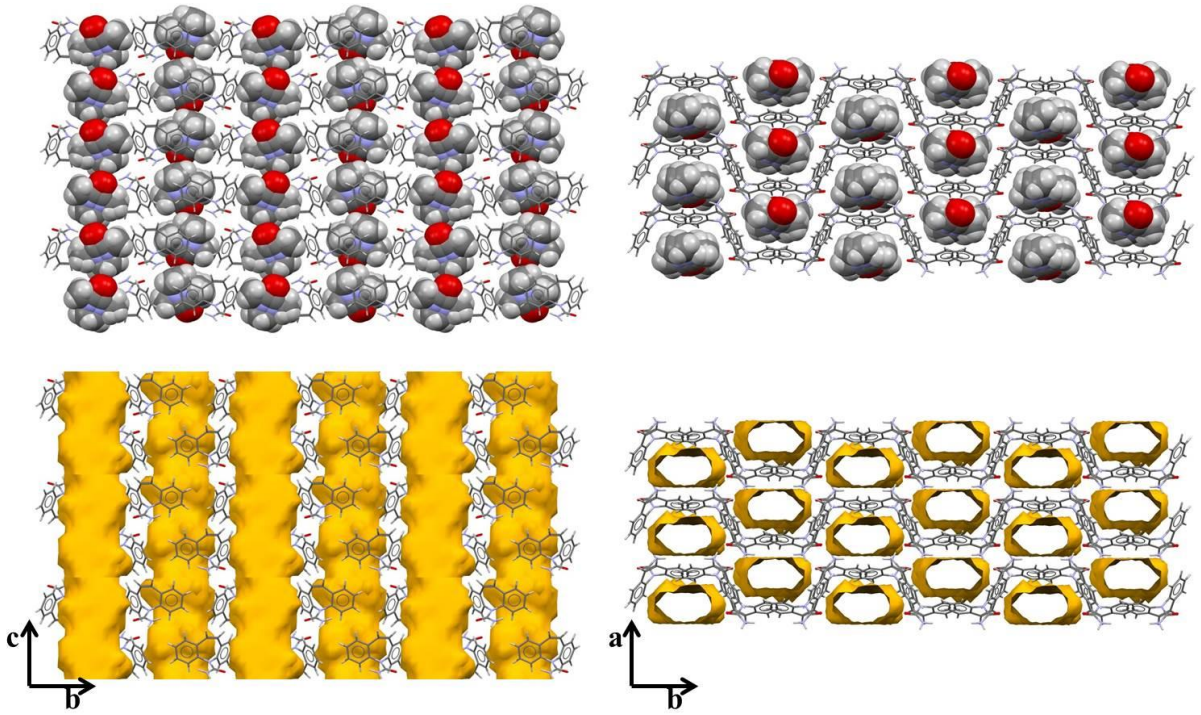

Figure 40 - Organization of DMA molecules in the CBZ:DMA solvate. The solvent molecules are highlighted in spacefill (top row) and the virtual voids are also shown (bottom row).

3.2.10 CBZ benzoquinone cocrystals (CBZ:BZQ and 2CBZ:BZQ)

A CBZ benzoquinone cocrystal was first described by Fleishman et.al (2003) as part of a crystal engineering study of carbamazepine synthons in multicomponent materials. This form has a 2:1 stoichiometry and is reported in the CSD as UNEYOB. The 2CBZ:BZQ cocrystal was initially obtained by slow solvent evaporation starting from a 1:1 proportion of CBZ and BZQ (the solvent used was not reported). In our screening studies, however, a 1:1 stoichiometry was also crystallised. The CBZ:BZQ cocrystal was initially obtained from a slurry in ethanol at high proportions of BZQ, following the reactive crystallization method proposed by Rodriguez-Hornedo and her colleagues. Later, CBZ:BZQ was also obtained from cooling and other slurry experiments, always with high quantities of unreacted BZQ. Full details and the observed phase diagram are presented in Chapter 4.

With respect to its crystal structure, the CBZ:BZQ cocrystal consists of dimers of CBZ ($R^2_2(8)$, N–H···O: D=2.902 Å, d=1.996 Å, θ=177.17º, θ^{AB}=n/a). The dimers are linked to two molecules of BZQ through N–H···O hydrogen bond between the amine group of CBZ and the carbonyl from BZQ (D=2.985 Å, d=2.140 Å, θ=157.43º) (Figure 41).

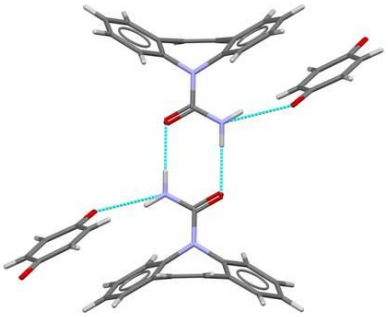

Figure 41 - Main hydrogen bonds observed in the CBZ:BZQ cocrystal.

Additional contacts exist from aromatic and BZQ C–H groups to neighbouring CBZ carbonyl groups. From the interaction map it is indeed shown that the diene portion of BZQ and the CBZ benzene rings occupy favourable regions for hydrogen bond donors (Figure 42). The BZQ carbonyl which is not hydrogen bonded to the CBZ dimer is stabilized by surrounding aromatic groups (C–H···O, D=3.503 Å, d=2.601 Å, θ=158.65º).

The packing of CBZ:BZQ resembles the CBZ:DMA solvate, except for the fact that the different layers along b are stacked in the same direction. The lattice is also a subtype of the translational stacking mode which produces coformer molecules intercalating the CBZ dimers along *a*. The solvent molecules interact via stacking to the CBZ aromatic ring accounting for -28.8 kJ mol^{-1} of intermolecular energy. In comparison, the energetic relationship between the

CBZ dimer, CBZ:coformer molecules and the CBZ:CBZ "stacked" molecules (paired to BZQ) correspond to -34.2 kJ mol^{-1}, -32.8 kJ mol^{-1} and -20.0 kJ mol^{-1}.

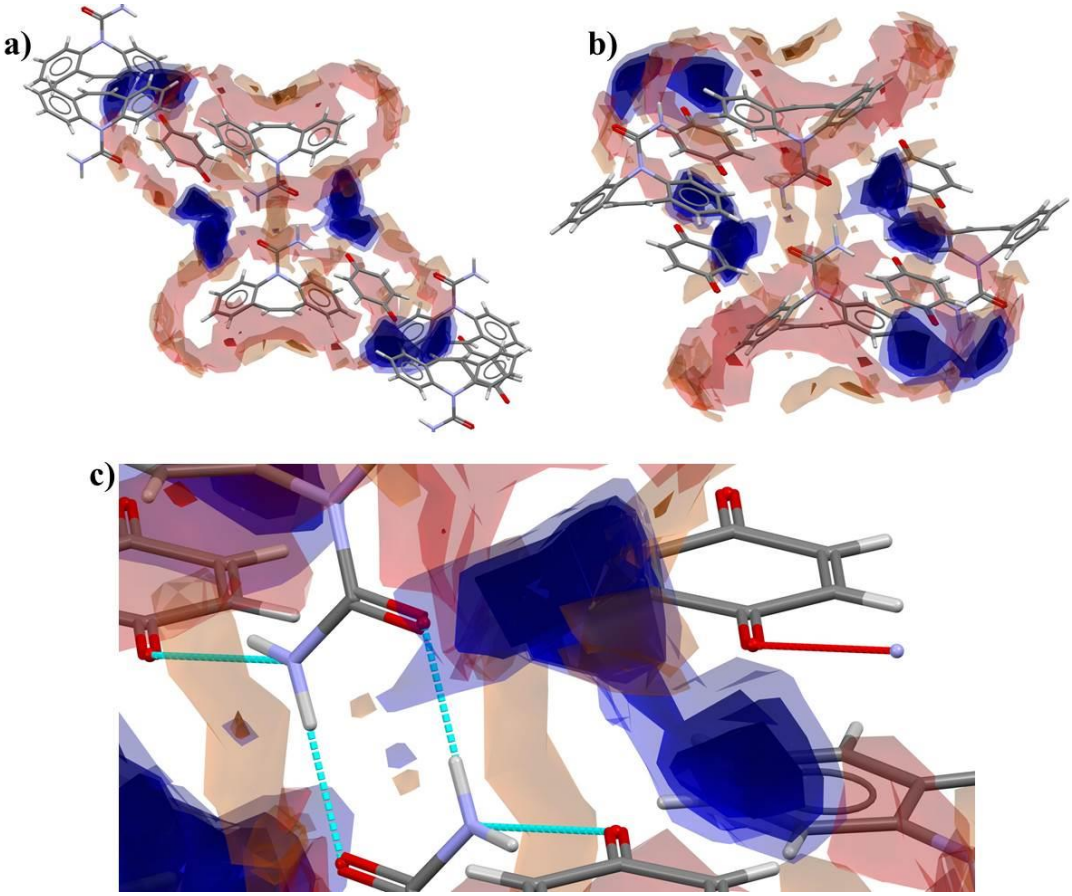

Figure 42 - The interaction map of the CBZ dimer bonded to BZQ molecules in CBZ:BZQ show missing regions of favourable interactions. These regions are occupied by CBZ aromatic groups and BZQ diene portions. a) shows contacts around the BZQ carbonyl which is not bonded to the CBZ dimer; and b) shows the contacts around the dimers and the respective hydrogen bonded BZQ (zoomed in c).

The BZQ molecules are also arranged in large channels along the *c* axis leading to a honeycomb-like lattice (Figure 44). The surface of the channel is also composed of dibenzoazepine portions of CBZ and the polar fragments of amine and carbonyl in the $R^2_2(8)$ motis. The channels, however, do not present a surface as smooth as the DMA solvate, which might also be related to the DMA disordered structure. The volume related to the BZQ arrangement corresponds to 274.83 $Å^3$ and is equivalent to 32.0% of the unit cell. The calculated BFDH morphology corresponds to blocks.

The analysis of CBZ:DMA and CBZ:BZQ paired stacking motif show that the interweaving coformer molecules are critical to this type of packing arrangement. In this case, lower coformer activities during the crystallization or during desolvation and sublimation experiments may lead to the collapse of the structure not because of strain along the channel, but as a response to the stacking disruption. This behaviour is unusual for inclusion channelled materials in which the coformer do not normally affect the packing of the host. While

CBZ:DMA did not show additional solvated forms during the screening, the BZQ system had already reported a cocrystal with an intermediate stoichiometry (as previously mentioned). It suggests that in the case of BZQ cocrystals, the structure do not collapse upon sublimation, but rearrange at lower BZQ activities.

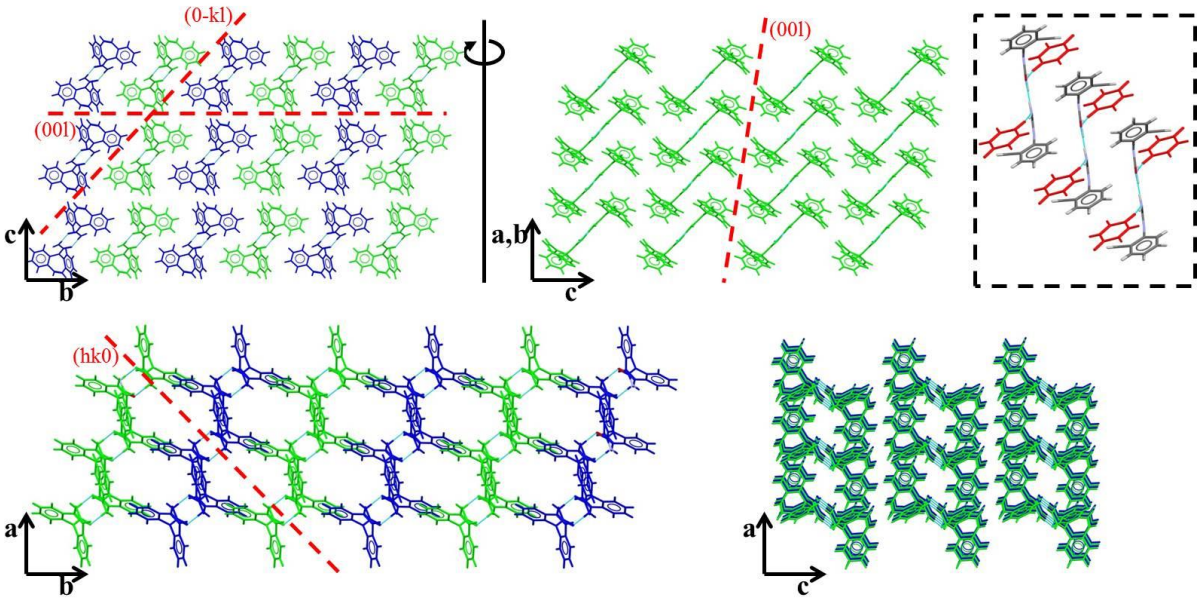

Figure 43 - Packing of CBZ molecules in CBZ:BZQ cocrystal (BZQ molecules are omitted). The colours of the molecules (green and blue) distinguish layers of dimers along b that present the same orientation down *a*. Details include: the clipping illustrating the translational stacking of the dimers paired with BZQ molecules (in red), and the (hk0), (0-kl) and (00l) planes.

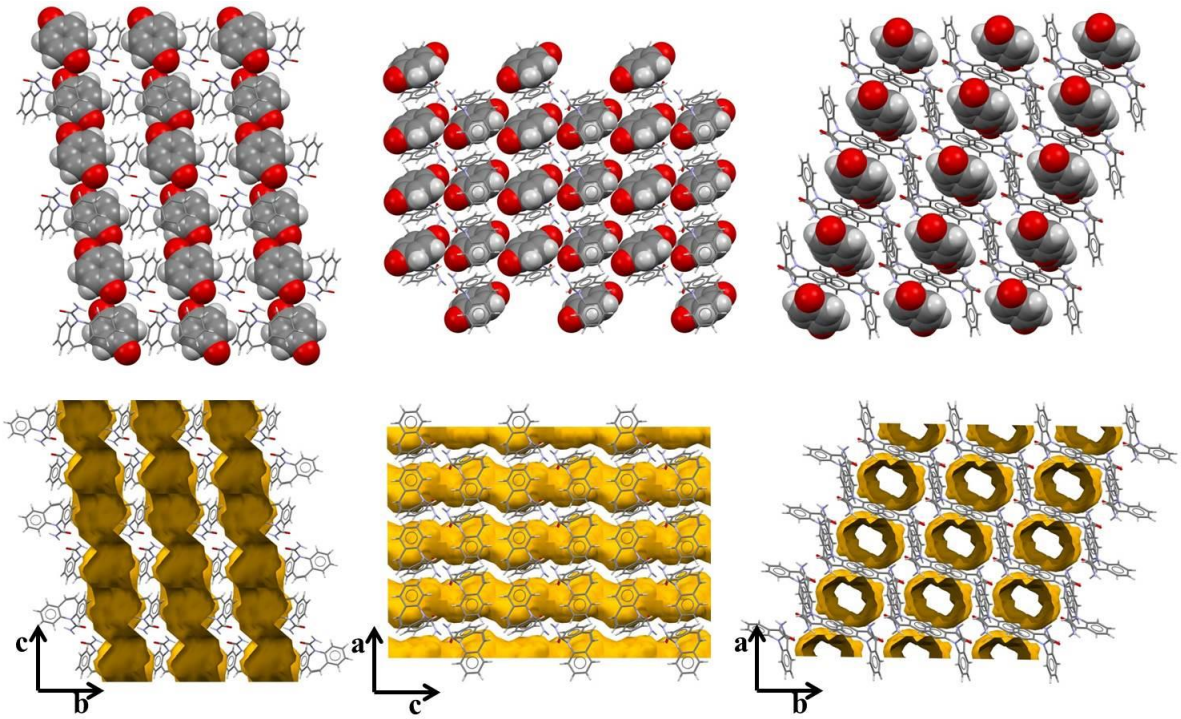

Figure 44 - Organization of BZQ molecules in the CBZ:BZQ cocrystal. The coformer molecules are highlighted in spacefill (top row) and the virtual voids are also shown (bottom row).

The reported 2CBZ:BZQ cocrystal also consists of dimers of CBZ ($R^2_2(8)$, N–H···O: D=2.900 Å, d=2.027 Å, θ=171.38º, θ^{AB}=n/a). The dimers are linked to one molecule of BZQ through an N–H···O hydrogen bond between the amine group of CBZ and the carbonyl from BZQ (D=3.116 Å, d=2.323 Å, θ=149.72º) (Figure 45). Additional C–H contacts are also observed from aromatic and BZQ C–H groups to a neighbouring CBZ carboxamide. From the interaction maps it is shown that the diene portion of BZQ occupies favourable regions of hydrogen bond donors around the CBZ carbonyl, while there is one region around the BZQ carbonyl which is not ideally occupied. This missing region is located between stacked CBZ molecules.

The packing of 2CBZ:BZQ is composed of stacked CBZ dimers along *c* (Figure 46). It resembles the 1:1 cocrystal, except for the fact that CBZ molecules stack in opposite directions along *b* and the BZQ molecules do not intercalate the stacks. The coformer, in this case, interacts via stacking with other BZQ molecules perpendicularly distanced by 3.208 Å. With respect to the energetic relationship between molecules in the structure, the stacking of BZQ molecules accounts for only -9.5 kJ mol^{-1} of intermolecular energy. In contrast, the CBZ dimer, CBZ:coformer hydrogen bonded molecules and the CBZ stacked molecules correspond to -33.1 kJ mol^{-1}, -22.6 kJ mol^{-1} and -46.4 kJ mol^{-1}.

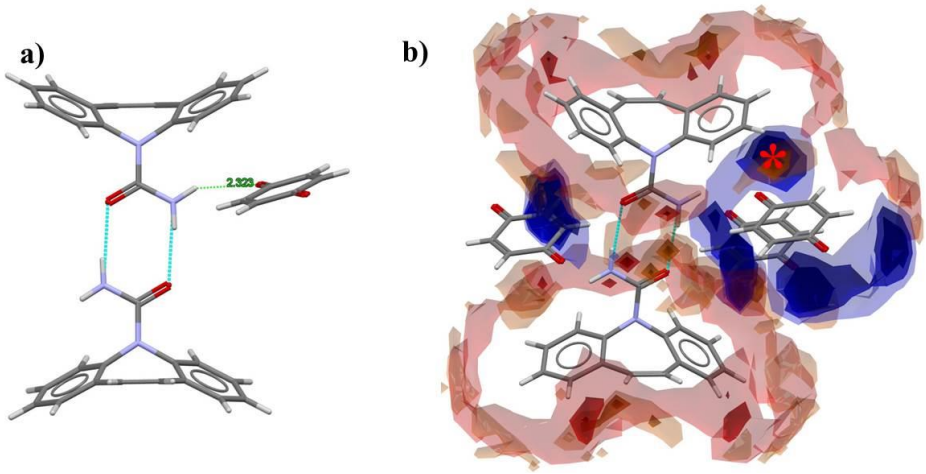

Figure 45 - Main hydrogen bonds observed in the 2CBZ:BZQ cocrystal (a). The interaction map of the CBZ dimer bonded to the BZQ molecule show missing regions of favourable contacts that are filled by additional interactions with other BZQ molecules (b). The star shows a region around the coformer carbonyl that does not present complementary groups of interaction.

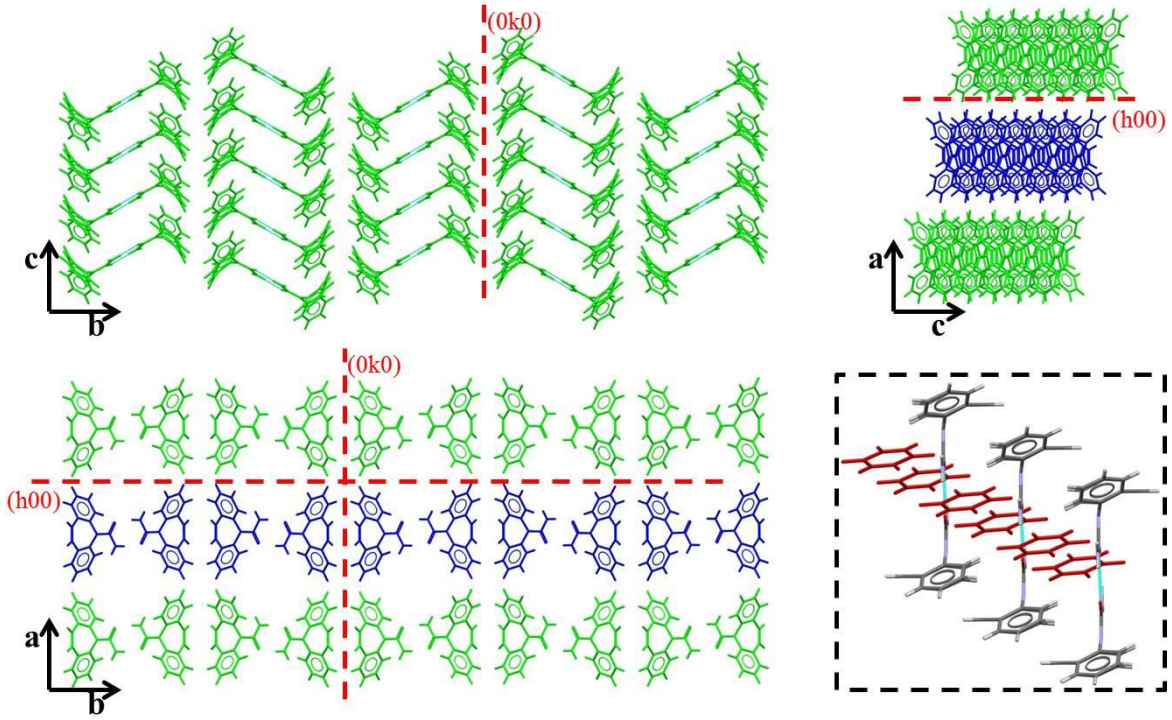

Figure 46 - Packing of CBZ molecules in 2CBZ:BZQ cocrystal (BZQ molecules are omitted). As a comparison to the previous structures, molecules interacting via their dibenzoazepine portions were characterised in different colours (green and blue). In the 2CBZ:BZQ cocrystal, however, the layers of dimers present distinct orientation along *b*, while same orientation along *a*. Details include: the clipping illustrating the translational stacking of the dimers in comparison to the BZQ molecules (in red), and the (0k0) and (h00) planes.

Another interesting aspect deriving from the interactions of molecules in this stacked structure are the low interaction energies between planes on (0k0) and (h00). Also, while (0k0) is formed only by the dibenzoazepine portion of CBZ molecules, the (h00) is formed by the aromatic parts of CBZ and runs through BZQ molecules. Without taking into account any energy comparison, it is interesting to observe that the geometric parameters of these planes related to the molecular axis of the CBZ dimers also differ and may play distinct role when the coformer sublimes.

The BZQ molecules in 2CBZ:BZQ are arranged in channels along the *c* axis (Figure 47). The channels give rise to a smooth surface composed of the aromatic portions of CBZ and the polar fragments of amine and carbonyl in $R^2_2(8)$ motif. The volume related to the BZQ arrangement corresponds to 267.55 $Å^3$ and is equivalent to 19.2% of the unit cell. The calculated BFDH morphology corresponds to needles, with the main crystal axis running along the channels.

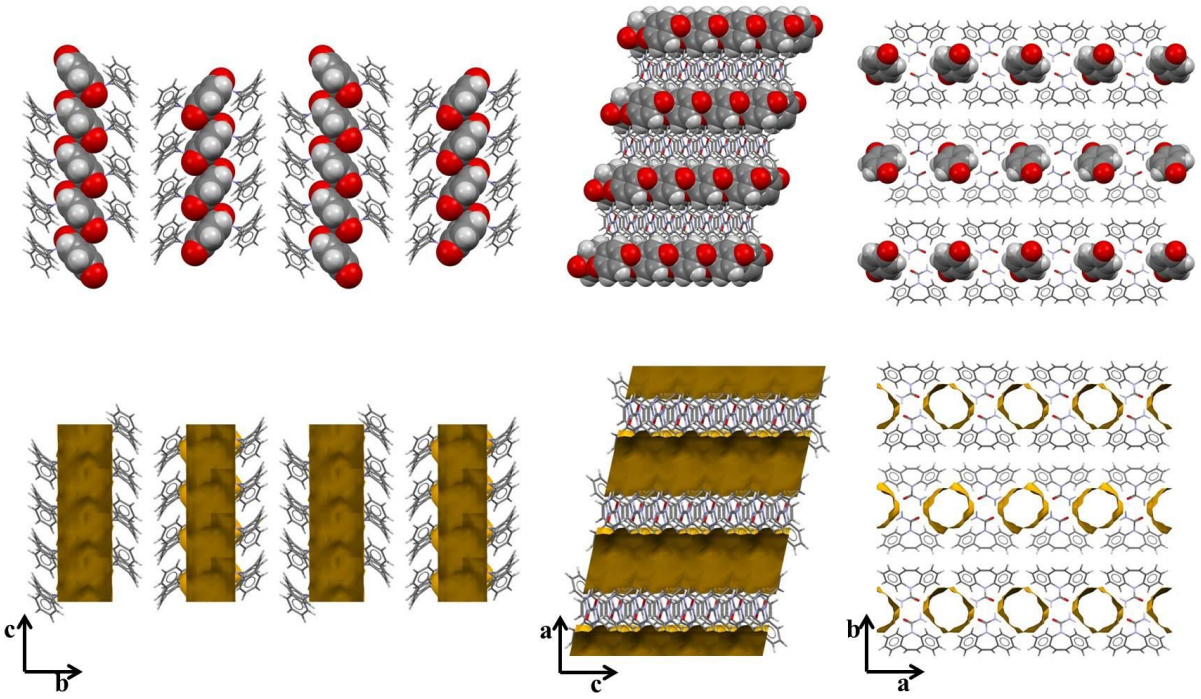

Figure 47 - Organization of BZQ molecules in the 2CBZ:BZQ cocrystal. The coformer molecules are highlighted in spacefill (top row) and the virtual voids are also shown (bottom row).

3.2.11 CBZ oxalic acid cocrystal (2CBZ:OXA)

The 2CBZ:OXA cocrystal is very similar to the structure of 2CBZ:BZQ. Screening experiments, however, did not result in additional cocrystals of different stoichiometry. The structure was previously reported in the CSD as MOXWUS, however the file did not contain information concerning the oxalic acid molecules as the authors used SQUEEZE during the crystal solution and refinement and characterised the cocrystal as CBZ:X. In order to get a better understanding of the structure and the hydrogen bonding to the coformer, new single crystal data was collected and the proposed model is discussed below. The crystallography data for both structures, however, are, shown in Table 2.

The 2CBZ:OXA cocrystal consists of dimers of CBZ composed of non-equivalent CBZ molecules tilted by 6.40º ($R^2_2(8)$, N–H···O: D_1=2.896 Å, d_1=1.873 Å, θ_1=169.26º, and D_2=2.829 Å, d_2=1.797 Å, θ_2=172.66º). This particularity is a result of the interaction to an oxalic acid molecule presenting twisted carboxylic groups in different planes (Figure 48). While one carboxylic portion bonds to the amine and carbonyl groups of different CBZ molecules interacting in one dimer (O–H···O: D_1=2.568 Å, d_1=1.538 Å, θ_1=173.51º; and N–H···O: D_2=2.829 Å, d_2=2.189 Å, θ_2=118.92º), the other carboxylic group from the same molecule bonds to the amine and the carbonyl of different CBZ molecules stacked along *c* (N–H···O: D_1=2.864 Å, d_1=1.906 Å, θ_1=153.16º; and O–H···O: D_2=2.531 Å, d_2=1.508 Å, θ_2=166.77º). It

is suggested that the complexity of the twisted conformation of oxalic acid is the reason why SQUEEZE was applied in the previous attempt of solving the structure.

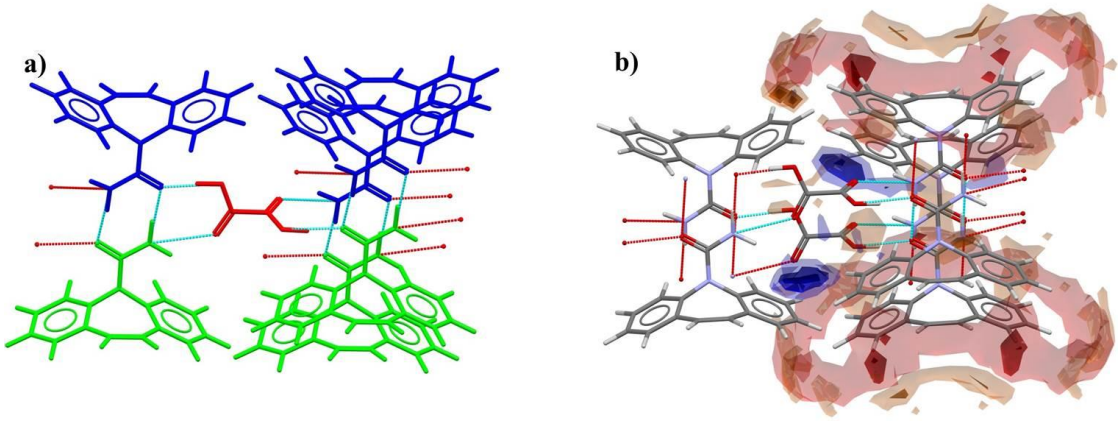

Figure 48 - Main hydrogen bonds observed in the 2CBZ:OXA cocrystal showing the non-equivalence of molecules and the twisted conformation of the oxalic acid molecules (a). The interaction map of the CBZ dimer bonded to the coformer show missing regions of favourable contacts that do not present complementary groups of interaction.

Additionally, C–H contacts are also observed from aromatic groups to neighbouring CBZ carboxamide. The interaction map shows, however, regions around the oxalic acid carbonyl that are not favourably occupied and do not form hydrogen bonds. These regions fall in between stacked benzene rings in a very similar way as observed in 2CBZ:BZQ.

The crystal structure of 2CBZ:OXA is composed of stacked CBZ dimers along *c*, which form different layers of opposite directions along *b* (Figure 49). The structure also shows probable slip planes on (0k0) and (h00) and hence the same characteristics which were described for 2CBZ:BZQ. With respect to the energetic relationship between, the stacked CBZ molecules correspond to the stronger interactions in the structure (-42.0 kJ mol^{-1}/-41.6 kJ mol^{-1} for both independent molecules 1 and 2). In turn, the intermolecular energy of the CBZ dimer, CBZ_{dimer}:coformer and CBZ_{stack}:coformer molecules correspond to -37.8 kJ mol^{-1}, -30.7/-18.0 kJ mol^{-1} and -28.2/-30.2 kJ mol^{-1}, respectively.

The OXA molecules in arrangein channels along the *c* axis (Figure 50). The channels present a smooth surface composed by the aromatic portions of CBZ and the polar fragments of the amine and carbonyl in $R^2_2(8)$ motifs. The volume related to the OXA arrangement corresponds to 206.90 $Å^3$ and is equivalent to 15.7% of the unit cell. These values are very similar to the voids reported in the MOXWUS structure (226.20 $Å^3$ and 16.6%). The calculated BFDH morphology corresponds to needles, with the main crystal axis running along the channels.

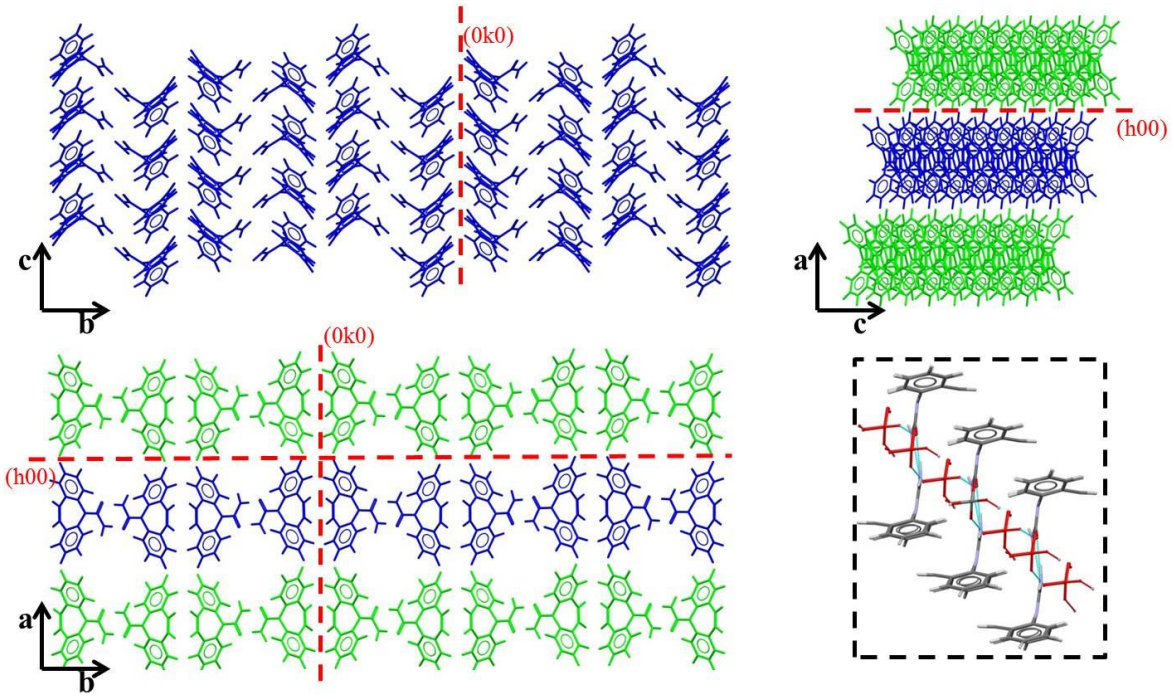

Figure 49 - Packing of CBZ molecules in 2CBZ:OXA cocrystal (OXA molecules are omitted). As a comparison to the previous structures, molecules interacting via their dibenzoazepine portions were characterised in different colours (green and blue). In the 2CBZ:OXA cocrystal, however, the layers of dimers present distinct orientation along *b*, while same orientation along *a*. Details include: the clipping illustrating the translational stacking of the dimers in comparison to the OXA molecules (in red), and the (0k0) and (h00) planes.

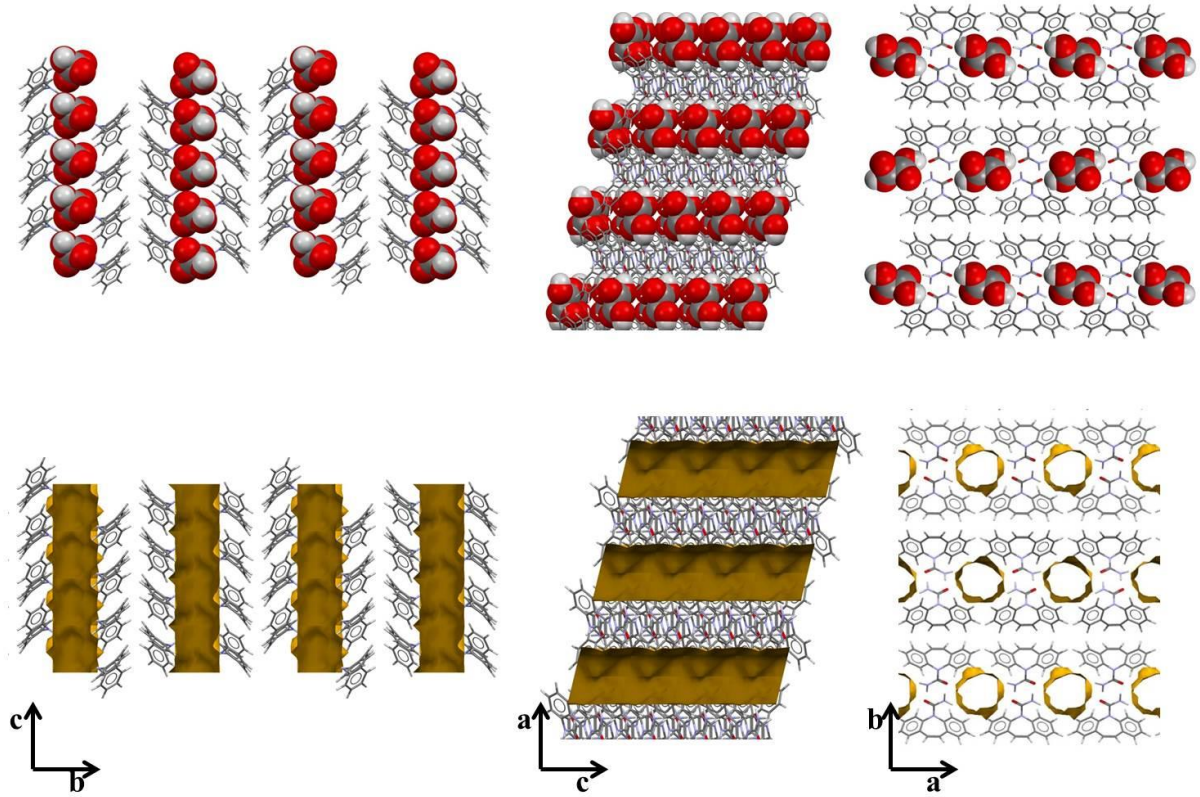

Figure 50 - Organization of OXA molecules in the 2CBZ:OXA cocrystal. The coformer molecules are highlighted in spacefill (top row) and the virtual voids are also shown (bottom row).

3.2.12 CBZ dihydrate (CBZ:2H_2O)

The literature reports the structure of CBZ dihydrate in two different space groups, monoclinic and orthorhombic. The crystallographic data for both structures is shown in Table 2, but only the $P2_1/c$ structure is analysed herein. The selection of this cif was made in order to avoid the disorder observed in the orthorhombic model since the disorder complicates the analysis of the hydrogen bond network and a comparison with other multicomponent forms of CBZ.

The structure is very similar to 2CBZ:BZQ and 2CBZ:OXA. The asymmetric unit consists of one CBZ and two non-equivalent molecules of water in a monoclinic cell. The CBZ is arranged in dimers ($R^2_2(8)$, N–H···O: D=2.867 Å, d=1.904 Å, θ=174.37º, θ^{AB}=3.28º) linked to molecules of water through O–H···O hydrogen bonds between the hydroxyl group of water and the carbonyl of CBZ (D=2.831 Å, d=1.765 Å, θ=158.20º) (Figure 51). Weaker N–H···O hydrogen bonds are also stablished between the amine of CBZ and the water oxygen (D=3.099 Å, d=2.434 Å, θ=146.09º). The molecules of water are bound to one another along *b* and *c*, and form an intricate hydrogen bond network along the (channel) axis *c*. Aromatic C–H groups form additional contacts to neighbouring CBZ carboxamide group. The interaction maps show that other water molecules occupy regions. It is worth mentioning, however, that the hydrogen donors are slightly offset and fall in the third level of the map contour, while the hydrogen acceptors fall in the first level of statistically most favourable interactions.

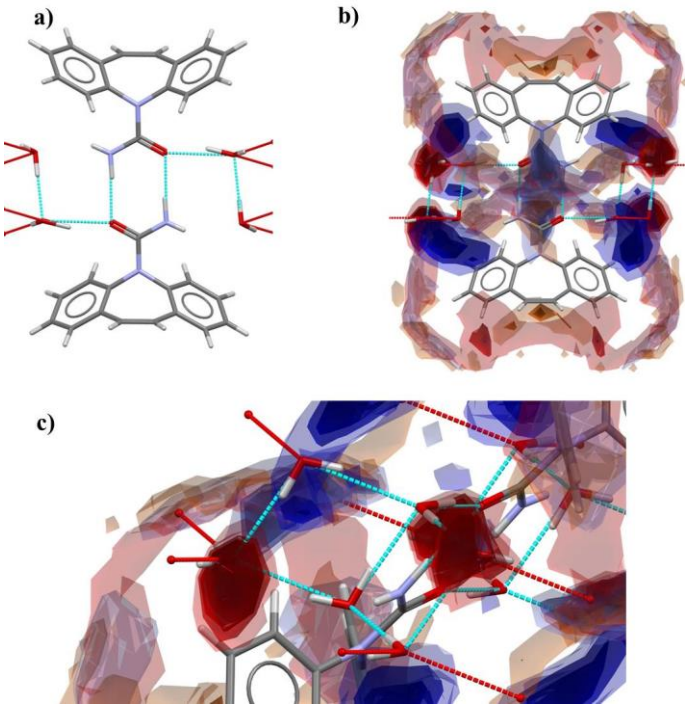

Figure 51 - Main hydrogen bonds observed in the CBZ:2H_2O (a). The interaction map of the CBZ dimer bonded to the water molecules show missing regions of favourable contacts occupied by water molecules.

The packing of CBZ:2H_2O is composed of stacked CBZ dimers along *c* (Figure 52). These stacks form different layers of opposite directions along *b* leading to small interactions on (0k0) and (h00). With respect to the energetic relationship between molecules in the structure, the stacked CBZ molecules correspond to the stronger interactions in the structure (-50.1 kJ mol^{-1}). In turn, the intermolecular energy of the CBZ dimer, CBZ:water and water1:water2 molecules correspond to -37.5 kJ mol^{-1}, -29.9 kJ mol^{-1} and -16.7 kJ mol^{-1}, respectively.

The water molecules are arranged in channels along the *c* axis (Figure 53). The channels present a smooth surface described by the aromatic portions of CBZ and the polar fragments of the amine and carbonyl in $R^2_2(8)$ motifs. The volume related to the H_2O arrangement corresponds to 261.18 $Å^3$ and is equivalent to 19.2% of the unit cell. The calculated BFDH morphology corresponds to needles, with the main crystal axis running along the channels.

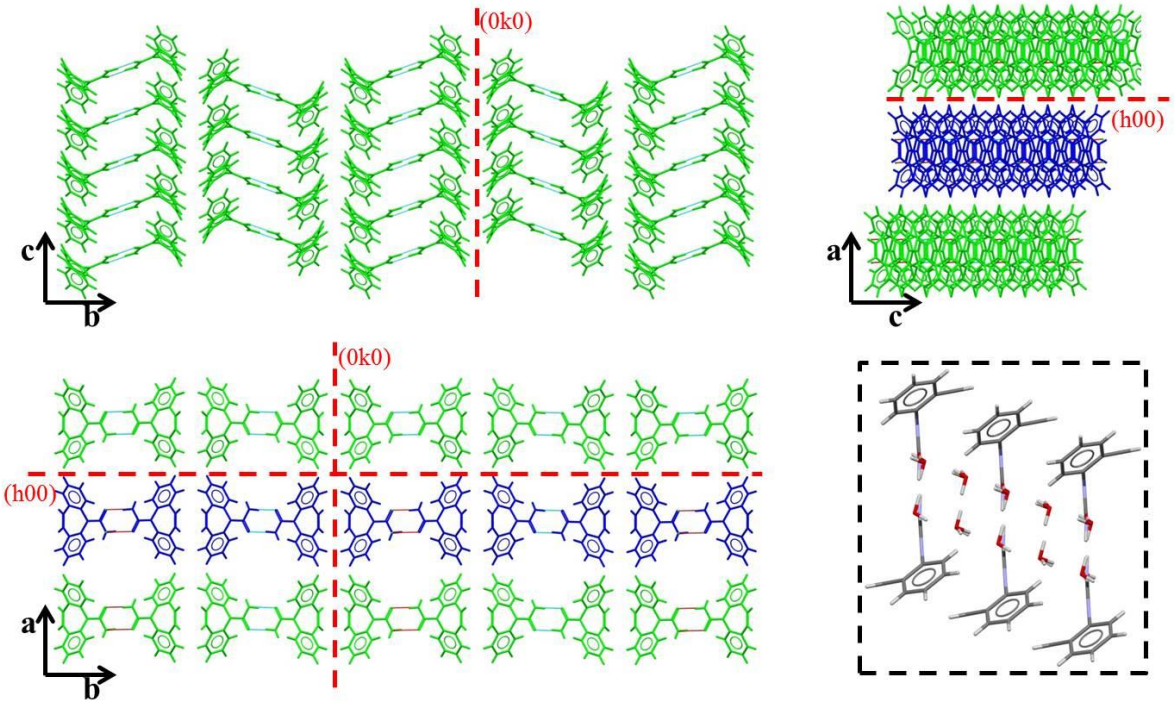

Figure 52 - Packing of CBZ molecules in CBZ:2H_2O (H_2O molecules are omitted). As a comparison to the previous structures, molecules interacting via their dibenzoazepine portions were characterised in different colours (green and blue). In CBZ:2H_2O, however, the layers of dimers present distinct orientation along *b*, while same orientation along *a*. Details include: the clipping illustrating the translational stacking of the dimers in comparison to the water molecules (in red), and the (0k0) and (h00) planes.

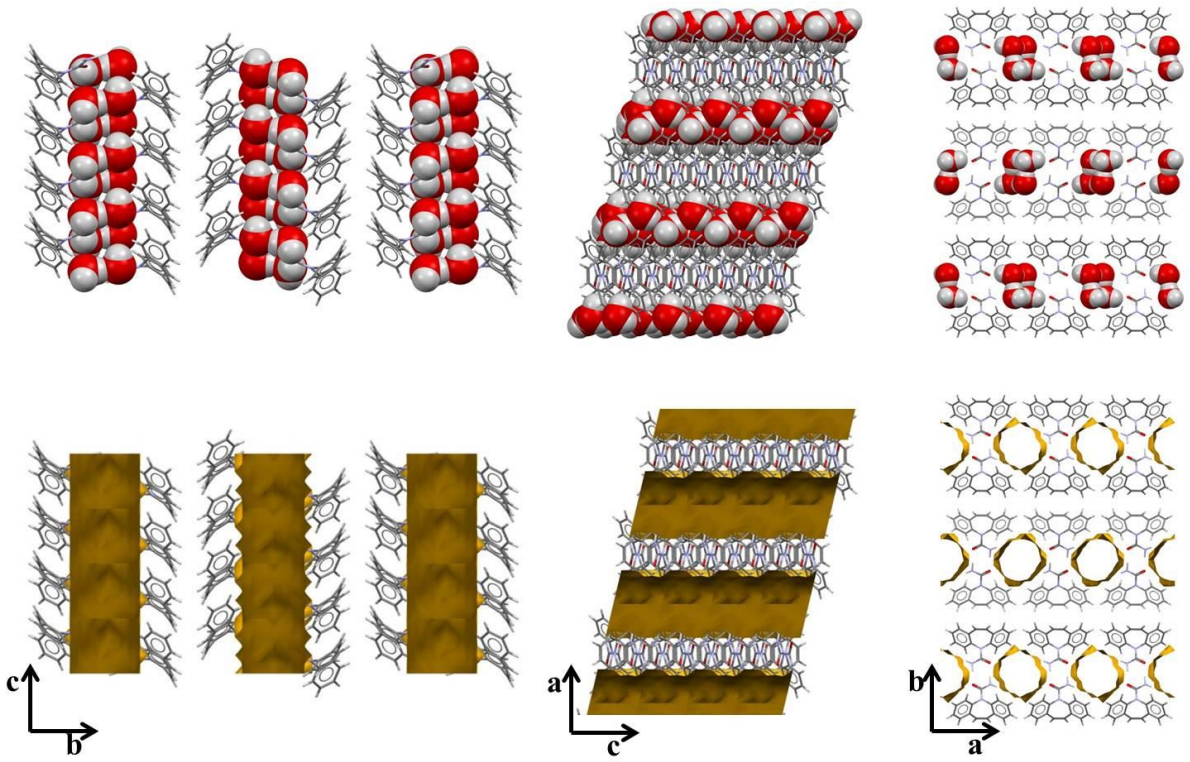

Figure 53 - Organization of H_2O molecules in CBZ:2H_2O. The water molecules are highlighted in spacefill (top row) and the virtual voids are also shown (bottom row).

3.2.13 CBZ formamide solvate (CBZ:FORM)

The CBZ:FORM asymmetric unit consists of two CBZ and two formamide molecules in a triclinic cell (Figure 54). In contrast to the oxalic acid cocrystal, the non-equivalent CBZ molecules are not interacting within a dimer, but are forming different dimers with neighbour molecules displaced along the *a* axis ($R^2_2(8)$, N–H···O: D_1=2.922 Å, d_1=2.064 Å, θ_1=164.75º, θ^{AB}=6.99º; and N–H···O: D_2=2.872 Å, d_2=1.998 Å, θ_2=171.39º, θ^{AB}=3.63º). This particularity is also a result of the interaction with the formamide molecules. Two independent solvent molecules form dimers with a $R^2_2(8)$ motif tilted by 8.26º (N–H···O: D_1=2.889 Å, d_1=2.017 Å, θ_1=170.25º, and N–H···O: D_2=2.941 Å, d_2=2.072 Å, θ_2=172.68º). The formamide dimers intercalate and form distinct hydrogen bonds to the different CBZ molecules. From one side of the formamide dimer, a $R^2_4(8)$ motif is formed as the amine and the carbonyl groups of formamide hydrogen bond to the carbonyl and the amine groups of two CBZ molecules interacting in one dimer (D_1=2.974 Å, d_1=2.216 Å, θ_1=144.04º, and D_2=2.875 Å, d_2=2.068 Å, θ_2=152.09º). From the other side of the formamide dimer, in turn, the amine and the carbonyl groups hydrogen bond to the carbonyl and the amine groups of other two CBZ molecules stacked along *c* (D_1=2.941 Å, d_1=2.066 Å, θ_1=172.43º, and D_2=2.911 Å, d_2=2.140 Å, θ_2=145.82º). Aromatic C–H groups form additional contacts to neighbouring CBZ carboxamide.

The interaction maps show that neighbour CBZ and formamide molecules occupy appropriate regions of favourable interaction in the structure.

The packing of CBZ:FORM is composed of stacked CBZ dimers along *a* (Figure 55). Stacks of opposite directions along *b* and *c* form a network of CBZ dimers which are different to the previous structures. The lattice, however, has similar weakly interacting planes on (0kl) and (0k-l), while the geometric parameters of the dimer planes are different. With respect to the energetic relationship between molecules in the structure, the stacked CBZ molecules contribute to the stronger interactions (-44.3 and -44.2 kJ mol^{-1}, for both CBZ independent molecules 1 and 2). In turn, the intermolecular energy of the CBZ dimers 1/2, CBZ1:solvent1/CBZ1:solvent2, CBZ2:solvent1/CBZ2:solvent2 and solvent:solvent dimers correspond to -31.7/34.3 kJ mol^{-1}, -18.9/-21.9 kJ mol^{-1}, -23.1/-21.3 kJ mol^{-1}, -27.8 kJ mol^{-1}, respectively.

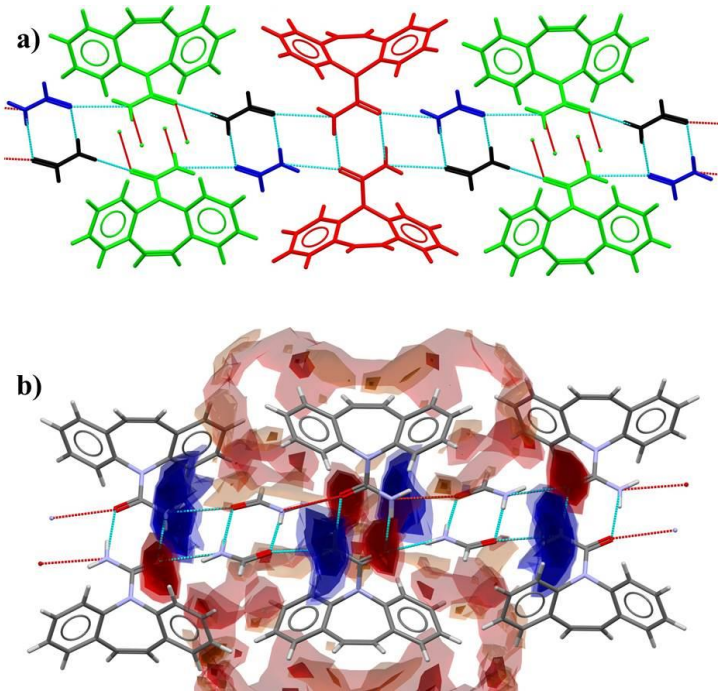

Figure 54 - Main hydrogen bonds observed in the CBZ:FORM (a). The interaction map of the CBZ dimer bonded to formamide molecules shows missing regions of favourable interactions occupied by the carboxamide portions of CBZ.

The solvent molecules are arranged in channels along the *a* axis (Figure 56). The channels present a smooth surface composed by the aromatic portions of CBZ and the polar fragments of the amine and carbonyl in the CBZ $R^2_2(8)$ motifs. The volume related to the formamide arrangement corresponds to 221.36 $Å^3$ and is equivalent to 15.8% of the unit cell. The calculated BFDH morphology corresponds to needles, with the main crystal axis running along the channels.

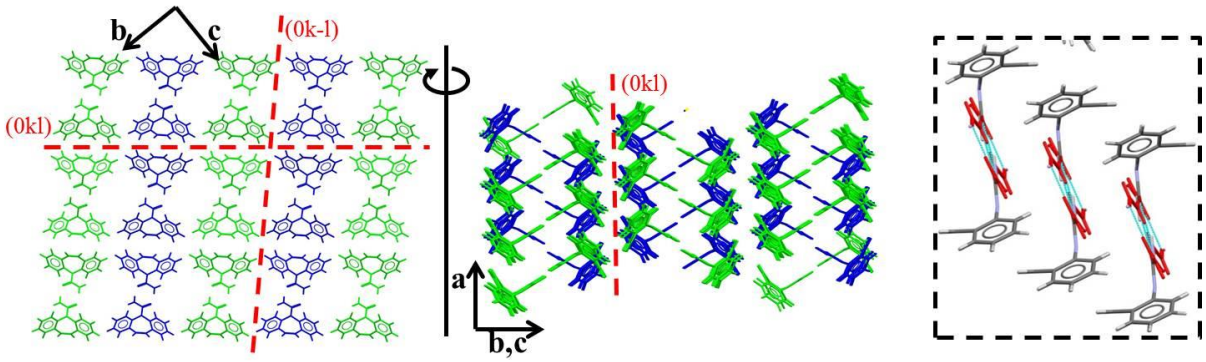

Figure 55 - Packing of CBZ molecules in CBZ:FORM (formamide molecules are omitted). As a comparison to the previous structures, molecules interacting via their dibenzoazepine portions were characterised in different colours (green and blue). In CBZ:FORM, however, neighbouring dimers present distinct orientation along *b* and *c*. Details include: the clipping illustrating the translational stacking of the dimers in comparison to the formamide molecules (in red), and the (0kl) and (0k-l) planes.

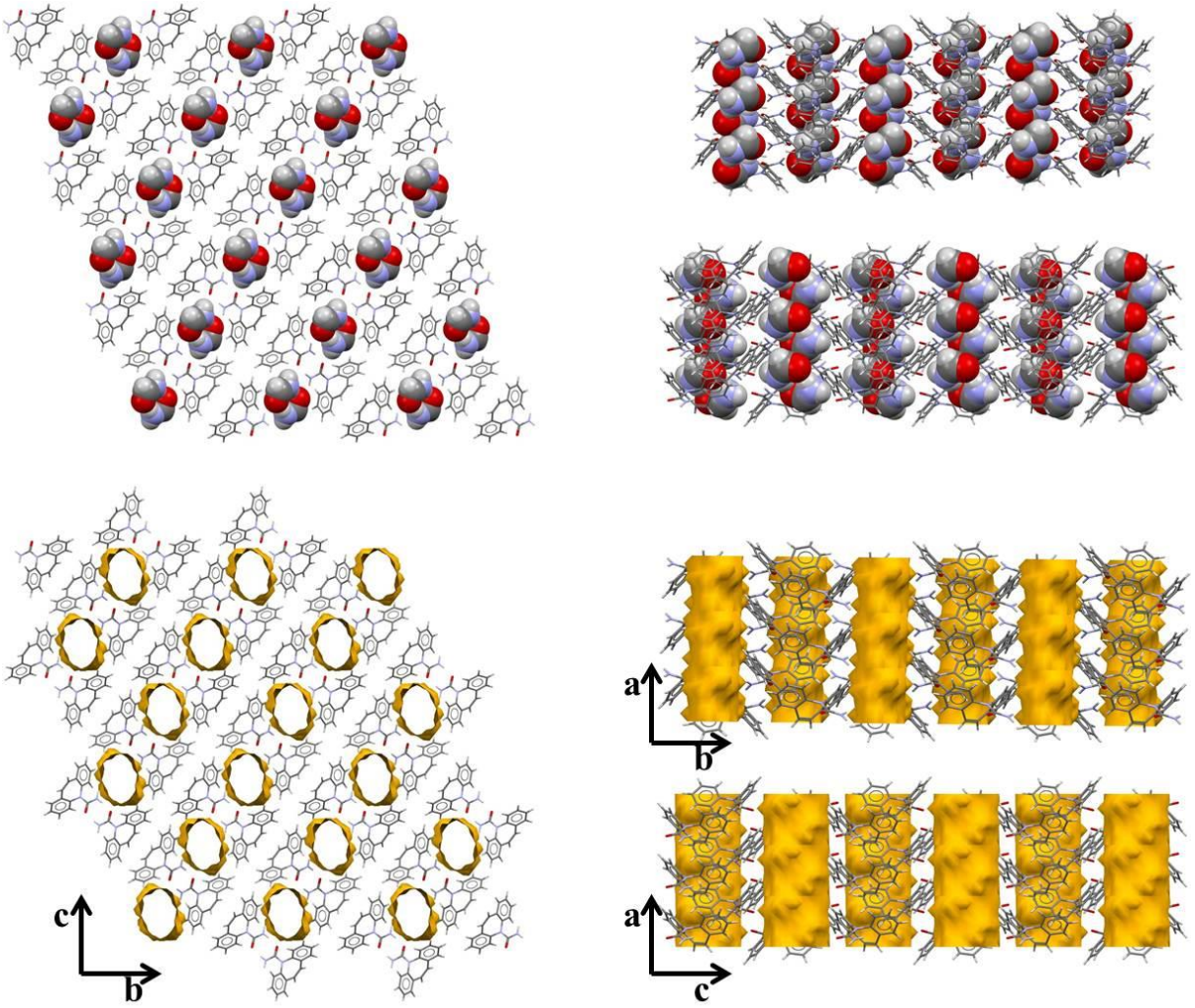

Figure 56 - Organization of formamide molecules in the CBZ:FORM solvate. The solvent molecules are highlighted in spacefill (top row) and the virtual voids are also shown (bottom row).

3.2.14 CBZ dioxane solvate (2CBZ:DIOX)

The 2CBZ:DIOX monoclinic structure consists of CBZ dimers tilted by 2.96º ($R^2_2(8)$, N–H···O: D=2.905 Å, d=2.076 Å, θ=173.51º) linked to one disordered molecule of dioxane (Figure 57). The disorder of dioxane is complex, seemingly a mixture of static and thermal disorder. Aromatic C–H groups form additional contacts to a neighbouring CBZ carboxamide group. Perhaps because of the disorder, the interaction map is not very clear. It is possible, however, to observe that dioxane molecules occupy regions of favourable interactions around the CBZ dimer.

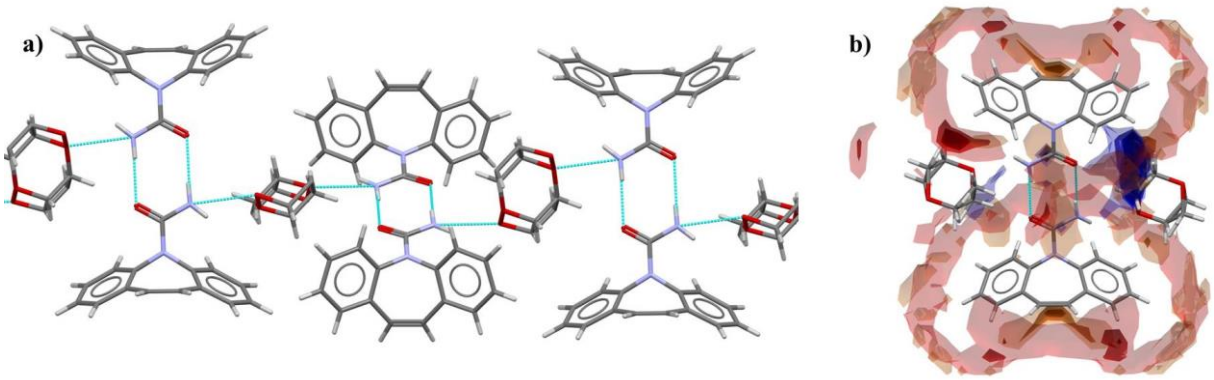

Figure 57 - Main hydrogen bonds observed in the 2CBZ:DIOX (a). The interaction map of the CBZ dimer bonded to the dioxane molecules shows missing regions of favourable interactions occupied by other solvent molecules.

Similar to CBZ:FORM, the packing of 2CBZ:DIOX is composed of stacked CBZ dimers along *b* (Figure 58). Stacks of opposite directions along *a* and *c* form a network of CBZ dimers similar to the structure of CBZ:FORM. The lattice also has similar weak interactions on (h0l) and (h0-l) with distinct geometric parameters in regard to the planes of the dimers. With respect to the energetic relationship between molecules in the structure, the stacked CBZ molecules contribute to the stronger interactions in the structure (-48.2 kJ mol^{-1}). In turn, the intermolecular energy of the CBZ dimer, CBZ:solvent and solvent:solvent molecules correspond to -30.0 kJ mol^{-1}, -27.5 kJ mol^{-1} and -32.3 kJ mol^{-1}, respectively.

The solvent molecules arrangein channels along the *b* axis (Figure 59). The channels present a smooth surface composed by the aromatic portions of CBZ and the polar fragments of the amine and carbonyl in $R^2_2(8)$ motifs. The volume related to the dioxane arrangement corresponds to 237.82 $Å^3$ and is equivalent to 16.8% of the unit cell. The calculated BFDH morphology corresponds to needles, with the main crystal axis running along the channels.

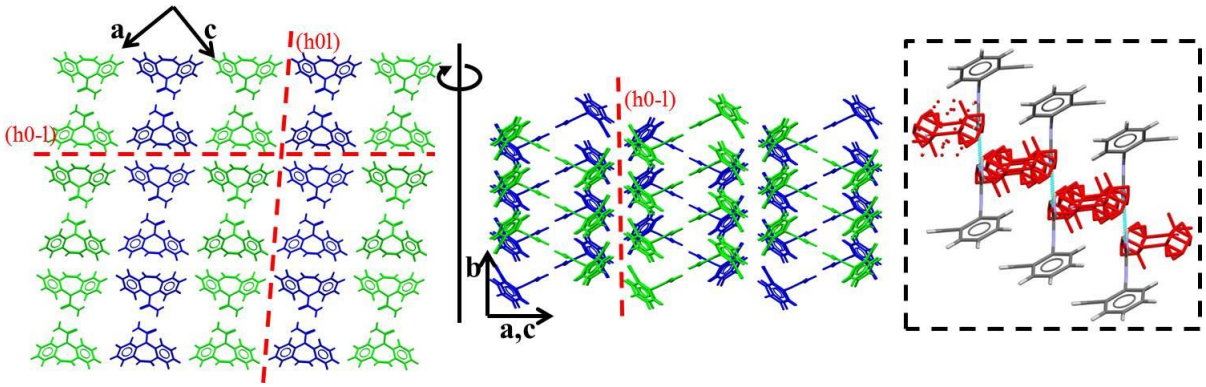

Figure 58 - Packing of CBZ molecules in 2CBZ:DIOX (dioxane molecules are omitted). As a comparison to the previous structures, molecules interacting via their dibenzoazepine portions were characterised in different colours (green and blue). In 2CBZ:DIOX, however, neighbouring dimers present distinct orientation along *a* and *c*. Details include: the clipping illustrating the translational stacking of the dimers in comparison to the dioxane molecules (in red), and the (h0l) and (h0-l) planes.

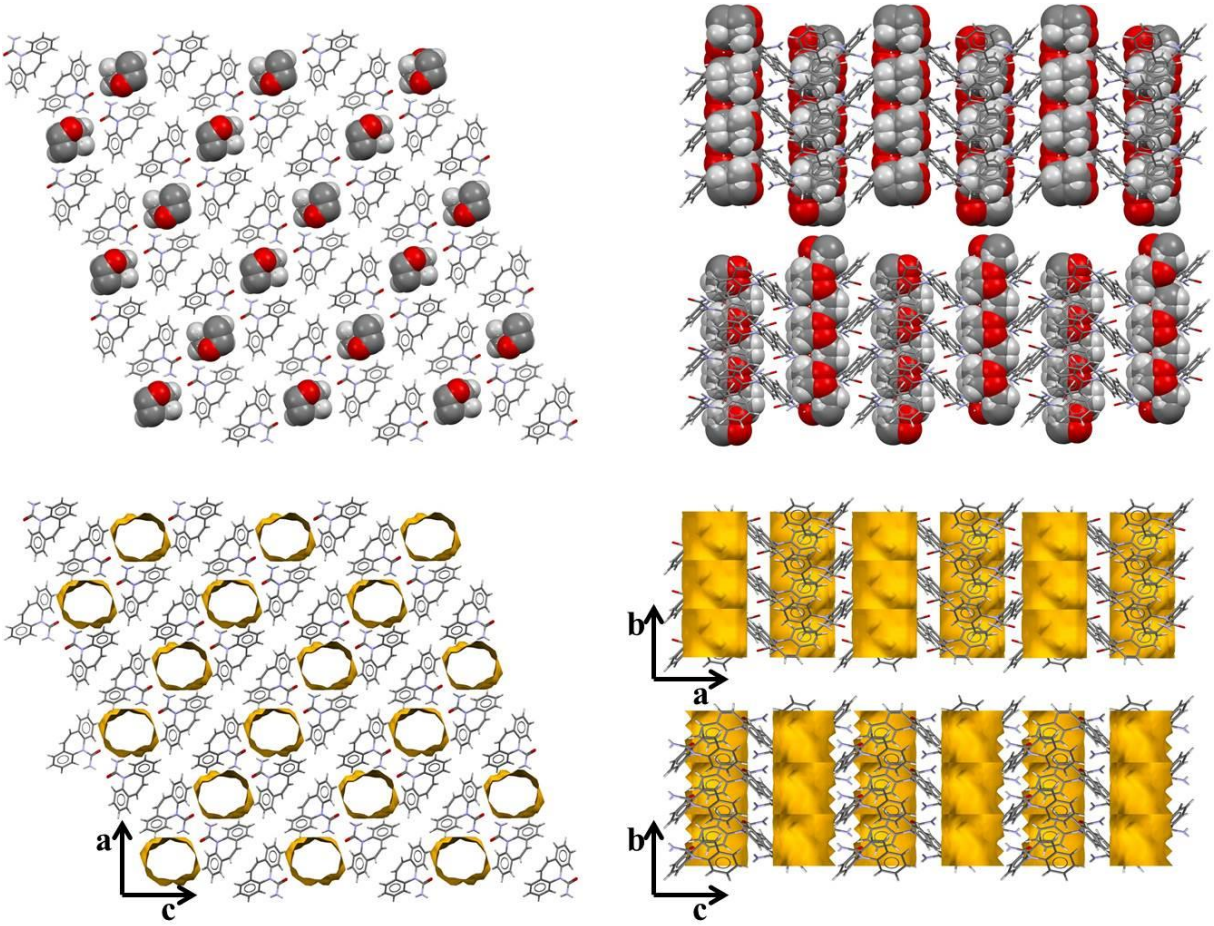

Figure 59 - Organization of dioxane molecules in the 2CBZ:DIOX solvate. The solvent molecules are highlighted in spacefill (top row) and the virtual voids are also shown (bottom row).

3.2.15 CBZ nitromethane solvate (CBZ:NIT)

The CBZ:NIT monoclinic structure consists of CBZ dimers ($R^2_2(8)$, N–H···O: D=2.874 Å, d=1.954 Å, θ=172.96º, θ^{AB}=7.89º). The dimer is linked to two molecules of nitromethane through N–H···O hydrogen bonds between the amine group of CBZ and the nitro

group of NIT (D=2.959 Å, d=2.379 Å, θ=126.35º) (Figure 60). Aromatic C–H groups form additional contacts to neighbouring CBZ carboxamide and to a second NIT N–O group. The interaction maps show that neighbouring nitromethane methyl groups occupy regions of favourable interaction around nitro groups of neighbouring molecules. The methyl groups are disordered in the structure.

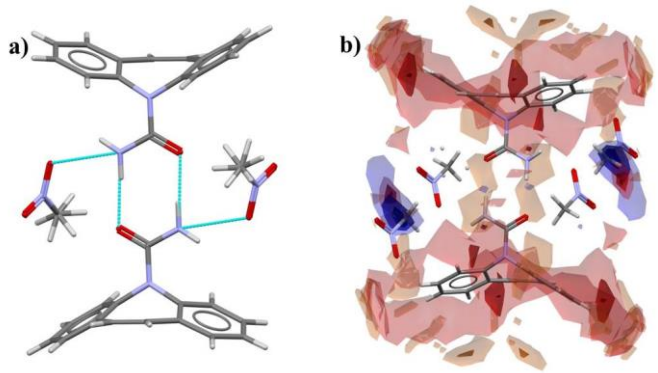

Figure 60 - Main hydrogen bonds observed in the CBZ:NIT (a). The interaction map of the CBZ dimer bonded to nitromethane molecules show missing regions of favourable interactions occupied by other solvent molecules.

Crystal packing of is composed of one-dimensional stacked CBZ dimers along *b* (Figure 61). The stacks are translated along *a* and show different orientations along *c*, resulting in a zig-zag network. The lattice is similar to that for the structures of 2CBZ:BZQ, 2CBZ:OXA and CBZ:2H_2O, except that the stacks are not aligned but slightly displaced along *c* by 2.594 Å. This characteristic interrupts the plane along the dibenzoazepine portions of CBZ, while the weak plane parallel to the axis of the dimers is still present (h0l). With respect to the energetic relationship between molecules in the structure, the stacked CBZ molecules contribute to the stronger interactions in the structure (-43.0 kJ mol^{-1}). In turn, the intermolecular energy of the CBZ dimer, CBZ:solvent and solvent:solvent molecules correspond to -34.4 kJ mol^{-1}, -10.9 kJ mol^{-1} and -6.6 kJ mol^{-1}, respectively.

Solvent molecules are arranged in channels along the *b* axis (Figure 62). Although the channels present a very similar chemical environment, the previously discussed packing characteristics lead to channels that are not as smooth and circular as found in the other related solvates and cocrystals. The volume occupied by the nitromethane corresponds to 288.25 $Å^3$ and is equivalent to 19.7% of the unit cell. The calculated BFDH morphology corresponds to needles, with the main crystal axis running along the channels.

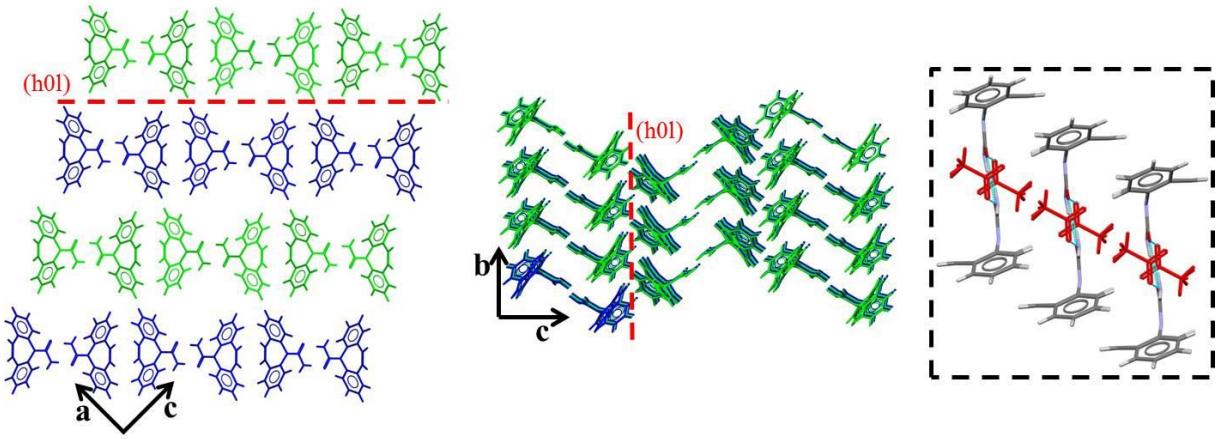

Figure 61 - Packing of CBZ molecules in CBZ:NIT (nitromethane molecules are omitted). As a comparison to the previous structures, molecules interacting via their dibenzoazepine portions were characterised in different colours (green and blue). In CBZ:NIT, however, the layers of dimers present distinct orientation along *c*, while same orientation along *a*. Details include: the clipping illustrating the translational stacking of the dimers in comparison to the nitromethane molecules (in red), and the (h0l) plane.

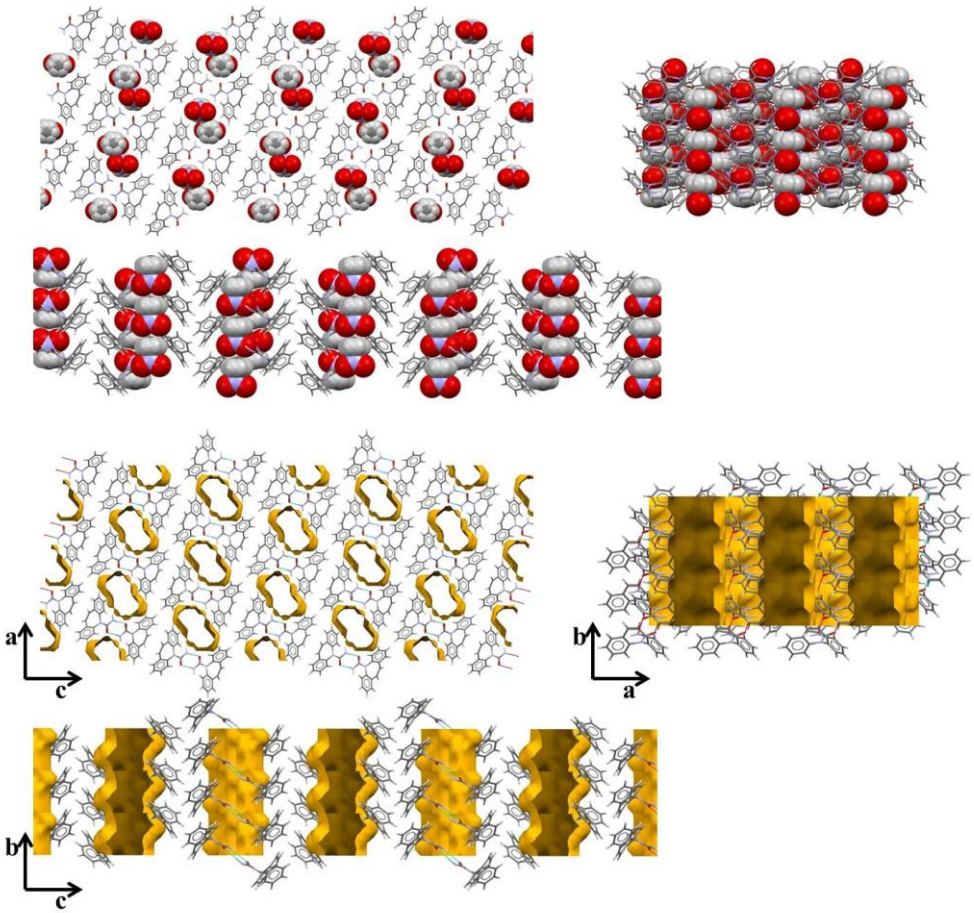

Figure 62 - Organization of nitromethane molecules in the CBZ:NIT solvate. The solvent molecules are highlighted in spacefill (top row) and the virtual voids are also shown (bottom row).

3.2.16 CBZ trifluoroethanol solvates (CBZ:TFE and 2CBZ:TFE)

The first structure in the CBZ:TFE system was described by Lohani et.al (2005). It had a 1:1 stoichiometry and was reported in the CSD as SAPDUJ. It was first obtained by slow

evaporation of a TFE solution. In our screening studies, however, a 2:1 stoichiometry was also crystallised. The 2CBZ:TFE cocrystal was first obtained from a slurrying experiment in ethanol:TFE at low proportions of TFE. Later, a 2CBZ:TFE form was also obtained from cooling and further slurry experiments, again always with low activities of TFE. Full details and the corresponding phase diagram are presented in Chapter 4.

The CBZ:TFE asymmetric unit consists of two CBZ and two TFE molecules in a triclinic cell (Figure 63). The CBZ dimers are formed by two independent molecules tilted by 6.59º ($R^2_2(8)$, N–H···O: D_1=2.905 Å, d_1=2.049 Å, θ_1=164.05º; and N–H···O: D_2=2.820 Å, d_2=1.956 Å, θ_2=166.66º). Only one molecule of CBZ in the dimer forms hydrogen bonds to the two independent molecules of TFE. While one hydrogen bond is formed from the TFE hydroxyl to the CBZ carbonyl (O–H···O: D=2.634 Å, d=1.805 Å, θ=169.31º), the N–H group of CBZ hydrogen bonds to the oxygen of another TFE hydroxyl (N–H···O: D=3.035 Å, d=2.444 Å, θ=124.90º). The two independent TFE molecules also form hydrogen bonds down the *a* axis (O–H···O: D=2.698 Å, d=1.859 Å, θ=177.64º), which link different stacked dimers via $R^6_6(16)$ motifs. Aromatic C–H groups form extra contacts to neighbouring CBZ carboxamide groups and TFE hydroxyls. Additional contacts are also observed from TFE C–H and F groups to the CBZ carboxamide. The interaction map illustrates the effect of these additional interactions as they occupy regions near the CBZ carboxamide and the solvent molecules.

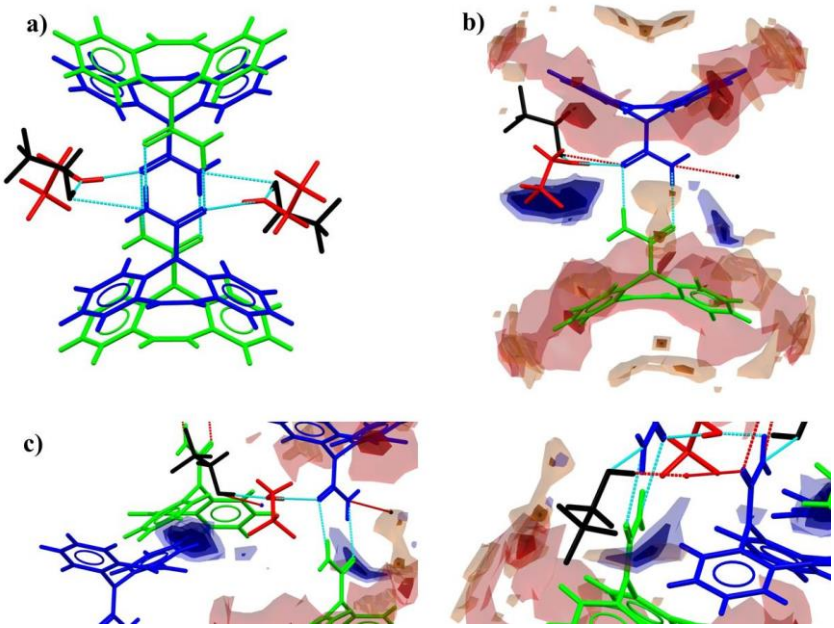

Figure 63 - Main hydrogen bonds observed in the CBZ:TFE (a); the colours show the independent molecules in the structure. The interaction maps of the CBZ dimer bonded to solvent molecules show missing regions of favourable interactions near the CBZ carboxamide and the solvent (b). The details in (c) show these regions are occupied by CBZ dibenzoazepine portions and TFE C–H and F groups.

The packing of CBZ:TFE is composed of one-dimensional stacked CBZ dimers along *a* (Figure 64). The stacks are translated along *b* and *c* resulting in two-dimensional layers,

which arrange the CBZ dimers stacked in the same direction throughout the crystal. Similarly to CBZ:NIT, the stacks in CBZ:TFE are not aligned. In this case, however, the displacement is observed along the dimer main axis (5.800 Å) and along the dibenzoazepine axis (2.592 Å). These characteristics interrupt the planes along the dibenzoazepine portions of CBZ and creates a new set of (0k-l) planes intersecting $R^2_2(8)$ motifs and the dibenzoazepine. The (0kl) slip system parallel to the dimer axis is also changed as the molecules of CBZ are displaced, but it still runs across the solvent channels. The calculated BFDH morphology corresponds to needles, with the main crystal axis running along the channels.

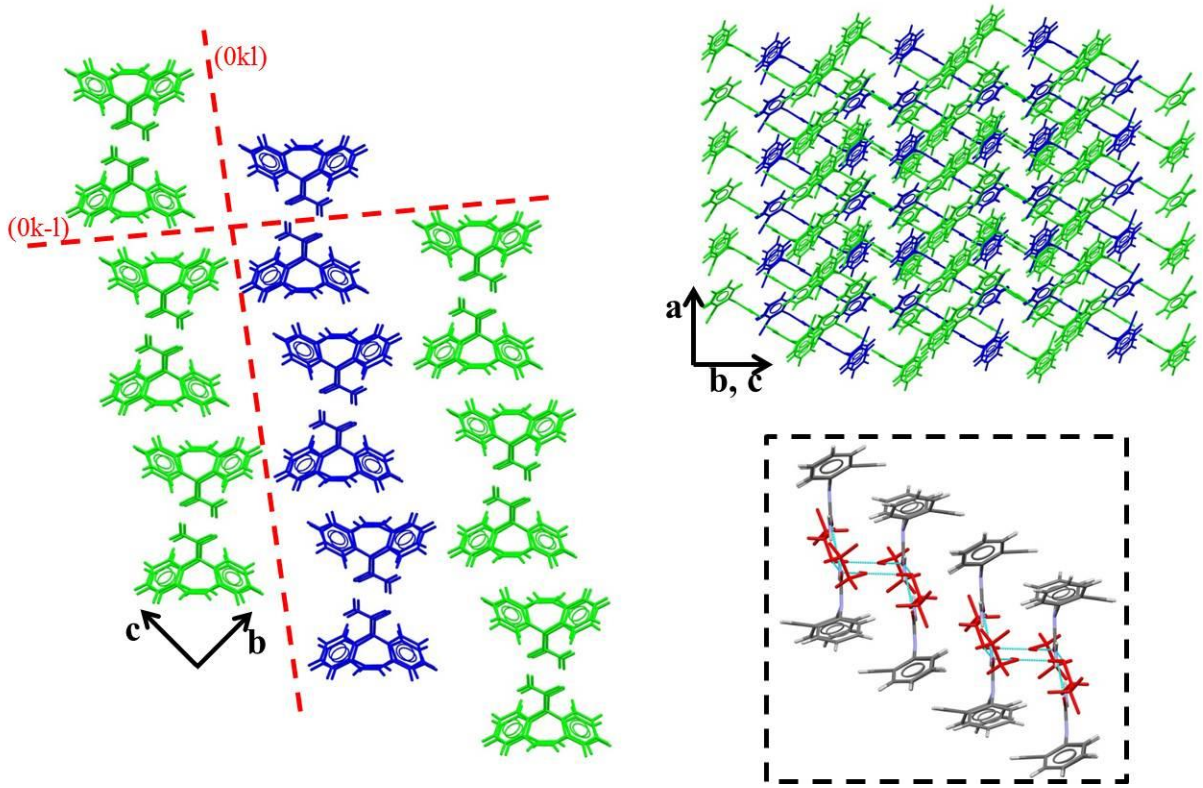

Figure 64 - Packing of CBZ molecules in CBZ:TFE (trifluoroethanol molecules are omitted). As a comparison to the previous structures, molecules interacting via their dibenzoazepine portions were characterised in different colours (green and blue). In CBZ:TFE, however, the dimers present the same orientations throughout the lattice. Details include: the (0kl) and the (0k-l) planes, and the clipping illustrating the translational stacking of the dimers in comparison to the trifluoroethanol molecules (in red).

With respect to the energetic relationship between molecules in the structure, the stacked CBZ molecules contribute to the stronger interactions in the structure (-44.1 kJ mol^{-1} and -43.8 kJ mol^{-1}). In turn, the intermolecular energy of the CBZ dimer, CBZ:solvent1, CBZ:solvent2 and solvent1:solvent2 molecules correspond to -33.9 kJ mol^{-1}, -32.9 kJ mol^{-1}, -15.2 kJ mol^{-1} and -22.0 kJ mol^{-1}, respectively.

Solvent molecules are arranged in channels along the *a* axis which almost create layers on (0kl) (Figure 65). The channels present a surface composed of the aromatic portions of CBZ and the polar fragments of the amine and carbonyl in $R^2_2(8)$ motifs. The aromatic

portions, however, almost block and divide the channel into two portions (channels essentially shaped into a figure eight). The volume related to the trifluoroethanol corresponds to 412.78 $Å^3$ and is equivalent to 26.0% of the unit cell. The calculated BFDH morphology corresponds to needles, with the main crystal axis running along the channels.

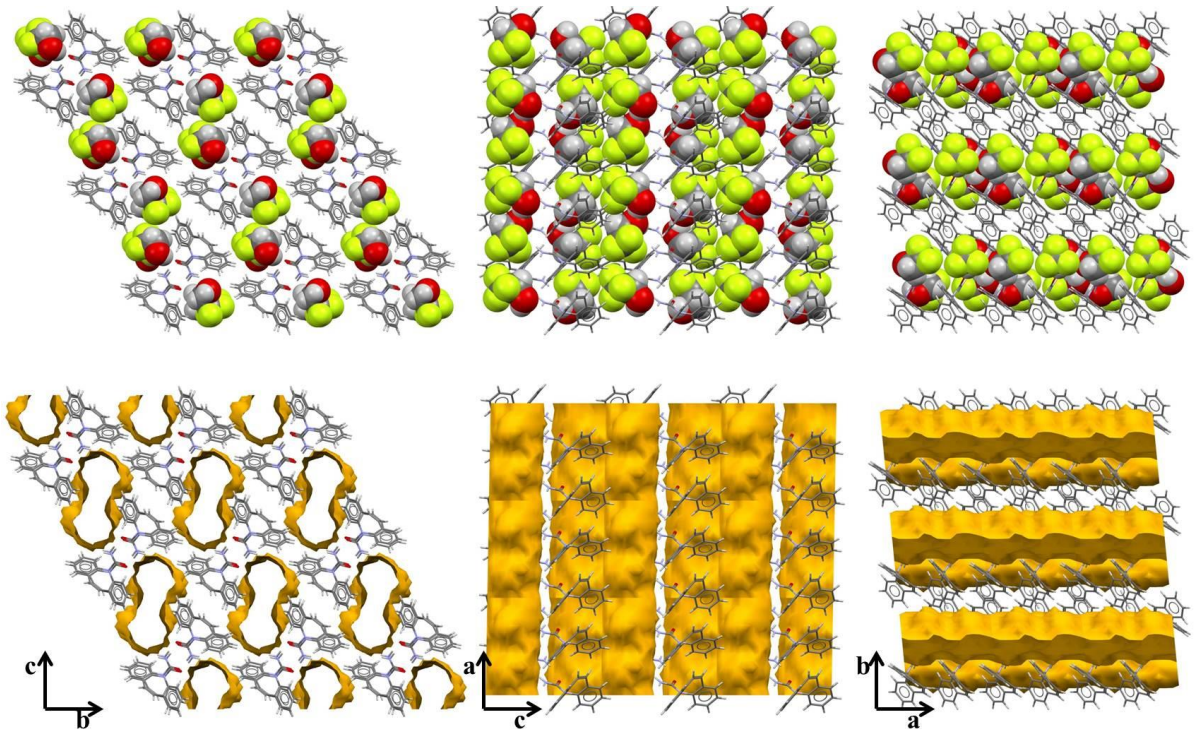

Figure 65 - Organization of trifluoroethanol molecules in the CBZ:TFE solvate. The solvent molecules are highlighted in spacefill (top row) and the virtual voids are also shown (bottom row).

It is interesting to compare the solvent arrangement in the reported CBZ:TFE structure and the arrangement in the new 2CBZ:TFE form. The shape and the surface of the channels are very similar in both structures; however, the orientation of the eight-shaped channel in regard to the CBZ dimer axis is different in 2CBZ:TFE (Figure 66). The volume related to the trifluoroethanol occupancy corresponds to 223.63 $Å^3$ and is equivalent to 16.0% of the unit cell. The calculated BFDH morphology corresponds to needles, with the main crystal axis running along the channels.

The packing of 2CBZ:TFE is composed of one-dimensional stacked CBZ dimers along *a* (Figure 67). The stacks are translated and combined along *b* in two different fashions: one layer has CBZ dimers associated to TFE molecules, while a second layer is formed only by CBZ dimers that are tilted with regard to the *c* axis. The aromatic portions of the dimers in the s layer interact to the solvent molecules from the next layer resulting in the characteristic 8-shaped channel. Because of this interaction, there is no weak interaction between these two layers. Two slip systems crossing the channels are identified on (0k-l) and (00l).

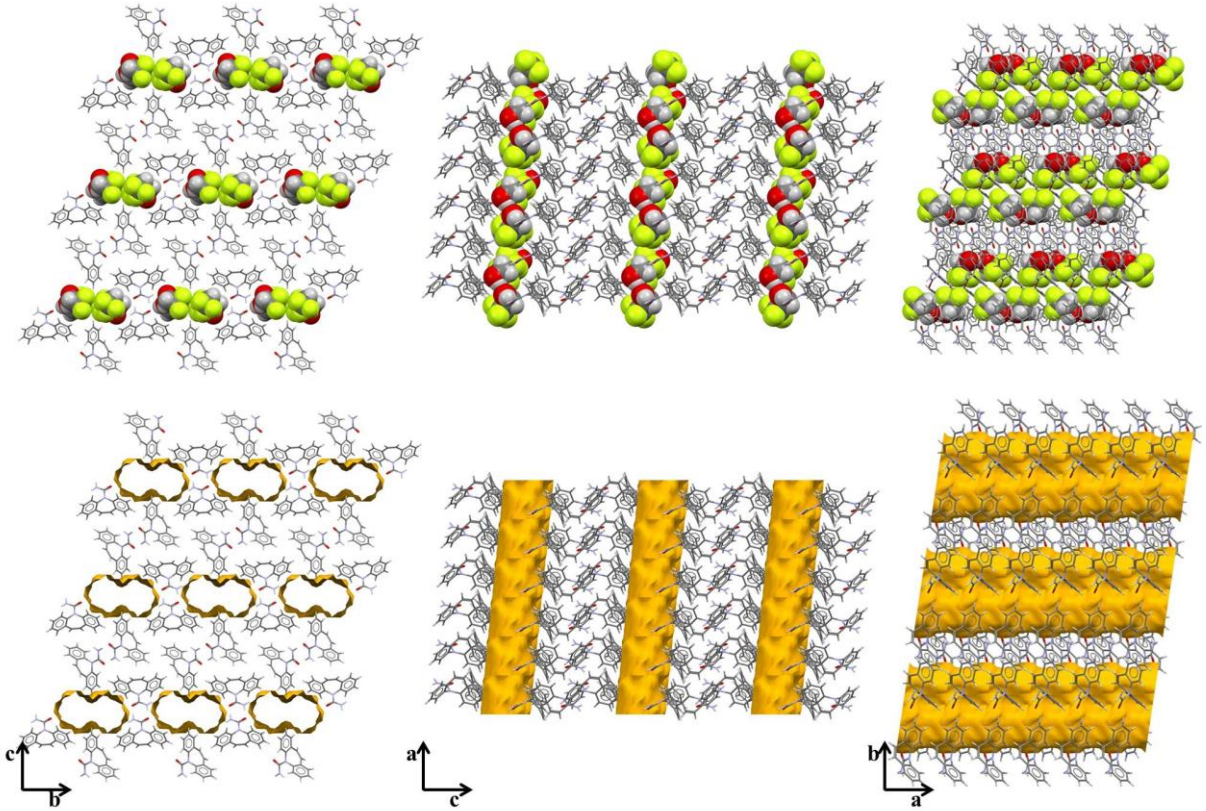

Figure 66 - Organization of trifluoroethanol molecules in the 2CBZ:TFE solvate. The solvent molecules are highlighted in spacefill (top row) and the virtual voids are also shown (bottom row).

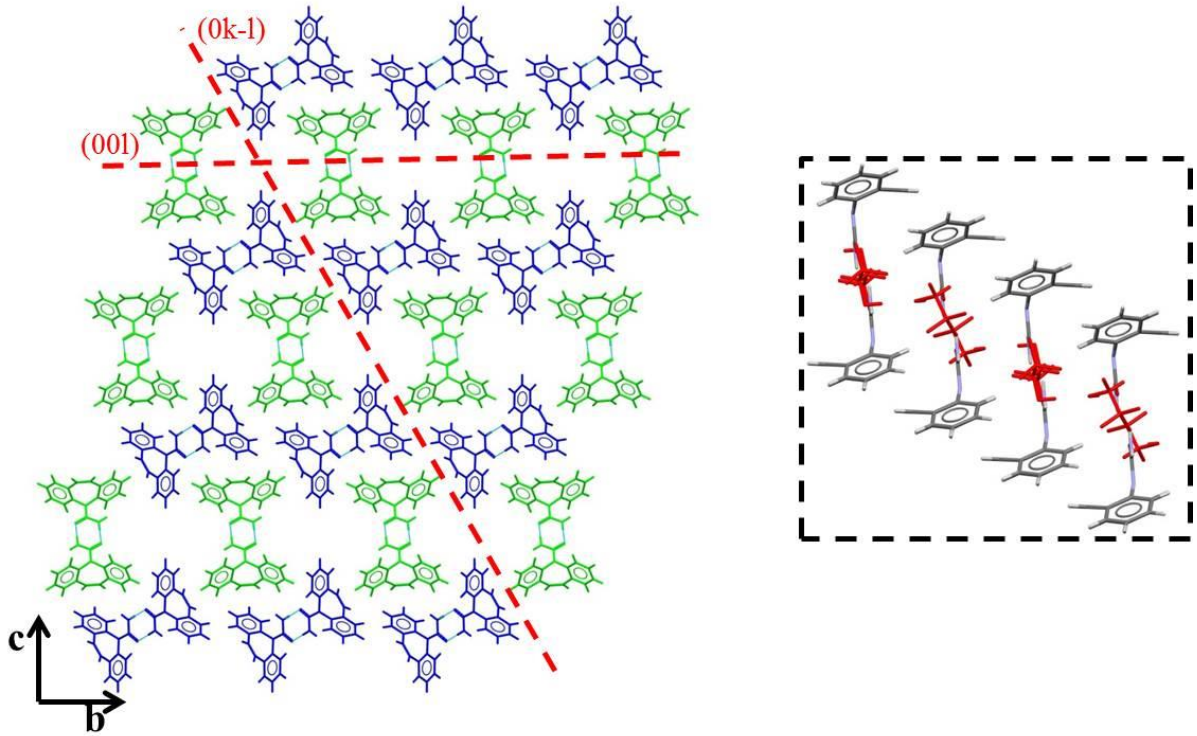

Figure 67 - Packing of CBZ molecules in 2CBZ:TFE (trifluoroethanol molecules are omitted). Details include: the clipping illustrating the translational stacking of the dimers in comparison to the trifluoroethanol molecules (in red), the CBZ layers 1 (green) and 2 (blue), and the (0k-l) and the (00l) planes.

The 2CBZ:TFE structure is also triclinic and consists of two CBZ and one disordered TFE molecule in the asymmetric unit. The solvent is disordered and can adopt one of two positions relative to CBZ along the *a* axis (Figure 68). The CBZ molecules form two different $R^2_2(8)$ dimers arranged in layers (N–H···O: D_1=2.878 Å, d_1=2.017 Å, θ_1=165.39º, θ_1^{AB}=8.40º; and N–H···O: D_2=2.893 Å, d_2=2.039 Å, θ_2=163.75º, θ_2^{AB}=9.16º). The TFE hydroxyl groups hydrogen bond to CBZ carbonyls along the a axis (O–H···O: D=2.791 Å, d=1.941 Å, θ=179.66º). The interaction maps show two regions of favourable interactions around the carboxamide in the dimers. The regions are occupied by aromatic groups along *b* and TFE molecules along *a*.

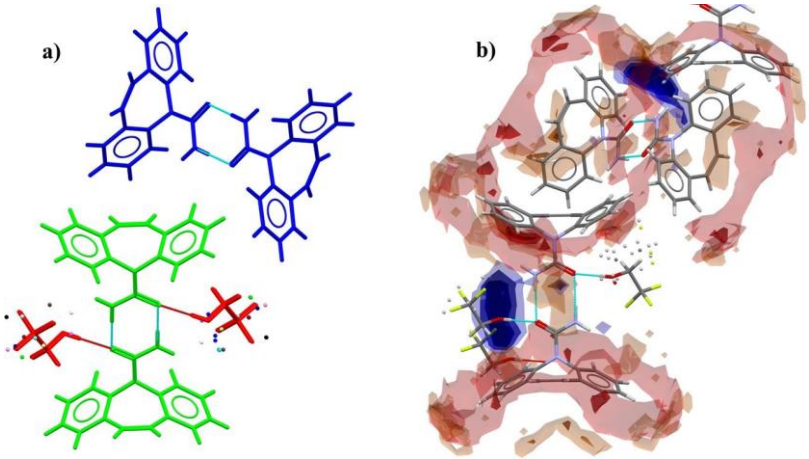

Figure 68 - Main hydrogen bonds observed in 2CBZ:TFE (a); the colours show the independent molecules in the structure. The interaction map of the CBZ dimer shows missing regions of favourable interactions occupied by CBZ aromatic portions and TFE molecules.

With respect to the energetic relationship between molecules in the structure, the stacked CBZ molecules coresond to the strongest interactions in the structure (-41.9 kJ mol^{-1} and -42.2 kJ mol^{-1}). In turn, the intermolecular energy of the CBZ dimer1, CBZ dimer2, CBZ1:CBZ2 and CBZ1:solvent molecules correspond to -33.4 kJ mol^{-1}, -32,7 kJ mol^{-1}, 17.8 kJ mol^{-1} and -29.7 kJ mol^{-1}, respectively.

3.2.17 CBZ trifluoroacetic acid solvate (CBZ:TFA)

The CBZ:TFA system was first studied by Fernandes et.al (2007) with the crystal structure reported as a solvate under the CSD code GINFOZ. Later, Eberlin, Eddleston & Frampton (2013) investigated the protonation state of CBZ:TFA and redetermined the structure at both 100 K and 270 K (CSD GINFOZ01 and GINFOZ02, respectively). The authors concluded that the CBZ:TFE solvate is best described as a salt with the acidic proton located at the mid-point between the acid and base. It is worth mentioning that the data collected at both

temperatures showed the same intermediate state structure, but the acidic hydrogen refined towards different groups. Although the difference was not large, the low temperature data showed the hydrogen refined towards the CBZ oxygen, while the high temperature data had the hydrogen biased towards the TFA oxygen.[199] Table 2 presents the crystallographic data of GINFOZ. The structures of salt and solvate are very similar and the GINFOZ solvate was selected for analysis in this section, although a comparison of the hydrogen bonding between the two models is presented below.

The CBZ:TFA solvate structure consists of $R^2_2(8)$ motifs between the CBZ carboxamide and the TFA, which presents disorder on the $–CF_3$ group (Figure 69). The hydrogen bonds in the ring are $N–H_{CBZ}\cdots O_{TFA}$ (D=2.889 Å, d=2.005 Å, θ=165.54º) and $O–H_{TFA}\cdots O_{CBZ}$ (D=2.433 Å, d=1.539 Å, θ=172.60º), and the functional groups are tilted by 14.48º. The CBZ N–H which is not involved in the CBZ:TFA dimer, also forms lateral hydrogen bonds to neighbouring TFE carbonyl along *b* ($N–H_{CBZ}\cdots O_{TFA}$: D=2.966 Å, d=2.296 Å, θ=133.46º). These interactions form chains following the screw axis relating the CBZ:TFA dimers. In other words, it means neighbour dimers are oriented in different directions and one dimer interacts with two other dimers along *b*.

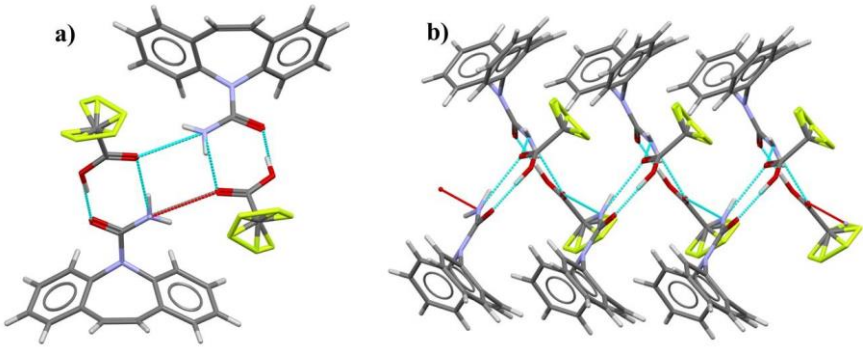

Figure 69 - Main hydrogen bonds observed in CBZ:TFA (a). The CBZ:solvent dimers that interact through the $R^2_4(8)$ motif are arranged in different directions (b).

Aromatic C–H groups form additional interactions to neighbouring CBZ carbonyls, which are observed in the interaction map of CBZ:TFA solvate. The TFA salt reported in GINFOZ01 show similar regions of favourable interactions around the CBZ:TFA dimers (Figure 70). As expected, the bond parameters in the salt are also very similar within the $R^2_2(8)$ dimer ($N–H_{CBZ}\cdots O_{TFA1}$: D=2.894 Å, d=2.042 Å, θ=169.03º; and $O–H_{CBZ}\cdots O_{TFA2}$: D=2.432 Å, d=1.266 Å, θ=168.23º; tilted by 15.64º) and in the lateral hydrogen bond ($N–H_{CBZ}\cdots O_{TFA1}$: D=2.938 Å, d=2.311 Å, θ=129.09º).

The packing of CBZ:TFA is mainly composed of a one-dimensional translational stacking of CBZ molecules along *b* (Figure 71). Along the (h0-l) plane, CBZ molecules of different orientations interact via their dibenzoazepine portions, while CBZ molecules of same

orientation show stacking of parallel-displaced benzene rings distanced by 3.185 Å. These interactions form layers of CBZ along the (h0-l) plane.

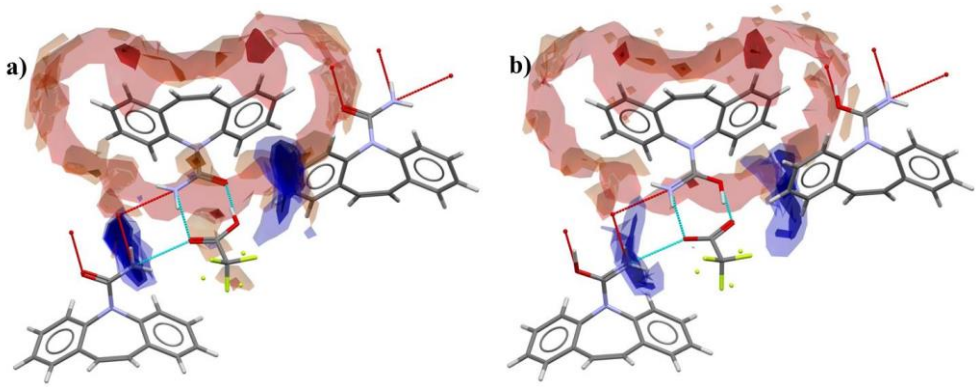

Figure 70 - The interaction map of the CBZ:solvent dimer shows missing regions of favourable interactions occupied by neighbouring CBZ molecules. The solvate (a) and the salt (b) models of the CBZ:TFA structure are shown.

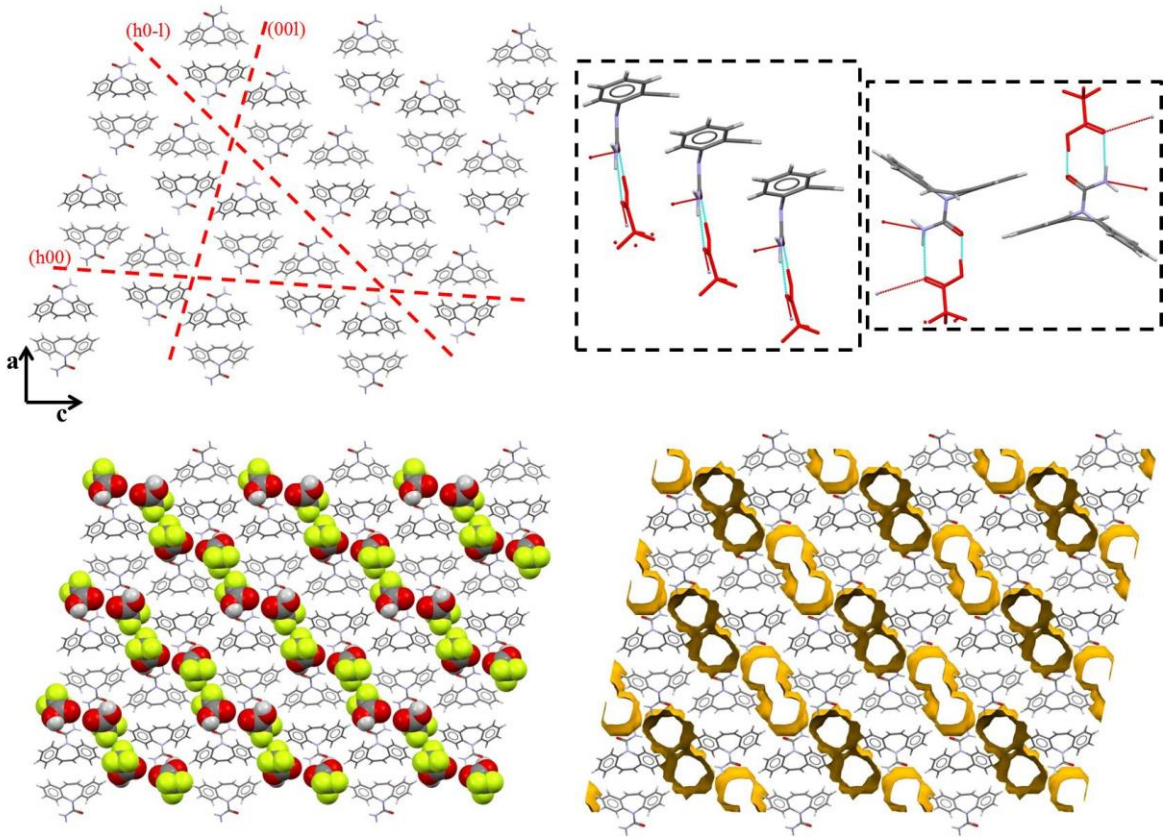

Figure 71 - Packing of CBZ molecules in CBZ:TFA exhibiting the slip planes, TFA molecules highlighted in spacefill and the virtual voids originated from the solvent (trifluoroacetic acid molecules are omitted when appropriate). Details include: the clipping illustrating the translational stacking of the dimers in comparison to the trifluoroacetic acid molecules (in red), and the benzene stacking.

With respect to the energetic relationship between molecules in the structure, the translational stacking of CBZ molecules contribute to the stronger interactions in the structure (-40.1 kJ mol^{-1}). In turn, the intermolecular energy of the CBZ:solvent dimer, CBZ:solvent in

the lateral hydrogen bond and the CBZ:CBZ molecules stacked by their benzene portions correspond to -31.5 kJ mol^{-1}, -20.6 kJ mol^{-1} and -22.8 kJ mol^{-1}, respectively.

Solvent molecules arrangein channels along the *b* axis (Figure 71). The channels present an irregular surface composed of the aromatic and the carboxamide portions of CBZ. The benzene groups almost block and divide the channel in two portions (creating eight-shaped channels) and the channels are almost connected along the (h0-l) plane, forming layers. Slip systems crossing the channels are identified on (h00) and (00l). The volume related to the trifluoroacetic acid arrangement corresponds to 362.0 $Å^3$ and is equivalent to 23.0% of the unit cell.

3.2.18 CBZ acetic acid solvate (CBZ:ACA)

Similar to the CBZ:TFA structure, the CBZ:ACA solvate consists of $R^2_2(8)$ motifs between the CBZ carboxamide and the ACA (Figure 72). The hydrogen bonds in the ring are $N–H_{CBZ}\cdots O_{ACA}$ (D=3.016 Å, d=2.208 Å, θ=152.43º) and $O–H_{ACA}\cdots O_{CBZ}$ (D=2.552 Å, d=1.666 Å, θ=167.64º), and the functional groups are tilted by 26.55º. In the case of CBZ:ACA, however, the CBZ N–H which is not involved in the dimer, forms lateral hydrogen bonds to neighbouring ACA carbonyl on the same plane of the dimer ($N–H_{CBZ}\cdots O_{ACA}$: D=2.919 Å, d=2.323 Å, θ=125.08º). These interactions form $R^2_4(8)$ motifs between two CBZ:ACA dimers, meaning that these neighbour dimers are oriented in the same direction. Aromatic CBZ C–H and ACA methyl groups form additional interactions to neighbouring carbonyls in the structure. From the interaction maps it is shown that the $R^2_4(8)$ motifs present a favourable geometry and the aromatic groups occupy additional regions of interactions around the dimers.

The packing of CBZ:ACA is composed of one-dimensional translational stacking of CBZ molecules along *a* (Figure 73). While weak planes are not easily identifiable, the (0k0), (00l) and (0k-l) are slip systems along which the CBZ molecules can potentially move. With respect to the energetic relationship between molecules in the structure, the translational stacking of CBZ molecules contribute to the stronger interactions in the structure (-44.2 kJ mol^{-1}). In turn, the intermolecular energy of the CBZ:solvent dimer and the CBZ:solvent in the lateral hydrogen bond correspond to -35.4 kJ mol^{-1} and -16.5 kJ mol^{-1}, respectively.

Solvent molecules arrangein channels along the *a* axis (Figure 73). The channels are small and present an irregular surface composed by the aromatic and the carboxamide portions of CBZ. The volume related to the acetic acid arrangement corresponds to 250.03 $Å^3$ and is equivalent to 16.9% of the unit cell.

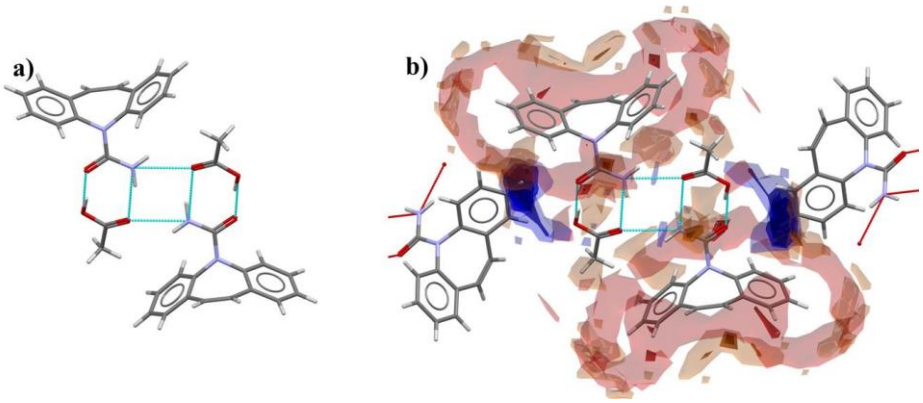

Figure 72 - Main hydrogen bonds observed in the CBZ:ACA (a). The interaction map of the CBZ:solvent dimer shows missing regions of favourable interactions occupied by CBZ aromatic portions (b).

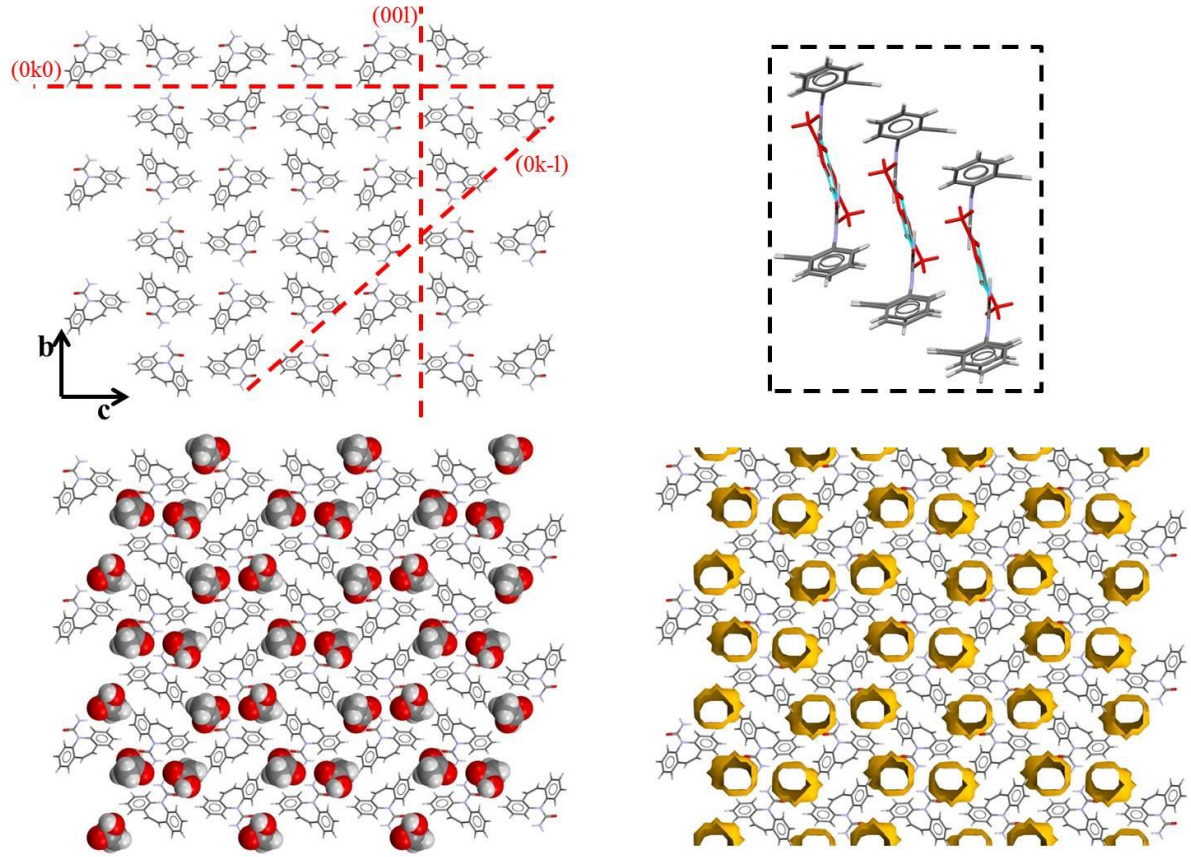

Figure 73 - Packing of CBZ molecules in CBZ:ACA exhibiting the (0k0), (00l) and (0k-l) planes, the ACA molecules highlighted in spacefill and the virtual voids originated from the solvent (acetic acid molecules are omitted when appropriate). Details include the clipping illustrating the translational stacking of the dimers in comparison to the acetic acid molecules (in red).

3.2.19 CBZ formic acid solvate (CBZ:FA)

The CBZ:FA solvate crystal structure consists of $R^2_2(8)$ motifs between the CBZ carboxamide and the FA (Figure 74). The hydrogen bonds in the ring are $N–H_{CBZ}\cdots O_{FA}$ (D=2.939 Å, d=2.133 Å, θ=151.84º) and $O–H_{FA}\cdots O_{CBZ}$ (D=2.548 Å, d=1.720 Å, θ=167.94º), and the functional groups are tilted by 27.16º. Similar to the CBZ:ACA, the CBZ N–H which is not involved in the dimer, forms lateral hydrogen bonds to neighbouring FA carbonyl on the

same plane of the dimer ($N–H_{CBZ}\cdots O_{FA}$: D=2.894 Å, d=2.157 Å, θ=140.89º). These interactions form $R^2_4(8)$ motifs between two CBZ:FA dimers, meaning that these neighbour dimers are oriented in the same direction. Aromatic CBZ C–H groups form additional interactions to neighbouring carbonyls in the structure. From the interaction maps it is shown that the $R^2_4(8)$ motifs present a favourable geometry and the aromatic groups occupy additional regions of interactions around the dimers.

The packing of CBZ:FA is also composed of one-dimensional translational stacking of CBZ molecules along *a* (Figure 75). The planes (0k0), (00l) and (0k-l) are likely slip systems along which the CBZ molecules can potentially move, although they are not as well-defined as in CBZ:ACA. With respect to the energetic relationship between molecules in the structure, the translational stacking of CBZ molecules contribute to the stronger interactions in the structure (-41.9 kJ mol^{-1}). In turn, the intermolecular energy of the CBZ:solvent dimer and the CBZ:solvent in the lateral hydrogen bond correspond to -33.7 kJ mol^{-1} and -20.5 kJ mol^{-1}, respectively.

It is interesting to compare the structure of the three CBZ solvates formed by carboxylic acids described in this chapter. As the size of the solvent molecule decreases, the CBZ packing rearranges in such a way leading to the variation of solvent arrangement from almost a layer to a pocket. The solvent molecules in CBZ:FA arrangein small pockets (Figure 75). The aromatic and the carboxamide portions of CBZ compose the surface of these FA pockets. The volume related to the acetic acid arrangement corresponds to 126.99 $Å^3$ and is equivalent to 9.4% of the unit cell.

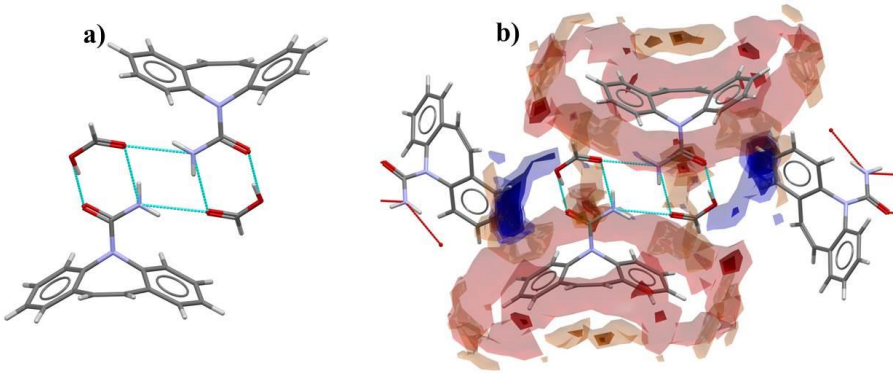

Figure 74 - Main hydrogen bonds observed in the CBZ:FA (a). The interaction map of the CBZ:solvent dimer shows missing regions of favourable interactions occupied by CBZ aromatic portions (b).

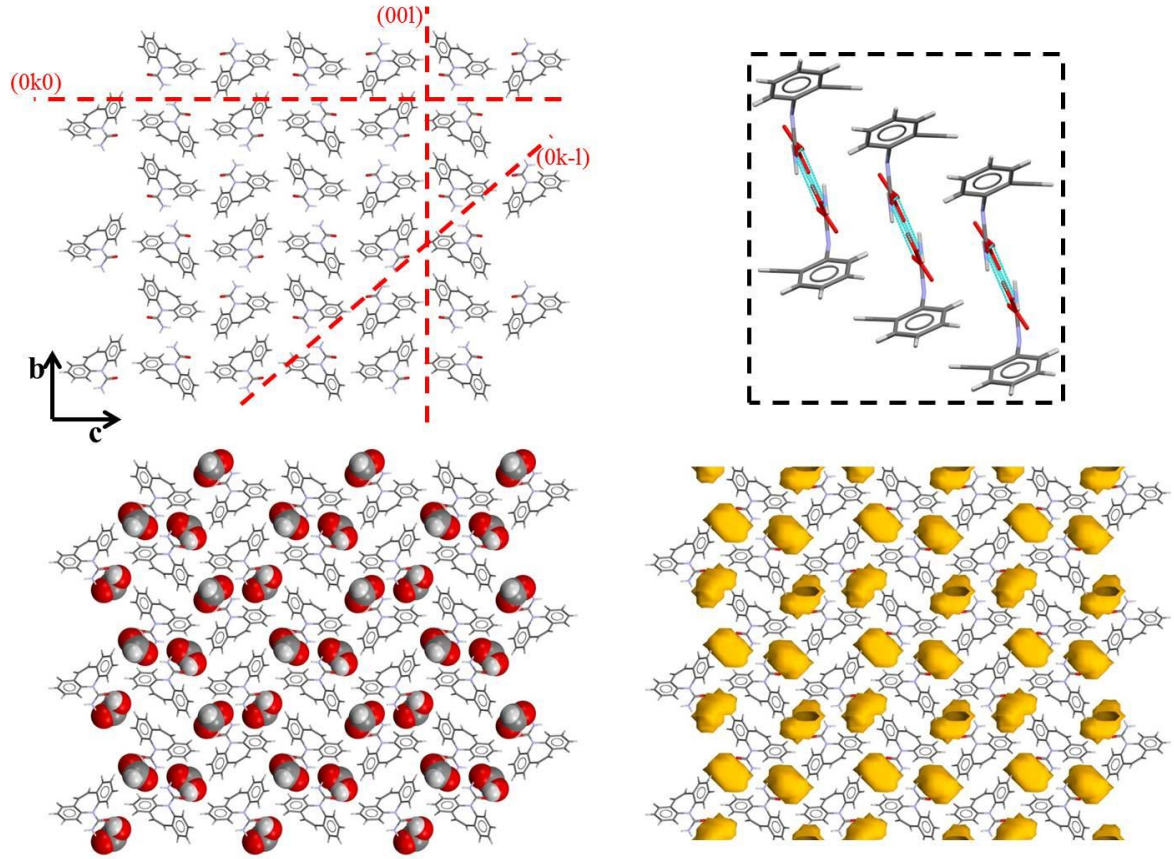

Figure 75 - Packing of CBZ molecules in CBZ:FA exhibiting the (0k0), (00l) and (0k-l) planes, the FA molecules highlighted in spacefill and the virtual voids originated from the solvent (formic acid molecules are omitted when appropriate). Details include the clipping illustrating the translational stacking of the dimers in comparison to the formic acid molecules (in red).

3.3. Comparison of structures

As mentioned in Chapter 1, the literature has used two main approaches to compare structures of crystals subjected to desolvation and phase transformations: the analysis of crystal packing and the calculation of the intermolecular interactions between the molecules in the crystals. While the analysis of packing focuses on the comparison of parent and daughter phases and on the arrangement of the guest molecules, the analysis of the intermolecular interactions indicates how strong the contact is between the host and guest. Taking the example of a channel solvate, the ease of molecular migration along the channel is expected to decrease as a result of strong intermolecular interactions of the guest and the walls of the channel. The stress along the channel may be released by the formation or movement of dislocations as well as by crack formation within the resulting host lattice, which may facilitate the desolvation process. It is difficult, however, to weigh or separate the influence of both aspects (packing and intermolecular interactions) on the outcome of stress induced transformations. In this context, the geometrical characterization of the slip systems existing within the lattice is proposed as an alternative, and perhaps more quantitative, tool to study molecular movements in the crystals.

These three aspects, packing, intermolecular interactions and geometrical parameters, are presented in this section and will be considered further in Chapter 8.

Following the analysis of the CBZ multicomponent structures, it is possible to categorize the materials into five different groups. Group 1 is formed by structures which contain intersecting channels of solvent molecules and pairs of CBZ molecules related by herringbone stacking (CBZ:ACE, CBZ:DMSO and CBZ:DMF) while the other groups show translational stacking. Group 2 is composed of channelled materials showing the coformer paired between two CBZ molecules (CBZ:DMA and CBZ:BZQ). This characteristic leads to channels formed by the dibenzoazepine portion of the CBZ molecules, while the other groups (1, 3, 4 and 5) show cavities formed from the aromatic and the carboxamide portions of CBZ. Groups 3 and 4 have channels between two sets of CBZ dimers, as shown in Figure 76.

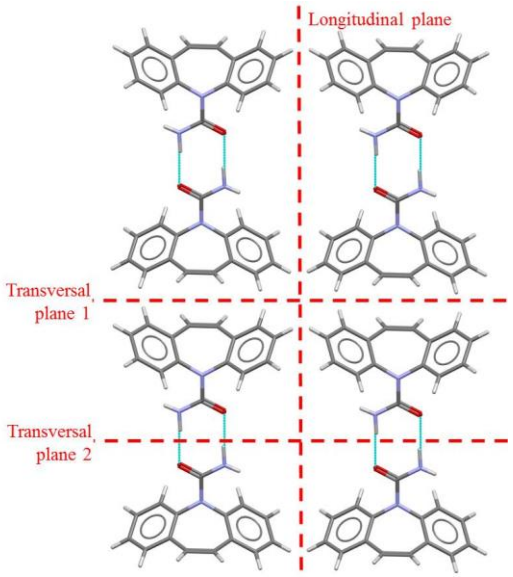

Figure 76 - Representation of different planes typically seen in the CBZ crystal forms, especially in Groups 3 and 4. The nomenclature of the planes is also used in the analysis of the geometric parameters of the structures.

The structures in Groups 3 (2CBZ:BZQ, 2CBZ:OXA, CBZ:2H_2O, CBZ:FORM, 2CBZ:DIOX and CBZ:NIT) and 4 (CBZ:TFE and 2CBZ:TFE) are essentially very similar. They change as a function of the displacement of neighbouring dimers along the axes which are longitudinal and/or transversal to the CBZ molecules. This leads to the disruption of the planes formed along the dibenzoazepine groups and/or through the channel between the dimers, respectively. Group 5 structures do not contain CBZ dimers, but a $R^2_2(8)$ motif between a CBZ molecule and a solvent molecule. This results in different solvent arrangements from layer-like to pocket, which seems to derive from the shrinkage of the CBZ host lattice as a function of the decreased size of the solvent molecule (from CBZ:TFA to CBZ:ACA and CBZ:FA).

This classification and the comparison of the CBZ multicomponent structures given above agree with that reported previously in the literature.[181,183] The similarities of the crystal

structures is shown in Table 3. The packing similarities were obtained from Mercury® by comparison of a cluster of 15 molecules, allowing molecular differences and small molecular components (tolerance of 20% for distance and 20 º for angles).

Variations in the results of reportedly very similar structures reflect differences in the lattice geometry. The comparison of CBZ:ACE and CBZ:DMF is an example. While the qualitative analysis has shown similar structural features, Figure 77 shows that the angles of the unit cells differ, which may have been the reason why packing similarities have only shown 3 similar CBZ molecules out of 15 in Table 3. With a change of the tolerance to 40% in Å and to 40º, the comparison shows an increased similarity of 6 CBZ molecules out of 15. A comparable situation is observed within the 2CBZ:BZQ, 2CBZ:OXA and CBZ:2H_2O structures. The three lattices show very similar structural features and cell parameters. 2CBZ:OXA and CBZ:2H_2O, however, only show 13 similar CBZ molecules out of 15. In this case, the difference is attributed to a distinct angle between the CBZ dimers and the plane along the dibenzoazepine moieties, which will be shown later in this section.

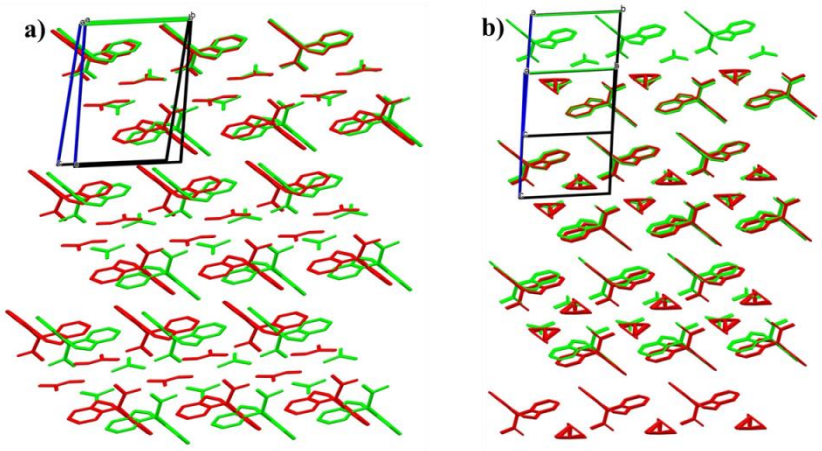

Figure 77 - Packing similarities within crystal structures of Group 1: *(a)* CBZ:ACE versus CBZ:DMF, and *(b)* CBZ:ACE versus CBZ:DMSO. While the three structures present the same type of CBZ arrangement, shows poorer similarity with CBZ:DMF due to different geometric parameters. Hydrogens are excluded to facilitate the interpretation.

The packing similarity of the multicomponent materials to the CBZ polymorphs appears to be a consequence of the stacking modes of CBZ in the structures. Group 1 showed higher similarities to CBZ Form III, which also contains herringbone stacking. Groups 3, 4 and 5, in turn, have higher similarities to CBZ Form I along the axis which give rise to translational stacking. As expected, Group 2 did not show clear comparative results, although it is a sub-type of translational stacking.

Table 3 - Crystal packing similarity results within the different CBZ multicomponent materials studied in the present work and their comparison to CBZ polymorphs* (from Mercury®, CSD).

		CBZ polymorphs				1			2		3						4		5	
		CBZ I	CBZ III	CBZ IV	CBZ V	CBZ:ACE	CBZ:DMSO	CBZ:DMF	CBZ:DMA	CBZ:BZQ	2CBZ:BZQ	2CBZ:OXA	CBZ:2H_2O	CBZ:FORM	2CBZ:DIOX	CBZ:NIT	CBZ:TFE	2CBZ:TFE	CBZ:TFA	CBZ:ACA
1	CBZ:ACE	2/15	7/15	2/15	2/15	-	-	-	-	-	-	-	-	-	-	-	-	-	-	-
	CBZ:DMSO	2/15	8/15	2/15	1/15	15/15	-	-	-	-	-	-	-	-	-	-	-	-	-	-
	CBZ:DMF	3/15	3/15	3/15	1/15	3/15	3/15	-	-	-	-	-	-	-	-	-	-	-	-	-
2	CBZ:DMA	2/15	2/15	2/15	1/15	2/15	2/15	2/15	-	-	-	-	-	-	-	-	-	-	-	-
	CBZ:BZQ	3/15	2/15	2/15	1/15	2/15	4/15	2/15	8/15	-	-	-	-	-	-	-	-	-	-	-
3	2CBZ:BZQ	5/15	2/15	2/15	1/15	4/15	4/15	4/15	2/15	4/15	-	-	-	-	-	-	-	-	-	-
	2CBZ:OXA	6/15	2/15	2/15	2/15	4/15	4/15	4/15	2/15	4/15	15/15	-	-	-	-	-	-	-	-	-
	CBZ:2H_2O	3/15	2/15	2/15	1/15	4/15	4/15	4/15	2/15	4/15	15/15	13/15	-	-	-	-	-	-	-	-
	CBZ:FORM	5/15	3/15	2/15	1/15	2/15	2/15	2/15	2/15	2/15	5/15	7/15	5/15	-	-	-	-	-	-	-
	2CBZ:DIOX	5/15	3/15	2/15	1/15	2/15	2/15	2/15	2/15	4/15	5/15	4/15	5/15	15/15	-	-	-	-	-	-
	CBZ:NIT	6/15	2/15	2/15	1/15	2/15	4/14	2/15	2/15	4/15	8/15	8/15	6/15	9/15	9/15	-	-	-	-	-
4	CBZ:TFE	6/15	2/15	2/15	2/15	3/15	3/15	2/15	2/15	3/15	6/15	6/15	4/15	6/15	6/15	6/15	-	-	-	-
	2CBZ:TFE	12/15	2/15	2/15	2/15	2/15	2/15	2/15	2/15	2/15	6/15	6/15	3/15	6/15	7/15	6/15	6/15	-	-	-
5	CBZ:TFA	3/15	1/15	1/15	1/15	2/15	1/15	2/15	1/15	1/15	3/15	4/15	3/15	5/15	5/15	5/15	3/15	3/15	-	-
	CBZ:ACA	3/15	1/15	1/15	1/15	1/15	1/15	1/15	2/15	2/15	3/15	3/15	4/15	3/15	3/15	3/15	6/15	3/15	3/15	-
	CBZ:FA	3/15	1/15	1/15	1/15	1/15	1/15	1/15	1/15	1/15	3/15	3/15	3/15	3/15	3/15	3/15	6/15	3/15	3/15	15/15

* The results of CBZ Form II packing similarities are not presented as no matches were found. It is worth remembering, however, that CBZ II is very similar to CBZ I (15 CBZ molecules out of 15) and the structure also shows translational stacking.

Table 4 - Morphology and coformer virtual cavity analysis of the different CBZ multicomponent materials. Packing coefficient is also provided. Data from Mercury®, CSD.

Group	Structure	BFDH	Reported (CSD) morphology	Cavities per area ($Å^{-2}$)[2]	Cavities per volume ($Å^{-3}$)[3]	Cavities per volume normalized ($x10^{-5}$)[4]	Volume% of cavities[5]	Weight% of coformer	Packing coefficient
1	CBZ:ACE	Block	-	0.011 / 0.010	0.0026	1.73	20.0	19.73	0.69
	CBZ:DMSO	Block	Block	0.011 / 0.009	0.0025	1.23	25.7	24.85	0.71
	CBZ:DMF	Block	Plate	0.011 / 0.009	0.0025	1.65	19.5	23.63	0.70
2	CBZ:DMA	Block	Plate	0.014	0.0012	0.26	25.9	26.94	0.71
	CBZ:BZQ	Block	Plate*	0.014	0.0012	0.42	32.0	31.39	0.69
3	2CBZ:BZQ	Needle	-	0.007	0.0014	0.54	19.2	18.62	0.72
	2CBZ:OXA	Needle	Needle*	0.007	0.0015	0.73	15.7	16.00	0.73
	CBZ:$2H_2O$	Needle	Block and needle	0.007	0.0015	0.56	19.2	13.23	0.69
	CBZ:FORM	Needle	-	0.007	0.0014	0.65	15.8	16.01	0.69
	2CBZ:DIOX	Needle	Needle*	0.007	0.0014	0.60	16.8	15.72	0.75
	CBZ:NIT	Needle	Needle	0.007	0.0014	0.48	19.7	20.53	0.71
4	CBZ:TFE	Block	Prism	0.006	0.0006	0.15	26.0	29.75	0.67
	2CBZ:TFE	Block[1]	Needle*	0.004	0.0007	0.32	16.0	17.47	0.71
5	CBZ:TFA	Needle	Block	0.007	0.0013	0.35	23.0	32.55	0.71
	CBZ:ACA	Needle	-	0.014	0.0027	1.08	16.9	20.27	0.69
	CBZ:FA	Needle	-	-	0.0029	2.32	9.4	16.30	0.71

*Data collected in the present work. Structures not yet reported in the CSD.

[1] Calculated from the doubled unit cell which presents TFE molecules in two possible positions (static disorder).

[2] Number of cavities per area of the unit cell's surface crossed by the cavities. Two faces are characterized in Group 1, as the structures present channels along two directions. The values in Group 1 are relative to *axc* and *bxc* faces, respectively. CBZ:FA was not characterized as the solvent is arranged in pockets.

[3] Number of cavities per volume of the unit cell.

[4] Number of cavities per volume of the unit cell divided by the volume occupied by the cavities.

[5] Virtual volume of the cavities calculated from the removal of the coformer molecules from the cif files.

Table 5 - Comparison of the intermolecular interactions in the different CBZ multicomponent materials as a function of the parameters of hydrogen bonds, HB, and intermolecular energy, E^{AB}. Data from Mercury®, CSD.

Group	Structure	$HB_{CBZ \rightarrow coformer}$		$E^{AB}_{CBZ \rightarrow coformer}$	$E^{AB}_{coformer \rightarrow coformer}$[4]	$E^{AB}_{CBZ\ dimer}$	$E^{AB}_{CBZ\ stack}$
		Number	d, θ (Å, º)	(kJ mol^{-1})	(kJ mol^{-1})	(kJ mol^{-1})	(kJ mol^{-1})
1	CBZ:ACE	1	2.275, 142.09	-23.9	-8.0	-30.5	-44.5
	CBZ:DMSO[1]	1	-	-27.8	-11.4	-28.3	-44.4
	CBZ:DMF	1	1.963, 154.47	-32.4	-6.9	-30.6	-45.2
2	CBZ:DMA[1]	1	-	-39.3	-6.5	-33.0	-13.7
	CBZ:BZQ	2	2.140, 157.43 2.601, 158.65	-32.8 -6.5	-9.9	-34.2	-20.0
3	2CBZ:BZQ	2	2.323, 149.72	-22.6	-9.5	-33.1	-46.4
	2CBZ:OXA	4	1.508, 166.77 2.189, 118.92 1.538, 173.51 1.906, 153.16	-30.2 -18.0 -30.7 -28.2	-4.9	-37.8	-42.0 -41.6
	CBZ:2H_2O	2	1.765, 158.20 2.434, 146.09	-29.9 -13.2	-16.7	-37.5	-50.1
	CBZ:FORM	4	2.216, 144.04 2.068, 152.09 2.066, 172.43 2.140, 145.82	-18.9 -21.9 -23.1 -21.3	-27.8	-31.7 -34.3	-44.3 -44.2
	2CBZ:DIOX[2]	2	-	-27.5	-32.3	-30.0	-48.2
	CBZ:NIT[1]	1	2.379, 126.35	-10.9	-6.6	-34.4	-43.0
4	CBZ:TFE	2	1.805, 169.31 2.444, 124.90	-32.9 -15.2	-22.0	-33.9	-43.8 -44.1
	2CBZ:TFE[3]	1	1.941, 179.66	-29.7	-22.3	-33.4	-41.9
		0	-	-	-	-32.7	-42.2

Group	Structure	$HB_{CBZ \rightarrow coformer}$		$E^{AB}_{CBZ \rightarrow coformer}$	$E^{AB}_{coformer \rightarrow coformer}$ [3]	$E^{AB}_{CBZ\ dimer}$	$E^{AB}_{CBZ\ stack}$
		Number	d, θ (Å, º)	(kJ mol^{-1})	(kJ mol^{-1})	(kJ mol^{-1})	(kJ mol^{-1})
5	CBZ:TFA[1]	3	2.005, 165.54 1.539, 172.60 2.296, 133.46	-31.5 -20.6	-4.6	-	-40.1
	CBZ:ACA	3	2.208, 152.43 1.666, 167.64 2.323, 125.08	-35.4 -16.5	-4.0	-	-44.2
	CBZ:FA	3	2.133, 151.84 1.720, 167.94 2.157, 140.89	-33.7 -20.5	-	-	-41.9

[1] Structure presents rotational disorder. Hydrogen bond parameters have not been measured.

[2] Structure presents a complex disorder state. The E^{AB} was calculated from the doubled unit cell.

[3] Structure presents static disorder and the E^{AB} was calculated from the doubled unit cell. Also, one set of CBZ dimers do not hydrogen bond to TFE molecules.

[4] For simplification, $E^{AB}_{coformer \rightarrow coformer}$ expresses the intermolecular energy between the two closest coformer molecules.

Table 4 shows that, in general, materials with higher similarities to CBZ Form I have also shown predicted needle morphologies. Structures similar to Form III resulted in predicted block morphologies. This characteristic is attributed to the similarities of the unit cell dimensions of these materials. A needle morphology is essentially observed in highly anisotropic CBZ structures which have a translational stacking mode, and experimental data tends to agree with the predicted crystal shape. It is suggested that the formation of a CBZ:CBZ stack contributes to the formation of a CBZ dimer, and vice-versa, as these events occur along the same axis. Group 2 shows diverse unit cells and a different type of stacking compared to the other groups, which reflects the prediction of blocks and the description of plate-like crystals from experimental data. The prediction of block morphologies while experiments show more anisotropic crystals (Groups 2 and 4), may reflect the existence of important interactions between molecules in the crystal and between crystal and crystallization environment.

Table 4 also presents an analysis of the "virtual cavities" in the CBZ multicomponent materials as a function of number, area and volume. Virtual cavities are the spaces which would be left if the solvent could be removed without movement of the remaining host molecules. In general, characterization of the cavities helps to discriminate amongst the types of coformer arrangements observed within the structures and distinguish the different groups. It is clear that, although the structures in Groups 4 and 5 have correlations in their intermolecular interactions and packing, they show significant variations in the arrangement of the solvent. Also, intersecting channels, small channels and pockets show a higher number of cavities per volume of the unit cell normalized to the volume of the cavities. The opposite situation exists in Group 2, as the channels are lower in number but larger in size. The distinction in packing coefficient among the different multicomponent materials is not as clear as the correlations made from the analysis of the virtual cavities.

A comparison of the hydrogen bond patterns in the CBZ materials is complicated by the fact that some structures had disordered solvent. As an alternative, intermolecular energy calculations using the UNI force-field potential were performed in Mercury, and the combination of these two approaches is shown in Table 5. In general, the dimension of the hydrogen bonds followed the same trend observed on the basis of intermolecular energies. As expected, stronger intermolecular interactions are observed between CBZ and coformer molecules linked via O–H···O hydrogen bonds from dicarboxylic acids and alcohols (2CBZ:OXA, CBZ:TFE, 2CBZ:TFE, CBZ:TFA, CBZ:ACA and CBZ:FA). In the case of Group 5, the interactions are even stronger owing to the formation of $R^2_2(8)$ motifs between CBZ and solvent molecules. Strong interactions between CBZ and the coformer are also observed in Group 2, possibly as a result of the coformer being paired between the

dibenzoazepine portions of CBZ molecules. DMF within the CBZ:DMF structure also shows stronger interactions to CBZ in comparison to the other structures in Group 1, which may reflect the differences in the solvent arrangement.

CBZ:BZQ, CBZ:2H_2O and CBZ:TFE show significantly different magnitudes of CBZ:coformer interactions in the same structure. It means that, in the case of CBZ:2H_2O and CBZ:TFE, one solvent molecule interact very strongly to CBZ, while the other non-equivalent solvent molecule weakly interacts to CBZ. In the case of CBZ:BZQ, the strong and the weak interactions take place in the same molecule, but in distinct carbonyls. Bearing in mind that BZQ and TFE systems present other multicomponent structures of lower coformer stoichiometry, one might think about the contribution of these weak interactions to the molecular movements in the CBZ:BZQ and CBZ:TFE crystals.

The interactions between guest molecules are, in general, much weaker. Exceptions are found in CBZ:2H_2O, CBZ:FORM, 2CBZ:DIOX, CBZ:TFE and 2CBZ:TFE. Strong interactions are present in CBZ:FORM as a result of a $R^2_4(8)$ motif formed between formamide molecules arranged in a dimer. In the case of CBZ:2H_2O, CBZ:TFE and 2CBZ:TFE, the strength of coformer interactions is explained by their nature which corresponds to O–H···O hydrogen bonds. In the case of 2CBZ:DIOX, however, the result might be an artefact from the disorder of dioxane molecules along the channel.

The strongest intermolecular interactions are observed between CBZ molecules in a dimer and between CBZ pairs related by stacking. While the hydrogen bonds in the CBZ dimer do not change expressively within the different structures, the stacking interactions in Group 2 diverge from the other groups. This result could actually be anticipated because of the type of coformer-paired stacking in CBZ:DMA and CBZ:BZQ. On the other hand, no such distinction was demonstrated between the intermolecular energy of CBZ molecules related by herringbone and translational stacking.

Up to this point, the packing and the intermolecular interactions in CBZ multicomponent materials have been discussed. The structure analysis has shown that different stacking modes form different types of crystallographic planes in the lattices. Yet, differences are also seen in structures which are considered isostructural. The characterization of the geometric parameters of the planes in these structures was used as a tool to assess these differences. For example, considering a CBZ dimer, planes may be formed along the transversal or the longitudinal axes (as shown in Figure 76). Longitudinal planes run along the lateral side of a dimer and cross the solvent cavity. Transversal planes are observed crossing the carboxamide groups or along the dibenzoazepine portions of CBZ molecules. Although planes intersecting strongly hydrogen bonded regions, such as the CBZ dimers, are not weak planes as

they may show higher resistance to molecular movements, they are occasionally characterized in this section.

The geometric parameters characterized were the angles between different dimers along the transversal and longitudinal planes, the tilt angles of the molecular axis with respect to the planes, and the angles between the planes. The dimers' planes were calculated along the two aromatic carbon atoms neighbouring the nitrogen in the seven-membered ring of two CBZ molecules related in a dimer. This setting was used to avoid artefacts from the tilt of dimers and the coplanarity offset observed in some of the structures. In the case of Group 5, however, the planes between CBZ and solvent molecules were determined along the carboxamide and the carboxylic groups related in the $R^2_2(8)$ motif. The results obtained within Groups 1 to 5 are shown in different tables to facilitate the comparison of the structures.

The structures in Group 1 have only been characterized by means of the plane formed along the inverse-cup stacking on (00l). The angle between the dimers and the transversal plane in CBZ:ACE, CBZ:DMSO and CBZ:DMF did not vary considerably (Table 5). On the other hand, the structures in Group 2 presented significant changes in the geometric parameters of the slip systems and the dimers (Table 7). Considering the CBZ arrangement in CBZ:DMA and CBZ:BZQ, the main difference reflects the tilt of the CBZ dimers along the longitudinal plane.

The structures in Group 3 also present angled dimers along the longitudinal CBZ molecular axis (Table 8). In this case, while 2CBZ:BZQ, 2CBZ:OXA, CBZ:2H_2O and CBZ:NIT show dimers with the same orientation surrounding a cavity, CBZ:FORM and 2CBZ:DIOX show dimers tilted along the longitudinal planes by 117.56^o and 126.34^o, respectively. Another interesting aspect accounts for the angle between dimers related along the transversal plane. The results show that CBZ:2H_2O and 2CBZ:OXA are the two extremes of tilted dimers, the former being characterized by a smaller angle while the latter's is larger. This difference may reflect the constraint imposed by the interaction of the oxalic acid molecule with different CBZ dimers related by stacking.

As expected, the crystal forms in Groups 4 and 5 have shown different geometrical characteristics related to drastic changes in packing and coformer arrangement (Table 9 and Table 10). The planes in the structures present modified chemical environments and are interrupted along the dibenzoazepine, as in CBZ:TFE for instance. The comparison of CBZ:TFA, CBZ:ACA and CBZ:FA clearly show the structural changes related to the shrinkage of the lattices as the solvent molecule decrease in size. These differences are more evident along longitudinal planes..

Table 6 - Comparison of the geometrical relationship between dimers and planes in the CBZ multicomponent materials belonging to Group 1 (from Mercury®, CSD).

Couple of planes	Materials		
	CBZ:ACETO	CBZ:DMSO	CBZ:DMF
Dimer x (transversal)*	61.83º	64.12º	60.86º

* The (transversal) plane corresponds to (00l) planes. It shows characteristics of transversal 1 planes.

Table 7 - Comparison of the geometrical relationship between dimers and planes in the CBZ multicomponent materials belonging to Group 2 (from Mercury®, CSD).

Couple of planes	Materials	
	CBZ:DMA	CBZ:BZQ
Dimer x Dimer (along transversal 1)	0º	0º
Dimer x Dimer (along longitudinal)	35.62º	0º
Dimer x (transversal 1)*	38.83º	39.77º
Dimer x (transversal 2)†	50.71º	43.88º
Dimer x (longitudinal)♦	74.71º	47.90º
(transversal 1) x (longitudinal)	50.19º	43.93º
(transversal 2) x (longitudinal)	85.78º	70.23º
(transversal 1) x (transversal 2)	83.40º	83.57º

* The (transversal 1) plane corresponds to (001) planes, which are equivalent in both structures. It actually shows characteristics of transversal 1 and transversal 2.

† The (transversal 2) plane corresponds to the (100) plane in CBZ:DMA and to the (220) plane in CBZ:BZQ.

♦ The (longitudinal) plane corresponds to the (021) plane in CBZ:DMA and to (0-11) plane in CBZ:BZQ.

Table 8 - Comparison of the geometrical relationship between dimers and planes in the CBZ multicomponent materials belonging to Group 3 (from Mercury®, CSD).

Couple of planes	Materials					
	2CBZ:BZQ	2CBZ:OXA	CBZ:2H_2O	CBZ:FORM	2CBZ:DIOX	CBZ:NIT
Dimer x Dimer (along transversal)	122.40º	73.36º	134.71º	117.56º	126.34º	116.35º
Dimer x Dimer (along longitudinal)	0º	0º	0º	117.56º	126.34º	0º
Dimer x (transversal)*	61.2º	53.32º	67.35º	59.79º	63.16º	-
Dimer x (longitudinal)†	89.64º	89.13º	89.45º	86.76º	88.82º	89.50º
(transversal) x (longitudinal)	90º	90º	90º	84.01º	85.77º	-

* The (transversal) plane corresponds to (0k0) planes. It shows characteristics of transversal 1 planes.

† The (longitudinal) plane corresponds to (h00) planes along the CBZ dimer axis.

Table 9 - Comparison of the geometrical relationship between dimers and planes in the CBZ multicomponent materials belonging to Group 4 (from Mercury®, CSD).

	Materials	
Couple of planes	CBZ:TFE	2CBZ:TFE[1]
Dimer x Dimer (along transversal 2)	0º	^{a}0º / ^{b}0º
Dimer x Dimer (along longitudinal)	0º	^{a}0º / ^{b}0º
Dimer x (transversal 2)*	57.51º	^{a}55.72º / ^{b}75.19º
Dimer x (longitudinal)†	83.44º	^{a}76.16º / ^{b}52.93º
(transversal 2) x (longitudinal)	86.42º	$^{a/b}$59.91º

* The (transversal 2) plane corresponds to the (01-1) plane in CBZ:TFE (it shows characteristics of transversal 1 and transversal 2) and to the (002) plane in 2CBZ:TFE.

† The (longitudinal) plane corresponds to the (022) plane in CBZ:TFE and to the (01-1) plane in 2CBZ:TFE (it shows characteristics of longitudinal and transversal 1).

[1] The 2CBZ:TFE crystal structure presents two types of CBZ dimers, one hydrogen bonded to the TFE solvent molecule, and another which is not linked to TFE. The dimers are both represented on the table and identified as "^{a}" and "^{b}", respectively. The angle between the planes along the dimers is 57.31º.

Table 10 - Comparison of the geometrical relationship between dimers and planes in the CBZ multicomponent materials belonging to Group 5 (from Mercury®, CSD).

	Materials		
Couple of planes	CBZ:TFA	CBZ:ACA	CBZ:FA
Dimer x Dimer (along transversal 1)	71.80º	68.62º	71.53º
Dimer x Dimer (along longitudinal)	71.80º	68.62º	71.53º
Dimer x (transversal 1)*	54.95º	55.69º	54.24º
Dimer x (transversal 2)†	68.92º	48.30º	43.73º
Dimer x (longitudinal)♦	76.55º	68.63º	64.69º
(transversal1) x (longitudinal)	78.26º	90º	90º
(transversal 2) x (longitudinal)	61.21º	49.47º	50.22º
(transversal1) x (transversal 2)	40.53º	40.53º	39.78º

* The (transversal 1) plane corresponds to the (400) plane in CBZ:TFA and to the (010) planes in CBZ:ACA and CBZ:FA.

† The (transversal 2) plane corresponds to the (10-1) plane in CBZ:TFA and (01-1) planes in CBZ:ACA and CBZ:FA.

♦ The (longitudinal) plane corresponds to the (001) plane in CBZ:TFA and (004) planes in CBZ:ACA and CBZ:FA.

3.4. Conclusions

The past reports in the literature have used two main approaches to compare the crystal structures of materials subjected to desolvation and phase transformation: the analysis of crystal packing and intermolecular interactions between the molecules in the crystals. It is difficult, however, to weight or separate the influence of both aspects on the outcome of stress-induced transformations. In this context, the present chapter has proposed the geometrical characterization of the slip systems existing within the lattices of CBZ crystal forms as an alternative to study the molecular movements in the crystals.

In total, 14 solvates (including one hydrate) and three cocrystals were selected for the study of desolvation and sublimation reactions. The CBZ materials were grouped according to their structure similarities. It has been demonstrated both here and elsewhere in the literature that CBZ molecules tend to interact in dimers and via translational stacking. The main coformer arrangement was in channels, however, such channels have shown different characteristics. Potential weak planes have been identified and compared as they can also be influential with regards to molecular migration, surface characteristics and mechanical properties. Two main types of planes were characterized in relation to the CBZ dimers in the structures: (i) planes formed along the lateral side of a dimer which cross the solvent cavity (*i.e.* longitudinal planes), and (ii) planes crossing the carboxamide groups or along the dibenzoazepine portions of CBZ molecules (*i.e.* transversal planes).

It is interesting to be noted that sets of equivalent crystallographic planes have shown geometric differences not only within polytypic structures (2CBZ:BZQ, 2CBZ:OXA and CBZ:2H_2O, compared to CBZ:FORM and 2CBZ:DIOX, and to CBZ:NIT), but also among strictly isostructural materials (2CBZ:BZQ, compared to 2CBZ:OXA and to CBZ:2H_2O). It is concluded therefore that the nature of the coformer do not affect only the intermolecular interactions, but also the CBZ lattice (even in more rigid isostructural solids). The influence of the structural similarities and differences of packing, intermolecular interactions and geometrical parameters on the properties of the materials will be considered in the further chapters, especially in Chapter 8.

CHAPTER 4 – The preparation of carbamazepine and carbamazepine multicomponent materials at laboratory scale

4.1. Introduction

Various methods for preparing multicomponent materials are described in the literature.[18,52] The most common and successful techniques include solution crystallization, slurrying and grinding, with each method presenting differing challenges. For example, while solution crystallization is the preferred approach since it is easily scaled-up, differences in the solubility of the components in a system often lead to the precipitation of separate phases. This characteristic has implications in the preparation of multicomponent forms. In the case of cocrystals, due to the existence of skewed phase diagrams because of components having different solubilities, the preparation methods have been typically approached in two ways: reaction crystallization and solid-solid grinding (neat and liquid assisted).

Reaction crystallization follows the equilibrium between cocrystal and cocrystal formers in solution.[47] It is essentially a slurry method in which increasing amounts of one coformer are added to a solution pre-saturated with the other component, which causes the crystallization environment to shift to a region where the cocrystal is stable. Grinding, however, is effective for producing cocrystals because the composition in a grinding jar is already set within the stoichiometric domain where the cocrystal is the most stable form, regardless of solubility. The limitations of the reaction crystallization and grinding techniques are, however, the kinetics and the influence of seeding effects, the possible formation of an amorphous phase, the physical stability of the materials, the large-scale production and the absence of any significant control over the crystal habit.

With these points in mind, the main aim of the Chapter 4 is to describe the preparation of various samples at small batches (*circa* 1 gram) which will be suitable for the specific study of stress-induced transformations of CBZ multicomponent materials. As desolvation reactions are thought, in some instances, to proceed via an amorphous intermediate,[114] one major concern of the work was to avoid the influence of seeds, defects and extensive amorphous content on the outcome of the proposed experiments. Therefore, to avoid possible interferents, solution crystallization was the chosen method typically used in this work. Eventual crystal habit and surface variations of the resulting cocrystals and solvates are tested

in this chapter as a function of the solution concentration and, in the case of needle-like crystals, the crystallization environment. In order to change the crystallization environment/conditions, specific ethanolic solutions of the respective coformer were prepared along with CBZ.

Prior to the crystallization experiments, the equilibrium solubility of the corresponding solid phase was determined in different solution compositions. The aim of these equilibrium solubility measurements is to find the conditions under which distinct crystalline phases occurred and to calculate accurate concentration/supersaturation conditions to be used in subsequent cooling crystallization experiments, however, other considerations are also made throughout the text. The solubility was assessed in saturated solutions generated by slurrying CBZ in an appropriate ethanol:coformer proportion and allowing them to equilibrate for at least 24 hours. After the system reached equilibrium, the solid phase was separated from the mother liquor and analysed by PXRD, while the amount of CBZ remaining in solution was quantified by UV spectrometry or LC analyses. The resulting filtered solids were additionally characterized by SEM and optical microscopy. Chapter 2 provides more details of the solubility determination method described above. The CBZ concentration of the solution phase at each ethanol:conformer proportion was combined with the PXRD analysis of the solids to determine the equilibrium solubility of the respective solid. The data is plotted as the molar proportion of coformer in ethanol against the amount of dissolved CBZ in solution in $mg.mL^{-1}$. One additional graph of the CBZ/BZQ system was plotted with the molar concentration of CBZ against the molar concentration of BZQ in solution.

An exception to the equilibrium solubility procedure described above was in the preparation of the cocrystal of CBZ with oxalic acid. The preparation of this crystal form involved solution crystallization using the same solvent and condition reported in the literature (ethyl acetate).[196] No preliminary phase diagram of CBZ solubility as a function of OXA concentration in ethyl acetate was studied.

Except in the case of 2CBZ:OXA, ethanol was chosen in the experiments as a common solvent for a variety of reasons: it is frequently used in crystallization studies, it has no reported multicomponent phases with CBZ and it provides moderate CBZ solubility. The concentration of the crystallization solutions was defined in relation to the measured solubility of the equilibrium solid phase in the respective solvent mixture. In general, the concentrations ranged from two-fold (2xS), to four-fold (4xS) and six-fold (6xS) of the solubility values, when appropriate.

Cooling crystallization was used to preserve the activity of the solvents during nucleation. The solutions were prepared by solubilizing CBZ by heating and with stirring in the corresponding solvent mixture. The solutions were further cooled to precipitate without the

addition of seeds. The cooling rate was set to 5 $^{o}C.min^{-1}$ and no agitation was used to avoid particle breakage. Chapter 2 provides more details of the general crystallization method described above. Any additional experiments are described as necessary in the following text. Appendix 2 characterizes the preferred orientation of the samples. It presents the powder diffraction patterns indexed with the main reflections. Although the crystals were not indexed by single crystal X-ray diffraction, their dominant surface was inferred by the preferred orientation seen in the PXRD patterns. In the case of CBZ:$2H_2O$, it was also possible to identify and differentiate the crystal surfaces because they present visually different properties (*i.e.* cracks).

4.2. Results and discussion

4.2.1. The equilibrium solubility of the different CBZ multicomponent solids

The equilibrium solubility of CBZ and the different CBZ multicomponent solids as a function of binary solvent mixtures of ethanol and coformer is shown in Figure 78. The diagrams generally illustrate two regions of stability. One region has CBZ Form III as the stable solid, while a second has the multicomponent solid as the stable solid. In some experiments, mixtures of both phases were obtained possibly because the system had not reached equilibrium, or the system was at an eutectic point. It is also noteworthy that the minimum concentration of BZQ required to crystallize the cocrystal is considerably lower than the minimum amount of the liquid coformers required to crystallize the respective solvates. The analysis of the cocrystal literature shows that this is a common characteristic of cocrystalline phases.[200]

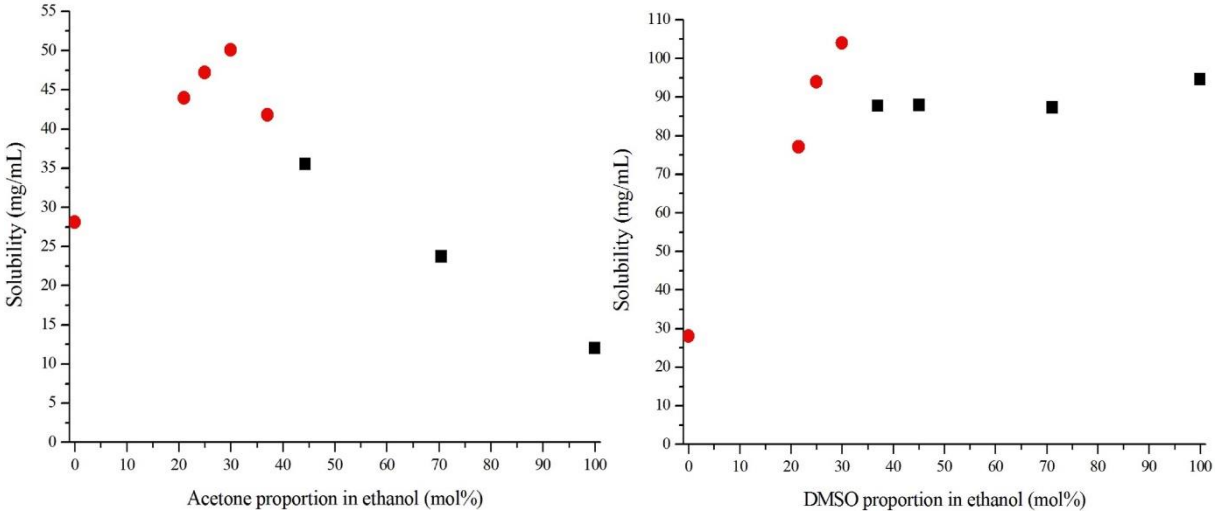

(Figure 78 continues in the next page)

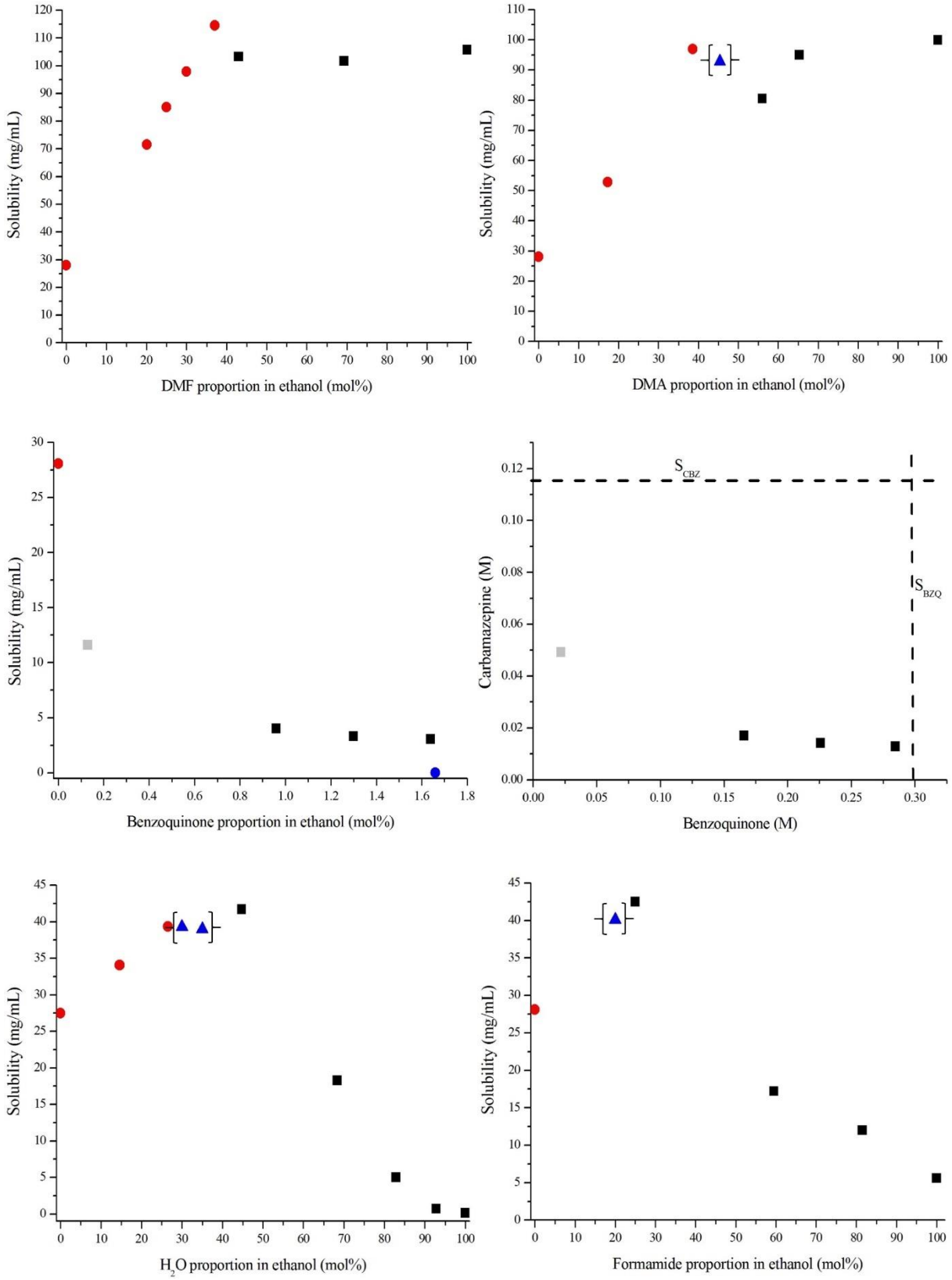

(Figure 78 continues in the next page)

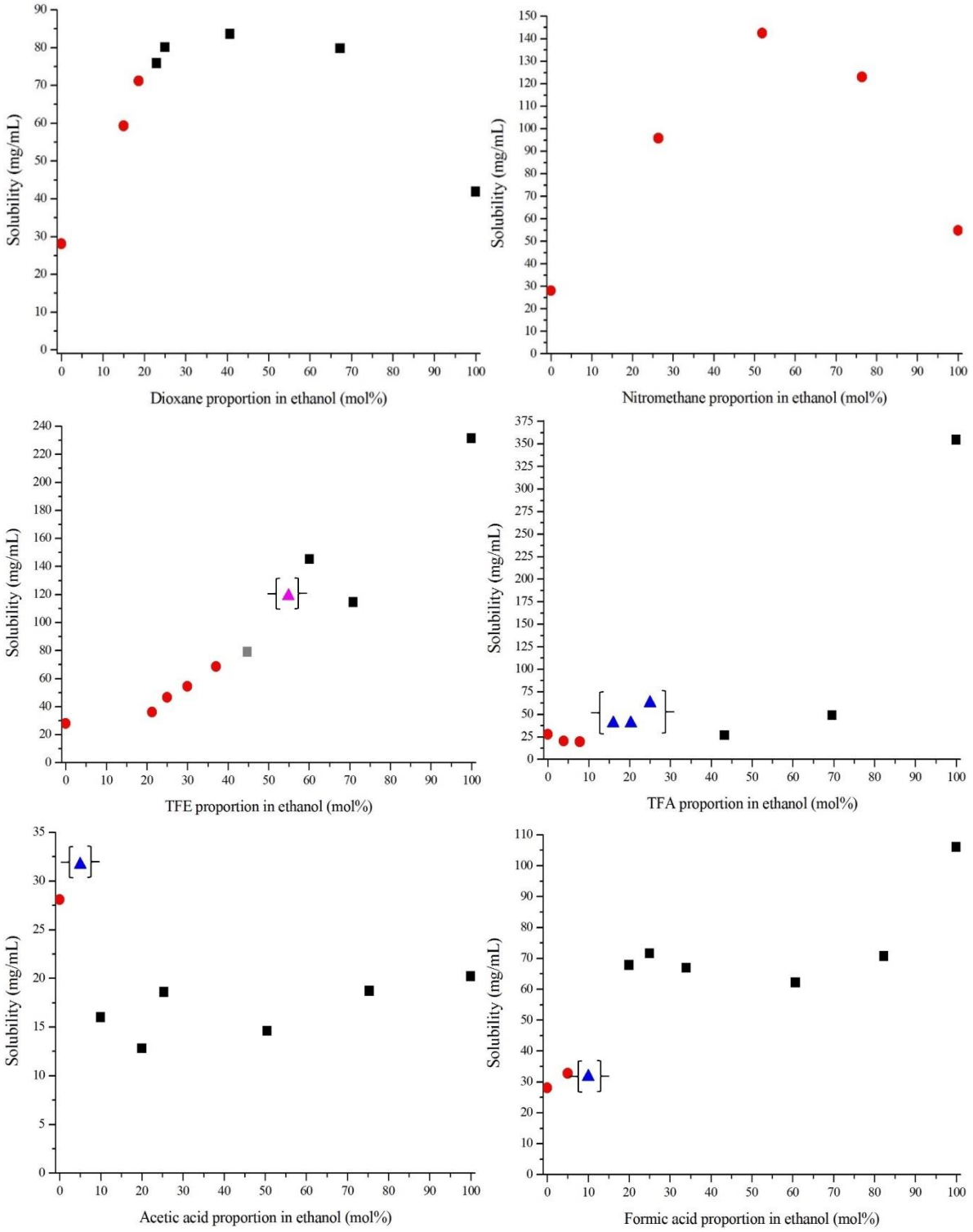

Figure 78 – Equilibrium solubility diagrams of CBZ multicomponent forms (room temperature). The graphs combine the results of solution quantification and solid phase identification to show the solubility and the stability regions of different CBZ crystal forms in ethanol:conformer. The data is plotted as the molar proportion of coformer in ethanol against the amount of dissolved CBZ in solution in $mg.mL^{-1}$, but one additional graph of the CBZ/BZQ system was plotted with the molar concentration of CBZ against the molar concentration of BZQ in solution. The symbols and their colour show the identity of the solid phases at the corresponding solvent composition: red circles represent CBZ Form III; squares CBZ multicomponent phases (grey and black colours symbolise different stoichiometric cocrystal forms); and blue circles BZQ (only in the respective graphs of the CBZ/BZQ system). Regions characterized as mixtures of Form III and multicomponent phase are shown in between brackets and represented by blue triangles. In the case of the CBZ/TFE system, a mixture of solvates of different stoichiometry is represented by pink triangles.

Another issue observed in the profiles of Figure 78 is demonstrated by the CBZ/DMF system. While the solid-state characterization has shown that slurrying CBZ in 37 mol% of DMF in ethanol leads to Form III, it is possible that this point is supersaturated in regards to the solubility of the solvate. It suggests that more time was required for the system to equilibrate (it is possible that heat/cool cycles should be applied during slurrying as an attempt to avoid such possible kinetic effects). Similar situations were also observed for CBZ:ACE, CBZ:DMSO, 2CBZ:DIOX and CBZ:TFE/2CBZ:TFE systems. It appears that this feature is common in regions where the activity of the coformers is close to the eutectic point of the solubility curves of both phases. Another possible explanation is that the solubility profiles indeed characterize the different solubility tendencies in the ethanol mixtures as the solution environment changes.

We note that CBZ:DMA and CBZ:NIT have also shown a few particularities during their solubility studies. Figure 78 demonstrates that slurrying experiments in nitromethane:ethanol did not result in solvate formation in any proportion of the coformer (even at 100%), although CBZ:NIT was obtained from cooling crystallization. Repetition of the experiments and the grinding of CBZ Form III with two equivalents of NIT also did not result in solvate formation. While preliminary experiments in dimethyl acetamide:ethanol have shown a similar effect, the results were not reproducible and repetition of the slurry experiments sometimes lead to the formation of the DMA solvate. Possibly coincidental, CBZ:DMA could only be obtained by slurrying after single crystals were prepared from preliminary cooling crystallizations in the same laboratory.

Different hypothesis accounting for kinetic and thermodynamic effects were raised in an attempt to understand what caused such behaviour in the CBZ:DMA and CBZ:NIT solvates. Kinetics may have influenced the results based on the time needed to reach the equilibrium in solution or possibly because of energetic barriers and templating on the surface of mother particles. Similarly, thermodynamic effects could also play a role when the CBZ solvates are metastable or are physically unstable. To have a better understanding of these phenomena, additional experiments were attempted. For example, slurry experiments were performed for one week rather than 24 hours, and the effect of the starting materials (CBZ Form III or the respective CBZ solvate) on the slurrying outcome was investigated. Extra care was also taken by collecting PXRD patterns of the solids directly harvested from solution with no drying step (the so-called "*wet cake*" in the case of slurries). To investigate the physical stability of the solvates, the single crystals of CBZ:DMA and CBZ:NIT obtained from cooling crystallization were systematically analysed after filtration.

The diffraction patterns shown in Figure 79 and Figure 81 summarize the NIT and DMA studies. They show that one-week slurries of CBZ Form III in DMA or NIT lead to the formation of CBZ:DMA or CBZ Form III (with traces of CBZ:2H_2O), respectively. The slurry generated from single crystals of CBZ:DMA and equilibrated for 24 hours, however, resulted in CBZ Form I or Form I with minor quantities of CBZ:DMA. Slurries of CBZ:NIT obtained from cooling crystallization could not be performed because of stability issues. The results show that, while the CBZ:DMA filtered crystals are stable for months under normal conditions, CBZ:NIT single crystals become opaque very quickly after being harvested from solution. The SEM micrographs of CBZ:NIT crystals analysed a few hours after filtration also indicate that desolvation has occurred (Figure 80). The PXRD patterns suggest CBZ:NIT single crystals stored at room temperature evolved to mixtures of CBZ polymorphs (Forms I, II and III) and CBZ:2H_2O (Figure 79).

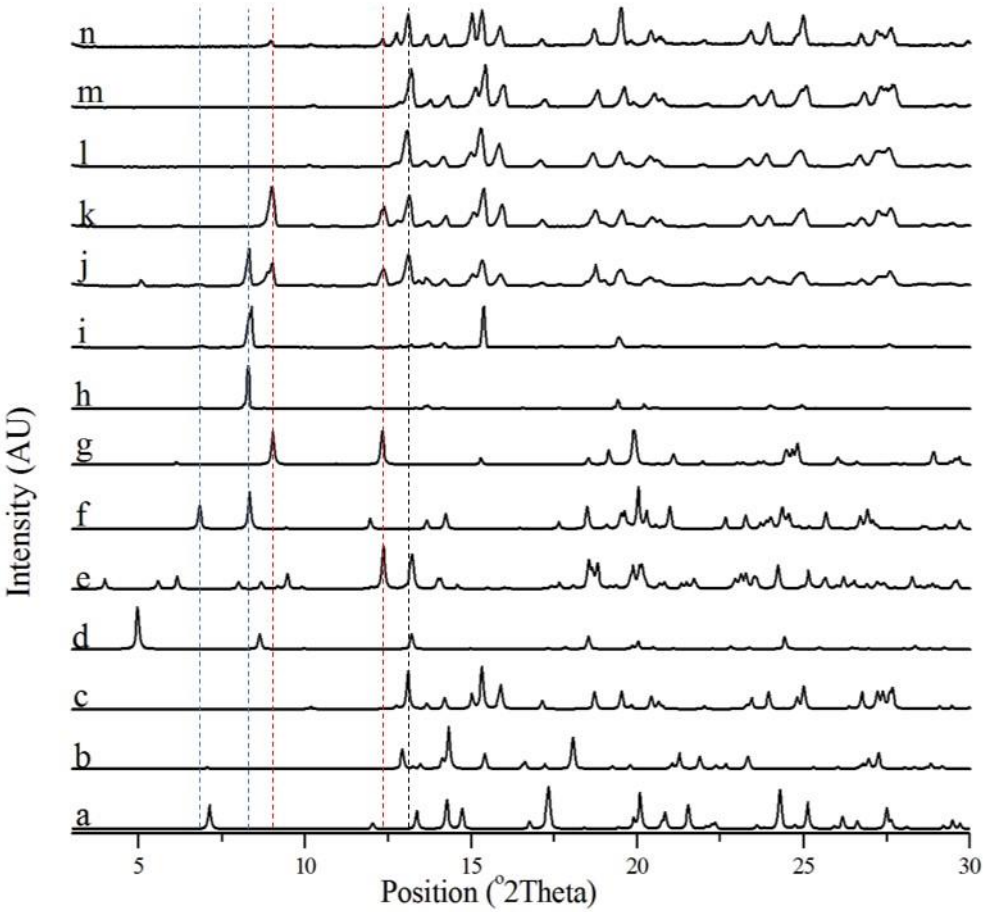

Figure 79 - Summary of slurrying, grinding and cooling solution crystallization experiments of CBZ:NIT. The calculated patterns of reference materials are added for clarification (*a*: CBZ V; *b*: CBZ IV; *c*: CBZ III; *d*: CBZ II; *e*: CBZ I; *f*: CBZ:NIT; *g:* CBZ:2H_2O). The experimental PXRD patterns are displayed on the top (*h*: CBZ:NIT wet single crystals; *i*: CBZ:NIT filtered single crystals; *j*: CBZ:NIT filtered single crystals stored for one day; *k*: CBZ:NIT filtered single crystals stored for 4 months; *l*: sample obtained from grinding of CBZ with two equivalents of NIT, 25 Hz for 30 min; *m*: sample obtained from slurrying of CBZ in NIT for 24h; *n*: sample obtained from slurrying of CBZ in NIT for 1 week).

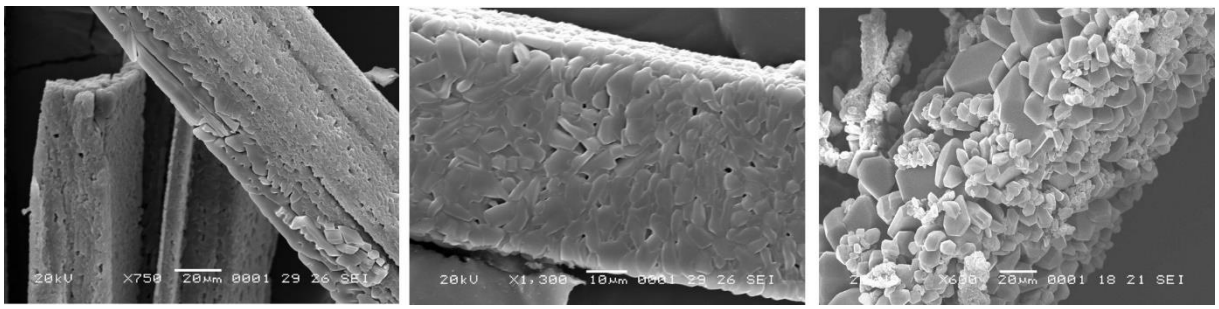

Figure 80 - Scanning electron micrographs of CBZ:NIT single crystals obtained from cooling solution crystallization and exposed to room conditions for a few hours.

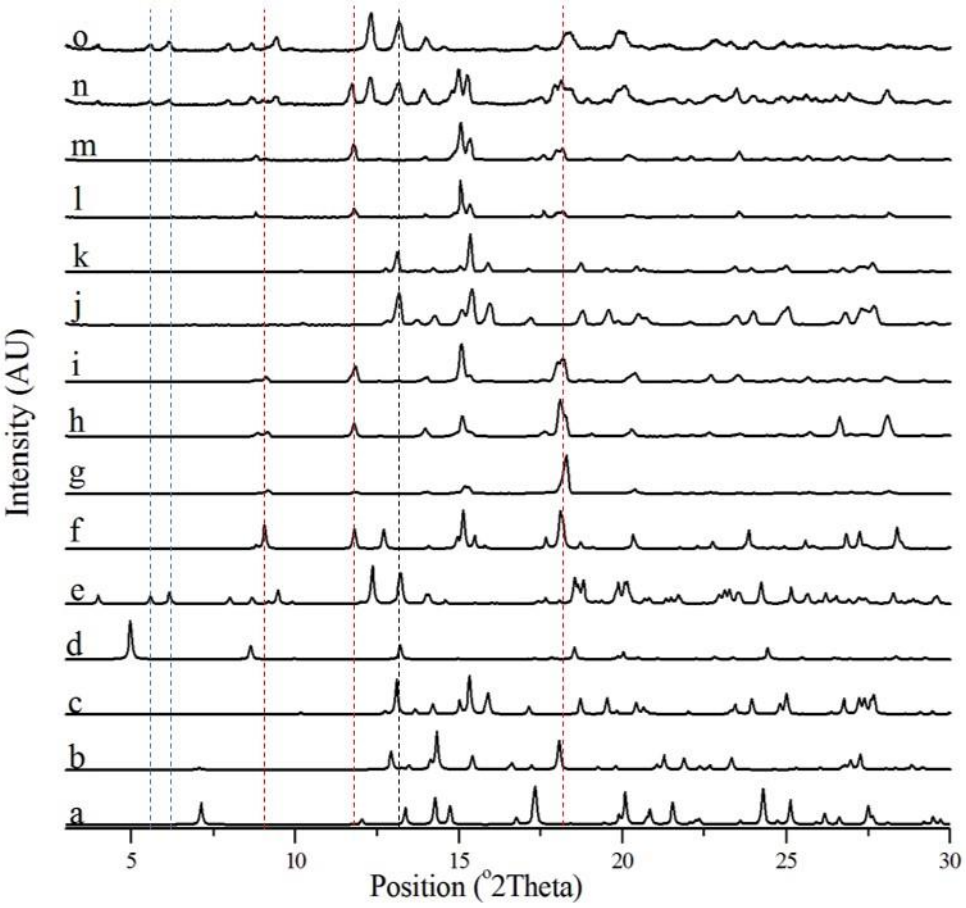

Figure 81 - Summary of slurrying, grinding and cooling solution crystallization experiments of CBZ:DMA. The calculated patterns of CBZ:DMA and CBZ polymorphs are added for clarification (*a*: CBZ V; *b*: CBZ IV; *c*: CBZ III; *d*: CBZ II; *e*: CBZ I; *f*: CBZ:DMA). The experimental PXRD patterns are displayed on the top (*g*: CBZ:DMA filtered single crystals; *h*: CBZ:DMA filtered single crystals stored for one day; *i*: CBZ:NIT filtered single crystals stored for 4 months; *j*: sample obtained from grinding of CBZ with two equivalents of DMA, 25 Hz for 30 min; *k:* first sample obtained from slurrying of CBZ in DMA for 24h; *l*: latter sample obtained from slurrying of CBZ in DMA for 24h; *m*: sample obtained from slurrying of CBZ in DMA for 1 week; *n*: sample obtained from slurrying of CBZ:DMA single crystals for 24h; *o*: replicate of sample obtained from slurrying of CBZ:DMA single crystals for 24h).

The existing literature reports that single crystals of CBZ:DMA and CBZ:NIT were obtained only by slow solvent evaporation at low temperature (2-4 ºC).[195] A first automated screening using cooling crystallization, isothermal crystallization and cooling with solvent evaporation (with and without agitation) did not result in a solvate with DMA or NIT.[154] The

crystallization low temperature experiments were suggested after the authors combined their experimental data using a Random Forest Classification. They found that three of the screened solvates (i.e. CBZ:DMA, CBZ:NIT and CBZ:methyl pyrrolidone) which gave negative results in the initial studies, were likely to be formed if the properties of the solvents were taken into account. The authors also report that the solvates start to desolvate after removal of the crystals from solution or upon storage at room temperature.[195]

From the present experimental data it is suggested that, while the behaviour of CBZ:NIT may be a consequence of its physical instability, the case of CBZ:DMA is not clear. Kinetics may be affecting the nucleation and the equilibrium of the solvate dissociation/crystallization reactions. The factor that may cause the dissociation of the solvate to be faster than its crystallization in an environment with maximum solvent activity is still open to question. One possibility is that the mechanical shear stresses in the slurry promote desolvation of CBZ:DMA to CBZ Form I and the kinetics of formation of CBZ:DMA from these particles does not follow the same mechanism as when the reactant is Form III. It is also likely, however, that the similar solubility of CBZ polymorphs and CBZ:DMA also contributes to the reproducibility problem. The amount of dissolved CBZ in pure DMA slurries which resulted in Form III, Form I and CBZ:DMA was 95.4 $mg.mL^{-1}$, 105.2 $mg.mL^{-1}$ and 99.9 $mg.mL^{-1}$, respectively It is difficult, however, to make firmer conclusions as the characterization analyses were static and no information is known about the real course of the crystallization reaction and its underlying mechanisms.

The stability characteristics of CBZ:NIT make it unsuitable for the proposed desolvation experiments. A similar characteristic was observed in 10CBZ:THF, which is also complicated by its similarity to CBZ Form II. In this scenario, although the structure of both materials, CBZ:NIT and 10CBZ:THF, were initially selected and will be eventually discussed in Chapter 8, the materials will not be characterized further. Although previous studies have reported that CBZ:DMA is not stable,[195] this crystal form will be assessed as marked spontaneous desolvation was not observed in the sample which was prepared herein.

Although the investigations of CBZ interactions in solution is not part of the scope of the present work, the effect of such aspects on the crystallization outcome will be considered in the following sections, but only CBZ:$2H_2O$ will be investigated in depth (Section 4.2.3.1). The relationship between crystal habit, solution environment and crystal structure is discussed in Chapter 8.

4.2.2. The crystallization experiments

4.2.2.1. CBZ polymorphs I - V

CBZ polymorph I was obtained by melting, by sublimation and by heating Form III or CBZ:2H_2O above 150 ^oC. Form II crystallized from evaporation and slow cooling experiments in toluene, tridecane and THF solutions. Form III crystallized from slow cooling and evaporation of solutions in solvents that do not form solvates with CBZ. Depending on the initial concentration of the solutions, the different methods sometimes resulted in mixtures of CBZ polymorphs, which then converted to pure Form III over time. Mixtures of Forms II and III were obtained from 1-butanol, cyclopentanone, ethyl acetate and scaled-up toluene solution experiments, while mixtures of Forms I, II and III occasionally crystallized from ethanol. Crystallization of Forms IV and V was attempted from methanolic solutions containing polyvinylpyrrolidone and from sublimation over dihydrocarbamazepine, respectively. The trials were, however, not successful.

Figure 82 shows the crystals of Form I as very thin whiskers/needles. Form II, in turn, shows acicular crystals (Figure 83). In the case of Form III, Figure 84 shows the crystals as blocks/prisms. Depending on the crystallization conditions, these crystals varied in size.

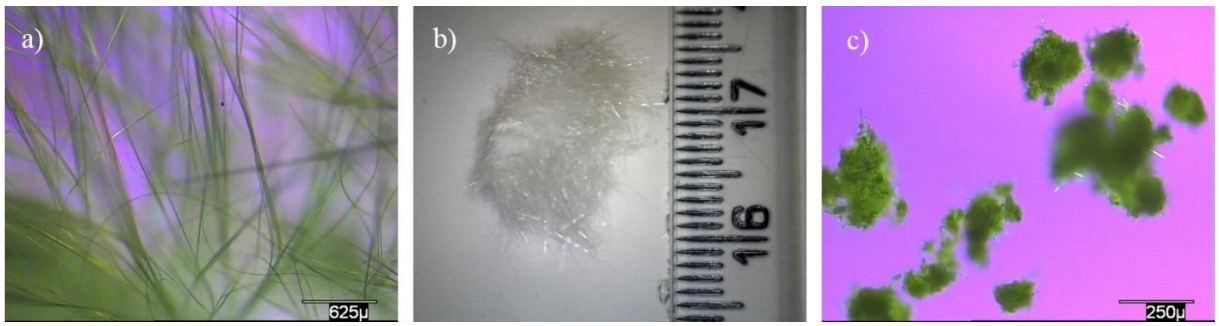

Figure 82 - CBZ polymorph I crystals obtained from sublimation (*a* and *b*) and heating of CBZ:2H_2O (*c*).

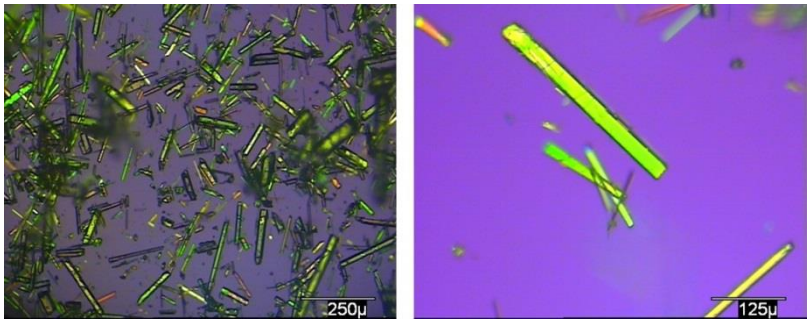

Figure 83 –CBZ polymorph II crystals obtained from cooling solution crystallization in 100% of THF (2xS).

Figure 84 – CBZ polymorph III crystals obtained from fast evaporation of a methanol solution (*a*), cooling crystallization in methanol at 2xS (*b*), and the commercial raw material (*c*).

4.2.2.2. CBZ acetone solvate (CBZ:ACE)

Crystals of CBZ:ACE were obtained from acetone by varying the concentration of the initial solution (2, 4 and 6 times the solvate solubility). Figure 85 shows that the crystals are large elongated prisms with relatively smooth surfaces. The morphology was not affected by the concentration of the starting solution.

4.2.2.3. CBZ N,N-dimethyl sulfoxide solvate (CBZ:DMSO)

Crystals of CBZ:DMSO were obtained from DMSO with an initial concentration of 6 times the solvate solubility (lower concentrations generally did not yield crystals). Figure 86 shows that the crystals are prismatic and relatively large, and generally present smooth surfaces. Occasionally the crystallized material resulted in agglomerated larger crystals with rough surfaces, as shown in Figure 87.

4.2.2.4. CBZ N,N-dimethyl formamide solvate (CBZ:DMF)

Crystals of CBZ:DMF were obtained from DMF with an initial concentration of 6 times the solvate solubility (lower concentrations generally did not yield crystals). Figure 88 shows that the crystals are prismatic and small relative to the previous materials. Occasionally, however, the crystallized material resulted in large crystals, as shown in Figure 89.

4.2.2.5. CBZ N,N-dimethyl acetamide solvate (CBZ:DMA)

The crystals of CBZ:DMA were obtained from DMA with an initial concentration of 4 and 6 times the solvate solubility. The results were not readily reproducible. Figure 90 shows that the crystals are prismatic with rough surfaces and irregular shapes. The PXRD

patterns collected without prior sample preparation (i.e. gentle grinding) show that the crystals have a preferred orientation, although the dominant crystal surface was not identified (Appendix 2, Figure 279).

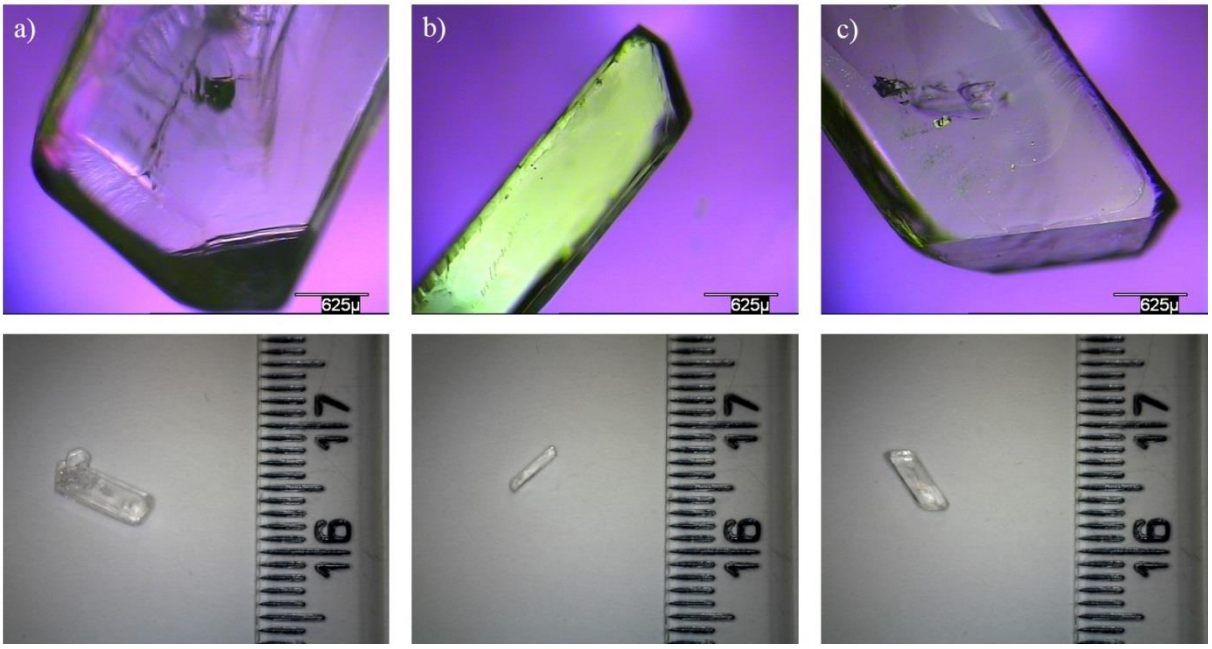

Figure 85 - CBZ:ACE crystals obtained from cooling solution crystallization in 100% of acetone. Labels *a*, *b*, and *c* indicate different samples crystallized from solutions with different initial concentrations of CBZ: 2xS, 4xS and 6xS, respectively.

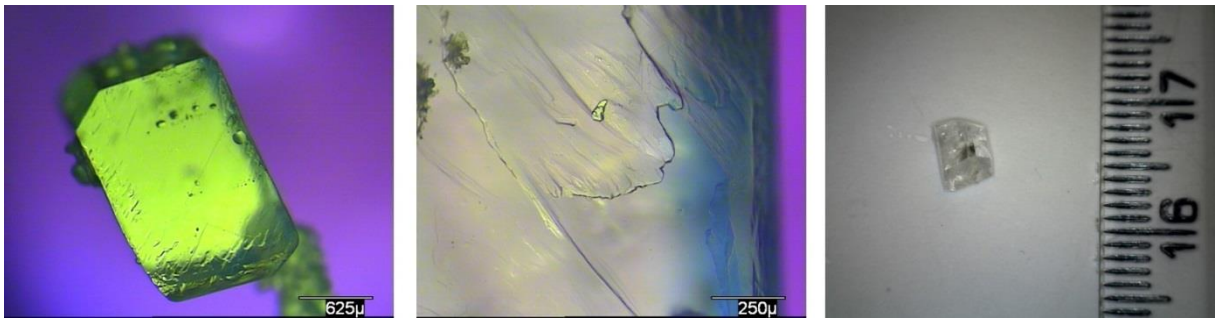

Figure 86 - CBZ:DMSO crystals obtained from cooling solution crystallization in 100% of DMSO (6xS).

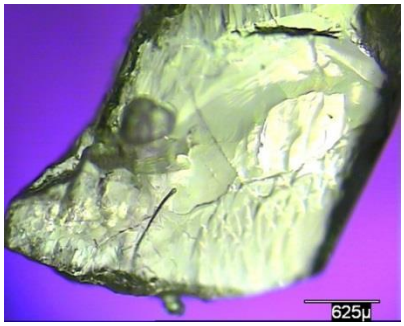

Figure 87 - CBZ:DMSO crystals with rough surface occasionally obtained in different batches of crystallization.

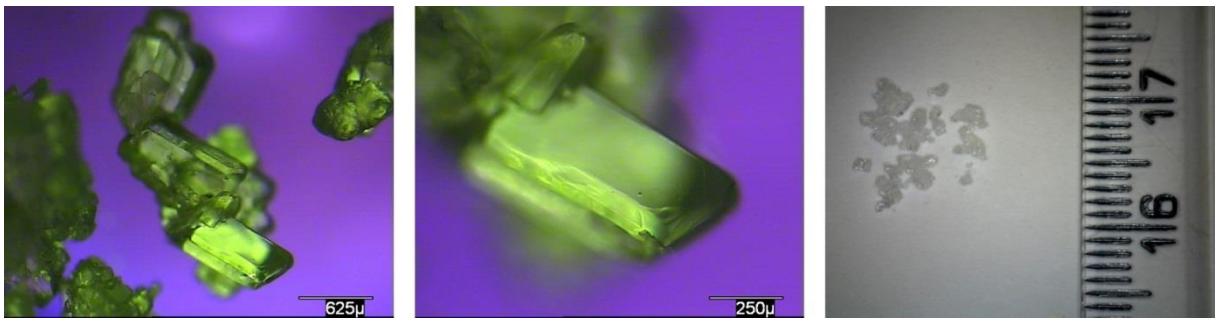

Figure 88 - CBZ:DMF crystals obtained from cooling solution crystallization in 100% of DMF (6xS).

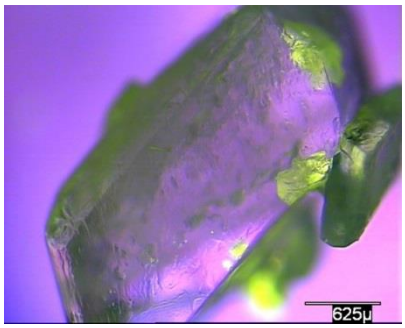

Figure 89 - CBZ:DMF big crystals occasionally obtained in different batches of crystallization.

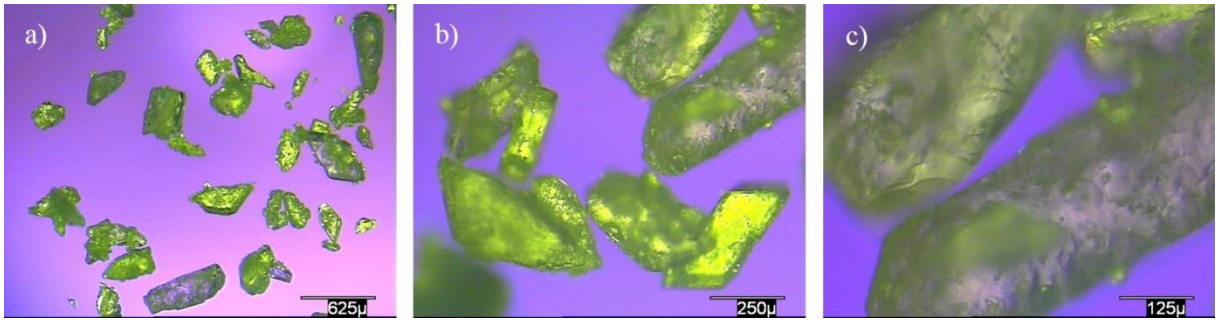

Figure 90 - CBZ:DMA crystals obtained from cooling solution crystallization in 100% of DMA (6xS).

4.2.2.6. CBZ benzoquinone cocrystals (CBZ:BZQ and 2CBZ:BZQ)

Crystals of CBZ:BZQ were obtained from ethanolic solutions. The initial concentration of CBZ and BZQ was defined in relation to one point in the phase diagram which had been previously characterized. The concentrations which yielded CBZ:BZQ cocrystals had 4 and 6 times more CBZ and BZQ than observed in the equilibrium condition (the results will be explored further in the Chapter). The PXRD patterns collected without sample grinding showed the crystals to have a preferred orientation on (001) and (002) planes and, therefore, suggest this is the dominant crystal surface (Appendix 2, Figure 280). Figure 91 shows that the crystals are prismatic, but have rough surfaces and occasionally round corners. As the concentration of BZQ in the solutions was much greater than its solubility, BZQ crystallized concomitantly to CBZ:BZQ. It is possible that the small particles sometimes observed on the

surface of the cocrystal are BZQ crystals crystallized from the evaporation of the remaining solution.

The crystals of 2CBZ:BZQ were also obtained from ethanolic solutions, but the initial amount of dissolved CBZ in relation to BZQ was higher than in the case of CBZ:BZQ. The concentration of CBZ and BZQ in the solution was also defined in relation to one point in the phase diagram that was characterized previously. The concentrations which yielded 2CBZ:BZQ cocrystals had 2, 4 and 6 times more CBZ and BZQ than was observed under equilibrium condition (the results will be explored further in the Chapter). The PXRD patterns collected without sample grinding show the crystals have preferred orientation on (0k0) planes and, therefore, suggest these are the dominant crystal surfaces (Appendix 2, Figure 281). Figure 92 shows that the crystals are needles with the aspect of the particles varying according to the initial concentration of the cocrystal formers. While lower concentrations lead to the crystallization of very thin needles, higher concentrations resulted in larger crystals. Larger needles were also obtained by preparing an ethanolic solution of 2CBZ:BZQ previously obtained by grinding experiments (100 $mg.mL^{-1}$) and performing a cooling crystallization experiment.

For comparison, Figure 93 shows the morphology of the BZQ raw material and the BZQ crystals obtained by sublimation. The PXRD patterns of as prepared BZQ single crystals show a preferred orientation on (20-1) plane, suggesting that (20-1) is the dominant crystal surface of BZQ crystals obtained by sublimation (Appendix 2, Figure 282).

4.2.2.7. CBZ oxalic acid cocrystal (2CBZ:OXA)

The crystals of 2CBZ:OXA were obtained from ethyl acetate in a manner similar to the method described in the literature. The method involved solution cooling crystallization experiments with an initial concentration of 27.0 $mg.mL^{-1}$ of the cocrystal previously obtained by grinding. The PXRD patterns suggest a preferred orientation on (h00) plane and, therefore, suggest this is the dominant crystal surface (Appendix 2, Figure 283). Figure 94 shows that the crystals exist as large needles with irregular or rough surfaces. Figure 95 shows the morphology of the OXA raw material for comparison.

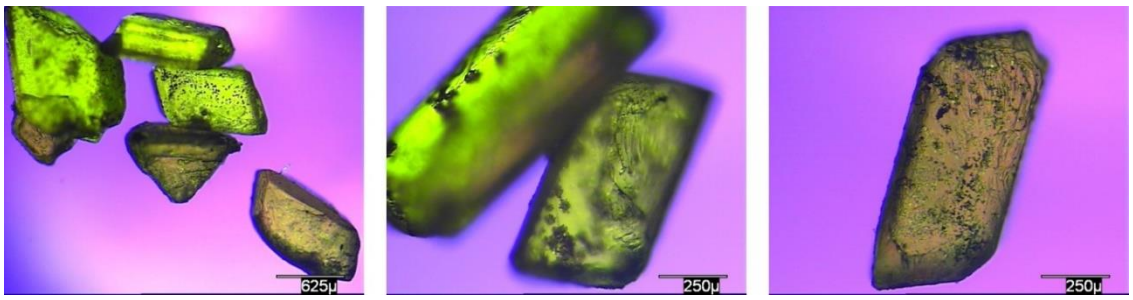

Figure 91 - CBZ:BZQ crystals obtained from cooling solution crystallization in ethanol with high concentration of BZQ. The sample's initial concentrations of CBZ and BZQ were 6xS.

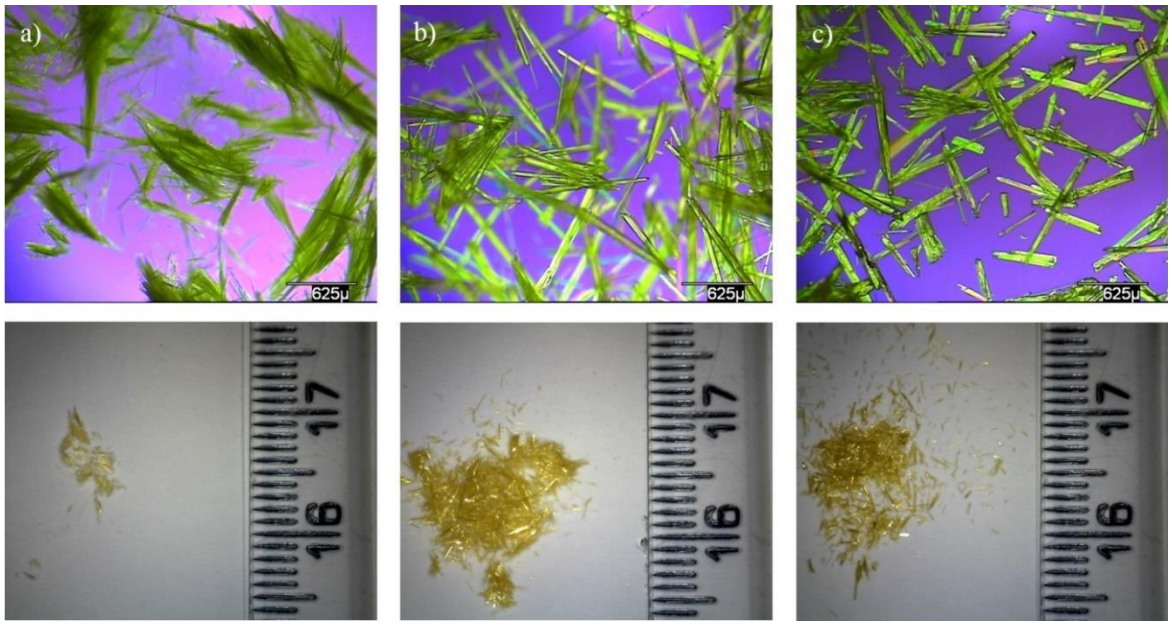

Figure 92 - 2CBZ:BZQ crystals obtained from cooling solution crystallization in ethanol with low concentration of BZQ. Labels *a* and *b* indicate samples crystallized from solutions with initial concentrations of CBZ and BZQ of 2xS and 6xS, respectively. Label *c* shows a sample obtained from cooling crystallization of a 100 $mg.mL^{-1}$ ethanolic solution prepared from 2CBZ:BZQ obtained from grinding.

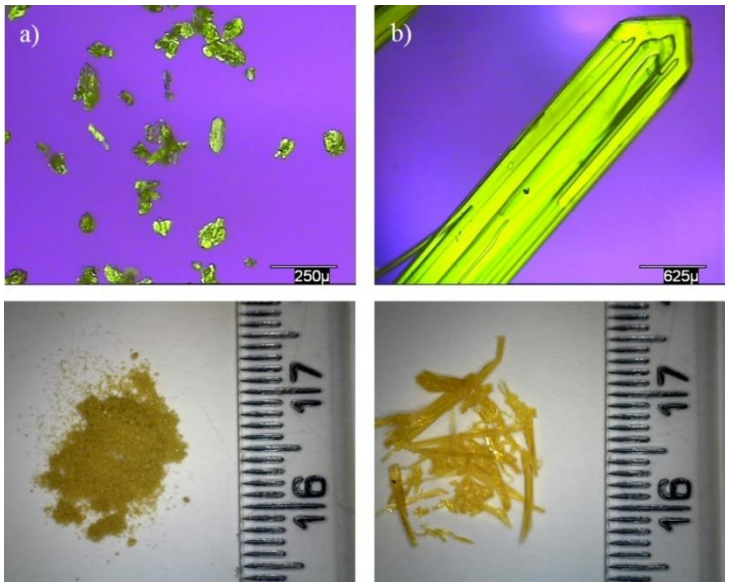

Figure 93 - BZQ samples. Label *a* represents crystals of the raw material, while label *b* shows a sample obtained from sublimation.

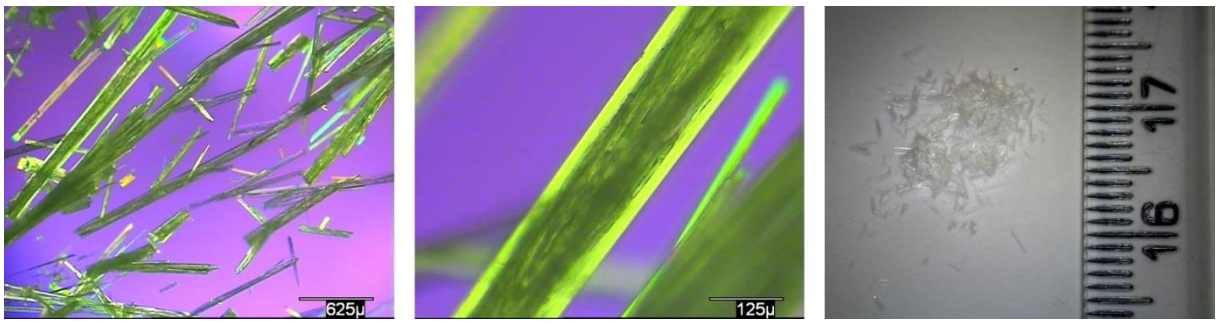

Figure 94 - 2CBZ:OXA crystals obtained from cooling solution crystallization in ethyl acetate.

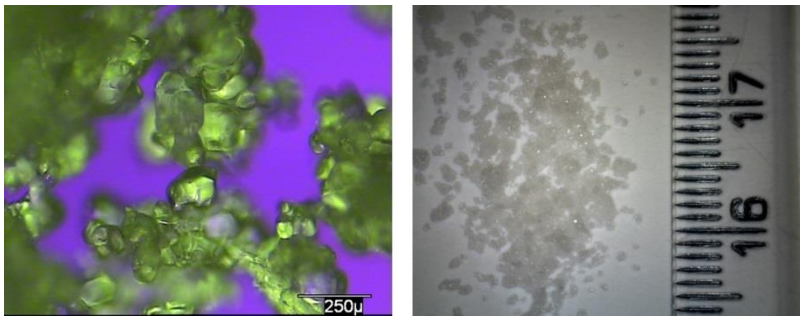

Figure 95 - OXA:2H_2O raw material.

4.2.2.8. CBZ dihydrate (CBZ:2H_2O)

The crystals of CBZ:2H_2O were initially obtained using different ethanol:water proportions and different initial CBZ concentrations (in a manner similar to the methods described in the literature).[162,163] Additional conditions will be further explored in this Chapter.

Figure 96 shows that the crystals are elongated needles which present different aspects depending on the crystallization conditions. The PXRD patterns show the crystals to have preferred orientation, but suggest the dominant surfaces differ in different conditions (Figure 284). CBZ:2H_2O obtained in high water activities show preferred orientation of (0k0) planes, while CBZ:2H_2O crystallized in low water activities show (h00) preferred orientation.

4.2.2.9. CBZ formamide solvate (CBZ:FORM)

The crystals of CBZ:FORM were obtained from different ethanol:formamide proportions and different initial CBZ concentrations (2xS, 4xS and 6xS). Figure 97 shows that, like the case of CBZ:2H_2O, the crystals are elongated needles which present variable aspects, depending on the amount of formamide in the solution. The PXRD patterns indicate the crystals have preferred orientation, but it is not clear if dominant surfaces are different for crystals prepared under different conditions (Appendix 2, Figure 285). CBZ:FORM obtained in solutions with high formamide activities show preferred orientation of (01-1) and (04-4) planes, while CBZ:FORM crystallized in low formamide activities show (022)/(01-2) and (033)

preferred orientation. It is noteworthy that the (0k-l) and the (0kl) planes in the CBZ:FORM structure are equivalent to the (h00) and the (0k0) planes in the CBZ:2H_2O structure, respectively.

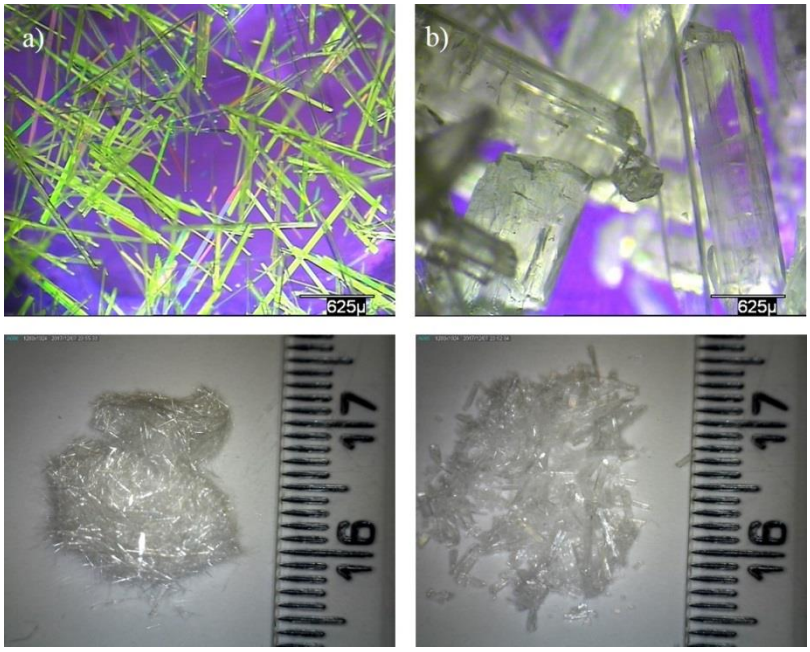

Figure 96 - CBZ:2H_2O crystals obtained from cooling solution crystallization in ethanol:water. Labels *a* and *b* indicate different samples crystallized from solutions with different initial concentrations of CBZ (6xS and 2xS, respectively) and different ethanol:water molar proportion (9:91 and 48:52, respectively).

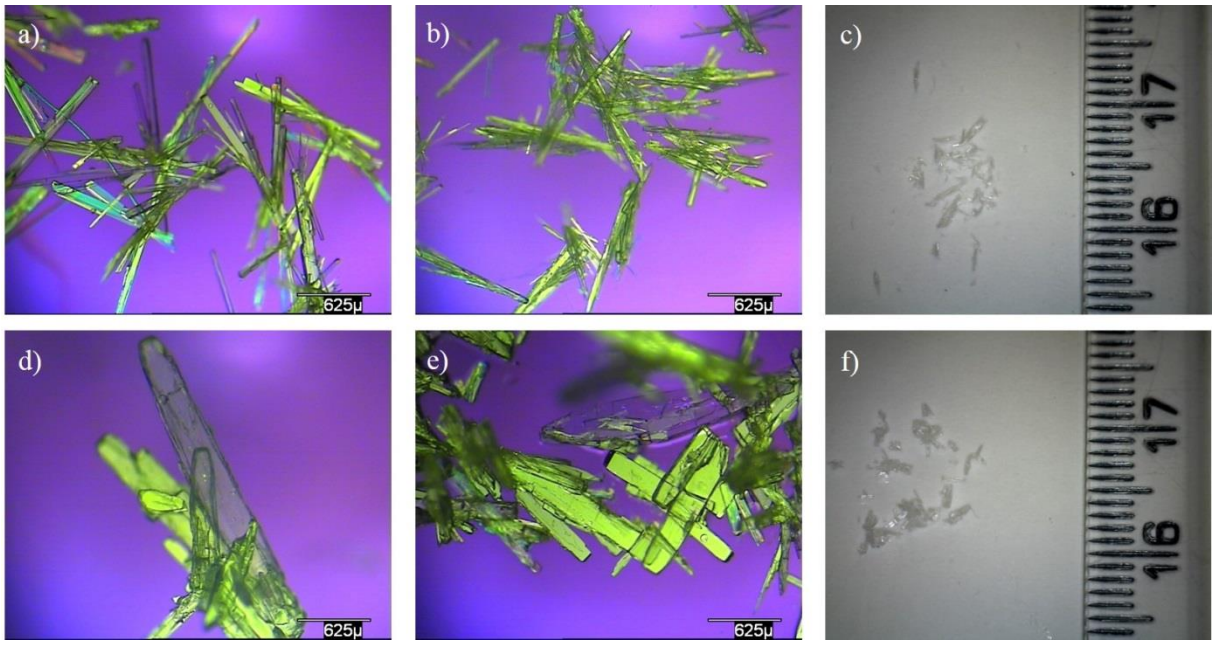

Figure 97 - CBZ:FORM crystals obtained from cooling solution crystallization in ethanol:formamide. The top row shows samples prepared in 100% of formamide, while the bottom row shows samples prepared in ethanol:formamide 75:25, n:n. Labels *a*, *b*, *c*, *d*, *e* and *f* indicate different initial concentrations of CBZ: 4xS, 6xS, 6xS, 4xS, 6xS and 6xS, respectively.

4.2.2.10. CBZ dioxane solvate (2CBZ:DIOX)

The crystals of 2CBZ:DIOX were obtained from different ethanol:dioxane proportions and different initial CBZ concentrations (2xS, 4xS and 6xS). Figure 98 shows that the crystals are elongated needles which present varied aspects depending on the amount of dioxane present, but the variation is not as marked as for CBZ:2H_2O and CBZ:FORM. In the case of 2CBZ:DIOX, higher activities of dioxane appear to result in thinner plate-like needles. The PXRD patterns show the crystals have preferred orientation and suggest the dominant surfaces are similar irrespective of the different crystallization conditions (Appendix 2, Figure 286). In contrast to CBZ:2H_2O and CBZ:FORM, 2CBZ:DIOX obtained in high and low dioxane activities show preferred orientation of (101), (20-2) and (30-3)/(11-1) planes. It is noteworthy that the (h0l) and the (h0-l) planes in the 2CBZ:DIOX structure are equivalent to the (h00) and the (0k0) planes in the CBZ:2H_2O structure, respectively.

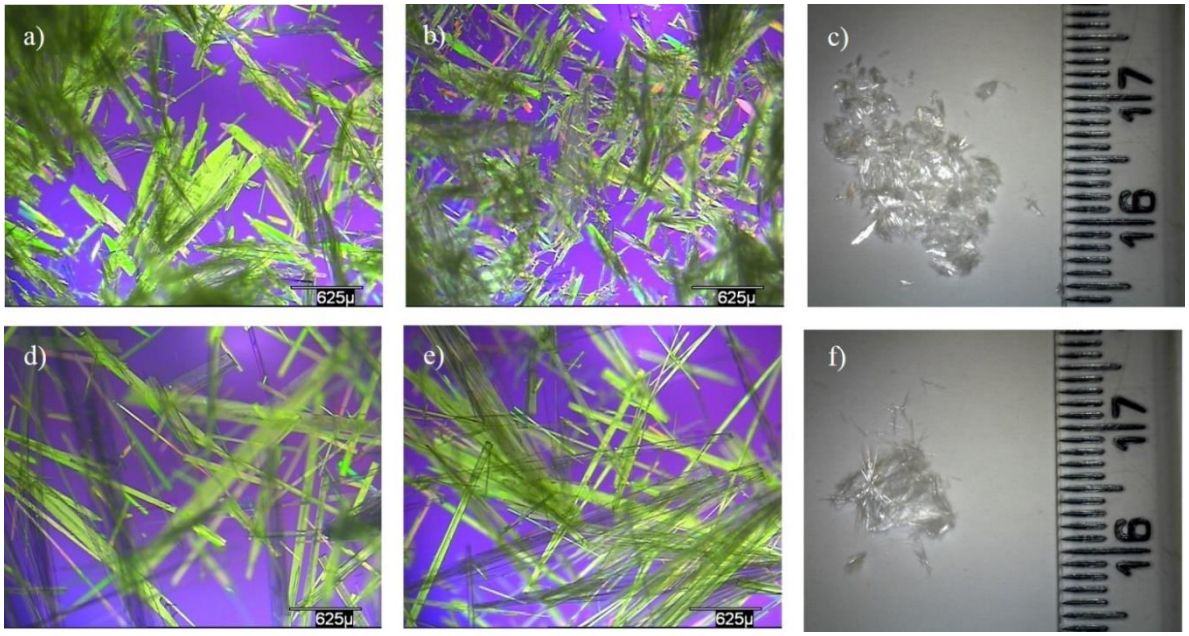

Figure 98 - 2CBZ:DIOX crystals obtained from cooling solution crystallization in ethanol:dioxane. The top row shows samples prepared in 100% of dioxane, while the bottom samples are prepared in ethanol:dioxane 75:25, n:n. Labels *a*, *b*, *c*, *d*, *e* and *f* indicate different initial concentrations of CBZ: 4xS, 6xS, 6xS, 4xS, 6xS and 6xS.

4.2.2.11. CBZ 2,2,2-trifluoroethanol solvates (CBZ:TFE and 2CBZ:TFE)

The crystals of CBZ:TFE and 2CBZ:TFE were obtained from 100:0 and 45:55 proportions of TFE:ethanol (n:n), respectively. The initial CBZ concentration of the solutions was 4xS with 6xS not resulting in clear solutions prior to the cooling. Figure 99 shows that both forms are characterized as needles, although CBZ:TFE seemed to be a somewhat more agglomerated than the low stoichiometry 2CBZ:TFE solvate. The PXRD patterns show the crystals have preferred orientations and suggest the dominant surfaces are (010)/(011) and (002)

in CBZ:TFE, and (01-1) in 2CBZ:TFE (Appendix 2, Figure 288). It is noteworthy that the (0kl) plane in the CBZ:TFE structure is equivalent to the (h00) plane in the CBZ:2H_2O structure.

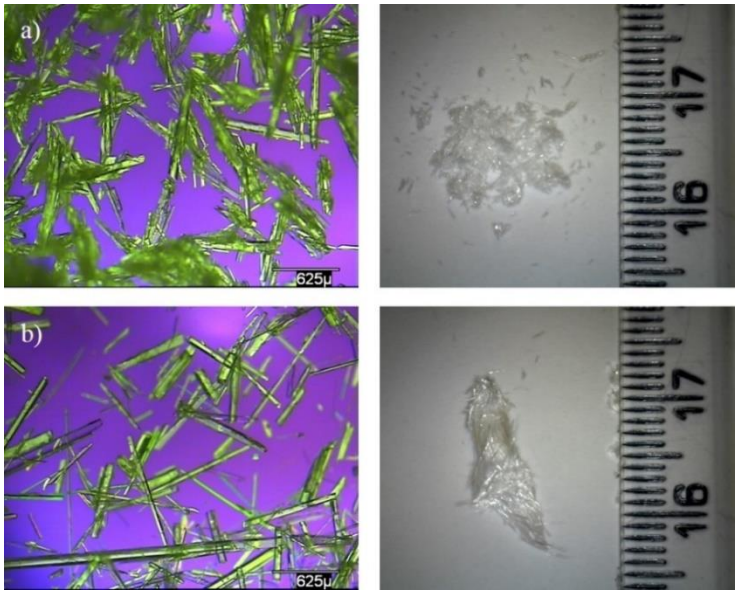

Figure 99 - a) CBZ:TFE crystals obtained from cooling solution crystallization in TFE (4xS); b) 2CBZ:TFE crystals obtained from cooling solution crystallization in ethanol:TFE 55:45, n:n (4xS).

4.2.2.12. CBZ 2,2,2-trifluoroacetic acid solvate (CBZ:TFA)

The crystals of CBZ:TFA were obtained in 100:0 and 43:57 proportions of TFA:ethanol (n:n), while the initial CBZ concentration of the solutions was 2xS and 2xS/4xS, respectively. Higher concentrations could not be assessed because they did not result in clear solutions prior to the cooling. Figure 100 shows that the crystals are needles which present a variable aspect depending on the experimental conditions. Higher activities of TFA resulted in larger and irregular needles. The PXRD patterns show the crystals to have preferred orientations and suggest that the samples prepared in higher TFA activities present the (202) and (30-1) dominant surfaces on the crystals (Appendix 2, Figure 289).

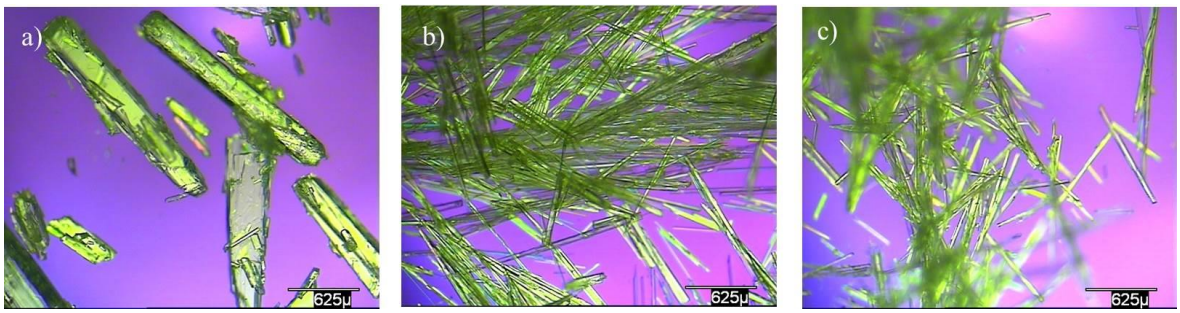

Figure 100 - a) CBZ:TFA crystals obtained from cooling solution crystallization in TFA (2xS); b) and c) CBZ:TFA crystals obtained from cooling solution crystallization in ethanol:TFA 57:43 (n:n) at 2xS and 4xS, respectively.

4.2.2.13. CBZ acetic acid solvate (CBZ:ACA)

The crystals of CBZ:ACA were obtained from different ethanol:ACA proportions and different initial CBZ concentrations (2xS, 4xS and 6xS). Figure 101 and Figure 102 show that the crystals are needles which present a variable aspect depending on the initial concentration of CBZ. Regardless the activity of ACA, higher concentrations of CBZ resulted in needles with a low aspect ratio. The PXRD patterns show that all the samples have similar preferred orientation and, therefore, suggest the difference in aspect ratio does not reflect a *tracht* change. Regarding the size of the crystals, it also varied occasionally, resulting in large crystals such as those shown in Figure 103.

4.2.2.14. CBZ formic acid solvate (CBZ:FA)

Crystals of CBZ:FA were obtained from different ethanol:FA proportions and different initial CBZ concentrations (2xS, 4xS and 6xS). Figure 104 shows the crystals are needles which present a variable aspect depending on the crystallization conditions. Similar to CBZ:ACA, at higher activities of FA, high concentrations of CBZ result in large CBZ:FA needles with a low aspect ratio. Figure 105, however, shows an opposite morphology correlation in the case of low FA activities. The characterization of the crystals has shown that low FA activities often resulted in mixtures of CBZ:FA and CBZ:2H_2O (Appendix 2, Figure 293) possibly deriving from residual water being present in the solution.

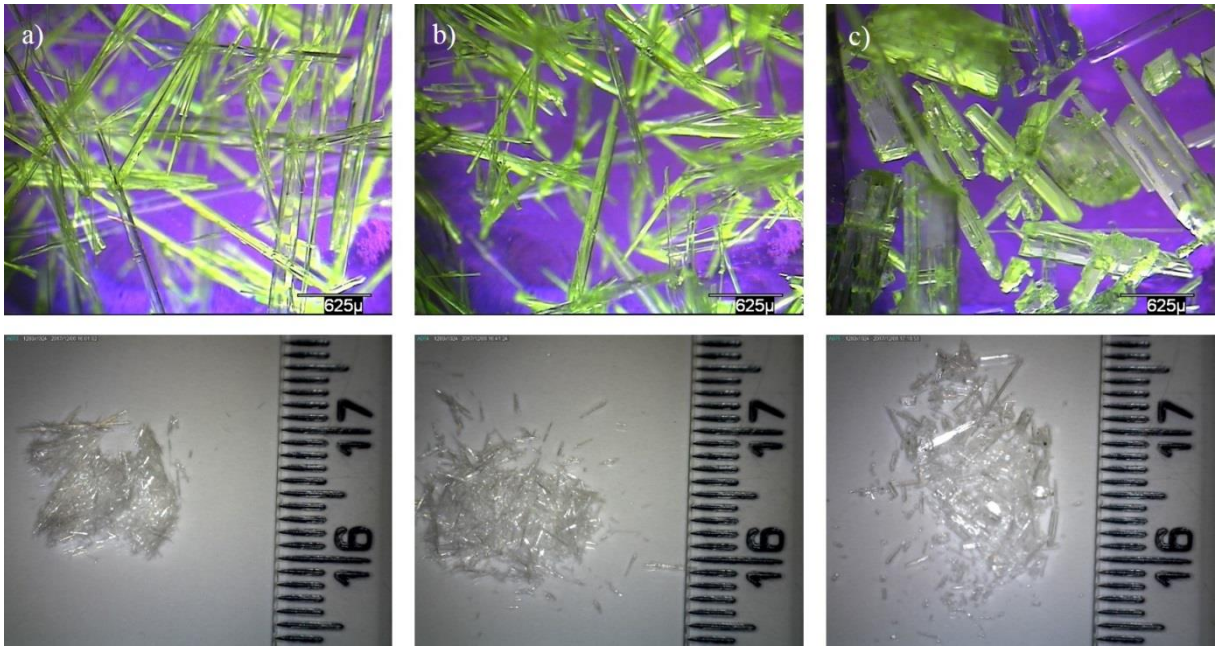

Figure 101 - CBZ:ACA crystals obtained from cooling solution crystallization in acetic acid. Labels *a*, *b* and *c* indicate different initial concentrations (2xS, 4xS and 6xS, respectively).

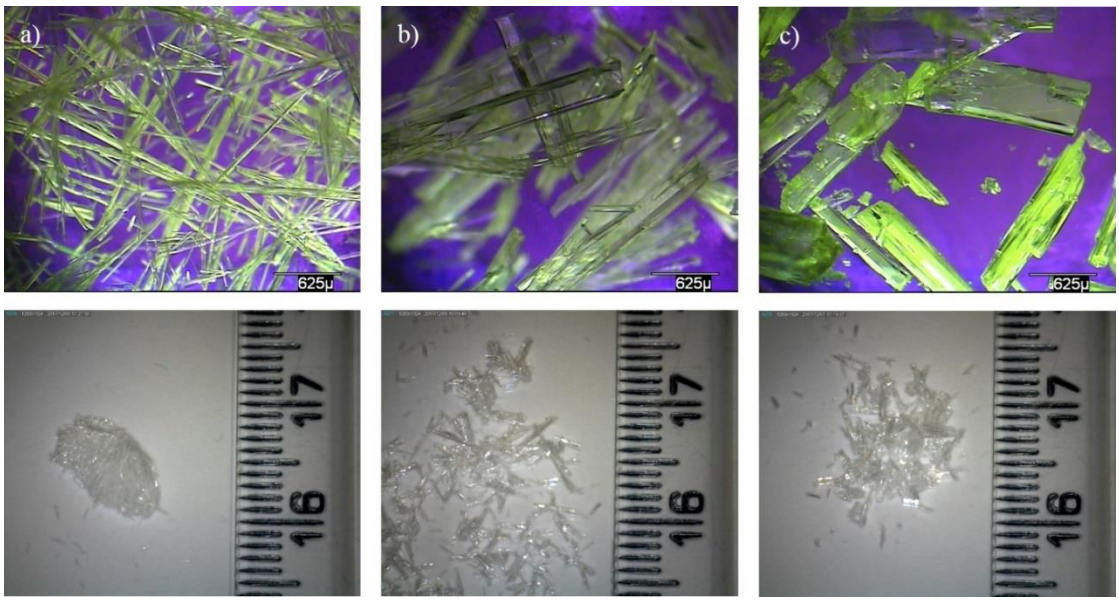

Figure 102 - CBZ:ACA crystals obtained from cooling solution crystallization in ethanol:acetic acid, 75:25 n:n. Labels *a*, *b* and *c* indicate different initial concentrations (2xS, 4xS and 6xS, respectively).

Figure 103 - CBZ:ACA large crystals occasionally obtained in different batches of crystallization.

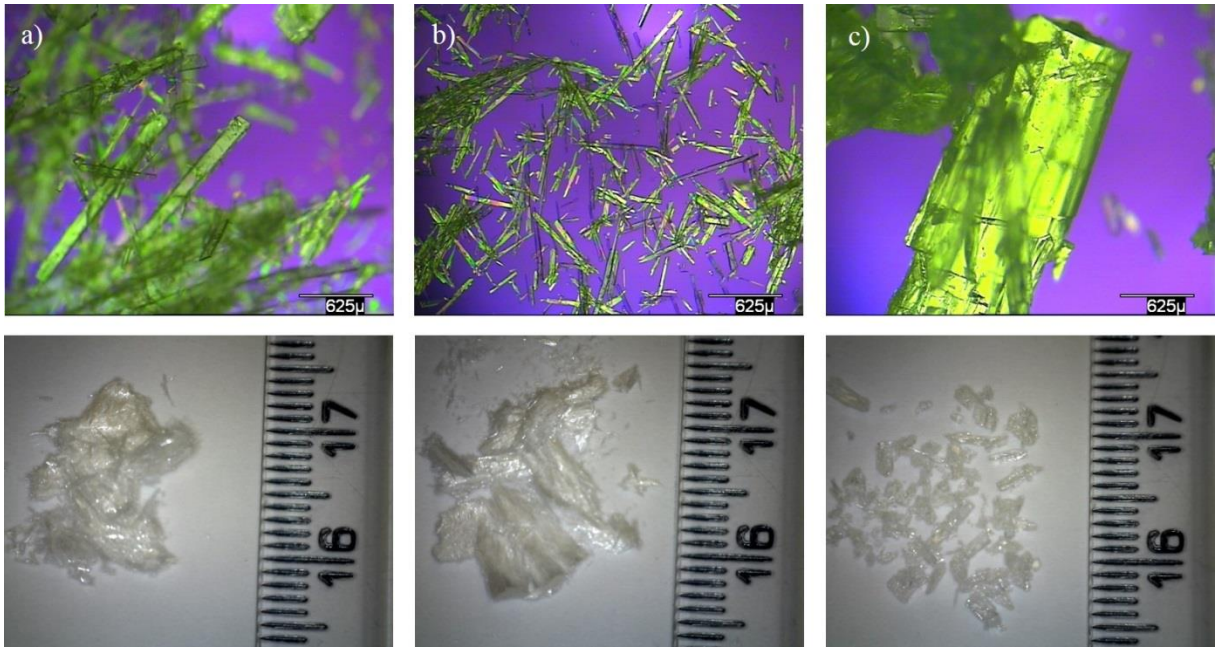

Figure 104 - CBZ:FA crystals obtained from cooling solution crystallization in formic acid. Labels *a*, *b* and *c* indicate different initial concentrations of 2xS, 4xS and 6xS, respectively.

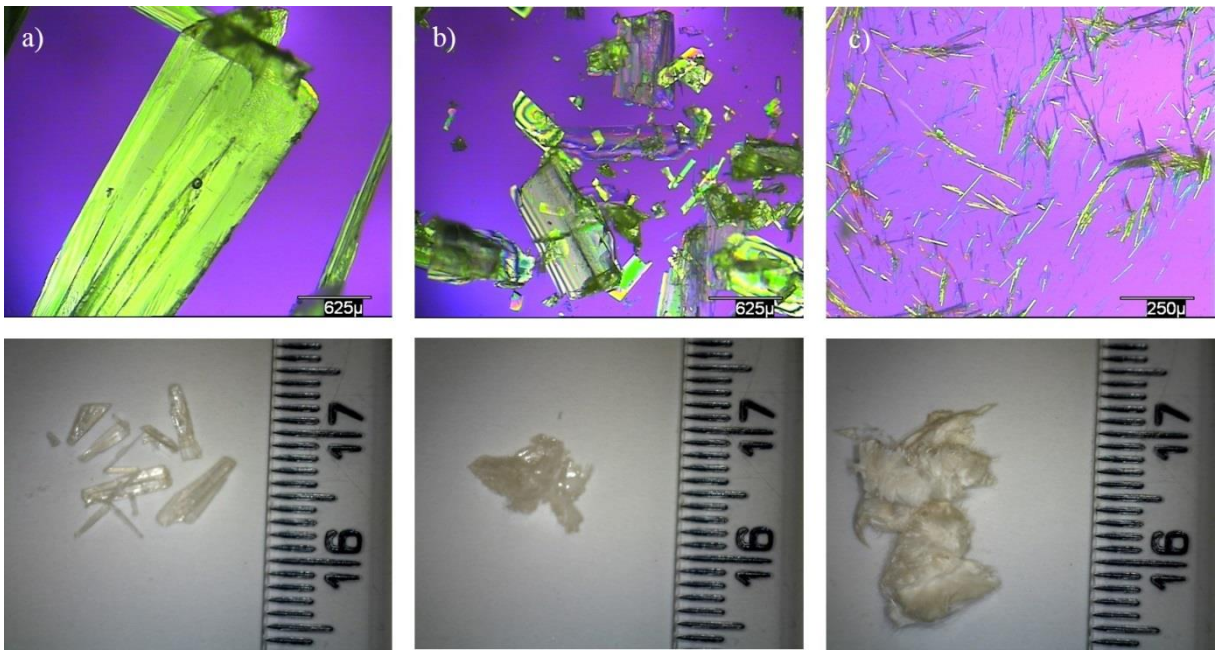

Figure 105 - Crystals obtained from cooling solution crystallization in ethanol:formic acid, 66:34 n:n. Labels *a*, *b* and *c* indicate different initial CBZ concentrations of 2xS, 4xS and 6xS, respectively.

4.2.3. Case studies illustrating the effect of solution environment on the crystallization of carbamazepine multicomponent materials

4.2.3.1. Case study 1: The crystallization of carbamazepine dihydrate

The first step in the development of a crystallization method for CBZ:2H_2O was to determine its domain of stability under the experimental conditions being used. This information was taken from the equilibrium solubility profile shown in Figure 78, which has demonstrated that CBZ:2H_2O is the thermodynamically most stable form above 45 mol% of water in ethanol. The SEM micrographs of the solids obtained from the slurries also characterize this region of stability by showing a significant change in the morphology of the samples obtained at different water activities (Figure 106). In this case, the resulting block-like morphology agrees with the calculated and reported morphologies of CBZ Form III, while the needles are characteristic of the dihydrate.

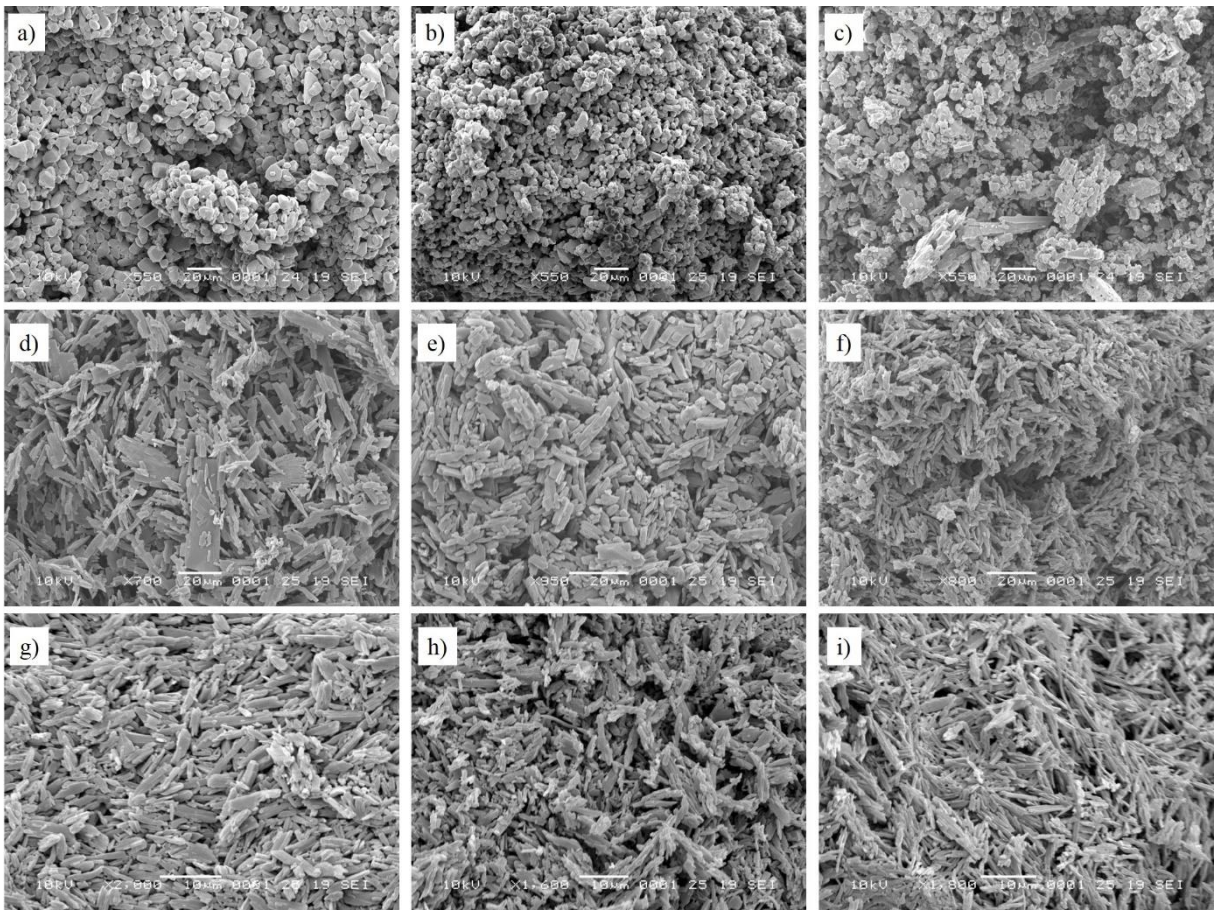

Figure 106 – SEM micrographs of CBZ slurried in ethanol:water mixtures of different water molar proportions (*a*: 0%; *b*: 15%; *c*: 26%; *d*: 45% ;*e*: 68%; *f*: 83%; *g*: 93%; *h*: 97%; *i*: 100%).

While the PXRD patterns of the slurries obtained in 26 mol% of water only show reflections which are characteristic of Form III (Appendix 3, Figure 294), the SEM micrographs occasionally showed needles among the small blocks of CBZ Form III (Figure 106). In the case of slurries of 30 mol% and 36 mol% of water, the PXRD was able to detect mixtures of Form III and CBZ:2H_2O (Appendix 3, Figure 294). Similarly, cooling crystallization experiments in ethanol:water proportions near the stability boundary of Form III and CBZ:2H_2O show that mixtures of both phases are obtained at 36 mol%, while pure CBZ:2H_2O crystals are obtained at 45 mol% of water (Figure 107). It is suggested that the mixtures resulting from slurrying and from the cooling crystallization are explained by the low chemical potential driving the reactions near the inflexion point of stability. The CBZ:2H_2O literature reports that the stability transition point is achieved when the water content is 19.6 wt% or 38.4 mol% (room conditions).[201] The literature have also demonstrated that temperature affects the water activity necessary to crystallize CBZ:2H_2O.[202]

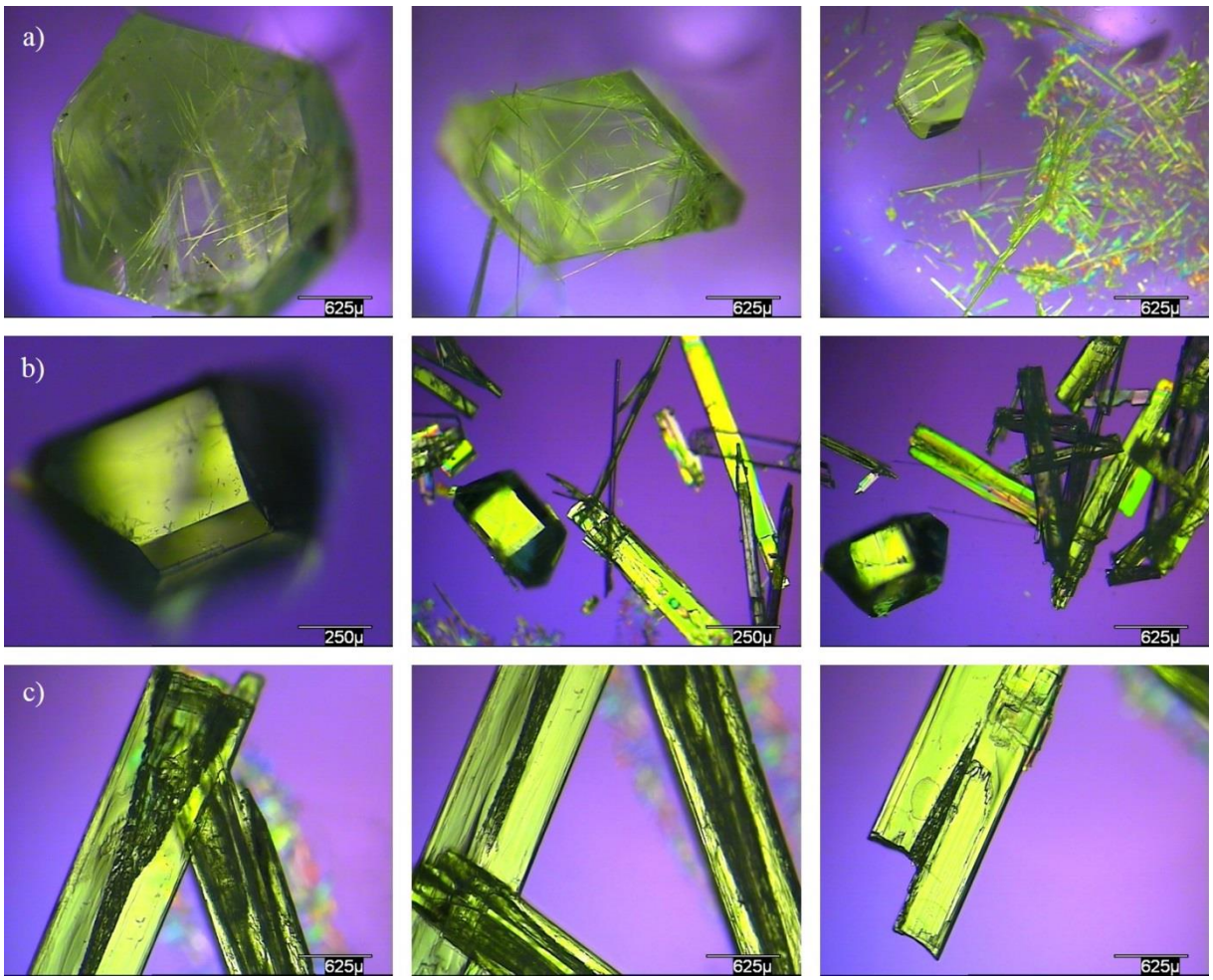

Figure 107 – Optical micrographs characterizing the outcome of CBZ crystallizations in water:ethanol mixtures (*a*: 26 mol%; *b*: 36 mol%; *c*: 45 mol%). The initial CBZ concentration was 2xS. It is noteworthy that cooling crystallization experiments at 26 mol% of water resulted in mixtures of big CBZ form III prisms and thin needles that may be characteristic of CBZ Form I, CBZ Form II and CBZ:2H_2O. While the PXRD analyses have identified the needles as CBZ I and II, it was unclear if the dihydrate was also present (Appendix 3, Figure 296 and Figure 295). The growth of needles over the prismatic crystals, however, recalls the surface interactions between crystals of CBZ Forms I and III, which have already been reported elsewhere.[165,166]

After this initial characterization, the preparation of CBZ:2H_2O crystals was first attempted by following similar methods to those used by Kachrimanis & Griesser[162] and Khoo *et al.*[163]. As suggested in the analyses of the literature in Chapter 1, the samples experimentally obtained in different ethanol:water mixtures resulted in needles which presented different *tracht* (Figure 96 and Figure 284). The analyses have characterized the preferred orientation in the samples and suggest that high water activities lead to a preferred (0k0) face while low water activities lead to a preferred (h00) face. In addition, the SEM images in Figure 108 suggest that these two different surfaces present distinct properties, which are explored further in Chapters 5 and 6.

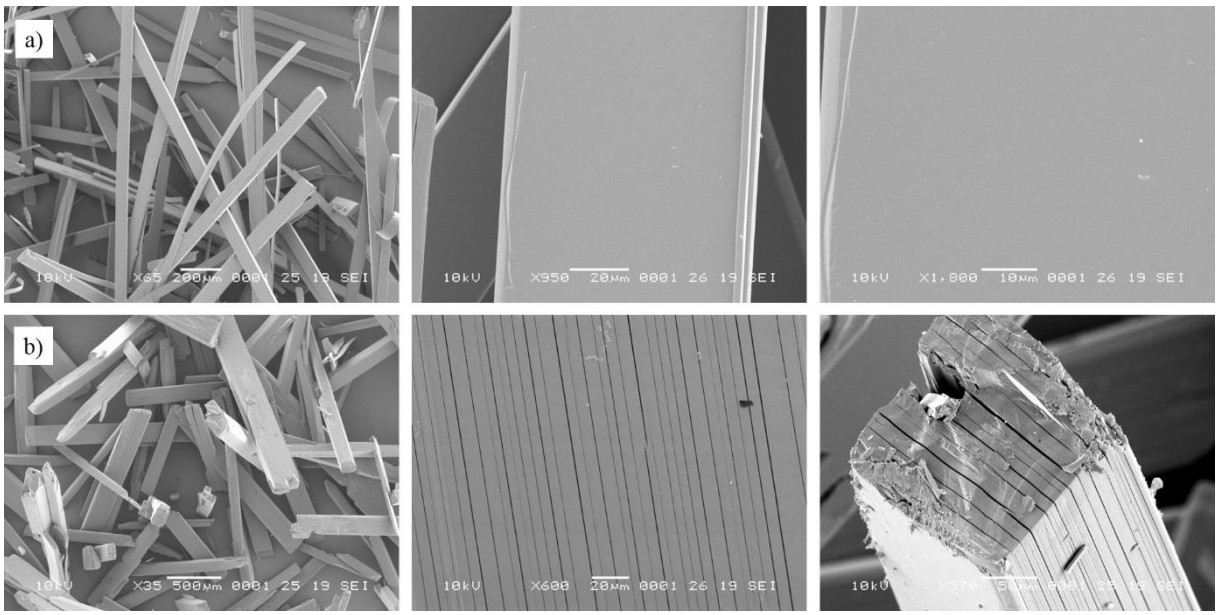

Figure 108 – SEM micrographs showing the differences on the surface of CBZ:2H_2O crystals obtained from cooling crystallization in 91 mol% (row *a*) and 52 mol% (row *b*) of water.

Different hypotheses have been proposed to explain the environment-driven *tracht* of the CBZ:2H_2O crystals, including the fact that differences in the mechanism of crystallization may affect the crystal habit because of different degrees of supersaturation and nucleation temperature. Another factor accounted for the composition of the crystallization solution, which may also play a role because of solvent adsorption and interactions on the crystal surface. In this case, the growth rates of (0k0) and (h00) may vary as a function of solvent environment, although it is not known which solvent (water or ethanol) was the most critical phase driving the crystallization outcome of CBZ:2H_2O.

A more careful analysis of the methods used by Kachrimanis & Griesser[162] and Khoo *et al.*[163] shows that they were actually not comparable as the initial concentrations of CBZ were different in relation to the solubility of CBZ:2H_2O in the respective ethanol:water proportions. While the system with low water activity used solutions of around 2xS, the system with high water activity used solutions of about 6xS. Equally important is that the supersaturation degree and the temperature of nucleation were not controlled during the cooling experiments. Thus, to investigate the crystallization behaviour of CBZ:2H_2O, a few modifications to the method were required. One set of experiments were performed by controlling only the ethanol:water proportion and varying the initial CBZ concentration and the cooling rate, with no seeding. In these conditions, the temperature at which nucleation starts was not the same for the different batches and increased initial concentrations are expected to lead to nucleation at higher temperatures. Other set of experiments, however, were performed at a fixed temperature of nucleation and growth. In these cases, supersaturation was generated by slow cooling of a saturated solution and adding seeds to trigger nucleation and crystal growth.

Different supersaturation degrees and different ethanol:water proportions were investigated at 25 and 40 ºC (the equilibrium solubility of CBZ in ethanol:water at different temperatures is shown in Appendix 3, Figure 297).

The results of the crystallization experiments are summarized in Table 11 and the corresponding SEM micrographs are shown in the Appendix 3 (Table 20 and Figure 298). They show that the supersaturation degree, the initial concentration of CBZ in the solution and the temperature of crystallization do not appear to change significantly the dominance of the (0k0) face in high activities of water nor the dominance of (h00) face in low water activities. It suggests that a change in the mechanism of growth is not the most influential factor on the *tracht* of CBZ:2H_2O crystals. The stronger correlation between the morphology of CBZ:2H_2O crystals and the crystallization conditions was the ethanol:water proportion. The characterization suggests that the dominance of (0k0) over (h00) takes place above 76 mol% of water. The analyses indicate no clear inflexion point in morphology, but subtle changes on the dominance of the surface as the water activity increases. It suggests that samples obtained at intermediate ethanol:water proportions may well be morphologically varied.

Table 11 – Comparison of the morphology* of CBZ:2H_2O crystals obtained at different crystallization conditions and methods.

C/S[a]	Water proportion (mol%)						
	52%[b]	52%[c]	68%[c]	76%[c]	83%[c]	91%[c]	91%[b]
1.2	(h00) Lath/Plate	(h00) Lath	(h00) Lath	(h00)+(0k0) Lath	(0k0) Lath	(0k0) Lath	(n/a)[d]
1.4	(h00) Lath	(h00) Lath	(h00) Lath	(h00)+(0k0) Lath	(0k0) Lath	(0k0) Lath	Needle
1.7	(h00) Lath	(h00) Lath	(h00) Lath	(h00)+(0k0) Lath	(0k0) Lath	(0k0) Lath	Needle
2.0	(h00) Lath	(h00) Lath	(h00) Lath	(h00)+(0k0) Lath	(0k0) Lath	(0k0) Lath	Needle
6.0	-	(h00) Lath/Plate	(h00) Lath	(h00)+(0k0) Lath	(0k0) Lath	(0k0) Lath	-

[a] Relation of concentration per solubility. This parameter is called "supersaturation degree" in the experiments where the supersaturation at the moment of nucleation was controlled ([b]), or is called "initial concentration" in the other experiments ([c]).
[d] The crystals obtained from crystallization in this experiment were insufficient for characterization.
* The nomenclature adopted for the shape of the crystals was adapted from Vatvani[60] (Appendix 3, Figure 299). In this classification, lath crystals are intermediates between needles and plates.

Figure 109 and Figure 110 characterize the CBZ:2H_2O samples resulting from cooling crystallizations performed at different cooling rates (without control of the supersaturation at the nucleation point and without seeding). Morphology deviations were observed at lower cooling rates for both water proportions (52 mol% and 91 mol%). In higher water activities, different to the previous experiments, the micrographs show an increase of the

(h00) significance in the crystals obtained at 1 ºC/day. At 52 mol% of water the dominance of (h00) was maintained in crystals resulting from the low cooling rate. In this case, however, the micrographs suggest the (0k0) face is replaced by the (hk0) face. It suggests that kinetics affect the growth of (0k0) face as the rate of its growth is increased at low cooling rates (especially at high proportions of water in ethanol). Alternatively, it may be that high cooling rates decrease the growth of (0k0) in relation to the (h00) growth.

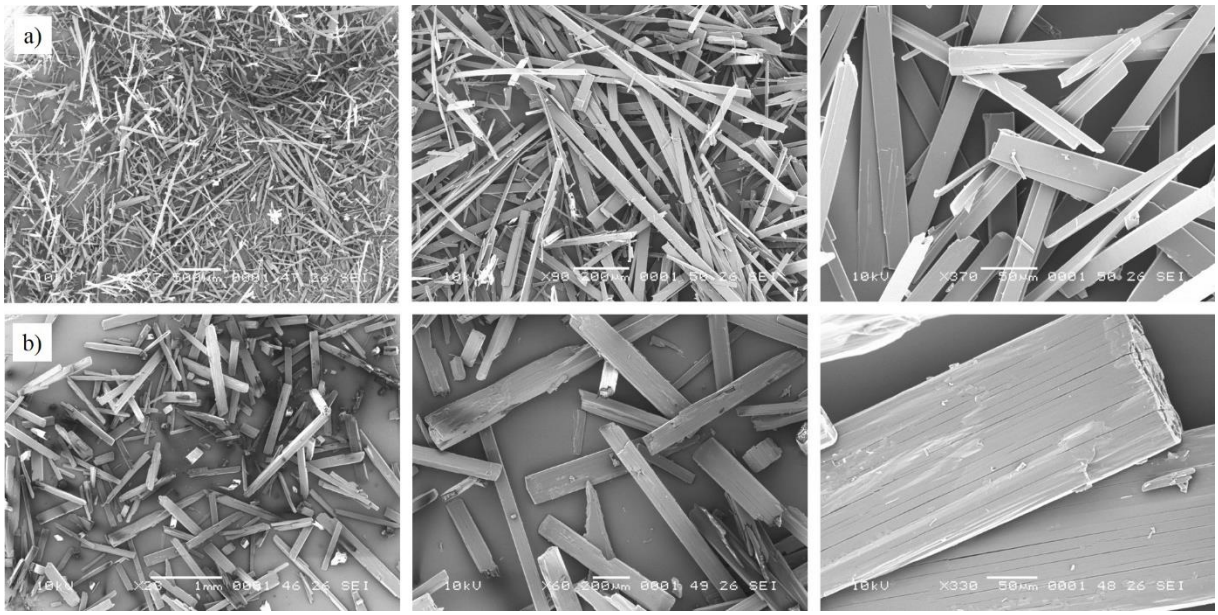

Figure 109 - SEM micrographs showing CBZ:2H_2O crystals obtained from cooling crystallization in 91 mol% (row *a*, 6xS) and 52 mol% (row *b*, 2xS). The cooling rate was fast and not controlled.

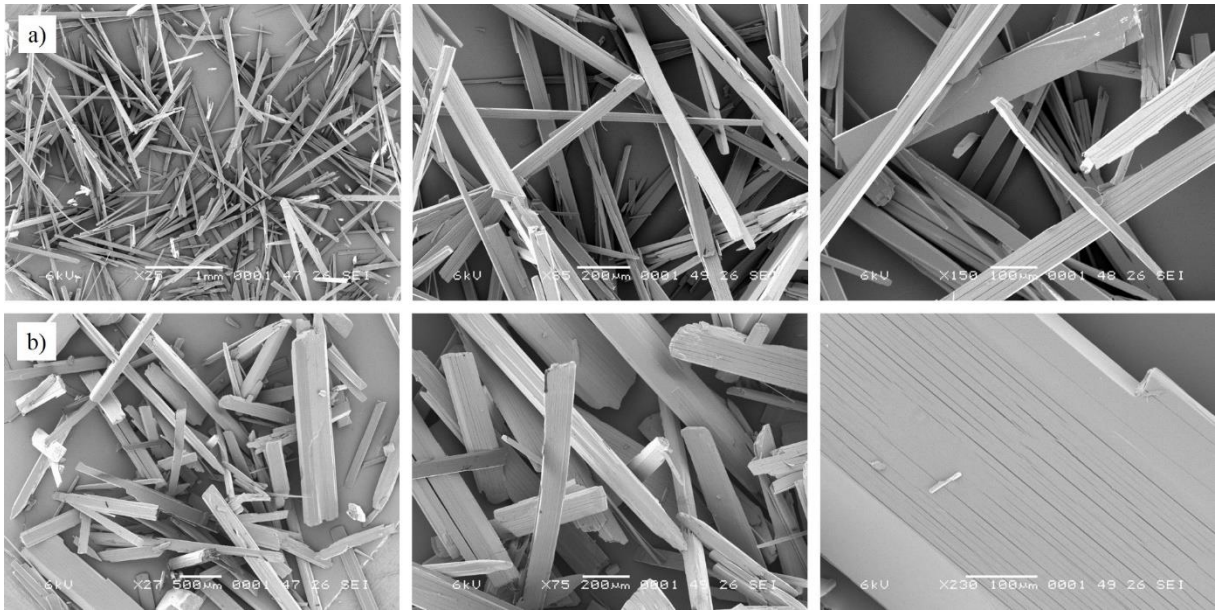

Figure 110 - SEM micrographs showing CBZ:2H_2O crystals obtained from cooling crystallization in 91 mol% (row *a*, 6xS) and 52 mol% (row *b*, 2xS). The cooling rate was 1 ºC/day.

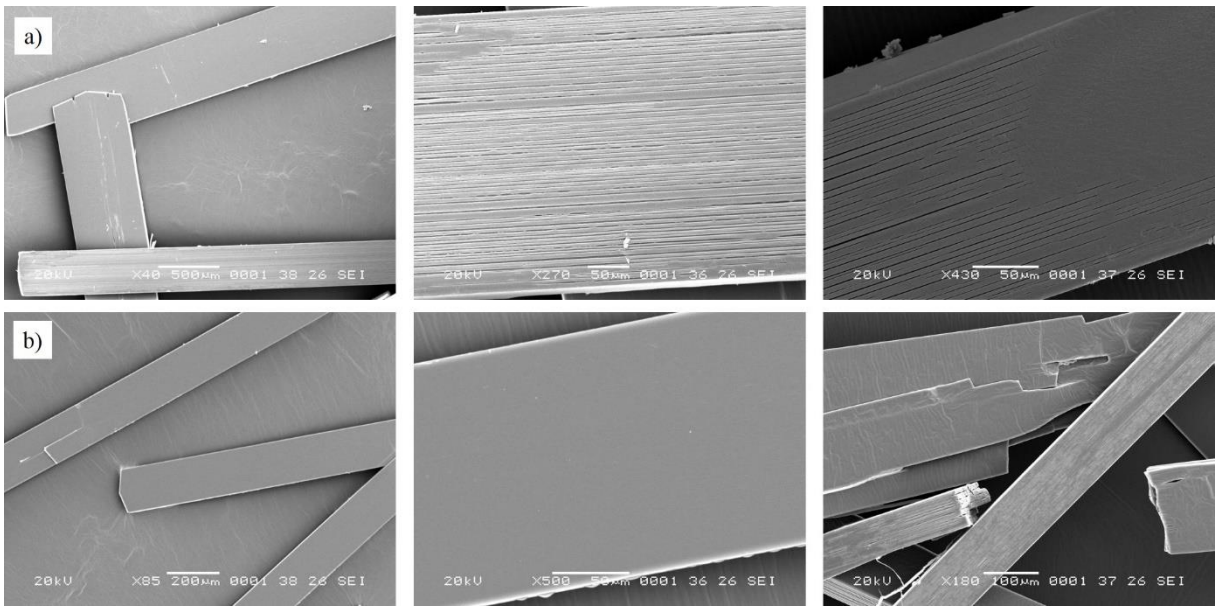

Figure 111 – SEM micrographs characterizing the outcome of CBZ crystallizations in isopropanol:water mixtures (row *a*: 59 mol% of water; row *b*: 93 mol% of water). The initial CBZ concentration was 2xS.

The effect of changes in the lipophilicity of the organic solvent on the morphology of CBZ:2H_2O was therefore investigated by performing cooling crystallizations in isopropanol. Figure 111 shows SEM micrographs of samples obtained in 41:59 and 7:93 isopropanol:water mixtures (n:n, 2xS). The experiments confirm that, in addition to the water content, the organic solvent also contributes to the growth morphology of the CBZ:2H_2O crystals. It is proposed that both ethanol and water play a role in the growth of (0k0) and (h00) crystal surfaces. As a non-crystallizing component, ethanol may work as an additive which adsorbs on the most lipophilic surface (0k0) leading to the decrease in its growth rate. The water molecules, in turn, increase the growth rate of the surface onto which they are preferentially bound (h00) because they are part of the crystal growth units.

The effect of additives on the growth crystals of CBZ:2H_2O has already been investigated by Rodriguez-Hornedo & Murphy[150] who showed that the presence of sodium taurocholate decrease the growth along the main axis of the CBZ:2H_2O needle-shaped crystals in water. As a result, different concentrations of the surfactant lead to distinctly crystal habits: 5 mM resulted in small plate-like crystals with (0k0) as the dominant face, while 9 mM concentration lead to prism shaped crystals. Comparative crystallization experiments in ethanol:water with sodium taurocholate were also performed in the present work (although the critical micellar concentration was not measured). Figure 112 and Figure 113 show the resulting crystals from these crystallizations. It is noted that the surfactant does not decrease the growth rate of (00l) as much as observed in water.[150] The effect of water activity on the preferred crystal surface was comparable to the crystallization in ethanol:water without additives (Figure 114). The size and the aspect ratio of the crystals obtained in high quantities of water was affected,

however. It is suggested that these crystals show large (0k0) surfaces because of the relative decrease in the rate of (00l) growth.

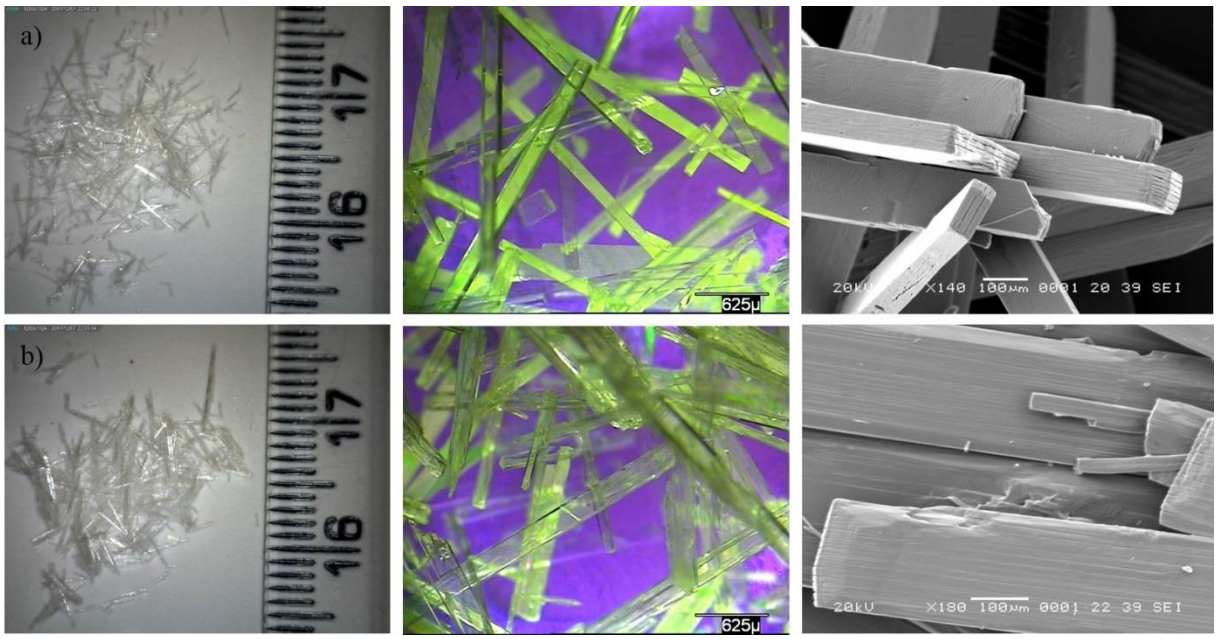

Figure 112 – Imaging of CBZ:2H_2O crystals obtained from cooling solution crystallization in ethanol:water solutions containing 5mM of sodium taurocholate. *a*: crystals obtained in 91 mol% of water (6xS). *b*: crystals obtained in 52 mol% of water (2xS).

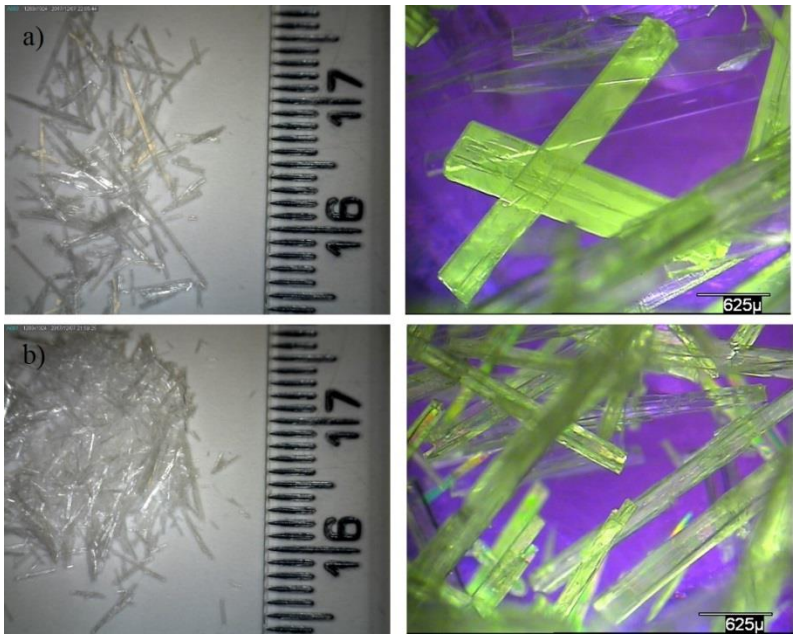

Figure 113 – Imaging of CBZ:2H_2O crystals obtained from cooling solution crystallization in ethanol:water solutions containing 9 mM of sodium taurocholate. *a:* crystals obtained in 91 mol% of water (6xS). *b*: crystals obtained in 52 mol% of water (2xS).

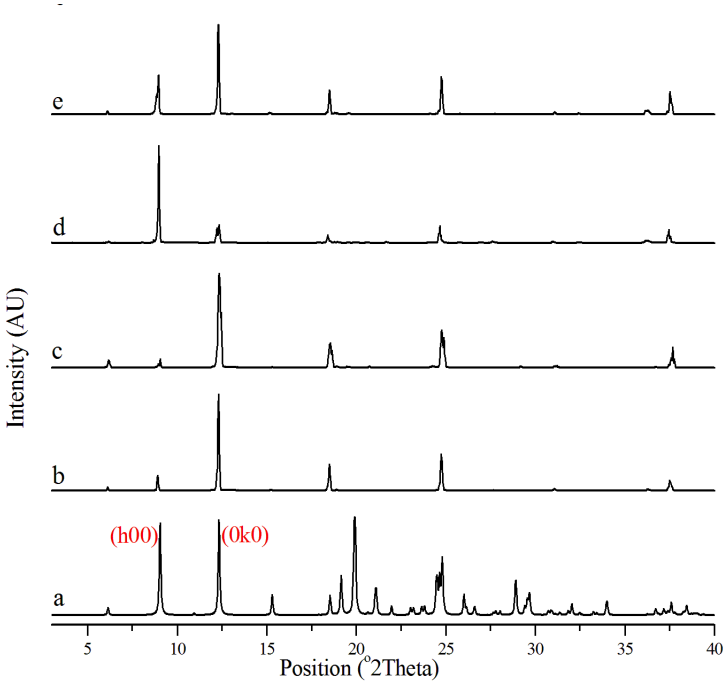

Figure 114 – PXRD patterns of CBZ:2H_2O crystals obtained from cooling solution crystallization in ethanol:water solutions containing sodium taurocholate. The *a* indicate the calculated pattern of FEFNOT02. The *b* and *c* indicate crystals obtained in 91 mol% of water with 5 mM and 9 mM of surfactant, respectively (6xS). The *d* and *e* indicate crystals obtained in 52 mol% of water with 5 mM and 9 mM of surfactant, respectively (2xS).

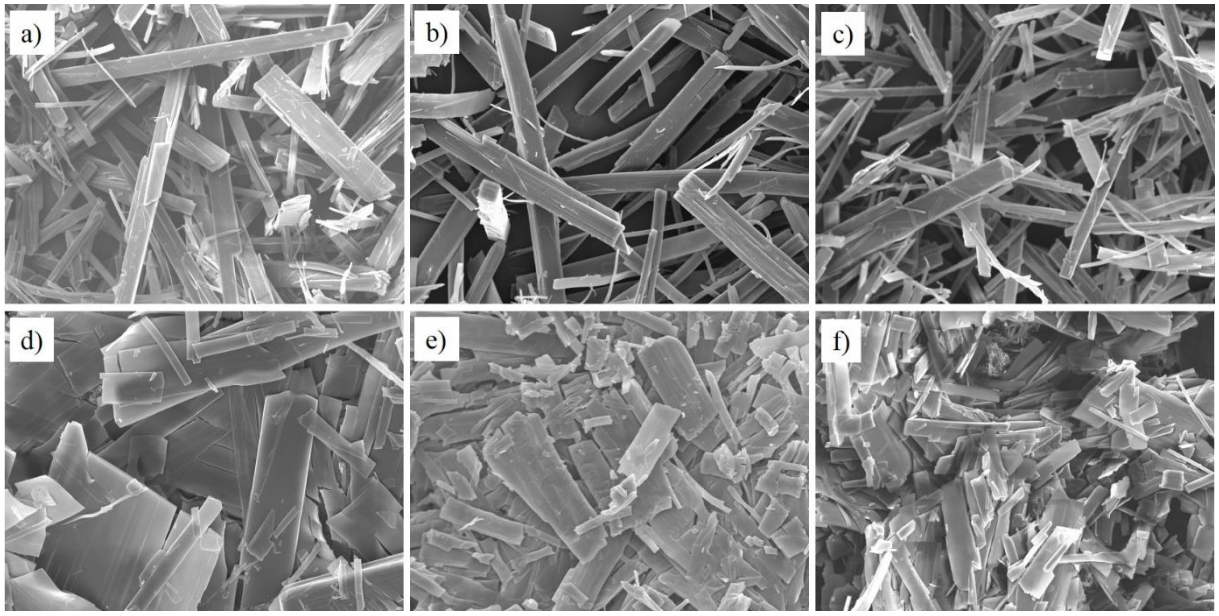

Figure 115 - SEM micrographs of CBZ:2H_2O crystals obtained from antisolvent addition of water in ethanolic solutions, followed by seeding. The *a*, *b* and *c* images indicate samples crystallized in a final concentration of 91 mol% of water (supersaturation degree of 1.2, 1.4 and 1.7, respectively). The *d*, *e* and *f* images indicate samples crystallized in a final concentration of 68 mol% of water (supersaturation degree of 1.2, 1.4 and 1.7, respectively).

Figure 115 shows the resulting crystals obtained from experiments in which supersaturation was generated via antisolvent addition of water into ethanolic solutions containing CBZ, and crystallization was induced by seeding. Different supersaturation degrees and two final ethanol:water proportions were tested, namely 68 mol% and 91 mol% of water.

Similarly to the other experiments described earlier, the results demonstrate that solvent nature affected the *tracht* of CBZ:2H_2O crystals. In this case, however, the crystals prepared in higher water proportions show equivalent (0k0) and (h00) growth. Higher ethanol proportions, in turn, resulted in crystals with (h00) preferred face. It was noteworthy that the crystals produced by antisolvent addition were considerably thin, which may result from the rate of water addition, the nature of the seeds used and/or, especially, the agitation.

The studies reported above illustrate how the crystallization environment and conditions can affect the crystal morphology such that crystals with different dominant surfaces (*tracht*) could be prepared. Although the overall shapes of the CBZ:2H_2O crystals were similar, the surfaces differed in their microscopic characteristics. Such differences are likely to affect the processability of the materials and their associated dehydration properties. This aspect is further considered in the following Chapters.

4.2.3.2. Case study 2: The crystallization of carbamazepine cocrystals with benzoquinone and oxalic acid

The preparation of CBZ cocrystals with BZQ and OXA was attempted initially by liquid assisted grinding using acetonitrile. Stoichiometric amounts of CBZ and the coformers (2:1, n:n) were used to make the reported 2CBZ:BZQ and 2CBZ:OXA cocrystals. The materials obtained from grinding were then used to prepare solutions that resulted in the corresponding single crystals by cooling crystallization.

After this first screening, the CBZ/BZQ system was selected for further study and reaction crystallization experiments were performed in order to assess the solubility of 2CBZ:BZQ in ethanol. The aim was to develop a better understanding of the required cooling crystallization conditions. The results were, however, unexpected - while 2CBZ:BZQ was formed at low concentrations of coformer, the slurries which contained large amounts of dissolved BZQ were in equilibrium to a solid which produced a new PXRD pattern. It was unclear, at the time, whether it was a mixture of 2CBZ:BZQ with an unknown material or a completely new form. Cooling crystallization experiments in ethanol solutions with different amounts of CBZ and BZQ showed a similar behaviour as that observed in the slurrying experiments (Figure 116). In this case, low quantities of BZQ in solution lead to the characteristic needles of 2CBZ:BZQ, while higher quantities lead to a mixture of large needles and small prisms. The large needles were identified as BZQ (CSD BNZQUI) and the prisms were characterized as CBZ:BZQ, a new cocrystal form of CBZ/BZQ.

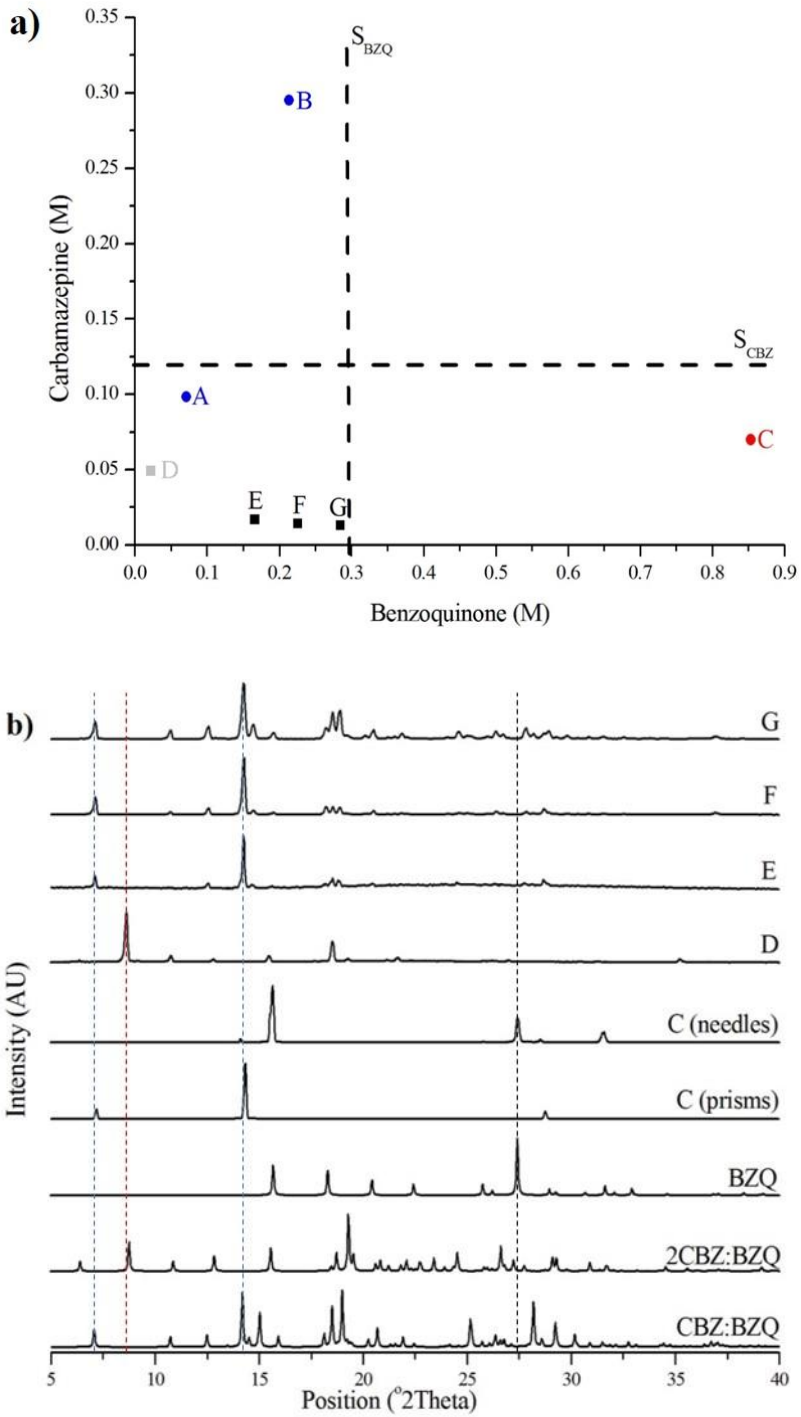

Figure 116 – Description of slurrying and cooling crystallization experiments performed for CBZ/BZQ. The graph in *(a*) shows the equilibrium solubility of the samples obtained from slurry (D, E, F and G) and compares it to the initial CBZ/BZQ concentrations used in cooling crystallization experiments (A, B and C). The solids obtained from the experiments A, B and D were characterized as 2CBZ:BZQ, while the materials C, E, F and G were characterized as CBZ:BZQ. In the case of C, CBZ:BZQ has also crystallized concomitantly to BZQ. The PXRD patterns in *(b)* characterize the different crystals obtained in sample C and the slurried samples D, E, F and G. The calculated patterns are also added for clarification.

Liquid assisted grinding experiments (30 minutes, 30 Hz) have also shown a similar trend - with Figure 117 showing that intermediate proportions of CBZ and BZQ formed a mixture of the reported and the new cocrystal. To investigate further the formation of CBZ:OXA, CBZ and OXA were also ground in a 1:1 proportion, but no unknown peaks were

observed in the PXRD patterns. The excess of coformers in the grinding experiments was also observed in the PXRD patterns by the presence of characteristic peaks of the starting materials.

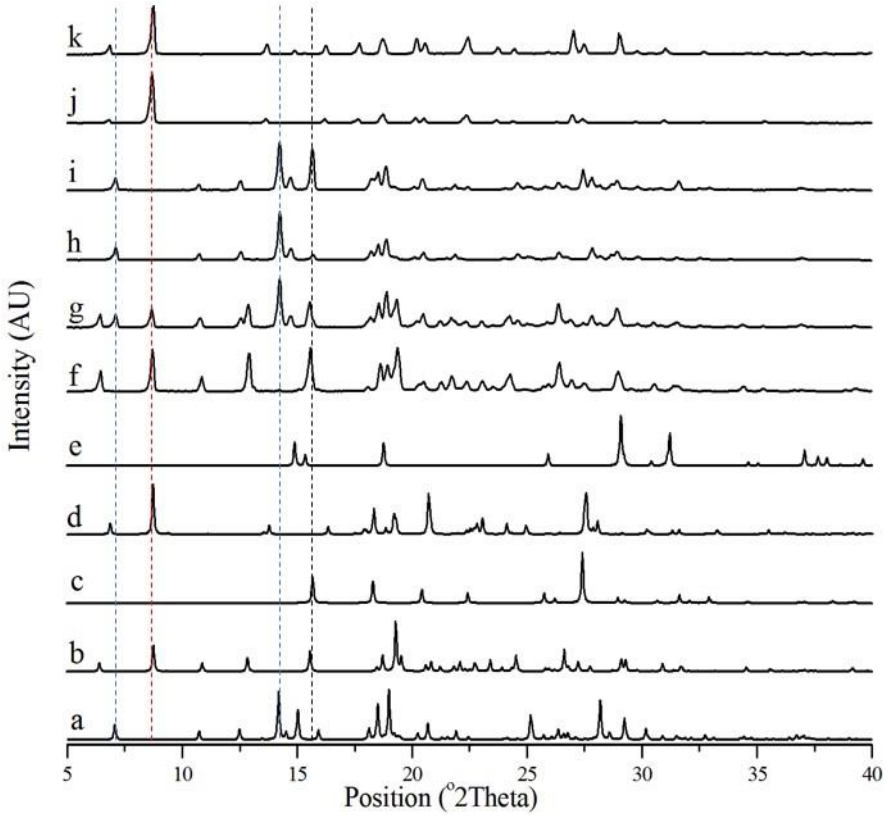

Figure 117 – PXRD patterns showing the results of liquid assisted grinding of CBZ/BZQ and CBZ/OXA with varied stoichiometric proportions. The calculated patterns of the cocrystals are added for clarification (*a*: CBZ:BZQ; *b*: 2CBZ:BZQ from UNEYOB; *c*: BZQ from BNZQUI; *d*: 2CBZ:OXA; *e*: OXA:2H_2O from OXACDH). The experimental PXRD patterns are displayed on the top (*f*: CBZ/BZQ in 1/0.5 proportion; *g*: CBZ/BZQ in 1/0.75 proportion; *h*: CBZ/BZQ in 1/1 proportion; *i:* CBZ/BZQ in 1/2 proportion; *j:* CBZ/OXA in 1/0.5 proportion; *k:* CBZ/OXA in 1/1 proportion).

The studies of CBZ/BZQ system illustrate another factor that is affected by the crystallization conditions: the crystal form. In this case, a cocrystal with a different stoichiometry resulted from different solution composition. Crystallization of different polymorphs would be another example. In the present study, no evidence of polymorphic forms of CBZ multicomponent phases were observed. Another system which have shown additional stoichiometry other than the reported one is CBZ/TFE. It is noteworthy that, while CBZ:TFE and 2CBZ:TFE present very similar needle-like morphologies, CBZ:BZQ and 2CBZ:BZQ have rather different crystal habits. Although changes in the solubility and morphology already affect the processability of organic solids, different stoichiometry may also affect (or not) the desolvation/sublimation properties of a material. This aspect is discussed further in Chapters 7 and 8.

4.3. Conclusion

It has been demonstrated that cooling solution crystallization is a suitable method to prepare CBZ multicomponent materials. Additionally, the determination of the equilibrium solubility of CBZ and CBZ multicomponent forms in different solution compositions provided useful information about their properties, such as stability. In practical terms, modifications in the solution composition have influenced the morphology and the stoichiometry of the resulting crystals.

Two new crystal forms were obtained: CBZ:BZQ and 2CBZ:TFE. It is likely that these new phases were not found in previous studies because the majority of the solvate crystallization experiments are usually performed in pure solvents (or low coformer concentrations, in the case of cocrystals). It illustrates the effectiveness of slurrying and grinding techniques on the characterization of the solid form landscape of cocrystals and solvates.

Differences in the growth of crystal surfaces result because of the crystallization environment. The aspect ratio of 2CBZ:BZQ, CBZ:2H_2O, CBZ:FORM, CBZ:TFA, CBZ:ACA and CBZ:FA crystals varied according to initial CBZ concentration and/or coformer proportion. In the case of CBZ:2H_2O, however, the results indicate that different dominant surfaces result from different coformer compositions giving rise to crystals with distinct *tracht*. CBZ:2H_2O was selected for additional experiments in alcohol:water and it was concluded that both solvents play a role in controlling crystal shape. The proposed hypothesis is that alcohol and water molecules affect the morphology by two different mechanisms of selective surface adsorption. While the lipophilicity of the alcohol decreases the growth rate of non-hydrogen-bonding crystal faces, the water molecules increase the growth of faces in which they are part of the growth unit through hydrogen bonding.

The formation of cracks on the (h00) face has facilitated its identification from the (0k0) CBZ:2H_2O surface, and it also suggests different surface characteristics. Samples containing (0k0) and (h00) preferred faces, in addition to the other crystals prepared in solution, will be used in the investigation of the bulk and surface properties of CBZ multicomponent materials upon stress-induced transformations.

CHAPTER 5 – The dehydration of carbamazepine dihydrate prepared and studied at laboratory scale

5.1. Introduction

Dehydration is a physical transformation that addresses the loss of water of crystallization and the accompanying lattice reorganization. These two phenomena are very difficult to separate and most likely occur simultaneously. This simultaneous nature is a major challenge associated with the prediction of the reaction outcome. Additionally, another aspect that complicates the process is the kinetic element, which may be seen by varying the rate of solvent loss, the particle size and morphology. In summary, the precise experimental conditions are likely to affect the outcome of the reaction and will have to be carefully controlled. In this context, the present chapter focusses on dehydration experiments of CBZ:$2H_2O$ subjected to temperature and moisture variations as well as the effect of vacuum applied to the sample. With respect to apparent inconsistencies concerning the dehydration studies reported in the literature, the effect of seed crystals upon the reorganization of the CBZ lattice during dehydration is also considered.

Two samples obtained from cooling crystallization at different ethanol:water proportions (see Chapter 4, Section 4.2.2.8) were selected for dehydration experiments. These methods of preparation of CBZ:$2H_2O$ provide samples with different *tracht* (*i.e.* different dominant crystal surfaces). CBZ:$2H_2O$ crystals obtained from high water activity solutions have shown a preferred orientation of (0k0) planes and hereafter will be referred to as the (0k0) dihydrate, while CBZ:$2H_2O$ crystallized in low water activities with (h00) preferred orientation will be identified as the (h00) dihydrate. Additionally, the influence of seeds on the outcome of the dehydration experiments is determined for CBZ:$2H_2O$ crystals obtained from slurrying experiments - which produces particles considerably smaller than the (0k0) and (h00) samples. Chapter 2 provides details of the general crystallization methods and Chapter 4 discuss the investigation of the crystallization characteristics of CBZ:$2H_2O$ (Section 4.2.3.1). When applicable, additional experiments and modifications are described in the following text.

5.2. The effect of vacuum on CBZ:$2H_2O$ crystals

The effect of vacuum on CBZ:$2H_2O$ crystals was initially observed during the preparation of samples for analysis by SEM. Images of CBZ:$2H_2O$ crystals freshly prepared

have shown the (h00) and the (00l) surfaces with significant numbers of cracks, while none were observed on the (0k0) surfaces (Figure 118). The analysis indicated two types of cracks corresponding to the (0k0) and the (h00) planes of the dihydrate structure. The (00l) surface shows both types of fractures, while the cracks visible on the (h00) surface were only related to the (0k0) planes. Figure 118 illustrates the difference between the crystal surfaces and identifies the fractures corresponding to the (0k0) and the (h00) planes. The images demonstrate that the different surfaces of the CBZ:2H_2O crystals show different susceptibility to defect formation.

It is suggested that the most important type of fracture on CBZ:2H_2O are the (0k0) cracks as they tend to cross-cut the entire crystals. A few cracks, however, do not propagate the whole length of the crystal. Figure 119 shows regions of incomplete crack propagation. Interestingly, this phenomenon was frequently seen in pairs of non-propagated cracks which developed to (or from) different crystal extremities. It is unclear whether the fractures have started or ended at the point where they meet. However, these findings suggest that the cracks are generated to release the various types of local stress and strain formed throughout the crystal.

The presence of strain is also demonstrated by a pattern of intersecting herringbone texture on the (h00) surface of fresh CBZ:2H_2O crystals analysed by SEM. Figure 120 shows that the different textures within the domains are related by an angle of 78.2±3.3^o, while the texture orientation is related to the main cracks by 36.1±2.5^o. It is noteworthy that Kachrimanis & Griesser[162] observed similar intersecting cracks related by 40.6±1.2° to the needle axis and crossing at 81.5±1.6° because of the thermal dehydration of CBZ:2H_2O crystals. The authors, however, reported the formation of these feature on the (0k0) surface as opposed to the (h00) described here.

The cracks parallel to the needle axis and which correspond to the (0k0) crystallographic planes have also been reported in the literature. Khoo *et al.*[163] attributed the formation of these cracks to the effect of early stages of dehydration on the (h00) surface. In the present work, it is suggested that the sputtering of the samples with gold prior to the microscopy analysis is the cause of the fractures (irrespective of whether they are related to dehydration or not). Coating of organic materials for conventional SEM analysis is used to improve charge dissipation and to minimize sublimation of the sample inside the SEM. While the vacuum inside the sputtering chamber is much lower than it is within the SEM microscope, the sputtering process may also be the source of sample damage. It was unclear, though, whether the cracks on the surface of CBZ:2H_2O crystals were artefacts from the sample preparation or if this characteristic was intrinsic to the fresh crystals.

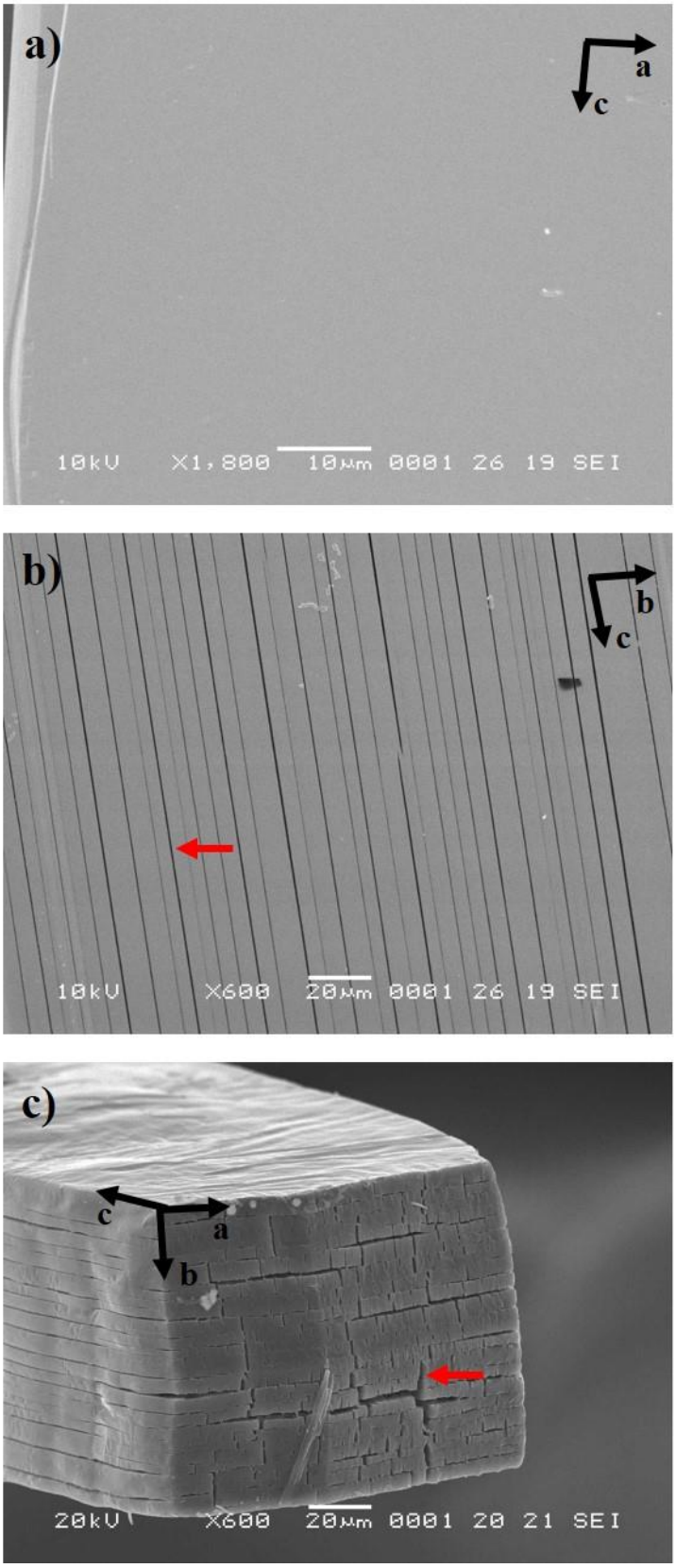

Figure 118 - SEM micrographs representative of the surfaces of CBZ:2H_2O crystals. *a*: (0k0) surface. *b*: (h00) surface, the arrow points to one crack corresponding to the (0k0) crystallographic plane. *c*: (00l), the arrow points to one crack corresponding to the (h00) crystallographic plane.

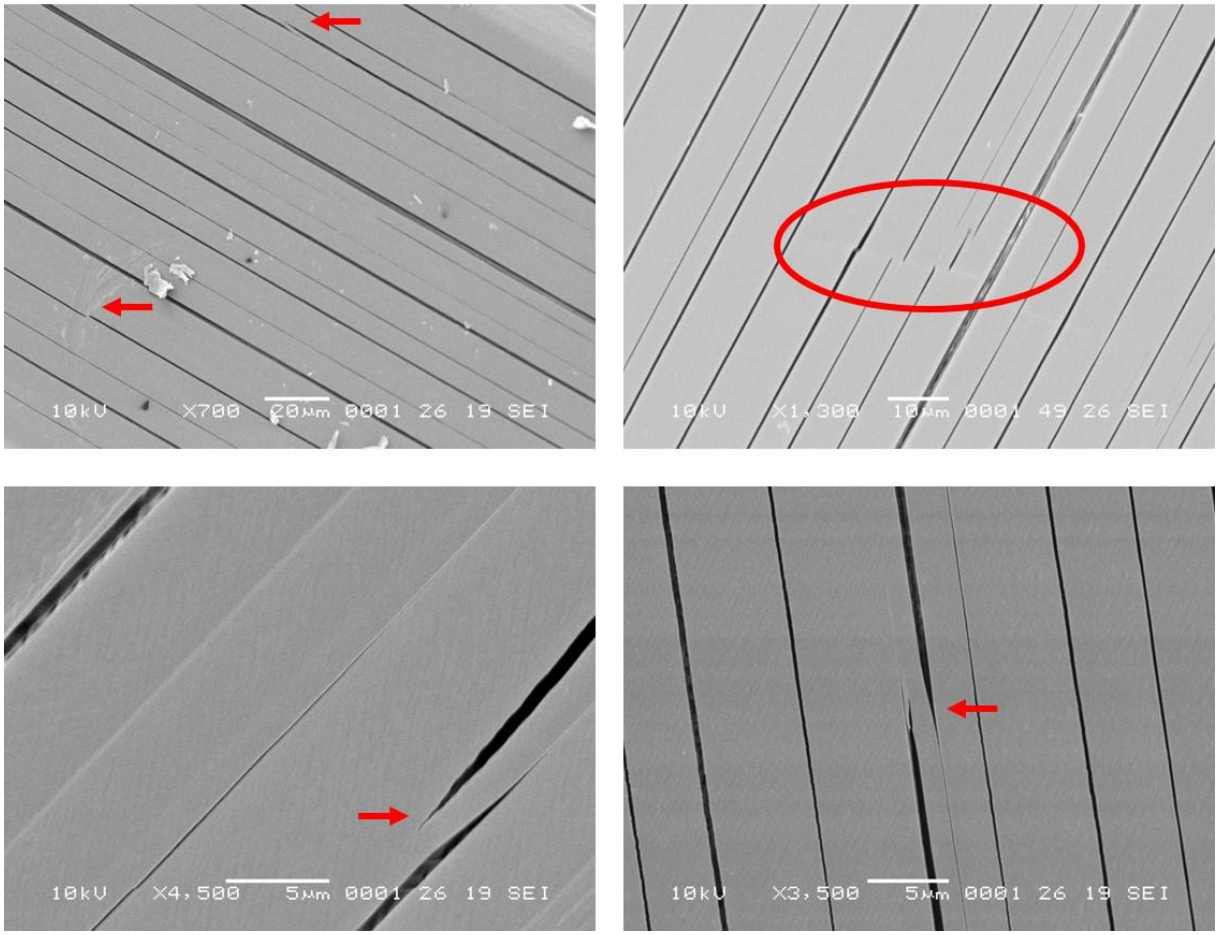

Figure 119 - SEM micrographs of CBZ:2H_2O (h00) surface showing incomplete crack propagation (indicated by the red arrow).

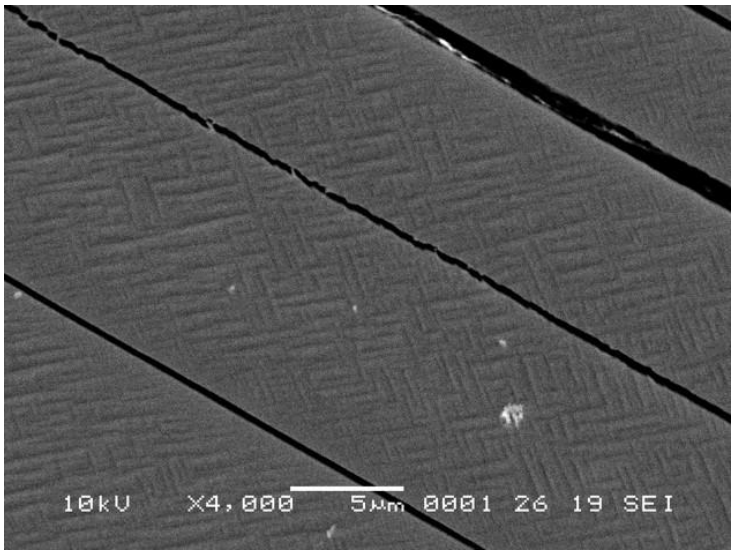

Figure 120 - SEM micrograph of CBZ:2H_2O (h00) surface showing the intersecting herringbone texture.

To answer this question the surface of fresh CBZ:2H_2O crystals were imaged by AFM at room temperature (Figure 121). The AFM analyses of (h00) fresh surfaces confirmed that the crystals did not show the cracks observed by SEM. The AFM images, however, did show that the (h00) face is composed of layers spaced by 7.5±0.7 Å along the needle axis. The (0k0) surfaces, in turn, show steps perpendicular to the needle axis and terraces of varied size.

Interestingly, the images suggest that the terraces on the (0k0) surface are formed by pairs of layers that present coincident edges. The measured distance between the paired layers is approximately half of the distance between two different terraces (12.5±0.6 Å and 25.8±1.2 Å, respectively).

Figure 122 shows the section of the height images of (0k0) and (h00) crystal surfaces. The graphs represent the height measurements on the terraces and along the step, and compare the height variations (*i.e.* the noise) on the terraces to the size of the steps. The baseline shows a large step size/noise ratio, which demonstrates a good vertical resolution. It confirms that the performed AFM measurements were sensible and can be appropriately used to measure the size of the steps on the surface of the CBZ:2H_2O crystals.

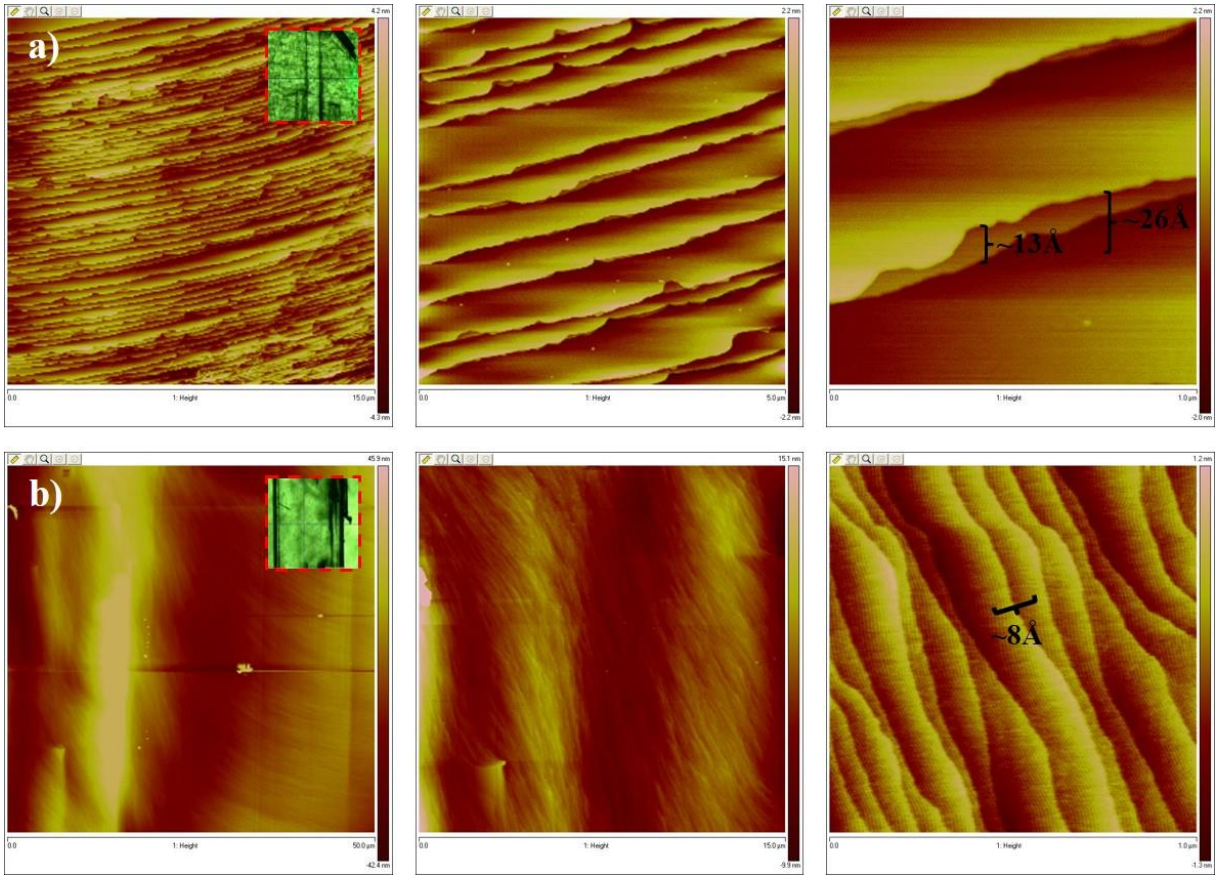

Figure 121 – AFM height images illustrating the topography of the surfaces of CBZ:2H_2O fresh crystals. *a*: (0k0) surface; scan size of 15 µm, 5 µm and 1 µm (left to right). *b*: (h00) surface; scan size of 50 µm, 15 µm and 1 µm. The optical micrographs show the orientation of the crystals during the analyses. The average step distances are shown on the images.

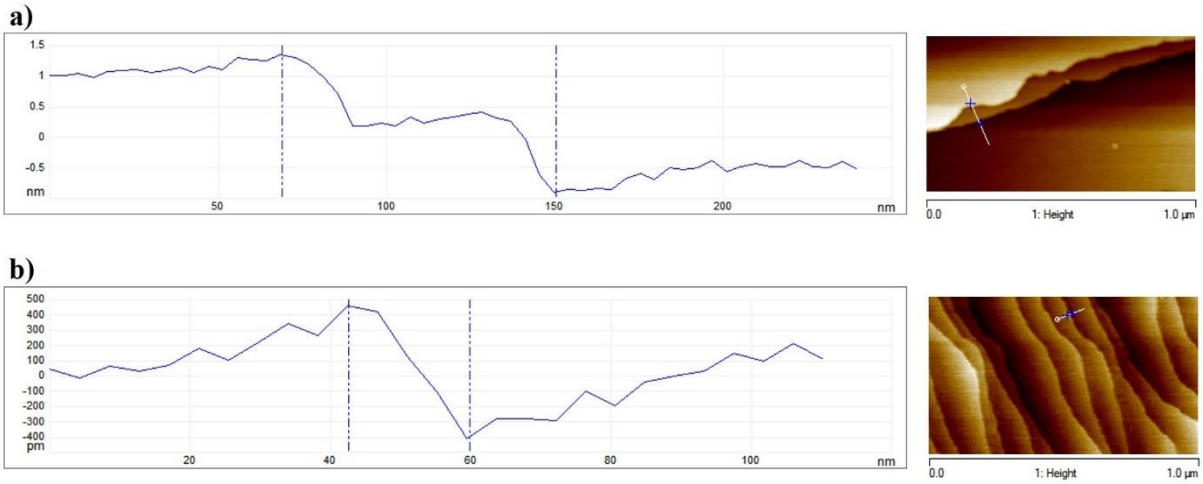

Figure 122 - Graphical representation of sections of AFM height images illustrating the step size to noise ratio on the surfaces of CBZ:2H_2O fresh crystals. *a*: (0k0) surface; *b*: (h00) surface. The height images on the right show the respective region that has been sectioned.

Additionally, a systematic study of the effect of vacuum on the dihydrate crystal surfaces over time was performed. It consisted of subjecting samples to the same vacuum used in the coater for 20, 30 or 40 minutes prior to gold sputtering. The resulting SEM images in Figure 123 show that the main artefacts from vacuum on the dihydrate surface are the cracks corresponding to the (0k0) crystallographic plane. The (0k0) surface presented less defects as a result from vacuum, namely roughness, and random and infrequent holes. The (h00) face developed the abovementioned patterns of fracture and intersecting texture, and holes. The (00l) face, in turn, was the most affected surface, showing cracks, roughness and the growth of small particles onto the surface as a function of time exposed to vacuum.

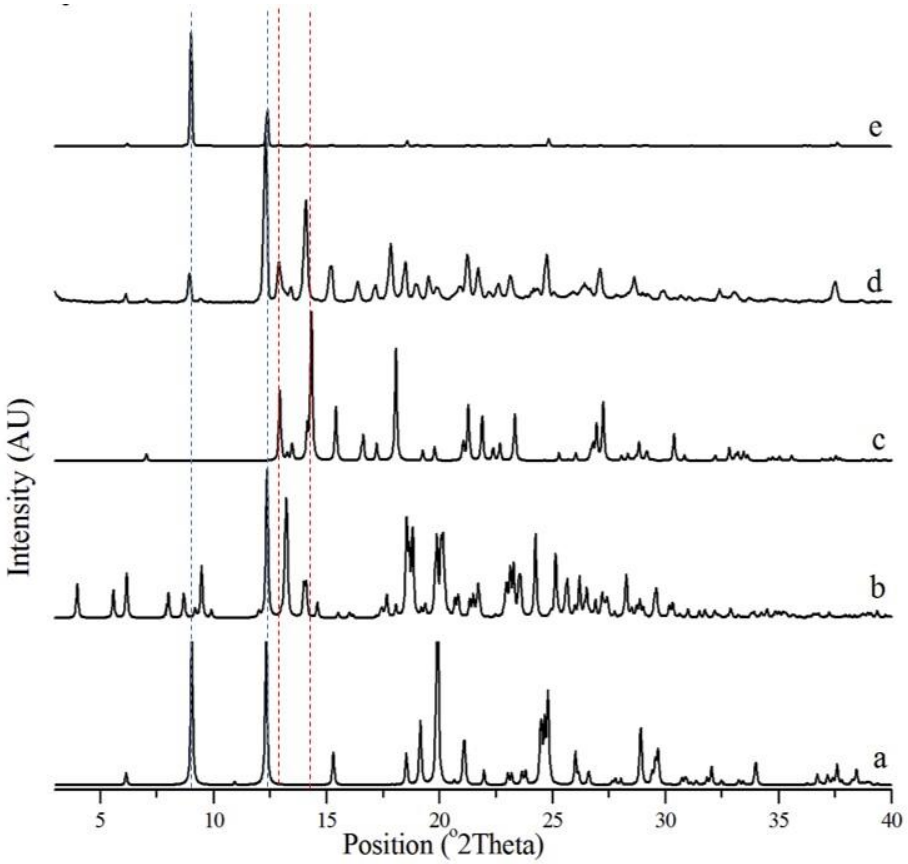

Figure 124 shows the effect of vacuum on the dihydrate lattice as analysed by PXRD. In these experiments, both (h00) and (0k0) samples were stored at room temperature under high vacuum for three hours, and subsequently analysed by PXRD, AFM and TGA. PXRD indicates that CBZ:2H_2O crystals subjected to these conditions show reflections of the dihydrate and anhydrous forms of CBZ. CBZ:2H_2O crystals with (0k0) dominant face develop additional reflections characteristic of CBZ Forms I and IV, while CBZ:2H_2O with (h00) dominant face show very minor diffraction peaks characteristic of CBZ Form I only. It is difficult to determine accurately the phase constitution because of preferred orientation. Both samples, however, had minimal or no residual water as measured by TGA, which suggests an isostructural dehydration process.

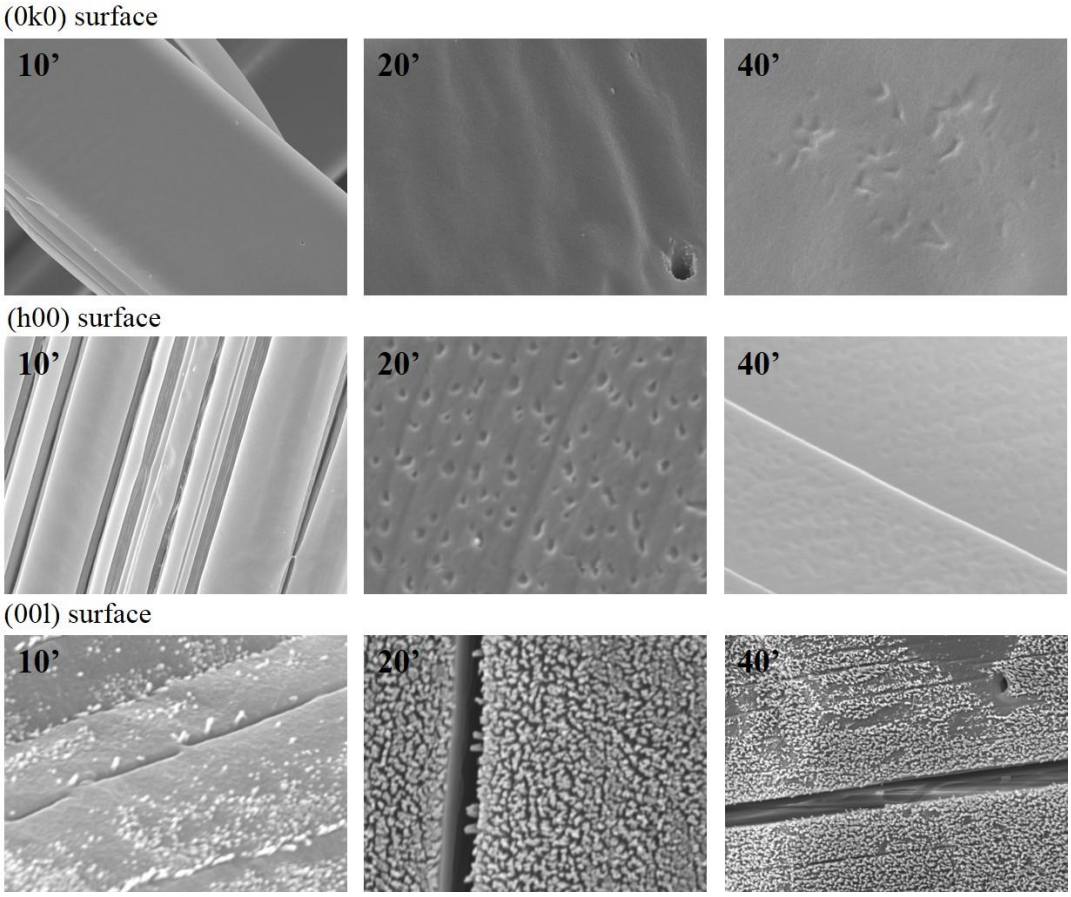

Figure 123 - SEM micrographs showing the CBZ:2H_2O surfaces after exposure to a vacuum of 0.02 mBar for 20, 30 or 40 minutes.

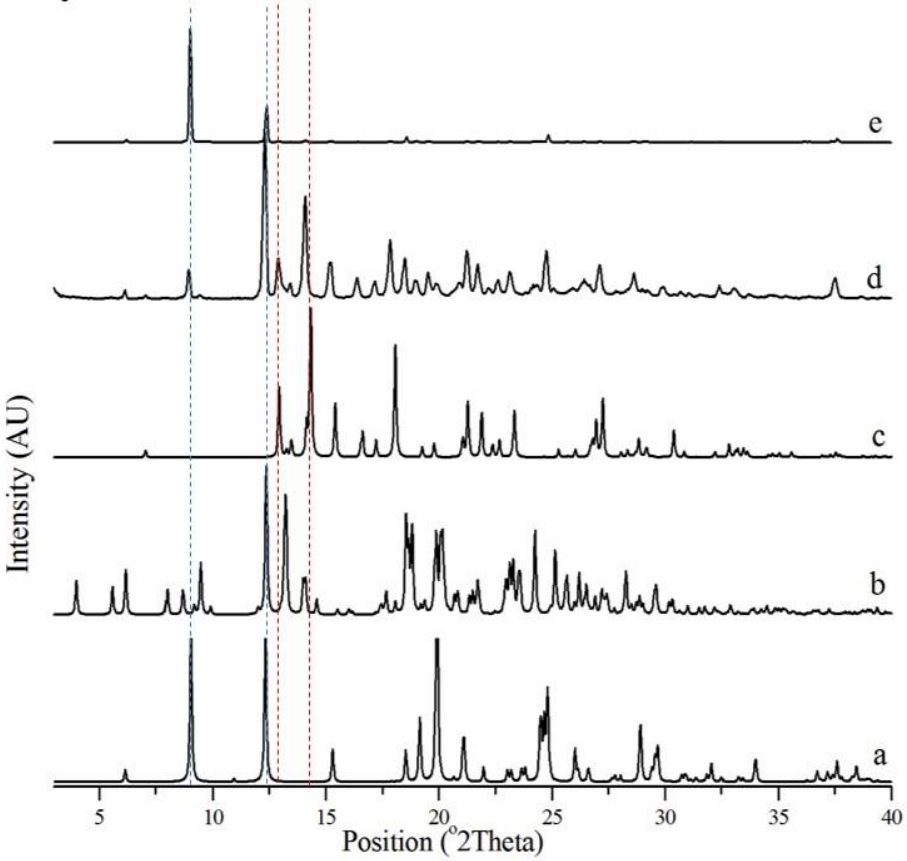

Figure 124 - PXRD patterns comparing (0k0) and (h00) CBZ:2H_2O samples stored for 3 hours under vacuum. The simulated patterns are added for clarification (*a*: CBZ:2H_2O from FENOT02; *b*: CBZ Form I from CBMZPN11; *c*: CBZ Form IV from CBMZPN12). *d*: (0k0) sample. *e*: (h00) sample.

AFM analysis of the samples stored under high vacuum for three hours show the disruption of the steps observed in the fresh samples, the formation of texture characterized by small domains, and the presence of holes (Figure 125). The oriented texture shown by AFM suggests anisotropy along the *c* axis of CBZ:2H_2O, although the orientation of the domains is different for the (h00) and (0k0) surfaces. The (h00) face show a pattern of intersecting domains like the intersecting texture characterized by SEM. The texture on the (0k0) surfaces, however, show acicular domains aligned along the *c* axis. It is noteworthy that a few remaining steps of CBZ:2H_2O are observed on the surfaces of the dehydrated samples. These steps illustrate the orientation of the dihydrate structural features in relation to the newly formed domains of the dehydrated material. The exact identity of the material is, however, unclear. PXRD bulk analysis suggests dehydration results in an isostructural anhydrous form, which subsequently rearranges to different anhydrous CBZ lattices. Regardless of the identification of the surface structure, the anisotropic surface features indicate the orientation of the strain direction and the molecular movements in the crystal as a consequence of water departure under vacuum.

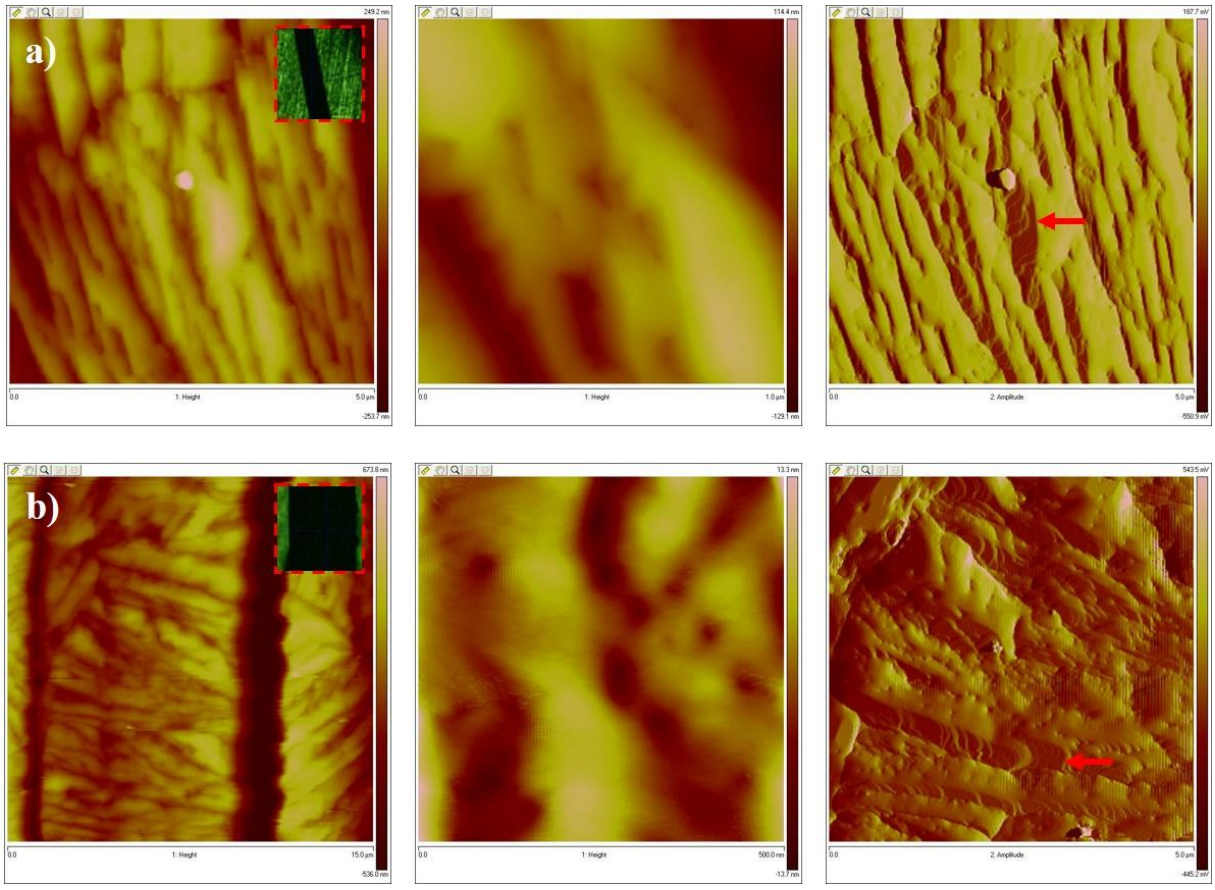

Figure 125 - AFM images illustrating the topography of the surfaces of CBZ:2H_2O crystals stored for 3 hours under vacuum. *a*: (0k0) surface; scan size of 15 µm, 5 µm and 1 µm (left to right). *b*: (h00) surface; scan size of 50 µm, 15 µm and 1 µm (left to right). The further right images are expressed in amplitude, while the others are height images. The optical micrographs show the orientation of the crystals during the analyses. The red arrows point to remaining steps from the fresh surfaces.

5.2.1. Transmission electron microscopy of CBZ dihydrate (CBZ:2H_2O)

The instability of CBZ:2H_2O under vacuum also challenged the TEM experiments. The bright field images obtained by conventional TEM show that the morphology agrees with previous experiments: *i.e.* needle-like crystals although sometimes showing tubular character (Figure 126). As the time of exposure to high vacuum increased, the particles developed holes that sometimes seemed to pass through the entire crystal thickness. The holes form as the time of exposure to vacuum increases. This phenomenon was not directly related to electron beam exposure and was observed in all the samples expected to be CBZ:2H_2O (Figure 126). Interestingly, no cracks were observed, which could be a result of the orientation of the crystals or their morphology/*tracht*.

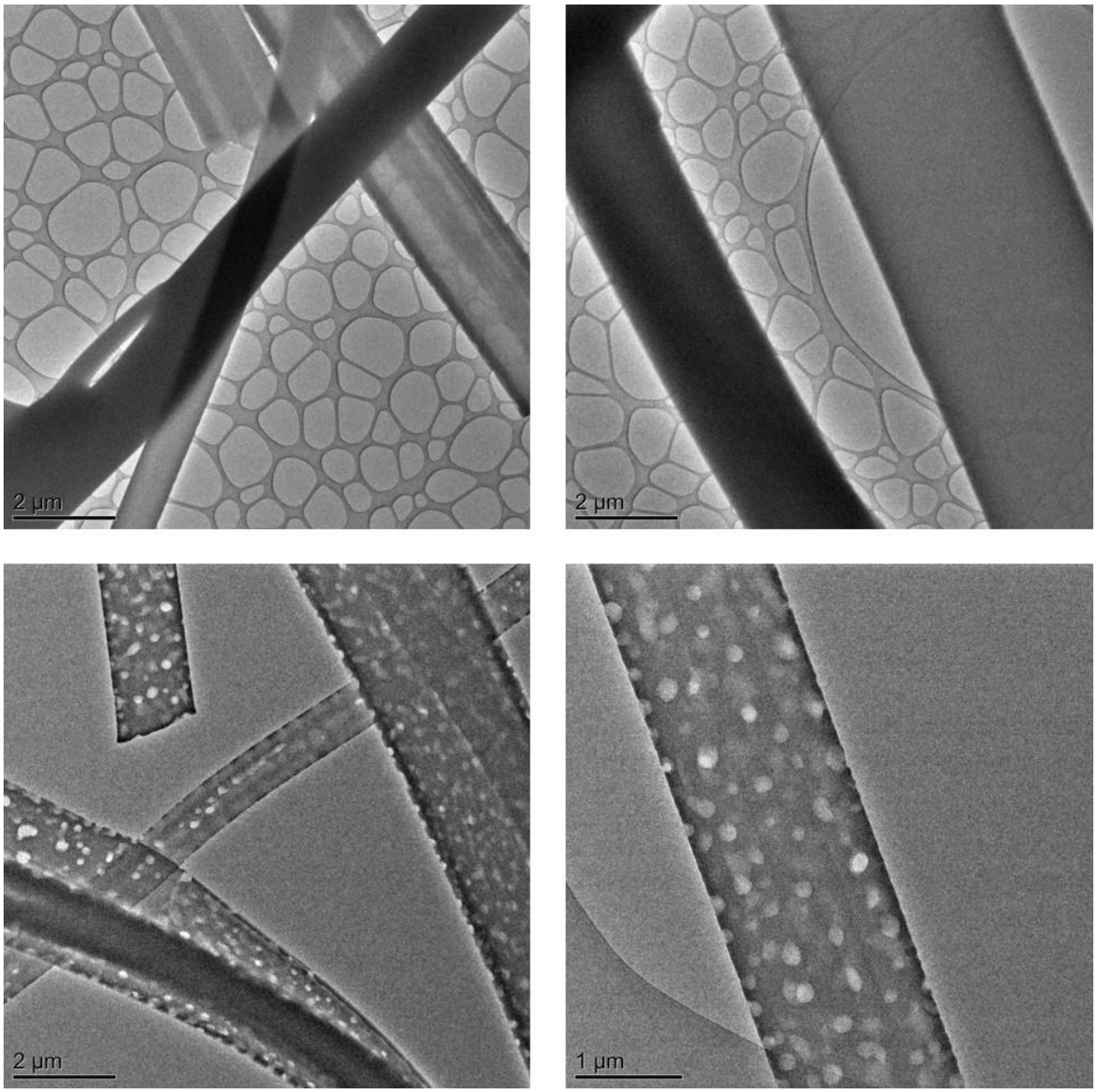

Figure 126 - TEM images of CBZ:2H_2O crystals. The top images show crystals at the beginning of the experiment, while the bottom images show crystals after a period inside the TEM chamber.

Figure 127 illustrates representative diffraction patterns collected in ambient temperature. Indexing of the electron diffraction patterns obtained for samples crystallized as CBZ:2H_2O was challenging and showed several possible matches. Attempts to group sets of *d*-spacings and the angles between the planes were not successful and no reliable indexing to known CBZ structures was possible. In some cases, zone axes were proposed, but the comparison with simulated zone axis diffraction patterns was ambiguous especially when there were just a few reflections in the patterns.

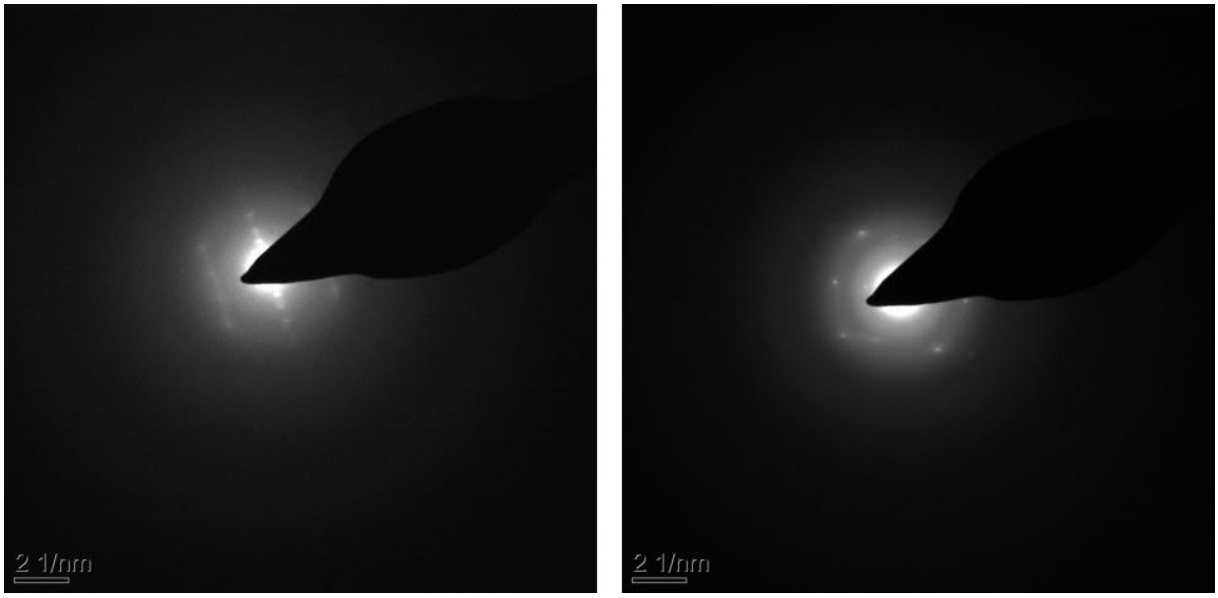

Figure 127 - TEM electron diffraction patterns of crystals expected to be CBZ:2H_2O.

In comparison, the diffraction patterns collected by conventional TEM of anhydrous CBZ materials were of significantly better quality. Figure 128 illustrates the indexing of two patterns obtained from specimens crystallized from THF. The patterns were individually reduced to three average *d*-spacings and three interplanar angles. These values were compared with *d*-spacings and interplanar angles of crystal planes of the anhydrous CBZ polymorphs (I, II, III, IV and V), but only the structure of polymorph II gave a good agreement to the experimental data. For the diffraction pattern in Figure 128a, d_1, d_2, d_3, θ_{12}, θ_{13} and θ_{23} were measured to be 9.84, 5.22, 4.82 Å, 97, 68 and 28^o respectively. The [010] zone axis was calculated to be a good match, with d1, d2 and d3 corresponding to the (100), (101) and (20-1) planes with calculated ideal values at 10.20 Å, 5.18 Å, 4.98 Å, 100, 71 and 29^o. On the other hand, the diffraction pattern in Figure 128c showed d_1, d_2, d_3, θ_{12}, θ_{13} and θ_{23} to be 17.86 Å, 5.21 Å, 5.22 Å, 101, 80 and 18^o, respectively. The [-1-21] zone axis was calculated to be a good match, with d1, d2 and d3 corresponding to the (2-10), (101) and (3-11) planes with value of

17.86 Å, 5.18 Å, 5.18 Å, 98, 82 and 17º. In both cases, therefore, the diffraction patterns could be satisfactory indexed.

Figure 129 displays the bright field images of samples characterized as CBZ polymorph II and polymorph I. It shows that the morphology of the particles agrees with the needle morphology expected for Forms II and I. Holes were not observed in the crystals. It leads to the conclusion that the holes observed in the crystals of CBZ:2H_2O after exposure to vacuum are not connected to the ability of CBZ to sublime. The experiments suggest that the holes are intrinsically related to CBZ dihydrate and its dehydration process under vacuum. Possibly, the formation of small and potentially more defective domains as a result of dehydration may be related to local sublimation and development of holes on the crystals analysed by TEM at room temperature.

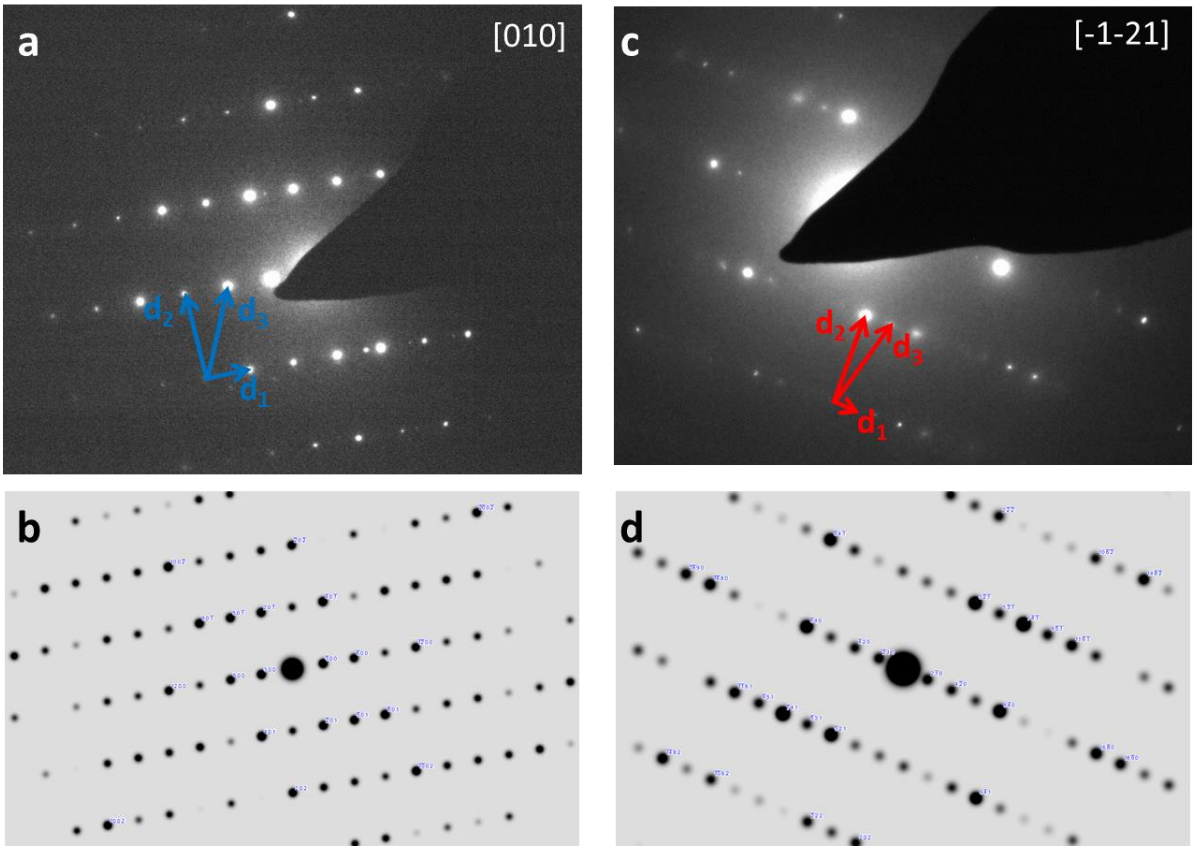

Figure 128 - Indexing of zone axis diffraction patterns of carbamazepine Form II. a) Experimental zone axis electron diffraction pattern of the [010] zone axis. b) Simulated electron diffraction pattern of the [010] zone axis from CSD structure CBMZPN03 (a = b = 35.454 Å, c = 5.253 Å, α = β = 90º, γ = 120º). c) Experimental zone axis electron diffraction pattern of the [-1-21] zone axis. d) Simulated electron diffraction pattern of the [-1-21] zone axis from CSD structure CBMZPN03.

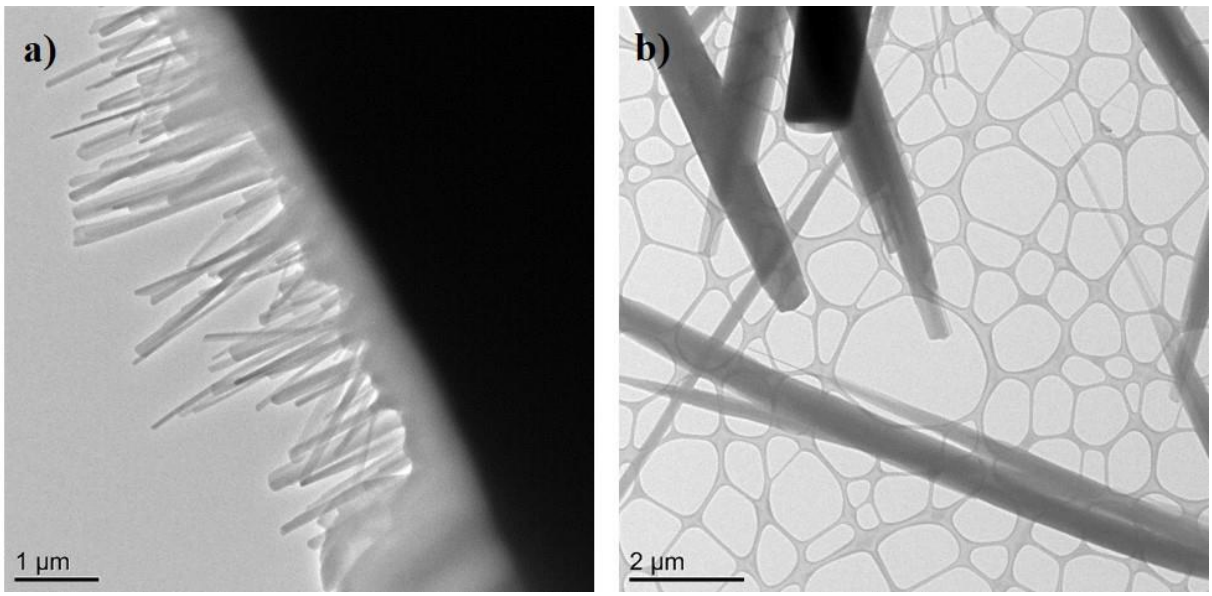

Figure 129 - TEM image of crystals of carbamazepine Form II (a) and samples expected to be polymorph I (b).

A solution to the quick and destructive departure of water molecules under vacuum was to perform cryo-TEM experiments, *i.e.* cool the sample to approximately 150K before and during examination. Figure 130 shows bright field images and diffraction patterns of such cooled CBZ:2H_2O samples. Holes did not develop during long periods of exposure to the TEM vacuum. Additionally, the quality of the diffraction patterns collected at low temperature has improved considerably.

Not all the diffraction patterns that were recorded during the cryo-TEM investigation of CBZ:2H_2O, however, could be indexed. In contrast to the samples analysed at room temperature, the indexing difficulty was not related to the quality of the diffraction patterns *per se*, but to the presence of several possible index matches, especially from high index zone axes (with associated small *d*-spacings). Figure 131 a and b show the bright field image and diffraction pattern for one cooled CBZ:2H_2O crystal. Although the rows parallel to the indexed (0k0) row of spots (k = even) were faint, it was possible to reduce the pattern to three average *d*-spacings and three interplanar angles (d_1, d_2, d_3, θ_{12}, θ_{13} and θ_{23} were measured to be 13.65, 2.24, 2.23 Å, 90.4, 85.2 and 5.0^o, respectively). Figure 131 c and d show that the [100] and the [101] zone axes were calculated to be good matches to the experimental data. In the case of the [100] zone axis, d1, d2 and d3 correspond to the (020), (002) and (01-2) planes, with respective values of 14.36, 2.35, 2.34 Å, 90.0, 85.3 and 4.7^o. The values are also very similar to the geometric parameters of the [101] zone axis, with d1, d2 and d3 corresponding to the (020), (20-2) and (2-1-2) planes, 14.36, 2.34, 2.33 Å, 90.0, 85.3 and 4.7^o.

Figure 131 shows that both zone axes are structurally very similar. It is suggested that the crystal face imaged corresponds to a view close to the (h00) CBZ:2H_2O surface. It is noteworthy that there is no evidence of crack formation along the main axis of the crystal and

no hole formation. A different outcome, however, was observed as the temperature of the sample was increased to room temperature. Figure 132 shows the bright field images and the diffraction patterns of the samples that were initially cooled, maintained under vacuum and then warmed to room temperature. The crystals developed holes at temperatures above 0 ^{o}C, like the holes observed in the TEM experiments at room temperature. Additionally, the quality of the diffraction patterns decreased and clearly resembled the patterns shown in Figure 127.

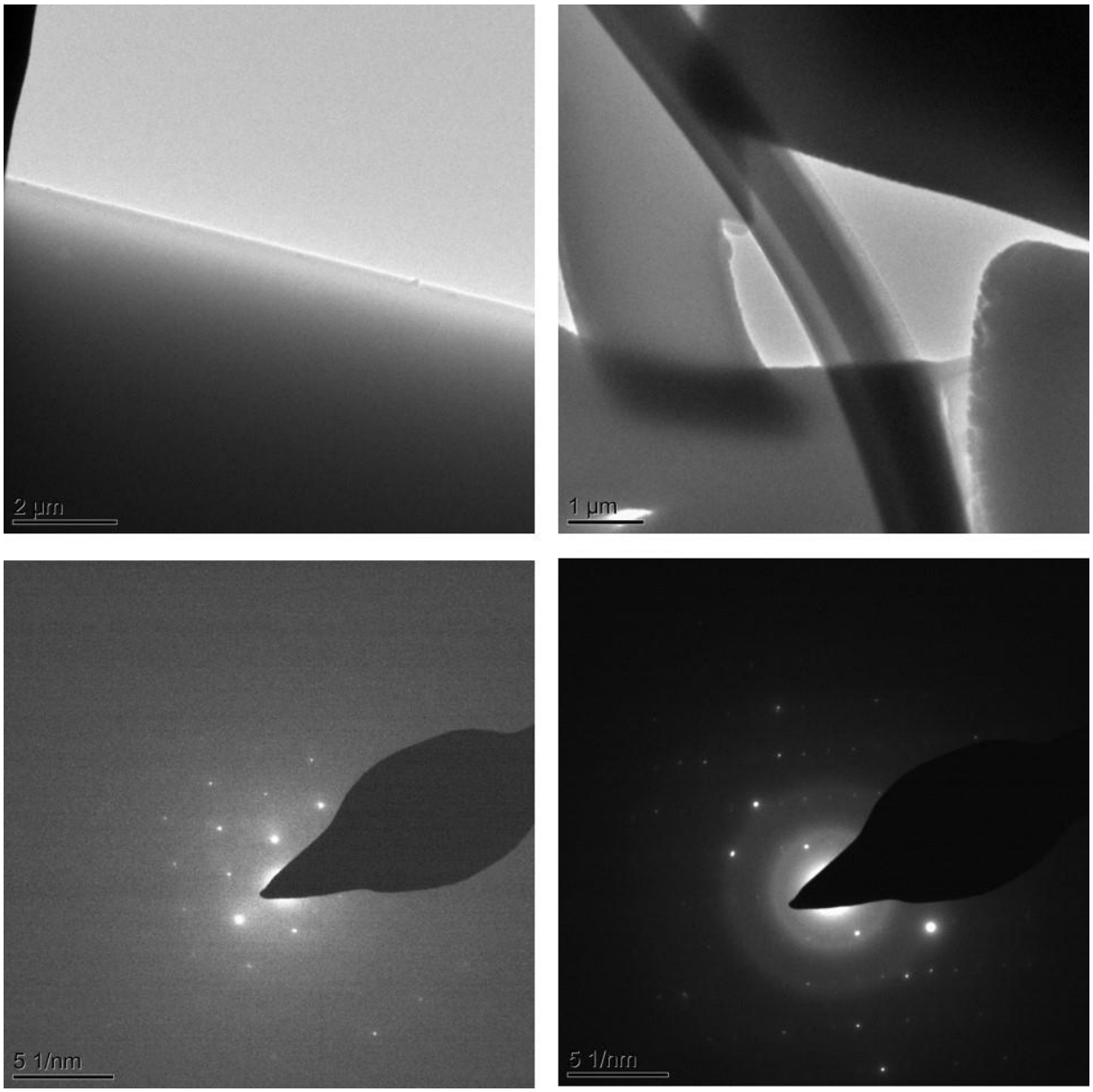

Figure 130 - Cryo-TEM images (top) and electron diffraction patterns (bottom) of crystals of CBZ:2H_2O.

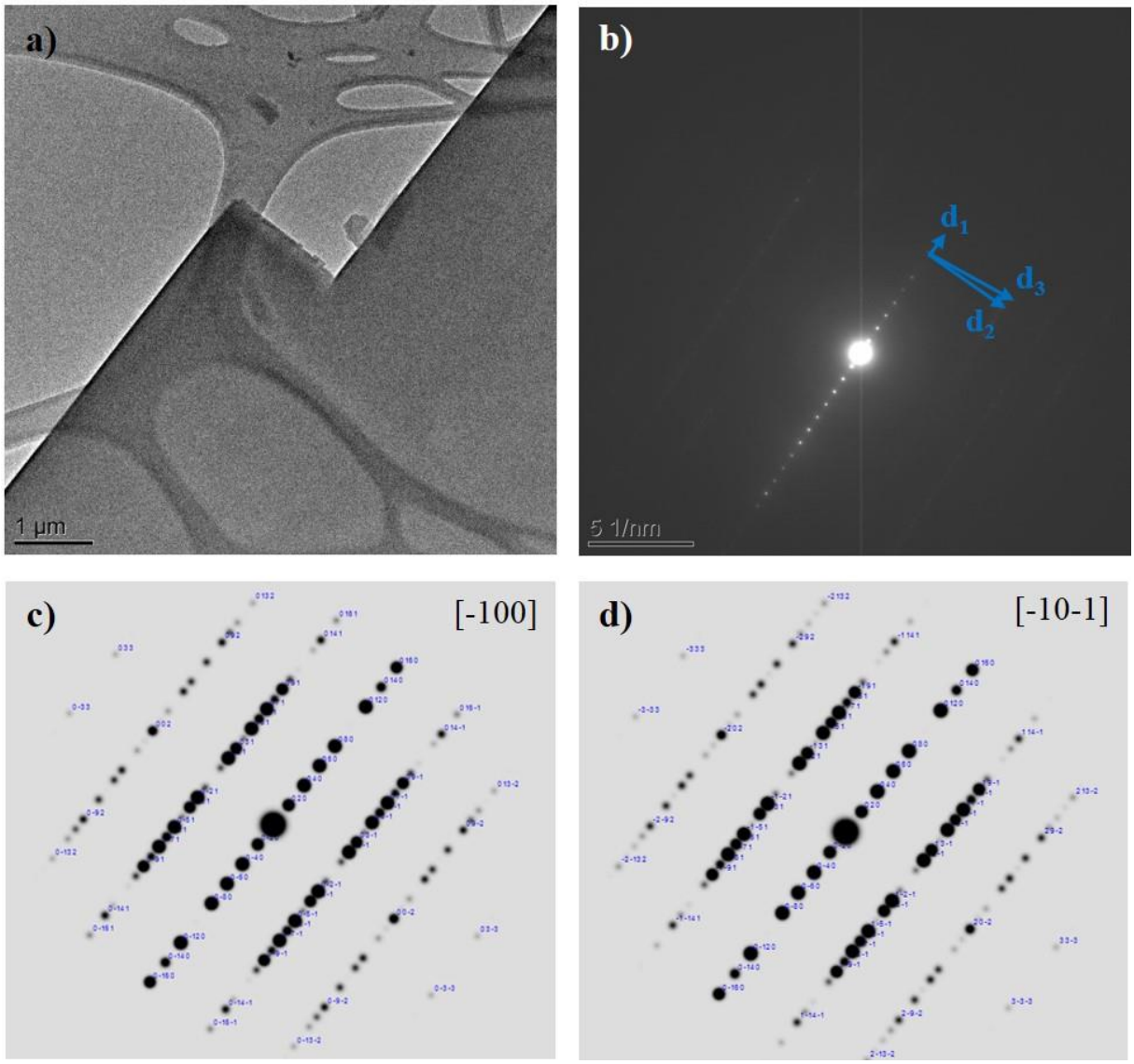

Figure 131 - Indexing of zone axis diffraction pattern of CBZ:2H_2O obtained from cryo-TEM experiments. *a)* Bright field image. *b)* Experimental zone axis electron diffraction pattern. *c)* Simulated electron diffraction pattern of the [100] zone axis from CSD structure FEFNOT02 (a=10.066, b=28.719 Å, c=4.831 Å, α=γ=90º, β=103.45º). *d)* Simulated electron diffraction pattern of the [101] zone axis from CSD structure FEFNOT02.

These results demonstrate that as temperature decreases, the movement of the molecules is also decreased and the lattice of CBZ:2H_2O remains stable in vacuum under cryogenic conditions. The opposite situation is characterized by an increase in molecular movement as thermal energy increases. This phenomenon expands the understanding of the destructive effect of vacuum on CBZ:2H_2O crystals that has been shown in Section 5.2. In this case, the strain caused by the combination of temperature and vacuum is suggested to overcome the fracture toughness of the material and to induce its dehydration (although crack formation and dehydration may not always be correlated).

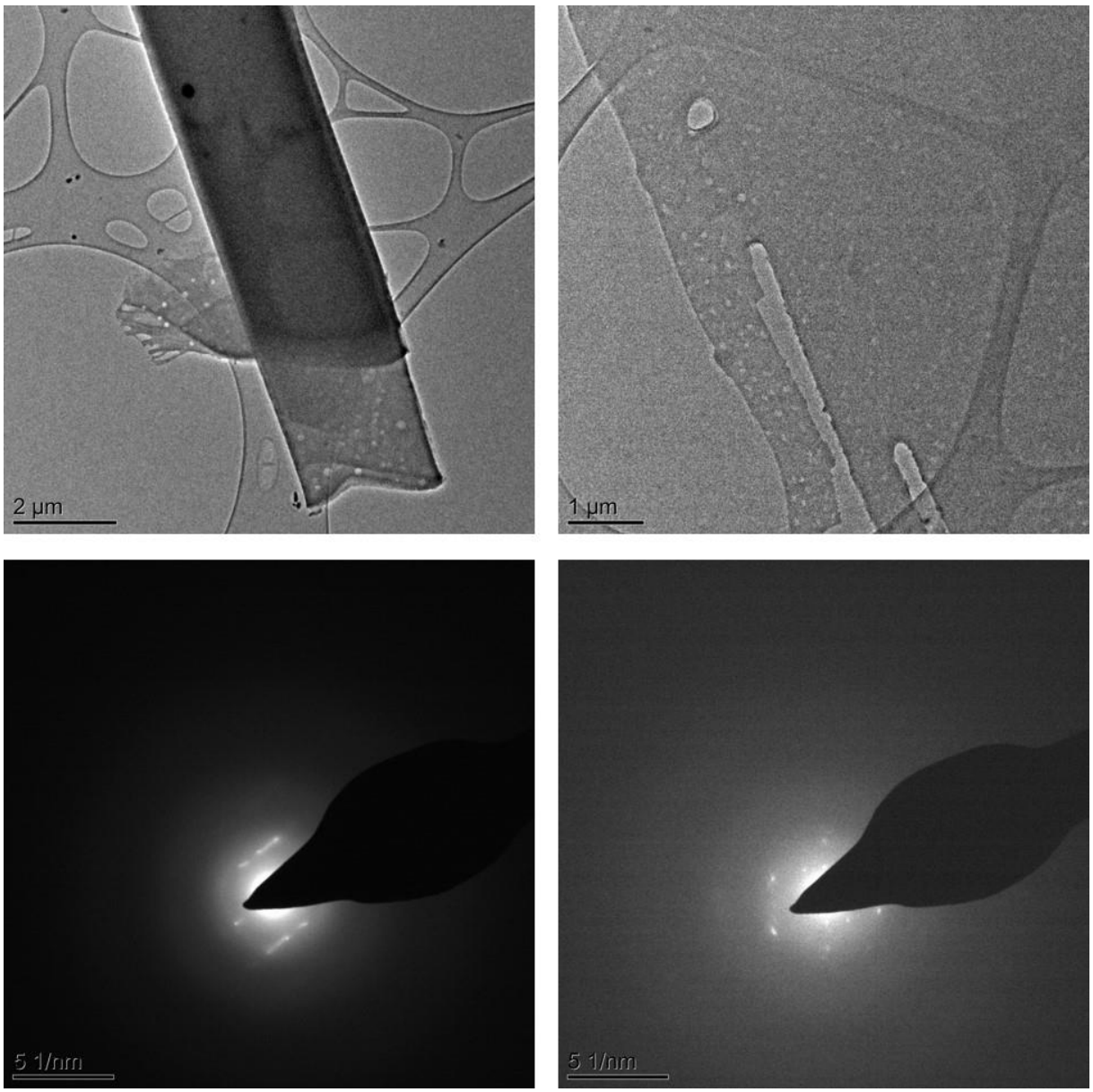

Figure 132 - TEM images and electron diffraction patterns of crystals of CBZ:2H_2O that were first frozen, stored under vacuum and then heated up.

5.3. The effect of temperature on the dehydration of CBZ:2H_2O

Crystals of CBZ:2H_2O turn opaque as a result of heating, while the original shape of the crystals is maintained. The micrographs obtained by hot stage microscopy show the crystals lose birefringence in the temperature range 50-90 ºC (Figure 133 and Figure 134). Regardless the differences in crystal size between (h00) and (0k0) samples, the (h00) crystals appear to become opaque at a slightly lower temperature than the (0k0) samples. The (0k0) crystals, in turn, show splitting along the needle axis and 'jumping crystals' before they lose birefringence. Above 140 ºC, both samples show whiskers growing on the surface of the crystals, which may be correlated to the growth of CBZ Form I. Melting occurs at approximately 190 ºC.

The formation of bubbles is observed when (h00) crystals immersed in silicon oil are heated, while the (0k0) crystals do not show a similar effect (Figure 135). When detected, the bubbles appear to originate from the central parts of the crystals, and not from the edges, perhaps demonstrating that the water does not leave the lattice only by moving along the crystal channels. Instead, the molecules may be released via alternative routes. Interestingly, the bubbles observed for (h00) crystals were only visible above 100 ^{o}C and continued until about 140 ^{o}C, which is far beyond the range of temperature corresponding to the birefringence loss (60-90 ^{o}C). This may suggest that dehydration of (h00) samples starts on the surface, while bulk water release starts at higher temperatures. The interpretation of these results, however, requires caution as the crystal-silicon interaction may affect the dehydration reaction. *In situ* PXRD with heating of (h00) samples immersed in oil have shown that, under these conditions, the dihydrate lattice changes above 90 ^{o}C (Figure 136). Instead, experiments performed in air have shown lattice changes above 70 ^{o}C.

The thermal analyses have shown that the experimental conditions influence the results and the TGA and the DSC curves vary considerably with sample size, heating rate and the specific configuration of the specimen crucible (*i.e.* open, closed or pinhole arrangement). To minimize kinetic effects on heat transfer, pressure and composition inside the crucible, the following experimental procedures were selected to the qualitative analyses of CBZ:2H_2O samples by TGA/DSC: a small sample size (~ 1 mg), open crucibles and low heating rates (1 ^{o}C.min^{-1}). Under these conditions, the analyses were sample-discriminative. Figure 137 illustrates the difference of the TGA curves of distinct dihydrate samples. While the (0k0) crystals show one single weight loss ending at about 65 ^{o}C, the (h00) crystals show a TGA curve with different slopes, resembling a two-step process finishing at approximately 90 ^{o}C. The same characteristic is observed in the DSC experiments. The (0k0) samples show one endothermic event followed by an exothermic event above 70 ^{o}C. CBZ:2H_2O (h00), in turn, displays two non-resolved endothermic events at higher temperatures and no visible exothermic event.

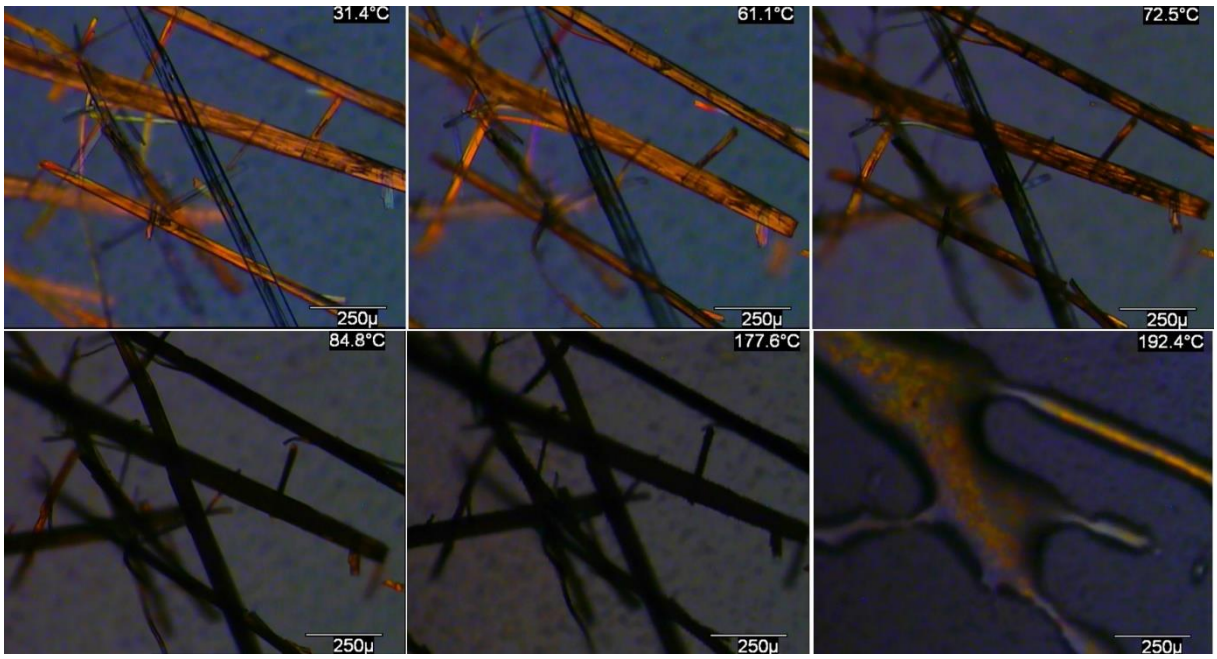

Figure 133 – Optical micrographs of CBZ:2H_2O sample (0k0) at different temperatures under polarized light (heating rate of 10 $^oC.min^{-1}$).

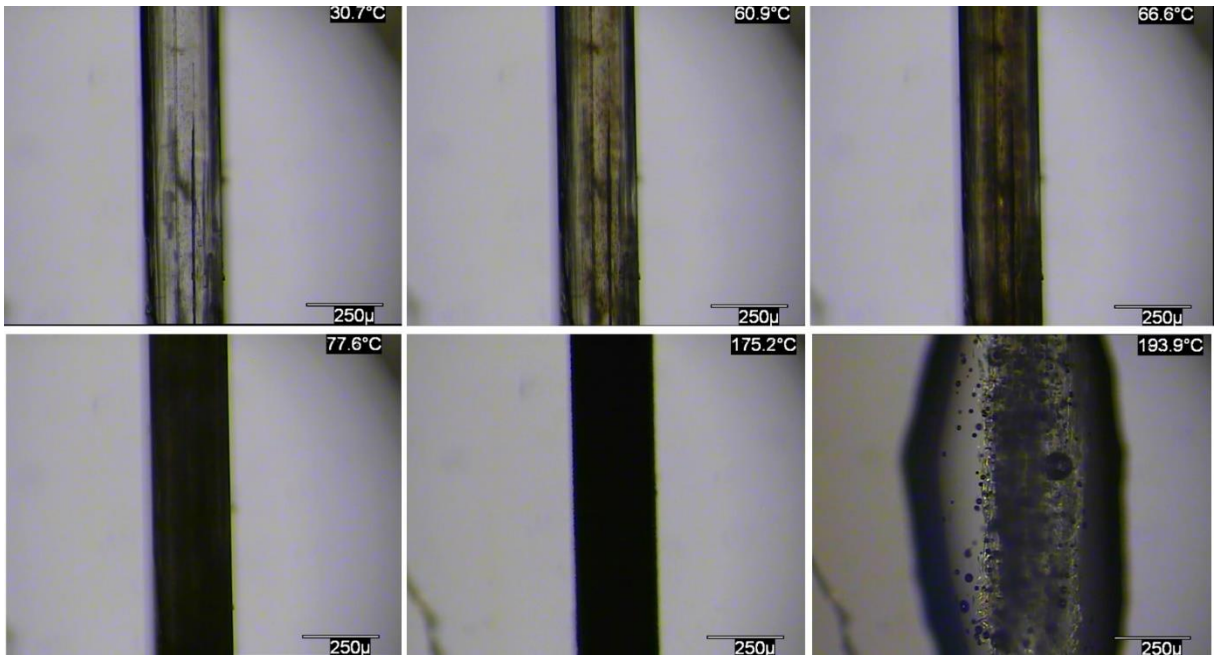

Figure 134 – Optical micrographs of CBZ:2H_2O sample (h00) at different temperatures under polarized light (heating rate of 10 $^oC.min^{-1}$).

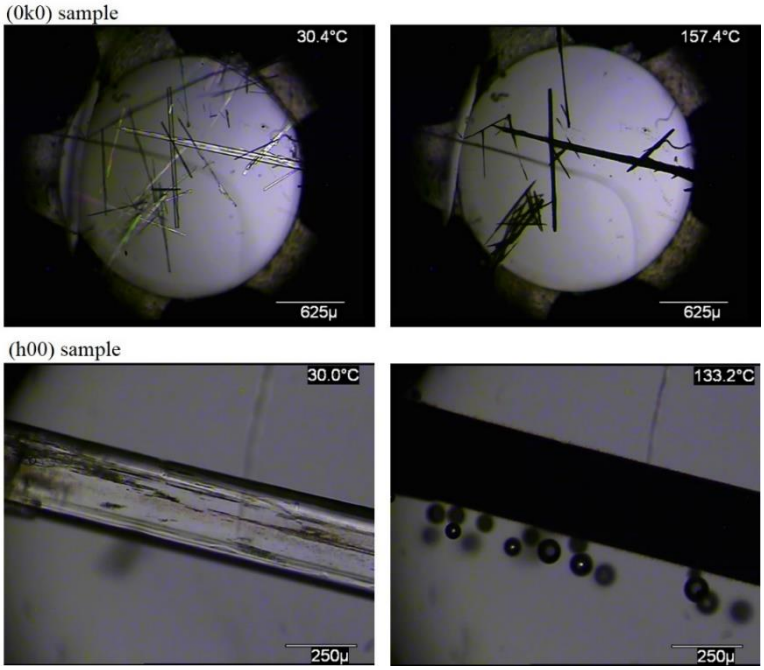

Figure 135 – Optical micrographs of CBZ:2H$_2$O samples (0k0) and (h00) immersed in silicon oil at different temperatures and under polarized light (heating rate of 10 ^{o}C.min^{-1}).

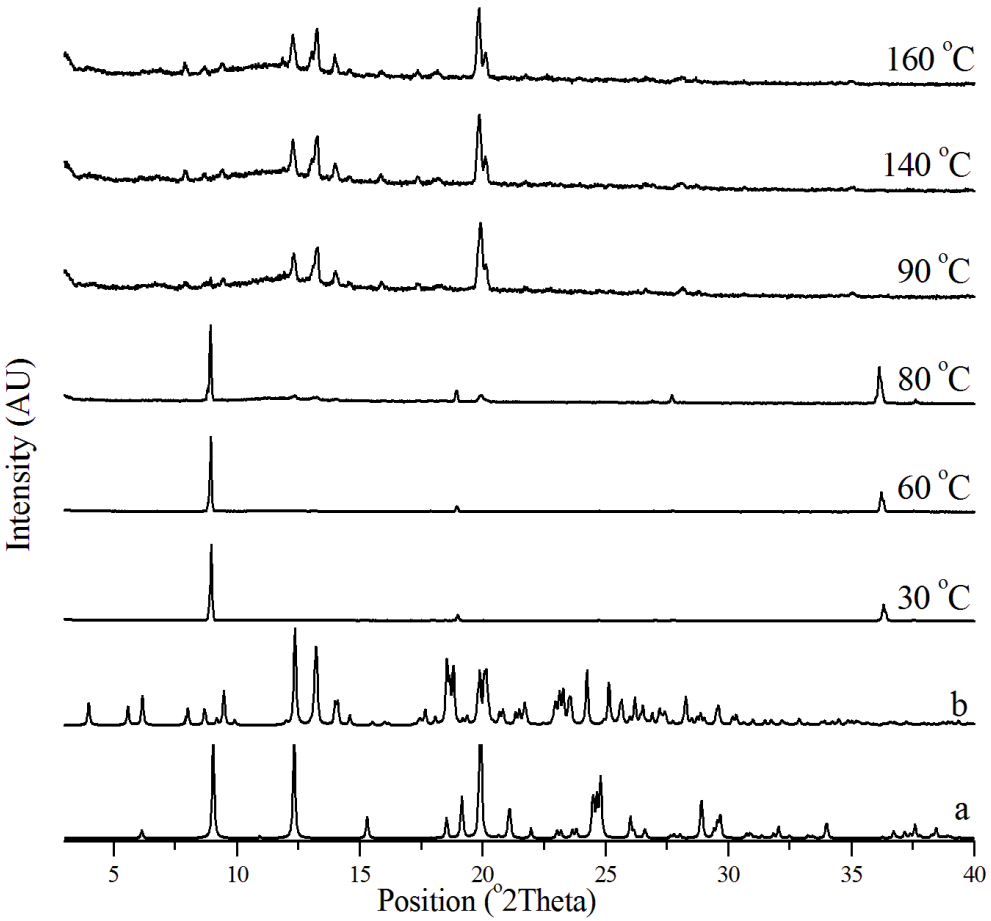

Figure 136 - *In situ* variable temperature PXRD patterns of CBZ:2H$_2$O sample (h00) in oil embedding (1 ^{o}C.min^{-1}, 30-180 ^{o}C). *a*: CBZ:2H$_2$O from FEFNOT. *b*: CBZ Form I from CBMZPN11.

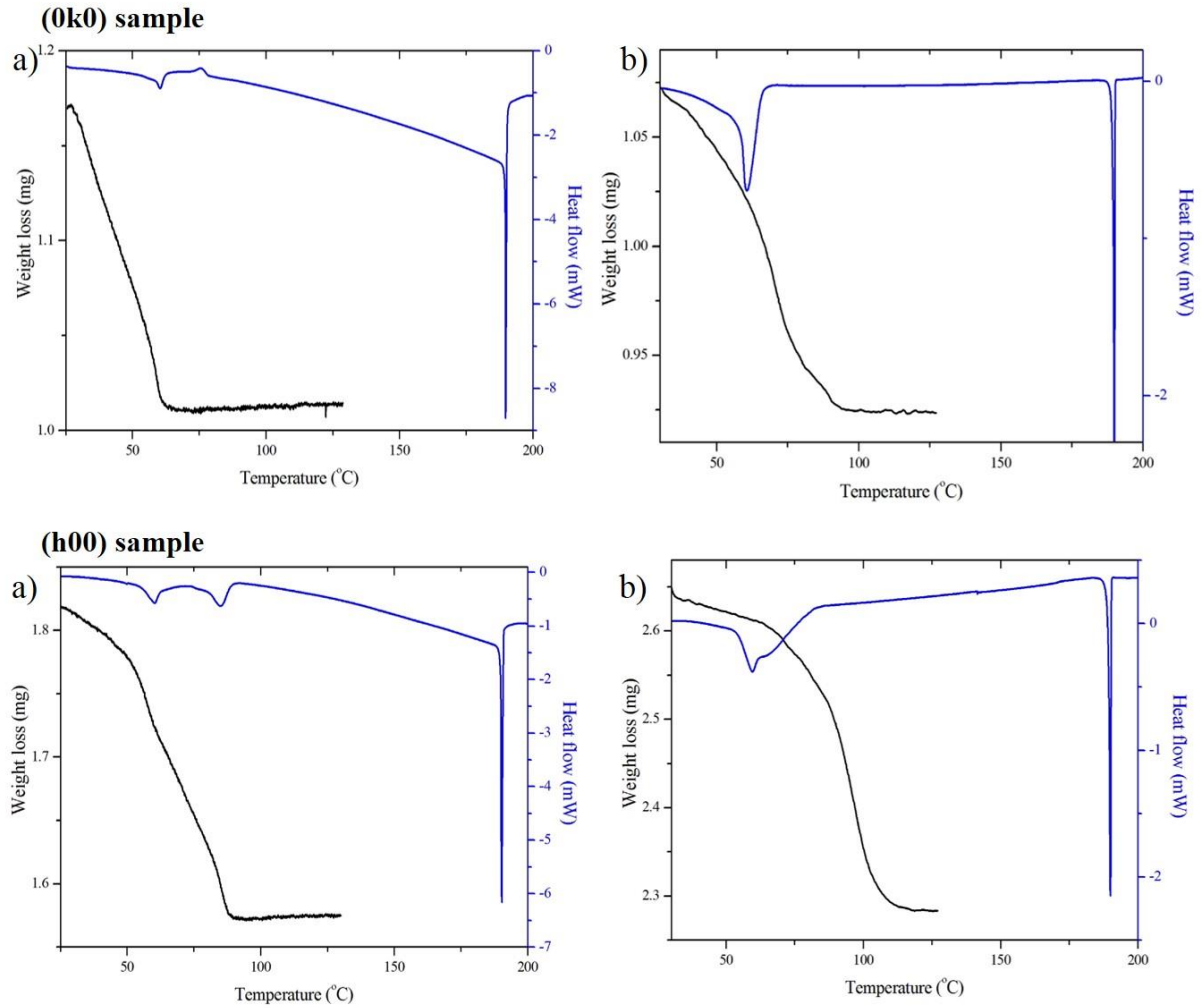

Figure 137 - DSC and TGA thermal characterization of CBZ:2H_2O samples (0k0) and (h00). *a:* open pan, 1 $^oC.min^{-1}$, N_2. *b:* perforated lid, 10 $^oC.min^{-1}$, N_2.

Associated *in situ* PXRD non-isothermal heating experiments showed that the dehydration of the (0k0) and (h00) samples results in the formation of CBZ polymorph I with poor crystallinity and amorphous character. Figure 138 and Figure 139 illustrate the results of experiments performed at 1 $^oC.min^{-1}$. For (0k0) samples, the patterns show some detectable peaks of CBZ Form I at 60 ^{o}C, with a clear phase transformation seen at 70 ^{o}C. This region approximately corresponds to the recrystallization event observed by DSC. The (h00) crystals show detectable peaks of Form I and complete phase transformation at 65 ^{o}C and 75 ^{o}C, respectively. These temperatures correspond to the intermediate region between the endothermic events observed during the dehydration by DSC.

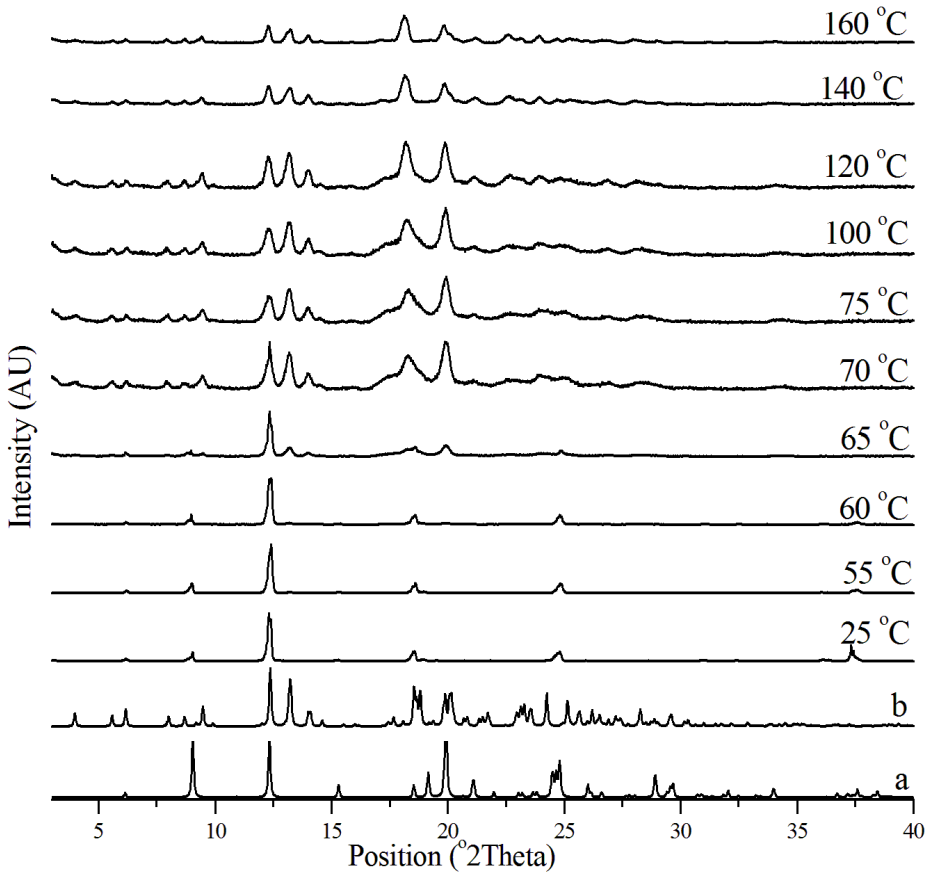

Figure 138 - *In situ* variable temperature PXRD patterns of CBZ:2H_2O (0k0) sample (1 °C.min^{-1}, 25-160 °C). *a*: CBZ:2H_2O from FEFNOT. *b*: CBZ Form I from CBMZPN11.

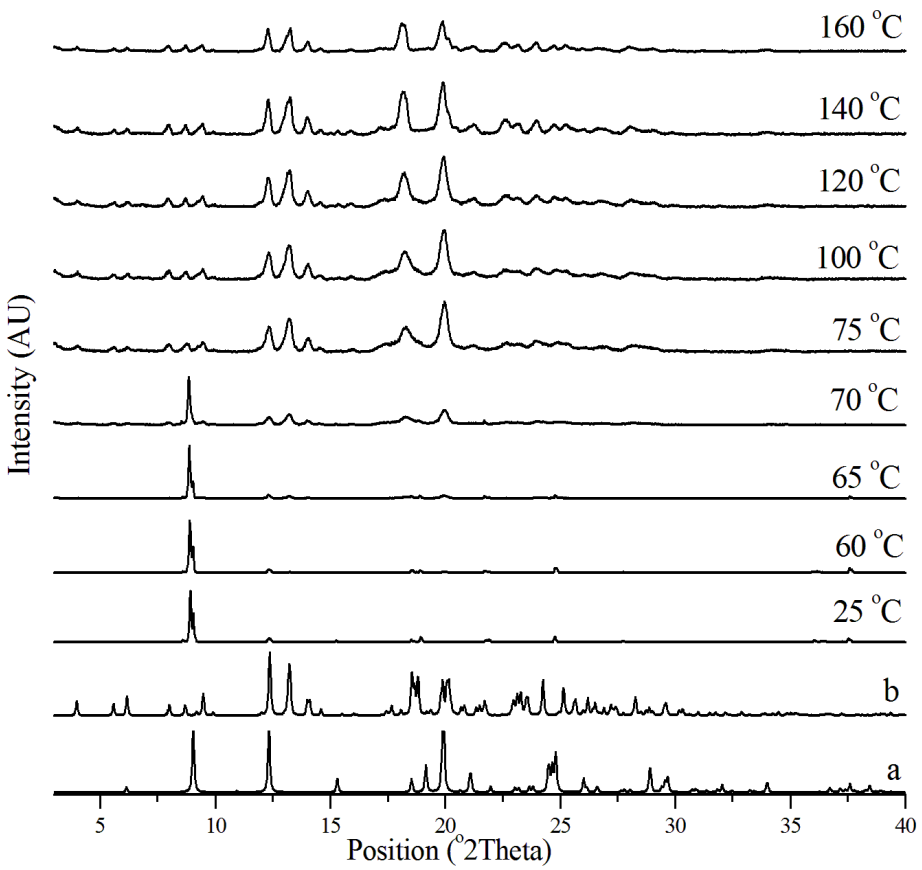

Figure 139 - *In situ* variable temperature PXRD patterns of CBZ:2H_2O (h00) sample (1 °C.min^{-1}, 25-160 °C). *a*: CBZ:2H_2O from FEFNOT. *b*: CBZ Form I from CBMZPN11.

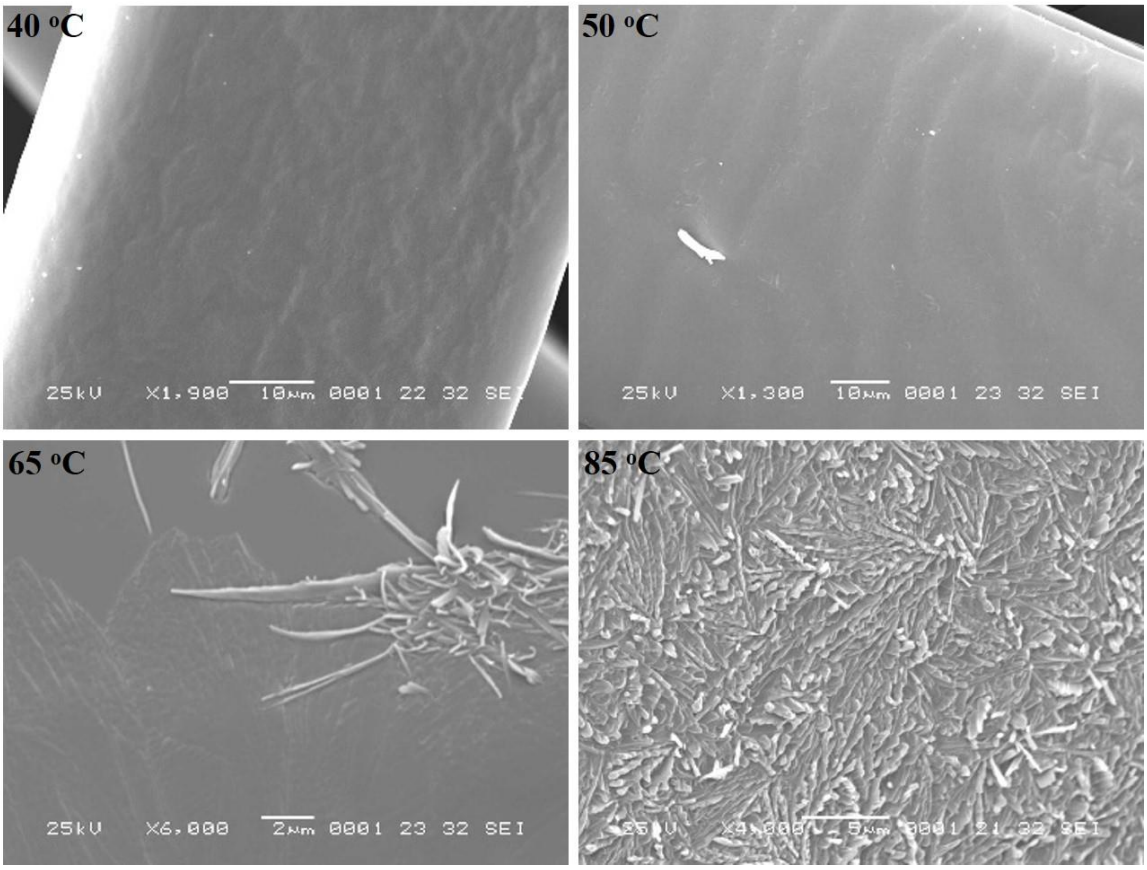

Figure 140 - SEM micrographs of CBZ:2H_2O (0k0) sample after heat treatment to different temperatures under N_2 (heating rate of 1 °C.min^{-1}).

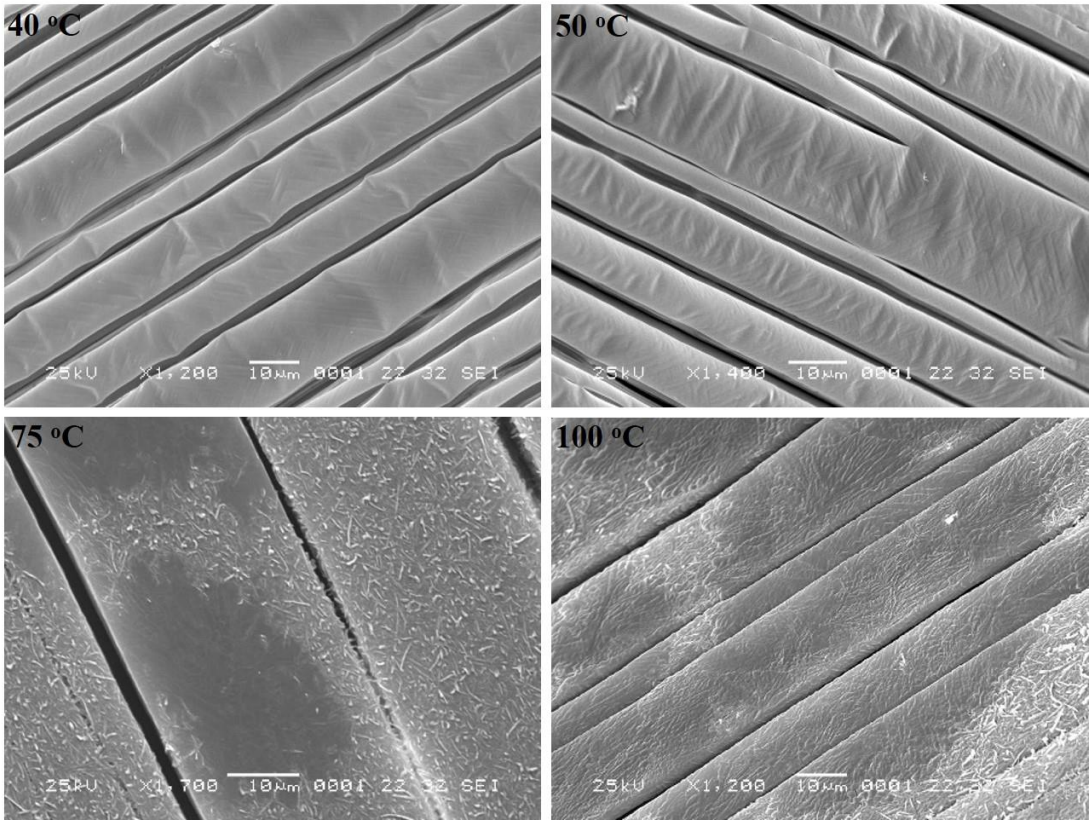

Figure 141 - SEM micrographs of CBZ:2H_2O (h00) sample after heat treatment to different temperatures under N_2 (heating rate of 1 °C.min^{-1}).

SEM analyses of (0k0) and (h00) samples subjected to thermal dehydration are shown in the Figure 140 and Figure 141. The images show that the first surface modification upon heating corresponds to an increase in roughness. Evidence of recrystallization (*i.e.* appearance of needle-like product) is observed at higher temperatures, at and above 65 ^{o}C and 75 ^{o}C for (0k0) and (h00) surfaces, respectively. The formation of diffusive domains/whiskers on (0k0) and (h00) surfaces are correlated to the surface reorganization into CBZ Form I.

Overall, the combined results show that water departure and recrystallization are concurrent processes in the (h00) samples, while (0k0) shows a first step of isomorphic dehydration followed by the formation of CBZ anhydrous Form I. This explains the shape of the TGA and DSC curves, especially for the (h00) sample. In this case, the "two-step" dehydration process seen in the thermal analyses is related to the effect of simultaneous exothermic and endothermic events on the heat flow response measured by the equipment.

5.4. The effect of humidity on the dehydration of CBZ:2H_2O

In order to explore the effect of humidity on the dehydration of CBZ:2H_2O (0k0) and (h00) crystals, samples were stored under different humidity and temperature conditions. Figure 142 to Figure 147 show how dehydration evolves over time at 0% RH and 22, 30 or 40 ^{o}C. Although the samples were ground in preparation for PXRD analyses, the patterns still showed evidence of preferred orientation. For this reason, the intensity decay of the peaks will not be evaluated further. The combination of TGA and PXRD measurements of the samples, however, shows that the crystal lattice changes only after removal of a considerable amount of water and dehydration results in the formation of CBZ polymorph IV (with minor amounts of polymorph I).

The formation of CBZ Form IV as a major component from the dehydration of (0k0) and (h00) samples, however, was not reproducible. Replication of the experiment at 0% RH and 40 ^{o}C resulted in CBZ Form I in both samples analysed (Figure 148 and Figure 149). It is proposed that small quantities of humidity may have affected the outcome of the dehydration process. In fact, isothermal dehydration experiments performed in environments containing water vapour resulted in pure CBZ Form I. Figure 150 and Figure 151 show how dehydration evolves over time at 11% RH and 30 ^{o}C. In comparison to the CBZ polymorph IV formed by dehydration, the dehydrated material that results in CBZ Form I show broader reflections with low intensity and the presence of an amorphous halo. These results suggest a difference in crystallinity and crystallite size between the two materials, which may indicate that the mechanism of formation of CBZ anhydrous polymorphs from CBZ:2H_2O changes in the presence of water.

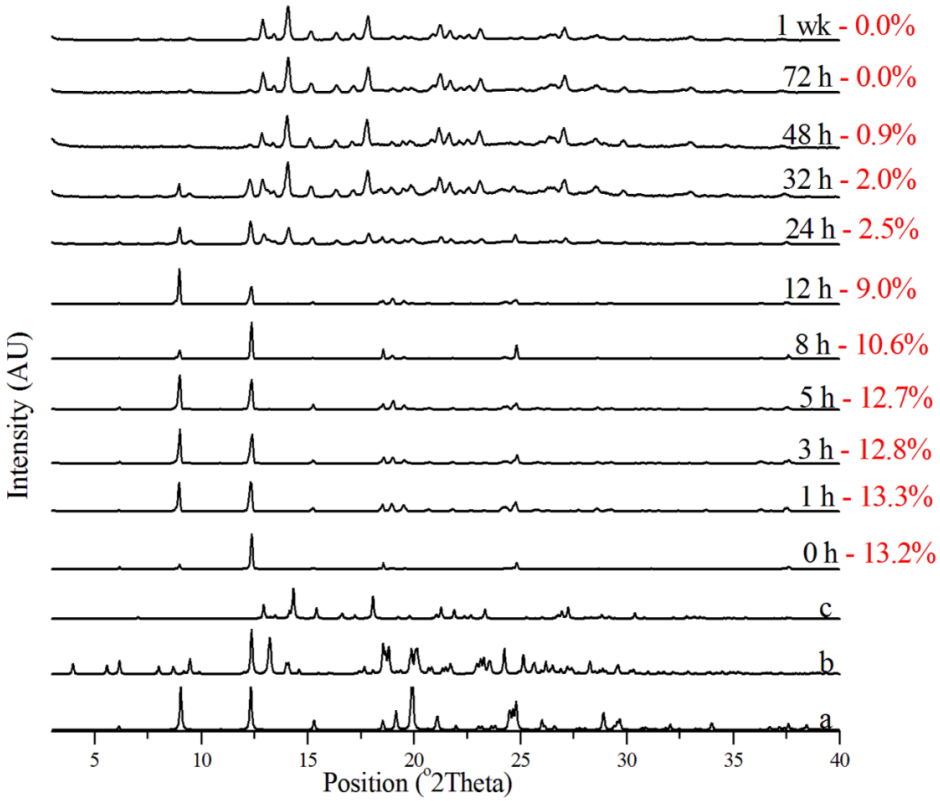

Figure 142 - *Ex situ* analyses of CBZ:2H$_2$O (0k0) sample stored at 22 ºC and 0% RH over time. The graphs correspond to the PXRD patterns and the respective water content was determined by TGA. The starting material show significant preferred orientation. *a*: CBZ:2H$_2$O from FEFNOT. *b*: CBZ Form I from CBMZPN11. *c*: CBZ Form IV from CBMZPN12.

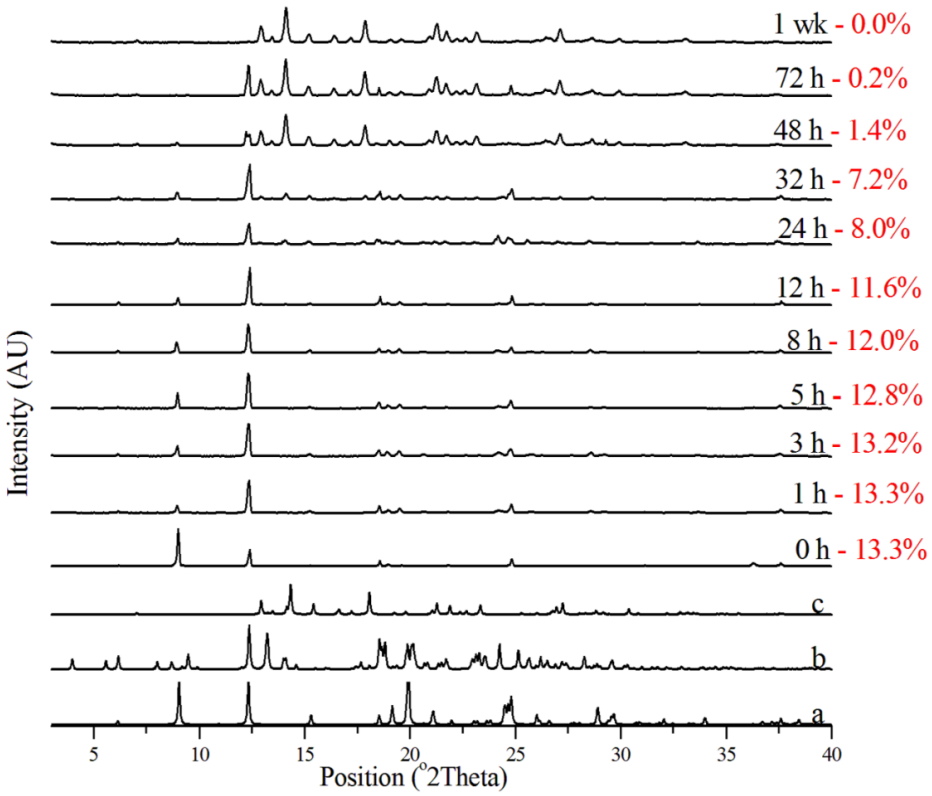

Figure 143 - *Ex situ* analyses of CBZ:2H$_2$O (h00) sample stored at 22 ºC and 0% RH over time. The graphs correspond to the PXRD patterns and the respective water content was determined by TGA. The starting material show significant preferred orientation. *a*: CBZ:2H$_2$O from FEFNOT. *b*: CBZ Form I from CBMZPN11. *c*: CBZ Form IV from CBMZPN12.

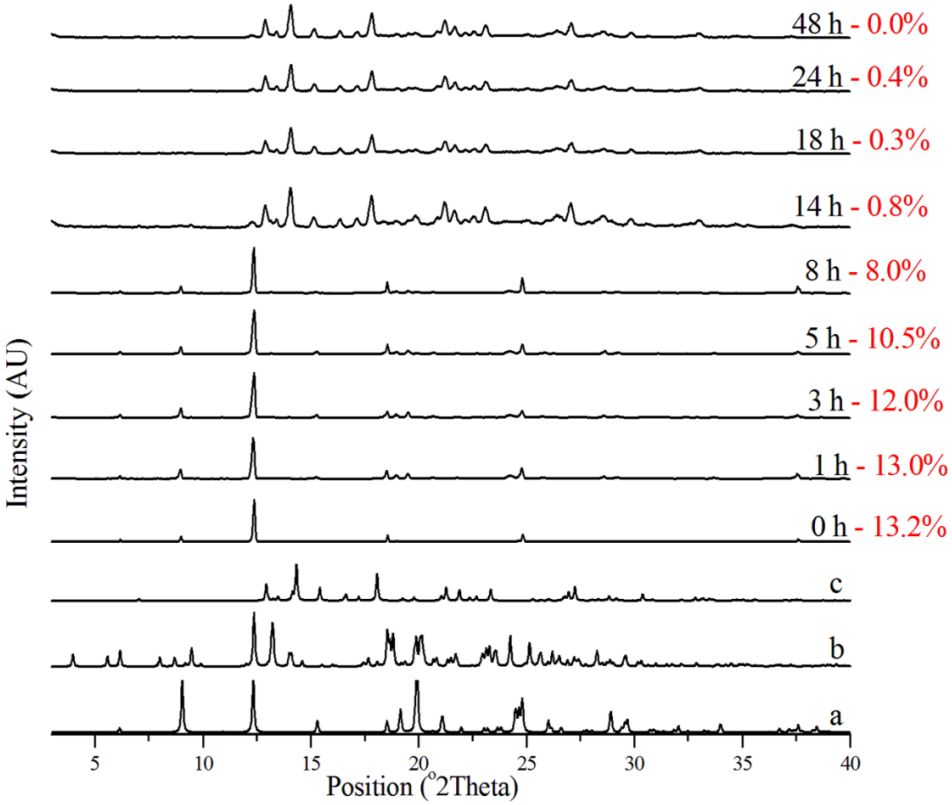

Figure 144 - *Ex situ* analyses of CBZ:2H_2O (0k0) sample stored at 30 ºC and 0% RH over time. The graphs correspond to the PXRD patterns and the respective water content was determined by TGA. *a*: CBZ:2H_2O from FEFNOT. *b*: CBZ Form I from CBMZPN11. *c*: CBZ Form IV from CBMZPN12.

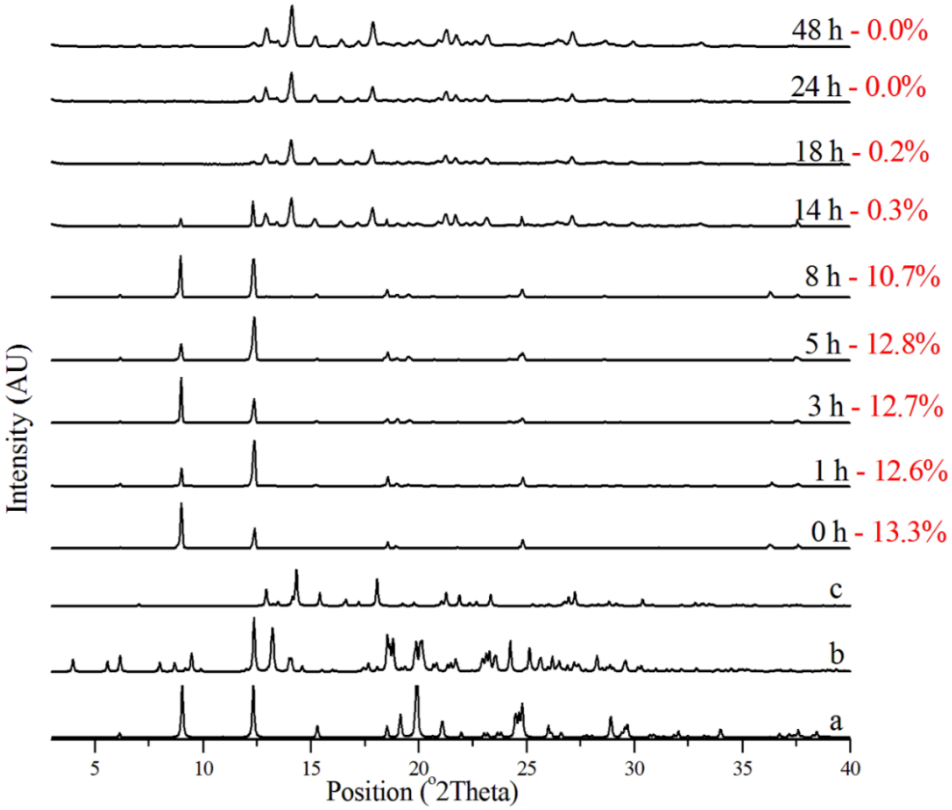

Figure 145 - *Ex situ* analyses of CBZ:2H_2O (h00) sample stored at 30 ºC and 0% RH over time. The graphs correspond to the PXRD patterns and the respective water content was determined by TGA. *a*: CBZ:2H_2O from FEFNOT. *b*: CBZ Form I from CBMZPN11. *c*: CBZ Form IV from CBMZPN12.

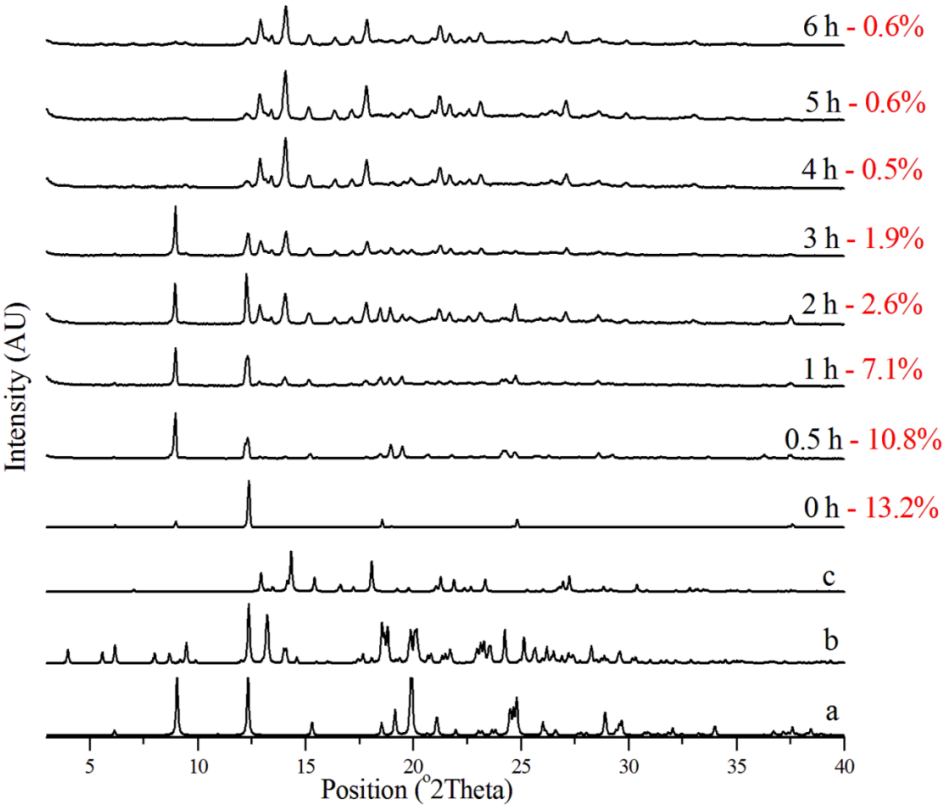

Figure 146 - *Ex situ* analyses of CBZ:2H$_2$O (0k0) sample stored at 40 ºC and 0% RH over time. The graphs correspond to the PXRD patterns and the respective water content was determined by TGA. *a*: CBZ:2H$_2$O from FEFNOT. *b*: CBZ Form I from CBMZPN11. *c*: CBZ Form IV from CBMZPN12.

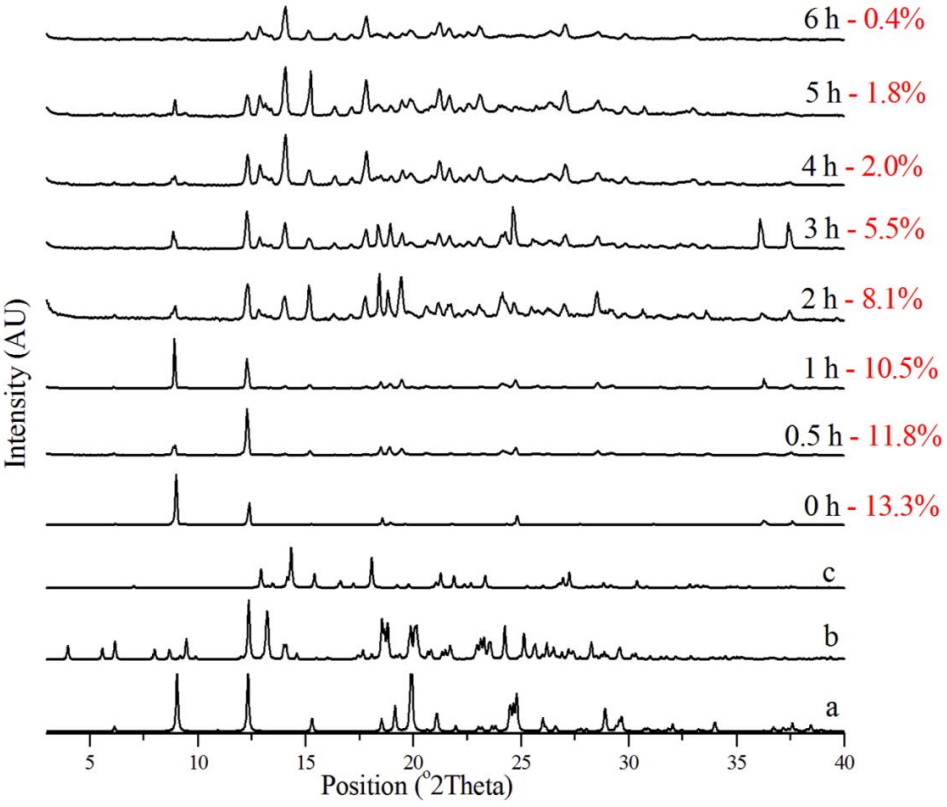

Figure 147 - *Ex situ* analyses of CBZ:2H$_2$O (h00) sample stored at 40 ºC and 0% RH over time. The graphs correspond to the PXRD patterns and the respective water content was determined by TGA. *a*: CBZ:2H$_2$O from FEFNOT. *b*: CBZ Form I from CBMZPN11. *c*: CBZ Form IV from CBMZPN12.

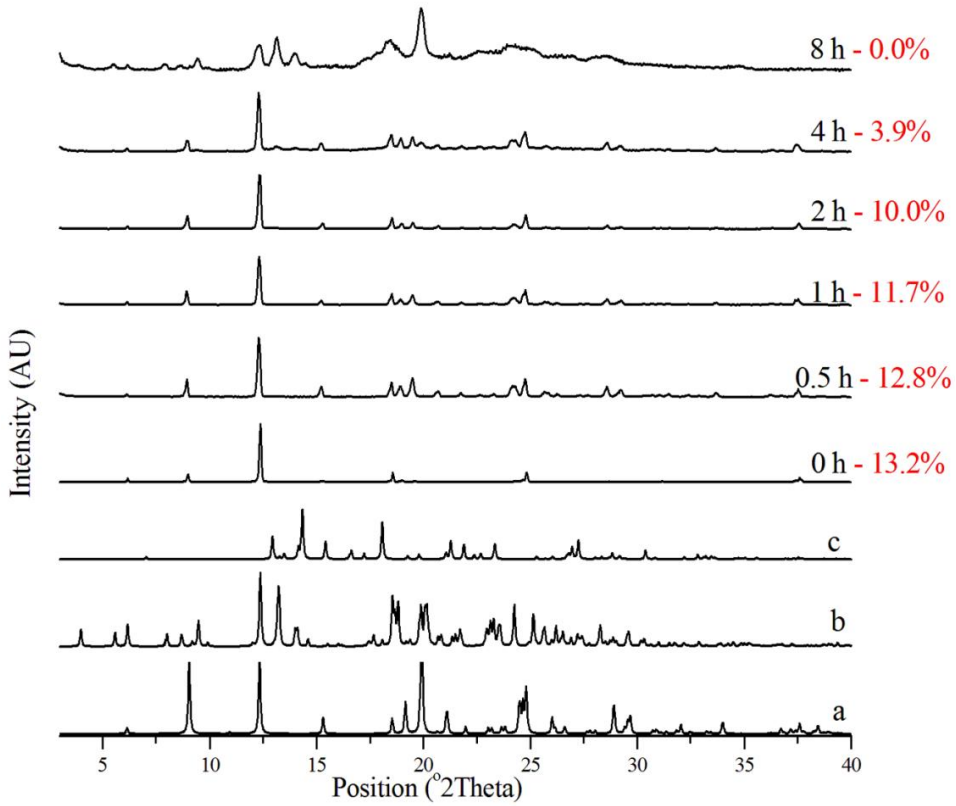

Figure 148 - Replicate of *ex situ* analyses of CBZ:2H$_2$O (0k0) sample stored at 40 ºC and 0% RH over time. The graphs correspond to the PXRD patterns and the respective water content was determined by TGA. *a*: CBZ:2H$_2$O from FEFNOT. *b*: CBZ Form I from CBMZPN11. *c*: CBZ Form IV from CBMZPN12.

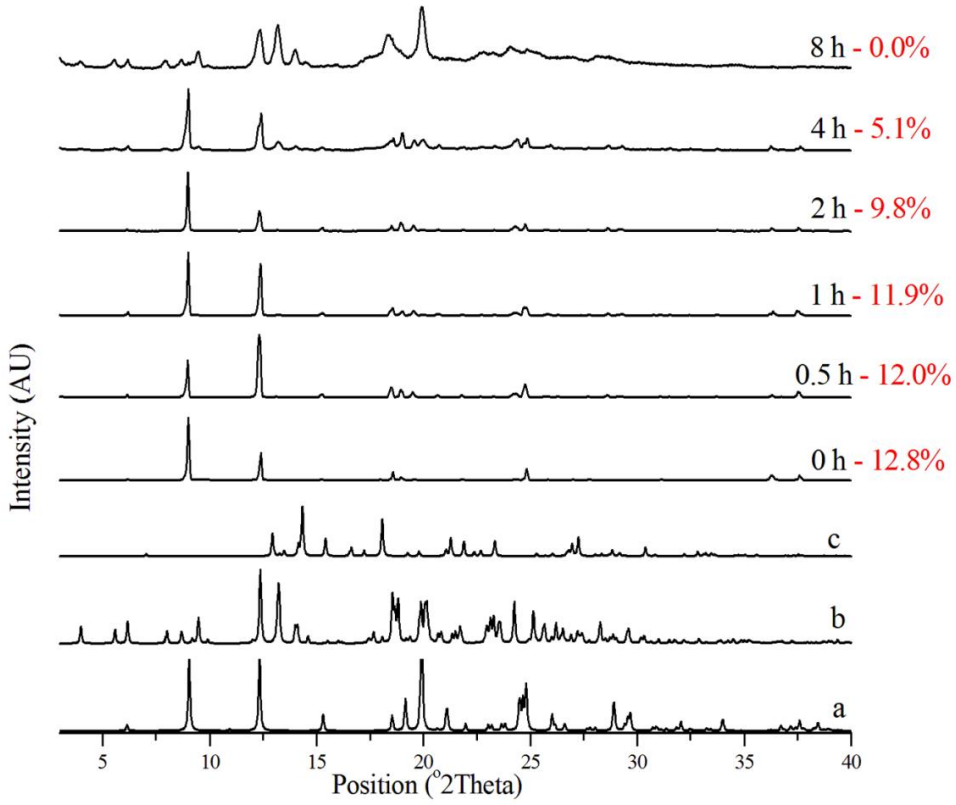

Figure 149 - Replicate of *ex situ* analyses of CBZ:2H$_2$O (h00) sample stored at 40 ºC and 0% RH over time. The graphs correspond to the PXRD patterns and the respective water content was determined by TGA. *a*: CBZ:2H$_2$O from FEFNOT. *b*: CBZ Form I from CBMZPN11. *c*: CBZ Form IV from CBMZPN12.

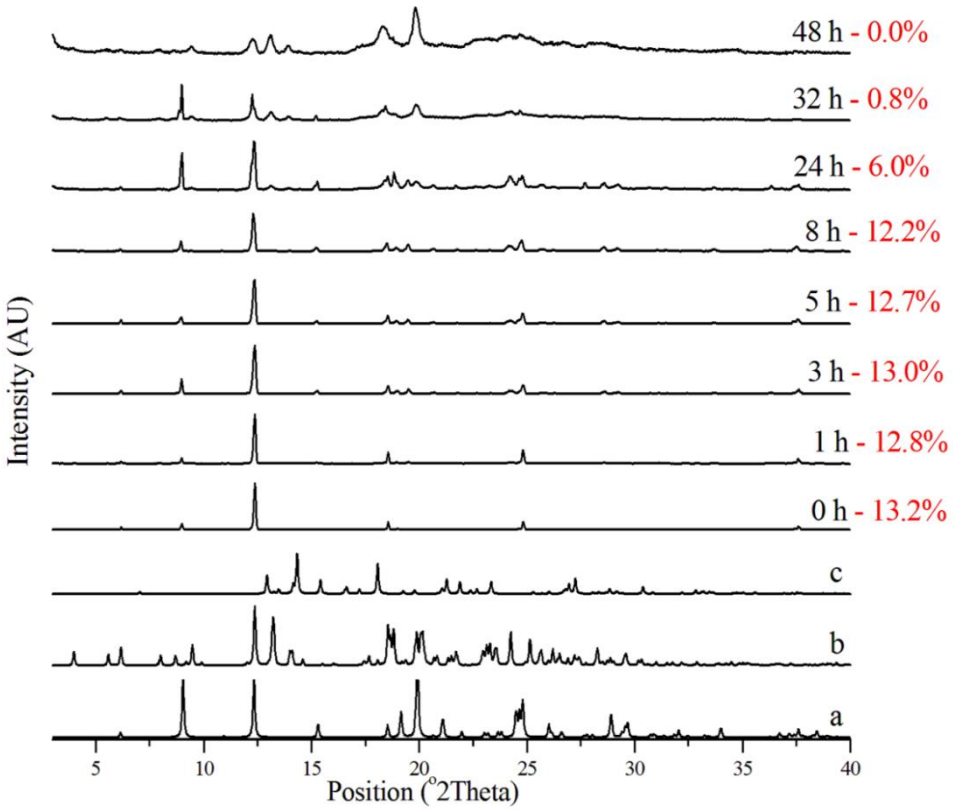

Figure 150 - *Ex situ* analyses of CBZ:2H_2O (0k0) sample stored at 30 ºC and 11% RH over time. The graphs correspond to the PXRD patterns and the respective water content was determined by TGA. *a*: CBZ:2H_2O from FEFNOT. *b*: CBZ Form I from CBMZPN11. *c*: CBZ Form IV from CBMZPN12.

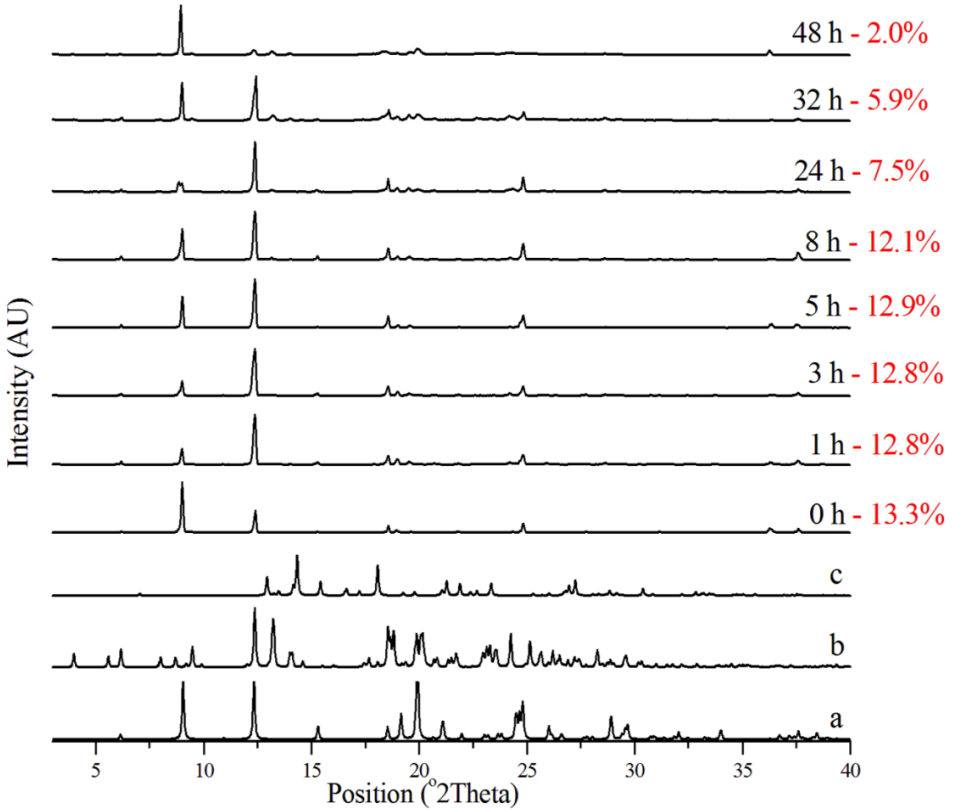

Figure 151 - *Ex situ* analyses of CBZ:2H_2O (h00) sample stored at 30 ºC and 11% RH over time. The graphs correspond to the PXRD patterns and the respective water content was determined by TGA. *a*: CBZ:2H_2O from FEFNOT. *b*: CBZ Form I from CBMZPN11. *c*: CBZ Form IV from CBMZPN12.

The (0k0) and (h00) dehydrated surfaces of samples treated isothermally at 40 ºC and 0% humidity are shown in Figure 152. The images represent samples that resulted in CBZ Form IV and Form I as major components (shown in Figure 146 to Figure 149). While the general morphology of the needle crystal is maintained, the dehydrated samples (characterized as CBZ Form IV) show round domains on the surfaces. A few whiskers have been observed and the (0k0) surface also shows texture. The dehydrated samples identified as CBZ polymorph I, in turn, show surfaces covered with whiskers.

The imaging of the CBZ:2H_2O surfaces at different stages of dehydration prior to the complete formation of CBZ anhydrous Form IV shows more details about the structural reorganization in the samples (Figure 153 and Figure 154). The (h00) surfaces do not change considerably over time, which may suggest that dehydration starts on the surface and no further surface structural rearrangement takes place as the bulk dehydration proceeds. The early stages of the dehydration, by comparison, result in cracks on the (0k0) surface. These cracks are related to the needle axis by an angle of 41.5±2.0º, as reported by Kachrimanis & Griesser.[162]

In the case of samples dehydrated at 40 ºC and 0% humidity which resulted in CBZ Form I the results show the progressive formation of domains oriented along the needle axis and whiskers forming across the (0k0) surface (Figure 155 and Figure 156). The whiskers of CBZ Form I are mainly formed from regions containing the newly formed domains, small cracks and holes. It is also evident from the imaging of (h00) samples that the whiskers of polymorph I originate from areas showing cracks and holes. It is noteworthy that initial stages of dehydration result in deformed areas that are crystallographically oriented. These areas contain holes aligned in such a way to suggest they would eventually form a crack. In the case of the (0k0) surfaces, the small holes are aligned to the *a* axis, corresponding to the (00l) planes crosscutting the needle. The (h00) surface, in turn, shows small holes aligned with the intersecting texture that has been previously described. It demonstrates that the initial molecular movements promoted during dehydration into Form I result in tensile forces along the needle axis, which affect differently the different crystal surfaces of CBZ:2H_2O.

Figure 157 shows the AFM analyses of the samples dehydrated at 40 ºC and 0% RH that resulted in polymorph I. It shows the disruption of the steps observed in the fresh samples and the formation of small domains. The (h00) surface shows cracks and a significant texture, while the (0k0) surface shows less oriented domains. The defects formed are very similar to the defects observed after the dehydration experiments performed under vacuum (Section 5.2).

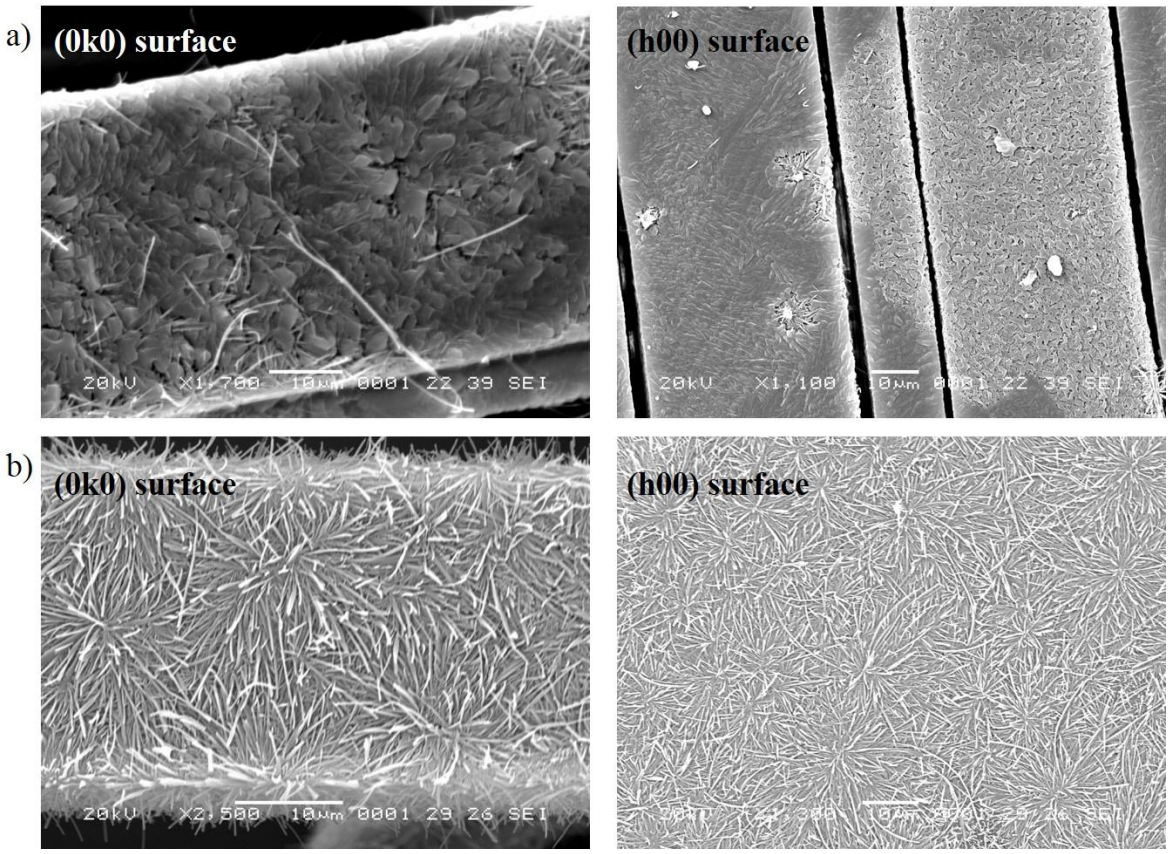

Figure 152 - SEM micrographs of CBZ:2H_2O surfaces stored at 40 ºC and 0% RH. Although the preparation of the samples was, in theory, the same, the outcome of the dehydration was different. *a*: product characterized as CBZ polymorph IV. *b*: product characterized as CBZ polymorph I.

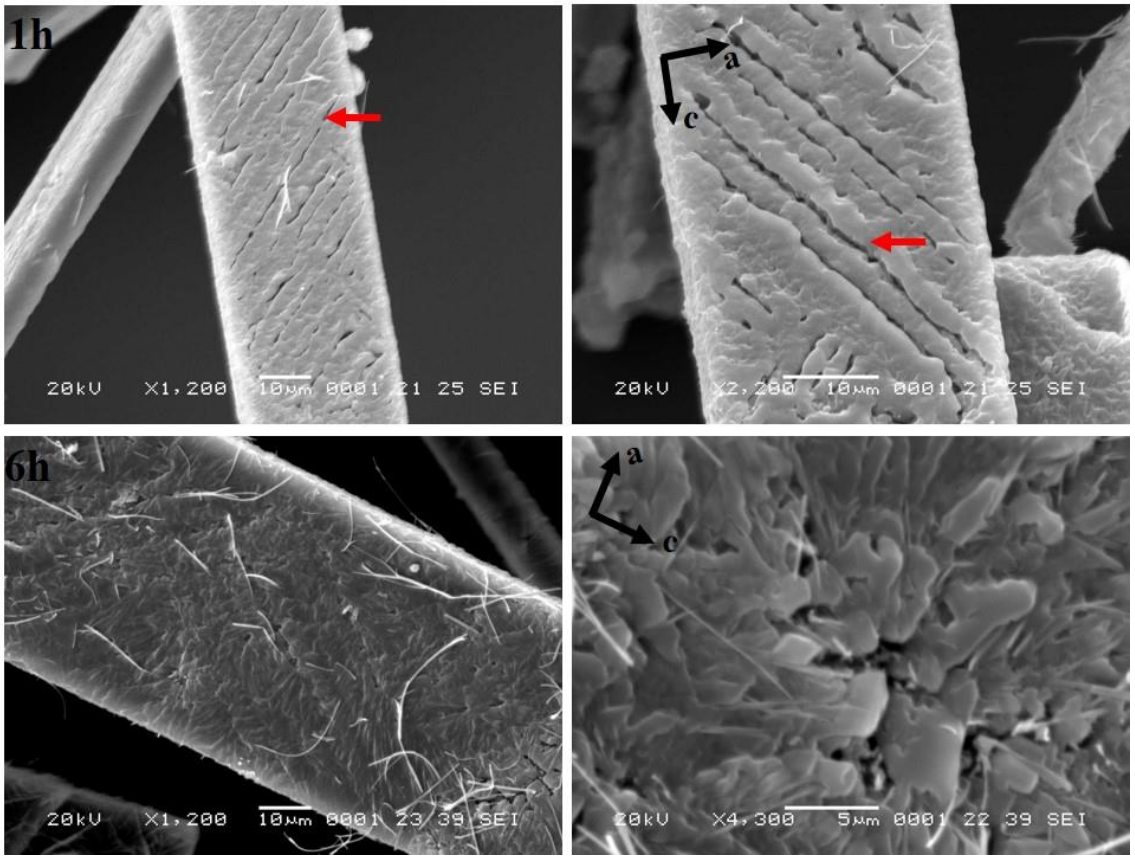

Figure 153 - *Ex situ* SEM analyses of CBZ:2H_2O (0k0) sample stored at 40 ºC and 0% RH over time. The dehydration product was characterized as CBZ polymorph IV. The red arrows indicate cracks.

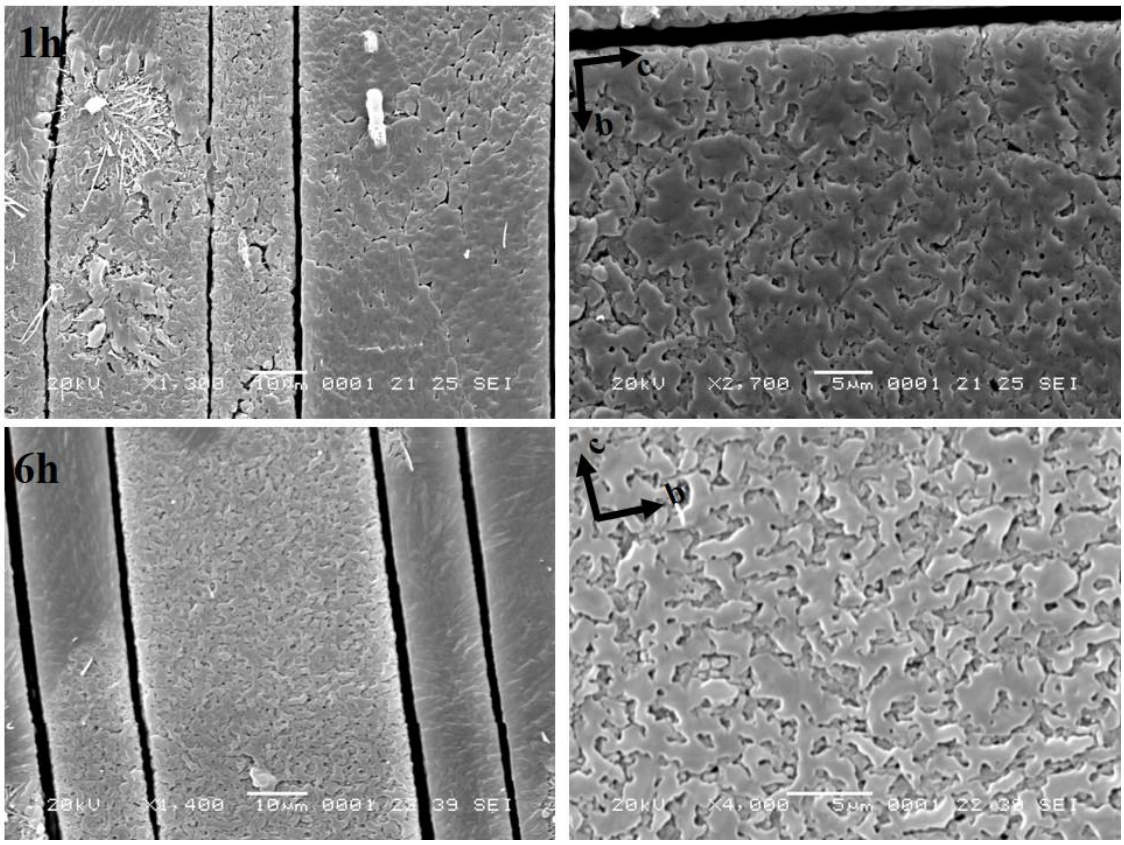

Figure 154 - *Ex situ* SEM analyses of CBZ:2H_2O (h00) sample stored at 40 ºC and 0% RH over time. The dehydration product was characterized as CBZ polymorph IV.

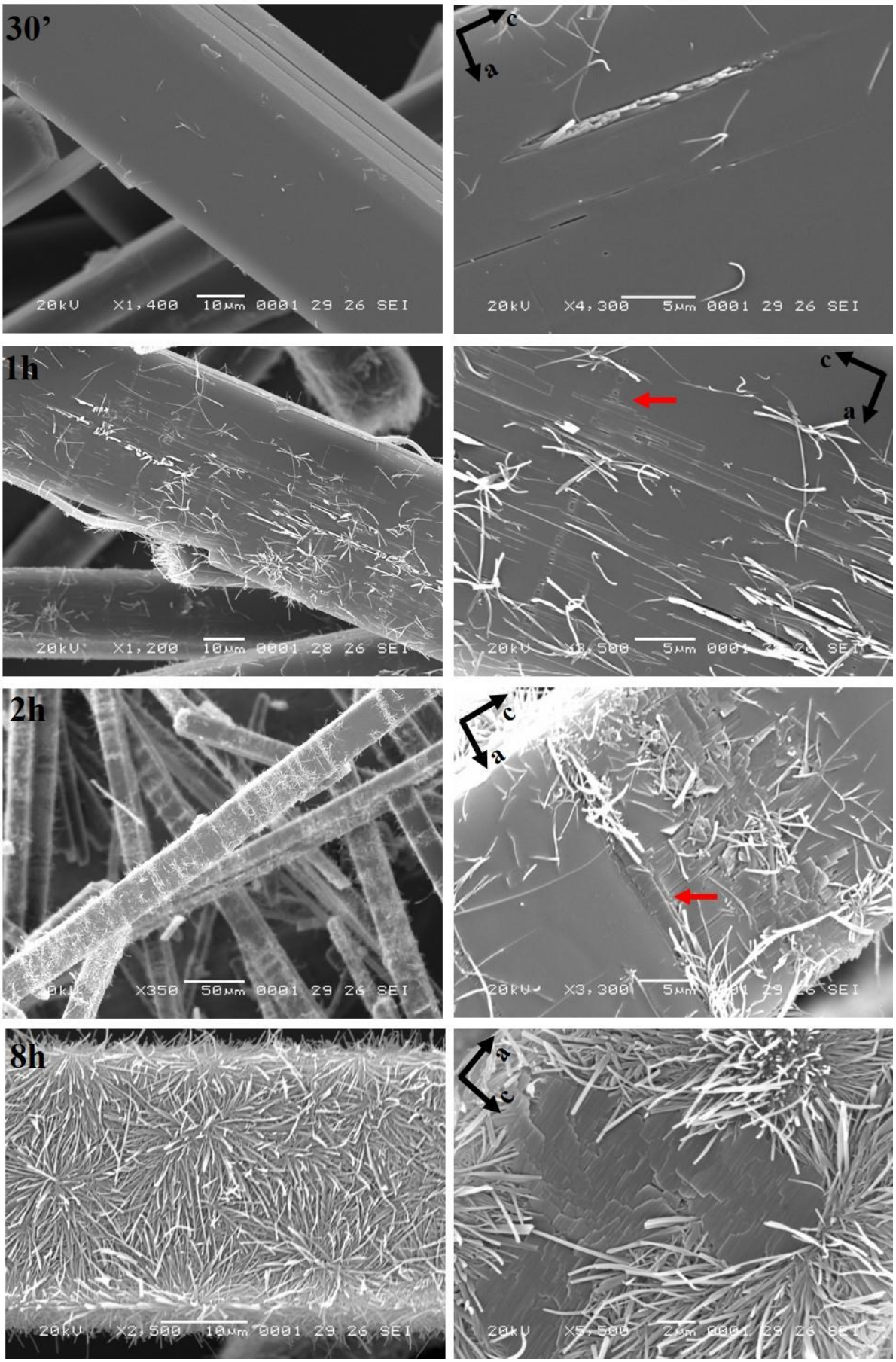

Figure 155 - *Ex situ* SEM analyses of CBZ:2H_2O (0k0) sample stored at 40 ºC and 0% RH over time. The dehydration product was characterized as CBZ polymorph I. The red arrows indicate crystallographically oriented defects.

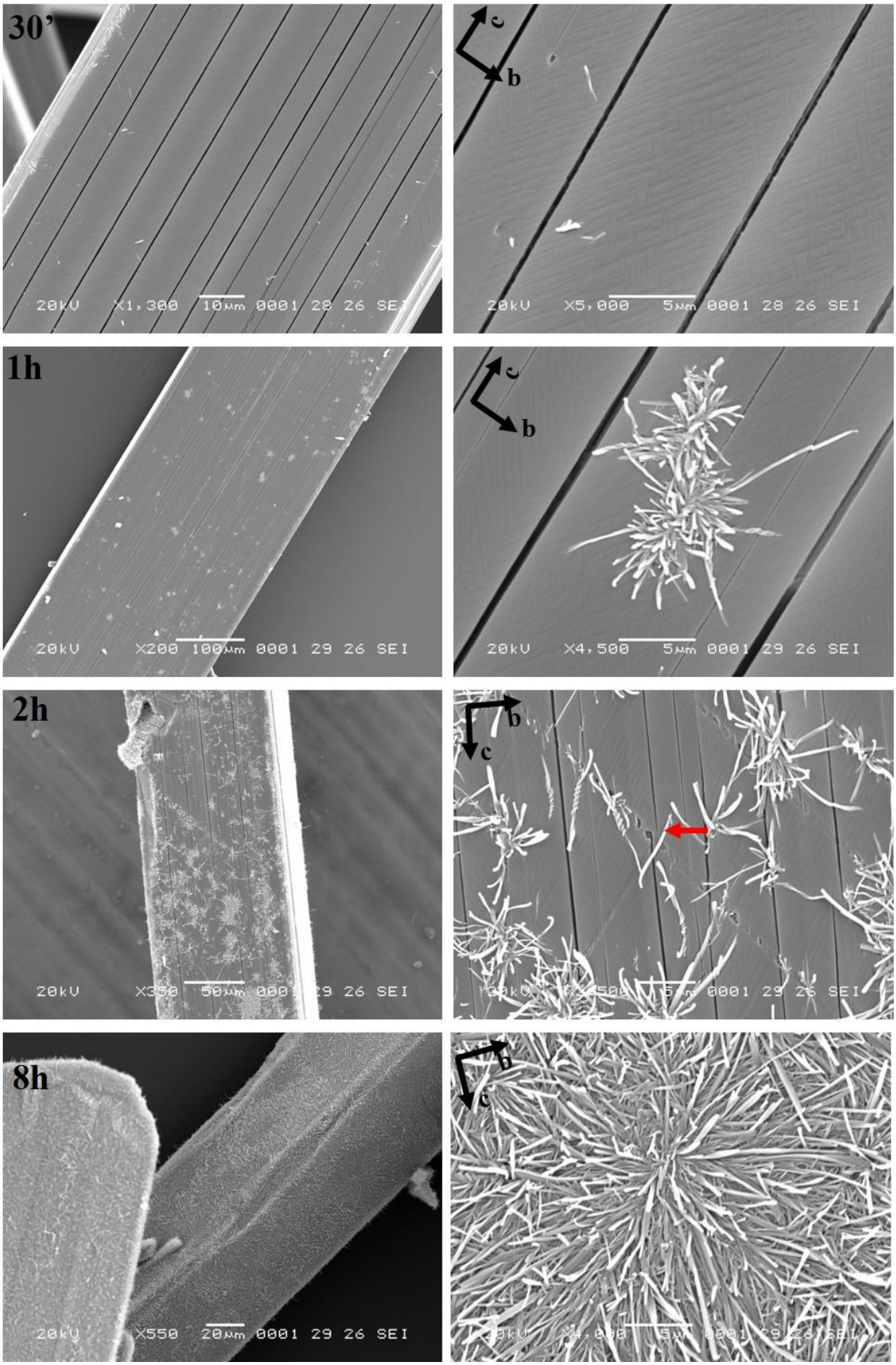

Figure 156 - *Ex situ* SEM analyses of CBZ:2H_2O (h00) sample stored at 40 ºC and 0% RH over time. The dehydration product was characterized as CBZ polymorph I. The red arrow indicate crystallographycally oriented defects.

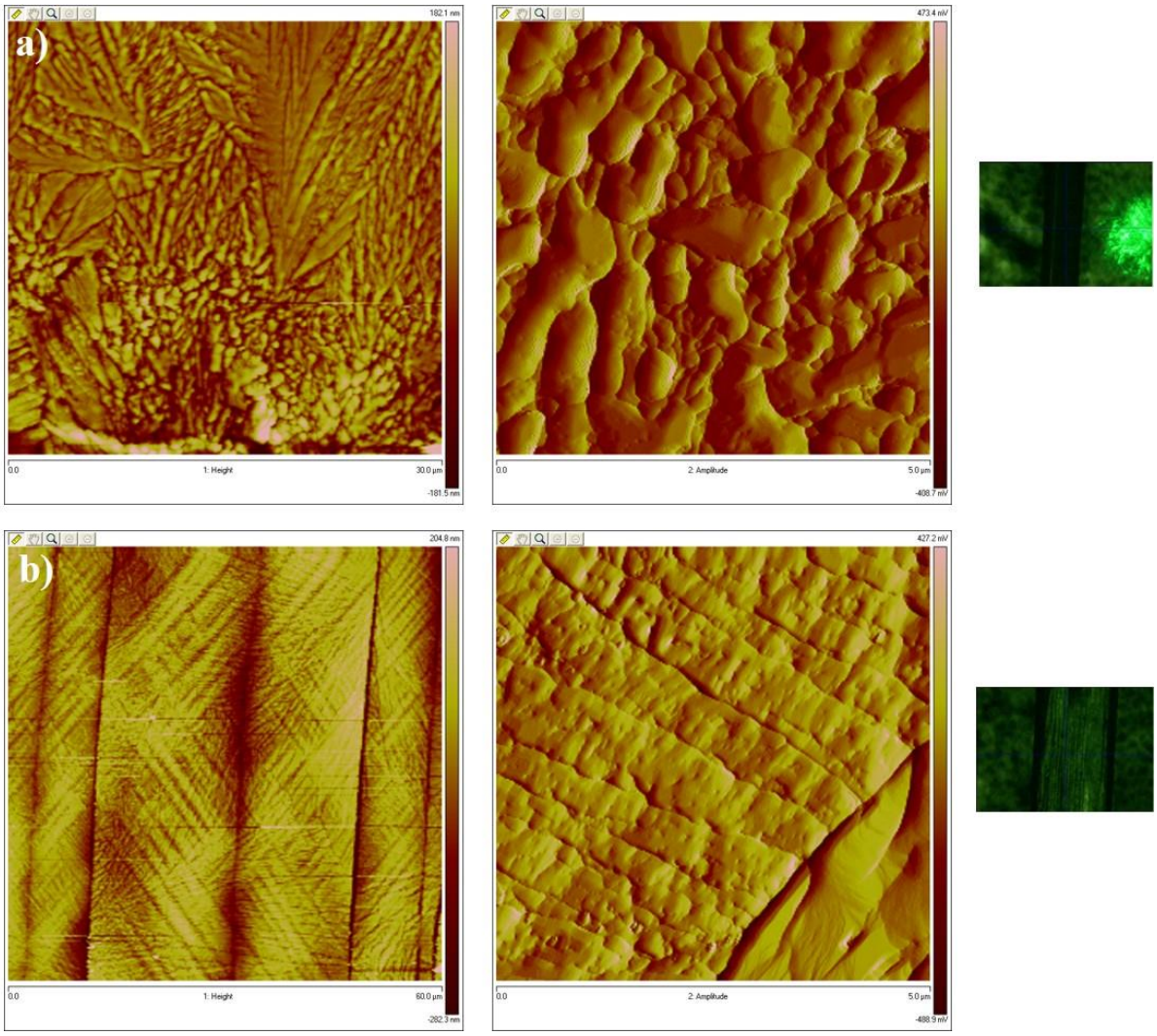

Figure 157 - AFM images illustrating the topography of the surfaces of CBZ:2H_2O crystals stored at 40 ºC and 0% RH. *a:* (0k0) surface; scan size of 30 µm and 5 µm, height and amplitude images (left to right). *b:* (h00) surface; scan size of 60 µm and 5 µm, height and amplitude images (left to right). The optical micrographs show the orientation of the crystals during the analyses.

5.5. The effect of seeds on the dehydration of CBZ:2H_2O

The influence of humidity on the outcome of CBZ:2H_2O dehydration suggests that nucleation and growth processes considerably affect the reorganisation of CBZ molecules and are also considerably affected by the environment. If this is the case then the presence of seeds is also expected to change the dehydration outcome. This hypothesis was tested in different samples of CBZ:2H_2O prepared by slurrying of CBZ Form I or Form III. Different slurrying conditions were used - namely the solvent (water or ethanol:water), the amount of CBZ in proportion to the solvent, the duration and the temperature of slurrying (with or without annealing cycles at higher temperatures). Although all the samples prepared from slurrying were characterized as CBZ dihydrate, the dehydration under non-isothermal heating programs in dry environment (N_2) consistently resulted in different outcomes.

Figure 158 and Figure 159 show how the dehydration evolves with increase in temperature (1 ^{o}C.min^{-1}) in the case of CBZ:2H$_2$O samples obtained from polymorph I or III slurried in water, respectively. The samples prepared from Form I show evidence of dehydration commencing at 55 ^{o}C with diffraction peaks of Form I being detected. For samples prepared from Form III, the PXRD patterns show evidence of dehydration commencing at 50 ^{o}C when reflections of Form I and Form III become detectable. The mixture evolves to the formation of pure polymorph III as the temperature increases, with Form III converting to form I above 150 ^{o}C.

While the CBZ:2H$_2$O samples prepared from Form I show the same behaviour at different heating rates, the dehydration of samples prepared from Form III only results in Form III as a result of slow heating. Figure 160 shows how the dehydration evolves with increase in temperature with heating rates of 10 and 20 ^{o}C.min^{-1} for both the CBZ:2H$_2$O samples prepared from slurrying. It shows that at high heating rates the seeds of Form III do not drive the recrystallization process, illustrating the kinetic character of the seeding effect.

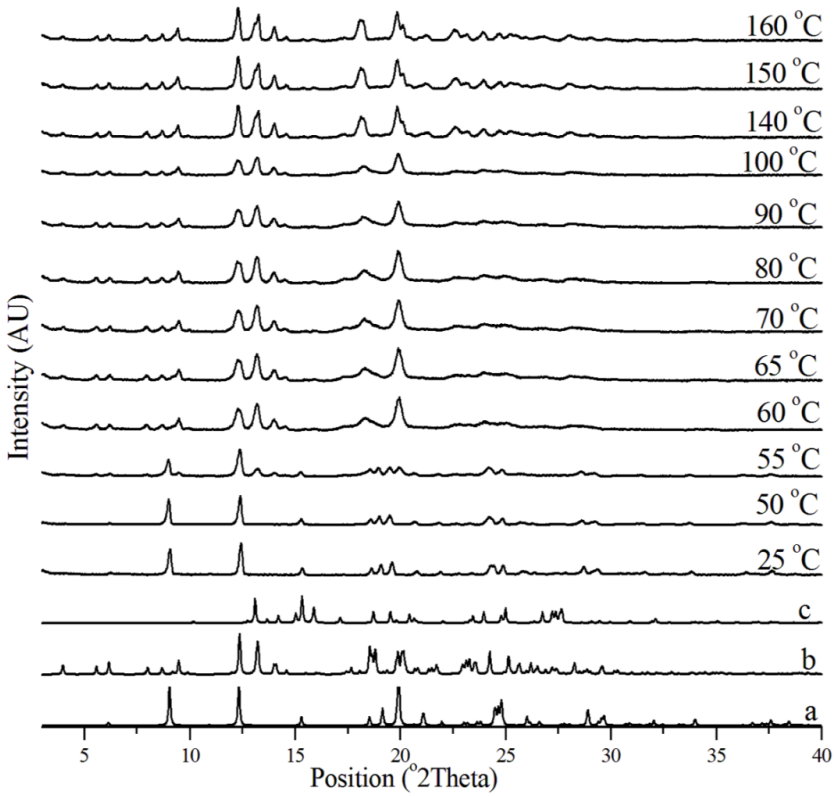

Figure 158 - *In situ* variable temperature PXRD patterns of CBZ:2H$_2$O prepared from slurrying of CBZ Form I in water (1 ^{o}C.min^{-1}, 25-160 ^{o}C). *a*: CBZ:2H$_2$O (FEFNOT02). *b*: CBZ I (CBMZPN11). *c*: CBZ III (CBMZPN01).

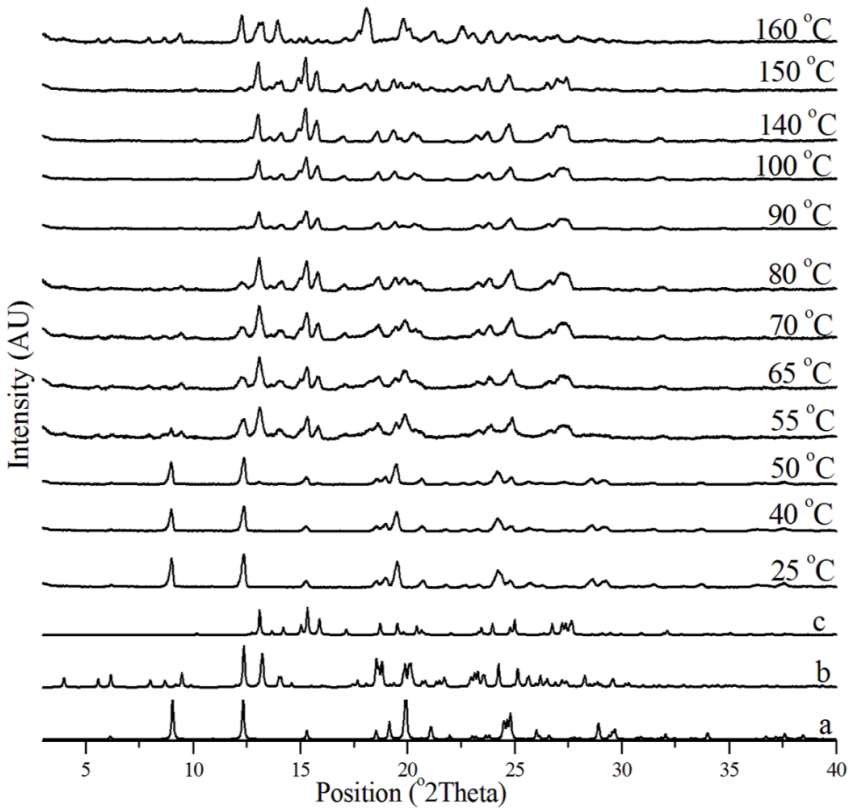

Figure 159 - *In situ* variable temperature PXRD patterns of CBZ:2H_2O prepared from slurrying of CBZ Form III in water (1 ºC.min^{-1}, 25-160 ºC). *a*: CBZ:2H_2O (FEFNOT02). *b*: CBZ I (CBMZPN11). *c*: CBZIII (CBMZPN01).

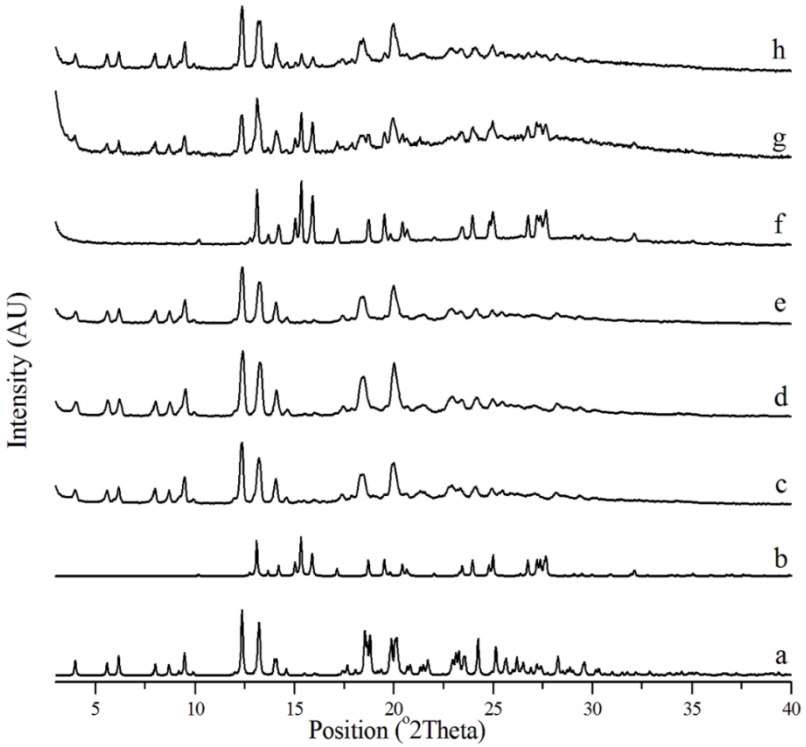

Figure 160 - *Ex situ* PXRD patterns of CBZ:2H_2O samples heated until 120 ºC at different heating rates. The patterns in *c*, *d* and *e* show the dehydration outcomes of a sample prepared from slurrying Form I in water (1, 10 and 20 ºC.min^{-1}, respectively). The patterns in *f*, *g* and *h* show the dehydration outcome of a sample prepared from slurrying Form III in water (1, 10 and 20 ºC.min^{-1}, respectively). The calculated patterns of polymorph I and polymorph III are added for clarification (*a*: CBZ Form I from CBMZPN11; *b*: CBZ Form III from CBMZPN01).

The thermal behaviour of both CBZ:2H_2O samples obtained from slurrying of CBZ Forms I or III appear to be very similar. The analyses at 1 $^oC.min^{-1}$ show one single event of weight loss ending at about 45 ^oC, which corresponds to a single endothermic event in the DSC. At about 60 ^oC, the samples show one exothermic event that indicates recrystallization. The shape of the thermal curves resembles the behaviour of the (0k0) sample, although the characteristic thermal events of the slurried materials occur at lower temperatures than for (0k0). It is proposed that particle size affects the thermal characteristics of the dihydrate samples. The only difference observed between the samples obtained from slurrying are drifts in the heat flow baseline of samples that resulted in CBZ Form III obtained after dehydration experiments performed at 1 $^oC.min^{-1}$. The abrupt changes have been consistently observed in a temperature range that corresponds to the formation of CBZ Form III after dehydration, as shown in Figure 159.

It is suggested that the DSC heat flow shifts are related to the crystallization of CBZ polymorph III and directly measure the change in the heat capacity of the material with recrystallization. In this case, as Form III is the most stable form of CBZ, the observed events are expected to be exothermic with heat flow out of the sample. Additionally, heat flow shifts may also be indirectly related to recrystallization as an artefact from the movements of the particles. In particular, changes in crystal morphology during the formation of Form III may result in changes in the contact of the sample and the crucible, which will affect the heat transfer from the sample holder to the DSC cell.

Figure 162 and Figure 163 show how the morphology of the particles evolves in dry environment (N_2) with a temperature ramp of 1 $^oC.min^{-1}$. CBZ:2H_2O samples that resulted in Form III showed clearly different particles to those which formed Form I crystals. The results indicate that the isostructural dehydrated product seen until 50 ^oC is characterized by particles that are very similar to the fresh material, except for the fact that they seem to bridge each other. As the temperature increases, thin needles develop on the surface, which can be correlated to the exothermic events observed in the DSC. In the case of CBZ:2H_2O slurried samples obtained from CBZ III, the materials start showing round domains and particles above 75 ^oC.

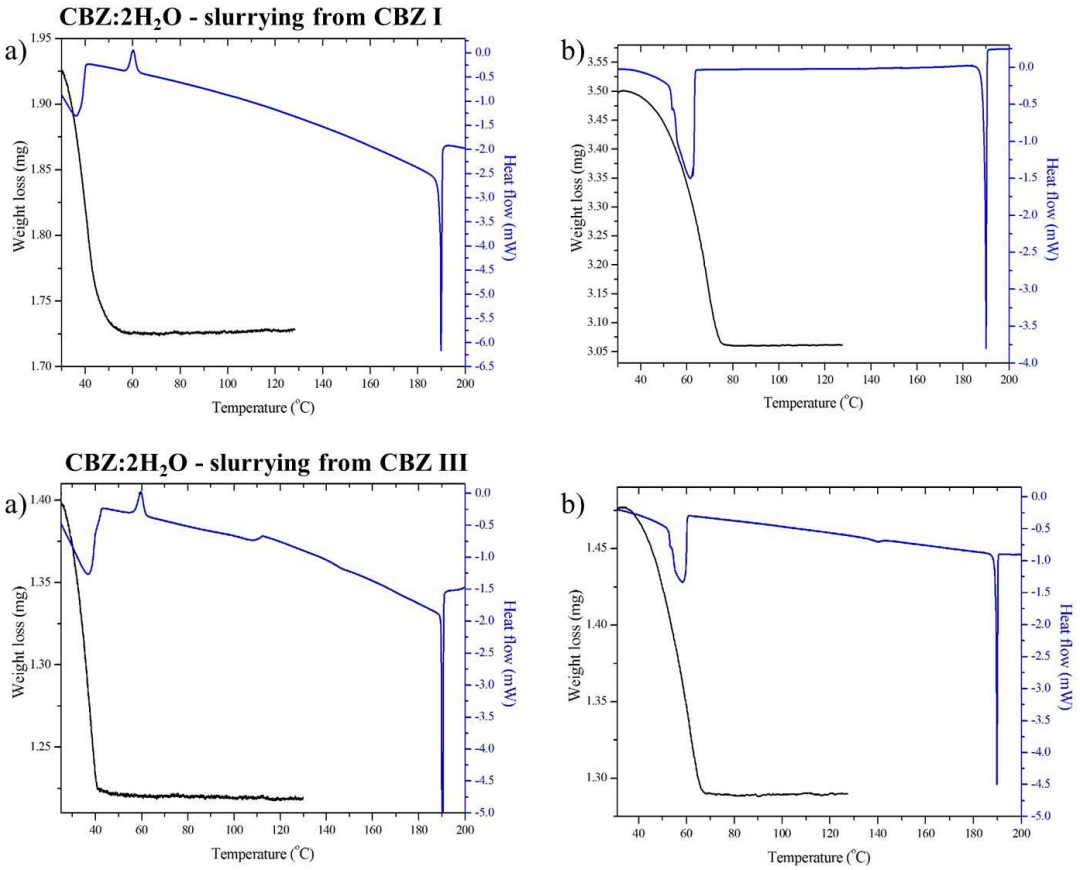

Figure 161 - DSC and TGA thermal characterization of CBZ:2H_2O samples prepared from slurrying of CBZ Forms I or III in water. *a*: open pan, 1 $^oC.min^{-1}$, N_2. *b*: perforated lid, 10 $^oC.min^{-1}$, N_2.

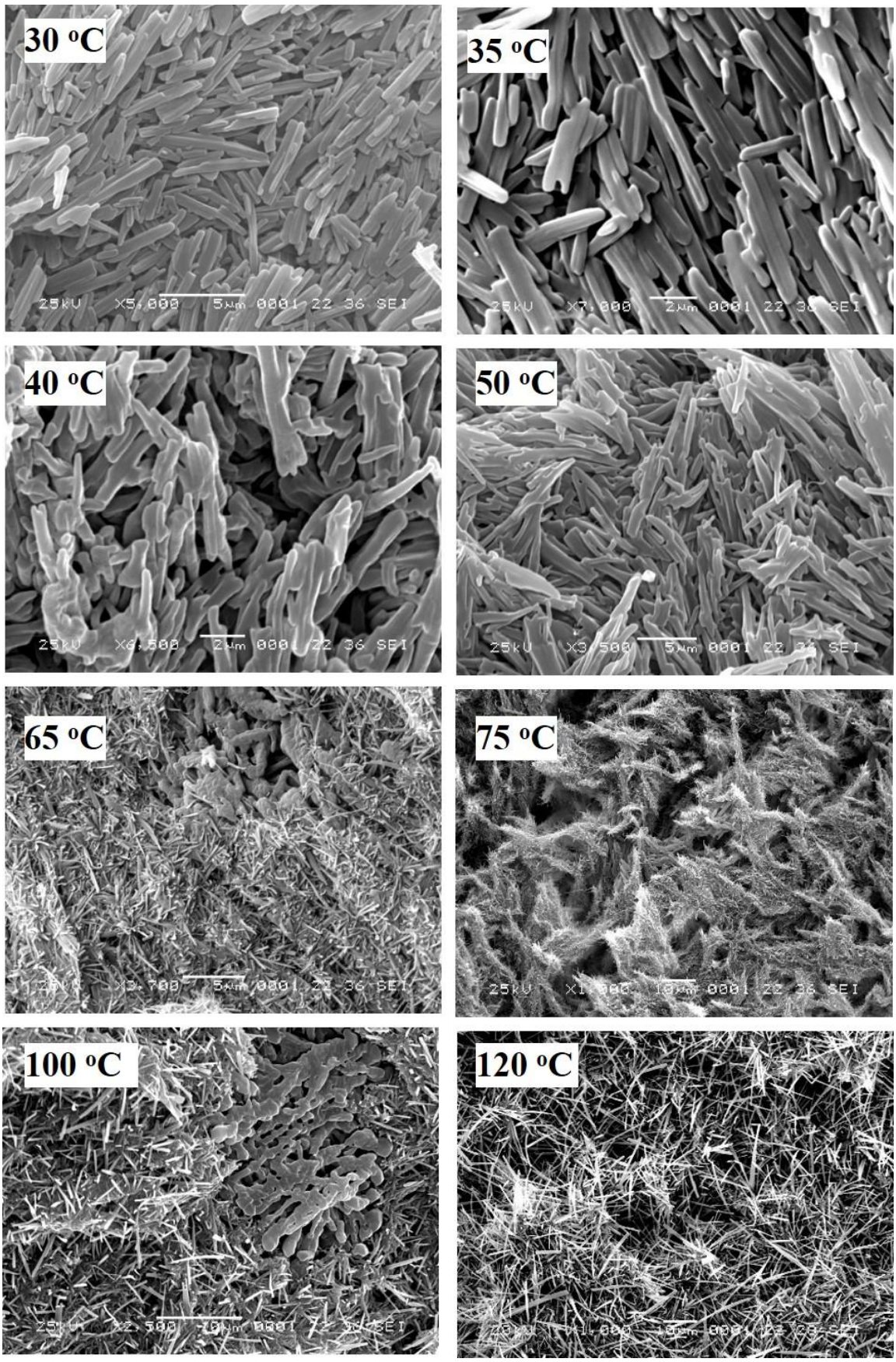

Figure 162 - SEM micrographs of CBZ:2H_2O heated until different temperatures under N_2 (heating rate of 1 $^oC.min^{-1}$). The sample was prepared from slurrying of CBZ Form I

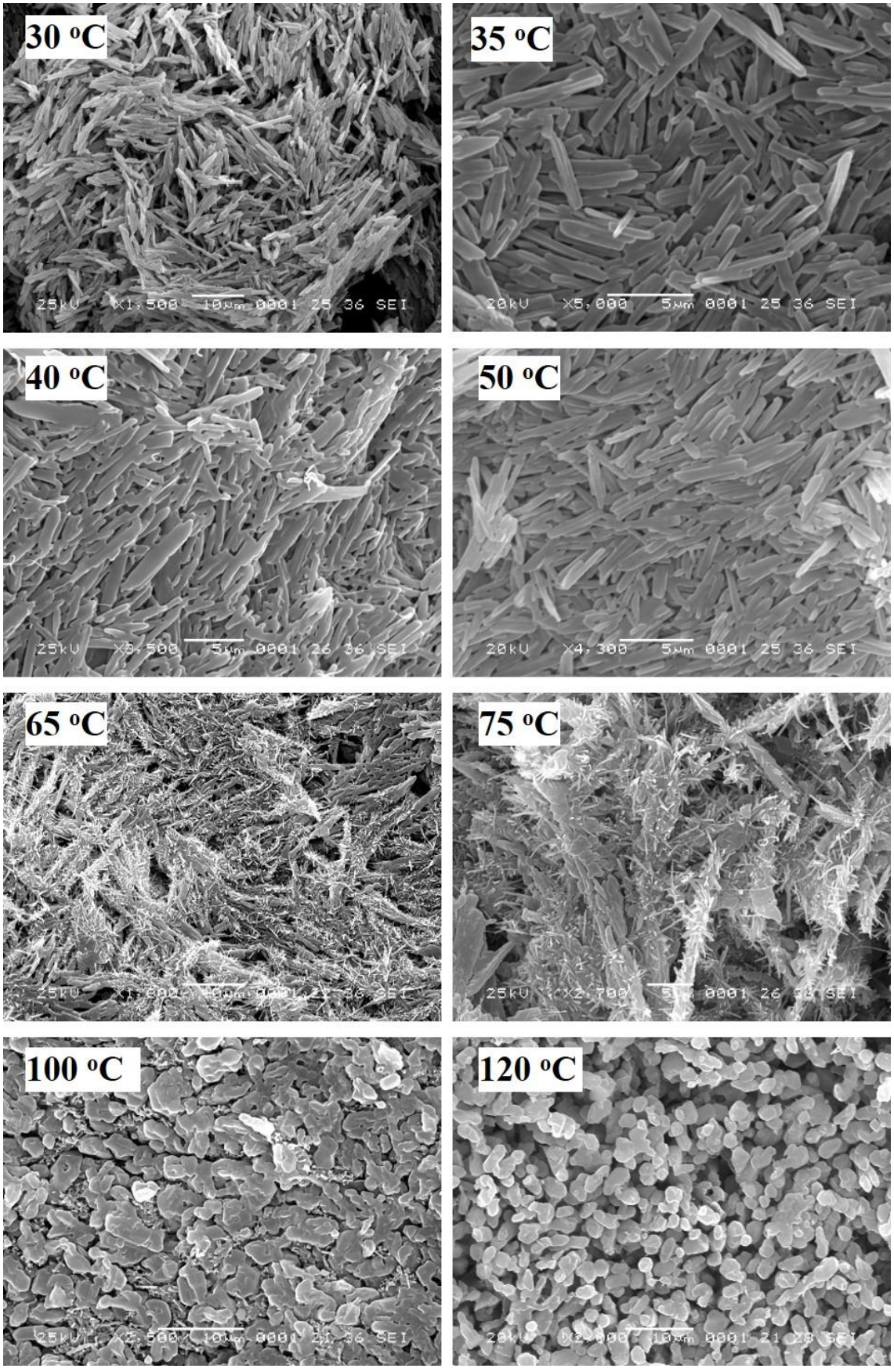

Figure 163 - SEM micrographs of CBZ:2H_2O heated until different temperatures under N_2 (heating rate of 1 $^oC.min^{-1}$). The sample was prepared from slurrying of CBZ Form III.

5.6. Conclusions

It has been demonstrated that the removal of water from the lattice of CBZ:2H_2O and the recrystallization into a new anhydrous form may be simultaneous events, depending on the aspect ratio of the dihydrate crystals. It is suggested, however, that the CBZ sublattice within CBZ:2H_2O is relatively stable even after loss of the water molecules and forms an isostructural anhydrous structure. This stability appears to be dependent on temperature and time, and may have implications on the subsequent resulting crystallization process of polymorphs of CBZ.

The polymorphic outcome of dehydration is shown to be dependent on the experimental conditions. Samples subjected to high temperatures or stored in the presence of water vapour result in the formation of CBZ polymorph I, while dry environments lead to polymorph IV. Samples which have been non-isothermally dehydrated in the presence of seeds of Form III or Form I, resulted in Form III or Form I, respectively. In general, CBZ I formed upon dehydration shows pronounced peak broadening and amorphous content, while CBZ IV product crystals gave sharper peaks and no background halo in the PXRD pattern. In the case of Form III product crystals, the peaks were broader. It is suggested that these microstructural differences may be related to the mechanism of dehydration.

The studies have shown that large crystals of CBZ:2H_2O become polycrystalline upon dehydration, although the external morphology do not change significantly. The nature of the polycrystalline domains, however, are different. Although the comparison between bulk PXRD and surface imaging is not always possible, the results suggest a correlation between phase identity and surface domains. CBZ polymorph I dehydrated materials show whiskers covering the crystal faces, while polymorph IV shows round domains on the surfaces. In the case of smaller crystals prepared from slurrying, the dehydration leads to particle shattering and a significant change in morphology, *i.e.* round particles and whiskers characterized as Form III and Form I, respectively.

The imaging of the crystal surfaces during the ongoing process of dehydration has also demonstrated different features. Samples isothermally dehydrated which resulted in CBZ polymorph I and crystals covered with whiskers, show evidences of strain along the *c* axis as cracks and intersecting texture on the (h00) surface, and aligned holes perpendicular to the needle axis on the (0k0) surface. In the case of samples dehydrated into CBZ polymorph IV and presenting round surface domains, the crystals show evidences of strain along the *c* axis as cracks and intersecting texture on the (h00) surface, and cracks angled by approximately 40^o to the needle axis on the (0k0) surface. Regardless of whether the different surface features captured during the ongoing process of dehydration are attributed to the distinct molecular

movements and strain resulting in the formation of anhydrous CBZ or not, the findings show the CBZ:2H_2O crystal surfaces present different properties.

The analyses of the fresh crystals also indicate the distinct characteristics of the faces. It was demonstrated that the dihydrate crystals are composed of (0k0) layers, which are piled-up, and show different *tracht* depending on the relationship between the size of the (0k0) surface and the amount of (0k0) layers. It is suggested that these layers are structurally related to weak planes in the dihydrate as dehydration has resulted in cracks cross-cutting the crystals and visible on the (h00) and the (00l) surfaces. In fact, these cracks are always observed in crystals analysed by SEM, fresh and dehydrated, as artefacts from vacuum, which was also challenging during TEM analyses.

In conclusion, the results of the present Chapter illustrate how the dehydration outcome is affected by the environment conditions. Even subtle differences in humidity are expected to change the nucleation and growth processes during the formation of anhydrous CBZ after water removal. The crystals present poor mechanical properties, as they are prone to breakage. It is suggested that the brittleness of the material is surface specific and related to the crystals' topography. The studies illustrate the importance of combining bulk and surface characterization to expand the understanding of decomposition reactions, such as dehydrations.

CHAPTER 6 – The properties of carbamazepine dihydrate prepared at large scale

6.1. Introduction

The crystallization studies of CBZ:2H_2O samples prepared at laboratory scale resulted in amounts of approximately 1g (Chapter 4) and the characterization of the samples (Chapter 5) has provided useful information about the intrinsic bulk and surface properties of the dihydrate. An important further step corresponds to the application of the results of these studies to the understanding of particle attrition and breakage arising during filter bed drying. Such studies are being performed at the University of Leeds (School of Chemical and Process Engineering). The experimental work performed by Leeds, however, required much larger quantities of material than were possible to be prepared in Cambridge or Leeds. As a result, AbbVie in their Chicago laboratories agreed to prepare quantities of CBZ:2H_2O at the kilogram scale. In this context, the main aim of the present chapter is to describe the crystallization methods adopted and to characterize and compare the properties of these large batches of CBZ:2H_2O subsequently used by Leeds in their attrition studies.

In order to improve the scalability from laboratory to factory, maximize yield and have batch-to-batch robustness, the method adopted by AbbVie involved solution crystallization via anti-solvent addition (i.e. addition of water in which the dihydrate is less soluble). It means that, different to the laboratory scale crystallization described in Chapter 4, the large-scale process did not use changes in temperature as the crystallization driving force. In the scaled-up experiments, a binary solvent mixture of ethanol and water was employed with the composition of the ethanol/water mixture changing during the water addition from a high ethanol concentration, to a predominantly aqueous environment. Other differences consisted of the use of agitation inside the reactor and the use of crystal seeds - seeds were not used in the standard cooling crystallization method performed in the laboratory.

The development of the crystallization process and the preparation of CBZ:2H_2O was done by Dr Kushal Sinha in AbbVie Inc. (Chicago, Illinois, USA). The results of the preliminary characterization and the description of the crystallization experiments developed in AbbVie are reproduced in Section 6.2 (with permission). The solid-state properties of CBZ:2H_2O produced in these experiments (approximately 1 Kg) were experimentally tested and analysed at Cambridge and Leeds. The results of the work developed in Cambridge are presented in Sections 6.3 and 6.4 (*N.B.* breakage experiments were performed in collaboration

to Professor Mojtaba Ghadiri and Wei Pin Goh, from the University of Leeds). Subsequently, one batch of 9 Kg was produced and is being evaluated in attrition studies by Leeds). Analysis of this material was not performed by Cambridge because of lack of time.

6.2. The crystallization of CBZ:2H_2O at the kilogram scale scale

The crystallization variables assessed in the scaled-up production of CBZ:2H_2O can be considered as (i) the effect of the seeds and (ii) the mixing used during crystallization. While a first set of experiments did not use seeds, later sets of experiments involved the addition of externally prepared seeds - namely "dry" seeds, "wet" seeds - made by stirring "dry" seeds in high dispersion instruments, and "wet" seeds prepared by *in situ* seed generation. The *in situ* formation of seeds occurs via vigorous and controlled mixing of a supersaturated solution. In this methodology, *in situ* primary nucleation generates the first solid nuclei, which is then followed by secondary nucleation and crystal growth. In the case of addition of "dry" seeds, secondary nucleation dominates the process.[203,204]

Figure 164 shows the resulting crystals of the two initial crystallization experiments which aimed to prepare *ex situ* seeds of CBZ:2H_2O. One method involved the reverse addition of CBZ ethanol:water solution into the crystallizer containing water as the antisolvent. Both solutions were maintained at 65 ^oC until addition was complete, resulting in a final ethanol:water proportion of 20:80 (v:v). A second method examined the forward addition of antisolvent into the crystallizer containing CBZ ethanol:water solution until a similar final ethanol:water proportion of 20:80 (v:v) was obtained. In this case, the ethanolic solution was maintained at 65 ^oC, while the water was charged at 25 ^oC. Both methods used successive heat and cool cycles after the solutions were mixed to improve the growth and the population homogeneity of the resulting crystals.

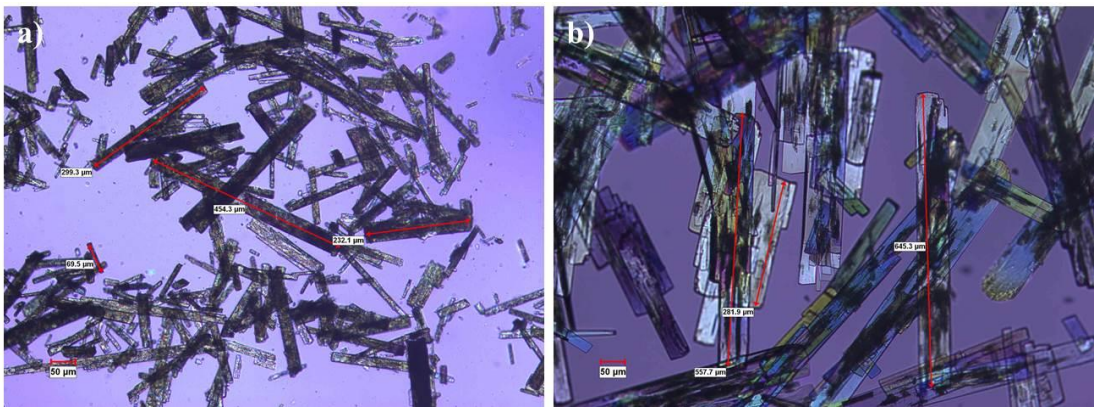

Figure 164 - Optical micrographs of samples prepared by different methodologies and intended to be used as *ex situ* seeds in future experiments (reproduced from Sinha[205] with permission). *a*: sample crystallized from reverse addition of CBZ ethanol:water solution in water. *b*: forward addition of antisolvent in CBZ ethanol:water solution.

The optical micrographs in Figure 1 suggest that the crystals produced from reverse addition of solvent do not seem to be single particles. The PXRD analyses show that these crystals are in fact CBZ polymorph III (Appendix 4). Considering the morphology of the crystals, it is unlikely that they formed directly as Form III, but rather dehydrated after CBZ:2H_2O itself was crystallized. The reason why dehydration has occurred is unclear. The sample obtained from forward addition of anti-solvent, in turn, was characterized by PXRD as CBZ:2H_2O and crystals from this batch were subsequently selected as a source of seeds for other crystallizations.

Figure 165a shows the crystals prepared by the forward addition of anti-solvent into a CBZ ethanol:water solution equilibrated with "dry" seeds at 50 ^oC (low supersaturation and final ethanol:water proportion of 20:80 v:v). The images show plate-like particles with little or no agglomeration. Although the characteristics of the sample have reasonably met the initial specifications, it was proposed that *in situ* seed generation could be used to improve the aspect ratio of the crystals. In this case, a first investigation was performed using wet milling of seeds. Figure 165b shows the crystals produced by a combination of forward anti-solvent addition, wet milling of "dry" seeds and heat and cool cycles (low supersaturation and final ethanol:water proportion of 20:80, v:v). It demonstrates indeed that aspect ratio of the resulting crystals was improved by wet milling and suggests that *in situ* seed generation could be subsequently used.

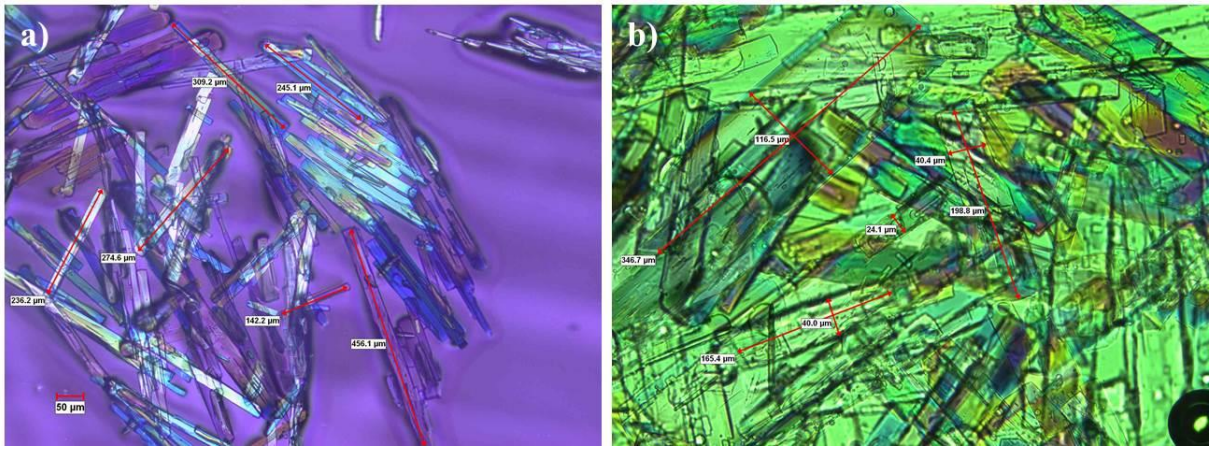

Figure 165 - Optical micrographs of CBZ:2H_2O samples prepared by different methodologies and intended to be used in the preparation of large amounts of the material (reproduced from Sinha[205,206] with permission). *a*: sample crystallized from forward addition of antisolvent in CBZ ethanol:water (80:20, v:v) solution equilibrated with "dry" seeds. *b*: sample crystallized from "wet" seeds. The seeds were prepared by wet milling "dry" seeds.

Initially, two batches of approximately 600 and 400 grams were prepared by using "wet" seeds. The properties of these materials are characterized in the following sections. Another important aspect of the crystallization of CBZ:2H_2O, however, is the toxicity of the drug. CBZ is a potent material and a skin sensitizer. Although these characteristics may be

easier to control in small-scale experiments, the crystallization of large-scale batches require the compliance to strict good manufacturing practices and the use of appropriate manufacturing plants. There are specific protocols of quality assurance, which must be validated if a foreign material, such as *ex situ* seeds, is used during the crystallization. The approval of the transfer and storage of such materials is a long process, which can be avoided by using *in situ* seed generation.[205,206] Another additional concern about the preparation and use of *ex situ* seeds is the physical stability of the crystals with time, especially if the targeted product is metastable or is a labile hydrate/solvate. In this case, while the first kilogram of CBZ:2H_2O was prepared by using "wet" seeds made by stirring "dry" seeds in high dispersion instruments, a method involving the forward addition of antisolvent and *in situ* seed generation was selected to scale up the crystallization of CBZ:2H_2O to a 9-Kg batch. As previously mentioned, the characterization of this material will not be described in the present chapter.

6.3. The characterization of CBZ:2H_2O crystallized by AbbVie

The samples obtained from AbbVie were characterized to evaluate their chemical purity and solid-state properties. Two batches were produced following the same methodology and were fully characterized. Although the results of chemical purity are shown for both samples, the solid-state analyses are only illustrated by the results obtained from the characterization of the larger batch.

The observed elemental compositions based on CHN analyses and TGA data, and the corresponding calculated compositions of CBZ:2H_2O dihydrate are summarised in the Appendix 4 (Table 21). The observed molecular formulas of $C_{15.0}H_{15.6}N_{2.0}O_{3.0}$ and $C_{15.0}H_{16.9}N_{2.0}O_{3.0}$ are in good agreement with the calculated $C_{15}H_{16}N_2O_3$ formula. The measurements of 13.3% and 13.2% of weight loss obtained from TGA data are consistent to the theoretical calculated values of water content (13.2%). In addition, solution NMR analyses demonstrated that the sample was chemically pure with no contaminant detected. The ^{1}H solution spectrum showed characteristic chemical shifts and integration values while the ^{13}C spectrum showed the presence of 15 chemically distinct carbons in the sample (Appendix 4, Figure 301).

Figure 166 compares the experimental PXRD pattern of the sample with a calculated pattern for CBZ:2H_2O and the CBZ anhydrous polymorphs reported in the literature. The sample shows extensive preferred orientation of the (h00) plane, which was not overcome by gentle grinding with mortar and pestle.

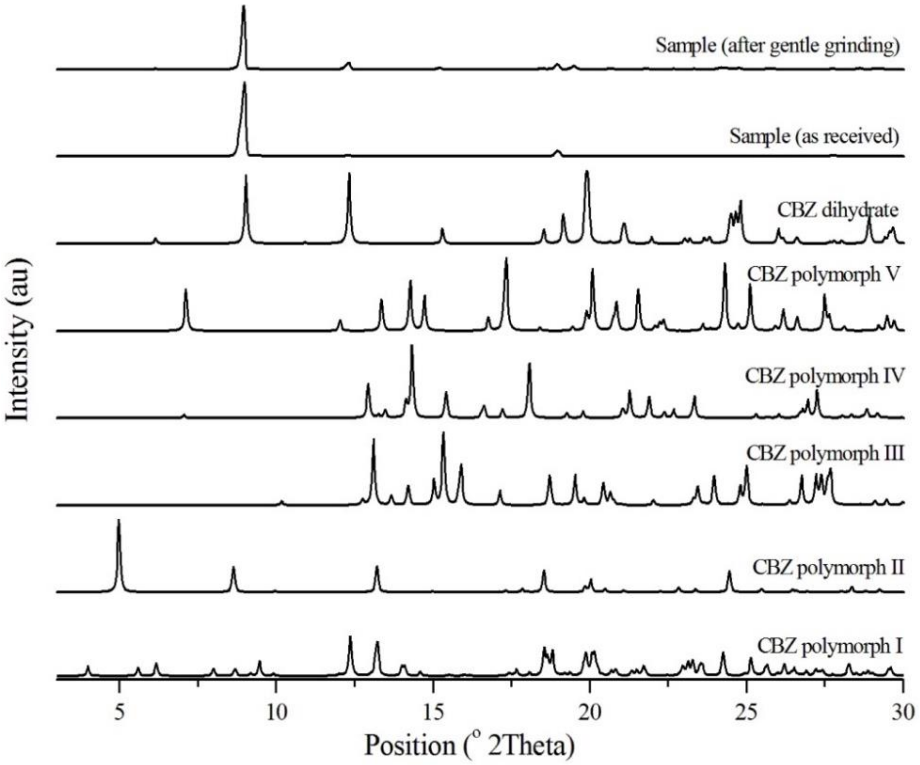

Figure 166 - PXRD patterns of the CBZ:2H_2O sample crystallized in large scale. The calculated patterns of CBZ dihydrate and CBZ anhydrous polymorphs I, II, III, IV and V are added for comparison (CSD codes FEFNOT02, CBMZPN11, CBMZPN03, CBMZPN01, CBMZPN12 and CBMZPN16, respectively).

The morphology of the samples crystallized at large scale also suggest preferred orientated. Optical micrographs show plate-like crystals and heterogeneous particle size distribution (Figure 167). Differences in the refracted light at the edges of the particles suggest that different regions of individual particles have uneven thickness. The crystals appear to be fragile, as fractured edges are also observed. The chipping of the crystals is related to the breakage along the (00l) and (0k0) crystallographic planes.

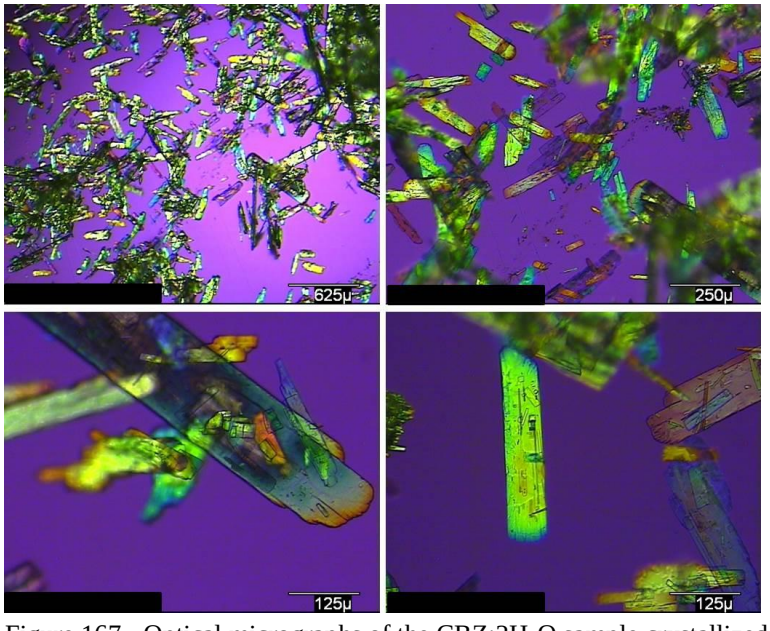

Figure 167 - Optical micrographs of the CBZ:2H_2O sample crystallized in large scale (polarized light).

Figure 168 shows the SEM micrographs of the samples and illustrate their surface features. The plate crystals show cracks and intersecting texture on the dominant face, which are typical of the (h00) surfaces as previously characterized. Although the majority of the cracks on the (h00) surface imaged by SEM are artefacts from vacuum, it is noteworthy that cracks and fractured edges were also observed by optical microscopy. It is proposed that particle attrition has caused the breakage, but it is unclear whether it occurs during crystallization, filtration, drying or even possibly transportation from Chicago. Interestingly, the materials prepared by small-scale *in situ* seed generation characterized in Figure 165 did not show the fractures seen in the samples prepared in large-scale and transported from the USA to England (Figure 167 and Figure 168).

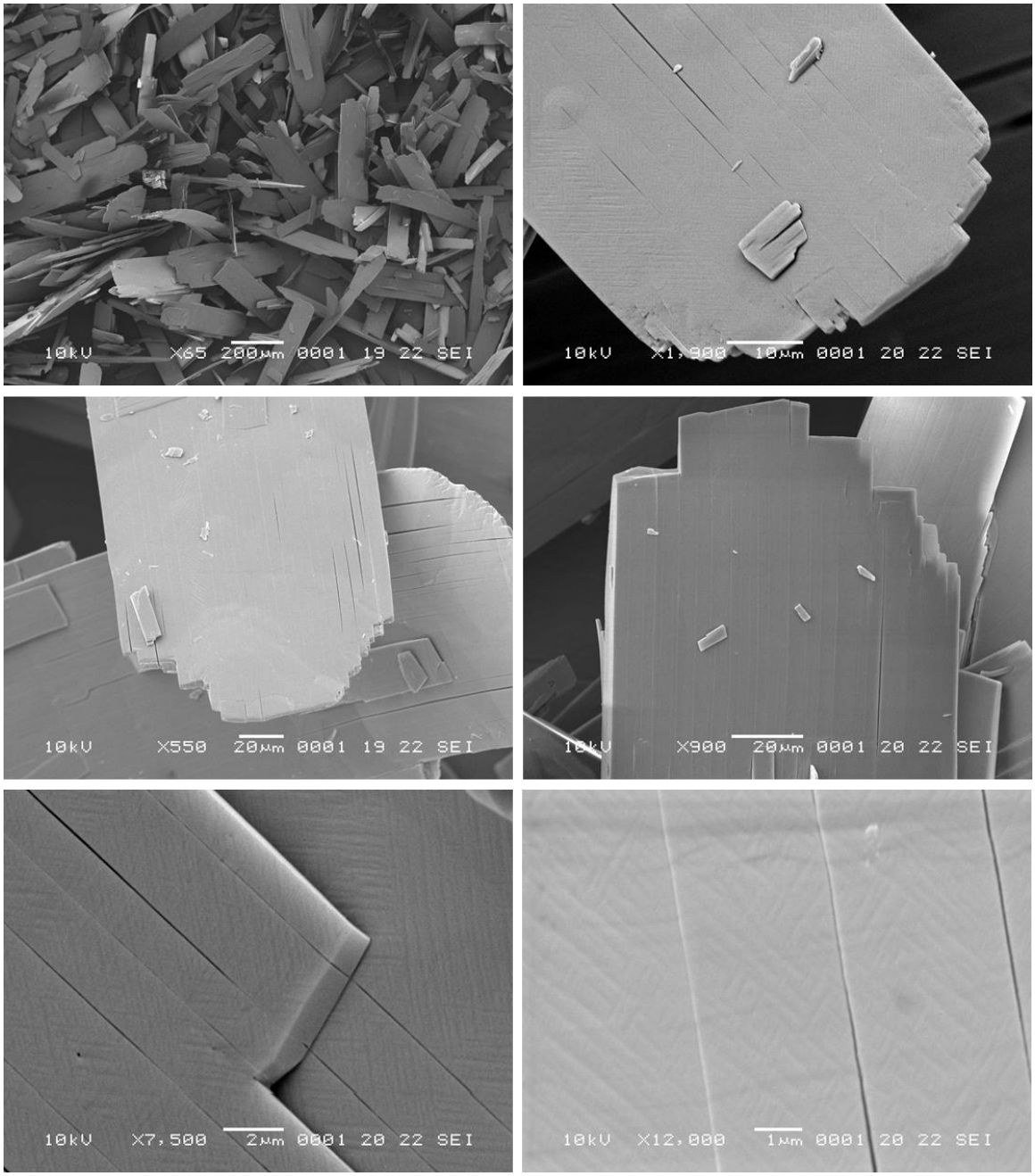

Figure 168 - SEM micrographs of the CBZ:2H_2O sample crystallized in large scale.

Crystals similar in thickness were obtained in laboratory scale experiments by combining anti-solvent addition, high final proportion of ethanol in water, "dry" seeds, low supersaturation and stirring (Figure 169). The large-scale batches, however, were prepared in a final ethanol:water proportion of 20:80 (v:v). In this solvent environment, the experimental procedures used in laboratory resulted in needle crystals with no specific dominant face (see Chapter 4). It is hypothesized that several parameters may kinetically affect the crystallization of CBZ:2H_2O, namely the anti-solvent addition rate, the agitation speed and, especially, the seeds (see comparison of "dry" and wet milled seeds in Appendix 4, Figure 302). The precise reason for these differences is not clear.

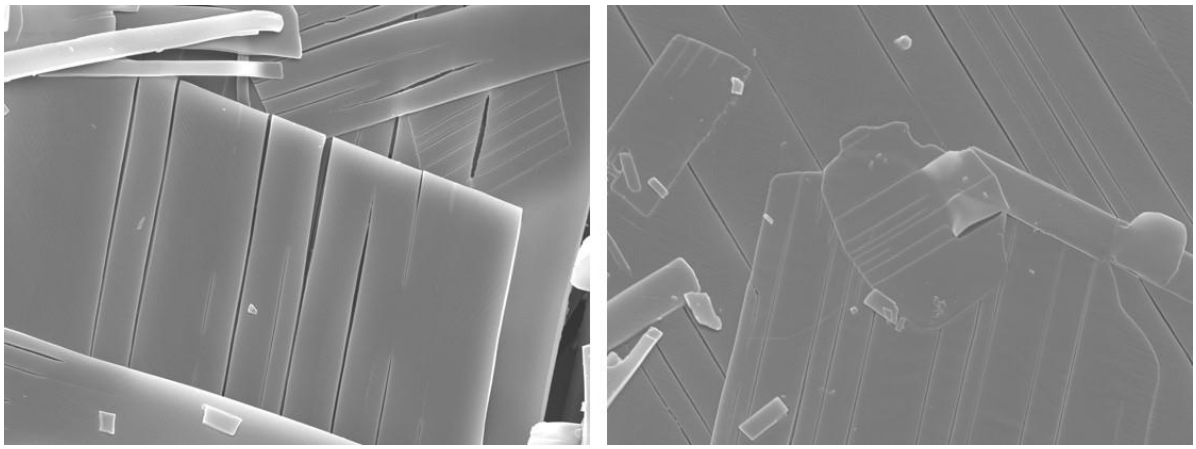

Figure 169 - SEM micrographs of CBZ:2H_2O crystallized by anti-solvent addition in laboratory scale (ethanol:H_2O 60:40 v:v, C/S = 1.2, with stirring)

Figure 170 shows the combined DSC and TGA curves of CBZ:2H_2O crystallized at large scale. The qualitative analyses of the thermal data show that the dehydration event of the sample resembles the behaviour of the (0k0) and the slurried dihydrate samples prepared in the laboratory. Although the materials present different morphologies and particle size, they are both very thin, which may explain the shape similarities of the thermal curves.

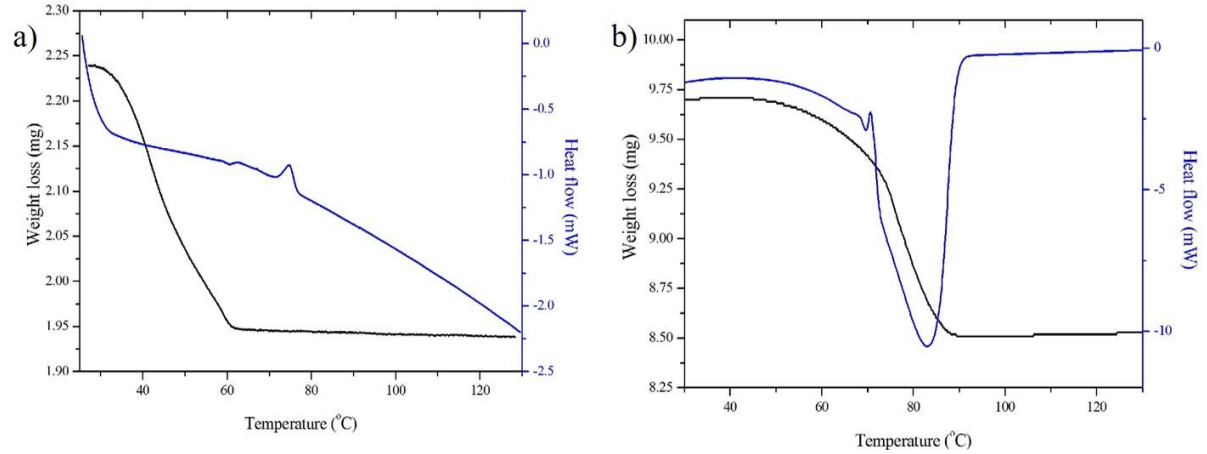

Figure 170 - DSC and TGA thermal characterisation of CBZ:2H_2O crystallized in large scale. *a:* 1 °C.min^{-1}, open pan, N_2. *b*: 10 °C.min^{-1}, perforated lid, N_2.

Table 12 compares the DSC measurements of different CBZ:2H_2O samples (measured at 10 $^oC.min^{-1}$ using a pin holed lid). In the case of the sample crystallized in large scale, the DSC analyses show one endothermic event in the range (38-106) ^oC (ΔH = 369.5±19.5 $kJ.g^{-1}$; T_{peak} = 81.0±2.5 ^oC) which corresponds to a weight loss of 13.28±0.01%. The melting event of CBZ was observed at 190.20±0.04 ^oC (ΔH_{fusion}=106.5±2.8 $kJ.g^{-1}$; T_{onset}=189.7±0.1 ^oC) and no event characteristic of the conversion from CBZ Form III into CBZ Form I was detected. These results suggest that the sample dehydrates and recrystallizes to CBZ polymorph I, which is also confirmed by *in situ* PXRD heating experiments (Figure 171). The PXRD patterns show lattice changes above 70 ^oC.

Table 12 - DSC quantitative data of different CBZ:2H_2O samples (10 $^oC.min^{-1}$, perforated lid, N_2).

CBZ:2H_2O	Dehydration			Melting		
	T_{onset} (^oC)	T_{peak} (^oC)	ΔH^1 ($kJ.g^{-1}$)	T_{onset} (^oC)	T_{peak} (^oC)	ΔH^2 ($kJ.g^{-1}$)
(0k0) sample	66.1	75.7	287.6	189.7	190.0	107.6
(h00) sample	85.9	92.6	299.9	189.4	190.1	102.2
Sample from slurry[3]	64.1	72.2	284.2	189.0	189.9	104.0
Scaled-up sample	70.6	81.0	369.5	189.7	190.2	106.5

[1] Relative to CBZ:2H_2O

[2] Relative to anhydrous CBZ

[3] CBZ:2H_2O sample obtained from slurrying of CBZ polymorph III

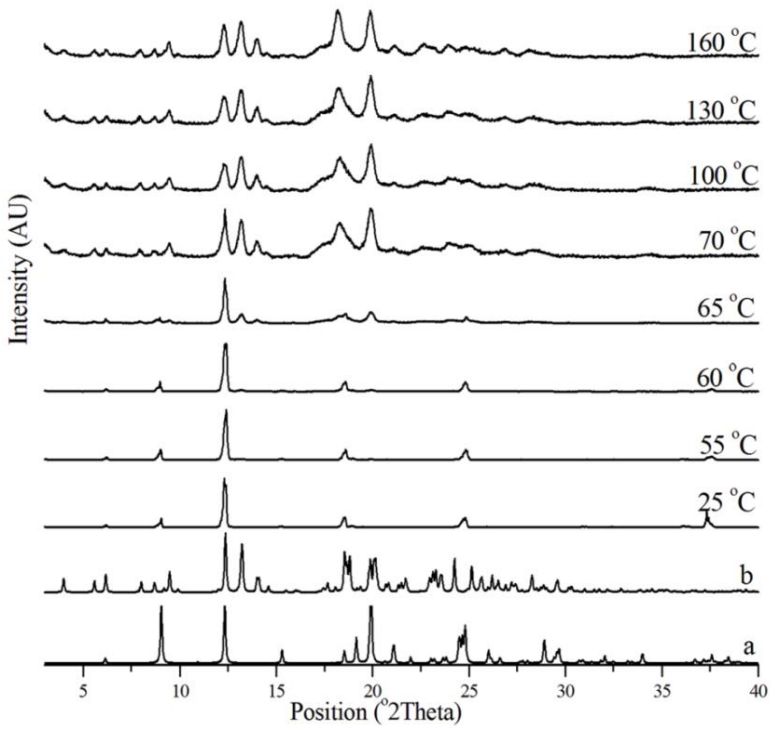

Figure 171 - *In situ* variable temperature PXRD patterns of CBZ:2H_2O crystallized in large scale (1 $^oC.min^{-1}$, 25-160 ^oC). *a*: CBZ:2H_2O from FEFNOT. *b*: CBZ Form I from CBMZPN11.

Optical micrographs collected during *in situ* heating experiments show two additional phenomena during dehydration: (i) jumping crystals and crack formation around 50-60 ^{o}C and (ii) darkening of the crystals around 60-75 ^{o}C (Figure 172). The darkening phenomenon, however, was not homogeneous as many crystals showed bright areas even after complete dehydration.

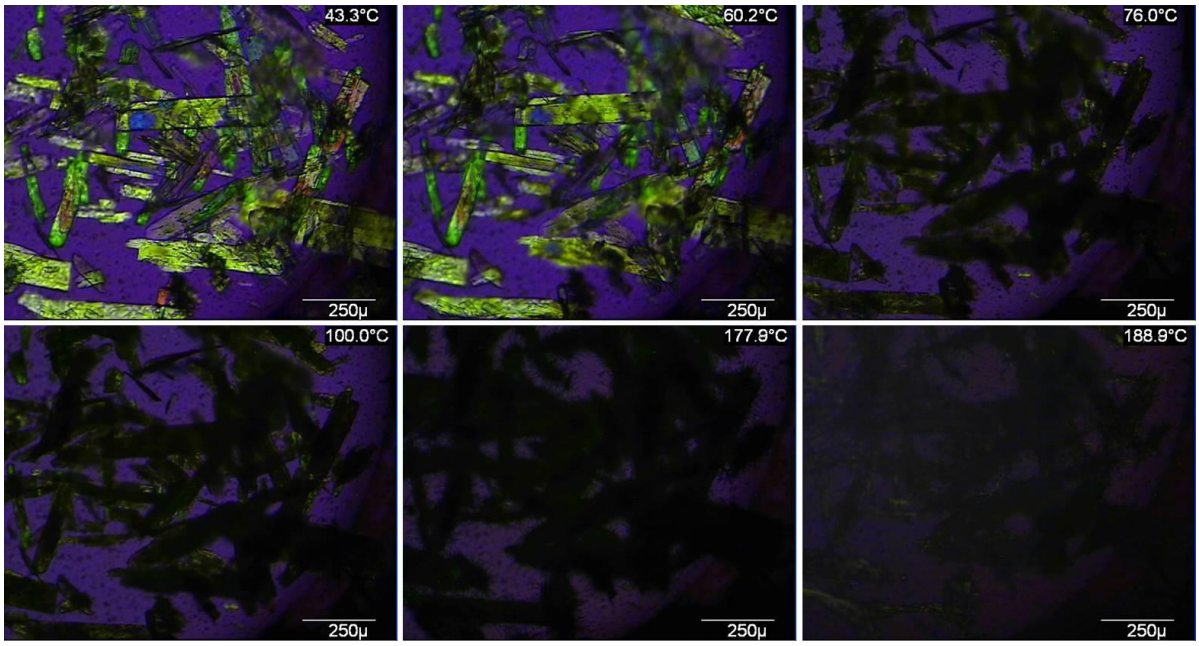

Figure 172 - Optical micrographs at different temperatures of CBZ:2H_2O crystallized in large scale (heating rate of 5 ^{o}C.min^{-1}, polarized light).

It is prorposed that the existence of bright and dark areas in a single crystal indicates the formation of a mixture of phases with the bright areas composed of dehydrated material that maintained the CBZ:2H_2O lattice, while those areas that lose birefringence correspond to dehydrated material which has recrystallized to CBZ polymorph I. It is unclear whether this would correspond to a characteristic of the sample prepared in large scale or if the other samples prepared in laboratory scale present the same behaviour but not detected because of crystal thickness. These findings are, however, noteworthy as they may result from crystal defects (*e.g.* disorder, twinning, dislocations). Also, regions in the dehydrated material which are isostructural to CBZ:2H_2O can act as seeds during the structural reorganization and influence the polymorphic outcome of the reaction.

6.4. The mechanical properties of CBZ:2H_2O crystallized in large scale

The characterization of the dihydrate samples crystallized in large scale has shown that the particles are fragile and susceptible to breakage. The brittleness of the particles, however, was not related to the dehydration of the crystals. The experiments show the samples

are chemically pure and present 100% of the expected water content. It is suggested that the breakage of the particles is purely related to their mechanical properties. In this case, breakage experiments were performed by using the Scirocco disperser of the Malvern Mastersizer 2000 and the Morphologi G3 apparatus from Malvern. These methodologies consist of impact tests in which particles are accelerated against a target resulting in breakage. Originally, both pieces of equipment have been used for imaging purposes and the acceleration of the particles was part of the dispersion stage of the analyses. Depending on the material and the impact velocity, however, the dispersion was known to cause undesirable particle breakage. Although this is inconvenient for image analyses, the principle and the technologies have been successfully applied as impact breakage test devices.[190,191]

Scirocco and G3 were combined in the analyses of CBZ:2H_2O particles as they provide distinct extent of breakage. Two different dispersion pressures were tested per equipment. Although an increase in the dispersion pressure affects the particle acceleration, the magnitude of the dispersion pressures of both equipment in relation to the impact velocity are not comparable.

Figure 173 and Figure 174 characterize the CBZ:2H_2O sample crystallized in large scale after the impact tests using G3. Although 1 bar of dispersion pressure has almost no effect on the particles, the experiments performed at 2 bar show breakage through sparse chipping. A few particles show evidences of fracture along regions corresponding to the (0k0) planes of the dihydrate structure. The overall particle shape and size, however, were not affected by the impact tests.

A different outcome was observed in experiments performed in the Scirocco device. Figure 175 and Figure 176 show how particle morphology changes as a function of the nozzle pressure. It is shown that particle size change considerably during the tests and breakage occurs through fragmentation, although chipping is also observed. It is evident that the samples subjected to the impact test with Sirocco mainly cleave along the (0k0) and the (00l) planes resulting in crystals with reduced dimensions along the *b* and *c* crystallographic directions.

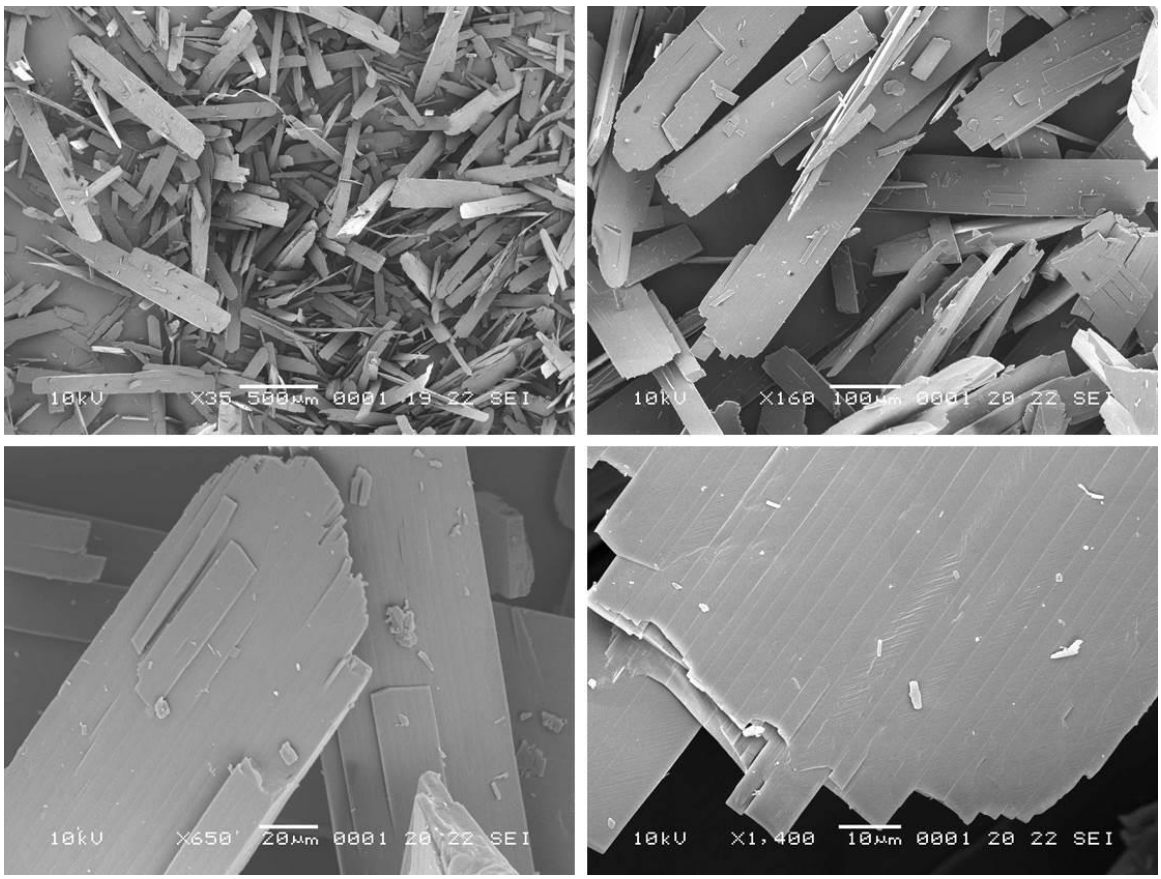

Figure 173 - SEM micrographs illustrating the results of impact tests on the CBZ:2H_2O sample crystallized in large scale (Morphologi G3, 1 bar of dispersion pressure).

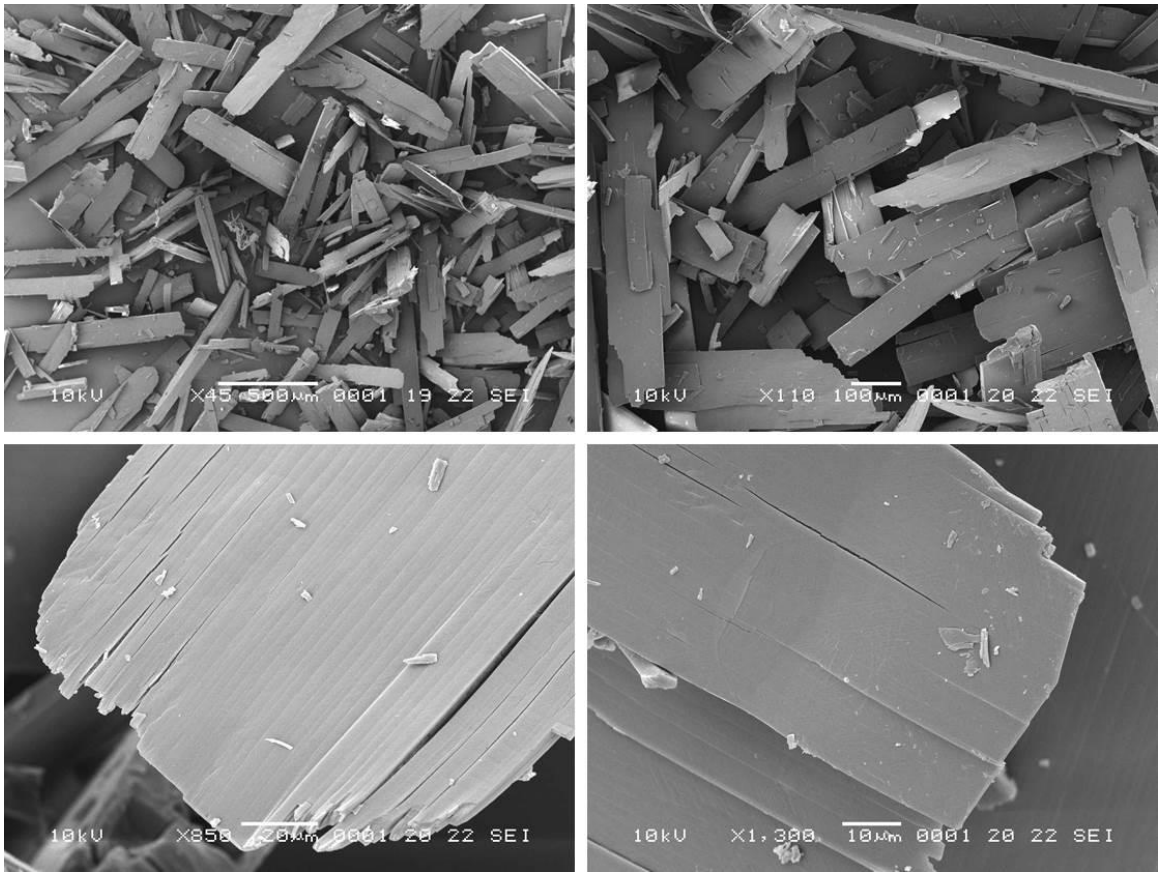

Figure 174 - SEM micrographs illustrating the results of impact tests on the CBZ:2H_2O sample crystallized in large scale (Morphologi G3, 2 bar of dispersion pressure).

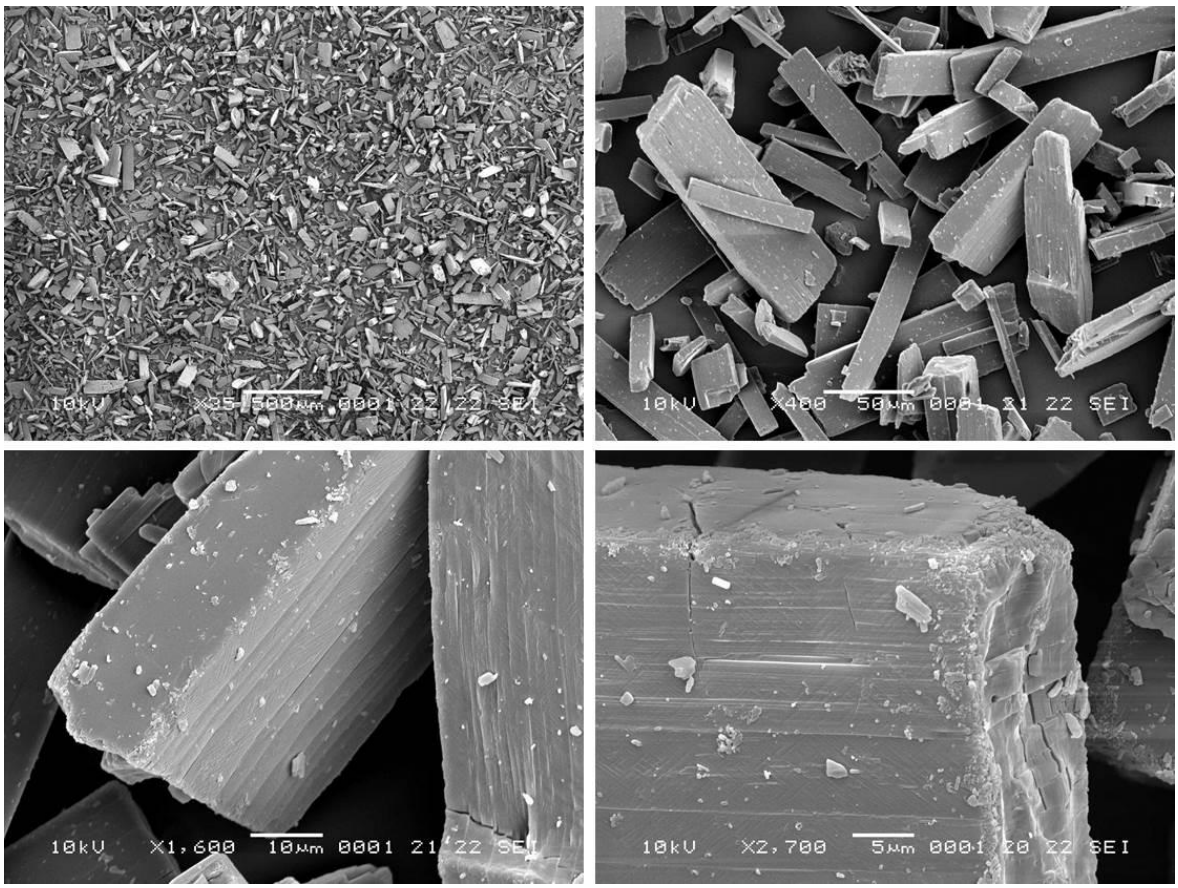

Figure 175 - SEM micrographs illustrating the results of impact tests on the CBZ:2H_2O sample crystallized in large scale (Scirocco disperser, 0.1 bar of dispersion pressure).

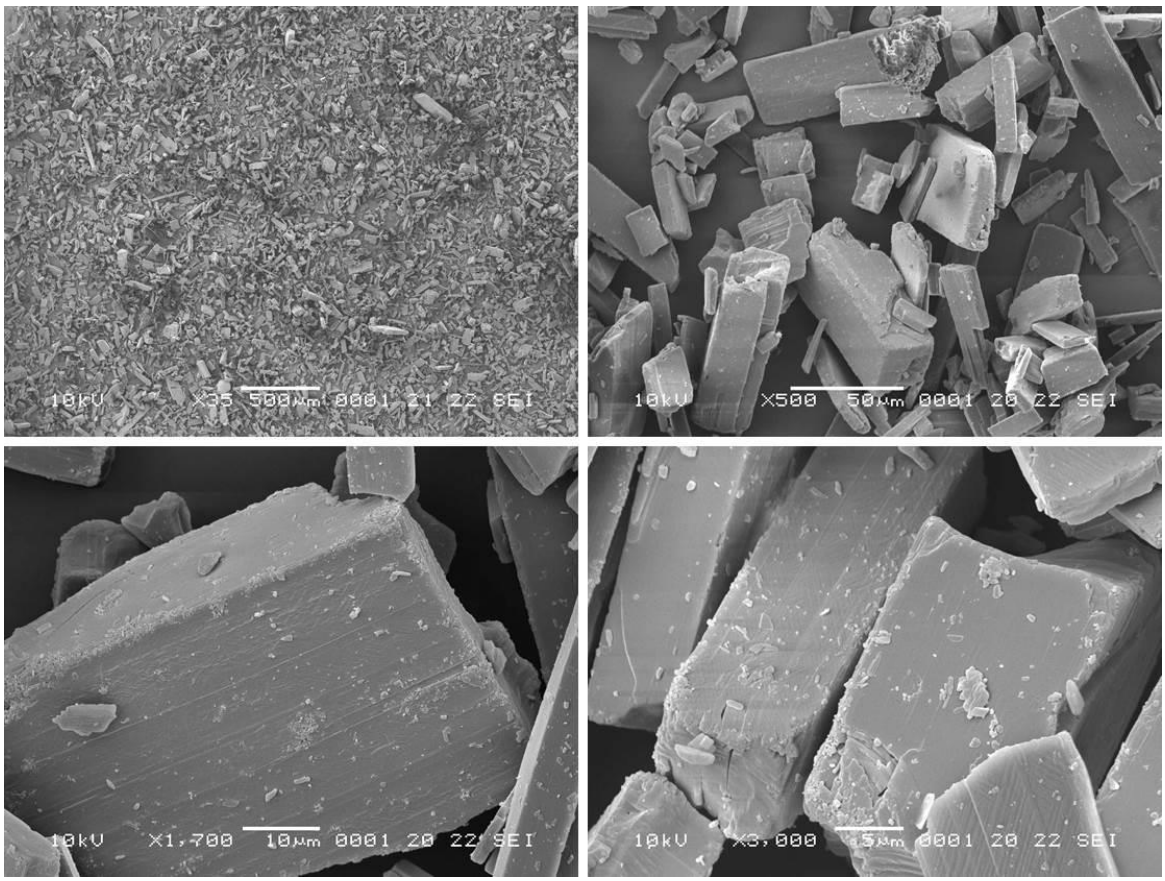

Figure 176 - SEM micrographs illustrating the results of impact tests on the CBZ:2H_2O sample crystallized in large scale (Scirocco disperser, 1 bar of dispersion pressure).

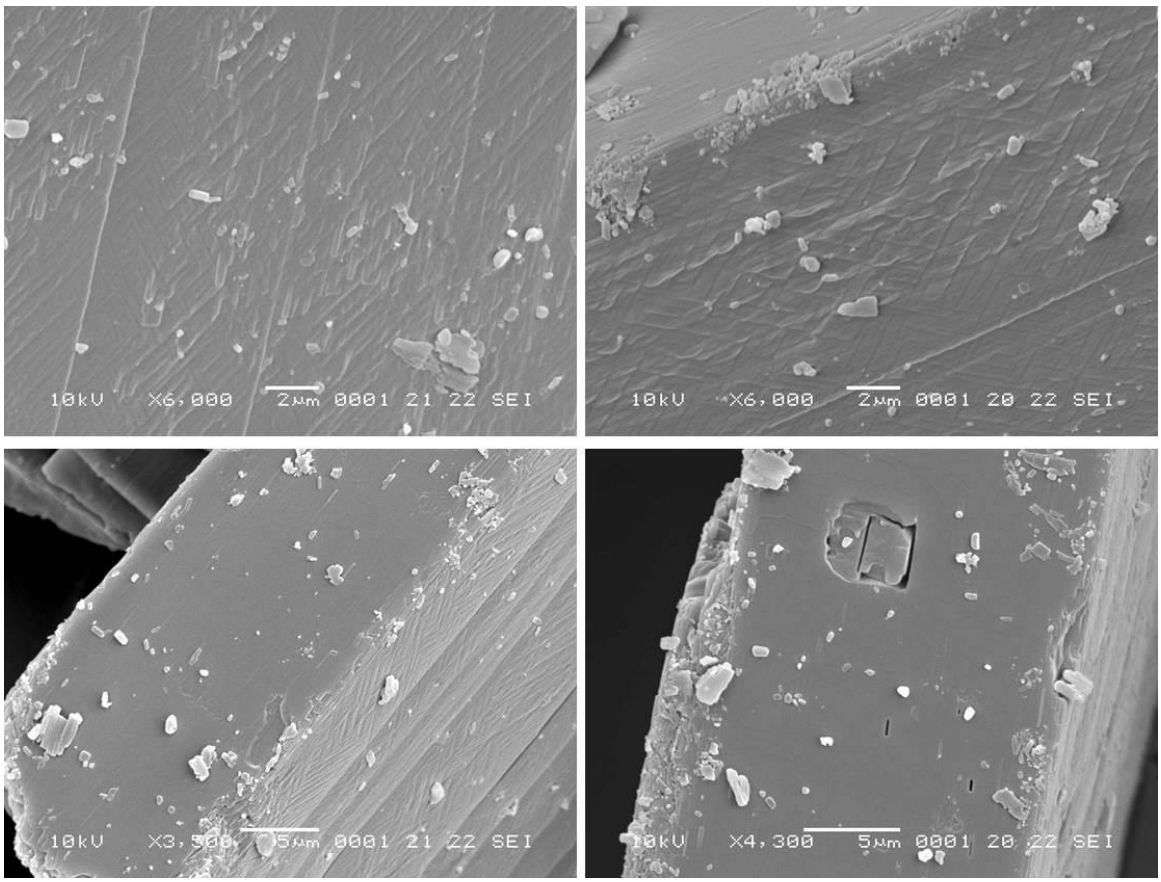

Figure 177 - SEM micrographs illustrating the effect of the impact tests on the surfaces of CBZ:2H_2O sample crystallized in large scale (Scirocco disperser, different dispersion pressures).

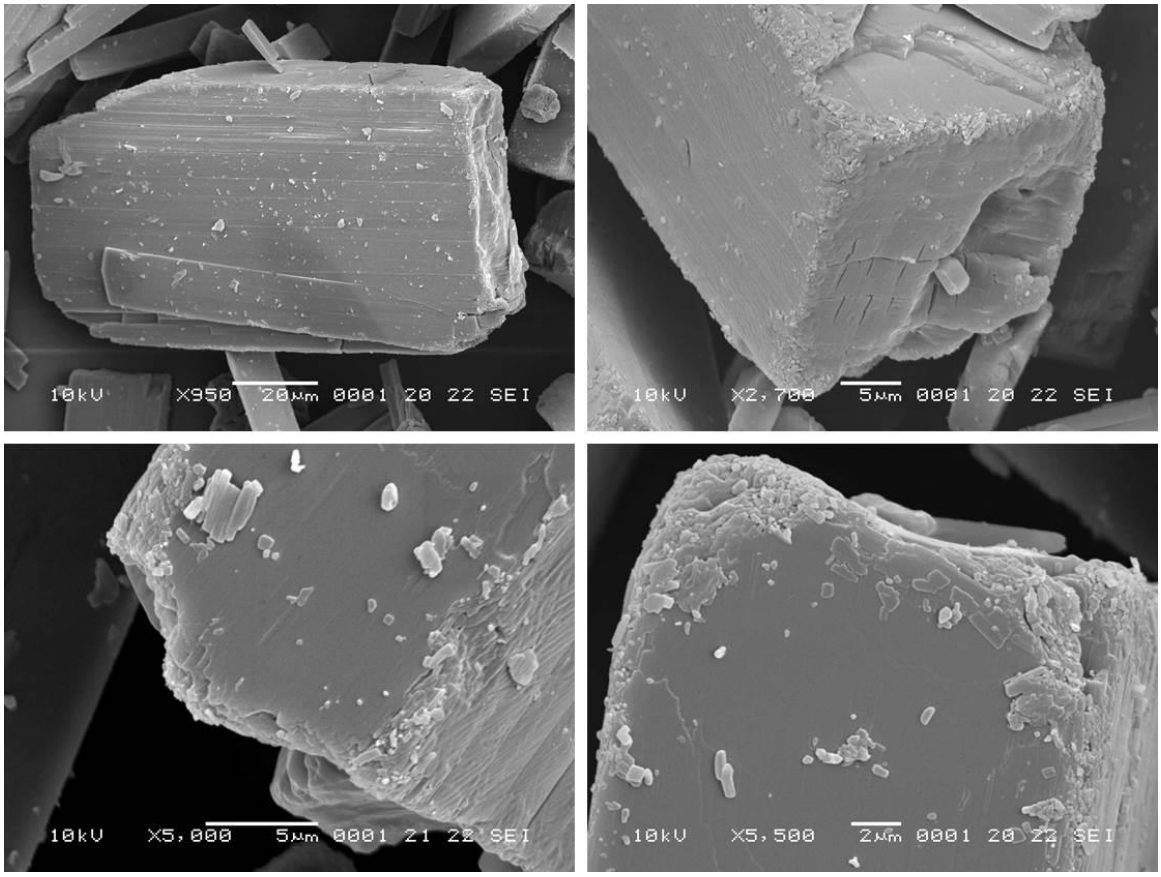

Figure 178 - SEM micrographs illustrating the effect of the impact tests on the extremity of the CBZ:2H_2O crystals prepared in large scale (Scirocco disperser, different dispersion pressures).

As a result of cleavage, new (0k0) and (00l) surfaces are generated. Figure 177 and Figure 178 compare the crystal surfaces of the fresh samples to the samples after the Scirocco impact test. It demonstrates that the new (00l) surfaces are, in general, rougher and more irregular than the sliced (0k0) surfaces. The surface features found on the (0k0) face after breakage are steps and, occasionally, holes. While the split of the crystals may generate the pattern of steps on (0k0), eventual holes on the surface can be correlated to the strain caused from the compression of the particle. It is suggested that the extensive texture observed on the (h00) surface also results from the strain caused by the impact, which leads to deformation as a way of releasing the stress.

6.5. Conclusions

The methodology selected to produce CBZ:2H_2O crystals at large scale involved anti-solvent addition and the use of "wet" seeds. Although laboratory scale samples prepared by antisolvent addition combined to stirring, high proportion of water in ethanol and "dry" seeds had provided needles with no dominant face, the comparable large-scale experiments resulted in crystals with an (h00) dominant face. In general, the experiments performed in Chapter 4 have shown that high ethanol proportions in water lead to crystals with (h00) as the dominant face, while high water proportions in ethanol tend to give crystals with (0k0) dominant. In the scaled-up processes, however, different procedures may have kinetically affected the crystallization of CBZ:2H_2O, especially the nature of the seeds.

The laboratory and scaled-up methods that use agitation during crystallization, have decreased the aspect ratio of the crystals. The generation of seeds via wet milling, however, seems to be more efficient in reducing growth along the needle axis. Another aspect that was common in the product obtained from both methods was the thickness of the particles.

It is suggested that the combination of thin crystals and (h00) preferred face results in the observed particle breakage of the materials. The fresh CBZ:2H_2O crystals have shown significant chipping and cracking along the corresponding (0k0) and (00l) crystallographic planes. The impact tests, in turn, have demonstrated particle breakage mostly on the (0k0) and (00l), but also on (h00) planes. It is noteworthy that the characterization of laboratory scale samples (fresh and dehydrated) suggest that the main cleavage planes are the (0k0).

The results illustrate how the translation of laboratory-scale studies to manufacturing is not as straightforward as an academic may experience. Figure 179 shows the crystals prepared in the final 9-kg scale batch of CBZ:2H_2O. It demonstrates that particle breakage and surface defects are common results from processing. In the case of labile materials,

such as hydrates, solvates and metastable polymorphs, these defects may play a role in solid-state physical transformations affecting the product. Additionally, quality assurance and toxicity may also be considered in the manufacturing of drugs. Therefore, CBZ:2H_2O has shown to be a very interesting model to test strategies used to balance varied issues, such as the crystal's aspect ratio and morphology, the thickness of the particles, the different characteristics of the crystal surfaces, the poor mechanical properties of the materials, the stability of the dihydrate, the potency and toxicity of CBZ. It has provided a big challenge to all the parts involved in the project, and the author would like to acknowledge the efforts from the engineers involved in the large-scale crystallization (AbbVie Inc.) and the importance of the mechanical behaviour assessment and particle attrition studies being performed in the University of Leeds. From an academic perspective, it is rewarding to be part of such a collaborative learning process and to contribute with the basic chemistry and structural analyses of the materials.

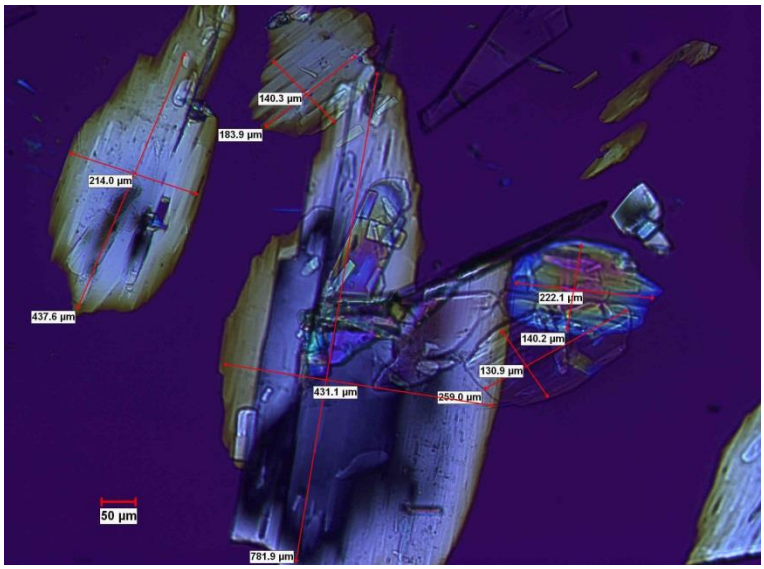

Figure 179- Optical micrographs of the CBZ:2H_2O sample crystallized in a 9-kg scale (polarized light). Methodology: anti-solvent addition combined to *in situ* seed generation; 20:80 (v:v) of final ethanol:water proportion; supersaturation degree of 1.14.

CHAPTER 7 - Further studies of carbamazepine solvates and carbamazepine cocrystals

7.1. Introduction

The literature and the structure analyses reported in Chapters 1 and 3 suggest that CBZ molecules act as rigid building blocks connected in very specific frameworks which are highly influenced by stacking. Therefore, CBZ forms stable host lattices that accommodate a variety of other included molecules, resulting in isostructural crystal forms. The structure similarities within the CBZ multicomponent materials studied herein lead to their classification in different groups, which aimed to facilitate the comparison of the properties of these materials. In this scenario, the previous chapters accounted for the preparation of samples and focused on the characterization of CBZ:2H_2O prepared in laboratory scale as well as in large batches. The present chapter, in turn, contemplates the characterization of the other CBZ multicomponent materials and their thermal properties. The comparison of the spectroscopic analyses and the quantitative thermal data is initially considered, while the thermal decomposition of each material is subsequently detailed. Since most of the samples decompose into CBZ Forms I or III and the literature is not very clear about their transition temperature, one section of this Chapter also provides a brief characterization of these polymorphs.

Two additional sections are devoted to supplementary experiments designed to compare CBZ:2H_2O with other CBZ multicomponent materials. In one of these sections, the effect of seeds is evaluated on the outcome of thermal decomposition of the 2:1 benzoquinone cocrystal, and the formamide and acetic acid solvates. Another section accounts for an alternative strategy of sample preparation. It involves the exchange of water for benzoquinone molecules, and vice versa, from crystals of CBZ:2H_2O and 2CBZ:BZQ which are already formed.

In summary, the main objective of the present Chapter is to investigate the thermal properties of the CBZ multicomponent forms which are useful to the discussion of the stress-induced transformations under the scope of this PhD thesis. How similar are the properties of the CBZ isostructural materials? And how dissimilar are materials classified in different groups?

7.2. Comparative IR and DSC/TGA analyses

IR spectroscopy has been used in this work as a tool to evaluate interactions and the chemical environment of the CBZ functional groups. Figure 180 to Figure 183 show the IR spectra of the materials, including CBZ:2H_2O, in comparison to the spectra of CBZ polymorphs I and III.

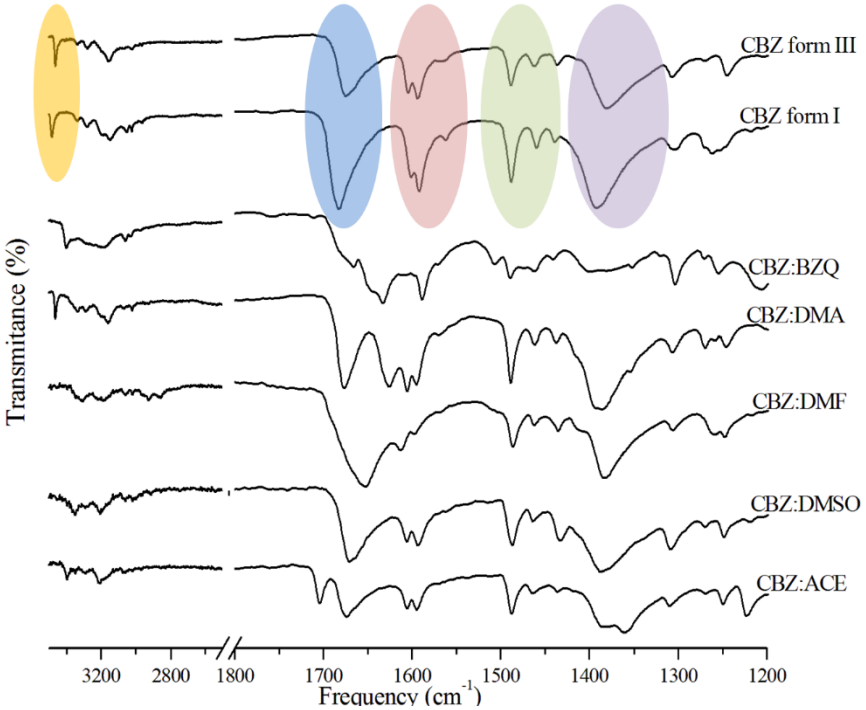

Figure 180 - IR spectra of CBZ materials classified in Groups 1 and 2 (see Chapter 3 for structure analysis). The spectra of Forms I and III are added for comparison and have specific regions highlighted.

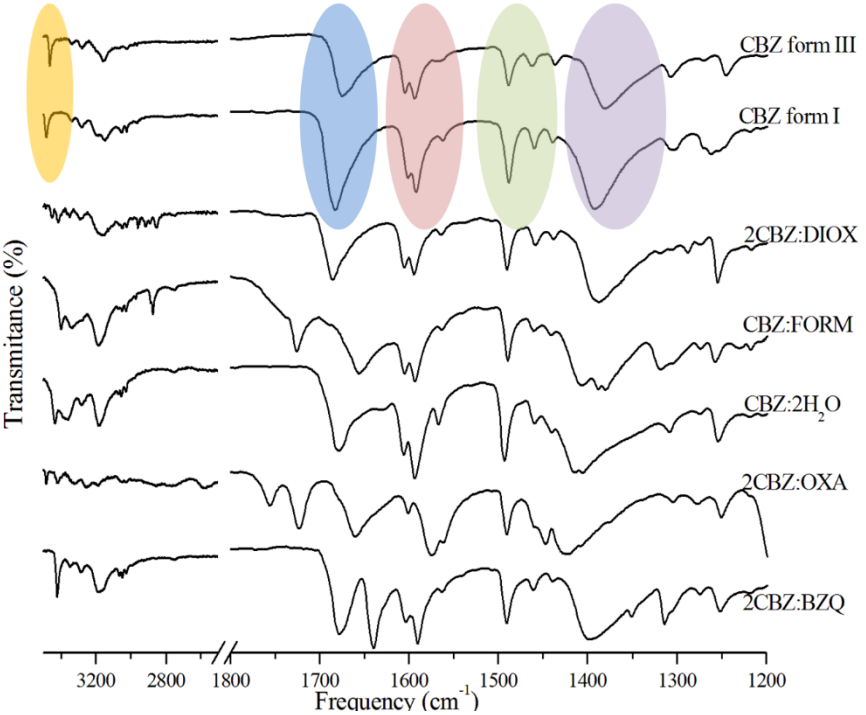

Figure 181 - IR spectra of CBZ materials classified in Group 3 (see Chapter 3 for structure analysis).

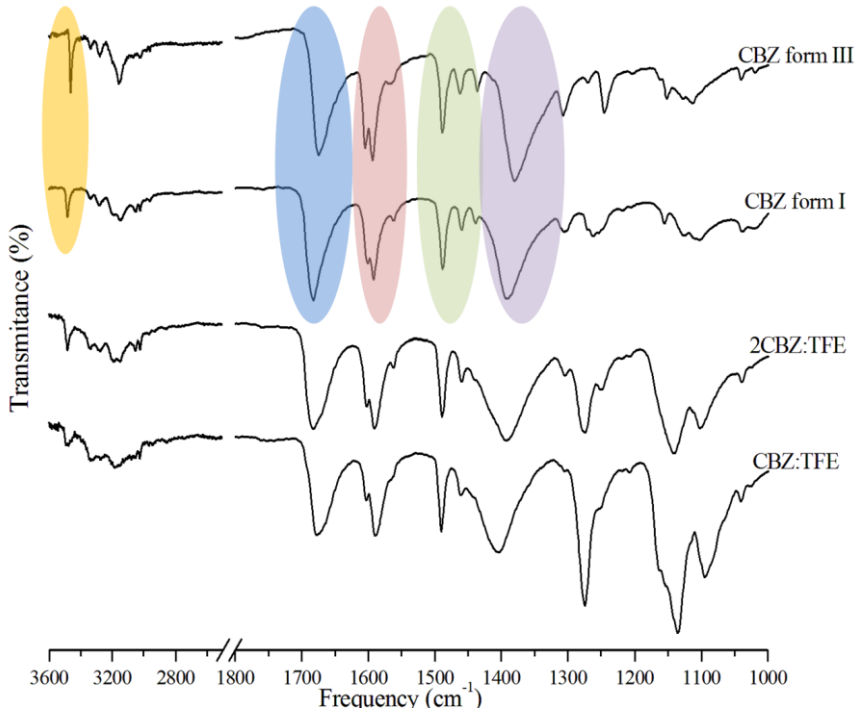

Figure 182 - IR spectra of CBZ materials classified in Group 4 (see Chapter 3 for structure analysis).

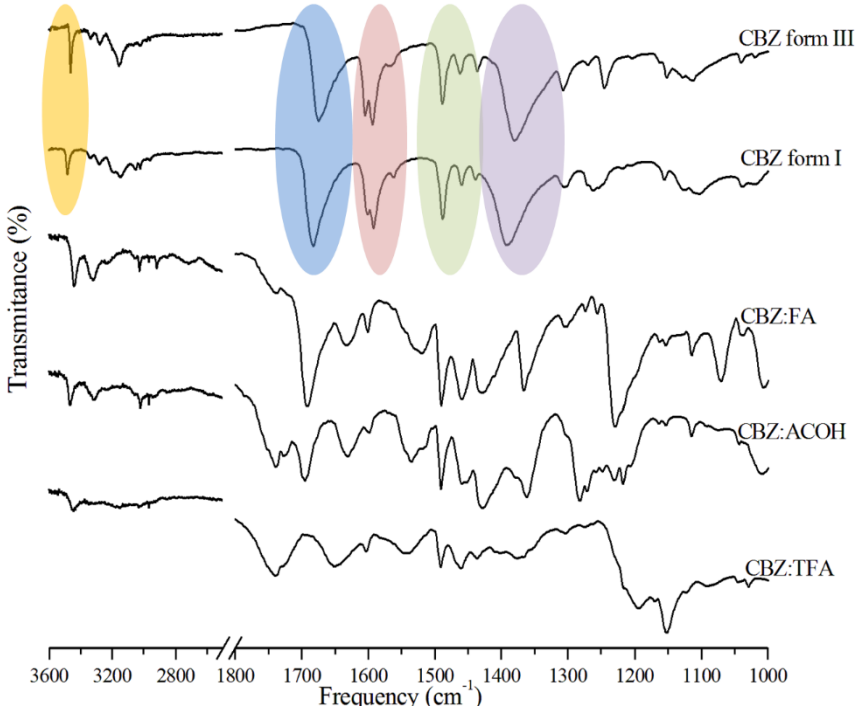

Figure 183 - IR spectra of CBZ materials classified in Group 5 (see Chapter 3 for structure analysis).

Five different regions are highlighted and attributed to specific chemical groups: (i) the N-H stretching (approximately 3500 cm^{-1}); (ii) the C=O stretching (approximately 1800-1600 cm^{-1}); (iii) the N-H bending (approximately 1650-1550 cm^{-1}); (iv) the C=C stretching (approximately 1500-1400 cm^{-1}); (v) the C-N stretching (approximately 1450-1300 cm^{-1}). Only minor differences are seen in the frequencies of vibration of CBZ Forms I and III. In the case

of the spectra of the multicomponent materials, the changes are generally related to the incorporation of the guest molecule in the lattice.

The materials classified in Group 1 present similar spectra. The stretch bands of the CBZ carbonyls in CBZ:ACE, CBZ:DMSO and CBZ:DMF are shifted to lower frequencies while the region around 3500 cm^{-1} shows broad and weak peaks, demonstrating that the amide group is hydrogen bonded. It is noteworthy that CBZ:ACE shows one additional C=O stretching band in higher frequencies than the CBZ carbonyl, which is attributed to the carbonyl of the acetone molecule. In the case of CBZ:DMF, the carbonyl of DMF is suggested to stretch in similar IR frequencies as the CBZ carbonyl, which results in one single but broad peak ranging from approximately 1750-1550 cm^{-1}, which also seems to superposed the N-H bending band. It is also suggested that this broad band reflects the additional hydrogen bonds between neighbouring DMF molecules in this solvate.

The structures classified in Group 2 also present similar spectra, although CBZ:BZQ shows broader peaks than CBZ:DMA. In both materials, additional peaks related to the carbonyl stretching of BZQ and DMA are located in between the C=O stretch and the N-H bending of CBZ. Similarly to what was observed in the spectra of Group 1, the C=O and N-H stretch bands from CBZ:BZQ and CBZ:DMA are also shown to be involved in hydrogen bonds. In this case, the peaks of both materials are shifted to lower frequencies than CBZ, although the shift is larger in CBZ:BZQ.

In comparison to CBZ:BZQ, the 2:1 cocrystal shows sharper peaks, which reflect differences in the vibration mode of the molecules and may illustrate the differences in the chemical environment of the BZQ carbonyls in the structures. Although in the case of 2CBZ:BZQ both carbonyls are hydrogen bonded to the same species, the BZQ molecules in the 1:1 cocrystal show carbonyls that interact to different groups.

The same analyses may explain why, in general, the structures classified in Group 3 show a wider variety of chemical shifts. Although not very clear in the N-H stretch region, the stretch bands of CBZ carbonyls show three different behaviours: (i) CBZ:DIOX shows a very minor blueshift; (ii) 2CBZ:BZQ and CBZ:2H_2O show minor redshift; and (iii) 2CBZ:OXA and CBZ:FORM show a considerable redshift. These results may be correlated to the nature of the interactions in the materials. While there is one only type of CBZ carbonyls in CBZ:DIOX, 2CBZ:BZQ and CBZ:2H_2O, there are two different types of CBZ carbonyls in 2CBZ:OXA and CBZ:FORM. This characteristic is also shown on the aspect of the C=O stretching bands of OXA and FORM as the structures also present two different types of carbonyls in molecules of OXA and FORM (bands above 1700 cm^{-1}). Interestingly, in the case of 2CBZ:OXA, the bands

related to the N-H bending are also significantly shifted to lower frequencies, which is not usually seen in the other CBZ multicomponent materials.

The comparison of the IR spectra of the materials in Group 4 (TFE solvates) to the CBZ polymorphs, show very minor differences, except for the presence of O-H bending bands (1300-1200 cm^{-1}) and C-F stretching bands (1300-1000 cm^{-1}). On the contrary, the materials classified in Group 5 show markedly different IR spectra, in comparison to the polymorphs but also to the other multicomponent forms. Starting from CBZ:FA, to CBZ:ACA and then to CBZ:TFA, it is clear that the CBZ carbonyl shifts to higher frequencies. In this case, while only a minor shift is seen in CBZ:FA, a significant shift is seen in CBZ:TFA, which leads to the superposition of the CBZ and TFA carbonyls. Also, the N-H bending bands of these materials change substantially and are also blueshifted. These findings are correlated to the interactions of CBZ and the solvent molecules in Group 5. While in the CBZ polymorphs I and III, and in the other multicomponent groups a CBZ molecule always forms a homodimer with other CBZ molecule, in Group 5 CBZ forms a heterodimer with the solvent. In this case, the hydrogen bonds change substantially because the interactions are not amide-amide anymore, but amide-carboxylic acid.

Interestingly, the literature has also suggested that the interaction of CBZ and TFA holds an intermediate ionic character. Eberlin, Eddleston & Frampton[199] report that CBZ:TFA solvate is best represented as a salt with the acidic proton located at the mid-point between the CBZ carbonyl and the TFA hydroxyl. Therefore, the shift of the C=O stretch band of CBZ:TFA to higher frequencies agrees with the literature. It also suggests that CBZ:FA and CBZ:ACA possibly present the proton in an intermediate position, while this characteristic may not be as significantly as in the case of the TFA solvate.

Although the IR spectra have shown correlations with the structural aspects of the CBZ multicomponent materials and the classification adopted in this work, the quantitative analyses of the thermal data have not demonstrated the same behaviour (Table 13). In general, no strong correlation was observed between the onset or the enthalpy of decomposition with the characteristics of the multicomponent forms such as packing similarities, solubility, strength of interactions and cavity volume. The only correlation was seen in Group 5, in which the onset of desolvation (and perhaps its enthalpy) seems to be related to the strength of the interactions between CBZ and coformer (shown by the analyses of the crystallographic data, but also by IR spectroscopy).

No correlation was stablished between thermal decomposition and the physical parameters of the guest molecules, such as their boiling points or sublimation temperatures, vapour pressure, viscosity, surface tension, heat of vaporization, dielectric constant and dipole

moment. This lack of apparent correlation may tell us that the onset of decomposition is influenced by a variety of factors, which are hard to interpret. Differences in particle size, however, may also affect the results. This is a difficult aspect to address when working with labile materials as comminution is usually avoided because it may introduce defects and promote an early decomposition, which can also affect the results.

Table 13 - Quantitative data obtained from thermal analyses of CBZ multicomponent materials[1].

Material	Decomposition			
	T_{onset} (°C)	T_{peak} (°C)	ΔH (kJ.mol^{-1})	Weight loss (wt%)
CBZ:ACE	79.8±2.9	87.3±4.2	48.7±1.7	19.6±0.4
CBZ:DMSO	100.8±1.1	106.7±1.3	56.8±1.2	24.6±0.3
CBZ:DMF	77.1±0.3	80.2±0.1	53.9±0.9	23.2±0.4
CBZ:DMA	76.6±2.0	79.5±4.5	62.5±1.4	26.8±1.4
CBZ:BZQ	146.2±13.6	159.9±9.2	82.5±4.0	31.3±0.3
2CBZ:BZQ	155.1±12.6	167.3±2.8	93.2±3.6	18.7±0.1
2CBZ:OXA[2]	156.3±1.4	160.2±0.6	58.8±0.8	-
CBZ:2H_2O (0k0) sample	66.1±0.2	75.7±1.7	78.3±2.3	13.2±0.1
CBZ:2H_2O (h00) sample	85.8±0.1	92.4±0.2	81.2±0.5	13.0±0.3
CBZ:FORM	144.5±0.1	147.3±1.8	50.7±3.8	16.9±0.4
2CBZ:DIOX	91.7±1.2	98.7±1.1	48.6±1.2	15.1±0.7
CBZ:TFE	68.4±0.7	78.1±1.0	51.0±1.7	29.7±0.4
2CBZ:TFE	97.2±0.4	108.1±3.4	50.9±0.1	16.9±0.1
CBZ:TFA[2]	128.4±2.0	134.2±0.1	104.8±1.0	-
CBZ:TFA[3]	120.5±5.2	124.8±0.7	72.6±0.7	33.0±0.9
CBZ:ACA	125.6±0.2	139.6±0.1	63.3±3.9	21.1±0.8
CBZ:FA	119.0±0.1	124.8±1.1	57.1±0.4	16.3±0.2

[1] DSC: 10 °C.min^{-1}, perforated lid, N_2; TGA: 10 °C.min^{-1}, open pan, N_2.
[2] Event occurs simultaneously to the chemical decomposition of CBZ.
[3] DSC: 1 °C.min^{-1}, perforated lid, N_2; TGA: 1 °C.min^{-1}, open pan, N_2.

Alternatively, Table 14 shows the vaporization enthalpy in kJ.mol^{-1} per formula unit of some of the CBZ multicomponent materials, while Figure 184 graphics the results. In general, it is seen that the experimental vaporization enthalpy tends to be lower than the calculated values. Interestingly, the difference between the calculated and experimental values obtained for CBZ:BZQ and 2CBZ:BZQ is significantly smaller in comparison to the CBZ solvates. CBZ:2H_2O and CBZ:FORM, in turn, show a greater difference amongst the results. It is suggested that these features are correlated to the presence (or not) of concomitant events during the vaporization of the guest molecules.

Concurrent reactions may considerably affect the enthalpy obtained from DSC data. Because of the nature of this transformation, decomposition frequently occurs with simultaneous events. In general, these events correspond to the release of one chemical entity and the recrystallization of the remaining host lattice, however, there is also the possibility that chemical decomposition and peritectic melting simultaneously occur. These simultaneous

events are difficult to avoid and suggest that the thermal curves need to be specifically and qualitatively analysed to have a better understanding of the thermal behaviour of the CBZ multicomponent materials.

Table 14 - Calculated vaporization enthalpies for the decomposition of multicomponent materials into different CBZ polymorphs.[a]

Crystal form	Vaporization enthalpy per formula unit ($kJ.mol^{-1}$)				
	Form I	Form II	Form III	Form IV	Form V
CBZ:ACE	66.4	70.6	60.0	65.5	67.5
CBZ:DMSO[b]	75.4	79.5	69.0	74.5	76.5
CBZ:DMF	79.5	83.7	73.1	78.6	80.6
CBZ:DMA	90.1	94.2	83.7	89.2	91.2
CBZ:BZQ	90.9	95.0	84.5	90.0	92.0
2CBZ:BZQ	100.2	108.5	87.4	98.3	102.4
2CBZ:OXA	141.3	149.6	128.5	139.5	143.5
CBZ:$2H_2O$	149.4	153.6	143.0	148.5	150.5
CBZ:FORM	92.8	97.0	86.4	91.9	93.9
CBZ:TFA	100.6	104.7	94.2	99.7	101.7
CBZ:ACA	84.0	88.1	77.6	83.1	85.1
CBZ:FA	81.3	85.4	74.9	80.4	82.4

[a] No calculations were performed for 2CBZ:DIOX, CBZ:TFE and 2CBZ:TFE due to complications related to the disorder of the solvent molecules.
[b] Calculated from UNEYIV01.

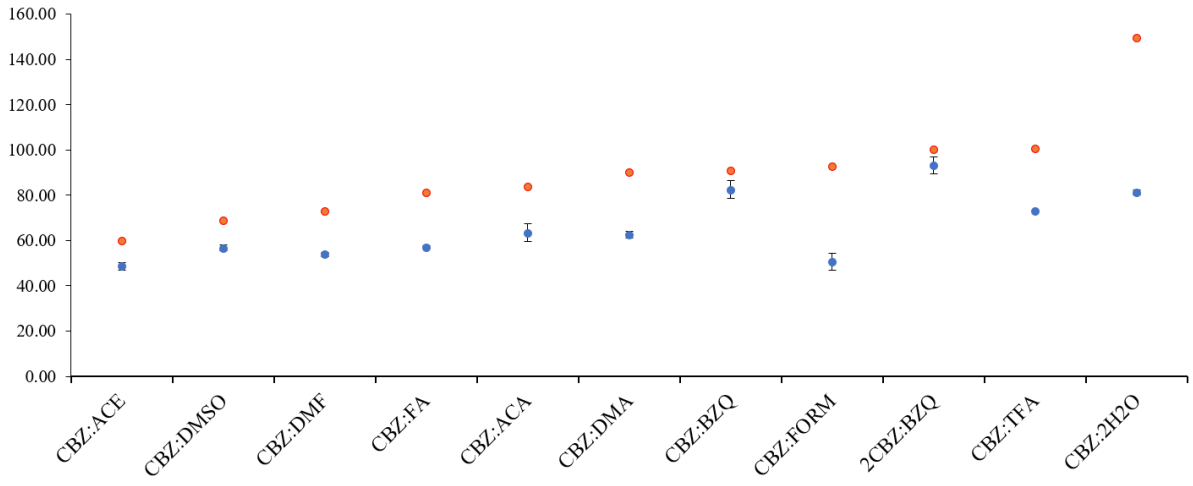

Figure 184 - Comparison of the calculated vaporization enthalpies (red circles) with the experimental decomposition enthalpies (blue circles) of a few CBZ multicomponent materials. The graph is plotted in regard to the polymorphic outcome experimentally obtained and discussed in the next Sections. The *x* axis classifies the materials in an increasing order of enthalpy ($kJ.mol^{-1}$, *y* axis).

7.3. The thermal decomposition

7.3.1. CBZ polymorphs I and III

The single crystals of CBZ polymorph I melt at about 190 ^{o}C and no other transformation is seen by optical microscopy during heating (Figure 185). The single crystals of polymorph III, in turn, show additional events taking place at about140 ^{o}C (Figure 186 and Figure 187). Interestingly, these events appeared to be different depending on the particle size. In the case of big particles of Form III, the crystals start fracturing above 145 ^{o}C, while small particles show the formation of whiskers on the surface of the crystals. This transformation corresponds to the conversion of Form III into Form I, which is the most stable form at high temperatures. It is unclear whether these findings show that the mechanism of transformation is dependent on particle size, or if defects on the surface of small crystals may catalyse the growth of whiskers. In other words, it may indicate that CBZ molecules sublime at high temperatures and recrystallize on the surface of the crystals of Form I, showing the characteristic whiskers. The literature has reported the formation of whiskers,[113,153] however, to the best of my knowledge, no fractures during the transformation have been previously reported.

These findings agree with the thermograms in Figure 188 and Figure 189. The TGA analyses of CBZ polymorphs I and III show two events of weight loss above 200 ^{o}C (experiments performed at 10 ^{o}C.min^{-1}). Just before the chemical decomposition of CBZ, the DSC curves of both polymorphs show one endotherm corresponding to melting at about 190 ^{o}C. The fusion event is equivalent in both samples, Form I and Form III, and it characterizes the fusion of polymorph I (T_{onset}=189.3 ^{o}C, T_{peak}=190.7 ^{o}C, ΔH_{fusion}=114.88 kJ.g^{-1}; and T_{onset}=188.9 ^{o}C, T_{peak}= 190.4 ^{o}C, ΔH_{fusion}=119.3 kJ.g^{-1}, respectively). Similarly to the results obtained from *in situ* optical microscopy, the DSC analyses show that Form III converts into Form I with heating. In this case, the heat flow curves of Form III show a small endothermic event at around 150 ^{o}C, which is correlated to the polymorphic transition.

As discussed in Chapter 1, although it is well accepted in the literature that Form I is the most stable polymorph at high temperatures,[45,46] the exact temperature of the transition from polymorph III to polymorph I is uncertain.[136,137,145,173,174] Aiming to test the transition temperatures described in previous studies, slurries of Form I or Form III were prepared in 1-butanol at 25 ^{o}C, 80 ^{o}C and 120 ^{o}C (reflux). 1-butanol was selected as a solvent because it does not form a solvate with CBZ and it has high boiling point. The slurries were equilibrated for 72 hours, filtered and the solids were analysed by PXRD. Figure 190 illustrates the *ex situ* PXRD patterns of the samples after slurrying and shows that all the samples converted to Form III

(minor quantities of Form II are detected in some experiments). These results show that Form III converts into Form I at temperatures above 120 ºC. Although the literature has demonstrated that the transition temperature in crushed and uncrushed CBZ Form III does not change, it was already described that heating rate affect the transition temperature.[145] It suggests that kinetics may play a role in the conversion of Form III into Form I and, in the present author's opinion, particle size, defects and sample size may affect the process as these factors may change the heat propagation.

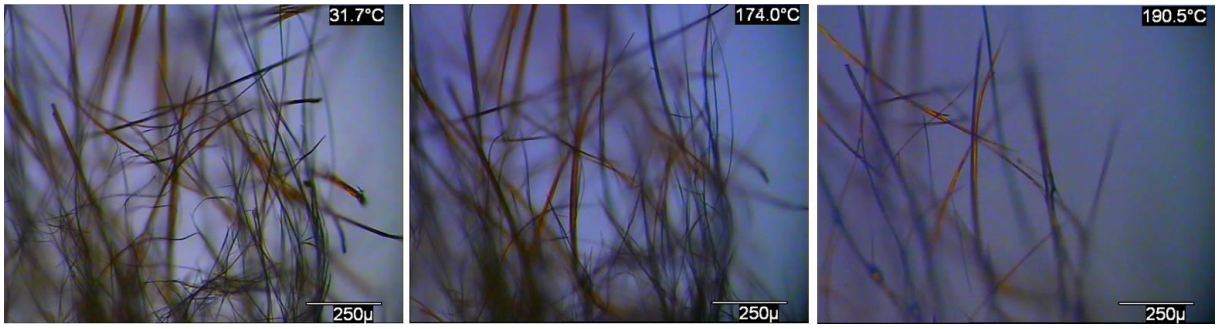

Figure 185 - Optical micrographs of CBZ Form I crystals at different temperatures under polarized light (heating rate of 10 ºC.min^{-1}).

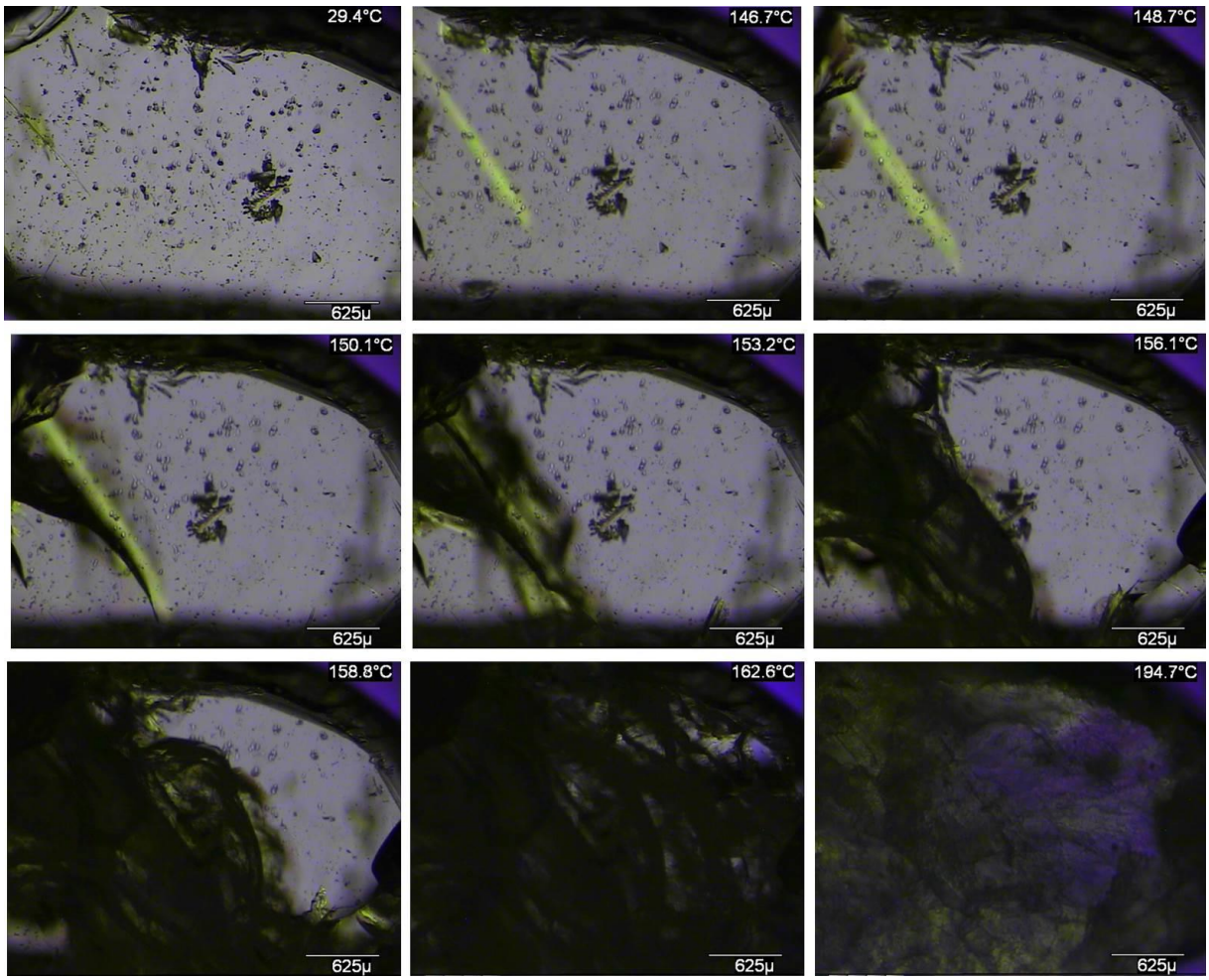

Figure 186 - Optical micrographs of CBZ Form III big crystals at different temperatures under polarized light (heating rate of 10 ºC.min^{-1}).

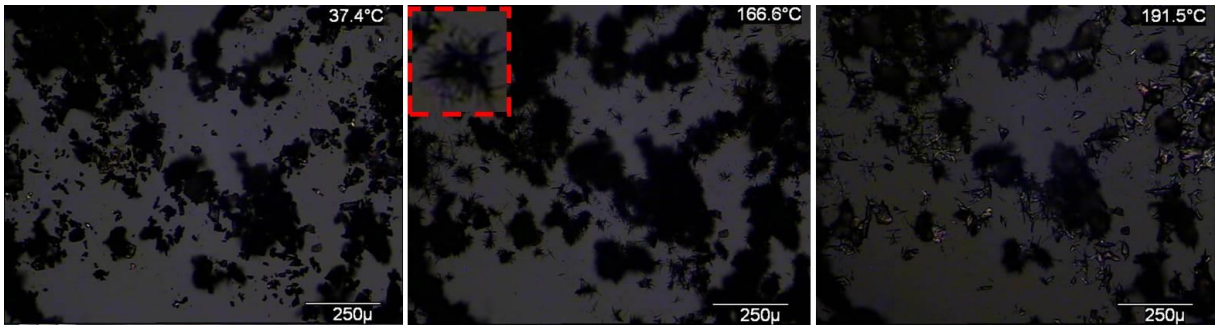

Figure 187 - Optical micrographs of CBZ Form III small crystals at different temperatures under polarized light (heating rate of 10 $^{o}C.min^{-1}$). The detail is a zoomed area showing the whiskers.

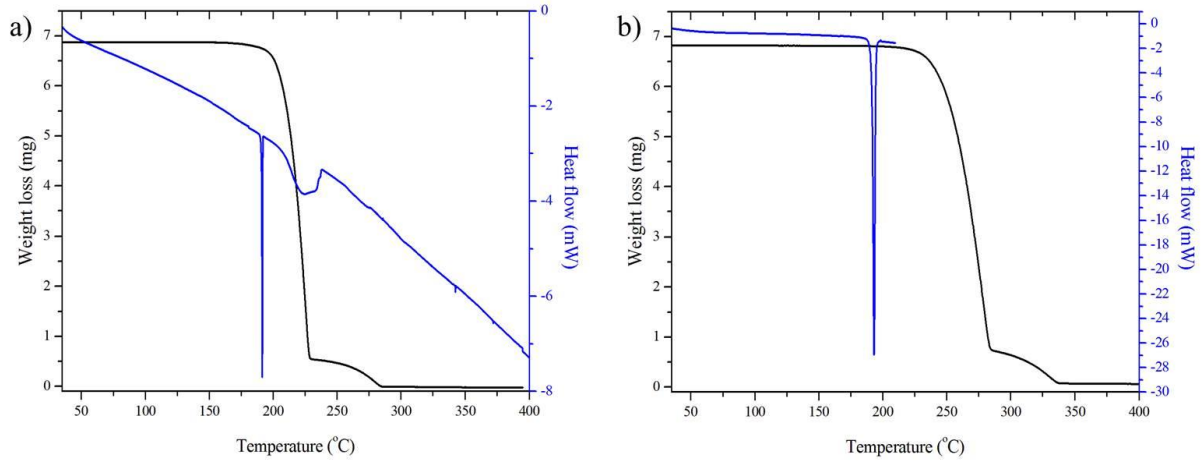

Figure 188 - DSC and TGA thermal characterisation of CBZ Form I. *a:* 1 $^{o}C.min^{-1}$, perforated lid, N_2. *b*: 10 $^{o}C.min^{-1}$, perforated lid, N_2.

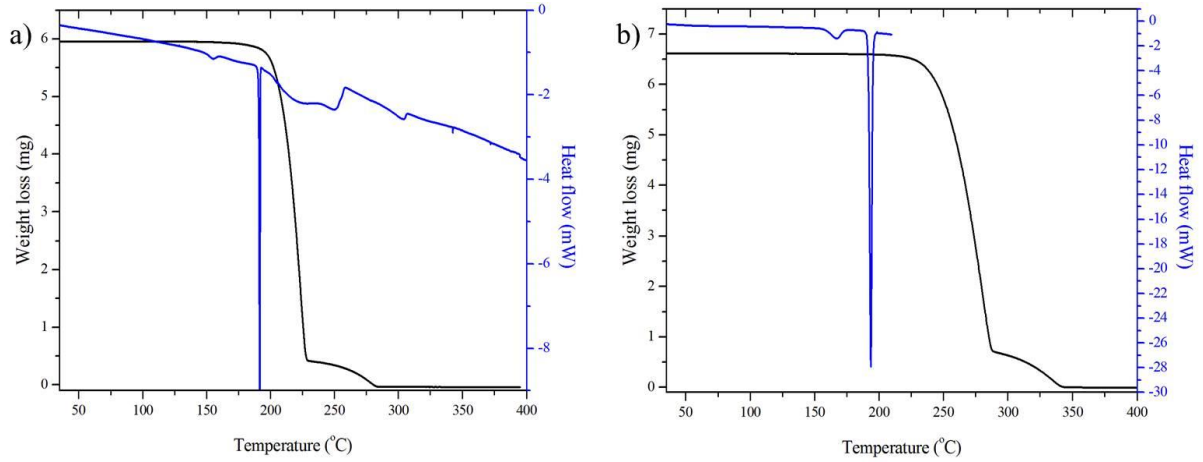

Figure 189 - DSC and TGA thermal characterisation of CBZ Form III. *a:* 1 $^{o}C.min^{-1}$, perforated lid, N_2. *b*: 10 $^{o}C.min^{-1}$, perforated lid, N_2.

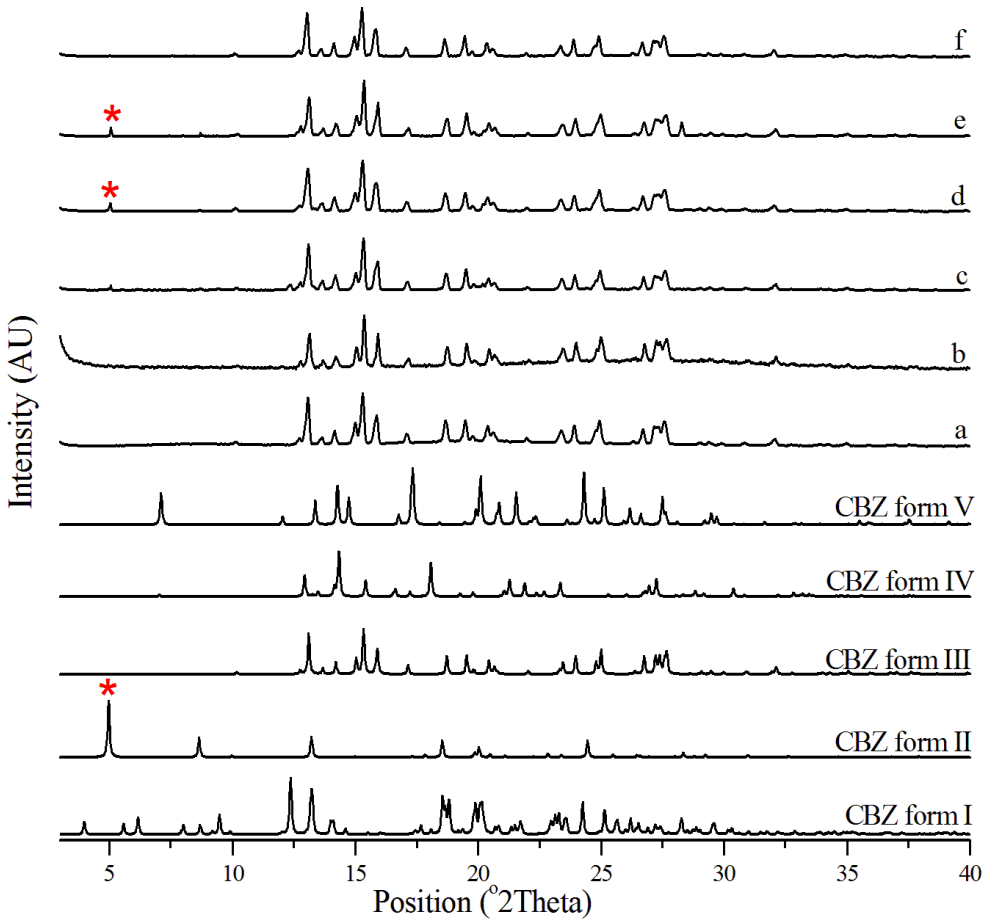

Figure 190 - PXRD patterns of the CBZ samples subjected to slurrying in 1-butanol at different temperatures for 72 hours. The starting material in *a*, *c*, and *e* was polymorph I, and the experimental temperatures were 25, 80 and 120 ºC, respectively. The starting material in *b*, *d*, and *f* was polymorph III, and the experimental temperatures were 25, 80 and 120 ºC, respectively. The calculated patterns of CBZ anhydrous polymorphs I, II, III, IV and V are added for comparison, and peaks of Form II are highlighted.

7.3.2. CBZ acetone solvate (CBZ:ACE), Group 1

Single crystals of CBZ:ACE turn opaque with heating while the original shape of the particles is maintained. Figure 191 shows the crystals lose birefringence in the range 55-75 ºC without marked formation of whiskers above 140 ºC. These findings agree with the thermograms in Figure 192. In this case, the TGA curve shows one single weight loss ending at about 100 ºC and the heat flow curve demonstrates that the desolvation is characterized by a relatively sharp endothermic event (T_{onset}=79.8 ºC). Additional endotherms are also seen before the characteristic melting of CBZ Form I, which occurs above 190 ºC. The endothermic events in the range 160-180 ºC can be correlated to the transition of Form III to Form I, while the endothermic event starting at about 185 ºC resembles the melting of Form III that has been described in the literature.[145,174]

It is noteworthy that the melting of Form III was not observable in every DSC experiment of CBZ:ACE. In the case of small crystals, only the solid-state transition of Form

III to Form I is detected. It is suggested that CBZ:ACE desolvates to polymorph III, which may convert to polymorph I at higher temperatures. In larger crystals, this transformation is sometimes not complete when the melting temperature of Form III is reached. In this case, the remaining Form III melts and recrystallizes as the triclinic polymorph just before its melting.

In situ PXRD with heating shows that the lattice gradually changes as the temperature increases, with a clear change seen above 90 ^{o}C (Figure 193). The experiments agree with the DSC data and demonstrate that the desolvation leads to polymorph III, while detectable reflections of Form I are observed above 160 ^{o}C.

Figure 194 shows *ex-situ* SEM analyses of CBZ:ACE crystals subjected to non-isothermal desolvation at 10 ^{o}C.min^{-1}. The images illustrate the formation of round domains and holes between a grain-like structure. Cracks are rarely seen, but when detected, the fractures are irregular and do not appear to be correlated to any crystallographic planes.

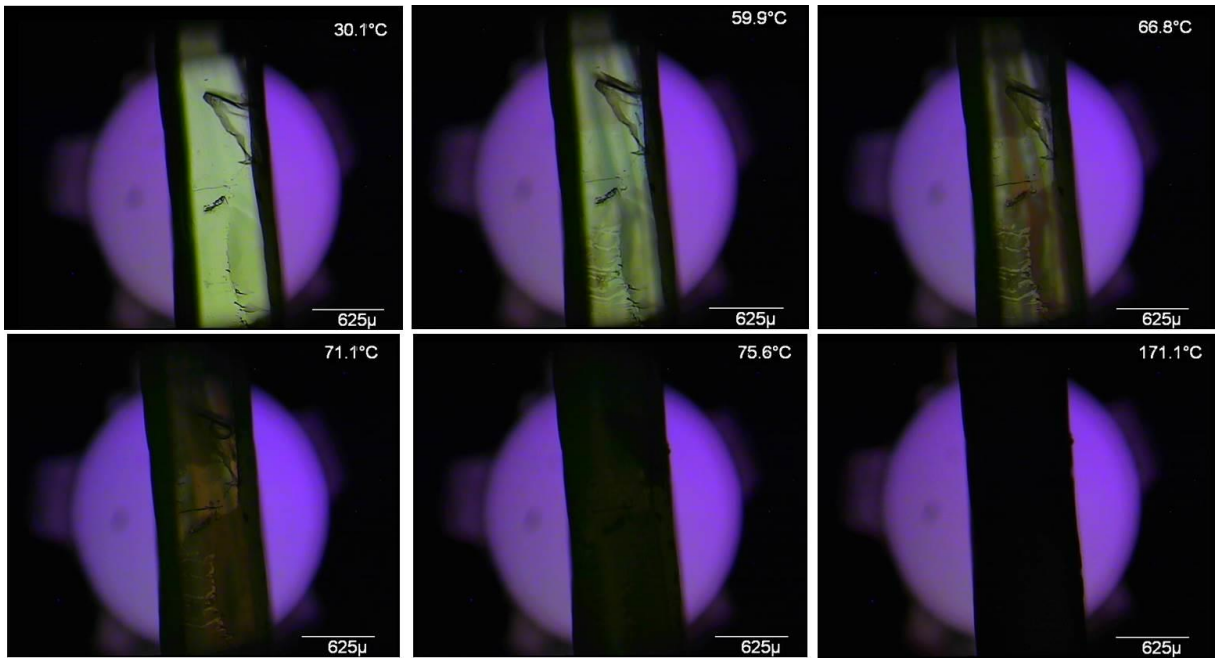

Figure 191 - Optical micrographs of CBZ:ACE crystals at different temperatures under polarized light (heating rate of 10 ^{o}C.min^{-1}).

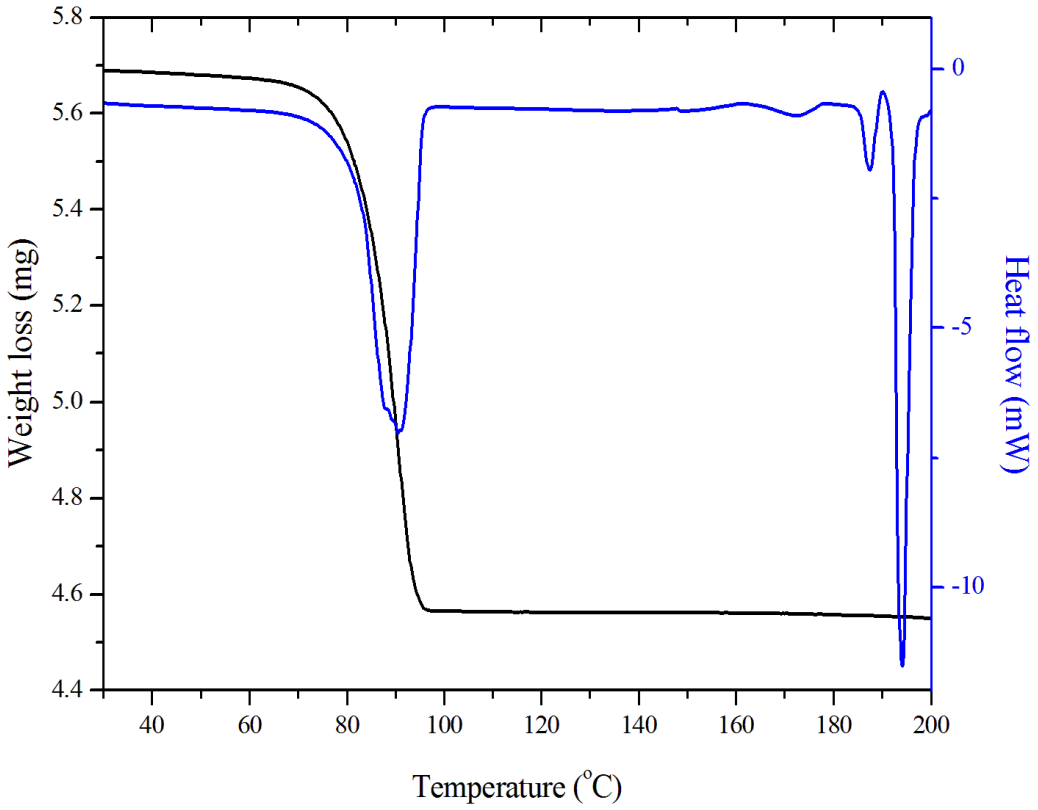

Figure 192 - DSC and TGA thermal characterization of CBZ:ACE crystals (10 °C.min^{-1},perforated lid, N_2).

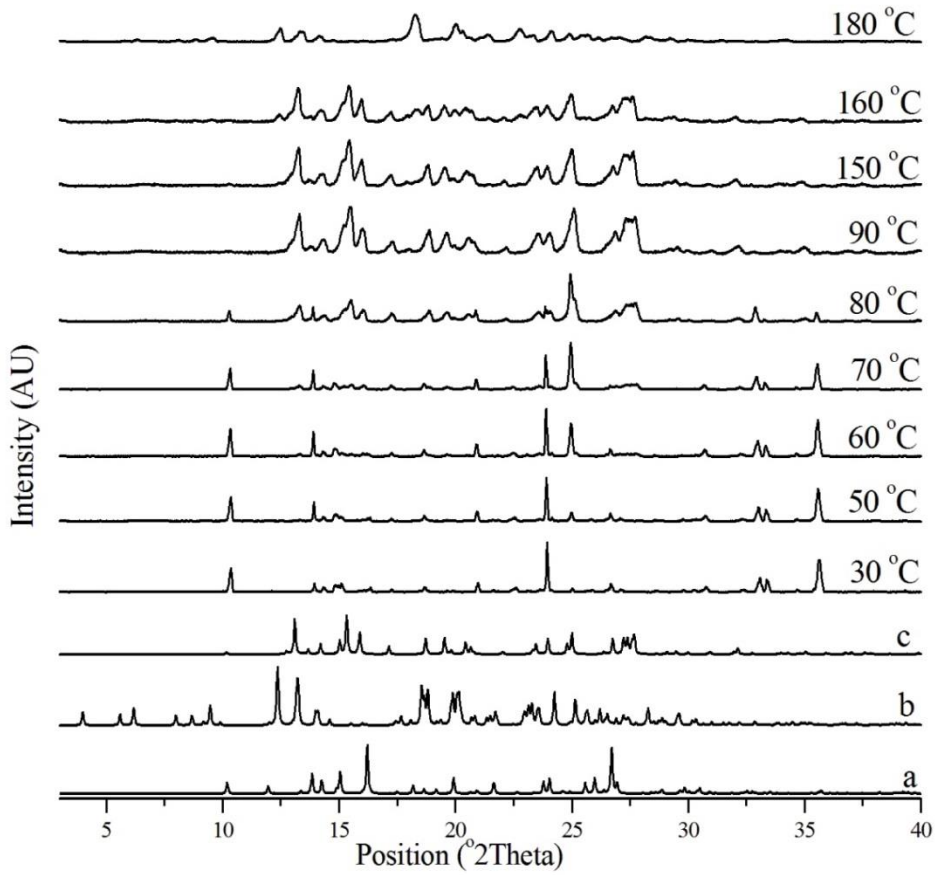

Figure 193 - *In situ* variable temperature PXRD patterns of CBZ:ACE crystals (10 °C.min^{-1}, 25-180 °C). *a*: CBZ:ACE from CRBMZA01. *b*: CBZ Form I from CBMZPN11. *c*: CBZ Form III from CBMZPN01.

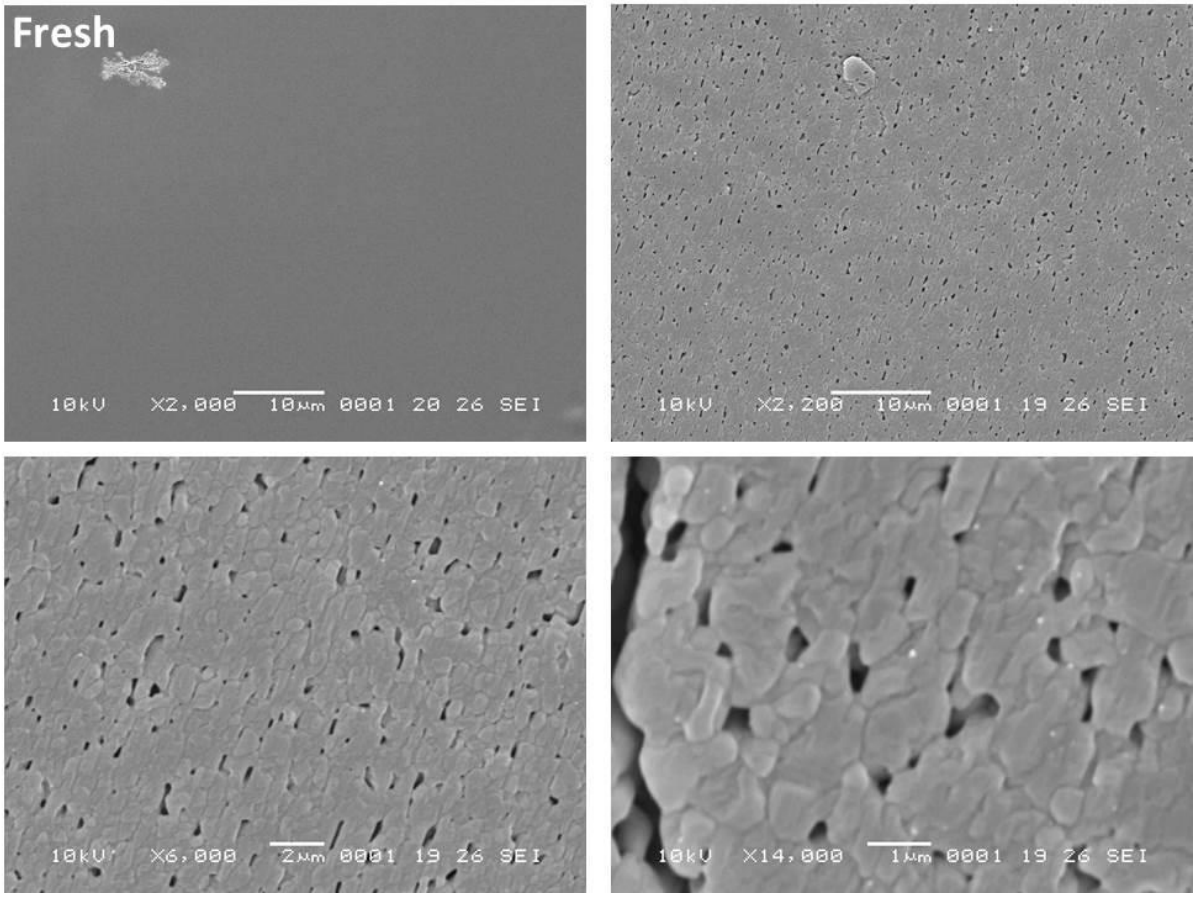

Figure 194 - SEM micrographs of CBZ:ACE crystal surfaces heated until 120 ºC under N_2 (heating rate of 10 ºC.min^{-1}). The fresh surface is added for comparison purposes.

7.3.3. CBZ dimethylsulfoxide solvate (CBZ:DMSO), Group 1.

In contrast to CBZ:2H_2O and CBZ:ACE, single crystals of CBZ:DMSO upon heating do not uniformly lose birefringence as desolvation proceeds. Figure 195 shows the development of opaque and round nuclei, which grow throughout the crystal as the temperature increases. The formation and growth of these nuclei results in the loss of the original shape of the crystals, as further illustrated by *ex-situ* SEM images of CBZ:DMSO subjected to non-isothermal desolvation at 10 ºC.min^{-1} (Figure 196). The SEM analyses show a substantial surface reorganization with the simultaneous formation of spherulites, round domains and particles on the original crystals. It is also observed that the rate of desolvation considerably affects the outcome of the transformation as experiments performed under mild conditions result in surfaces containing round domains and holes, similar to the desolvated CBZ:ACE surfaces. In the case of CBZ:DMSO, however, cracks are more frequently seen. While the fractures do not appear to be correlated to crystallographic planes in the solvate lattice, they seem to propagate along the edges of the surface of domains and through the holes.

PXRD analyses of samples subjected to isothermal desolvation at room temperature or to heating at 10 ºC.min^{-1} show that the surface variations are also correlated to

microstructural differences caused by crystal decomposition. While slow desolvation conditions result in the formation of CBZ polymorph III (Figure 197), faster desolvation leads to a more complex scenario (Figure 198). *In situ* PXRD with heating indicates reflections corresponding to Form III at 90 ^{o}C. The reflections show a gradual increase in intensity until a rapid transformation is detected at 110 ^{o}C. At this temperature, a mixture of CBZ:DMSO and polymorphs I and III are observed with the overall intensity of the reflections being low. These findings may indicate the formation of a peritectic mixture in which the solid solvate and anhydrous CBZ are mixed with liquid DMSO. It is suggested that DMSO is released from the solvate lattice and remains as a liquid within the crystal due to its high boiling point (189.0 ^{o}C). In this case it is possible that while the desolvation of CBZ:DMSO results in Form III, the recrystallization of the CBZ which had dissolved in the surrounding liquid DMSO results in Form I.

The DSC and TGA curves of the DMSO solvate collected at 10 ^{o}C.min^{-1} agree with this interpretation (Figure 199). The weight loss associated with desolvation shows varying slopes throughout the event, which may suggest different physical transformations arising from the heating of the crystals. This phenomenon is also observed in the DSC curve as the characteristics of the endothermic event of desolvation change as the temperature increases: the event begins as a sharp endotherm (T_{onset}=100.8 ^{o}C), but is followed by a broad event which lasts until about 170 ^{o}C. At approximately 175 ^{o}C, another endotherm indicates melting of Form III and recrystallization of Form I before it melts at about 190 ^{o}C.

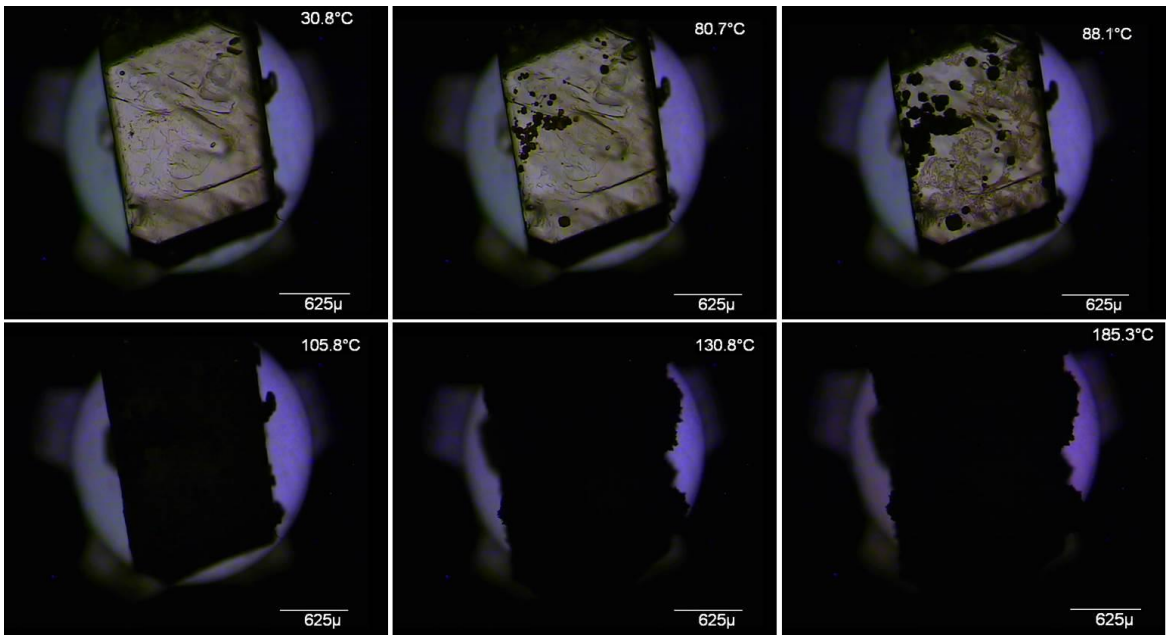

Figure 195 - Optical micrographs of CBZ:DMSO crystals at different temperatures under polarized light (heating rate of 10 ^{o}C.min^{-1}).

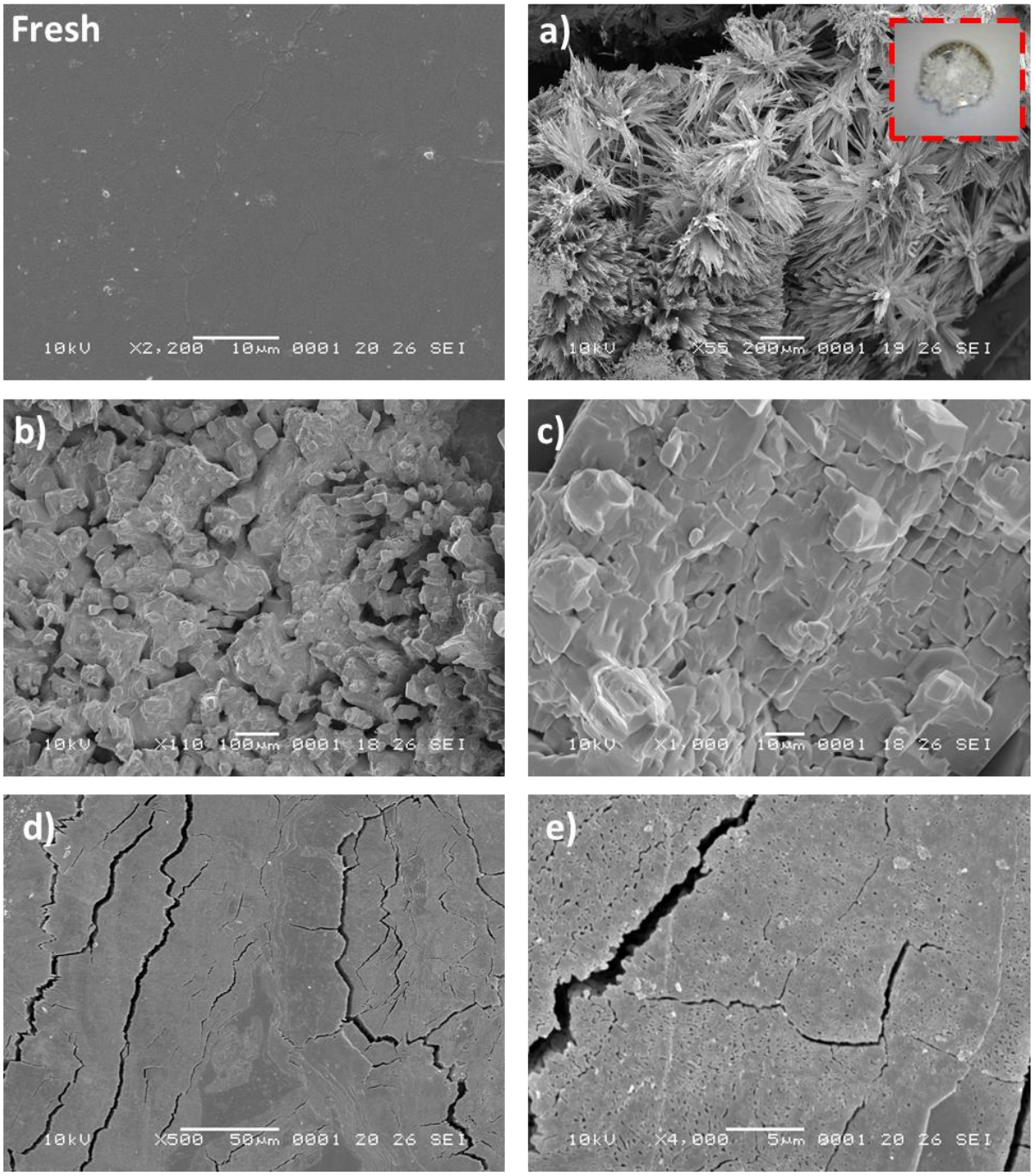

Figure 196 - SEM micrographs of CBZ:DMSO crystals subjected to desolvation (the fresh surface is added for comparison purposes). *a*: heated until 150 ºC (N_2, 10 ºC.min^{-1}); the detail shows a photograph of the sample after the experiment. *b* and *c*: heated until 110 ºC (N_2, heating rate of 10 ºC.min^{-1}). *d* and *e* : stored at 25 ºC (1 day, room conditions).

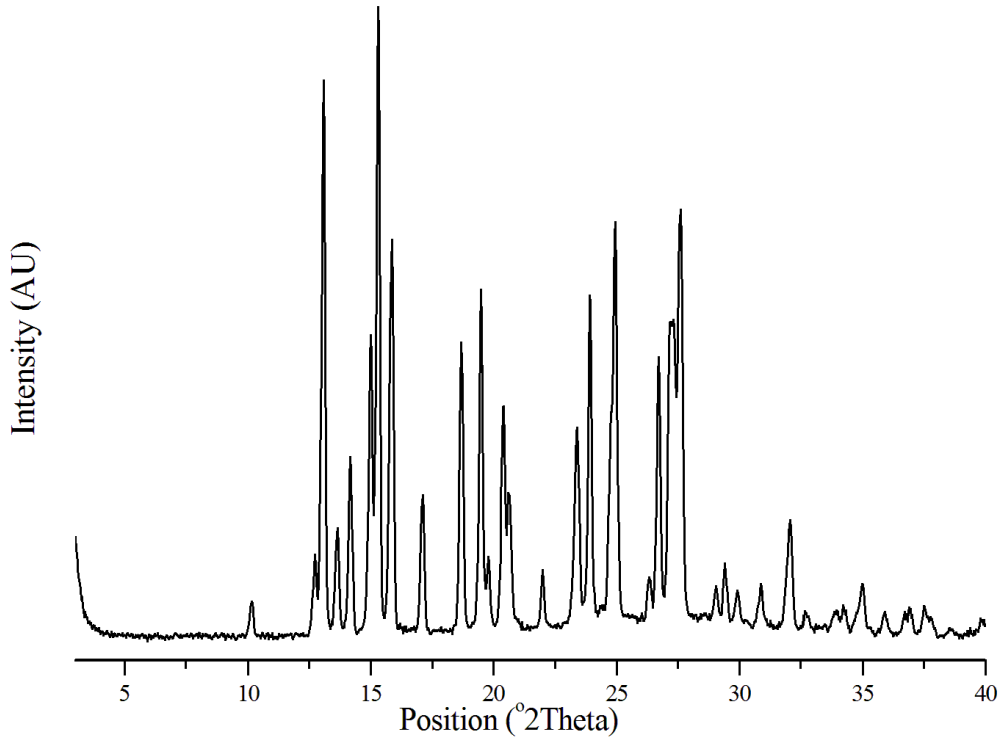

Figure 197 - *Ex situ* PXRD pattern of CBZ:DMSO crystals stored at 80 ºC for 5 h (N_2).

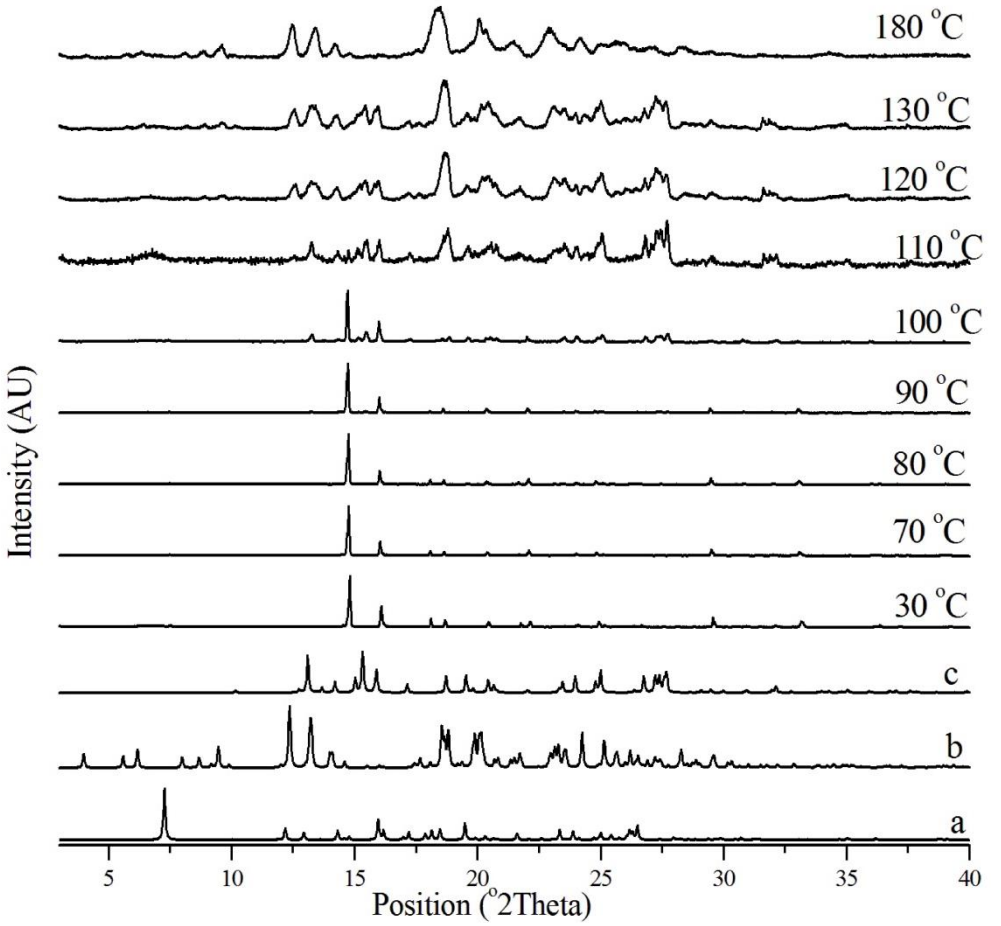

Figure 198 - *In situ* variable temperature PXRD patterns of CBZ:DMSO crystals (10 ºC.min^{-1}, 25-180 ºC). *a*: CBZ:DMSO from UNEYIV01. *b*: CBZ Form I from CBMZPN11. *c*: CBZ Form III from CBMZPN01.

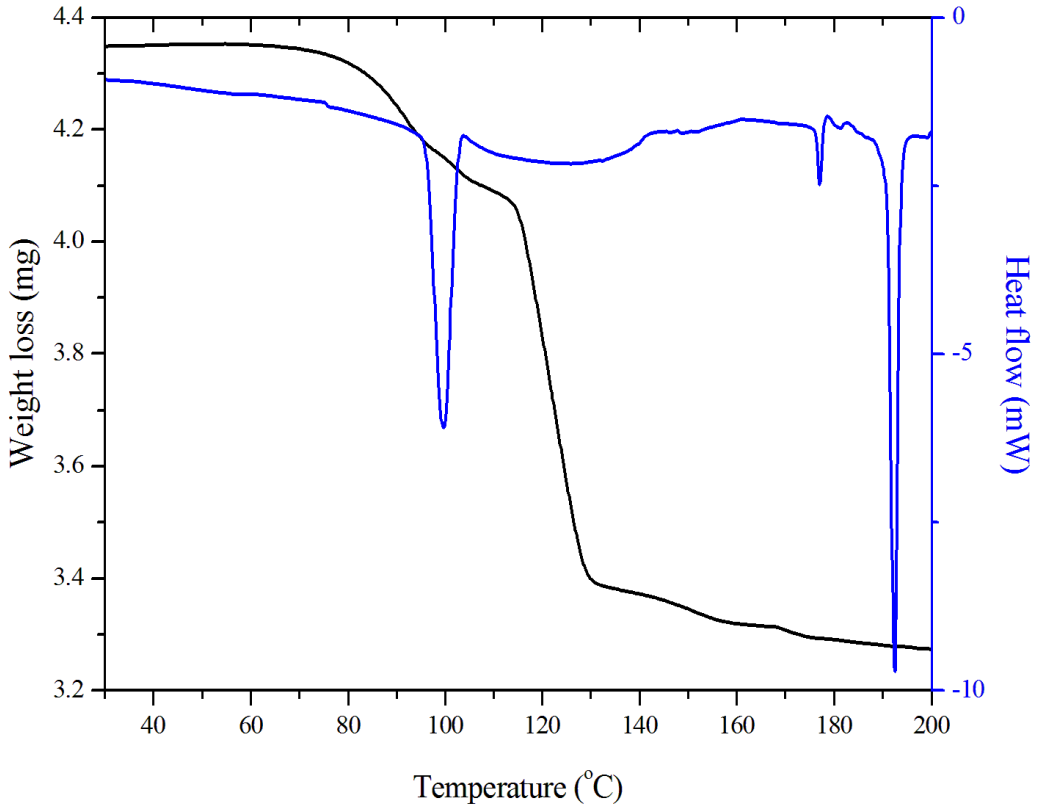

Figure 199 - DSC and TGA thermal characterization of CBZ:DMSO crystals (10 ^{o}C.min^{-1}, perforated lid, N_2).

7.3.4. CBZ dimethylformamide solvate (CBZ:DMF), Group 1.

The process of desolvation of CBZ:DMF crystals appears similar to that of CBZ:DMSO. The micrographs obtained by hot stage microscopy show that the crystals lose their original shape as a result of heating (Figure 200). *Ex-situ* SEM analysis of DMF solvate crystals subjected to non-isothermal desolvation at 10 ^{o}C.min^{-1} also illustrates this behaviour (Figure 201). The images show that desolvation leads to the formation of spherulites and other irregular structures and particles over the original crystals. Isothermal desolvation at room conditions is, however, not as destructive. In this case, the resulting surfaces shows round domains, holes in between the newly formed grains and cracks, comparable to that of CBZ:DMSO desolvated isothermally (Section 7.3.3) and to CBZ:ACE desolvated at 10 ^{o}C.min^{-1} (Section 7.3.2).

PXRD analysis show that samples subjected to mild desolvation conditions result in polymorph III (Figure 202). *In situ* PXRD investigation with heating at 10 ^{o}C.min^{-1}, in turn, show the crystals desolvate to CBZ Form III with evidence of Form I formation (Figure 203). The reflections of the new phase are detected at about 60 ^{o}C and show a gradual increase in intensity until complete lattice transformation is observed at 90 ^{o}C. In contrast to the behaviour of the DMSO solvate, CBZ:DMF does not seem to undergo such a rapid transformation and no evidence of a liquid phase is observed. Although it may be characterized as an analytical artefact

because the analyses were simply not able to detect the peritectic formation, other factors may also play a role. It is possible that the differences between CBZ:DMSO and CBZ:DMF reflect the differences in the boiling point of the released solvents, the particle size of the crystals and/or the strength of interaction between CBZ and the solvent molecules.

The DSC and TGA curves of the DMF solvate collected at 10 ^{o}C.min^{-1} are shown in Figure 204. One event of weight loss ending at about 160 ^{o}C with varying slope is linked to the desolvation of DMF. The heat flow curve shows that the endothermic event of desolvation changes in appearance during the decomposition as it begins as a sharp event at approximately 80 ^{o}C, but is followed by a broad endotherm which lasts until just above 145 ^{o}C. These characteristics illustrate different physical transformations arising from the heating of the crystals and may suggest that the solvent released from the lattice does not vaporize immediately after crystal decomposition. The thermal data demonstrate clear similarities between the CBZ:DMSO and CBZ:DMF. It is interesting that, although the acetone solvate is isostructural to the DMSO and DMF solvates, its thermal behaviour and the product obtained from heating are significantly different if compared to the other two materials (especially depending on the desolvation rate).

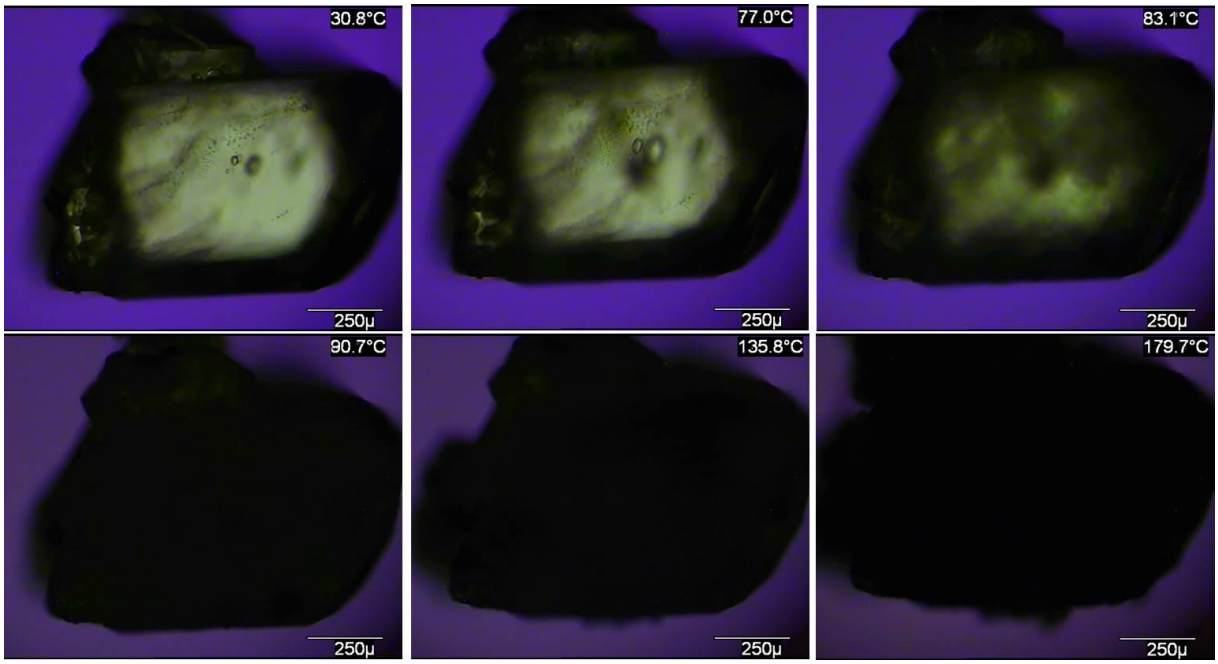

Figure 200 - Optical micrographs of CBZ:DMF crystals at different temperatures under polarized light (heating rate of 10 ^{o}C.min^{-1}).

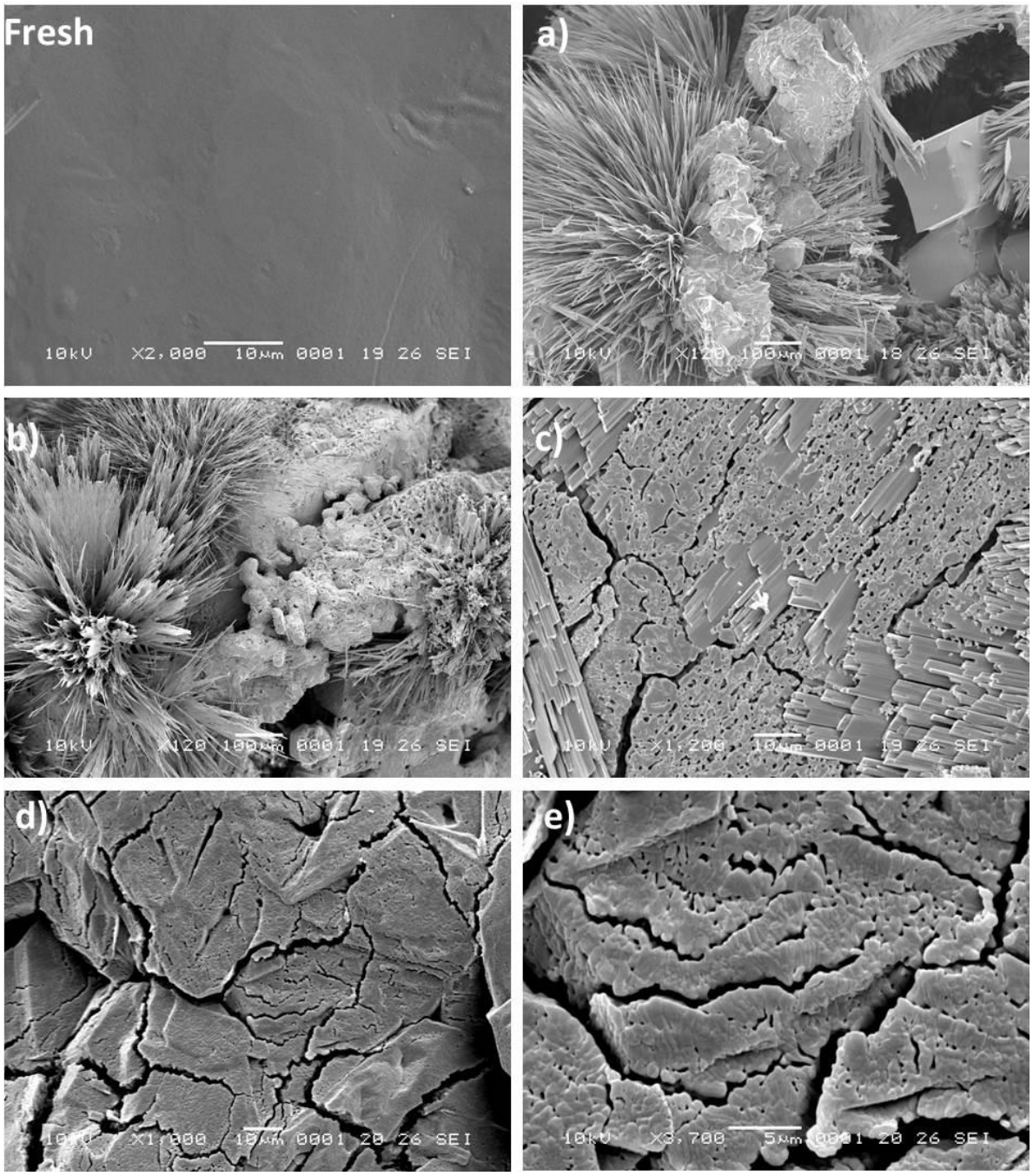

Figure 201 - SEM micrographs of CBZ:DMF crystal surfaces subjected to desolvation (the fresh surface is added for comparison purposes). *a* and *b*: heated until 150 °C (N_2, 10 °C.min^{-1}); the detail shows a photograph of the sample after the experiment. *c*: heated until 110 °C (N_2, heating rate of 10 °C.min^{-1}). *d* and *e* : stored at 25 °C (1 day, room conditions).

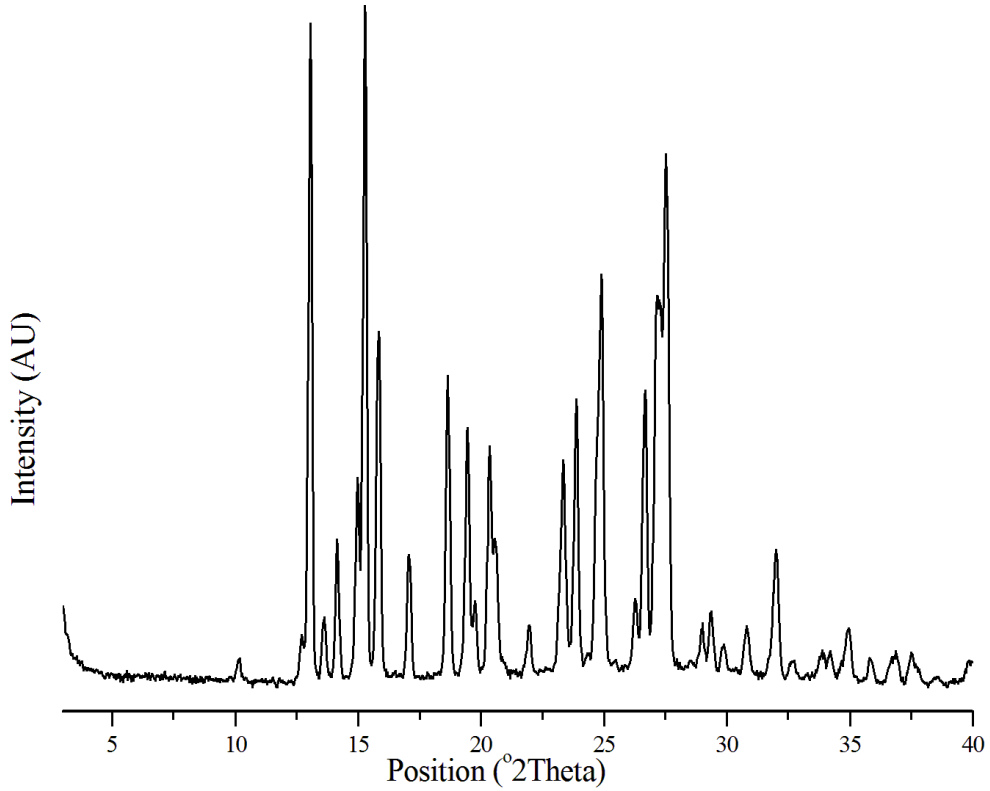

Figure 202 - *Ex situ* PXRD pattern of CBZ:DMF crystals stored at 50 ºC for 2 hours (N_2).

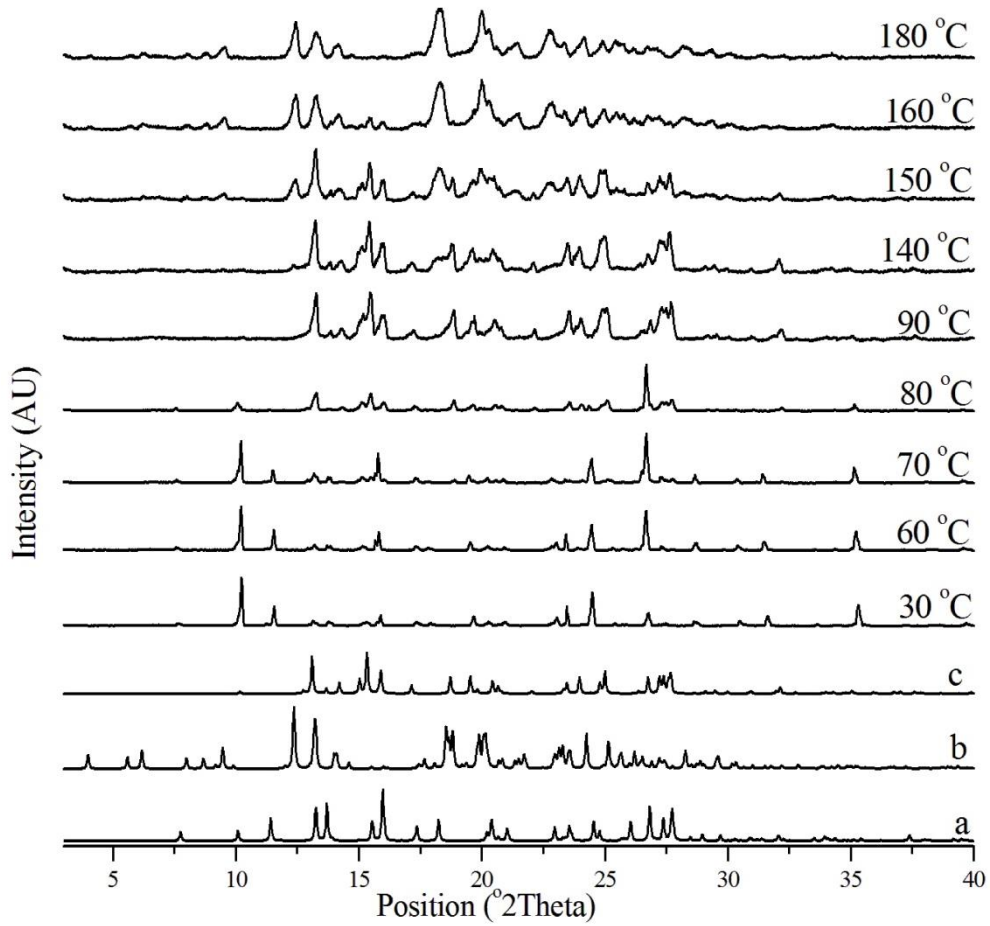

Figure 203 - *In situ* variable temperature PXRD patterns of CBZ:DMF crystals (10 ºC.min^{-1}, 25-180 ºC). *a*: CBZ:DMF from QANQUS. *b*: CBZ Form I from CBMZPN11. *c*: CBZ Form III from CBMZPN01.

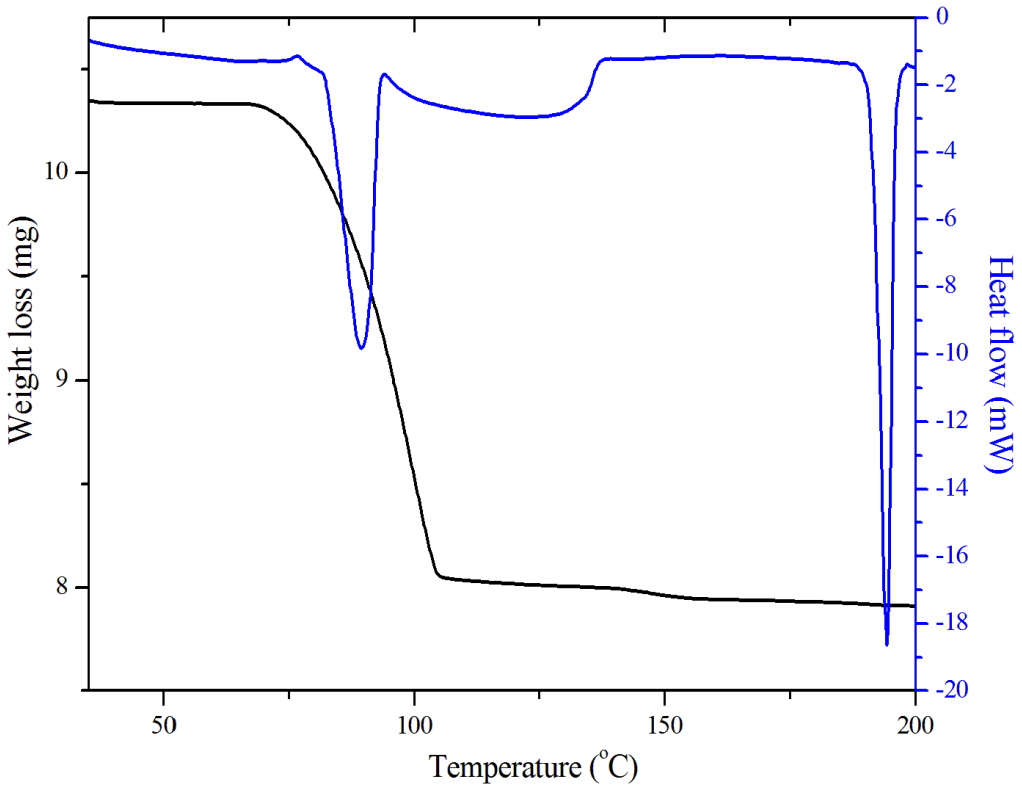

Figure 204 - DSC and TGA thermal characterization of CBZ:DMF crystals (10 ^{o}C.min^{-1}, perforated lid, N_2).

7.3.5. CBZ dimethylacetamide solvate (CBZ:DMA), Group 2.

As in the case of CBZ:DMSO and CBZ:DMF solvates, single crystals of CBZ:DMA turn opaque and lose their original shape upon heating. Figure 205 shows that the crystals do not lose birefringence uniformly but develop opaque and round nuclei which grow throughout the crystal as the temperature increases. E*x-situ* SEM analysis illustrates the reorganization of the surface after non-isothermal desolvation at 10 ^{o}C.min^{-1} and shows the development of whiskers and spherulites (Figure 206).

Figure 207 gives the corresponding DSC and TGA data. A single event of weight loss (ending at about 90 ^{o}C) is observed in the TGA, while the heat flow curve shows that desolvation is characterized by a single endothermic event (T_{onset}=76.6 ^{o}C). Although the desolvation endotherm is not symmetric, suggesting that concurrent physical transformations are taking place, the shape of the thermograms and the rate of weight loss are different to those observed for CBZ:DMSO and CBZ:DMF. Additionally, the melting event of the desolvated product consists of a broad endotherm that may consist of two events. It is unclear whether this behaviour is related to differences in particle size or if it is correlated to the melting of polymorphs III and I, suggesting that a mixture of phases is obtained from desolvation or that the conversion of Form III to Form I was not complete.

In situ PXRD shows that desolvation of CBZ:DMA results in Form III, which partially transforms to Form I above 170 ºC (Figure 208). The lattice gradually changes with increase in temperature, and a clear structural change is seen above 80 ºC. Although the outcome of desolvation observed from PXRD corresponds to polymorph III, the surface of the desolvated product does not show, curiously, the properties usually associated with this polymorph. The reasons why the PXRD analysis has only detected Form III as a result of desolvation are unclear. It is likely that differences in sample size may change the local environment during desolvation and kinetically affect the reaction.

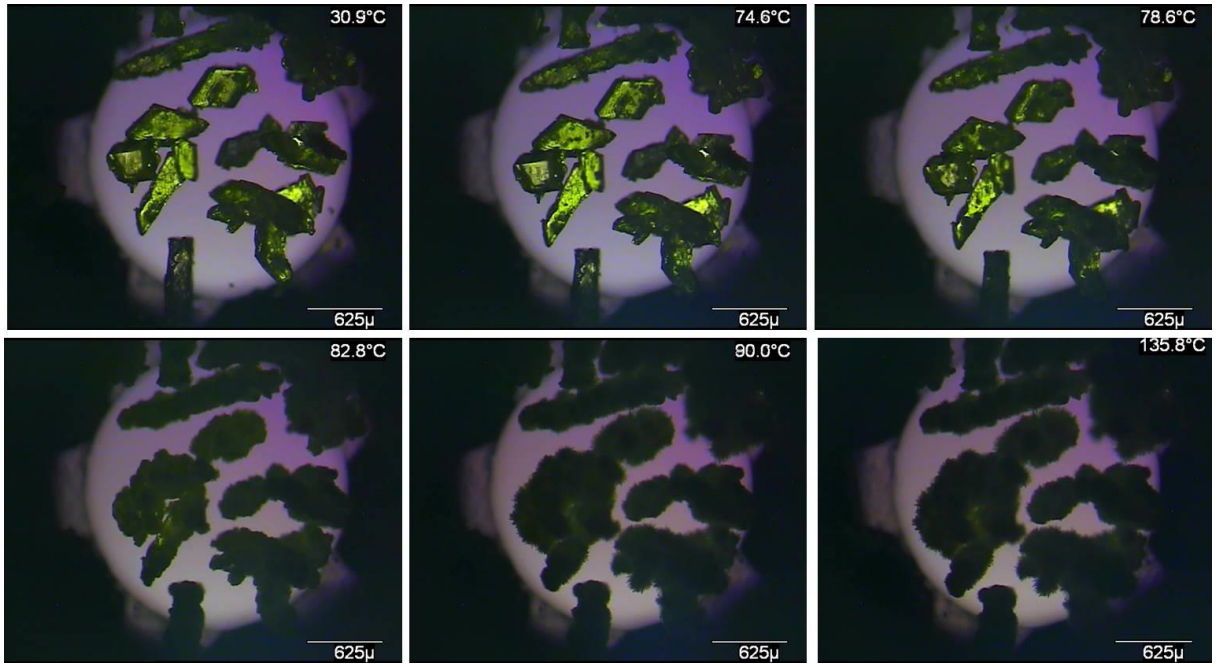

Figure 205 - Optical micrographs of CBZ:DMA crystals at different temperatures under polarized light (heating rate of 10 ºC.min^{-1}).

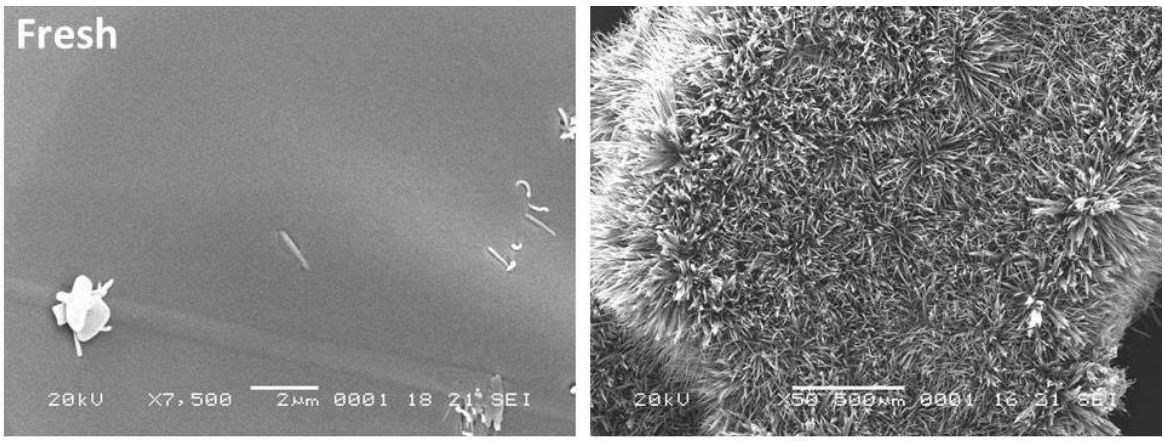

Figure 206 - SEM micrograph of CBZ:DMA crystals heated until 120 ºC (N_2, heating rate of 10 ºC.min^{-1}). The fresh surface is added for comparison purposes.

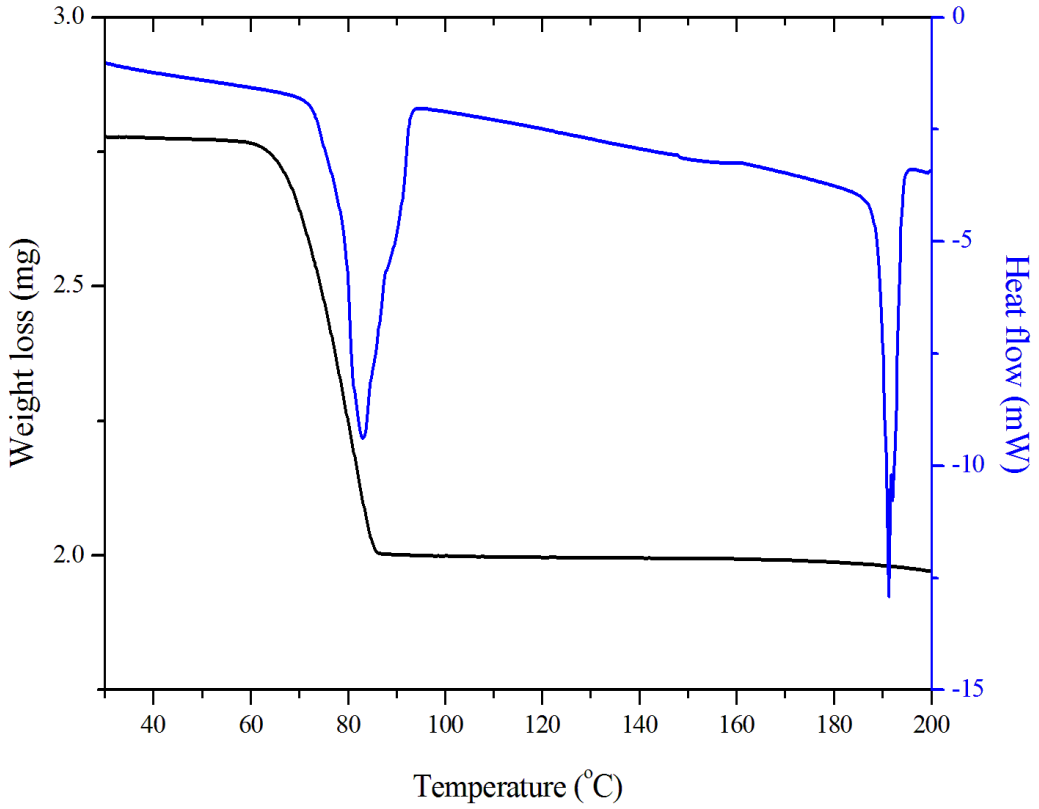

Figure 207 - DSC and TGA thermal characterization of CBZ:DMA crystals (10 °C.min^{-1}, perforated lid, N_2).

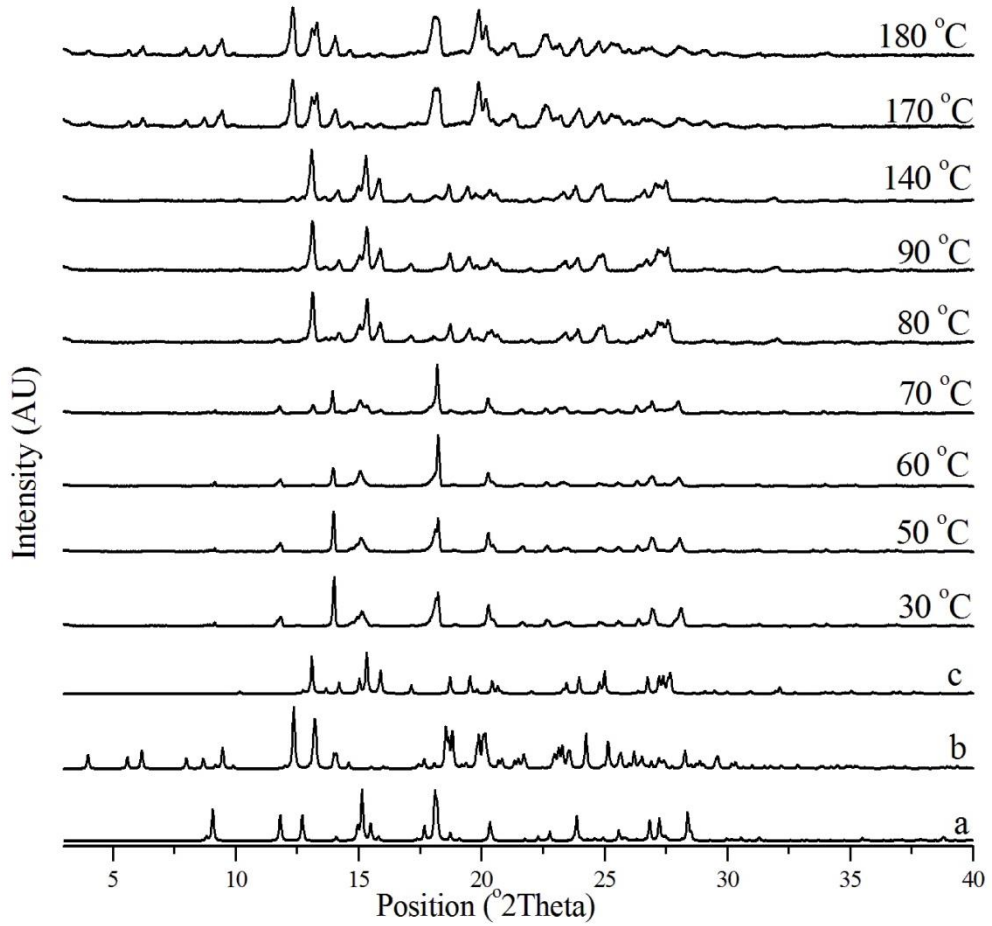

Figure 208 - *In situ* variable temperature PXRD patterns of CBZ:DMA crystals (10 °C.min^{-1}, 25-180 °C). *a*: CBZ:DMA from KIWBEY. *b*: CBZ Form I from CBMZPN11. *c*: CBZ Form III from CBMZPN01.

7.3.6. CBZ benzoquinone cocrystals (CBZ:BZQ and 2CBZ:BZQ), Group 2 and Group 3.

CBZ:BZQ

The single crystals of CBZ:BZQ do not lose birefringence uniformly as desolvation proceeds. Figure 209 shows the development of opaque regions above 90 ^{o}C, which apparently nucleate from defective regions on the surface and grow throughout the crystal with increase in temperature. The formation and growth of these nuclei leads to a substantial surface reorganization, but does not cause the loss of the crystal shape as seen for instance for CBZ:DMA. E*x-situ* SEM images of CBZ:BZQ crystals subjected to non-isothermal desolvation at 10 ^{o}C.min^{-1} are shown in Figure 210. They illustrate that sublimation of BZQ leads to the formation of whiskers over the original surface.

DSC and TGA curves are shown in Figure 211. A single event of weight loss ending at about 160 ^{o}C is observed by TGA, and the heat flow curve demonstrates that desolvation is characterized by a broad endothermic event (T_{onset}=146.2 ^{o}C). For comparison purposes, the sublimation of BZQ crystals is illustrated in Figure 212 and Figure 213. The TGA of BZQ shows a single weight loss between 60 to 160 ^{o}C, while the DSC curve displays two endotherms. These findings agree with the literature, which suggests that benzoquinone concomitantly melts and sublimes.[207] In this case, the sharp endotherm observed in the DSC curve may be assigned to the melting of BZQ, and the subsequent broad peak associated with sublimation. It may also be mentioned that the shape of the DSC curve of the coformer reflects changes in the pressure inside the sample holder. This is, however, unlikely as coupled TGA and heat flow curves collected in open crucibles have also shown the same behaviour as the experiments performed in perforated pans.

Optical micrographs collected during the heating of BZQ single crystals show evidences of concomitant processes of melting and sublimation described in the literature. Although it is not possible to determine which transformation starts the process, it is demonstrated that the sample sublimes layer-by-layer. The results indicate how the sublimation of coformer changes once the molecule is incorporated in the cocrystal lattice. While the single crystals of BZQ alone sublime and melt following a layer-by-layer process until the entire material is transferred to the vapour state, the sublimation of benzoquinone from the cocrystal results in the reorganization of the remaining CBZ into a new lattice.

In situ PXRD of CBZ:BZQ shows that the material gradually changes with the increase in temperature (Figure 214). The experiments demonstrate that the sublimation of BZQ first leads to the formation of the lower stoichiometric 2CBZ:BZQ cocrystal, which shows

detectable reflections above 100 ºC. Further sublimation of BZQ results in the conversion of 2CBZ:BZQ into CBZ Form I above 140 ºC. In summary, it demonstrates that the lower stoichiometry cocrystal is an intermediate in the decomposition of CBZ:BZQ.

Considering the polymorphic outcome of the decomposition reactions, another interesting aspect is the comparison of CBZ:BZQ and CBZ:DMA. Although the materials are structurally similar, they result in different CBZ polymorphs upon heating. It is suggested that the existence of a stable cocrystal form with an intermediate stoichiometry in CBZ/BZQ influences the mechanism by which lattice rearranges. In this case, a slower and progressive transformation is observed for the sublimation of CBZ:BZQ. Also, the similarities between 2CBZ:BZQ and Form I may affect the outcome of sublimation of the resulting BZQ cocrystals.

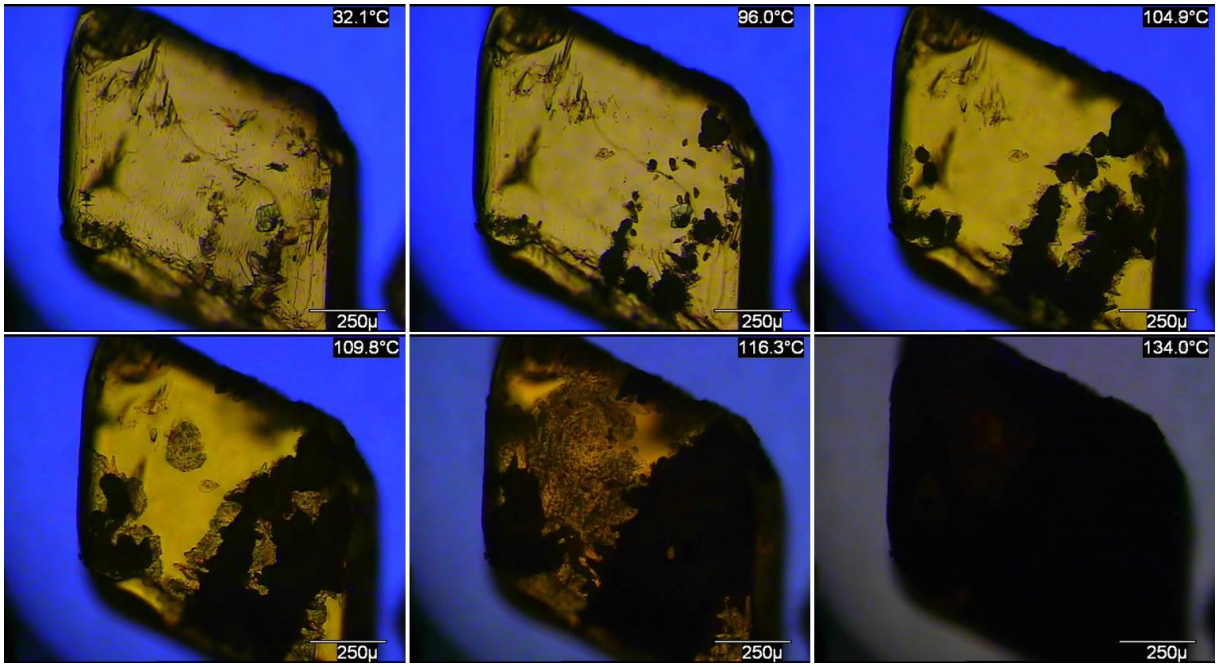

Figure 209 - Optical micrographs of CBZ:BZQ crystals at different temperatures under polarized light (heating rate of 10 ºC.min^{-1}).

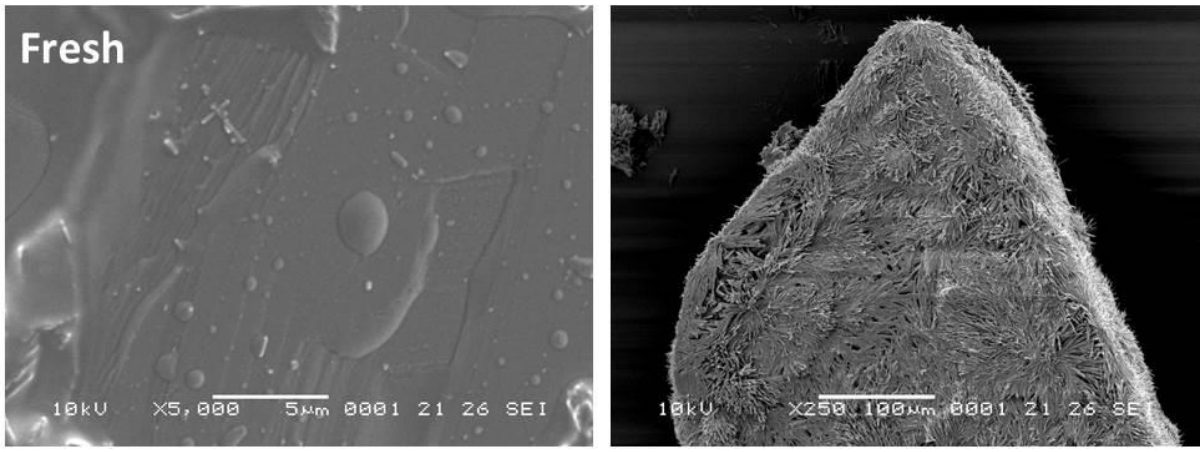

Figure 210 - SEM micrographs of CBZ:BZQ crystals heated until 150 ºC (N_2, heating rate of 10 ºC.min^{-1}). The fresh surface is added for comparison purposes.

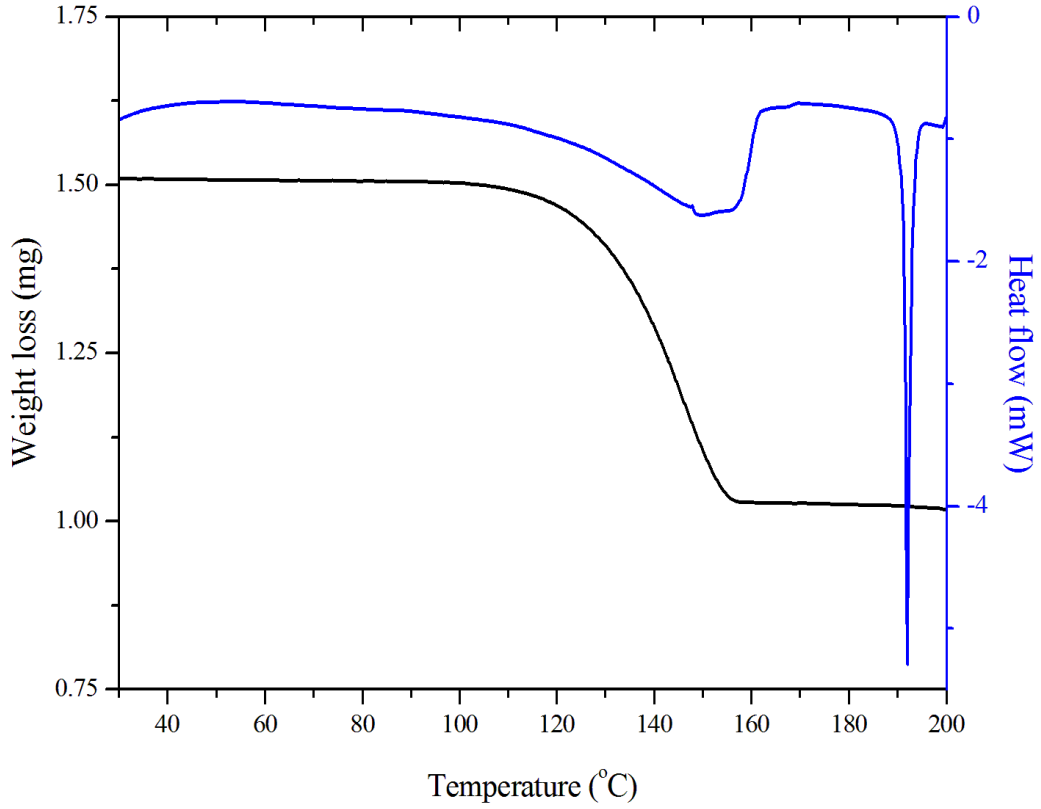

Figure 211 - DSC and TGA thermal characterization of CBZ:BZQ crystals (10 ^{o}C.min^{-1}, perforated lid, N_2).

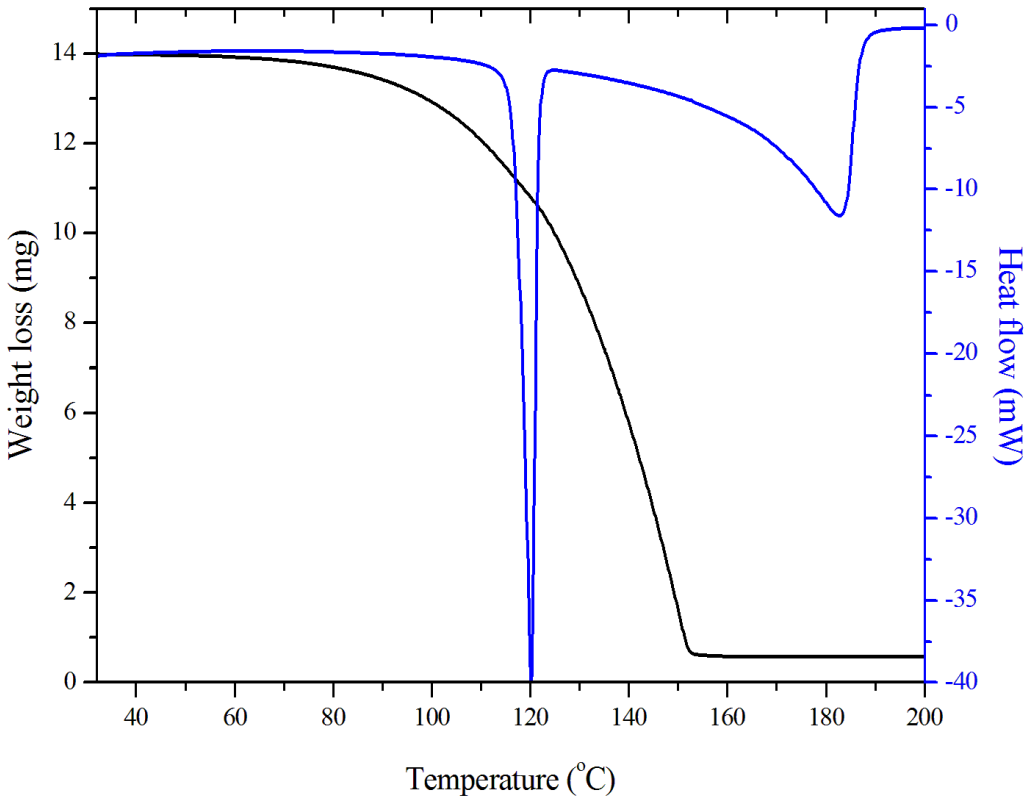

Figure 212 - DSC and TGA thermal characterization of BZQ crystals (10 ^{o}C.min^{-1}, perforated lid, N_2).

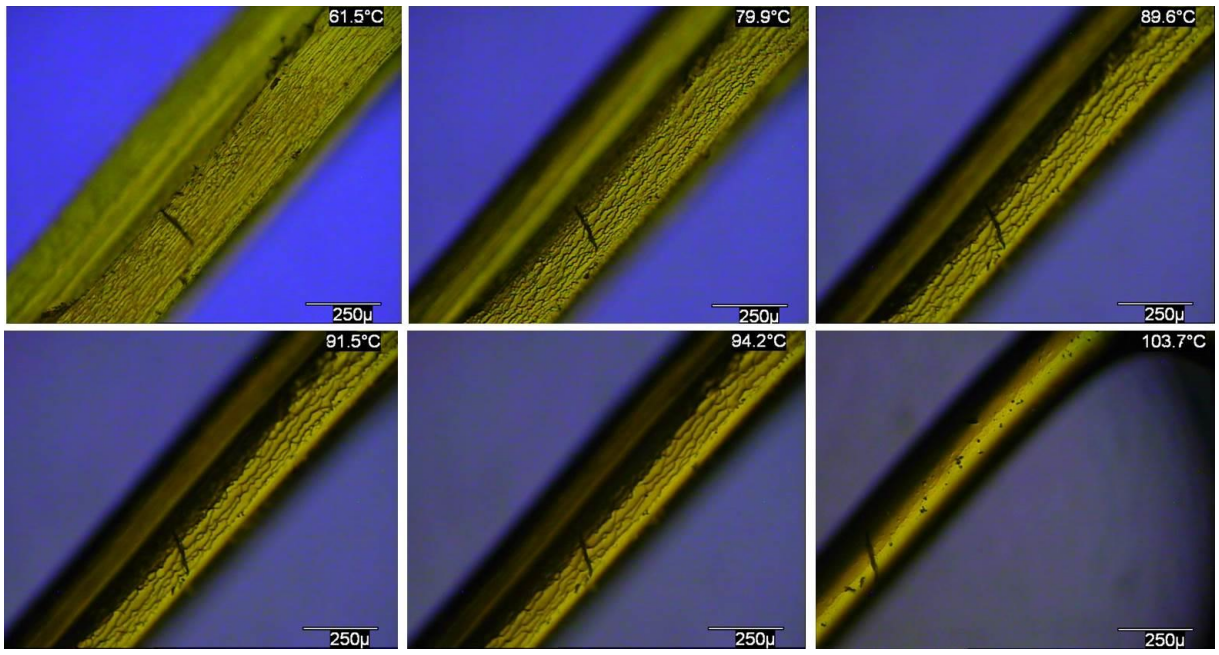

Figure 213 - Optical micrographs of BZQ crystals at different temperatures under polarized light (heating rate of 10 ^{o}C.min^{-1}).

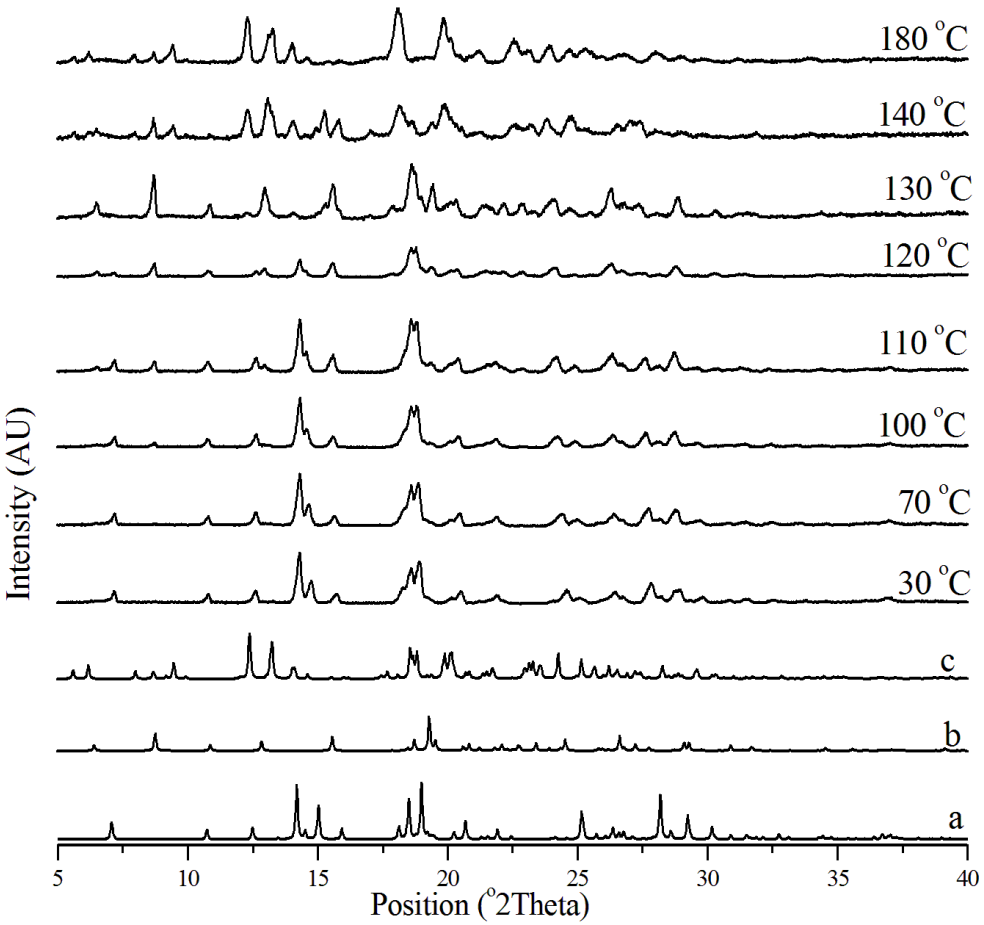

Figure 214 - *In situ* variable temperature PXRD patterns of CBZ:BZQ crystals (10 ^{o}C.min^{-1}, 25-180 ^{o}C). *a*: CBZ:BZQ from in-house data. *b*: CBZ Form I from CBMZPN11. *c*: CBZ Form III from CBMZPN01.

2CBZ:BZQ

The analysis of 2CBZ:BZQ samples prepared from solution also demonstrate that decomposition starts at a higher temperature than for CBZ:BZQ. Figure 215 shows the *in situ* PXRD heating experiments of 2CBZ:BZQ. It is shown that the CBZ material remaining from the decomposition of the cocrystal rearranges into polymorph I and the first detectable peaks of CBZ are seen above 120 ^{o}C. The DSC and TGA curves of the 2:1 cocrystal are very similar to the 1:1 cocrystal, while the onset temperature of sublimation appears to be slightly higher (T_{onset}=155.1 ^{o}C, Figure 216).

Although the thermal curves and the polymorphic outcome of decomposition of both BZQ cocrystals are the same, they have significantly different morphology and surface characteristics. Single crystals of 2CBZ:BZQ show needle-like morphology which uniformly turns opaque on heating and maintains the original shape of the particles, while whiskers are formed progressively on the surface of the particles (Figure 217). The *ex situ* SEM analyses of the crystals resulting from CBZ:BZQ sublimation show that the domains of the newly formed product are oriented along the needle axis (Figure 218). This surface rearrangement differs quite significantly from the behaviour of CBZ:BZQ subjected to heating experiments.

The 2:1 cocrystal is structurally similar to CBZ:2H_2O and the crystals prepared from solution crystallization resemble morphologically the dihydrate (0k0) samples. In fact, the product resulting from the decomposition of 2CBZ:BZQ shows similar characteristics to the product of dehydration of CBZ:2H_2O which resulted in Form I. It is noteworthy that the fresh cocrystal particles, however, do not appear to be prone to the formation of cracks as in the case of the dihydrate. The stability of the cocrystal under vacuum is shown by SEM, but also by conventional TEM analyses performed without cryogenic protection (Figure 218 and Figure 219, respectively). It is shown that the crystals do not develop cracks or holes during the TEM experiments. The diffraction patterns appear to be in agreement to the 2CBZ:BZQ structure and show high crystallinity, although the patterns were not fully indexed. Figure 219 shows the proposed indexing of the h00 row of spots with the largest *d*-spacings (10.40 Å) in the pattern. The streaking in the patterns and the evidence of extra reflections, however, lead to non-conclusive analysis of the pattern. Streaking was observed in several diffraction patterns and may be due to ordered stacking of layers in the crystals or possibly to stacking faults, thin ordered domains or finely twined structures.

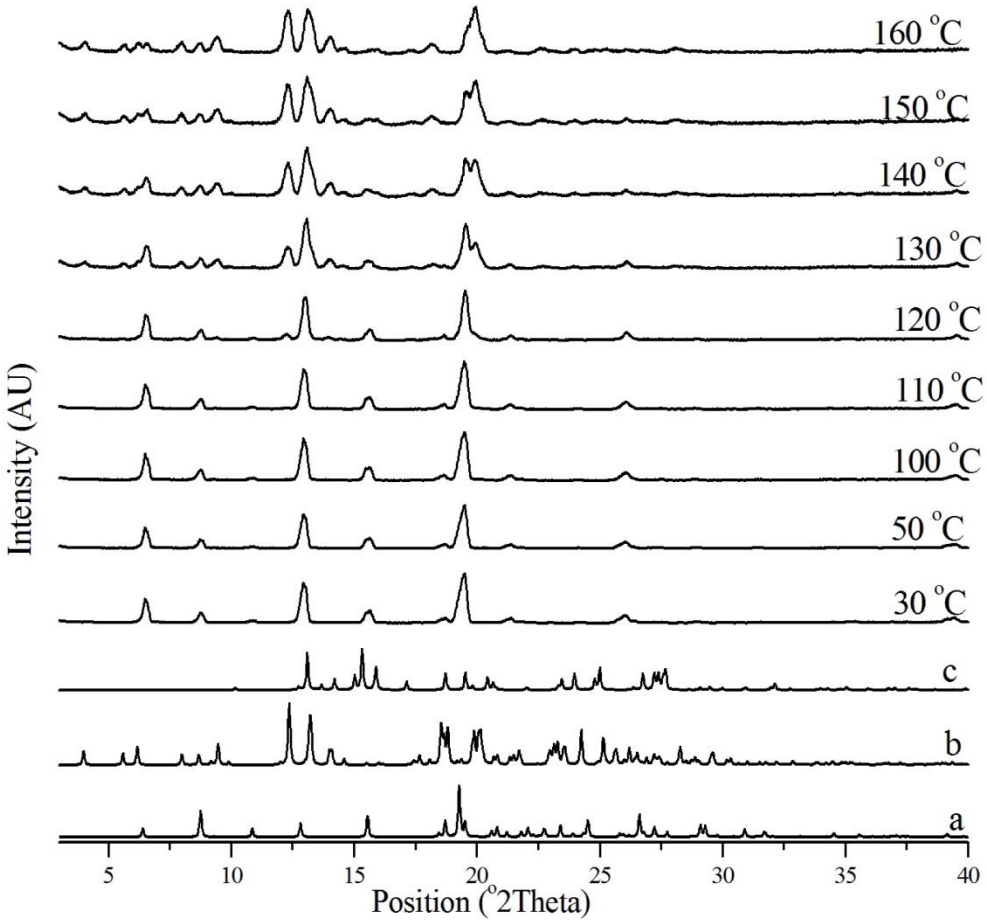

Figure 215 - *In situ* variable temperature PXRD patterns of 2CBZ:BZQ crystals (10 °C.min^{-1}, 25-180 °C). *a*: 2CBZ:BZQ from UNEYOB. *b*: CBZ Form I from CBMZPN11. *c*: CBZ Form III from CBMZPN01.

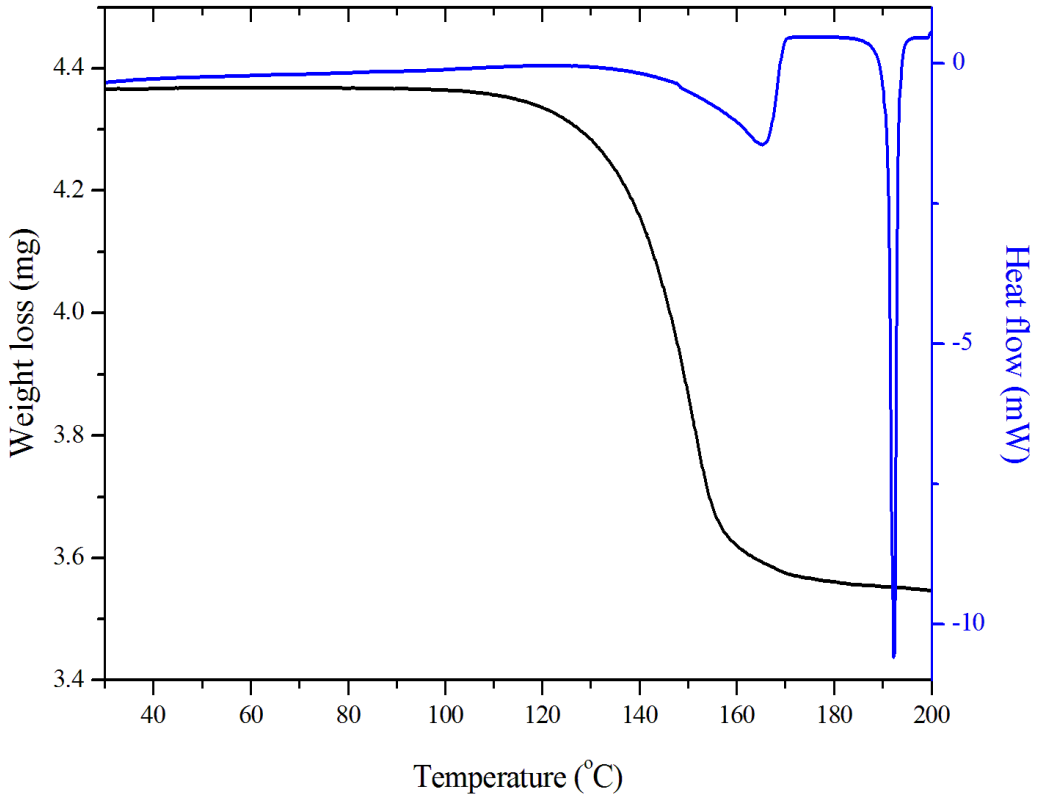

Figure 216 - DSC and TGA thermal characterization of 2CBZ:BZQ crystals (10 °C.min^{-1}, perforated lid, N_2).

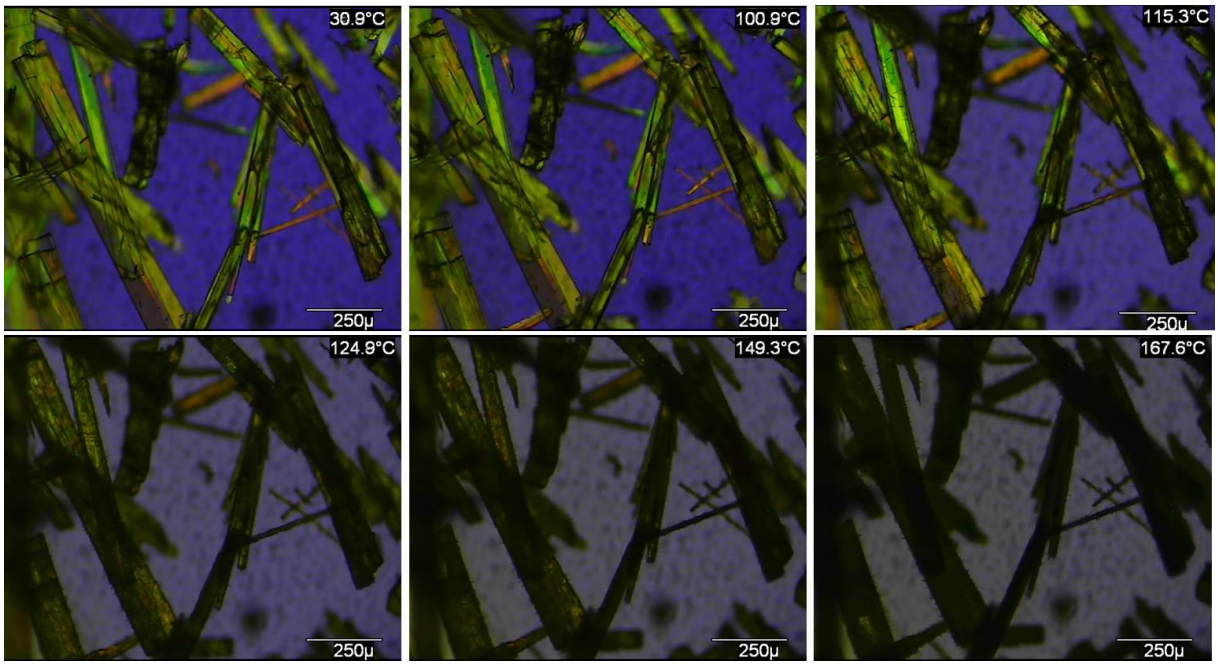

Figure 217 - Optical micrographs of 2CBZ:BZQ crystals at different temperatures under polarized light (heating rate of 10 $^{o}C.min^{-1}$).

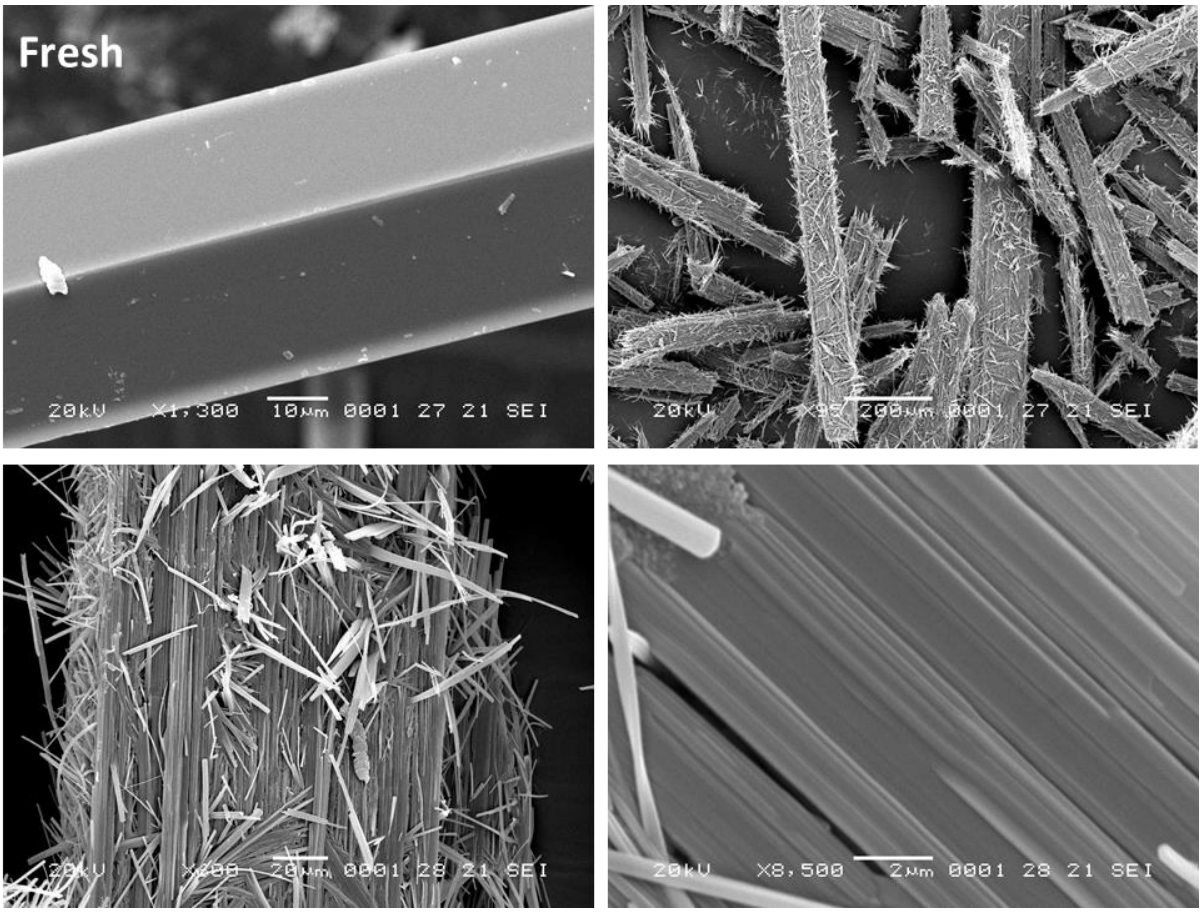

Figure 218 - SEM micrographs of 2CBZ:BZQ crystals heated until 150 ^{o}C (N_2, heating rate of 10 $^{o}C.min^{-1}$). The fresh surface is added for comparison purposes.

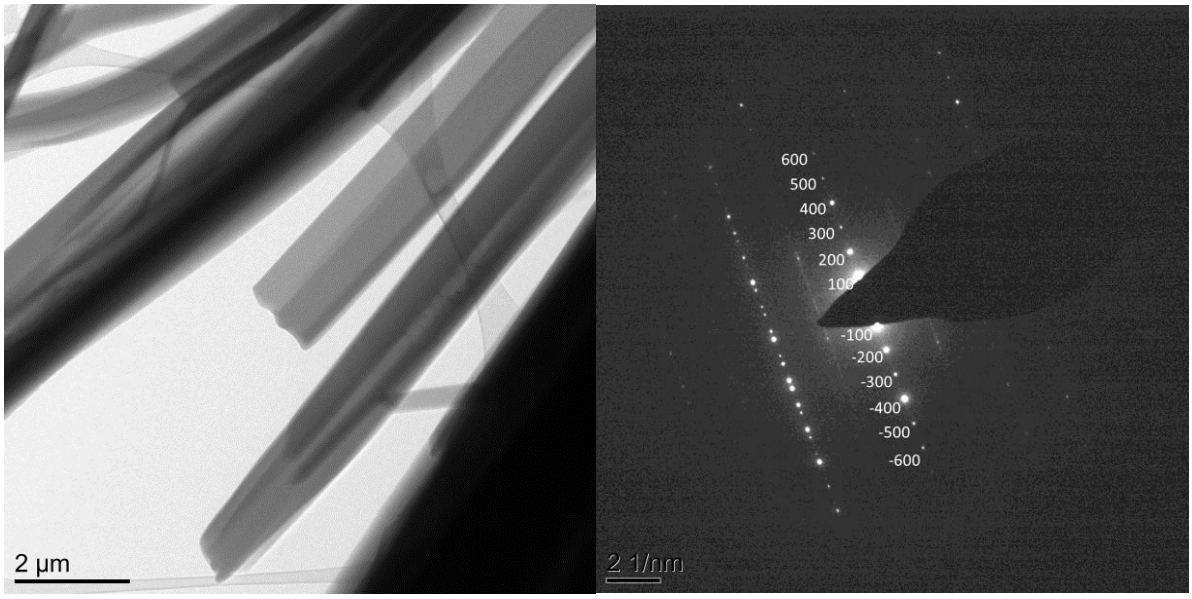

Figure 219 - TEM bright field image and diffraction pattern of crystals expected to be 2CBZ:BZQ (based on from CSD structure UNEYOB, a = 10.334 Å, b = 27.612 Å, c = 4.996 Å, α = γ = 90º, β = 102.275º).

7.3.7. CBZ oxalic acid cocrystal (2CBZ:OXA), Group 3.

Similarly to 2CBZ:BZQ, 2CBZ:OXA is also isostructural to CBZ:2H_2O. In the case of the oxalic acid cocrystal, however, the crystals prepared from solution crystallization show (h00) dominant face. The SEM imaging of the cocystal shows extensive defects and roughness characterized by cracks and particle collapse on the inner regions of the dominant (h00) crystal surfaces (Figure 220).

Figure 221 shows the optical micrographs taken during the hot stage analyses of 2CBZ:OXA. They demonstrate that the surface irregularities on (h00) are not an artefact of the vacuum during the SEM imaging or from the sputter coating of the particles but are most probably originated during the crystallization of the sample. The optical micrographs also illustrate that the crystals become opaque and show whiskers growing on the crystals above 130 ºC. Interestingly, the images demonstrate that the material concomitantly liquefy and sublime above 160 ºC. *In situ* PXRD heating experiments have not detected the formation of CBZ polymorphs upon heating, however, the diffractograms show evidences of lattice collapse and the formation of a liquid phase above 160 ºC (Figure 222).

The thermograms of the oxalic acid cocrystal provide further insights about its decomposition. Figure 223 shows the DSC and TGA curves of 2CBZ:OXA collected at 1 and 10 ºC.min^{-1}. The analyses show one sharp endothermic event in the range 150-175 ºC, which is followed by broad endotherms at higher temperature. Although the general results were reproducible, the experiments performed at slow heating rate suggest that exothermic events are also taking place during heating and are masked perhaps by the other events at higher rates.

Similarly, the TGA curve demonstrates the existence of concomitant reactions as three regions of weight loss without clear limits: (i) from approximately 140 to 160 ºC; (ii) from approximately 160 to 260 ºC; and (iii) above 160 ºC. The shape and the slopes of regions (ii) and (iii) are equivalent to the characteristics of the decomposition of CBZ (see Figure 188 and Figure 189). In the case of the OXA cocrystal, however, these events are shifted to lower temperatures. The results may demonstrate that the physical decomposition of the cocrystal accelerates the chemical decomposition of CBZ without a change in mechanism. As similar weight loss profiles were obtained from samples prepared by grinding and from samples crystallized in solution, it is unlikely that the surface defects and roughness observed on the single crystals of 2CBZ:OXA affect the instability of the CBZ crystals.

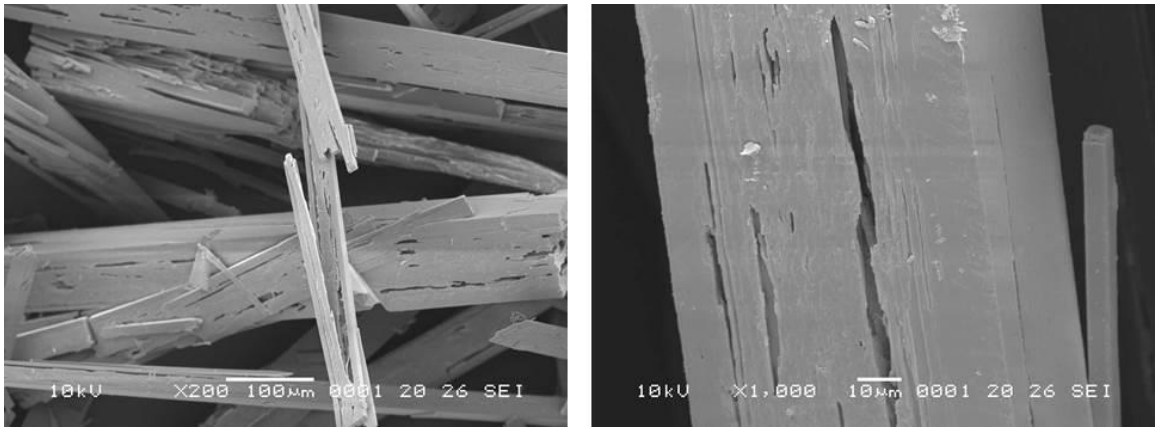

Figure 220 - SEM micrographs of 2CBZ:OXA crystals.

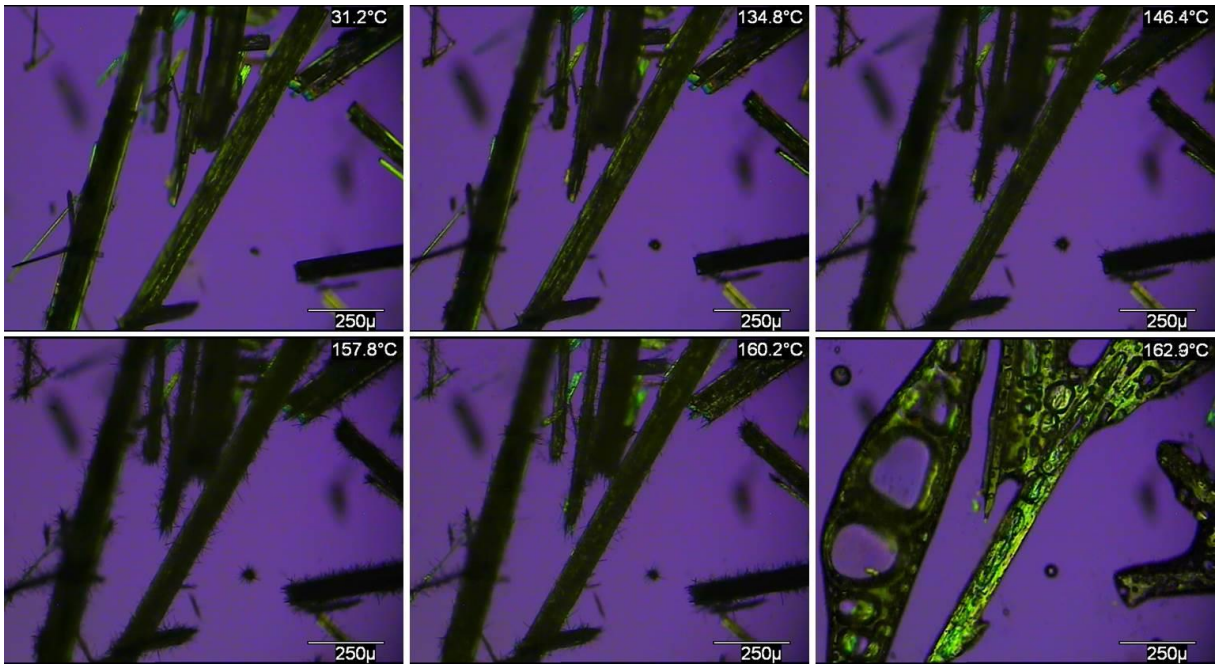

Figure 221 - Optical micrographs of 2CBZ:OXA crystals at different temperatures under polarized light (heating rate of 10 ºC.min^{-1}).

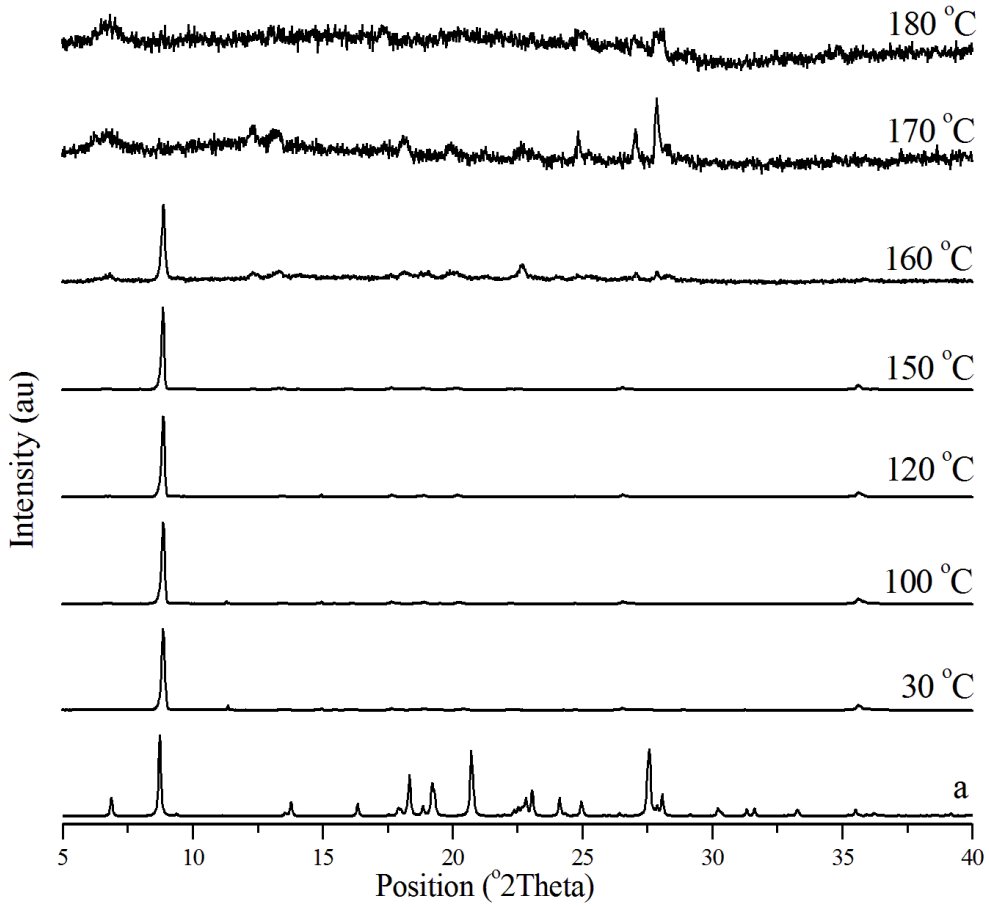

Figure 222 - *In situ* variable temperature PXRD patterns of 2CBZ:OXA crystals (10 °C.min^{-1}, 25-180 °C). *a*: 2CBZ:OXA from in-house data.

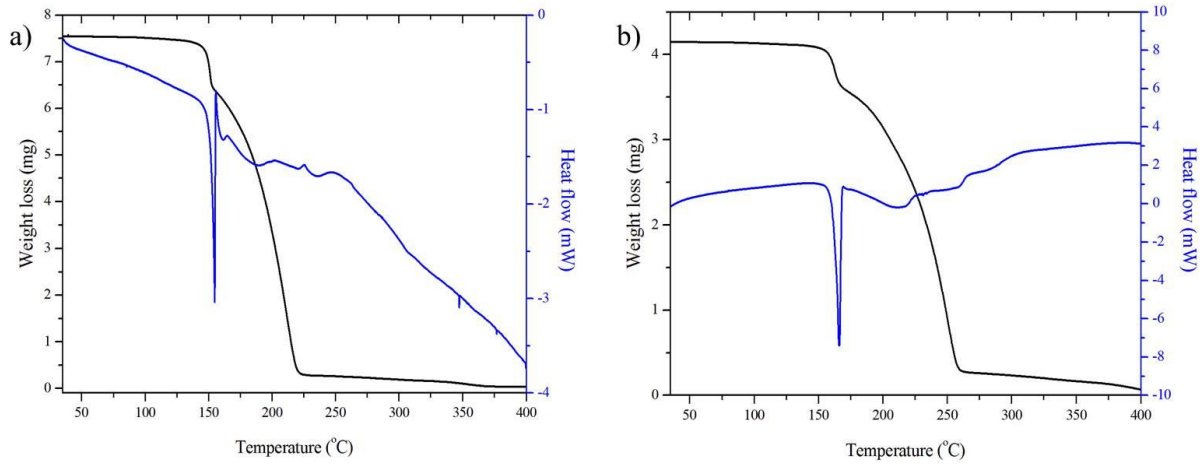

Figure 223 - DSC and TGA thermal characterisation of 2CBZ:OXA. *a:* 1 °C.min^{-1}, perforated lid, N_2. *b*: 10 °C.min^{-1}, perforated lid, N_2.

In situ micrographs collected during heating of oxalic acid alone also suggest that the decomposition of the conformer evolves with the concomitant formation of molten material and sublimation (Figure 224). Visual observations of the remaining residues suggest that not only pure sublimation is taking place, but also a chemical reaction. In fact, the literature reports that oxalic acid mainly decomposes into formic acid and carbon dioxide when heated above

130 ºC.[208,209] As both reaction products are expected to be vapours at these temperatures, the decomposition of oxalic acid may give rise to the characteristic weight loss behaviour observed in Figure 223, which can be misunderstood as simple melting with sublimation. It is then hypothesized that the thermal decomposition of oxalic acid is the main factor involved in the acceleration of CBZ decomposition in 2CBZ:OXA.

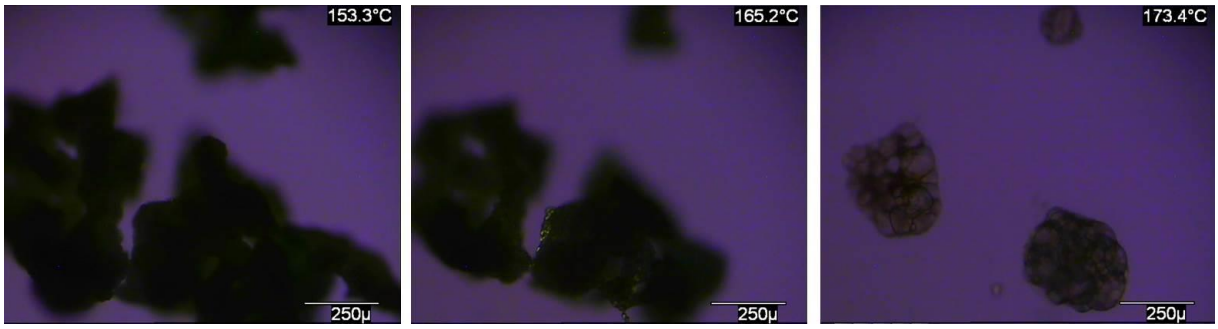

Figure 224 - Optical micrographs of OXA crystals at different temperatures under polarized light (heating rate of 10 ºC.min^{-1}).

The catalytic effect of oxalic acid on the rate of decomposition of other compounds has already been reported in the literature. Debenham & Owen[210] demonstrated that in the presence of oxalic acid in m-nitroperoxybenzoic acid leads to fusion during decomposition at about 78 ºC. The study shows that melting *per se* is not the reason for the acceleration in decomposition, although the authors were unclear whether the phenomenon was related to a direct reaction of oxalic acid with m-nitroperoxybenzoic acid, or if it was mediated by the formation of hydrogen bonds between them. In the case of 2CBZ:OXA, it is proposed that the formation of different species during the chemical decomposition of oxalic acid plays a major role.

The comparison of the characteristics of benzoquinone (which sublimes without decomposition) and oxalic acid (which decomposes with product sublimation) may explain the difference in the thermal behaviour of 2CBZ:BZQ and 2CBZ:OXA. It is demonstrated that, although the cocrystals are isostructural, their thermal behaviour is greatly influenced by the properties of the coformer.

7.3.8. CBZ formamide solvate (CBZ:FORM), Group 3.

Single crystals of CBZ:FORM turn opaque uniformly with heating and the overall shape of the particles is maintained, while whiskers are observed on the surface of the crystals above 150 ºC (Figure 225). These findings agree with the DSC and TGA curves of the solvate, which are illustrated in Figure 226. A single event loss is observed by TGA in the range 80-180

ºC. The heat flow curve shows desolvation as a sharp endotherm close to 147 ºC. The shape of the curve, however, suggests that the sample starts absorbing energy at a different rate at much lower temperatures. Exothermic events are seen above 150 ºC.

In situ PXRD detects reflections of CBZ Form I at 160 ºC and a rapid lattice change with an increase in temperature (Figure 227). Similar to that observed for CBZ:2H_2O (see Section 5.5, Chapter 5), the results demonstrate that the solvate undergoes isostructural desolvation and lattice modification only after the release of a significant amount of solvent. The temperature at which transformation to polymorph I is detected by PXRD can be correlated to the exothermic event observed by DSC.

Ex situ SEM analysis of the desolvated samples shows the formation of needle-like structures (Figure 228). Interestingly, the two main crystal surfaces show somewhat distinct behaviours. While the dominant face shows needle-like domains oriented along the particle axis, the other shows needles randomly arranged throughout the surface. Also, although the dominant surface of CBZ:FORM is structurally equivalent to the (h00) surface of CBZ:2H_2O, no cracks are detected during desolvation, nor do the fresh surfaces fracture as a consequence of vacuum as observed for CBZ:2H_2O - only random cracks have been seen during the analyses of the formamide solvate.

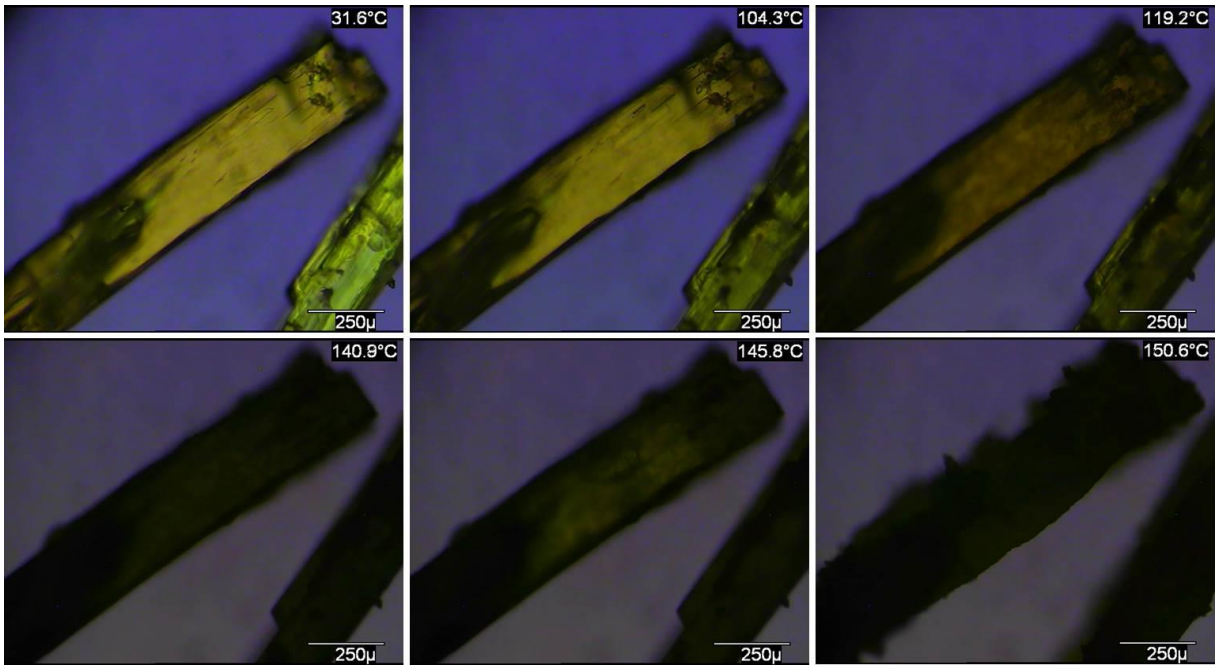

Figure 225 - Optical micrographs of CBZ:FORM crystals at different temperatures under polarized light (heating rate of 10 ºC.min^{-1}).

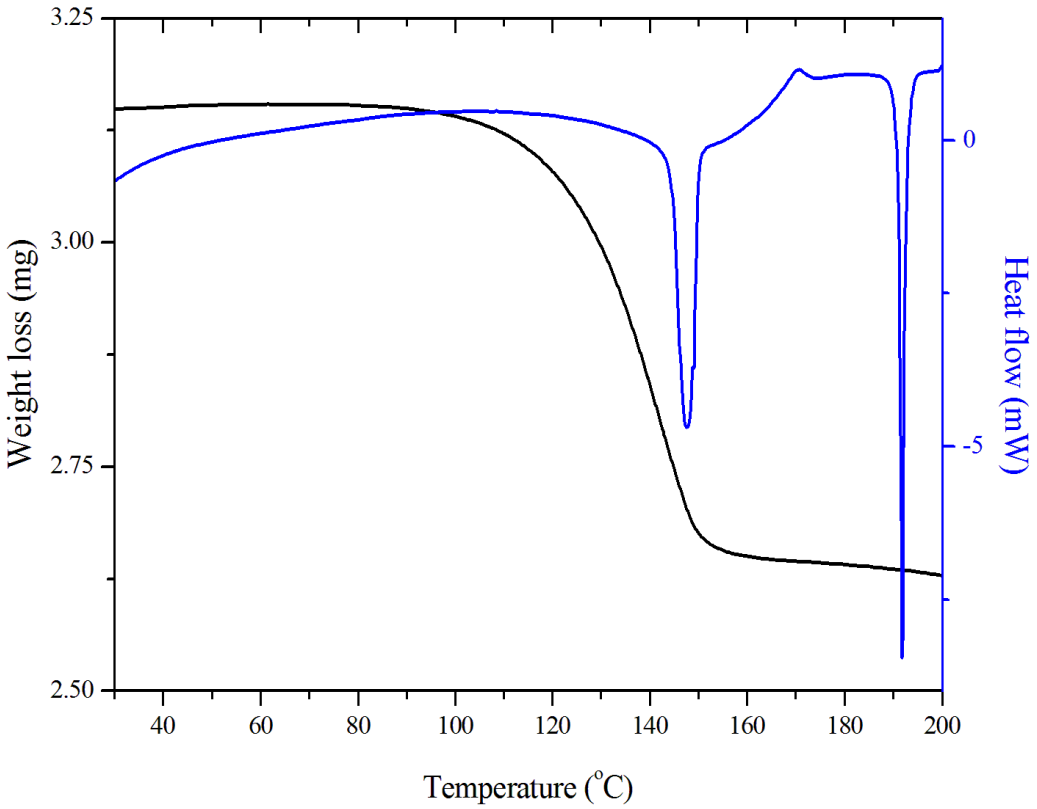

Figure 226 - DSC and TGA thermal characterization of CBZ:FORM crystals (10 ºC.min^{-1}, perforated lid, N_2).

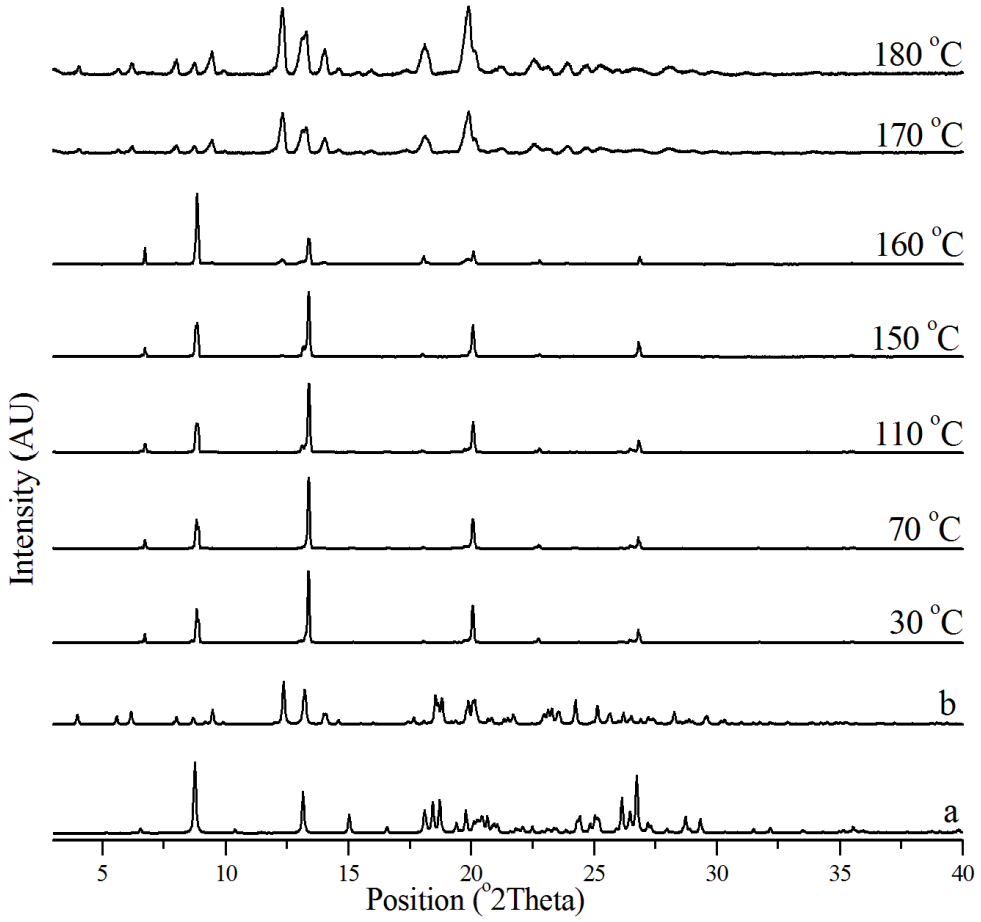

Figure 227 - *In situ* variable temperature PXRD patterns of CBZ:FORM crystals (10 ºC.min^{-1}, 25-180 ºC). *a*: CBZ:FORM from UNIBOI. *b*: CBZ Form I from CBMZPN11.

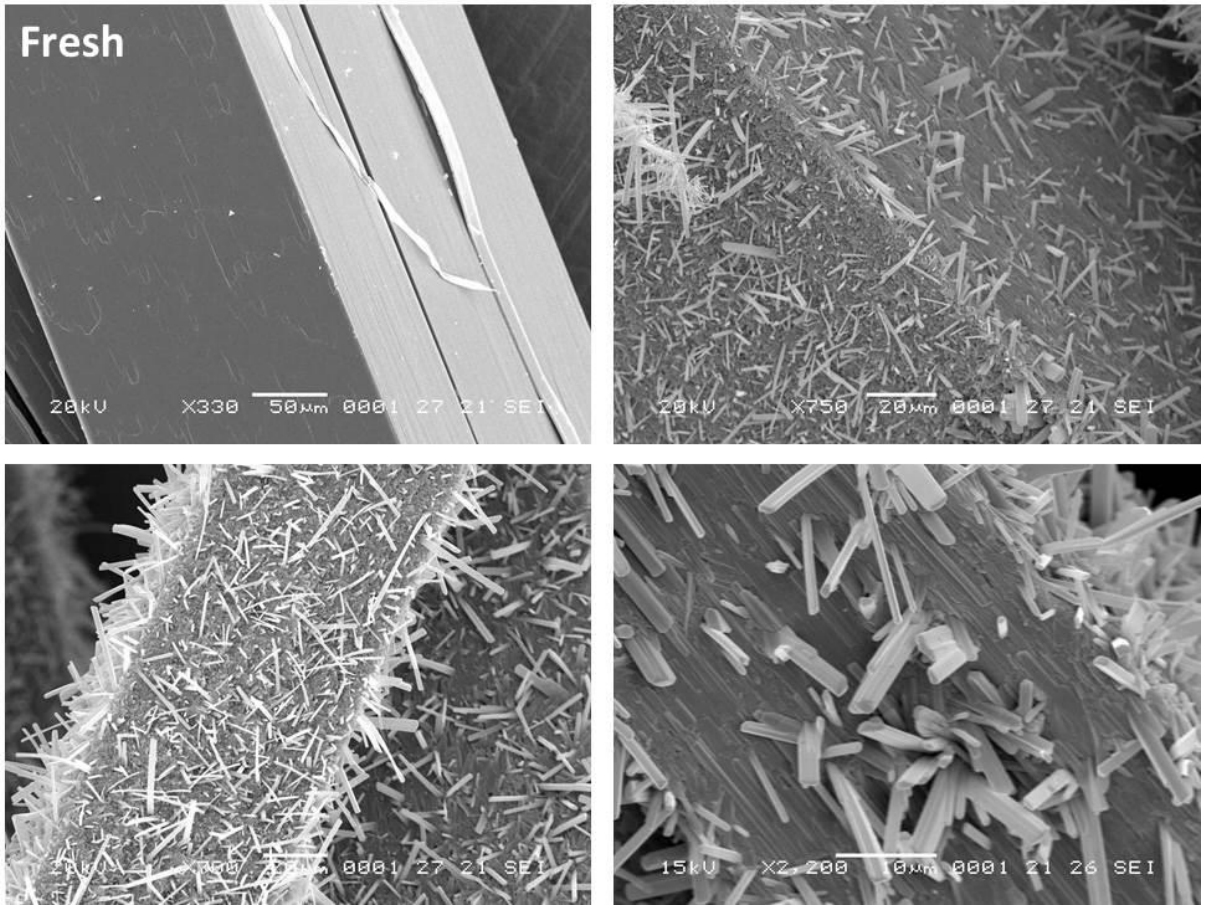

Figure 228 - SEM micrographs of CBZ:FORM crystals heated until 170 ºC (N_2, heating rate of 10 ºC.min^{-1}). The fresh surface is added for comparison purposes.

7.3.9. CBZ dioxane solvate (2CBZ:DIOX), Group 3.

Single crystals of 2CBZ:DIOX turn uniformly opaque on heating and the original shape of the particles is maintained (Figure 229). These findings agree with the DSC and TGA curves, which are illustrated in Figure 230. TGA shows one single event of weight loss in the range 70-120 ºC. The heat flow curve characterizes desolvation as a relatively broad endothermic event ending at about 120 ºC. The DSC curve also demonstrates baseline shifts in the range 150-170 ºC, which resemble exothermic transformations, such as possible recrystallization.

In situ PXRD shows detectable reflections of Form I above 90 ºC and a rapid lattice change with increase in temperature (Figure 231). Similar to 2CBZ:BZQ, the results demonstrate that the dioxane solvate does not form an isostructural desolvate as CBZ:2H_2O and CBZ:FORM do.

Ex situ SEM analyses of the desolvated samples show the formation of needles which are characteristic of CBZ Form I (Figure 232). As for CBZ:FORM, the main crystal surfaces show distinct behaviour. While one surface shows needles and domains oriented along

the particle axis, the other shows needles erratically arranged over the surface. No cracks are usually detected during desolvation, nor do the fresh surfaces fracture because of vacuum. Figure 232, however, displays an image of one sample in which perfectly aligned longitudinal cracks were formed upon heating. This behaviour was not frequently seen in desolvated 2CBZ:DIOX crystals and, although the structure is closely related to the dihydrate, only random cracks have been seen during the analysis of the dioxane solvate.

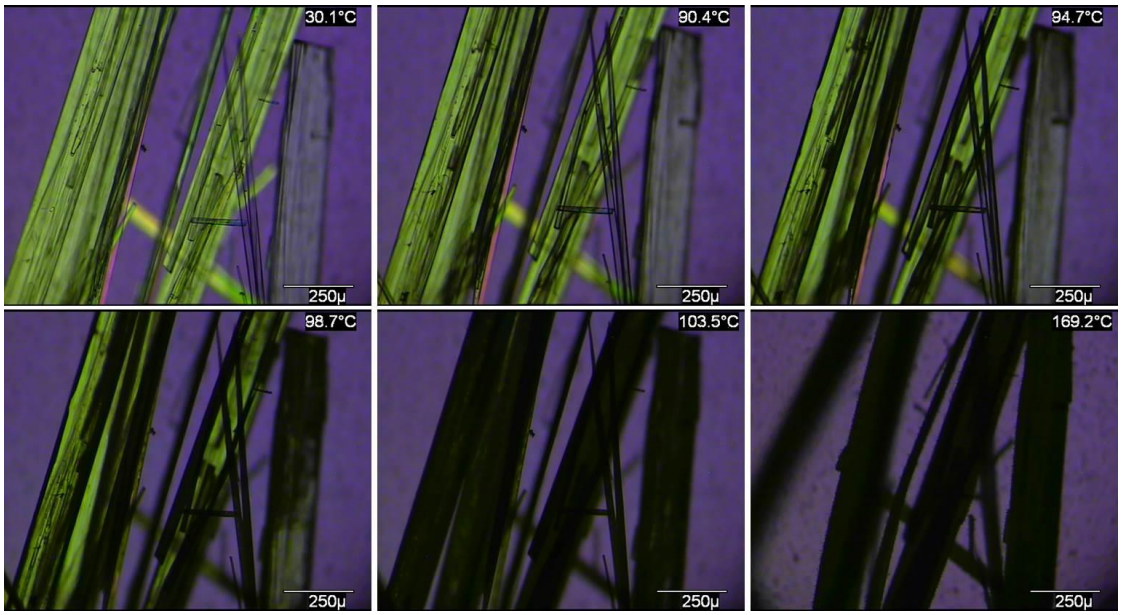

Figure 229 - Optical micrographs of 2CBZ:DIOX crystals at different temperatures under polarized light (heating rate of 10 ^{o}C.min^{-1}).

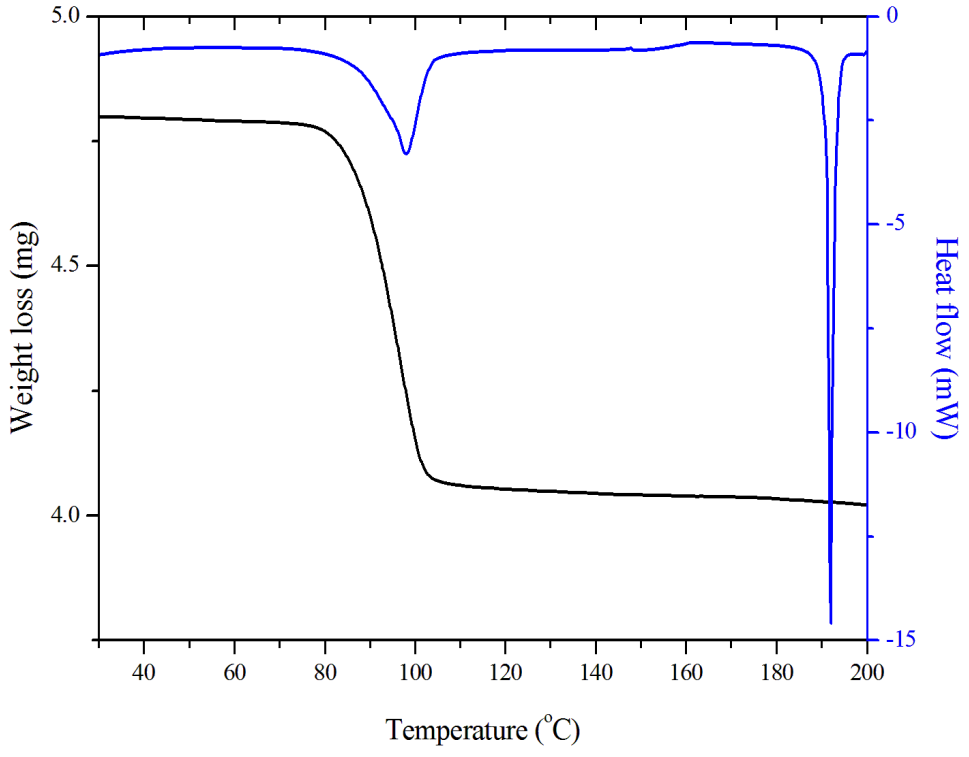

Figure 230 - DSC and TGA thermal characterization of 2CBZ:DIOX crystals (10 ^{o}C.min^{-1}, perforated lid, N_2).

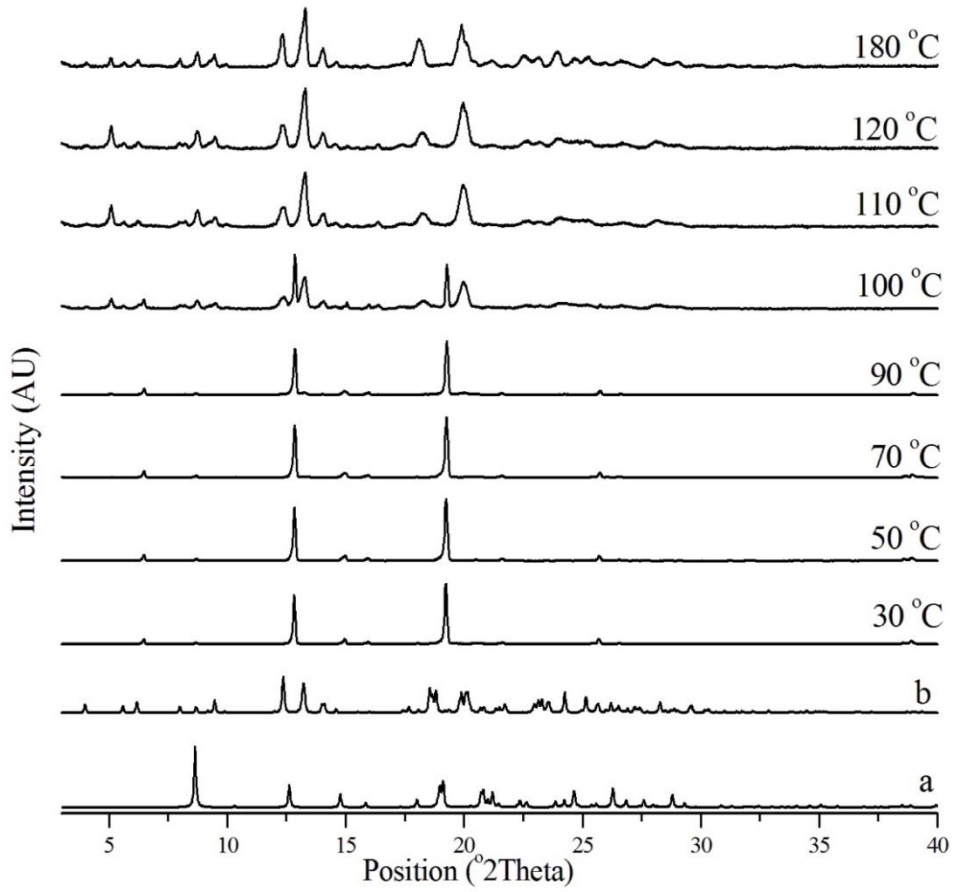

Figure 231 - *In situ* variable temperature PXRD patterns of 2CBZ:DIOX crystals (10 °C.min^{-1}, 25-180 °C). *a*: 2CBZ:DIOX from in-house data. *b*: CBZ Form I from CBMZPN11.

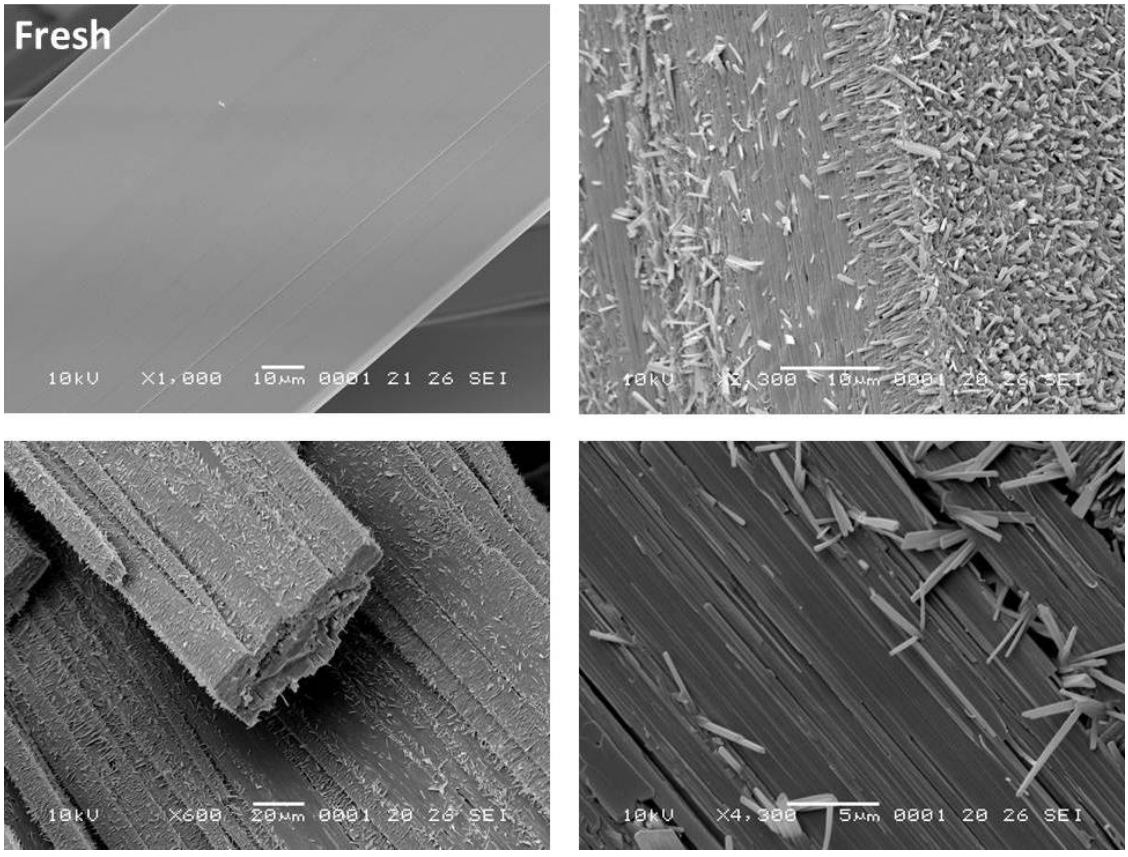

Figure 232 - SEM micrographs of 2CBZ:DIOX crystals heated until 120 °C (N_2, heating rate of 10 °C.min^{-1}). The fresh surface is added for comparison purposes.

7.3.10. CBZ 2,2,2-trifluoroethanol solvates (CBZ:TFE and 2CBZ:TFE), Group 4.

CBZ:TFE

Single crystals of CBZ:TFE exhibit fluctuations in colour upon heating (Figure 233). It is unclear whether this is related to molecular movement during crystal decomposition or to the formation of a peritectic mixture due to the release of TFE below its boiling point (74.0 ^{o}C). This effect is only visible at the initial stages of desolvation (~70 ^{o}C). As the desolvation proceeds (>75 ^{o}C), the material becomes polycrystalline and opaque under polarized light, while the original shape of the crystals is maintained. Figure 234 shows *ex situ* SEM images of CBZ:TFE crystals subjected to non-isothermal experiments at 10 ^{o}C.min^{-1}. It illustrates that desolvation of TFE leads to the formation of elongated domains, which develop holes between neighbouring grain surfaces. The alignment and the contact between domains frequently result in the formation of cracks that do not appear to follow any specific crystallographic orientation.

In situ PXRD experiments show that the desolvation of CBZ:TFE results in the formation of CBZ polymorph IV (Figure 235). Although minor peaks of the product are detected above 60 ^{o}C, a sudden lattice change is clearly seen above 80 ^{o}C. In contrast to the behaviour of the benzoquinone cocrystals, the experiments demonstrate that desolvation of the 1:1 trifluoroethanol solvate does not result in the formation of 2CBZ:TFE. It shows that the solvate with lower stoichiometry is not an intermediate of the decomposition of CBZ:TFE.

Figure 236 shows the DSC and TGA data. TGA demonstrates one event with two different slopes in the range 60-120 ^{o}C, while the heat flow curve collected at 10 ^{o}C.min^{-1} shows that desolvation is characterized by two unresolved endothermic events (T_{onset}=68.4 ^{o}C). Although the shape of the thermograms alone could indicate the existence of an intermediate form during desolvation, the combination of thermal analyses with other characterization techniques suggest that the findings only illustrate changes in the rate of desolvation. It is suggested that the recrystallization of CBZ at the final stages of desolvation may lead to a decrease in the rate of vaporization of TFE and desolvation of the remaining CBZ:TFE.

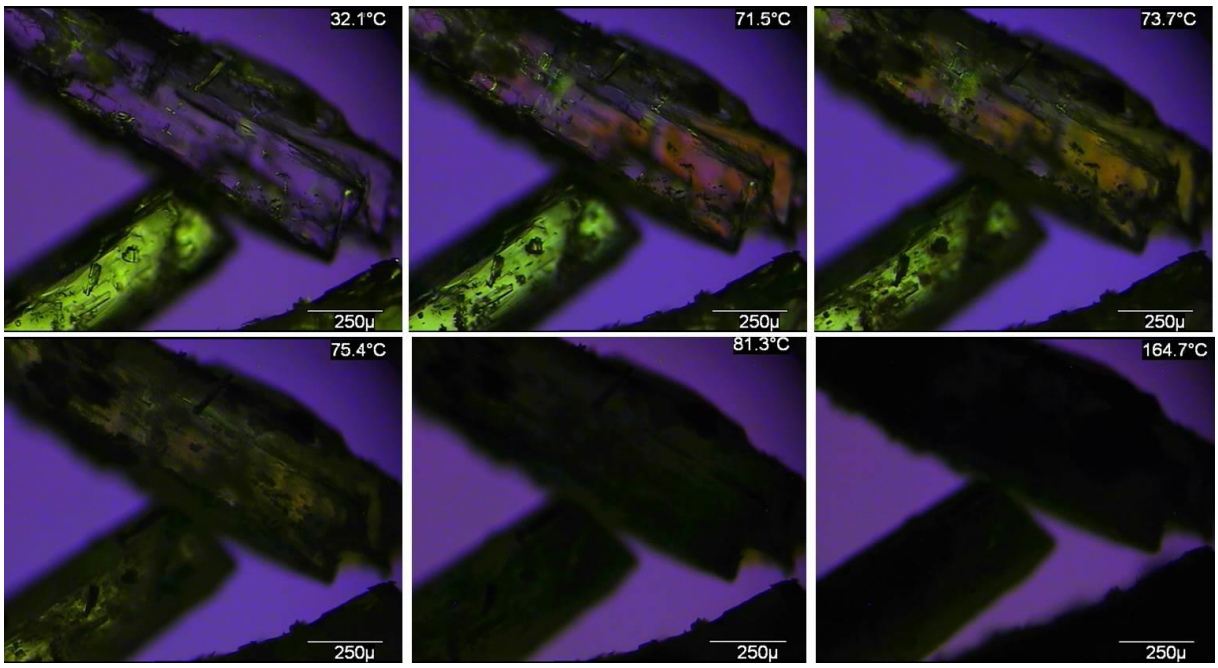

Figure 233 - Optical micrographs of CBZ:TFE crystals at different temperatures under polarized light (heating rate of 10 $^{o}C.min^{-1}$).

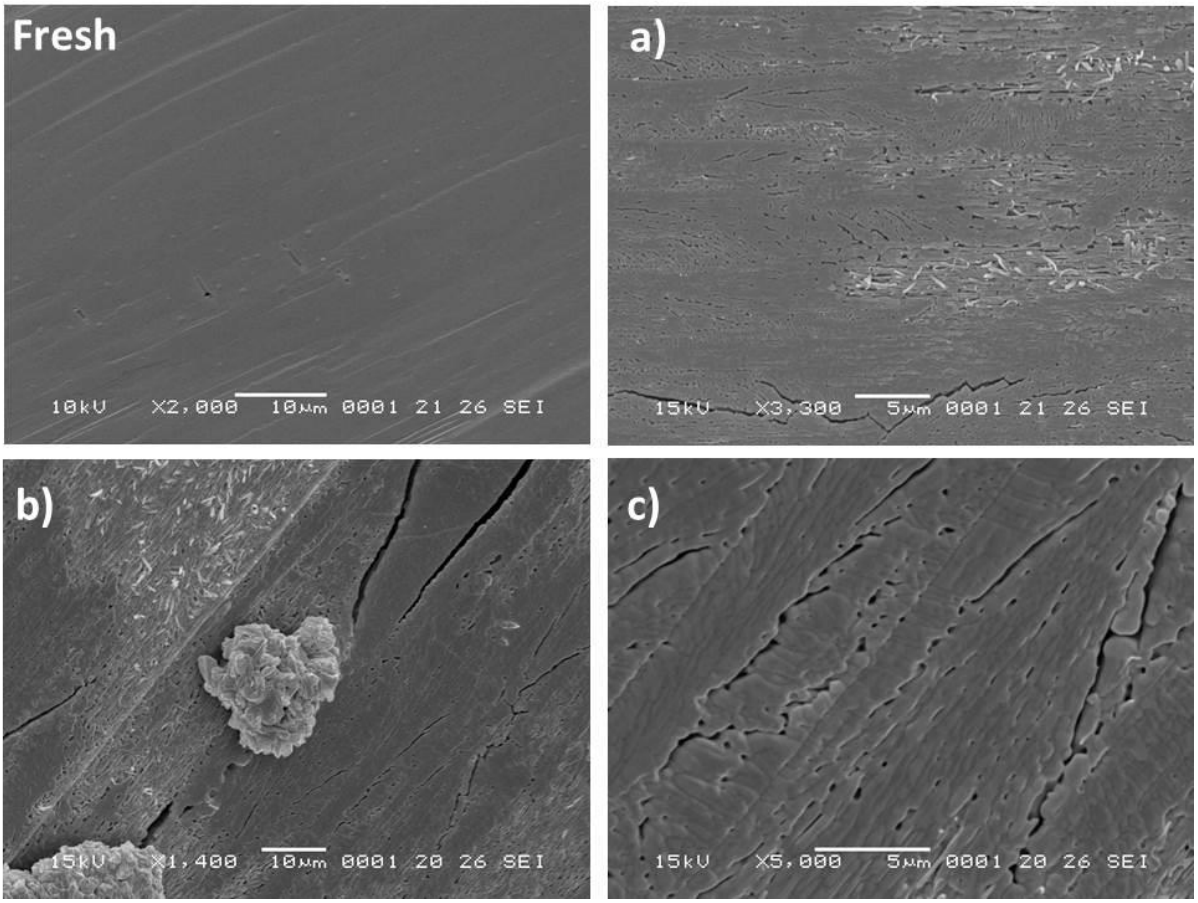

Figure 234 - SEM micrographs of CBZ:TFE crystals subjected to desolvation (the fresh surface is added for comparison purposes). *a* and *b*: heated until 120 ^{o}C (N_2, 10 $^{o}C.min^{-1}$). *c*: heated until 80 ^{o}C (N_2, heating rate of 10 $^{o}C.min^{-1}$).

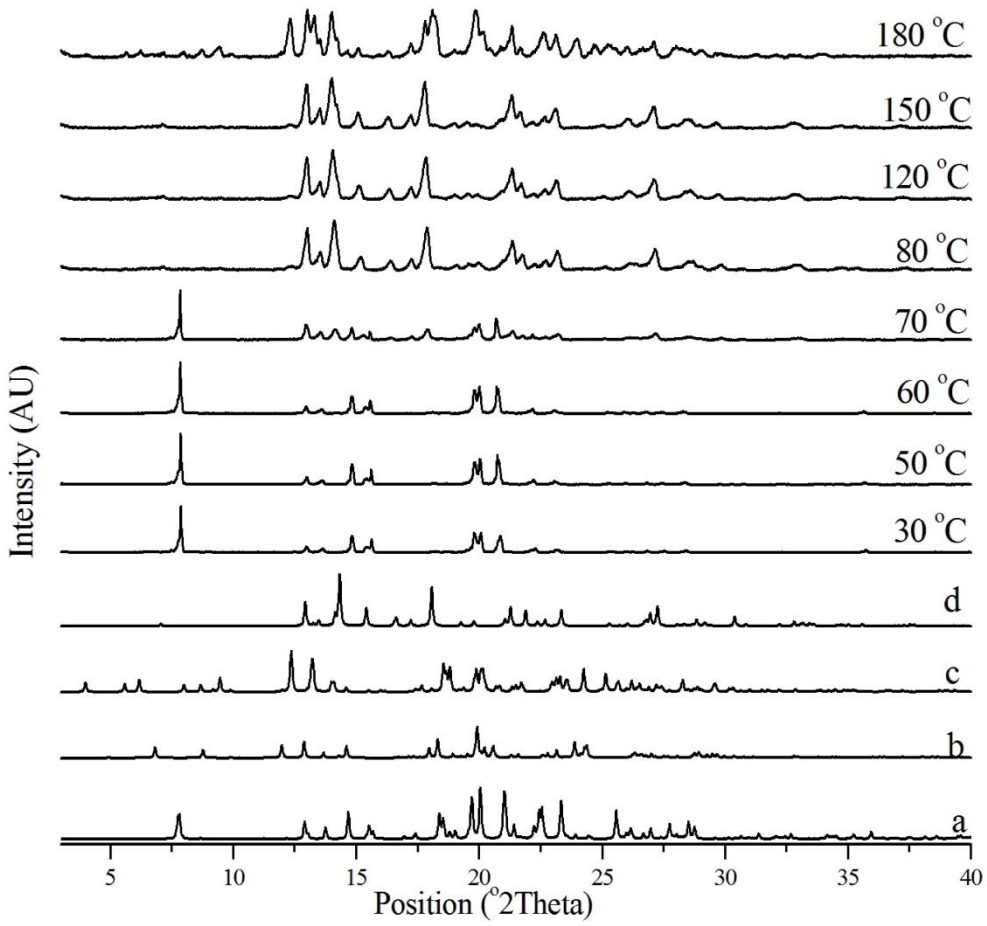

Figure 235 - *In situ* variable temperature PXRD patterns of CBZ:TFE crystals (10 ºC.min^{-1}, 25-180 ºC). *a*: CBZ:TFE from SAPDUJ. *b*: 2CBZ:TFE from in-house data. *c*: CBZ Form I from CBMZPN11. *d*: CBZ Form IV from CBMZPN12.

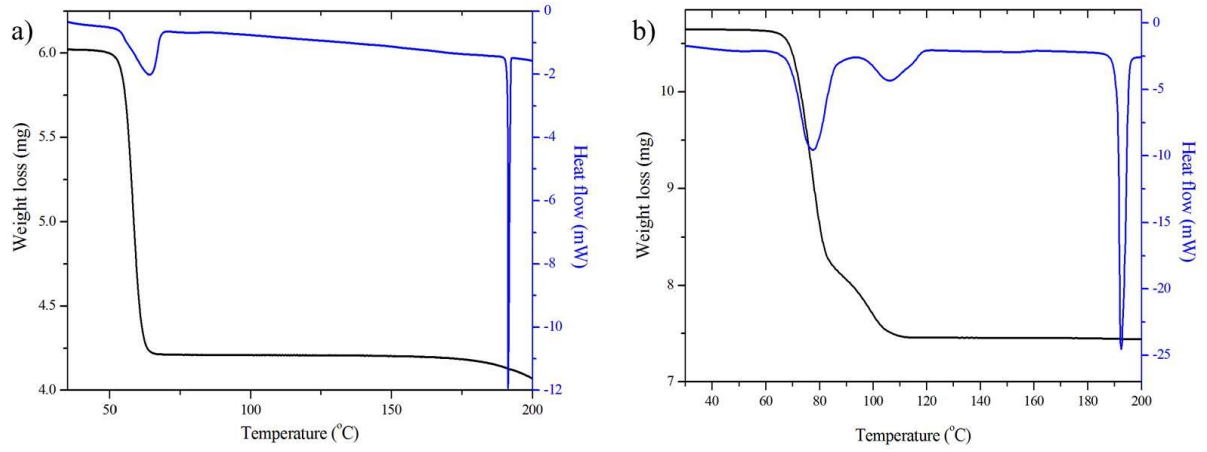

Figure 236 - DSC and TGA thermal characterisation of CBZ:TFE. *a:* 1 ºC.min^{-1}, perforated lid, N_2. *b*: 10 ºC.min^{-1}, perforated lid, N_2.

2CBZ:TFE

Analysis of 2CBZ:TFE crystals prepared from solution shows that decomposition starts at higher temperature than observed for CBZ:TFE. Figure 237 shows the *in situ* PXRD heating experiments of 2CBZ:TFE. The solvate lattice rapidly rearranges into CBZ polymorph I upon heating above 100 ºC. The DSC and TGA curves of the 2:1 solvate are also different

from the 1:1 form (Figure 238). TGA performed at 10 ^{o}C.min^{-1} shows a single weight loss in the range 80-130 ^{o}C, while the heat flow curve demonstrates that desolvation is characterized by an endothermic event with a T_{onset} of 97 ^{o}C.

Single crystals of 2CBZ:TFE turn opaque upon heating, while the original shape of the particles is maintained. Figure 239 shows that the crystals heterogeneously lose birefringence in the range 80-100 ^{o}C, while whiskers are formed above 150 ^{o}C. The *ex situ* SEM analyses of the materials resulting from desolvation show that the domains of the newly formed product are oriented along the needle axis (Figure 240). Considering the comparison of the TFE solvates to the BZQ cocrystals, the results show that the 1:1 and 2:1 solvates do not only show dissimilar surface characteristics between each other, but also exhibit different thermal curves and polymorphic outcome upon desolvation.

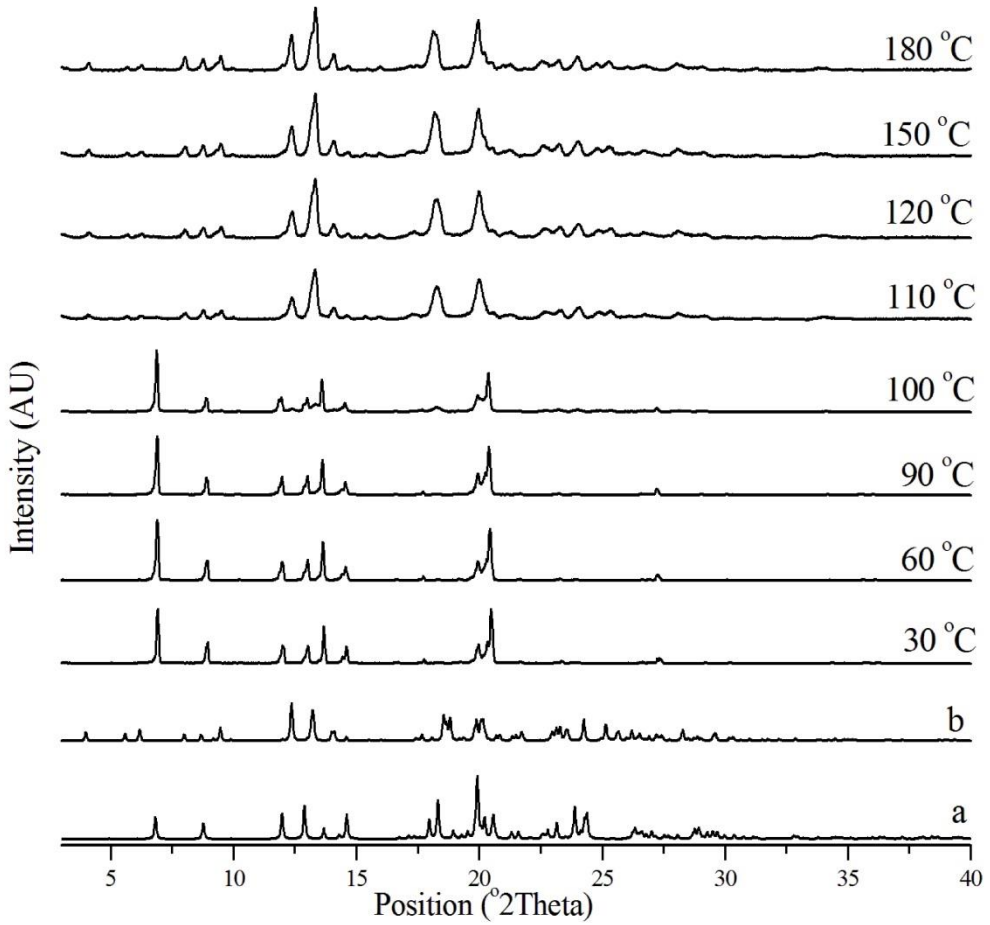

Figure 237 - *In situ* variable temperature PXRD patterns of 2CBZ:TFE crystals (10 ^{o}C.min^{-1}, 25-180 ^{o}C). *a*: 2CBZ:TFE from in-house data. *b*: CBZ Form I from CBMZPN11.

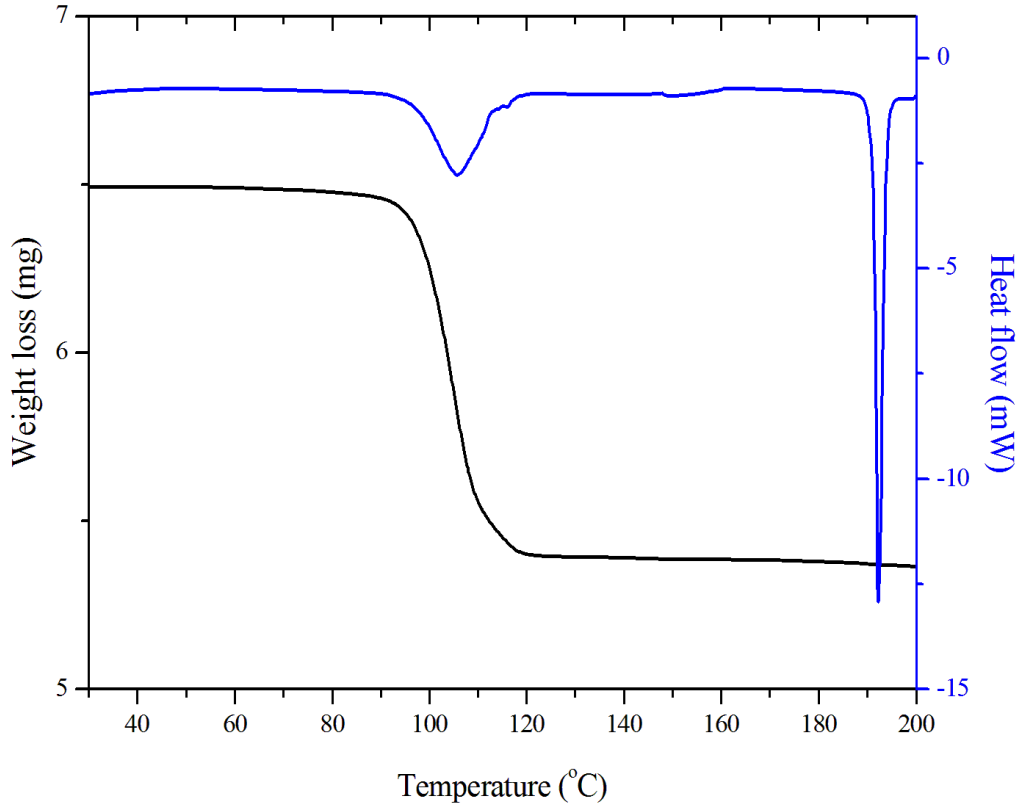

Figure 238 - DSC and TGA thermal characterization of 2CBZ:TFE crystals (10 $^{o}C.min^{-1}$, perforated lid, N_2).

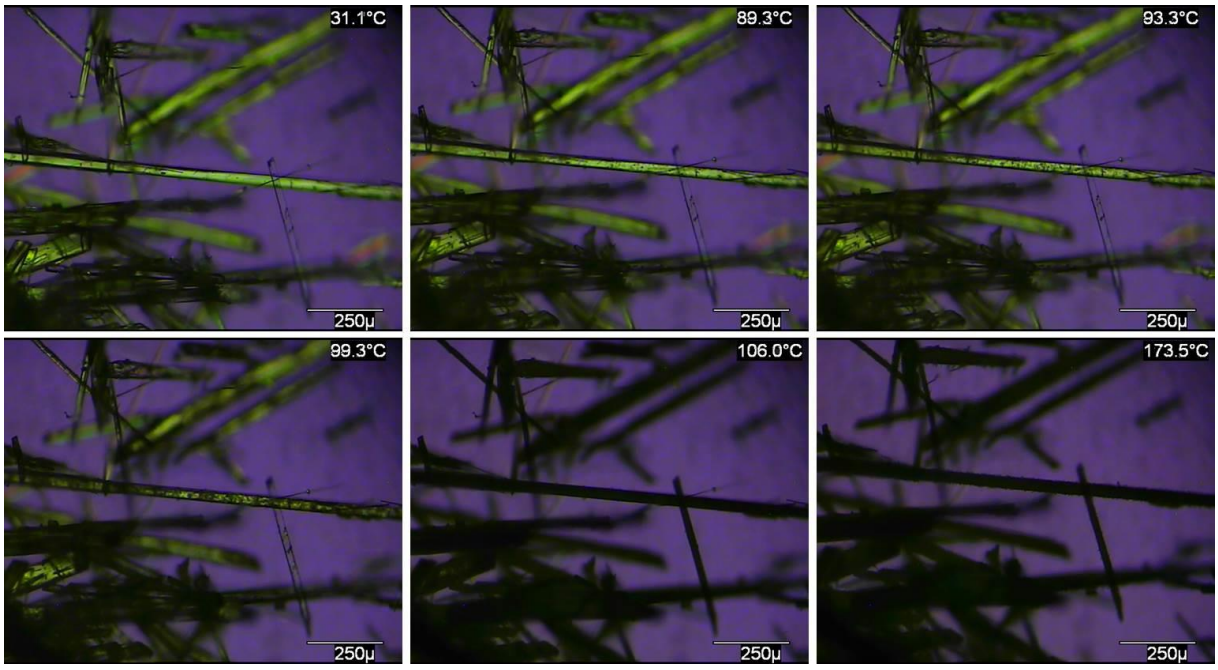

Figure 239 - Optical micrographs of 2CBZ:TFE crystals at different temperatures under polarized light (heating rate of 10 $^{o}C.min^{-1}$).

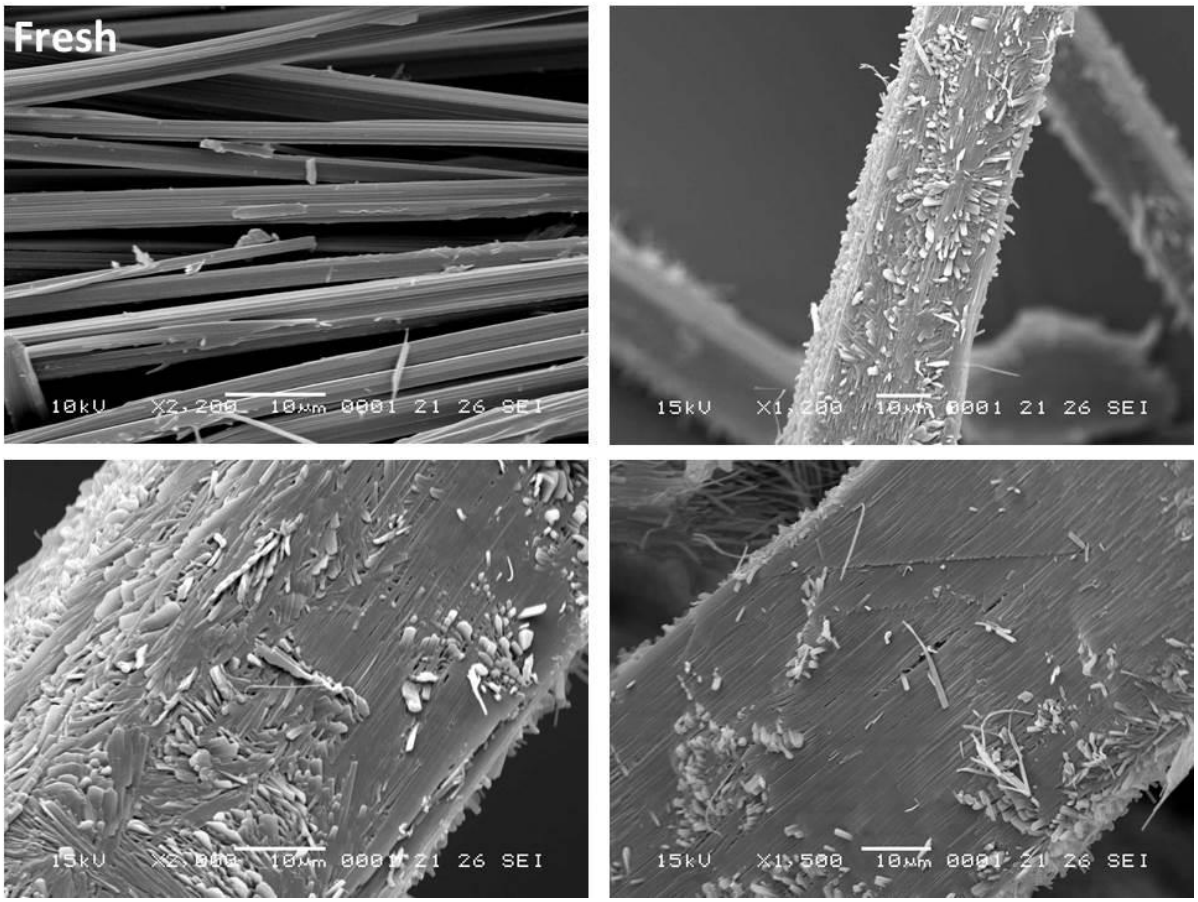

Figure 240 - SEM micrographs of 2CBZ:TFE crystals heated until 130 ºC (N_2, heating rate of 10 ºC.min^{-1}). The fresh surface is added for comparison purposes.

7.3.11. CBZ trifluoroacetic acid solvate (CBZ:TFA), Group 5.

The crystals of CBZ:TFA turn opaque on heating, with the original shape of the crystals maintained. Figure 241 shows the crystals lose birefringence above 100 ºC and whiskers appear to grow on the surface. Although *in situ* PXRD heating experiments performed at 10 ºC.min^{-1} did not detect CBZ polymorphs above 100 ºC, the diffractograms show evidences of lattice collapse and the formation of a liquid phase above 130 ºC (Figure 243). Visual observation has also shown that the reaction product was frequently molten (Figure 242).

The thermograms of the CBZ:TFA provide further insights about the desolvation process (Figure 244). The heat flow curves collected at 10 ºC.min^{-1} show an endothermic event that starts as a sharp endotherm (T_{onset}=128.4 ºC) but is followed by a broad event finishing above 140 ºC. As the temperature increases, two additional endothermic events are also observed. The endotherms can be correlated to three regions of weight loss that do not present clear limits in the TGA curves collected at 10 ºC.min^{-1}: (i) from approximately 80 to 175 ºC; (ii) from approximately 175 to 275 ºC; and (iii) above 275 ºC. Although it is suggested that the region (i) is related to the desolvation of CBZ:TFA and the (ii) and (iii) regions correspond to

the decomposition of CBZ, the analyses of the thermograms reveal additional information. Interestingly, the events in (ii) and (iii) are shifted to lower temperatures, as previously observed for 2CBZ:OXA (see Section 7.3.7). In the case of CBZ:TFA, however, the slopes of the curves collected at 10 ^{o}C.min^{-1} are not comparable to the characteristic slopes of CBZ decomposition.

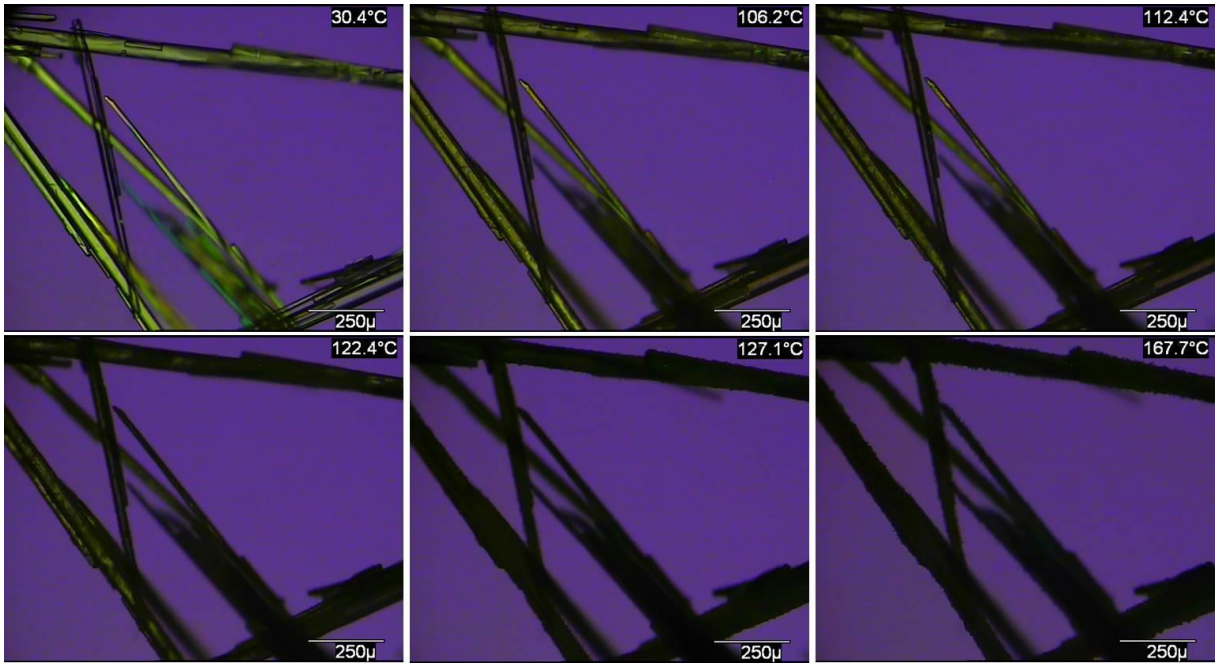

Figure 241 - Optical micrographs of CBZ:TFA crystals at different temperatures under polarized light (heating rate of 10 ^{o}C.min^{-1}).

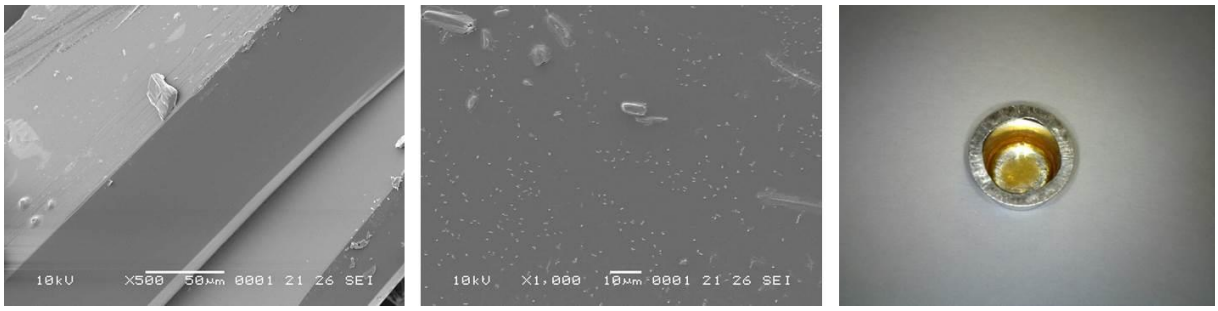

Figure 242 - SEM micrographs of CBZ:TFA crystals. The photograph on the right show the material which resulted from heating until 140 ^{o}C (N_2, heating rate of 10 ^{o}C.min^{-1}).

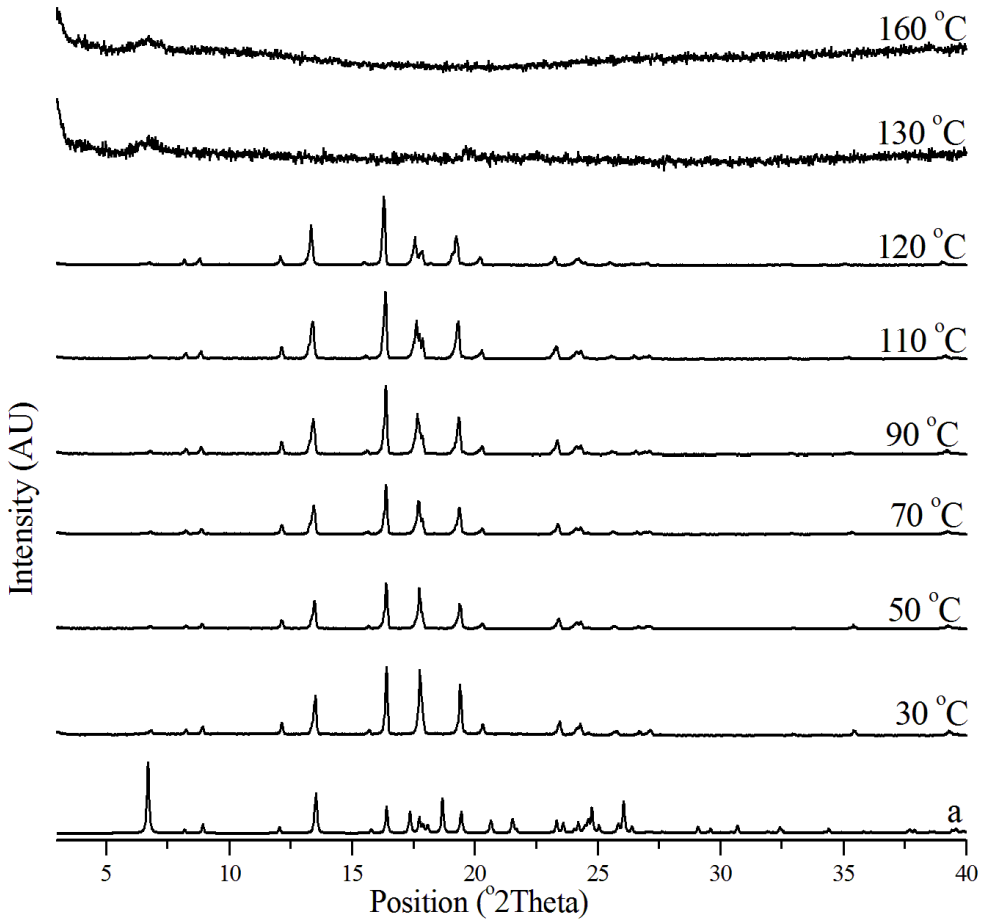

Figure 243 - *In situ* variable temperature PXRD patterns of CBZ:TFA crystals (10 ºC.min^{-1}, 25-180 ºC). *a*: CBZ:TFA from GINFOZ.

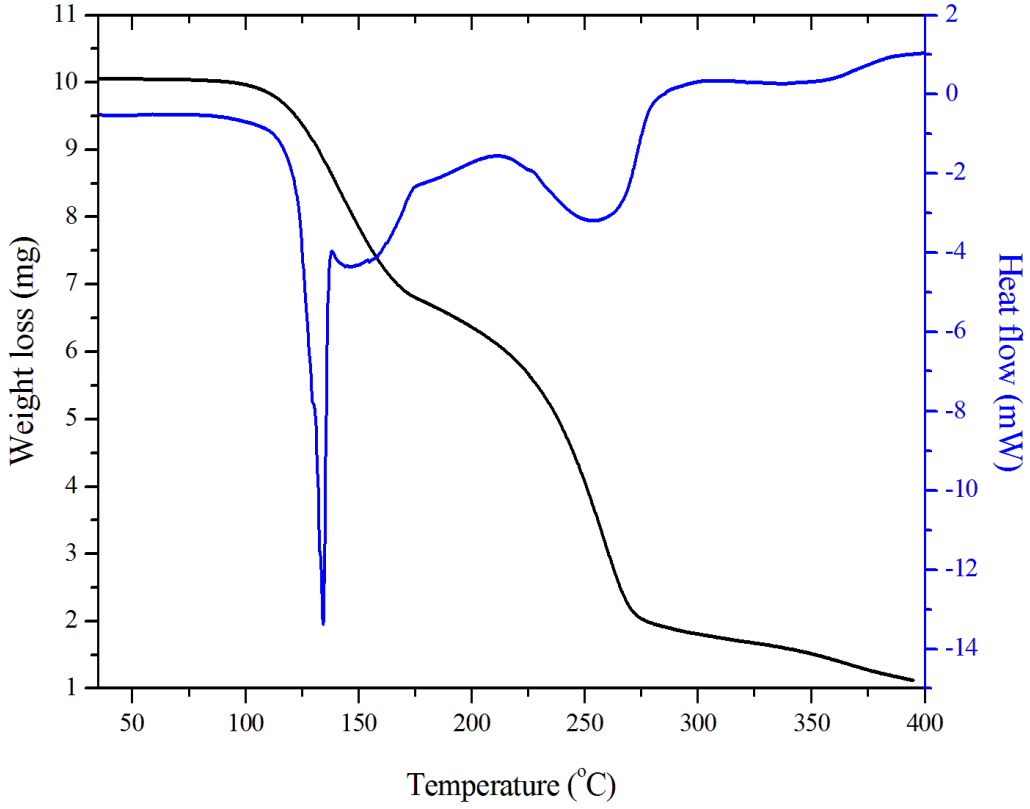

Figure 244 - DSC and TGA thermal characterization of CBZ:TFA crystals (10 ºC.min^{-1}, perforated lid, N_2).

Another difference in the behaviour of 2CBZ:OXA and CBZ:TFA is the effect of the heating rate on their thermal characteristics. Although the thermograms of 2CBZ:OXA do not differ whether they are collected at 1 or 10 $^{o}C.min^{-1}$, the CBZ:TFA thermograms do (Figure 245). At 1 $^{o}C.min^{-1}$ the TFA solvate shows three regions of weight loss: (i) from approximately 60 to 115 ^{o}C; (ii) from approximately 160 to 230 ^{o}C; and (iii) from approximately 230 to 275 ^{o}C. The regions (ii) and (iii) clearly correspond to the decomposition of CBZ, as seen in the thermal analyses of CBZ polymorphs. In contrast to the experiments performed at 10 $^{o}C.min^{-1}$, see Figure 64 shown earlier, the desolvation event resulting from non-isothermal heating at $1^{o}C.min^{-1}$ is clearly separated from the other weight loss events. The DSC curves collected at 1 $^{o}C.min^{-1}$ combine the desolvation events to one endothermic process which is moderately asymmetric (T_{onset}=120.5 ^{o}C). A second endotherm is also observed at higher temperatures between regions (i) and (ii) (T_{onset}=145.3 ^{o}C), which could be related to melting.

In situ PXRD (Figure 246) show no detectable peaks of CBZ polymorphs upon heating at 1 $^{o}C.min^{-1}$, but demonstrate the formation of a liquid phase above 130 ^{o}C. *In situ* optical micrographs collected during heating, however, show no clear evidences of melting, only the growth of whiskers on the surface of crystals which maintained their original morphology (Figure 247). Also, *ex situ* SEM images of samples heated until 140 ^{o}C at 1 $^{o}C.min^{-1}$ show needles and whiskers on the surface of the crystals (Figure 248). The inconsistencies between the characterization techniques may arise from the effect of sample size on mass and heat transfer. It is, however, clear that a liquid phase is likely to result from the desolvation of CBZ:TFA, whether it is characterized as melting, peritectic melting or decomposition.

In general, the results show that the rate of desolvation of CBZ:TFA affects the rate and mechanism of chemical decomposition of CBZ. It is suggested that TFA *per se* or the species formed during the decomposition of TFA may react with CBZ, although the exact mechanism involved in these reactions is unclear. The literature reports that trifluoroacetic acid thermally decomposes mainly into carbon dioxide, difluoromethyl trifluoroacetate, carbon monoxide, and trifluoroacetyl fluoride.[211,212] Different studies have also shown the decomposition of salts of trifluoroacetic acid and the use of this solvent as an ionizing agent promoting the degradation of various compounds at room conditions and at high temperatures.[213–215]

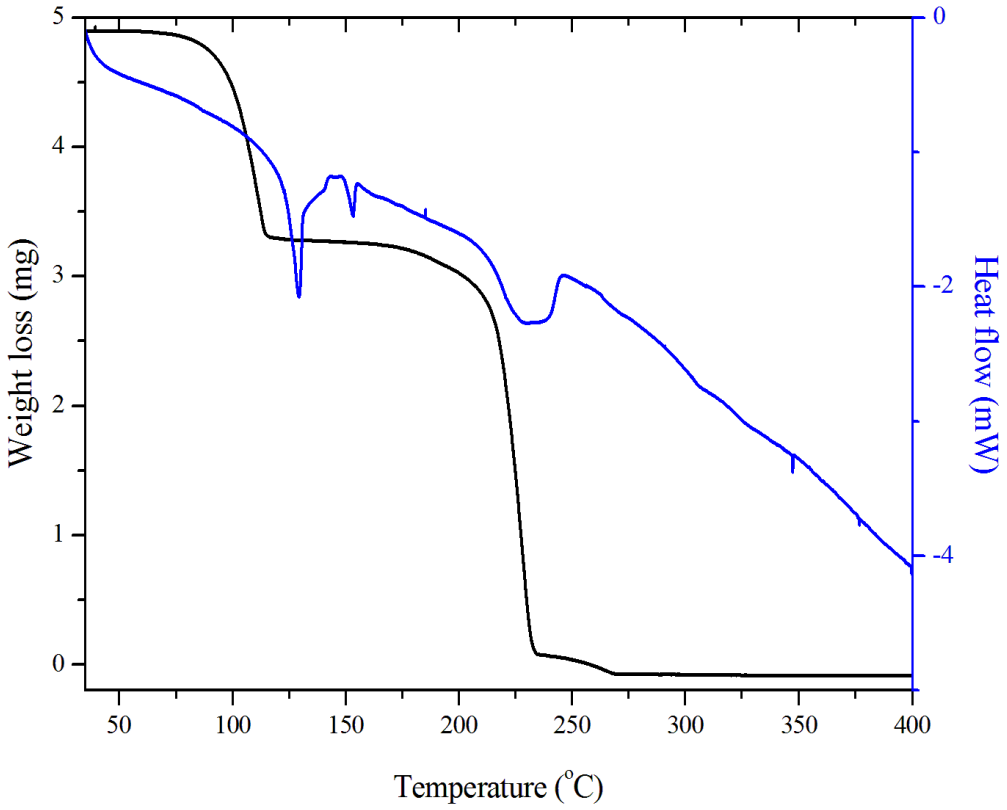

Figure 245 - DSC and TGA thermal characterization of CBZ:TFA crystals (1 °C.min^{-1}, perforated lid, N_2).

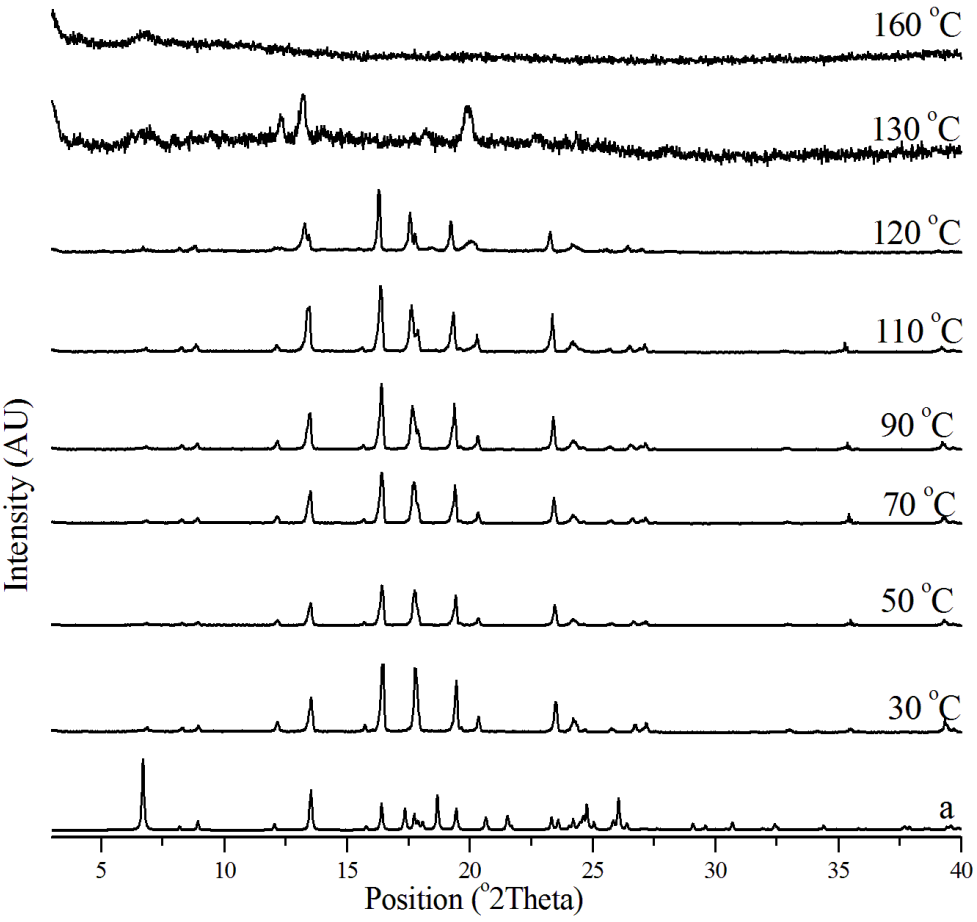

Figure 246 - *In situ* variable temperature PXRD patterns of CBZ:TFA crystals (1 °C.min^{-1}, 25-180 °C). *a*: CBZ:TFA from SAPDUJ.

Figure 247 - Optical micrographs of CBZ:TFA crystals at different temperatures under polarized light (heating rate of 10 $^{o}C.min^{-1}$).

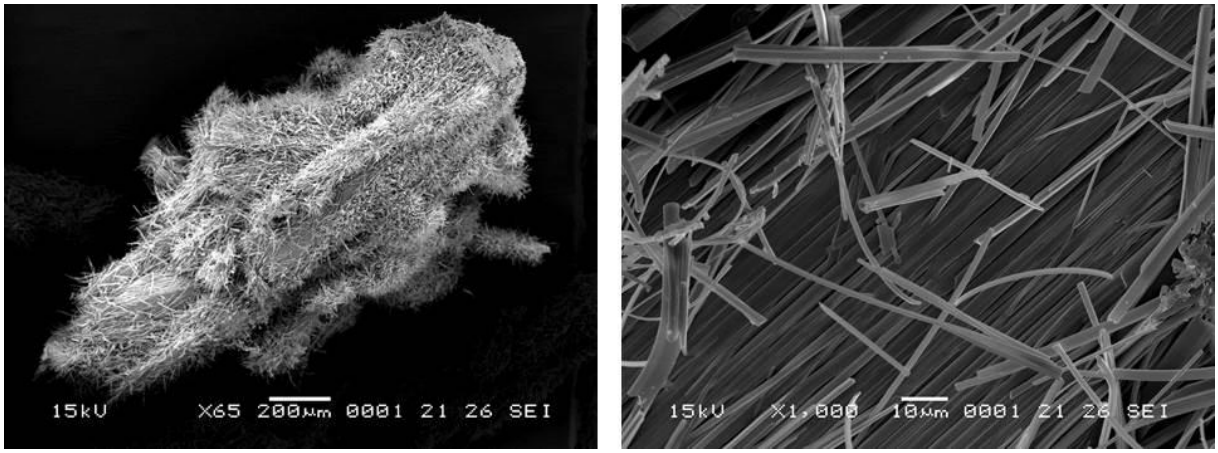

Figure 248 - SEM micrographs of CBZ:TFA crystals heated until 140 ^{o}C (N_2, heating rate of 1 $^{o}C.min^{-1}$).

Using the hypothesis that trifluoroacetic acid promotes the decomposition of CBZ, it is suggested that high heating rates change the thermal behaviour of the solvate because they shift the desolvation to higher temperatures at which TFA may decompose and/or the reaction of CBZ with trifluoroacetic acid is catalysed. Decomposition may also be facilitated in the molten state, which was experimentally evidenced in CBZ:TFA.

Considering all the materials analysed in the course of the present study, three were samples which clearly resulted in molten material after desolvation/dehydration: 2CBZ:OXA, CBZ:TFA and $[CBZ]_2[H_3O][Cl].2H_2O$[216,217]. Although out of the scope of the initial work, $[CBZ]_2[H_3O][Cl].2H_2O$ was synthesized with the aim of comparing its thermograms to the other materials, knowing that it has strong ionic interactions and presents packing similar to those of Group 3. $[CBZ]_2[H_3O][Cl].2H_2O$ shows DSC and TGA curves (Figure 249) which are

similar to the curves of CBZ:TFA and reminds us about another factor which may have also affected the thermal behaviour of CBZ:TFA: *i.e.* the ionic interaction between the constituents in the lattice. In this case, the desolvation of CBZ:TFA may result in point defects which are more destructive in nature (Schottky defects are types of point defects in ionic crystals). The rate of desolvation can affect the nature and the quantity of such defects, and, in the CBZ:TFA example, the rate of desolvation may also modify the ionization character of the species. Perhaps the properties of the desolvate product, such as melting, sublimation and stability, may vary as a consequence of ionization state during desolvation.

Analysis of the thermal behaviour of CBZ:TFA raises the following question: how is the temperature-mediated increase in molecular motion related to temperature-mediated changes in the nature of molecular interactions? Although both effects may not be separated from one another, testing if and how frequently a network may change from a hydrogen-bonded to an ionic character, and vice versa, as a function of temperature and heating rate may improve the overall understanding of solid state reactivity and defect formation in desolvation. To the best of my knowledge, the interplay between desolvation, Schottky defect formation and chemical decomposition are unexplored in molecular crystals and I found no examples in the literature. Although these phenomena are difficult to tackle experimentally, this could be an interesting field of study, especially considering that salts tend to be hydrated or solvated.

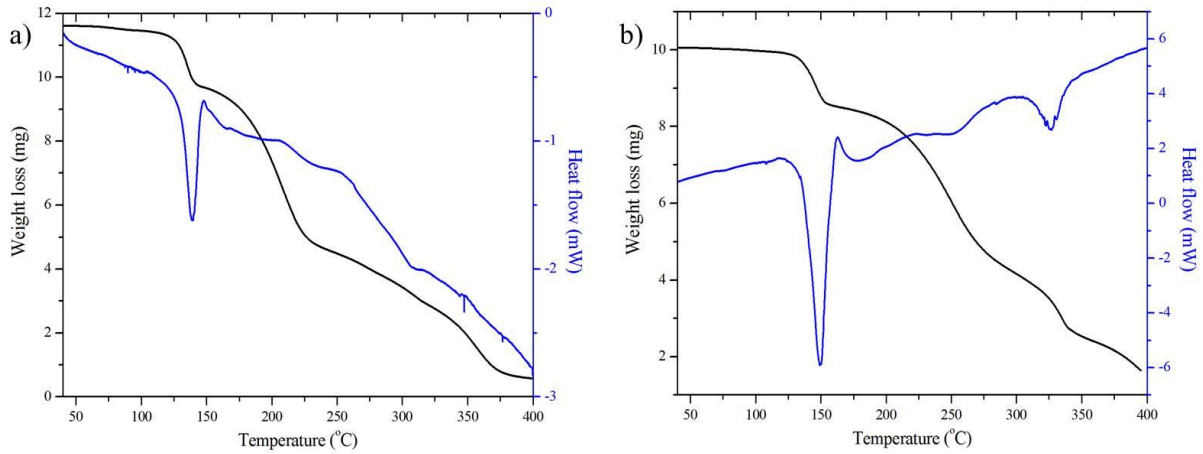

Figure 249 - DSC and TGA thermal characterisation of $[CBZ]_2[H_3O][Cl].2H_2O$. *a:* 1 °C.min^{-1}, perforated lid, N_2. *b*: 10 °C.min^{-1}, perforated lid, N_2.

7.3.12. CBZ acetic acid solvate (CBZ:ACA), Group 5.

Crystals of CBZ:ACA turn opaque upon heating and overall shape of the particles is lost. The crystals, however, do not uniformly lose birefringence as desolvation proceeds. Figure 250 shows the development of opaque nuclei above 100 °C, which grow throughout the

crystal as the temperature increases. The formation and growth of these nuclei results in the loss of the crystal shape above 150 ºC.

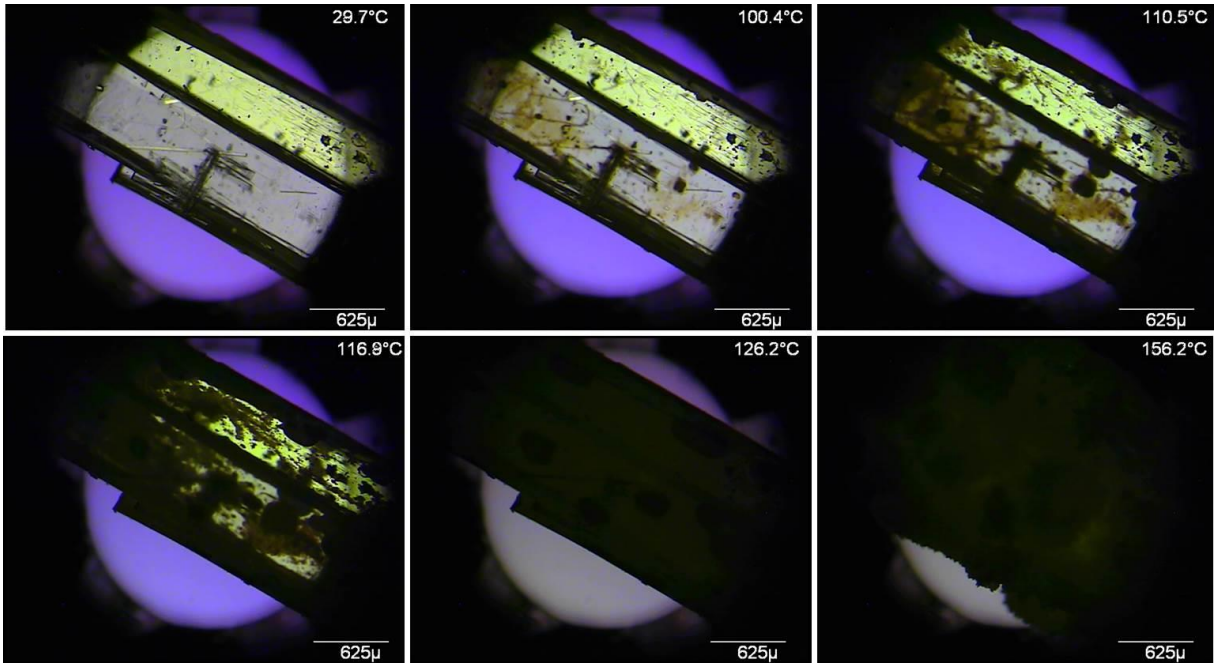

Figure 250 - Optical micrographs of CBZ:ACA crystals at different temperatures under polarized light (heating rate of 10 ºC.min^{-1}).

Ex situ SEM analyses of the desolvated samples show the formation of needle-like domains on the surface of the crystals (Figure 251). Interestingly, different faces show distinct behaviours characterized by oriented domains along the crystal axis or by needles erratically arranged on the surface. Evidence of melting was sometimes observed and characterized as spherulite growth on the crystal surface. No cracks were detected during desolvation, nor did the fresh surfaces fracture because of the vacuum.

DSC and TGA curves are illustrated in Figure 252. A single weight loss is observed in the range 80-140 ºC. The heat flow curve associates desolvation with one event (T_{onset}=125.6 ºC), which starts as a broad endotherm but becomes sharper as the temperature increases. This characteristic may be correlated to the existence of concomitant events, such as desolvation and melting or the formation of a peritectic mixture. The thermograms show a minor exothermic event after the endotherm assigned to desolvation.

In situ PXRD indicates detectable reflections of CBZ Form I at 160 ºC and a rapid lattice change with the increase in temperature (Figure 253). Similar to that observed in heating experiments of CBZ:2H_2O and CBZ:FORM (see Section 5.3, Chapter 5; and Section 7.3.8, Chapter 7, respectively), the results demonstrate that the acetic acid solvate undergo isostructural desolvation and shows lattice modification only after the release of a significant amount of solvent. The temperature in which transformation into polymorph I was detected by

PXRD can be correlated to the exothermic event observed by DSC. Although no liquid phase was detected by PXRD, it is suggested that a peritectic mixture may result from desolvation. Interestingly, crystals immersed in silicon oil and subjected to heating show the release of bubbles from approximately 100 to 145 ºC, while at approximately 150 ºC the crystals melt and recrystallize as needles (Figure 254).

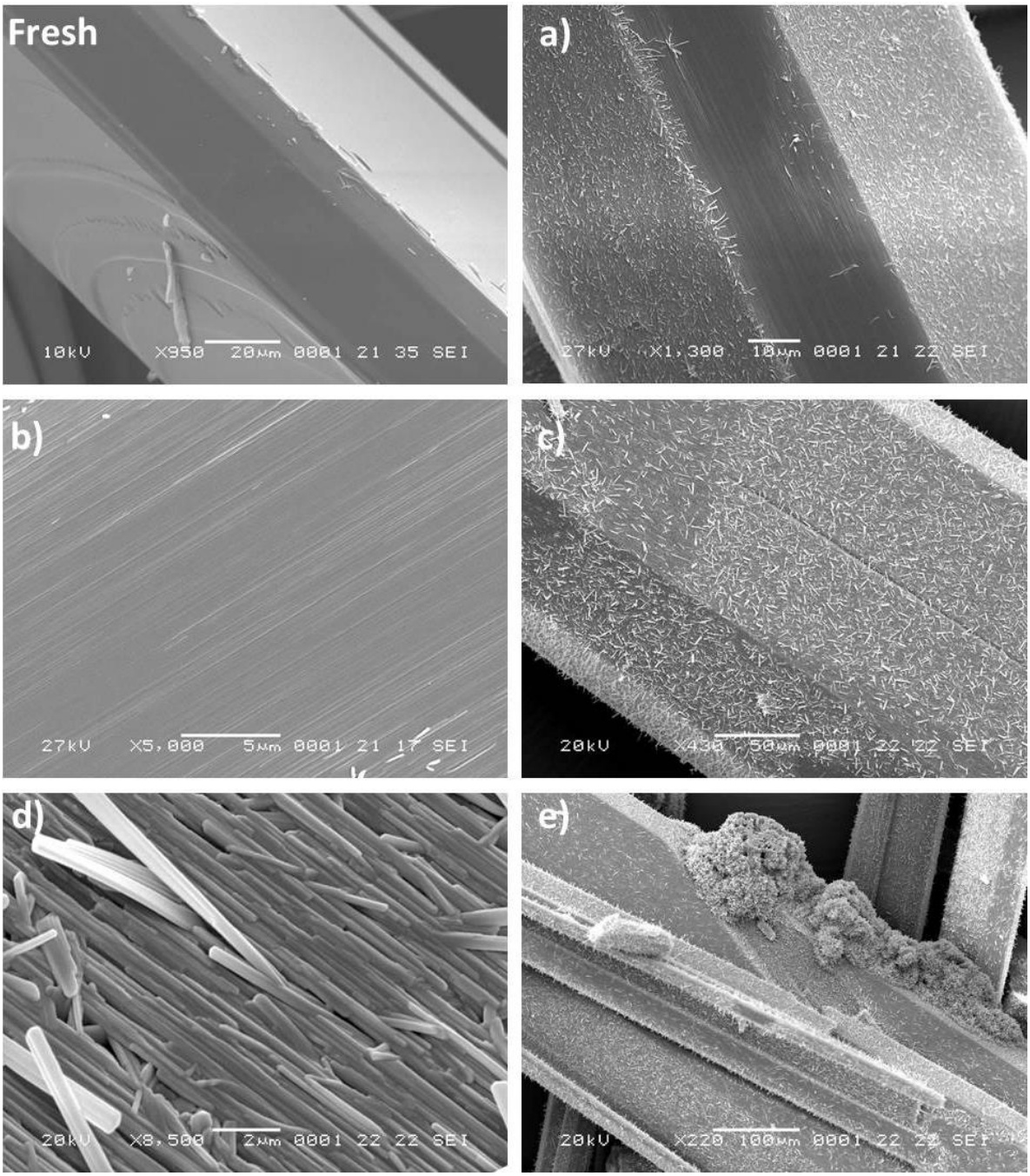

Figure 251 - SEM micrographs of CBZ:ACA crystals subjected to desolvation (the fresh surface is added for comparison purposes). *a*, *b* and *c*: heated until 100 ºC (N_2, 10 ºC.min^{-1}). *d* and *e*: heated until 150 ºC (N_2, heating rate of 10 ºC.min^{-1}).

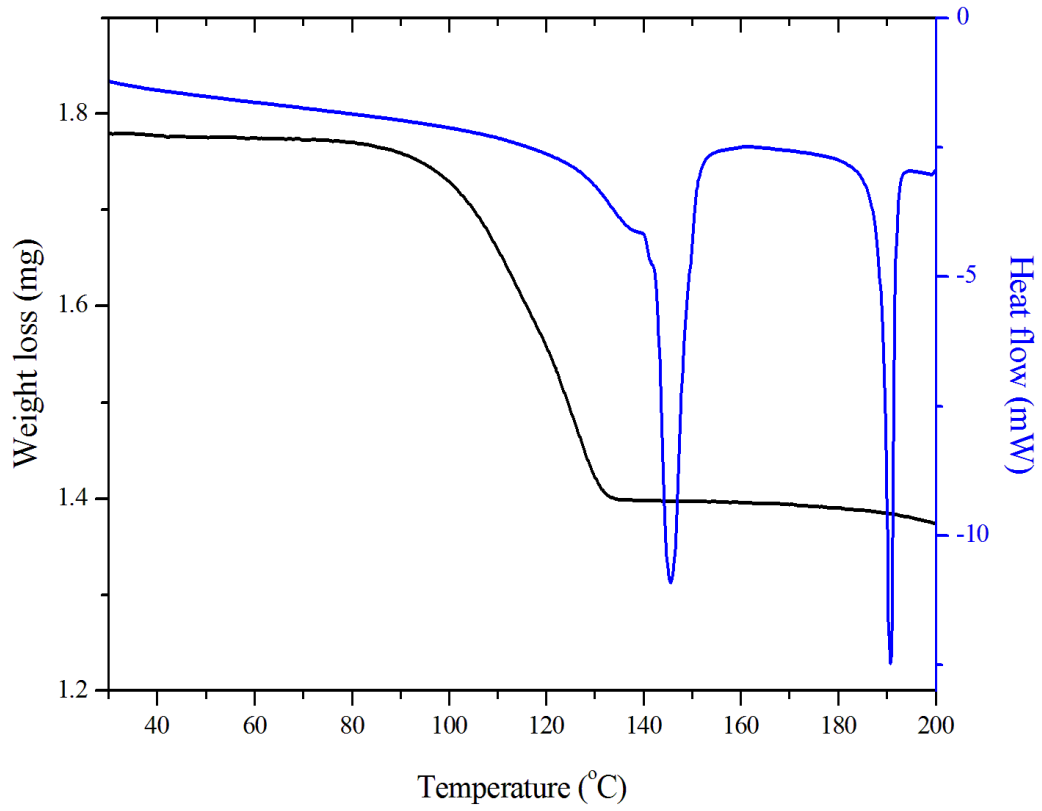

Figure 252 - DSC and TGA thermal characterization of CBZ:ACA crystals (10 °C.min^{-1}, perforated lid, N_2).

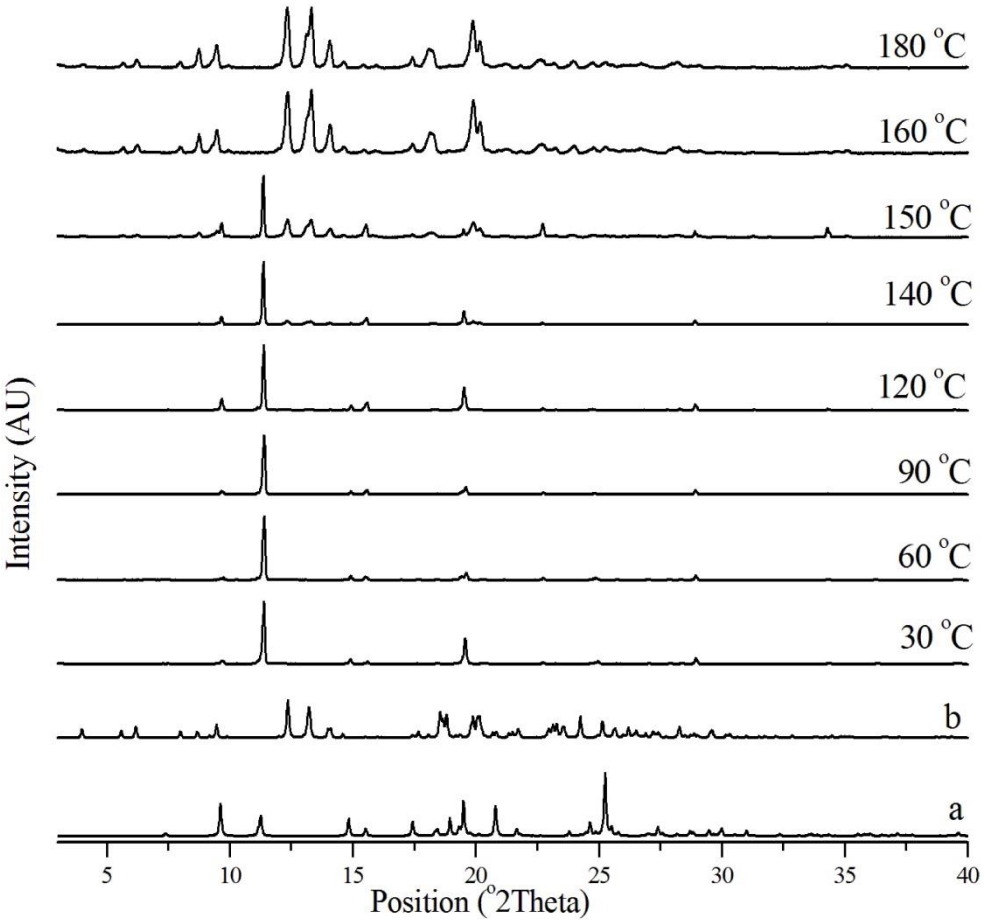

Figure 253 - *In situ* variable temperature PXRD patterns of CBZ:ACA crystals (10 °C.min^{-1}, 25-180 °C). *a*: CBZ:ACA from UNEZIW. *b*: CBZ Form I from CBMZPN11.

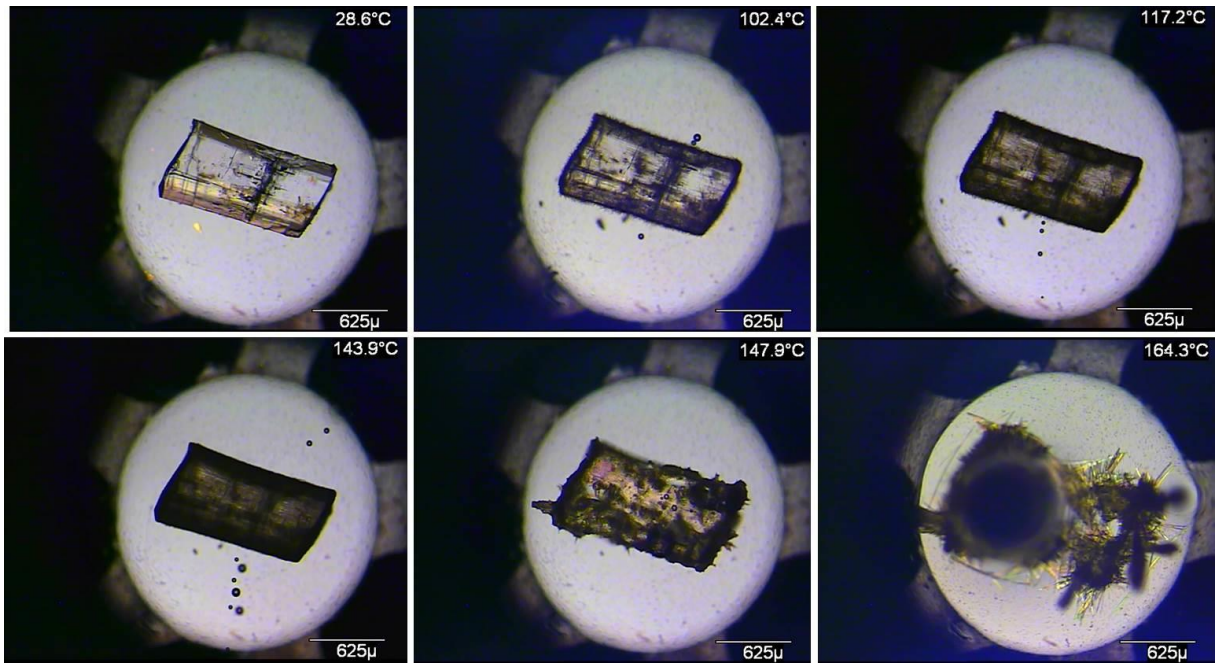

Figure 254 - Optical micrographs of CBZ:ACA crystals immersed in silicon oil and heated to different temperatures under polarized light (heating rate of 10 ^{o}C.min^{-1}).

7.3.13. CBZ formic acid solvate (CBZ:FA), Group 5.

CBZ:FA crystals turn opaque upon heating and lose original shape (Figure 255). At the initial states of desolvation, the crystals exhibit fluctuations in their colour and later show the development of opaque nuclei above 100 ^{o}C. The nuclei grow throughout the crystal as the temperature increases, causing the loss of the particles shape above 130 ^{o}C. It is suggested that these findings are related to the formation of a peritectic mixture as a result of the release of formic acid from the lattice.

Ex situ SEM analyses of the desolvated samples show the formation of needle-like domains characteristic of CBZ Form I (Figure 256). The surfaces show oriented domains along the crystal axis, but evidence of melting is also observed as spherulite formation. No cracks are detected during desolvation, nor do the fresh surfaces fracture because of vacuum.

The DSC and TGA curves are shown in Figure 257. A single weight loss is observed in the range 100-160 ^{o}C. The heat flow curve shows desolvation as one endothermic event (T_{onset}=119.0 ^{o}C) associated with other events, which may represent desolvation and melting or formation of a peritectic mixture. *In situ* PXRD indicates new reflections appearing above 110 ^{o}C, which gradually increase in intensity until a clear change is seen above 140 ^{o}C (Figure 258). The experiments agree with the observation by DSC and demonstrate that desolvation leads to CBZ polymorph I.

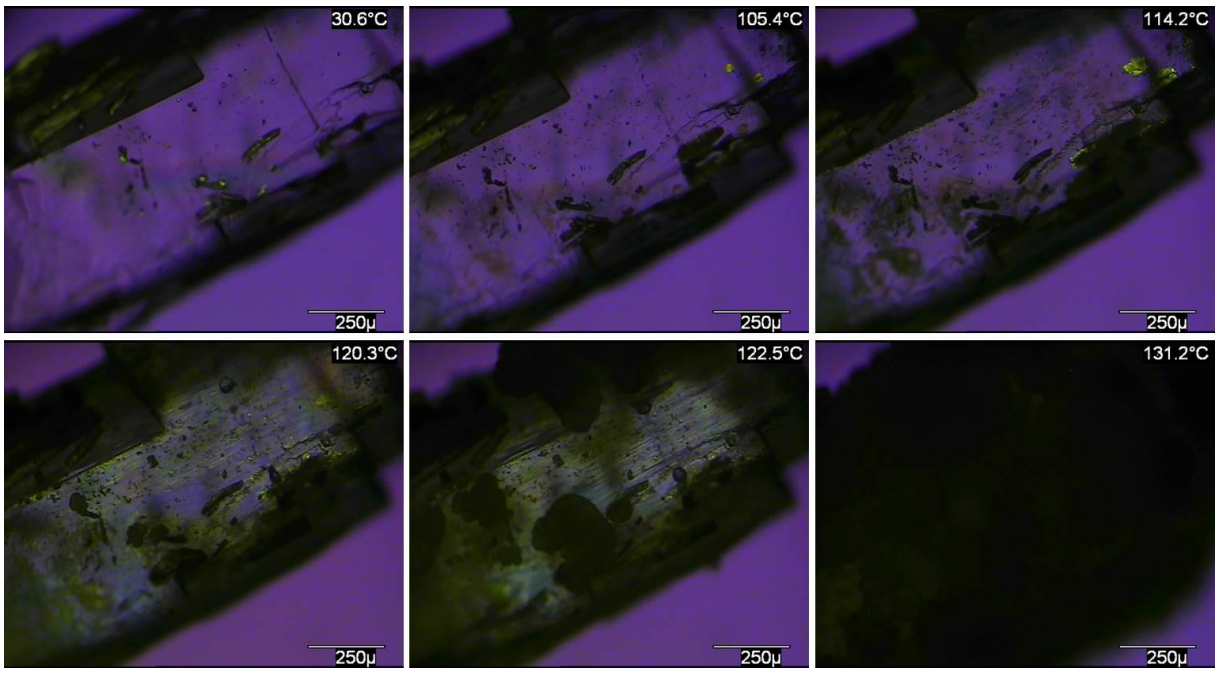

Figure 255 - Optical micrographs of CBZ:FA crystals at different temperatures under polarized light (heating rate of 10 $^{o}C.min^{-1}$).

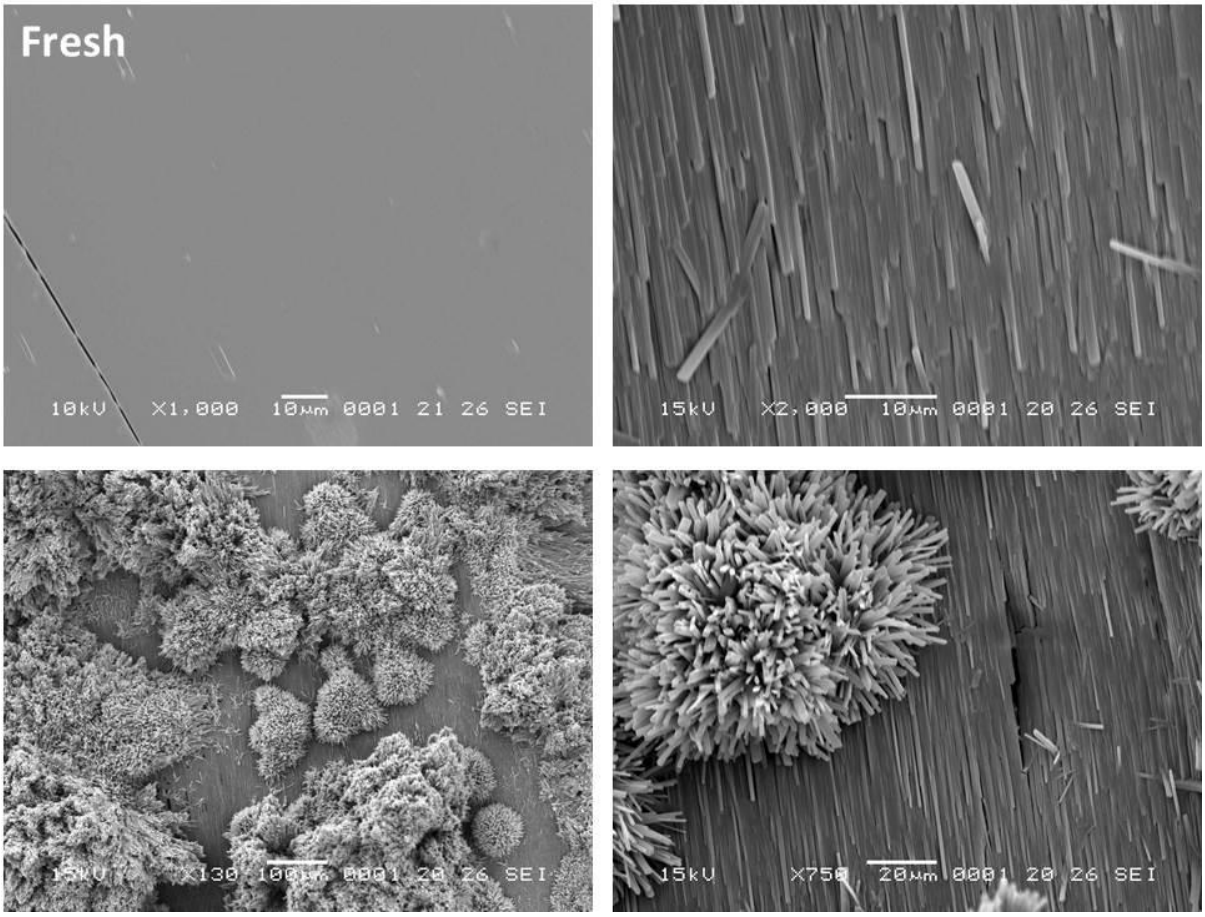

Figure 256 - SEM micrographs of CBZ:FA crystals heated until 165 ^{o}C (N_2, heating rate of 10 $^{o}C.min^{-1}$). The fresh surface is added for comparison purposes.

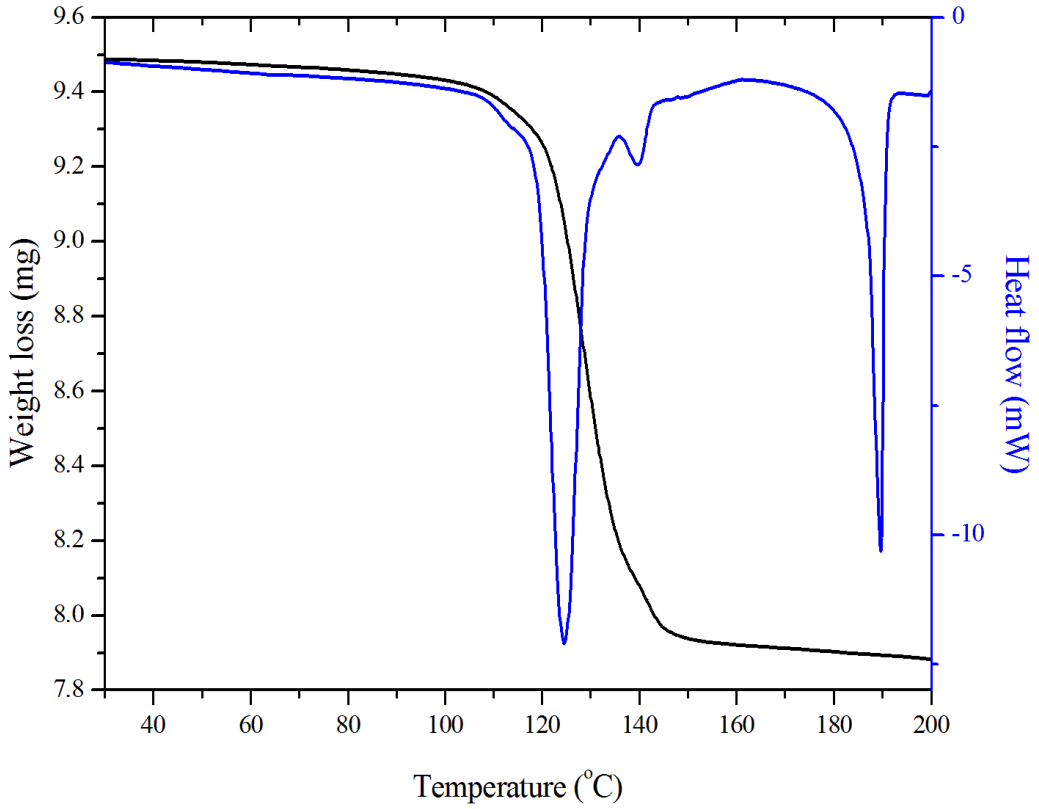

Figure 257 - DSC and TGA thermal characterization of CBZ:FA crystals (10 °C.min^{-1}, perforated lid, N_2).

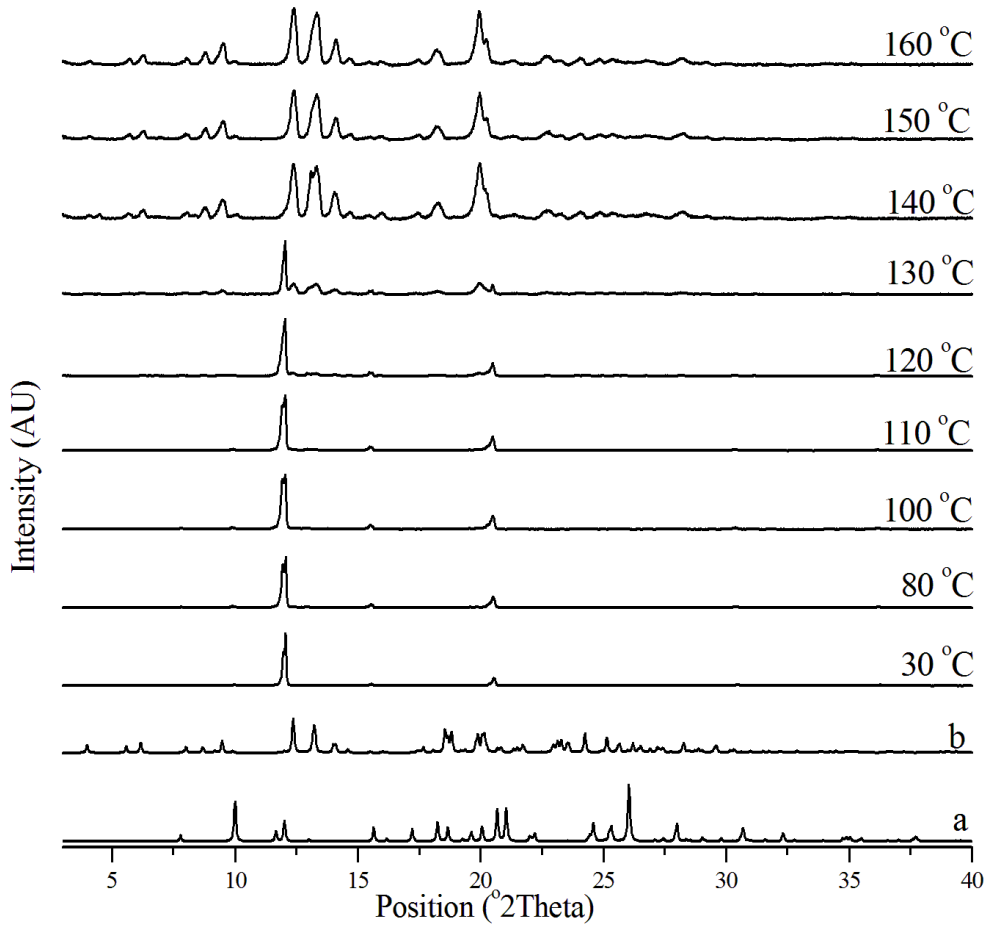

Figure 258 - *In situ* variable temperature PXRD patterns of CBZ:FA crystals (10 °C.min^{-1}, 25-180 °C). *a*: CBZ:FA from UNEZOC. *b*: CBZ Form I from CBMZPN11.

7.4. The effect of seeds on the outcome of the thermal decomposition of the carbamazepine benzoquinone cocrystal and the solvates with formamide and acetic acid

The effect of crystal seeds on the outcome of thermal decomposition has already been demonstrated for CBZ:2H_2O samples prepared by slurrying CBZ Form I or Form III (see Section 5.5, Chapter 5). It was shown that dehydration consistently resulted in different outcomes, depending on the origin of the dihydrate material (*i.e.* which were believed to be contaminated with residual seeds of the starting CBZ crystals). An additional question was raised as to whether the same behaviour would be observed in the thermal decomposition of other CBZ multicomponent materials. In the cases reported in the following, samples of 2CBZ:BZQ, CBZ:FORM and CBZ:ACA were prepared from either CBZ polymorph I or III and the outcome of their thermal decomposition was assessed. While the cocrystal of 2CBZ:BZQ was prepared by liquid assisted grinding, the solvates were prepared by slurrying. The 2CBZ:BZQ cocrystal was selected because it is structurally similar to CBZ:2H_2O, but decomposes at higher temperatures as well as contains a guest molecule which is solid under room conditions. The CBZ:FORM solvate also shows certain structural similarities to the dihydrate and also desolvates at high temperatures. In this case, however, there are indications that desolvation leads to melting or peritectic melting – see earlier. The CBZ:ACA, in turn, was selected because it has also shown evidences of formation of a liquid phase upon desolvation, although having only minor similarities to the dihydrate.

Figure 259 to Figure 264 show how the decomposition of the three systems evolves with the increase in temperature (1 $^oC.min^{-1}$). The PXRD patterns of the 2CBZ:BZQ samples again show new diffraction peaks above 100 ^oC, while the reaction gradually proceeds to completion at approximately 130 ^oC. The results, however, show clearly that cocrystals prepared from CBZ Form I decomposed into Form I, while cocrystals prepared from CBZ Form III decompose into Form III. Further, and as in the case of CBZ:2H_2O, the morphology of both products were significantly different (Figure 265).

Samples of CBZ:ACA show a different behaviour. In this case, new reflections are again seen above 75 ^oC, which gradually increase in intensity until the reaction is complete at approximately 100 ^oC. Both samples, however, desolvate into Form I. The starting form of CBZ used in the preparation of the samples clearly does not appear to drive the structural rearrangement after decomposition.

Finally, the experiments of CBZ:FORM were not reproducible. Although the *in situ* PXRD experiments in Figure 261 and Figure 262 show that desolvation results in different polymorphs depending on the starting material, the results were not consistent within different

experiments. It is suggested that the variations occur because the lattice of the desolvated material collapses very rapidly and decomposition occurs at temperatures in which CBZ Form III converts to Form I.

As already discussed in the case of CBZ:2H_2O, the present experiments illustrate the kinetic character of the seeding effect on solid-state reactions – a factor which is difficult to control. The present results, however, suggest that the mechanism of transformation influences the effect that seeds may have over the product obtained. For instance, it may be that reactions of desolvation which result in melting or the formation of a peritectic mixture are not equally affected by the presence of seeds, as a reaction which develops via recrystallization in the solid-state. The melting of a solid has been used in the literature as a method eliminating persistent seeds from a material, however, the effect of melting is not usually considered for transformations such as dehydration and desolvation. The remaining question is: why some systems are highly influenced by seeds, while others are not? Is it only influenced by the intrinsic characteristics of the seeds and the thermodynamic relationship between the crystal forms, or do the mechanisms of transformation play a role?

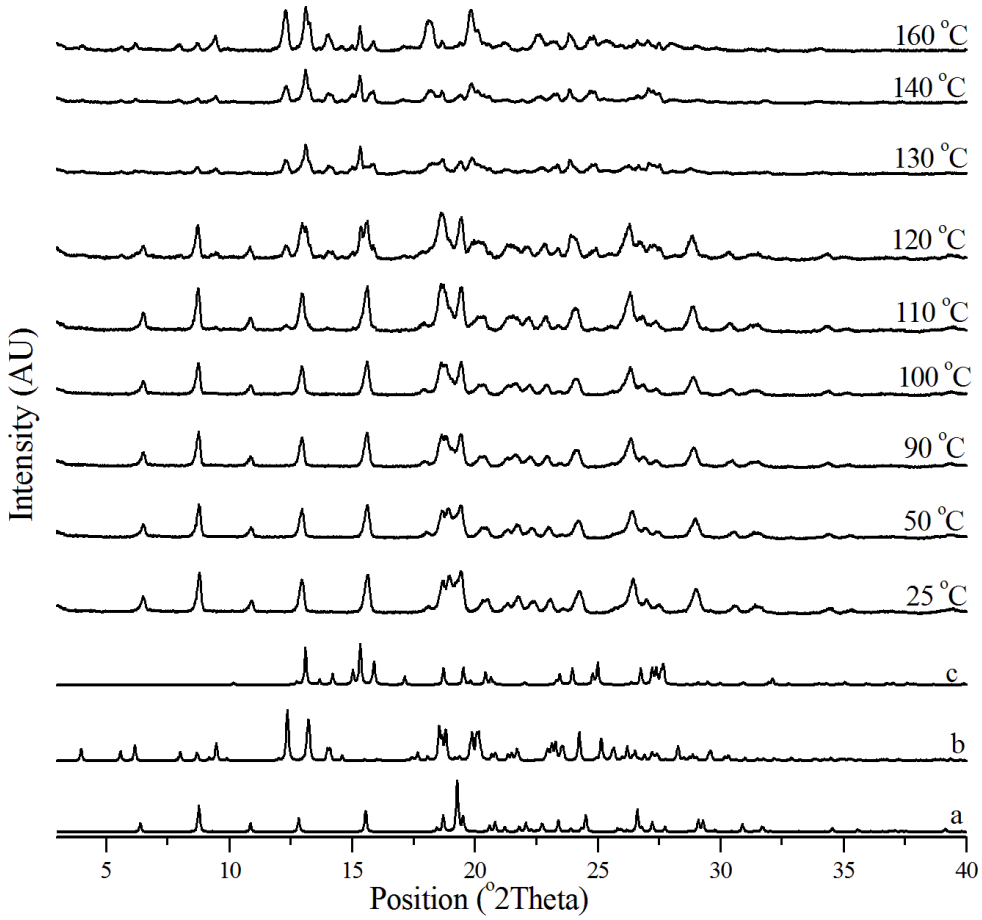

Figure 259 - *In situ* variable temperature PXRD patterns of 2CBZ:BZQ prepared from liquid assisted grinding of CBZ Form I and BZQ (1 °C.min^{-1}, 25-160 °C). *a*: 2CBZ:BZQ (UNEYOB). *b*: CBZ I (CBMZPN11). *c*: CBZ III (CBMZPN01).

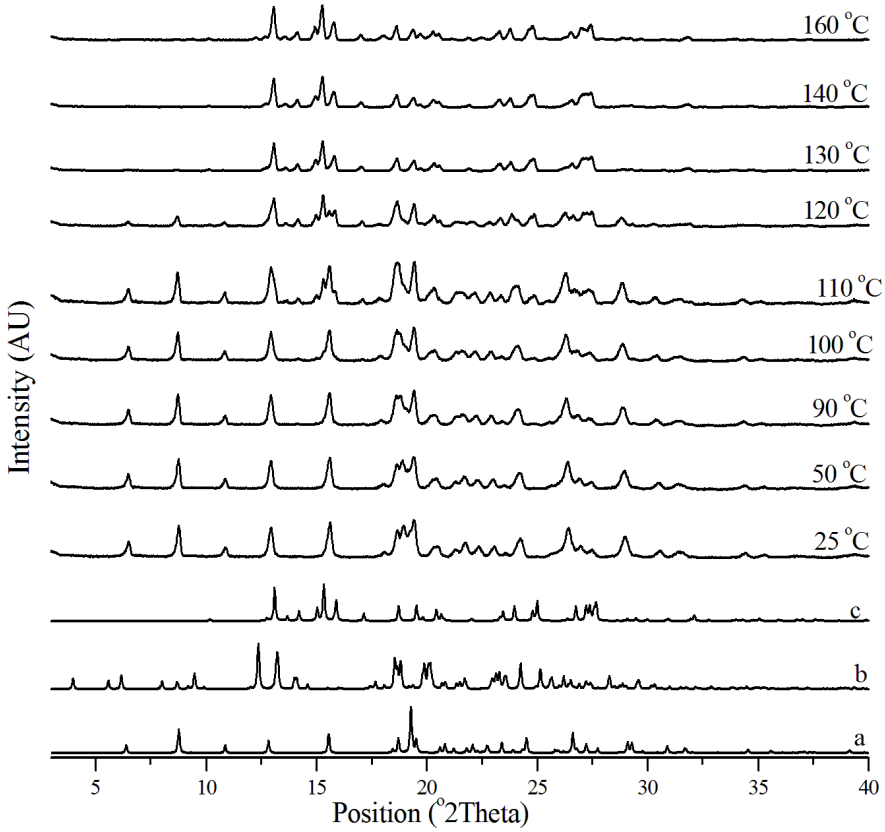

Figure 260 - *In situ* variable temperature PXRD patterns of 2CBZ:BZQ prepared from liquid assisted grinding of CBZ Form III and BZQ (1 ºC.min^{-1}, 25-160 ºC). *a*: 2CBZ:BZQ (UNEYOB). *b*: CBZ I (CBMZPN11). *c*: CBZ III (CBMZPN01).

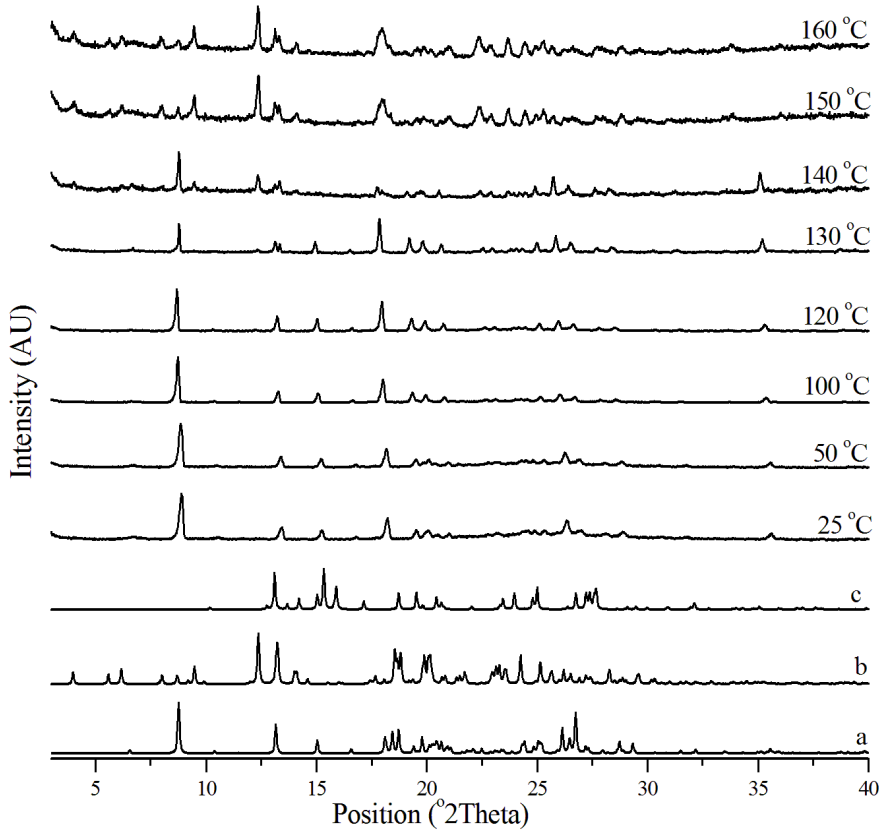

Figure 261 - *In situ* variable temperature PXRD patterns of CBZ:FORM prepared from slurrying of CBZ Form I in formamide (1 ºC.min^{-1}, 25-160 ºC). *a*: CBZ:FORM (UNIBOI). *b*: CBZ I (CBMZPN11). *c*: CBZ III (CBMZPN01).

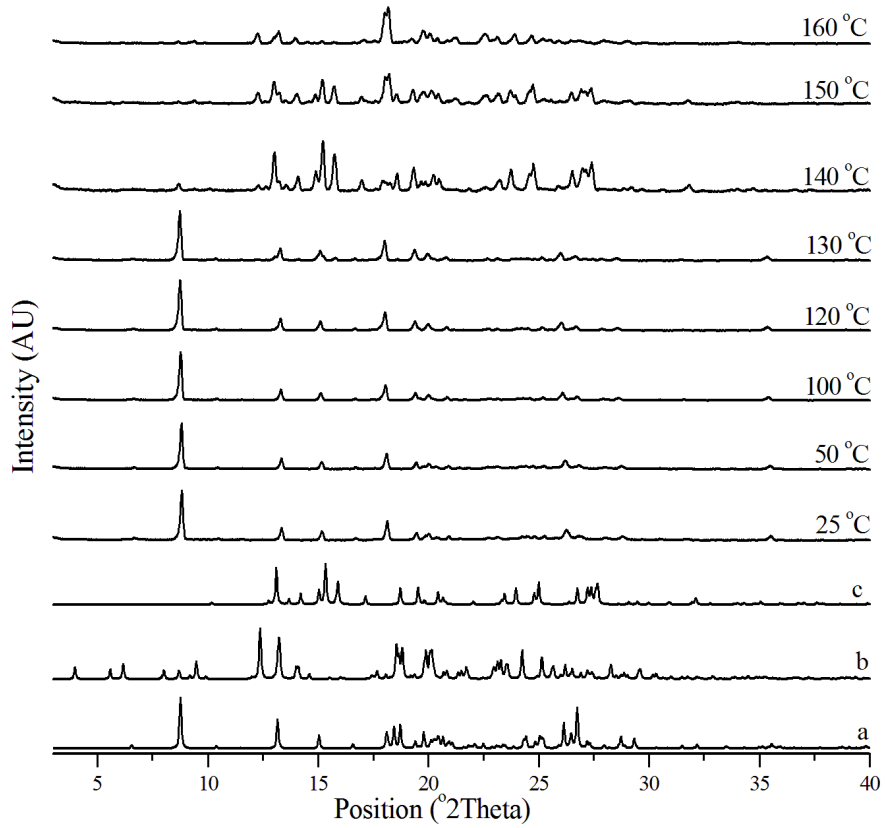

Figure 262 - *In situ* variable temperature PXRD patterns of CBZ:FORM prepared from slurrying of CBZ Form III in formamide (1 ºC.min^{-1}, 25-160 ºC). *a*: CBZ:FORM (UNIBOI). *b*: CBZ I (CBMZPN11). *c*: CBZ III (CBMZPN01).

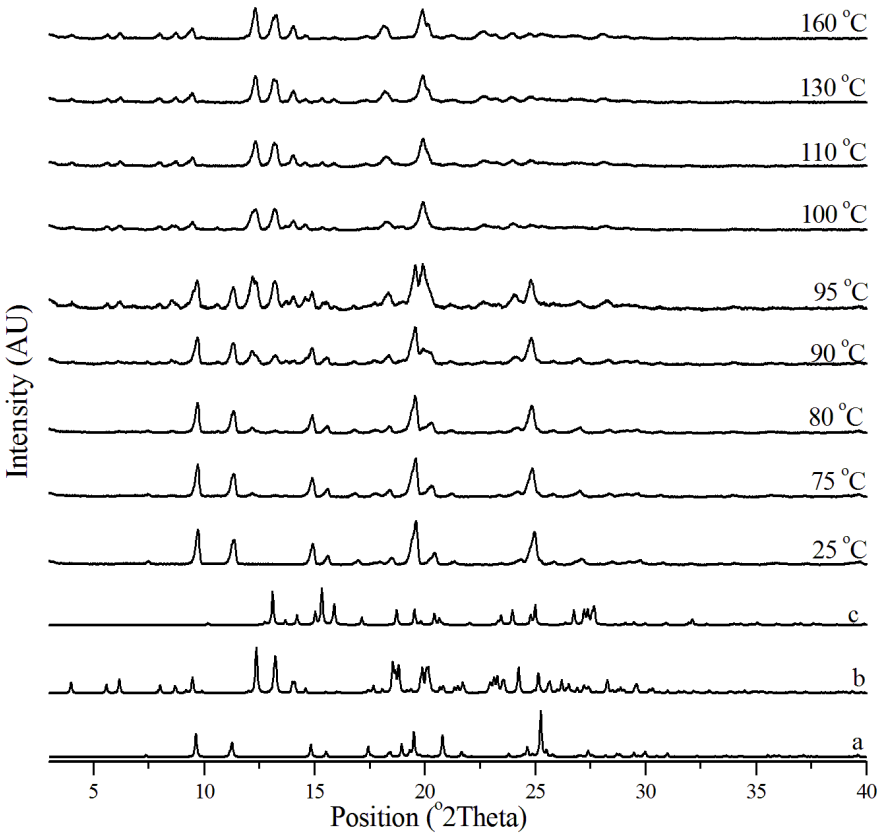

Figure 263 - *In situ* variable temperature PXRD patterns of CBZ:ACA prepared from slurrying of CBZ Form I in acetic acid (1 ºC.min^{-1}, 25-160 ºC). *a*: CBZ:ACA (UNEZIW). *b*: CBZ I (CBMZPN11). *c*: CBZ III (CBMZPN01).

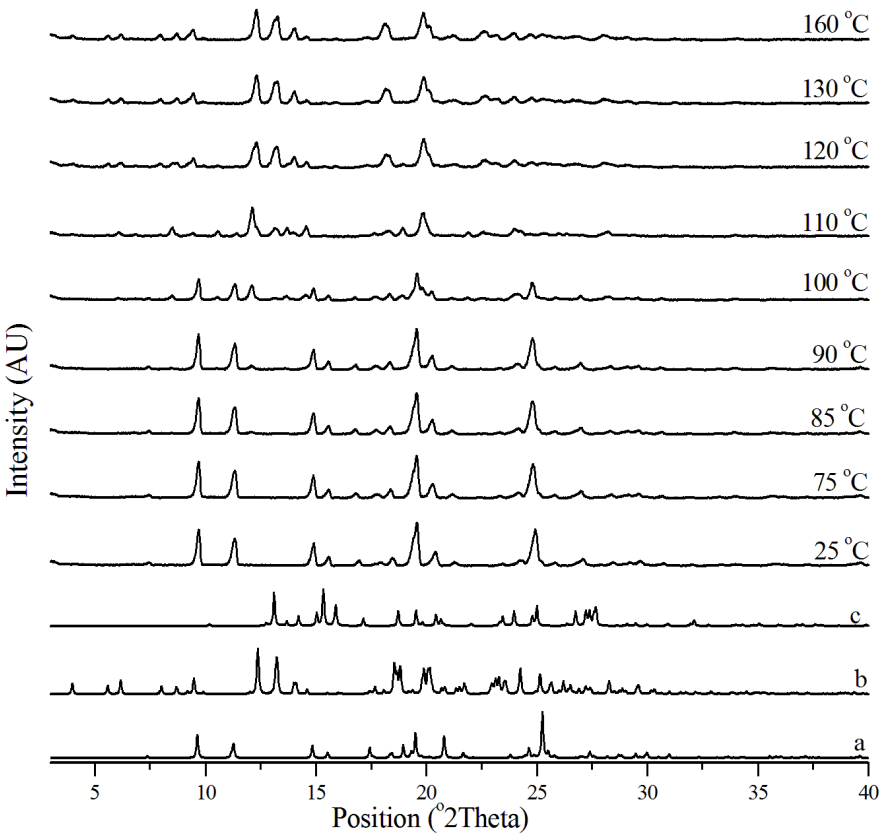

Figure 264 - *In situ* variable temperature PXRD patterns of CBZ:ACA prepared from slurrying of CBZ Form III in acetic acid (1 ºC.min^{-1}, 25-160 ºC). *a*: CBZ:ACA (UNEZIW). *b*: CBZ I (CBMZPN11). *c*: CBZ III (CBMZPN01).

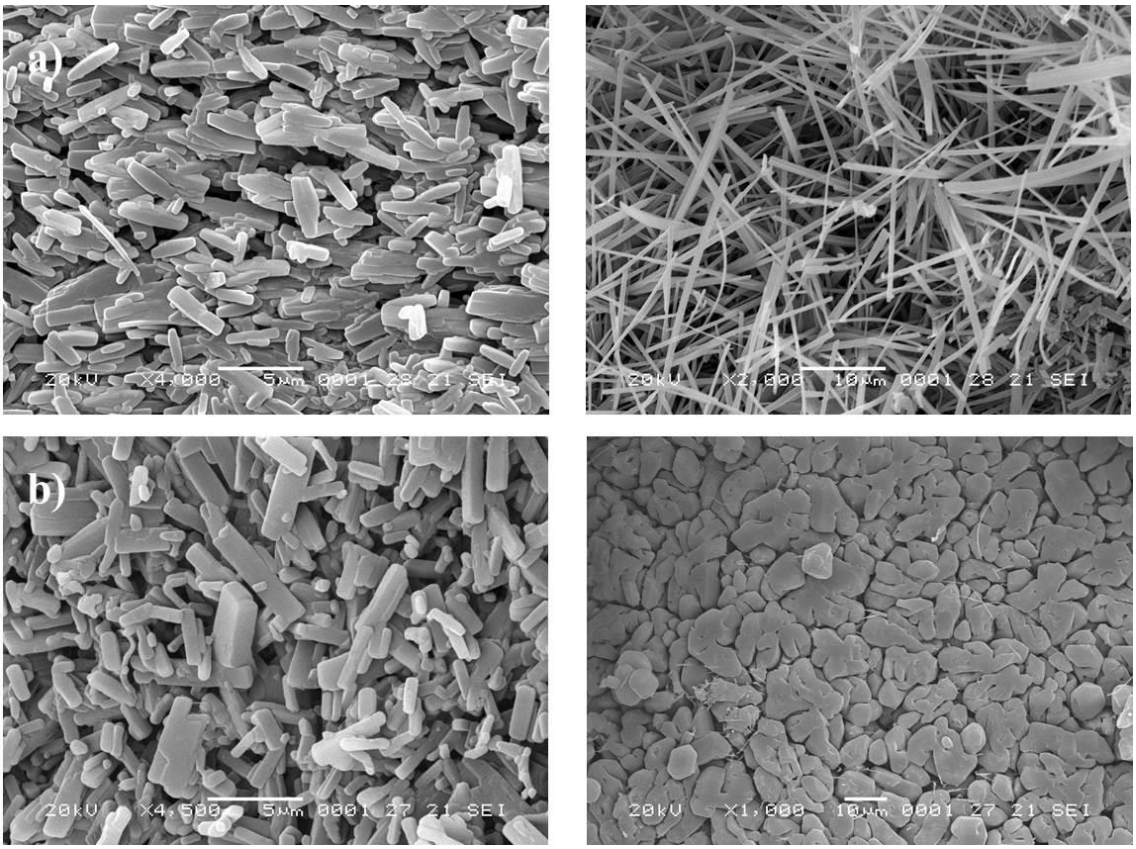

Figure 265 - SEM micrographs of 2CBZ:BZQ fresh samples (left) and 2CBZ:BZQ samples after being heated until 150 ºC (1 ºC.min^{-1}, N_2) (right). The samples were prepared by liquid assisted grinding of CBZ Form I (a) or CBZ Form III (b) with BZQ.

7.5. The interconversion of carbamazepine dihydrate and carbamazepine benzoquinone cocrystal

The results shown in Chapters 5 and 6 have demonstrated that CBZ:2H_2O crystals are prone to the formation of cracks. The characterization of the other CBZ multicomponent materials in the present chapter, however, has not identified the same property, neither in materials which are structurally similar to the dihydrate, nor in materials with markedly different structures. Although these results already illustrate the intrinsic characteristics of the materials, the comparison between structurally related materials would be more reliable if the crystals presented comparable morphology and size. To achieve this case, different crystallization strategies were used in attempt to prepare crystals of a desired and comparable *tracht* and size. The results of the crystallization attempts are described in Chapter 4.

An alternative strategy for sample preparation, however, considered the possibility of replacing the included (solvent) molecules from an already formed lattice. This technique could potentially provide crystals of different CBZ multicomponent materials with the same morphology and size. CBZ:2H_2O and 2CBZ:BZQ were selected for these interconversion experiments. The approaches adopted were as follows.

The preparation of the BZQ cocrystal from the dihydrate was evaluated (i) using a suspension of hydrate crystals in ethanol solutions containing CBZ and BZQ, and (ii) by storing vials of the dihydrate in chambers containing BZQ vapour generated either by solid BZQ or by a slurry of BZQ in ethanol. The reverse process *i.e.* the preparation of the dihydrate from the BZQ cocrystal, was tested by (i) suspending cocrystals in water and in ethanol:water solutions saturated with CBZ, and (ii) by storage of vials containing cocrystals in a humidity chamber at 98% RH, 25 ^oC. In none of the performed experiments was there evidence by PXRD that the crystals of 2CBZ:BZQ converted into CBZ:2H_2O. In the case of CBZ:2H_2O crystals stored in environments containing BZQ, however, the conversion was detected and the results are discussed herein.

Figure 266 to Figure 268 show the respective PXRD and TGA analyses of the products of CBZ:2H_2O samples stored in CBZ/BZQ solution (Figure 266) and in contact with BZQ vapour without the aid of ethanol vapour (Figure 267) and with ethanol vapour (Figure 268). (Note that because of the preferred orientation effects as well as the *tracht* effect on reflection intensities, the optimum region for assessment is close to 8^o two-theta, with in each case red corresponding to hydrate and blue to cocrystal).

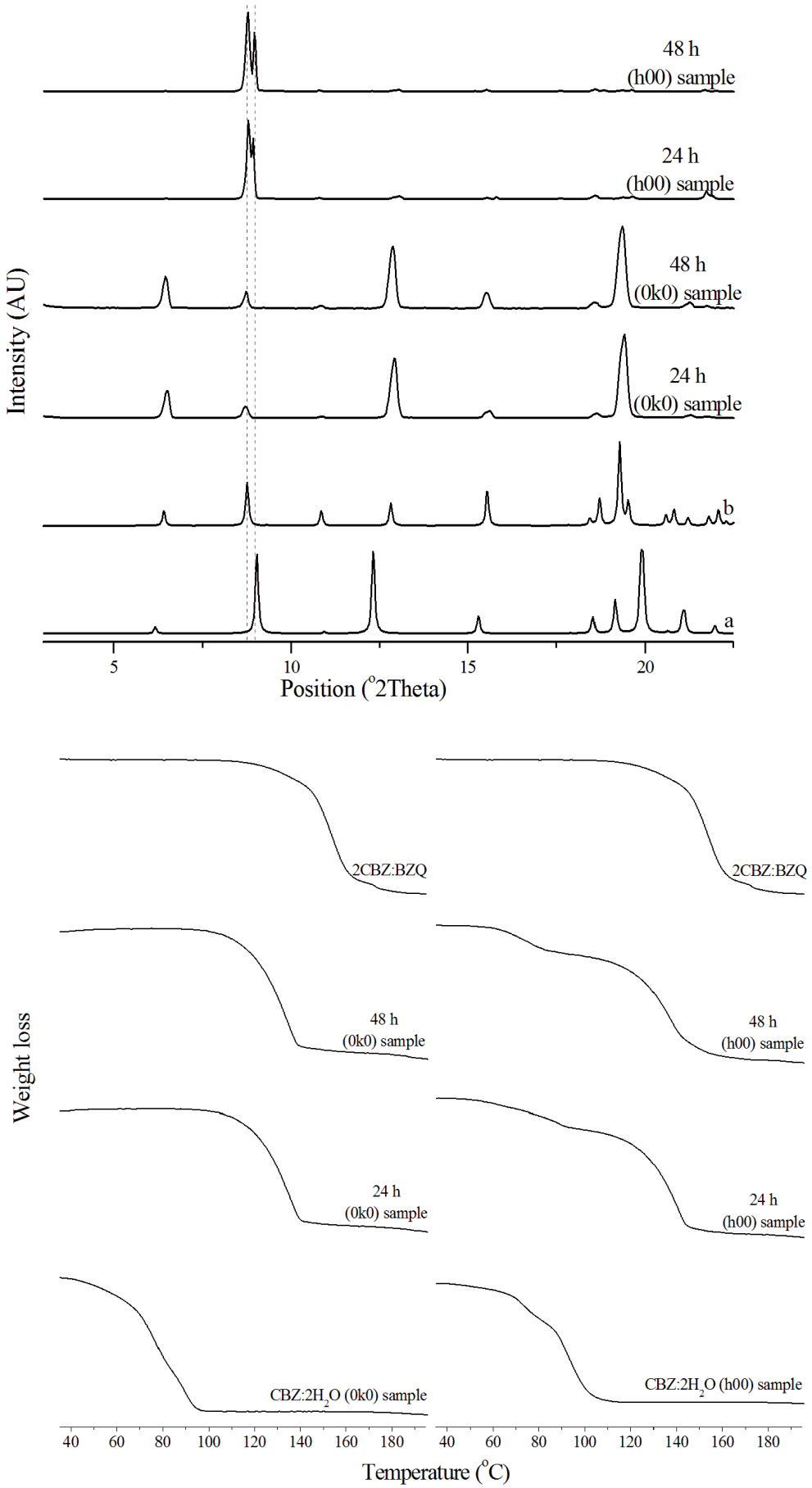

Figure 266 - Characterization of dihydrate samples immersed in ethanolic solutions containing CBZ and BZQ. The top graphs are *ex situ* PXRD patterns (*a* and *b* are the calculated patterns of CBZ:2H_2O and 2CBZ:BZQ); the graphs at the bottom are TGA curves (the curves of CBZ:2H_2O and 2CBZ:BZQ are added for clarification).

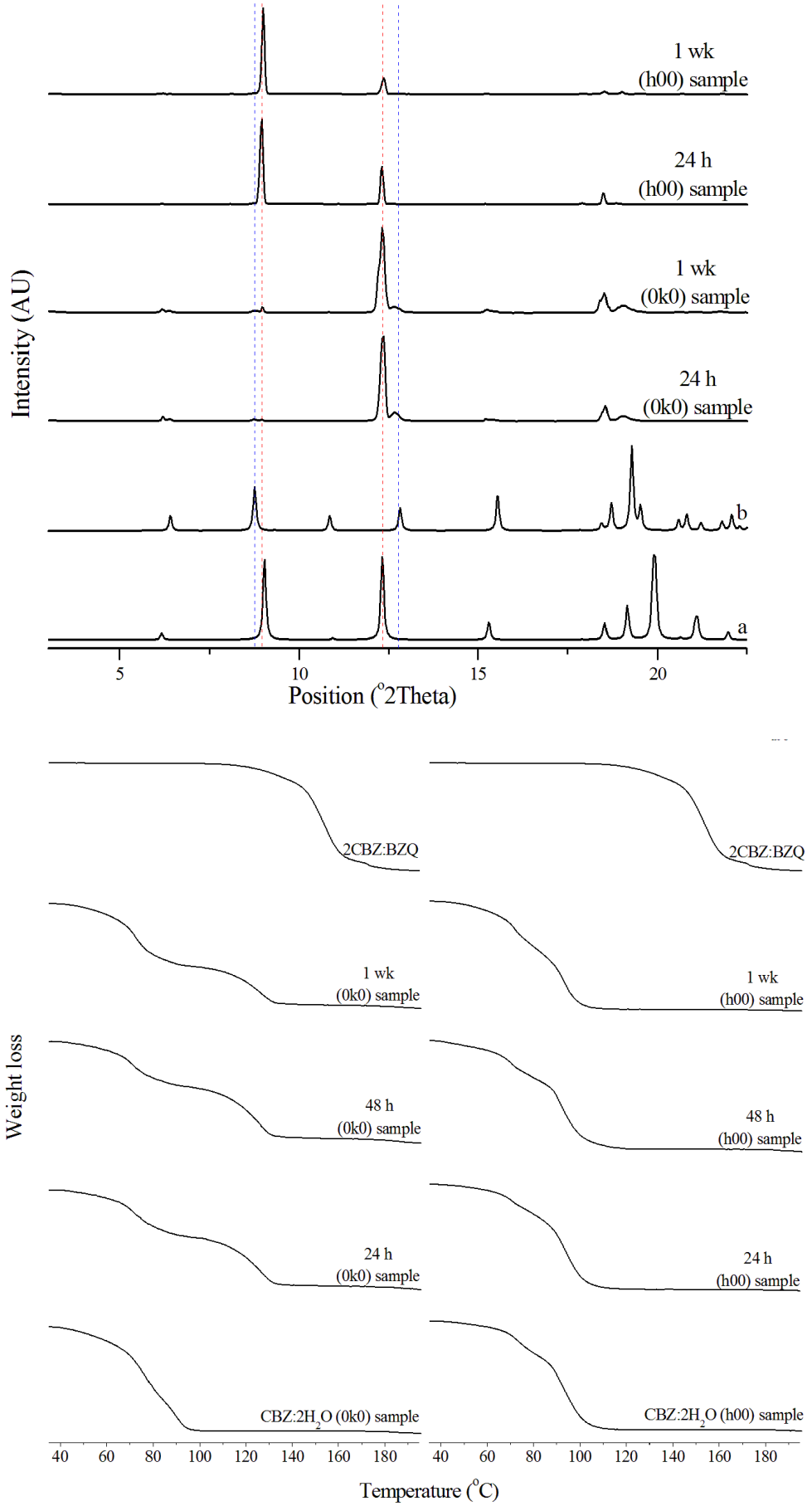

Figure 267 - Characterization of dihydrate samples subjected to BZQ vapour. The top graphs are *ex situ* PXRD patterns (*a* and *b* are the calculated patterns of $CBZ:2H_2O$ and 2CBZ:BZQ); the graphs at the bottom are TGA curves (the curves of $CBZ:2H_2O$ and 2CBZ:BZQ are added for clarification).

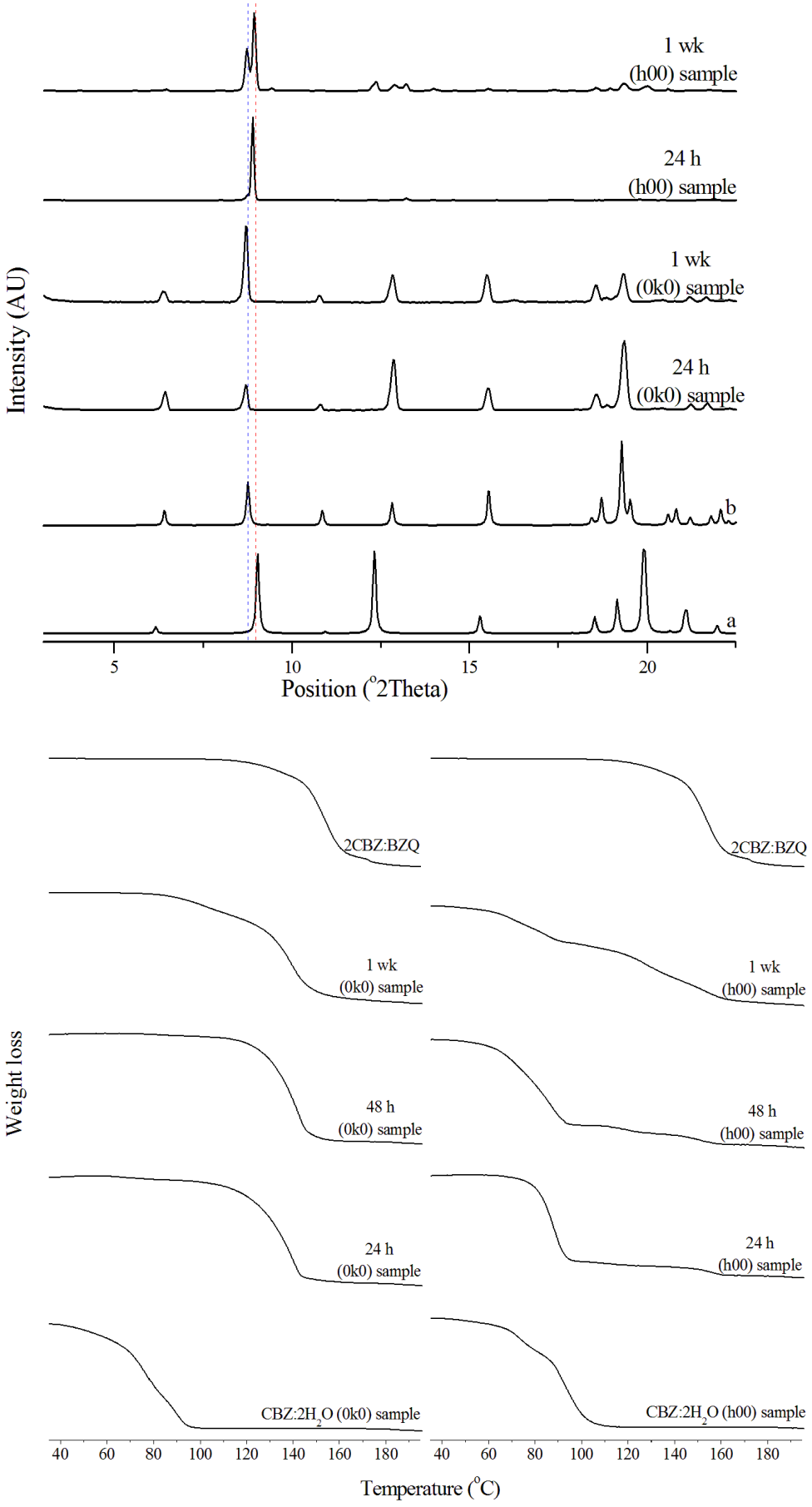

Figure 268 - Characterization of dihydrate samples subjected to BZQ and ethanol vapour. The top graphs are *ex situ* PXRD patterns (*a* and *b* are the calculated patterns of CBZ:2H$_2$O and 2CBZ:BZQ); the graphs at the bottom are TGA curves (the curves of CBZ:2H$_2$O and 2CBZ:BZQ are added for clarification).

It is seen clearly that the (0k0) dihydrate samples convert more rapidly to the cocrystal than the (h00) samples. This may possibly be due to their different particle sizes. As expected, the exchange of H_2O for BZQ molecules was favoured in solution. From the vapour phase the rate seems to be increased in the presence of ethanol vapour. The TGA data are perhaps more convincing in the changes in profile which exists between the different samples.

SEM and optical microscopy demonstrate the same behaviour observed by PXRD and TGA. The surface of the crystals resulting from the interconversion experiments in solution show significant rearrangement (Figure 269). In this case, although the new material may retain the original crystal shape, the particles are polycrystalline. (The yellow appearance of the crystals also indicates the extent of BZQ uptake). The crystals subjected to BZQ in the vapour phase, in general, did not show such a profound surface reorganization (Figure 270). Again the colour of the crystals suggest little BZQ uptake for (h00) crystals and more for (0k0) crystals.

It is noteworthy that compared with fresh CBZ:$2H_2O$ (h00) surfaces, the (h00) faces exposed to BZQ vapour do not present the same pattern of fractures. In this case, optical microscopy and SEM demonstrate the presence of short cracks on the main surface with the cracks clearly not cross-cutting the crystals. SEM also shows that the fractures are usually surrounded by areas containing recrystallized product (Figure 272). Although rougher, the (h00) surfaces exposed to BZQ and ethanol vapour, also show only random cracks (Figure 271 and Figure 273).

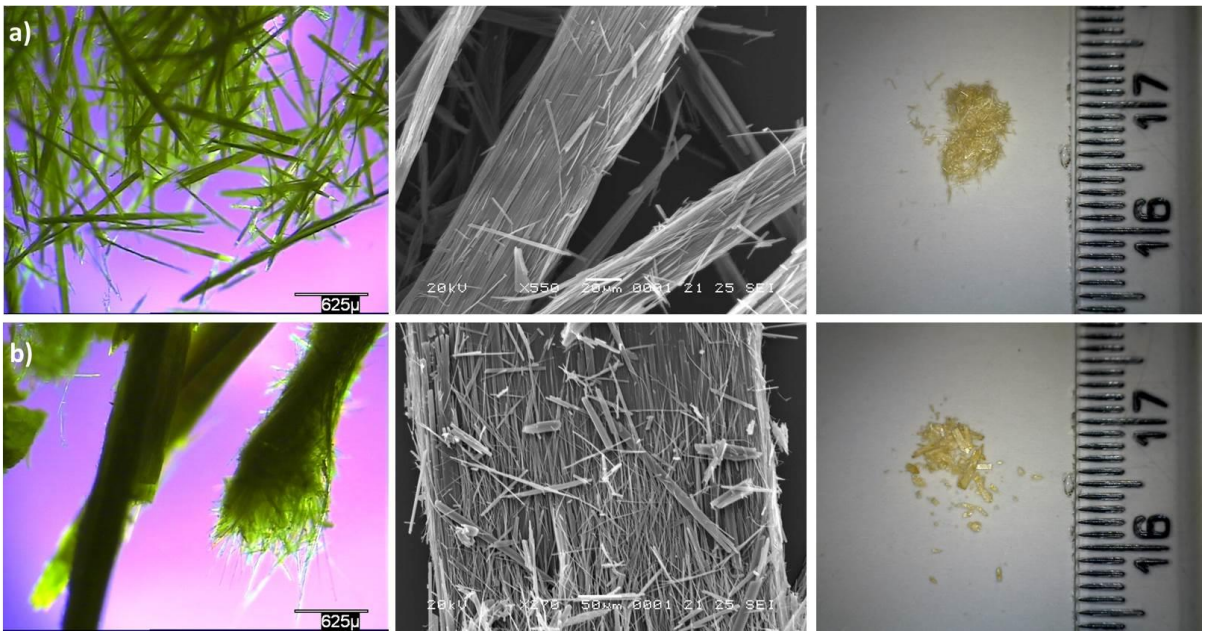

Figure 269 Micrographs of dihydrate samples immersed in ethanolic solutions containing CBZ and BZQ (48 h, 25 ^{o}C). *a*: (0k0) sample. *b*: (h00) sample.

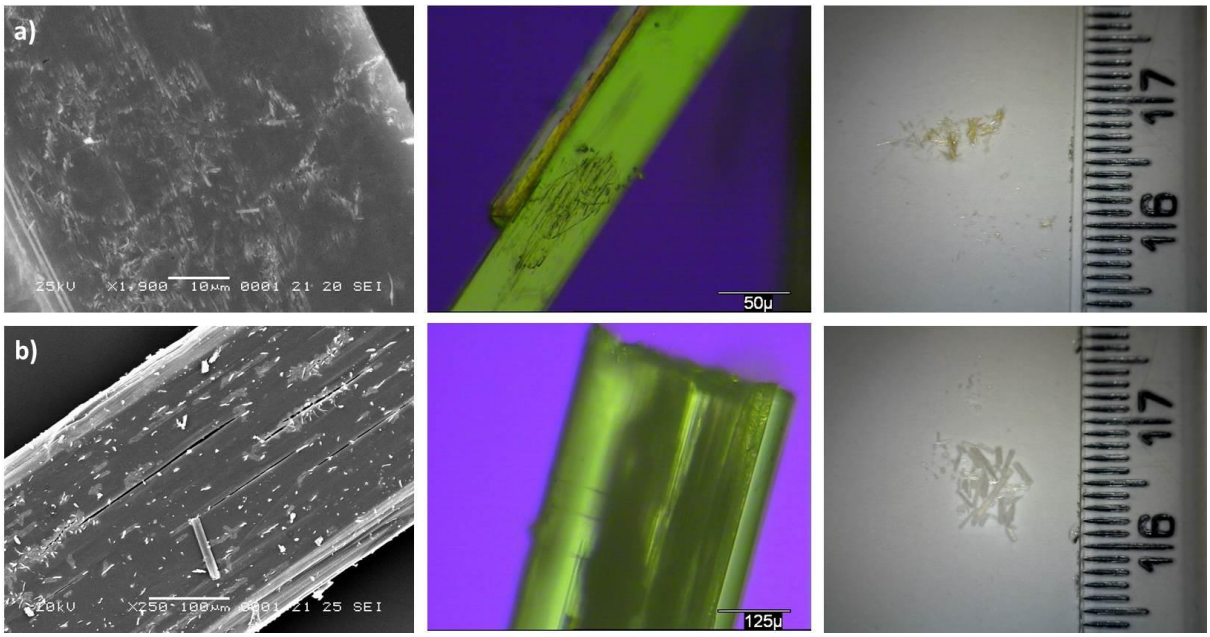

Figure 270 - Micrographs of dihydrate samples subjected to BZQ vapour (48 h, 25 ºC). *a*: (0k0) sample. *b*: (h00) sample.

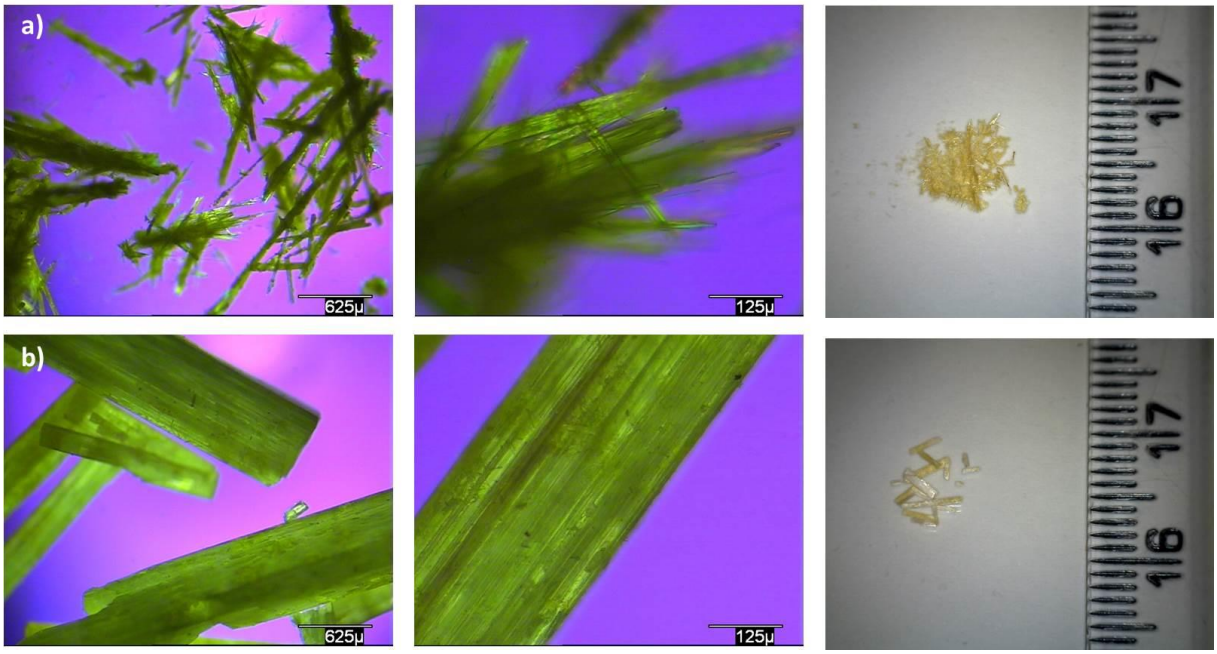

Figure 271 - Micrographs of dihydrate samples subjected to BZQ and ethanol vapour (48 h, 25 ºC). *a*: (0k0) sample. *b*: (h00) sample.

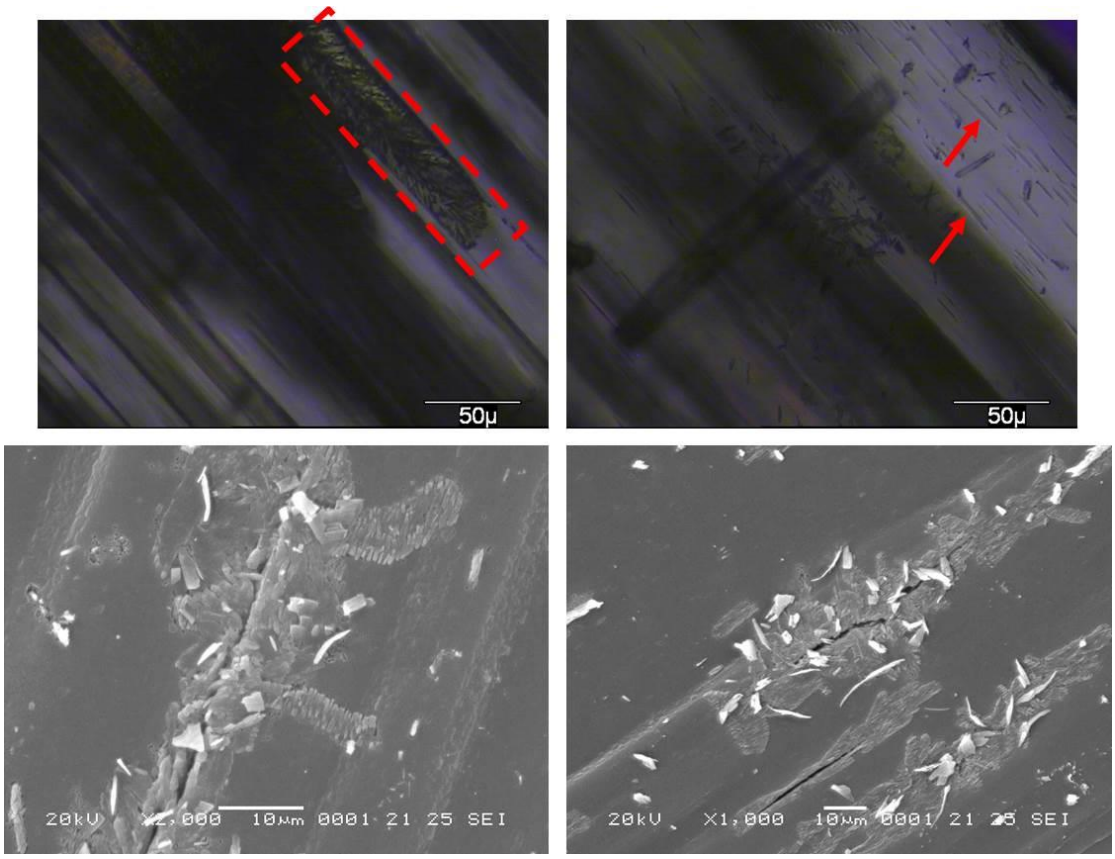

Figure 272 - Micrographs of dihydrate samples subjected to BZQ vapour (48 h, 25 ºC) highlighting the (h00) surface defects.

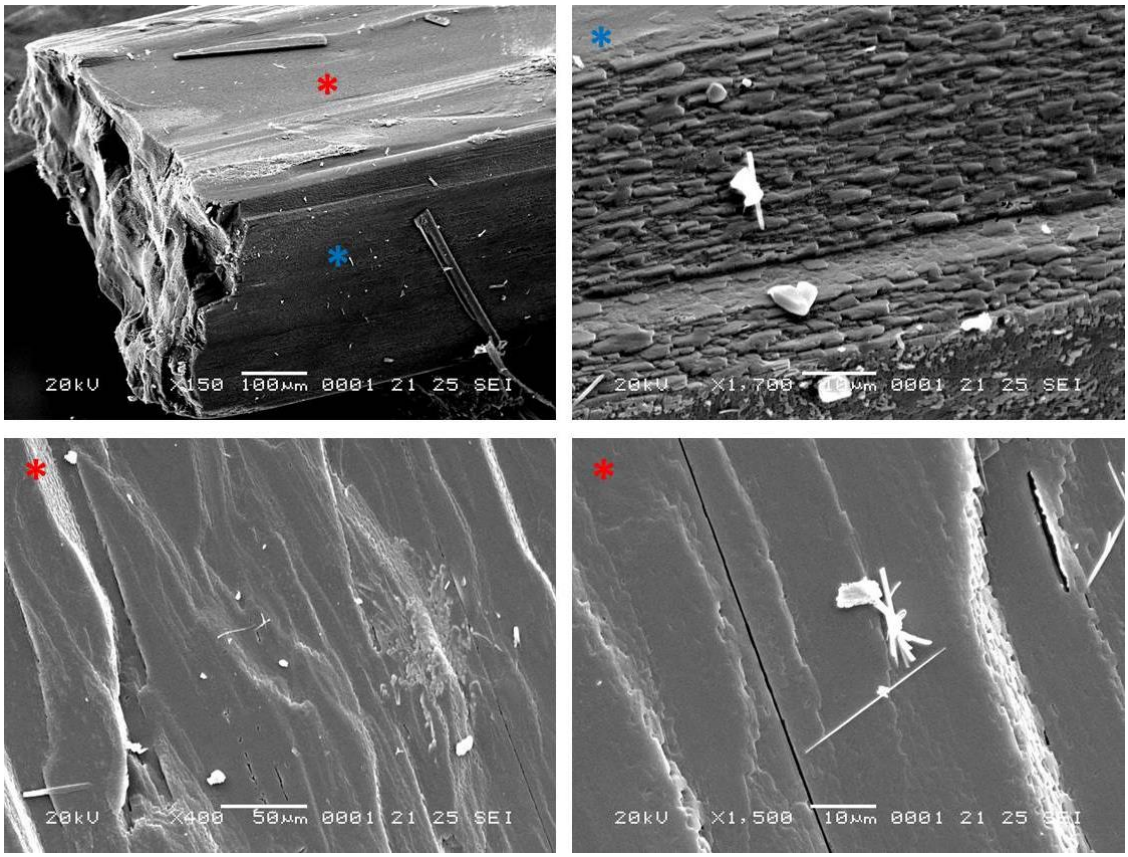

Figure 273 - Micrographs of dihydrate samples subjected to BZQ and ethanol vapour (48 h, 25 ºC) showing the surface characteristics and the relatively absent cracks on the (h00) face. The red star represents the (h00) surface while the blue star represents the (0k0) surface.

As none of the conditions resulted in complete exchange of the H_2O molecules with the maintenance of crystal and surface integrity, this approach was not used in the preparation of samples for thermal decomposition studies. The results, however, reinforce that the BZQ cocrystal is more stable than the dihydrate. Also, it is interesting that CBZ:2H_2O (h00) surfaces exposed to BZQ do not show as many cracks as in the fresh samples. It is unclear whether this effect results from the surface reorganization and from roughness, or if it is related to the intrinsic characteristics of 2CBZ:BZQ formed from the cast of CBZ:2H_2O.

7.6. Conclusions

It has been demonstrated that the removal of the guest molecule from the lattice of CBZ multicomponent materials and the accompanying recrystallization into a new form are likely to be simultaneous events. Other concurrent transformations have been evidenced during desolvation and sublimation, such as melting, peritectic formation and even chemical decomposition. It is suggested (and perhaps not surprising) that particle size, heating rate and temperature significantly affect the outcome of decomposition. In this scenario, the polymorphic outcome of seeded and non-seeded experiments is shown to be dependent on the experimental conditions, especially when sudden reactions and the formation of a liquid phase occur.

The materials classified in Group 1 of structural similarities (CBZ:ACE, CBA:DMSO and CBZ:DMF) tend to desolvate into CBZ Form III and show round domains and irregular cracks on the surface. Thermal experiments of materials from Group 3 (2CBZ:BZQ, 2CBZ:OXA, CBZ:2H_2O, CBZ:FORM and 2CBZ:DIOX) and Group 5 (CBZ:TFA, CBZ:ACA and CBZ:FA) resulted in Form I with the resulting crystals presenting needles-like domains on the surface. A correlation between phase identity and surface domains was also observed in samples of Group 2 (CBZ:BZQ) and Group 4 (CBZ:TFE and 2CBZ:TFE) subjected to thermal treatment. The outcome of decomposition of the related structures of BZQ cocrystals and TFE solvates, however, was not the same.

The studies have shown that different crystal surfaces present different properties, as the orientation of the polycrystalline domains change throughout the product crystal. This effect may be attributed to distinct molecular movements or strain resulting from the transformation. None of the materials, however, show cracks cross-cutting the crystals as observed in the case of CBZ:2H_2O. For instance, 2CBZ:BZQ is shown to be more stable than CBZ:2H_2O, although both materials are isostructural. In fact, dihydrate crystals subjected to

environments rich in BZQ vapour show surfaces with a different pattern of cracks. Regardless of whether these surface modifications are attributed to the intrinsic characteristics or not, the findings suggest that the brittleness of the crystals may change as a consequence of surface treatment.

In conclusion, the present chapter illustrates how the outcome of thermal decomposition is affected by the environment conditions. Although packing similarities have an important effect over solid-state reactivity, other kinetic factors may also considerably affect the product. As it has been exemplified over the course of the present work, the studies show the importance of combining bulk and surface characterization to expand our understanding of decomposition reactions.

CHAPTER 8 - Discussion

8.1. Introduction

The past chapters have shown the investigation of solid-state properties at play in the surface and structural reorganizations that result from the stress within crystals of labile CBZ multicomponent materials. The study of desolvation, dehydration and sublimation reactions upon thermal treatment (mainly) has focused in two main characteristics, namely the nature of the polymorphic outcome, and changes in surface, crystal shape and volume (especially when related to crystal breakage). Prior to the crystal decomposition studies, strategies of particle design, solubility determination and crystallization experiments were also performed. The main aim was to find the best conditions to prepare CBZ crystal forms suitable for the proposed study in a robust and reproducible manner. The different aspects and properties approached in the thesis are discussed in the following sections and are presented as an investigative framework to assess labile materials in studies of drying.

8.2. The crystallization of multicomponent forms of carbamazepine

8.2.1. The equilibrium solubility diagrams

The present work has demonstrated that the determination of the equilibrium solubility of CBZ and CBZ multicomponent forms in different solvent/coformer activities is an interesting tool for the solid-state chemist. Firstly, it can be used for screening of multicomponent forms containing different stoichiometric amounts of the components. For example, two new crystal forms were found by this approach: CBZ:BZQ and 2CBZ:TFE. These phases were not obtained by previous studies in the literature because the crystallization experiments undertaken were performed in low coformer concentrations and in pure solvent, respectively. Secondly, the diagrams of equilibrium solubility also provide information about the regions in which the desired crystal form is stable, helping in the development of suitable crystallization methods.

In solution, the most important information taken from the equilibrium solubility diagrams was the amount of dissolved CBZ in ethanolic solutions, which varied significantly amongst the different systems. In view of the apolar character of CBZ, it might be expected that less polar solvents would solubilize more of the drug then polar ones. In contrast, the experiments have shown that, for example, the initial addition of moderate quantities of water

to ethanol increases the solubility of CBZ Form III. This observation illustrates that solubility profiles show a more complex dependence rather than simply based on polarity and the "*like-dissolves-like"* principle. Solubility is a result of a dynamic equilibrium between crystallization and lattice dissociation. In the case of the studies presented here, two major features appear to affect the solubility: competing equilibrium reactions and changes in composition of the solution media.

The formation reaction of multicomponent materials, which is generalized in Equation 2, results, in fact, from the sum of two other reactions shown in Equation 3 and Equation 4. They express the solubilization and crystallization of the single component phase, and the crystallization of the multicomponent solid in equilibrium with the dissociation of its components. Following Le Chatelier's principle of chemical equilibrium, at lower activities of coformer B, the reaction in Equation 4 is not in equilibrium and shifts to the formation of reactants. In this case, the equilibrium constant which dominates the reaction progress is k_2 and the thermodynamically most stable solid phase is $A_{(s)}$. Equilibrium for Equation 4 is only reached at high activities of coformer B, which consumes $A_{(l)}$ and shifts the equilibrium of the reaction in Equation 3. In other words, an increase in concentration of coformer B, leads to the formation of $A_aB_{b(s)}$ at the expense of $A_{(s)}$ and the constant that dominates the reaction rate is k_1. The change in composition with the addition of coformer B results in an increase in the solubilization of $A_{(s)}$ until a point is reached where sufficient A is available to reach equilibrium for the formation of $A_aB_{b(s)}$. The solubility diagrams in Chapter 4 show this behaviour as a rise in the solubility of CBZ Form III with increase of concentration of the coformers in solution. It also shows the change in the direction of the reaction as the CBZ multicomponent form starts to be detected.

Equation 2

$$aA_{(s)} + bB_{(l)} \overset{K}{\rightleftharpoons} A_aB_{b(s)}$$

Equation 3

$$aA_{(s)} \overset{K_1}{\rightleftharpoons} aA_{(l)}$$

Equation 4

$$aA_{(l)} + bB_{(l)} \overset{K_2}{\rightleftharpoons} A_aB_{b(s)}$$

In the regions where the CBZ multicomponent materials are the most stable phases, changes in the composition of the solution still follow Le Chatelier's principle for CBZ:ACE, CBZ:BZQ and 2CBZ:BZQ, CBZ:2H_2O, CBZ:FORM and 2CBZ:DIOX. In these cases, an increase in the concentration of the coformer leads to a decrease in the solubility of the multicomponent solid. Deviations from this behaviour, however, are observed for CBZ:DMSO, CBZ:DMF, CBZ:DMA, CBZ:TFE and 2CBZ:TFE, CBZA:TFA, CBZ:ACA and CBZ:FA

where an increase in concentration of the coformer leads to either an increase in the solubility of the multicomponent solid or to a plateau in dissolved CBZ.

In general, the mechanism by which the predicted solubility behaviour is not seen experimentally may be related to a variety of effects such as: ionization of the species in solution, hydrogen bonding between the species and to complexation. In the case of ionization, the dissociation of the species in solution must be added to the general reaction scheme described in Equation 2. This modifies the equilibrium relationship and means that the solubility changes not only as a function of the concentration of the species, but also by the pH of the medium and the pKa of the ionisable molecules. Considering that the ionization of CBZ and the formation of salts has been reported in the literature in aqueous and non-aqueous solutions, it is possible that CBZ molecules ionize in some of the solvents, especially in the systems containing carboxylic acids.

While the pKa of trifluoroacetic acid, acetic acid and formic acid are low (0.19, 4.75 and 3.75 at 25 ºC, respectively), trifluoroethanol is not as acidic (pKa=12.37, 25 ºC).[218] It is unclear whether the high solubility of CBZ:TFE and 2CBZ:TFE solvates is related to ionization, or whether a different mechanism is involved. Similarly, the plateau in the solubility profiles of CBZ:DMSO, CBZ:DMF and CBZ:DMA cannot at the moment be explained. It is possible that the degree of ionization of CBZ may change with increased quantities of aprotic solvents, such as DMSO, DMF and DMA, but other phenomena could also be involved.

A further factor that must be considered is that mixtures of solvents will not necessarily behave as ideal solutions. In the case of ideal behaviour, the interactions of *like*- and *unlike-molecules* is the same and the activity coefficient is one, while non-ideal solutions show different affinities of interactions between *like*- and *unlike*. Under non-ideal conditions, the activity coefficient will be higher than one if the interactions of *like-molecules* are preferred, while activity coefficients of less than one suggest that interactions of *unlike-molecules* are energetically more favourable. Table 15 shows some values of γ_∞ (*i.e.* the activity coefficient at infinite dilution) related to the solvent mixtures studied in this work (the data for all the systems studied here are not available in the literature).[219–221] It is noteworthy that the systems which presented an increased or constant solubility value as a function of increase in coformer concentration (namely CBZ:DMSO, CBZ:DMF, CBZ:DMA, CBZ:TFE and 2CBZ:TFE and CBZ:ACA), have a value of γ_∞ less than one, indicating that strong interactions between ethanol and the coformers are favourable. In contrast, for the case of CBZ:ACE, CBZ:2H_2O, 2CBZ:DIOX and CBZ:NIT, γ_∞ is greater than one. Because of these interaction tendencies, the solvation of ions and undissociated molecules in these mixtures may also differ and there are likely to be differences in the solubility profiles of the respective solid phases. It is interesting

that the use of activity coefficients to study the solubility characteristics of pharmaceuticals in solvent mixtures has not been appreciated in the literature. The present analyses, however, show that this can be a useful tool to be investigated further.

Table 15 – Comparison of the activity coefficients at infinite dilution (γ_∞) of a few solvent systems used in the present work. It illustrates how the molecules of a solute A behave when surrounded by B molecules of a solvent.

Systems	γ_∞		
	Value	Temperature (K)	Reference
Ethanol in acetone	2.32	303.23	Dallinga et.al (1993)[1]
Acetone in ethanol	2.70	303.15	Dallinga et.al (1993)[1]
Ethanol in N,N-dimethylsulfoxide	0.533	298.15	Park et.al (1987)[1]
Ethanol in N,N-dimethylformamide	0.753	298.15	Park et.al (1987)[1]
Ethanol in N,N-dimethylacetamide	0.504	298.15	Park et.al (1987)[1]
Ethanol in water	3.76	298.15	Park et.al (1987)[1]
Water in ethanol	3.28	298.15	Schmidt (1980)[2]
Ethanol in 1,4-dioxane	2.49	298.15	Park et.al (1987)[1]
1,4-dioxane in ethanol	3.10	298.15	Park et.al (1987)[1]
Ethanol in nitromethane	8.24	298.15	Park et.al (1987)[1]
Nitromethane in ethanol	6.82	298.15	Park et.al (1987)[1]
Ethanol in 2,2,2-trifluoroethanol	0.245	298.15	Park et.al (1987)[1]
Ethanol in acetic acid	0.838	298.15	Park et.al (1987)[1]

[1] Work searched in Springer Materials

[2] Work searched in Dortmund Databank – DDB

8.2.2. Crystal growth and morphology

Modifications in the crystallization environment have also been used in this thesis to change the growth of specific crystal faces in the CBZ multicomponent forms. For example, the aspect ratio of 2CBZ:BZQ, CBZ:2H_2O, CBZ:FORM, CBZ:TFA, CBZ:ACA and CBZ:FA crystals varied with the solution composition and/or the initial CBZ concentration. It is suggested that these findings are a result of the anisotropy of the network of intermolecular interactions in the structures. In this case, a modification in the aspect ratio of the CBZ needle particles is mainly related to the kinetics of crystal growth of the face that is perpendicular to the elongation axis, which also corresponds to the axis containing the channels of guest molecules.

The crystals of CBZ:2H_2O and CBZ:FORM, however, have also shown that the crystal surfaces which are parallel to the needle axis also present distinct growth rates depending on the solvent composition. Consequently, this resulted in crystals with distinct dominant surfaces. Crystallization experiments of CBZ:2H_2O crystals in alcohol:water have concluded that both solvents influence crystal shape. While the lipophilicity of the alcohol seems to increase the growth rate of non-hydrogen bonding crystal faces (*e.g.* (0k0) surfaces) and leads to dominant (h00) surfaces, water molecules increase the growth of faces in which they are part of the growth unit through hydrogen bonding (*e.g.* (h00) surfaces) resulting in dominant (0k0)

surfaces. Figure 274 shows the identity of molecules observed on the different surfaces of CBZ:2H_2O and illustrates its crystal growth.

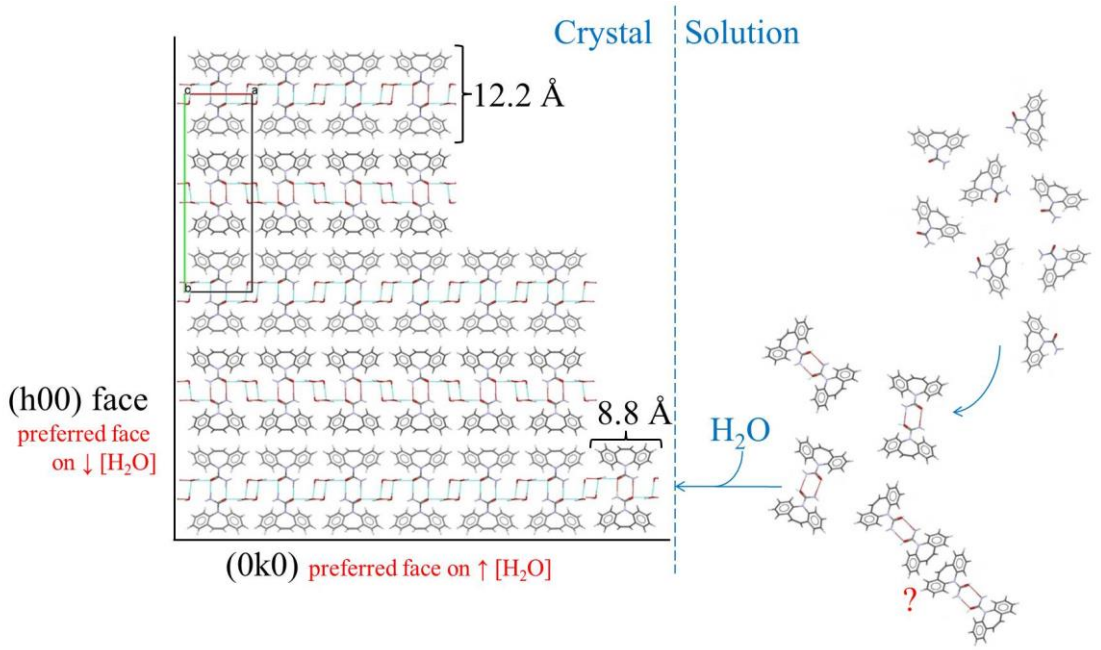

Figure 274 - Scheme showing the molecular arrangement on the (00l) plane of the CBZ:2H_2O structure. It illustrates the growth of the (0k0) and (h00) crystal surfaces and adds the size of the molecular units.

A comparison of the attachment energies within the materials which are isostructural to CBZ:2H_2O (Group 3) shows that the surface composed by the dibenzoazepine portions of CBZ molecules corresponds to the lowest absolute attachment energies in all the crystal forms (Table 16). It means that in a thermodynamically driven situation where the quantity of guest molecules does not limit the growth, this surface is therefore expected to grow slowly and to have morphological significance. As the quantity of guest molecules in the crystallization media decrease, in turn, the growth along the direction of CBZ:guest hydrogen bonds may be supressed because of kinetics.

A subsequent question was raised as to the reason why this kinetic effect is so pronounced in the case of CBZ:2H_2O? It is suggested that the difference in the hydrogen bonding character between both alcohol and guest molecule contribute to the findings obtained during the crystallization of CBZ:2H_2O in alcohol:water. Table 17 shows, for example, the comparison of the Hansen Solubility Parameters (HSP) of carbamazepine, ethanol and the other solvents used in the crystallization of materials classified in Group 3. The HSP is one of the different approaches used to understand and predict the solubility behaviour of a material.[222] The method is based on the molecular structure of the components and relates the total cohesion energy of a material to its solubility based on three energetic components which describe the possible interactions in solution. These components are the intermolecular dispersion forces,

the dipole-dipole polar interactions and the hydrogen bonding. In the present study, HSP was used to compare the hydrogen bonding contributions of the different molecules present during the crystallization. It was demonstrated that the hydrogen bond contribution to the total cohesion energy of water was of particular importance. A different scenario was seen in the HSP of the other guest molecules, which might explain the different behaviours seen during the crystallization of different CBZ multicomponent materials (formamide has shown an intermediate behaviour). The HSPs also help understanding the experimental evidences which have shown that an increase in the lipophilicity of the alcohol (ethanol *versus* isopropanol) also affected the kinetics of CBZ:2H_2O crystal growth. In this case, it can be inferred that the hydrogen bonding power is decreased in isopropanol.

Table 16- Attachment energy calculated for the CBZ multicomponent structures classified in Group 3.

Crystal form	Attachment energy[1,2]		
	hkl	d_{hkl} (Å)	E_{att} Total (kJ.mol^{-1})
2CBZ:BZQ	{0 2 0}	13.81	-20.6842
	{1 0 0}	10.10	-43.9063
2CBZ:OXA	{0 2 0}	12.85	-29.0315
	{1 0 0}	10.39	-56.8815
CBZ:2H_2O	{0 2 0}	14.36	-25.9131
	{1 0 0}	9.79	-46.0860
CBZ:FORM[3]	{0 1 1}	13.46	-28.1940
	{0 1 -1}	10.11	-53.2671

[1] The attachment energies of the 2CBZ:DIOX structure are not added because of errors found during the calculations (due to the disorder of the dioxane molecule). Results were only obtained for the doubled cell, but they are still being analysed.

[2] These values correspond to the lowest absolute attachment energies in the structures, except in CBZ:FORM. In the case of CBZ:FORM, other two planes have shown intermediate attachment energies in comparison to the planes shown on the table: (001) with -37.0246 kJ.mol^{-1}, and (010) with -39.4974 kJ.mol^{-1}. The results are not highlighted here, but they show differences in the predicted morphology from BFDH and the attachment energy method. It is suggested that it is a result of the symmetry in the CBZ:FORM (see Chapter 1) but the results are still being analysed.

[3] The (011) and the (01-1) planes correspond to the (020) and (100) planes in the other crystal forms, respectively.

Table 17 - Hansen Solubility Parameters of the carbamazepine and solvents used in the crystallization of CBZ:2H_2O, CBZ:FORM and 2CBZ:DIOX.

Component	Hansen Solubility Parameters[1] (MPa$^{1/2}$)		
	Dispersion	Permanent dipole	H bonding
Ethanol	15.8	8.8	19.4
Isopropanol	15.8	5.2	13.3
Water	15.6	16.0	42.3
Formamide	17.2	26.2	19.0
Dioxane	19.0	1.8	7.4
Carbamazepine	23.6	7.4	9.8

[1] The HSP values for the solvents were taken from www.hansen-solubility.com,[222] while the values of carbamazepine were taken from Grymonpre & Thommes[223].

One remaining factor, however, may have also affected the marked kinetic effect of solution composition in the crystallization of CBZ:2H_2O: the CBZ growth units. The AFM analyses of the (0k0) and (h00) surfaces of the dihydrate have shown steps which provide useful information about the growth units and the surface adsorption of CBZ molecules. It was shown that the (h00) surface had steps of 7.5±0.7 Å along the needle axis and presented a layer-like aspect as a consequence of its small terraces. The (0k0) surfaces, in turn, showed steps crossing the needle axis and terraces of larger size. Interestingly, the images demonstrated that the terraces on the (0k0) surface are formed by pairs of layers that have coincident edges. The measured distance between the paired layers is approximately half of the step distance between two different terraces (12.5±0.6 Å and 25.8±1.2 Å, respectively). Figure 274 illustrates how the molecules are arranged on the (0k0) and (h00) surfaces of CBZ:2H_2O and links the steps seen by AFM to the molecules on the respective surfaces. It shows that the steps on the (h00) surface can be related to the size of the dibenzoazepine portions of CBZ. The size of the steps on the (0k0) face, however, coincides the size of two dimers of CBZ.

Two hypotheses have been suggested to explain the size of the (0k0) steps and the reason why they are composed of a pair of layers. The first considers that the growth units of CBZ:2H_2O in solution corresponds to one CBZ dimer, but the interaction between two pairs of dimers along the *b* axis stabilizes the binding of the molecules to the surface. It is possible that the strength of interaction between two different dimers via their dibenzoazepine portion and the strain caused by the angle between them plays an important role in this behaviour. Another hypothesis, however, suggests that clusters larger than one CBZ dimer correspond to the growth units of CBZ:2H_2O. If this hypothesis is correct, it is also possible that the solution composition also modifies the formation of CBZ pre-nucleation clusters. For example, a more lipophilic environments could favour the interaction along the dibenzoazepine groups, as it has been suggested in the case of differences in outcome between using ethanol or isopropanol for crystallization. Both hypotheses are difficult to assess experimentally. Regardless of what mechanism leads to the formation of steps on the (0k0) surface which are composed by two pairs of dimers, this characteristic may also have affected the growth of (0k0). In this case, the pronounced kinetic effect of solvent composition on the crystallization of CBZ:2H_2O may not only be related to favouring the binding of CBZ on the (0k0) surface in low water contents, but also by adding stable molecular units on the surface that are larger than one dimer alone.

The crystallization studies of CBZ:2H_2O illustrate how the solution environment and experimental conditions can affect the particle morphology such that crystals with different dominant surfaces (*tracht*) could be prepared. Compared to previous reports from the literature,[11,69,71,72] the case of CBZ:2H_2O crystallized in alcohol:water is special because both

solvents play different and important roles in the crystallization outcome. Water acts as being part of the crystal lattice, while the alcohol modulates the hydrogen bonding character in solution. This effect is different than the surface "docking" effect alone.

Although the overall shapes of the CBZ:2H_2O crystals prepared in different ethanol:water proportions were similar, they differed in their microscopic properties. Considering the complexity of the solutions and crystallization apparatus in which a drug is commonly crystallized in industry, challenges related to these microscopic surface properties can be anticipated. In fact, it was shown in the present work that the combination of thin crystals and (h00) preferred face results in extensive particle breakage of CBZ:2H_2O samples crystallized in large-scale. The results illustrate how the translation of laboratory-scale studies to manufacturing is not straightforward. Also, in the case of labile material, such as hydrates, solvates and metastable polymorphs, breakage may play a role in solid-state transformations affecting the product.

8.2.3. Possible future work related to crystallization

– To evaluate the possibility of predicting the eutectic point of solubility between CBZ and the CBZ multicomponent forms in ethanolic solutions with increasing proportions of guest molecules. The use of the Hansen Solubility Parameters and the methodology described in McKenzie, Feeder & Hunter[224] and Calero et.al.[225] remain to be evaluated.

– To perform AFM experiments on the dominant surfaces of 2CBZ:BZQ and 2CBZ:DIOX in order to measure the size of the steps and compare them to the step size found on the (0k0) surface of the CBZ:2H_2O crystals. The aim would be to evaluate if the steps are composed of one or two CBZ dimers (or perhaps something different?). A better understanding of the growth of CBZ:2H_2O crystals, however, may be obtained from *in situ* crystallization experiments using AFM.

– To study the differences seen between using the BFDH calculation and the attachment energy method for predicting the morphology of CBZ:FORM crystals.

8.3. Stress-induced transformations of multicomponent forms of carbamazepine

Stress-induced transformations of organic solids are processes that may involve changes in the internal structure and/or in the shape and volume of a crystal due to stress. The

change in the internal structure usually leads to lattice rearrangement and the formation of different bulk crystal structures (*e.g.* polymorphs), but may also result in isostructural forms (*e.g.* some solvates and their desolvates). The deformation related to changes in shape and volume, in turn, results in different morphologies or the formation of macroscopic defects, such as cracks, holes and polycrystalline domains, which are usually evidenced on the surface of the materials. In this case, although atomic-scale processes and mechanisms are knowingly difficult to study in the solid-state, a combined analysis of bulk and surface may help correlate the nature of the starting materials and products with the kinematic processes occurring during the transformation. It is clear from the results shown in this study that combining both bulk and surface characterization provide different types of information well worth our attention.

Modifications of both the bulk and surface of solid materials occur as a result of stress and strain, *i.e.* distortions, being accumulated in the lattice. Depending on the nature of the material and its intrinsic characteristics, along with the pressure and the temperature of the environment, this 'stressed' transient state will transform to release the extra energy in one way or another. Additional factors may affect these transformations, such as the strain rate, the presence of defects, the molecular mobility in the material and the availability of fluids during the processes.

In the case of materials composed of host and guest molecules, stress may cause crystal decomposition due to the release of the guest molecule. Such processes have been studied in the present thesis in the form of dehydration, desolvation or sublimation, depending on the nature of the guest molecule at room temperature. From the perspective of the present work, different CBZ multicomponent materials were selected to evaluate the effects of the nature of the guest molecules, the hydrogen bonding strength of guest and host molecules, the packing and the coformer arrangement on the outcome of decomposition.

In general, temperature was selected as the external force driving crystal decomposition of hydrates, solvates and cocrystals of CBZ. The effect of temperature on introducing strain into the lattice was experimentally assessed in isothermal and non-isothermal experiments. In some cases, the response to different strain rates was evaluated by means of changing the condition of the experiments and the environment. The effect of the presence of fluids (liquids phases) during these processes was experimentally assessed by the visual observation of melting or peritectic formation. The nature of the materials and molecular mobility were indirectly evaluated by combining structural analyses and information of the intrinsic properties of the guest molecules alone. The differences in pressure and the presence of defects are, however, difficult to approach and a few considerations were made.

8.3.1. The nature of the polymorphic outcome after crystal decomposition

A comparison of the structures of CBZ multicomponent materials in the previous chapters has demonstrated that although most of the crystal structures containing CBZ molecules are held together by hydrogen bonding in the form of CBZ dimers, the strongest interactions within the crystals appears to be through the stacking of the molecules. In this respect, two main types of stacking were identified and correlated to the stacking of the resulting CBZ polymorphic form: *i.e.* translational stacking of dimers in Forms I and II and the herringbone/inversed-cup motif in the structure of Forms III and IV. On this basis it was shown that, in general, molecular rearrangement as a result of decomposition is highly influenced by the stacking motif of CBZ molecules in the solvate/cocrystal phase- for example, it was shown that solvates classified in Group 1 showed similar stacking to that of polymorph III and therefore subsequently tend to rearrange to Form III. Those multicomponent materials in groups 3 and 5, in turn, show similar stacking to that in polymorph I and tend to rearrange into Form I.

Further considerations about the internal structural reorganization of the CBZ multicomponent materials are needed, however. Varying the experimental conditions applied during the desolvation of CBZ:DMSO and CBZ:DMF (Group 1) were noted to result in different polymorphic outcomes to that described above and it was suggested that higher desolvation rates resulted in the formation of a liquid phase, thereby affecting the results obtained. With the boiling points of DMSO and DMF being relatively high, it was proposed that the collapse of the structures is then related to the formation of a peritectic mixture. In this case, the solvent released from the lattice remains in contact with the solid material and results in its dissolution (and subsequent recrystallization). This mechanism will be clearly different to the alternative cooperative solid-solid transformation pathway. It appears to be facilitated by the rate of desolvation.

Evidence for the formation of a liquid phase (without decomposition) was also proposed in CBZ:DMA (Group 2); CBZ:FORM (Group 3); CBZ:TFE (Group 4); and CBZ:TFA, CBZ:ACA and CBZ:FA (Group 5). Not all these materials, however, show higher onset temperature of desolvation than the boiling points of the respective solvent (see Chapter 7 for thermal data). It was suggested that lattice collapse and liquid phase formation might also be influenced by the stress resulting from solvent release. For example, in the case of CBZ:DMA, CBZ:TFE and CBZ:TFA, the volume of the cavities is relatively large and layers of the solvent are almost formed within the crystal, while CBZ:FA has guest molecules isolated in pockets. In both cases, desolvation is potentially more destructive than in typical channel-like structures. It is noteworthy that CBZ:DMSO and CBZ:DMF also show a different type of

solvent arrangement (intersecting channels), which may be coupled to other factors and give rise to the observed behaviour and the formation of a liquid.

Such transformations are likely to be a result of a combination of factors that are not, conceptually or experimentally, easily separated. For instance, in the investigation of the liquid phase observed during desolvation there is also the possibility that the lattice melts, especially in the examples where isostructural desolvation was evidenced (*e.g.* CBZ:FORM). It is unclear, however, whether the liquid observed in these studies corresponded to the formation of a peritectic, or if it was related to the melting of the desolvate lattice at high temperatures (or possibly a combination of both).

Another aspect that might contribute to both phenomena is the effect of the strength of interactions in introducing stress to the lattice. It was shown in Chapter 3 that in their respective solvates DMF, DMSO, DMA, TFE, TFA, ACA and FA strongly interact with the CBZ molecules. This was particularly likely in the case of materials belonging to Group 5, where CBZ molecules form heterodimers with the carboxylic acid. It is also worth noting that there is the possibility of ionization within the solvate and therefore the local stress caused by solvent release may, as a result, be particularly high. Thus, if only hydrogen bonds are considered, the probability of the structure collapsing because of desolvation is higher in structures that contain stronger interactions.

In the specific case of the TFE solvates, solvent interactions and arrangement appears to play a crucial role in the outcome of stress-induced transformations. The difference between the desolvation onset in CBZ:TFE and the boiling point of TFE is not large. The structure of the solvate shows, however, interesting features that may indicate that solvent release generates significant stress in the lattice. The solvent molecules in CBZ:TFE are strongly bound to one of the two CBZ independent molecules, while the other CBZ molecule is only hydrogen-bonded to CBZ within a dimer. In combination with these characteristics, it is also observed that the TFE molecules form hydrogen bonds between each other along the channels which, in addition, are almost interconnected to form layers. These factors may be correlated to the non-expected results observed in the case of the TFE 1:1 and 2:1 solvates. According to the structure analysis, CBZ Form I was the expected polymorphic outcome of the desolvation of both structures, and the 2:1 solvate was expected to be an intermediate in the desolvation of the 1:1 crystal form. Yet, the results have shown that the solvate with the higher stoichiometry desolvated directly to CBZ polymorph IV as the major phase, while the low stoichiometric form desolvated to give polymorph I. It is suggested that the solvent release in CBZ:TFE promotes a rapid collapse of the lattice before a 2:1 intermediate can be formed.

In contrast, in the case of the 1:1 and 2:1 BZQ cocrystals, the lower stoichiometric form was shown to be an intermediate of the sublimation process of the 2:1, and the decomposition of both materials, therefore, resulted in CBZ Form I. Although the interaction of CBZ and BZQ in the 1:1 cocrystal is as strong as in those CBZ multicomponent forms which showed the formation of a liquid phase, the lattice in CBZ:BZQ does not show evidence of such a collapse. It is suggested that the existence of an intermediate stable form, which provides stronger CBZ stacking interactions, coupled with the thermal behaviour of BZQ at high temperatures, affected the decomposition outcome of CBZ:BZQ. This analysis reminds us about CBZ:DMA. Although the DMA solvate shows similarities to CBZ:BZQ, the thermal behaviour of the two materials is considerably different. It is believed that the lack of an intermediate form of desolvation and the formation of a peritectic form influences the results obtained in the desolvation of CBZ:DMA.

In the case of CBZ:2H_2O, although a few studies in the literature have suggested the presence of a monohydrate form, none of the experiments in the present work have observed such an intermediate. It was observed, however, that depending on the particle size, the dihydrate crystals can undergo complete dehydration and then further recrystallize into anhydrous CBZ, or show simultaneous dehydration and recrystallization events. The results also showed that the experimental conditions again influence the kinetics of water loss and lattice rearrangement, which can be related to the different processes occurring during dehydration. It is suggested that the dehydration occurs via the release of water molecules following a cooperative mechanism. Depending on the kinetics of water loss, however, the material may present short range order with the domains formed upon dehydration being very small. In this case, there is no prominent structural filiation between parent and daughter phases and the lattice reorganisation is mainly influenced by nucleation and growth processes.[114] As a result, different polymorphic outcomes may be experimentally obtained - as in fact, they were.

Similarly, Khoo *et al.*[175] suggested that the kinetics of dehydration of CBZ:2H_2O is controlled by the internal diffusion of the water molecules, which will change with particle size. In other work, the same group suggested that molecular mobility and the relaxation period required to initiate nucleation after CBZ dehydration changes as a function of the experimental conditions.[163] In other words, nucleation and growth processes may explain the inconsistencies on the polymorphic outcome of CBZ dehydration reported in different studies in the literature and herein.

Following this consideration about nucleation, decomposition that leads to materials which show short range order or are more defective appear to be more affected by the presence of seeds during recrystallization than transformations which are mediated by a liquid

phase. As a common feature, though, the reactions that present an intermediate liquid phase tend to result in CBZ polymorph I. This finding is in agreement to the experiments performed in this study and to the previous literature,[140,149,166] which concludes that Form I is obtained from the molten state and is the most stable form at high temperature.

The formation of CBZ polymorph I from the molten, amorphous or highly defective state is not only related to its thermodynamic stability at higher temperature. CBZ Form I may also be formed because of crystal decomposition below the transition temperature between Forms III and I, for example. The reason for such transformation pathway may be explained by the Ostwald Rule of Stages.[76] It is expected that the unstable product of crystal decomposition, tends to transform into a crystal form via the smallest loss of free energy. This metastable polymorph is considered, however, a transient state and its formation and detection may be strongly affected by kinetic factors.

Kinetics was also shown to modulate the chemical decomposition of CBZ and TFA in the CBZ:TFA solvate. It was suggested that the rate of desolvation can modify and accelerate the mechanism of CBZ chemical decomposition. It was hypothesized that this phenomenon is related to the reactivity of CBZ in contact with TFA in the molten state, but also by ionic interactions which vary as a function of temperature in the solvate.[199] A slightly different behaviour was observed in 2CBZ:OXA. In this case, the chemical decomposition of the guest molecule only accelerated the decomposition of the CBZ host molecules in the molten material.

It is noteworthy from the discussions so far that packing, and more specifically the stacking pattern of CBZ molecules in the parent phase, is the main factor governing the polymorphic outcome of the stress-induced transformations studied herein. The product of physical decomposition, however, is frequently affected by the experimental conditions. These findings show that the effect of strain rate on molecular vibrations and diffusion need also to be considered. Although the vibrations within the CBZ molecular framework may also contribute to the lattice collapse, it is expected that the main sources of stress come from the release of the guest molecules because CBZ is not subjected to complex torsions and is, usually, held in dimers interacting via strong stacking forces. More than that, the guest components appear to affect the outcome of the reactions because of their own physical properties (*e.g.* boiling point, state at room temperature and reactivity). As a summary, it is concluded that three different factors have affected the polymorphic outcome of the transformations in CBZ multicomponent materials: the stacking mode of CBZ molecules, the interaction of CBZ and guest molecules, and the guest's physical properties.

In the literature, Petit & Coquerel[114] stated in their "Rouen 96" model that the polymorphic outcome of crystal decomposition depends on the destructiveness of the process

(see Figure 10, Chapter 1). The authors later added particle size and defects to this model.[226] In the case of particle size, they suggest that the formation of a product layer on the surface of large particles will affect the further release of the guest molecules. As the temperature increases, these particles undergo a destructive transformation, which explains why no structural correlation appears to exist between mother and daughter phases in such instances. Although the authors illustrate this behaviour with the example of a DMSO solvate which forms a peritectic mixture during desolvation, they do not discuss the effect of particle dissolution on the outcome.[227]

The findings from the present work, however, suggest that the formation of a liquid phase may significantly affect the results of desolvation reactions. As a take-home message, if I could somehow start this project again, I would first collect DSC/TGA data and compare the onset of physical decomposition to the boiling temperature of the guest material. My first question would be whether is there possibility of peritectic formation? If yes, my prediction about the polymorphic outcome would be based on the stability relationship between polymorphs at that specified temperature. If the answer was negative, in turn, I would proceed with structural analyses expecting that packing similarities between parent phases and the products play a role. It is known, however, that many factors other than structural similarities may affect the outcome of these transformations, such as the formation of defects and amorphous materials, and the diffusion throughout large particles, which gives rise to the dependence on experimental conditions. As it has been suggested that experimental conditions are influenced by strain rate, an alternative could be the computation of strain and stress generated by the increase in temperature. These calculations are expected to provide information to be used on the prediction of dehydration, desolvation and sublimation reactions. It could be a helpful tool for the solid-state chemist and the process engineer as it potentially provides combined information of the effect of host-guest strength (and nature) of interactions, the host lattice energy and the defects caused by molecular migration. To the best of my knowledge, no such model has been proposed and studied so far. To conclude, although experimental conditions may modify the mechanism of the processes and result in inconsistencies, it is believed that calculations from the structure of the materials may still provide information that could be used to explain their thermal behaviour.

8.3.2. Changes in surface structure, crystal shape and volume resulting from crystal decomposition

(a) General observations

Together with the changes of the internal crystalline structures described above, the CBZ multicomponent materials subjected to heat show surface modifications. In general, the transformations result in polycrystalline particles with retention of shape of the original crystals. It was shown that important information could be extracted from the analysis of the resulting surface features. For instance, the presence of spherulites was taken as indicative of the formation of liquid intermediate phase. Additionally the appearance and orientation of initial surface domains changed quite significantly depending on the polymorphic form obtained after the transformation.

The domains on the surface of those crystals correlated to the formation CBZ polymorph I were characterized as acicular or whisker-like, illustrating the anisotropy of product growth. In some cases, it was even observed that surfaces of the same crystal had domains oriented in different fashions. This orientation effect could be correlated to the direction of molecular transport, lattice rearrangement and/or crystallite growth.[228] Frequently, the domains on the dominant surfaces were oriented along the main particle axis, following the stacking direction of the CBZ molecules. These findings suggest that a certain degree of lattice continuity is maintained during the transformation and agrees with the hypothesis that packing influences the polymorphic outcome of these reactions.

The surfaces of the resulting crystals characterized as CBZ polymorph III or IV were smoother and, in general, presented holes and round domains. The literature has suggested that holes formed by the edges of different grains are possibly a consequence of the strain between two intersecting features.[229] For the systems reported here, it is suggested that tensile forces result in lattice collapse at the point where they intersect (Figure 275). Although it is unclear whether the intersecting features are related to the crystal structure of the materials (such as the intersecting channels of solvent molecules seen in Group 1), it is more likely that they correspond to the surface of the grains in the product. These areas are expected to be more susceptible to deformation or product sublimation, and hence to the formation of holes. The holes and the surface of the grains may also align and connect to form “macro-fractures” which propagate quite irregularly throughout the crystal with no crystallographic orientation.

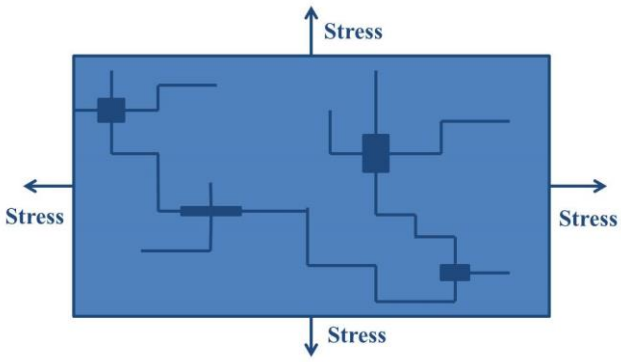

Figure 275 - Schematic representation of the formation of holes at the intersection of grain boundaries or planes which act as a source of stress (adapted from Tse *et al.*[229]).

(b) The surface of carbamazepine dihydrate crystals

In contrast to the cracks found on the surface of Group 1 materials, the crystals of CBZ:2H_2O show fractures which are clearly crystallographically oriented. Two different types of fractures were identified and were shown to be correlated to the different characteristics of the (0k0) and the (h00) planes. Because of these properties, the crystals exhibited surfaces that develop different types of cracks. The (00l) surface, for example, shows both types of fractures related to (0k0) and (h00) planes, while the cracks that are visible on the (h00) surface are solely related to (0k0) planes. The (0k0) surface, however, did not exhibit fractures. The reason for this is because while the (0k0) fractures tend to cross-cut the crystals, the (h00) cracks were shown to propagate only if confined between two (0k0) planes. The comparison of the attachment energies of both planes show that, indeed, the (0k0) plane presents the lowest attachment energy and thus corresponds to the most important cleavage plane in the structure (see Table 16). It explains why fractures along the (h00) plane only develop in constrained regions under high stress.

The cracks corresponding to the (0k0) crystallographic planes running parallel to the CBZ:2H_2O needle axis have been reported by Khoo *et al.*[163]. Additionally, Kachrimanis & Griesser[162] observed other type of cracks on the (0k0) face of the crystals. These cracks intersect at an angle of 81.5±1.6° and were related to the needle axis by 40.6±1.2°. Although no such fractures were usually observed in the present study, a similar pattern of texture (not cracks) was always found, but on the (h00) surface. In this case, the texture was composed of different domains which were related by an angle of 78.2±3.3º, while the orientation of the texture to the elongation axis was 36.1±2.5º.

Striations similar to these on the (h00) surface provide information about the movement history of the cracks, especially about the shear that was present before fracture.[228] For instance, Figure 276a illustrates that the textured domains show continuity across surfaces

separated by a crack. Figure 276b shows the corresponding structural features believed correlated to these striations - the dimers of CBZ and the (0k0) cleavage planes. It is indicated that, although the shear occurs between the dibenzoazepine portions of the CBZ molecules along the (0k0) plane, the stress direction runs parallel to the CBZ dimers. The findings on the (h00) surfaces suggest that the transport of water along the channels activates the movements of the CBZ dimers, while the stacking of the molecules resists the shear along the (0k0) plane.

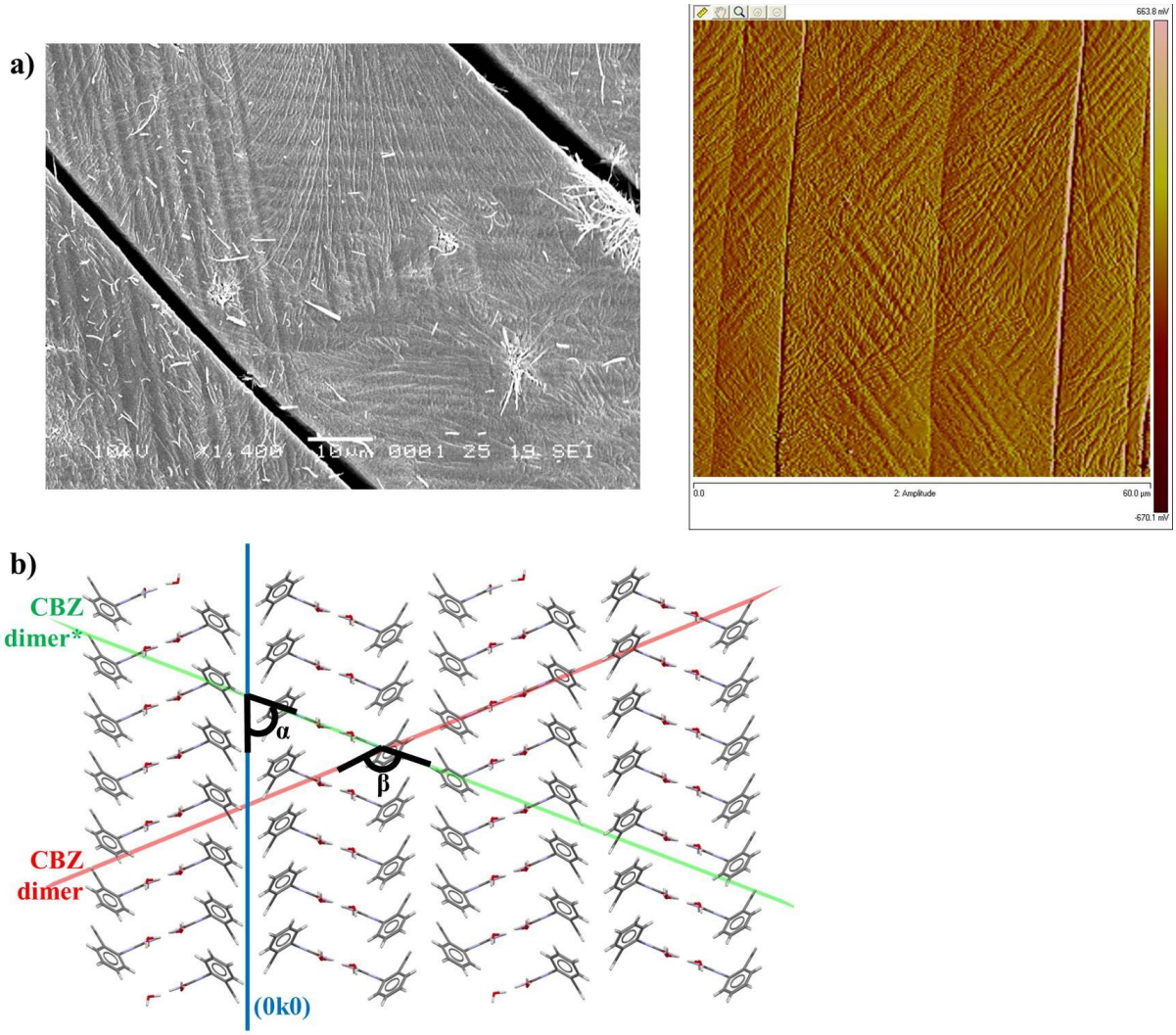

Figure 276 - The (h00) surface of CBZ:2H_2O crystals has shown striations as a result of stress. This figure shows *(a)* the surface of crystals dehydrated at 0% RH and 40 ºC (SEM and AFM-amplitude images), and *(b)* correlates the texture on the surface to the structure of CBZ:2H_2O (α=67.35º, β=134.71º).

Because of the molecular arrangement in the crystal, different surfaces show distinct responses to stress, as shown by the difference found between the (00l), (h00) and (0k0) surfaces. The analyses of samples which dehydrated into different polymorphs, however, suggest that the molecular arrangement in the parent phase may not be the only factor affecting the molecular movements. In this regard, although the general characteristics of the (h00) surfaces of the dihydrate did not change greatly, the (0k0) surfaces show differences depending

on the polymorphic outcome of the reaction. Samples dehydrated into polymorph I show aligned holes perpendicular to the needle axis on the (0k0) surface, while samples which resulted in polymorph IV show (0k0) surfaces with cracks angled by 41.5±2.0^{o} to the needle axis (similarly to the features reported by Kachrimanis & Griesser[162]). It is noteworthy that imaging of the ongoing process of dehydration showed that the surfaces of those crystals which dehydrated into polymorph I progressively changed with the course of the reaction, while crystals which dehydrated into Form IV apparently show a faster surface transformation. It is unclear whether the different surface features are directly attributed to distinct molecular movements and strain resulting from the formation of anhydrous CBZ Form I or IV, or if it illustrates the kinetics of the process in which the strain rate is expected to play a role. Regardless of the mechanisms which are involved in the formation of polymorph I *versus* polymorph IV from CBZ:2H_2O, the surface characteristics of the products agree with the remarks in the previous section: (i) the experimental conditions influence the kinetics of water loss and lattice rearrangement; and (ii) strain rate is important in stress-induced transformations.

A role for defects?: A further aspect that may influence the dehydration of CBZ:2H_2O, but is challenging to assess, is the presence of defects, such as twinning, and the disorder as proposed in the orthorhombic structural model of the dihydrate. In this case, the existence of striated domains in different directions on the (h00) surface can be the reflect of twinning in the crystals of CBZ:2H_2O. Harris *et al.*,[180] have studied a dihydrate sample and determined by X-ray analyses that the crystals were twinned in the proportion 5:1. They suggested that this twinning could be a domain-type disorder (with domain sizes of tens to hundreds of Å) or could occur on a microscopic level (multiple micro-twinning or penetration twinning), but no conclusive data was found in their study. Although the present work shows experimental evidences of boundary dimensions in SEM images of fresh crystals, and in AFM and SEM images of crystals after dehydration, care should be taken during the interpretation of these results because they were indirect measurements. The images present such domains as a consequence of the strain caused by the vacuum (in the case of SEM of fresh crystals) or by dehydration (in the case of AFM and SEM of dehydrated crystals), which also leads to cleavage. For the time being, the striated domains remain intriguing if not understood. If the twinning of the crystals was confirmed and an apparent single crystal of CBZ:2H_2O was actually characterized by smaller domains and different symmetry than the FEFNOT02 structure, it is expected that the mechanical strength would be affected. It is noteworthy, however, that the size of the domains is a sample-specific property which is highly influenced by the crystallization conditions and especially difficult to control in such samples.[4]

Information from impact testing: The surface characteristics of CBZ dihydrate crystals have suggested that the (h00) surface shows brittle behaviour and the (0k0) surface tends to be more plastic. These findings not only show that the (h00) surface will be more prone to cracks formation than the (0k0), but also suggests that particles in which the overall contribution of both surfaces is different (*e.g.* different dominant faces, *trachts* and thickness), may also show different susceptibility to breakage. In this case, it is suggested that decreasing the size of the (0k0) face will result in crystals with poorer mechanical properties. This characteristic was seen, in fact, in thin crystals prepared at a kilogram-scale, although this effect may also be combined with the influence of particle size on the properties of the material. It is known that particle size can affect the strength of a material because of the difference between surface and bulk mechanical properties: while the outer layers of a material are more brittle, the inner portions show plastic behaviour.[228]

The mechanical properties of the fresh crystals were assessed by impact tests in a dihydrate sample obtained at the kilogram-scale. It was shown that new (0k0) and (00l) surfaces were generated as a result of breakage, and the (h00) surface showed extensive texture from the strain caused by impact. While the striation on (h00) and the cleavage along the (0k0) plane have been previously correlated to structural features, the breakage perpendicular to the needle axis does not appear to be related to any weak plane in the structure. It is proposed, however, that strong compressive forces act on the crystals during impact and modify the lattice in comparison to a perfect non-stressed crystal. The stacking and the arrangement of CBZ molecules in the dihydrate structure appear to contribute to such behaviour.

Figure 277 illustrates this proposal and shows how the compression of the different crystal surfaces of a hypothetical CBZ:2H_2O crystal may lead to cleavage. This phenomenon has been previously characterized in bending crystals by the comparison of *in situ* X-ray diffraction data of bent and unbent crystal.[230] It is also possible, however, that the large bending force caused by the high aspect ratio of the particles also influences this breakage behaviour. In this case, *in situ* X-ray experiments of compressed dihydrate crystals along the needle axis would help in understanding the underlying mechanisms of breakage due to compression. Additionally, surface energy measurements could be useful in understanding the contribution of both surfaces to the overall particle properties and breakage behaviour.

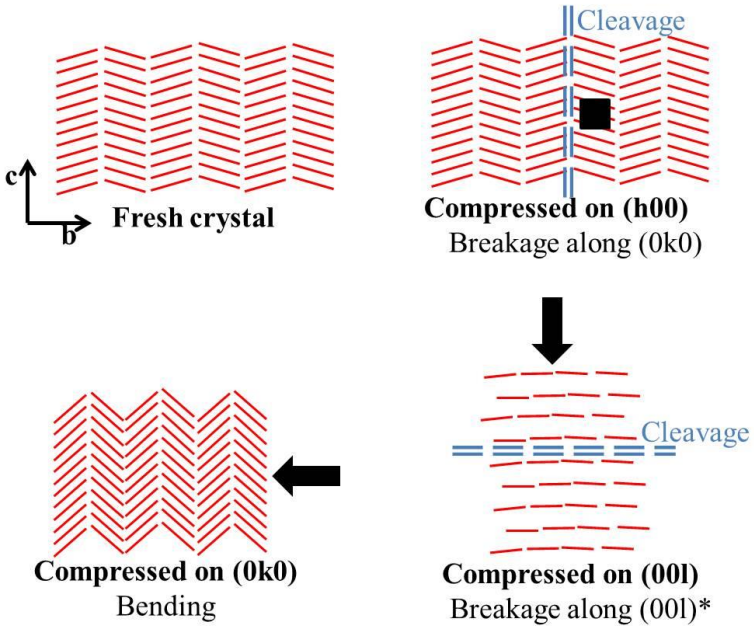

Figure 277 - Scheme illustrating the hypothetical effects of compression on the crystals of CBZ:2H_2O based on the experimental data and the structural analyses. The red lines correspond to the CBZ dimers projected on the (h00) plane, and the arrows show the direction of the compressive forces.

As a take-home message, the crystals of CBZ:2H_2O present poor mechanical properties and are prone to breakage due to both external mechanical forces applied to the crystals, but also due to internal stress generated during dehydration. It is suggested that the brittleness of the material is surface-specific and related to the crystal topography and structure. These characteristics raise one main question: why only CBZ:2H_2O crystals show such behaviour within the materials classified in Group 3, which are all structurally very similar?

(c) Comparing the Group 3 forms that are isostructural to the dihydrate

The response to stress due to vacuum and thermal treatment appeared to be different within the materials classified in Group 3 (2CBZ:BZQ, 2CBZ:OXA, CBZ:2H_2O, CBZ:FORM and 2CBZ:DIOX). It was shown that, although the materials are isostructural, CBZ:2H_2O is the only material which consistently developed surface cracks. In this regard, the next paragraphs revisit the structural analyses given in Chapter 3 as to answer the following question: why are CBZ:2H_2O crystals so prone to fracturing in comparison to the other isostructural forms in Group 3?

Consider the general case of heating a hypothetical CBZ multicomponent crystal from Group 3. The increasing temperature generates tensile stress within the crystal as the vibration of CBZ and guest molecules increase. The change in the position of the molecular units relative to each other creates, in turn, distortions or strain in the lattice. Consequently, two

different processes may take place: (i) fracture of the crystals, and (ii) movement of the guest molecules along the channels. The lattice will hold its structure until a certain amount of guest molecules is released and, then, the structure collapses. Considering this scenario, it is easy to understand why temperature, heating rate, pressure and particle size may affect the strain and, consequently, the mechanisms of dehydration, desolvation or sublimation. It shows that the packing of CBZ plays an important role in accumulating strain while the strength of interaction of CBZ and the guest molecules mainly acts on the stress generated once the temperature is increased.

The visual observation of CBZ packing in the structures of Group 3 has suggested that the weak planes are essentially the same. Two main planes were identified which appeared to cost the least energy for molecular movement: the planes along the dibenzoazepine groups and the planes which cross the channels and are longitudinal to the CBZ dimers. For simplification purposes, both planes will be respectively called (0k0) and (h00), although the correct crystallographic notation is different in CBZ:FORM and 2CBZ:DIOX.

The comparison of the attachment energies of both planes in the different structures of Group 3 shows that the (0k0) planes present the lowest values and correspond to the weakest cleavage planes (see Table 16). Although the chemical environment along these planes are very similar, the angles between the molecules and the planes, *i.e.* geometric parameters, are different in the different materials. Figure 278a illustrates the difference in the angles between CBZ dimers across the (0k0) planes of CBZ:2H_2O and 2CBZ:OXA, which present the biggest and the smallest angles in the structures of Group 3, respectively. In this case, if the orientation of the dimers in relation to the (0k0) plane is considered as a tensile axis in the structures of Group 3, it is easily seen that different angles between the dimers and plane may modify the lattice response to stress. Figure 278b also shows the components of this tensile axis projected on the (0k0) plane and the (00l) plane of the Group 3 structures. It demonstrates that, depending on the angle of the CBZ dimer, the stress produced on the (0k0) and the (00l) plane is different. In this situation, there are two main forces acting on (0k0) - which is the weakest plane in all the structures. The component that runs along the (0k0) plane contributes to slip movements and the component which is normal to the (0k0) plane, in turn, contributes to cleavage. They are both represented by the cosine and sine of the angle between the tensile axis and the plane, respectively.

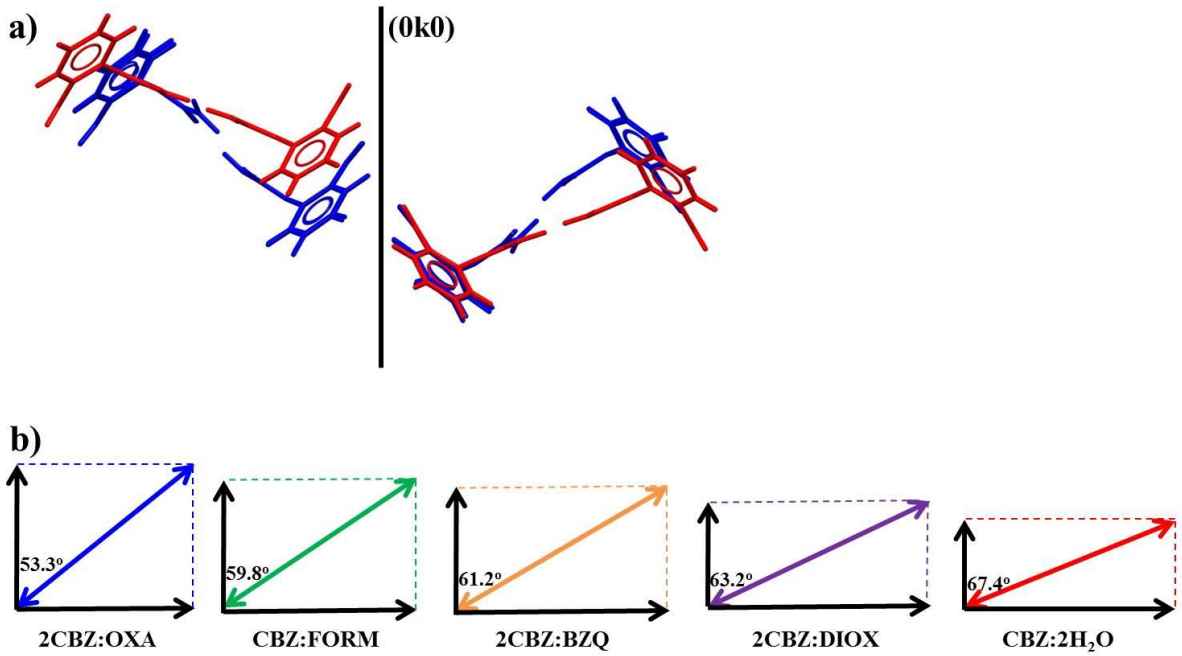

Figure 278 - It is suggested that the angle between the CBZ dimers and the (0k0) weak plane may modify the lattice response to stress. This figure illustrates (*a*) the difference of the CBZ dimers across the (0k0) plane in 2CBZ:OXA (molecules in blue) and CBZ:2H_2O (molecules in red). The graphical representations in (*b*) show the decomposition of tensile forces of same magnitude in the structures of CBZ multicomponent materials classified in Group 3. One component contributes to slip (along the (0k0) plane and represented by the *y* axis) and another to cleavage (perpendicular to the (0k0) plane and represented by the *x* axis).

From this relationship and assuming that the intermolecular energy between two CBZ molecules related through the (0k0) plane corresponds to the normal component of the tensile axis, it is possible to calculate the energy that the tensile stress along the CBZ dimer requires to overcome the energy of interaction of both molecules to form a crack. These calculations are detailed in Table 18. They illustrate a very simplistic model of a "monomolecular" cleavage scheme, but still allow the comparison of slip and cleavage contributions resulting from tensile stress in the structures of Group 3.

Table 18 - Hypothetical decomposition of the tensile stress forces along one CBZ dimer taking in consideration how the molecules are angled to the (0k0) plane and the strongest interaction of CBZ molecules across the plane.

Crystal form	α[1] (º)	Tensile stress[2] (kJ.mol^{-1})	Cleavage component of tensile stress[3] (kJ.mol^{-1})	Slip component of tensile stress[4] (kJ.mol^{-1})
2CBZ:OXA	53.3	25.2	20.2	15.0
CBZ:FORM	59.8	26.3	22.7	13.2
2CBZ:BZQ	61.2	25.8	22.6	12.4
2CBZ:DIOX	63.2	24.2	21.6	11.0
CBZ:2H_2O	67.4	23.6	21.8	9.1

[1] Angle between the plane of the CBZ dimer and the (0k0) plane.

[2] Calculated as the cleavage component divided by sinα.

[3] Interactions between two CBZ molecules related along the (0k0) plane. Obtained from Mercury® (UNI Intermolecular Potentials).

[4] Calculated as the product of the tensile stress and cosα.

The numbers show that, although the cleavage component is very similar for the different materials, the slip component varies. Interestingly, CBZ:2H_2O shows that less energy is needed to overcome the interaction which is normal to (0k0), while the same tensile stress provide less energy to slip in comparison to the other structures. It shows that, although the materials are isostructural, the orientation of the CBZ dimers in regard to the weak plane may play an important role on activating either fracture or frictional sliding (*e.g.* slip).

Frictional sliding is caused by edge dislocation movements that do not damage the crystals but are expected to slip through the crystal and 'heal'. It is difficult, however, to predict when the dislocation mode will be active and when the fracture mode will be active. As mentioned above, the comparison in Table 18 is very simplistic and only aims to facilitate the interpretation of the different geometric parameters related to the response of the lattice to stress in the different structures classified in Group 3. It is believed that it is not the CBZ lattice characteristics alone that contribute to the formation of cracks in the crystals of CBZ:2H_2O, but its combination to the intermolecular interactions between CBZ and water. The water molecules interact very strongly with the CBZ dimers, which could lead to a substantial stress being produced during the molecular movements. Additionally, the stacking of the CBZ molecules in the dihydrate is the strongest seen in the CBZ multicomponent materials analysed in the present work. In this case, strong stacking interaction may also facilitate the cleavage along (0k0) other than slip.

Defects and grain boundaries are also known to affect crack propagation and the strength of solid materials. In case the twinning of CBZ is confirmed, its effect on the mechanical properties may illustrate a balance of different aspects. The change in the orientation of the dimers can modify the strain in the lattice. It is also hypothesized that twinned domains may increase the local intensity of the tensile stress acting on the (0k0) plane, which reduces the local strength. The reverse behaviour is also a possibility as the existence of grain boundaries among the twinned domains may increase the toughness of the crystals.[4] In this case, it is said that the grain boundaries block the crack propagation and force cleavage to be reinitiated at each boundary.

The discussion above shows that CBZ:2H_2O is particularly prone to the formation of cracks because of a combination of the strength of interactions and the angle between the molecular axis and the weakest plane in the structure. The periodicity of the cracks on the surface is attributed to this combination of factors. It is suggested that there is a critical stress amount which can be tolerated by the lattice. Once the stress exceeds this value, a fracture propagates along the (0k0) plane. Considering the crystal structure of the CBZ:2H_2O, it is proposed that stress starts building up as the number of molecular layers increase along *b*

direction (the effect of defects, such as twinning, is unclear at the moment). In comparison, the crystal structures of the CBZ materials classified in Group 3, can tolerate a larger amount of critical stress because of their characteristics in regard to intermolecular interactions and geometrical parameters.

As a summary, four main messages have been learnt when considering the mechanical properties of the CBZ multicomponent materials classified in Group 3: (i) qualitative structural analyses and attachment energy calculations are not enough to understand a cleavage fracture along a weak plane; (ii) the orientation and the intensity of the tensile stress acting on a weak plane play important roles on cleavage; (iii) stacking and anisotropy give rise to interesting mechanical behaviour in organic materials; and (iv), as obvious as it may sound, slip and cleavage are different processes although they can occur along the same weak planes. It is expected that these learning messages can be applied to the study of the mechanical properties and crystal breakage of other organic solids.

8.3.3. Possible future work related to stress-induced transformations and mechanical properties

– To indent the crystal surfaces of the other multicomponent structures in Group 3 (2 CBZ:BZQ, 2CBZ:OXA, CBZ:2H_2O, CBZ:FORM and 2CBZ:OXA). The aim is to compare the Young Modulus of equivalent surfaces and relate the results with the structure.

– To compress CBZ:2H_2O crystals along the needle axis and perform *in situ* single X-ray experiments (before and during the compression). The aim is to evaluate how the stacking of the CBZ molecules change during compression and correlate the results with the impact tests.

– To collect single X-ray data and solve the structure of the same CBZ:2H_2O crystal before and after it is subjected to very mild vacuum conditions. The aim is to mimic the conditions to which the crystals were subjected during coating prior to SEM analyses. It was shown in the present work that the sputter coating leads to the formation of cracks on the surface of the dihydrate crystals. The aim is to check if it modifies the angle between dimers and (0k0) planes. It is known, however, that the X-ray data will show the average picture of the lattice and this may not be the most appropriate experimental set-up.

– To investigate the mechanical properties of other organic solids that are reported to fracture by combining the analysis of the strength of interactions and the angle between the molecular axis and the weakest plane in the structures.

CONCLUSION

The present thesis has investigated desolvation, dehydration and sublimation reactions as models of stress-induced transformations. The main aim was to study the surface and bulk properties of labile organic materials that are susceptible to crack formation and particle breakage. The materials selected for this study were carbamazepine multicomponent forms. In total, 14 solvates (including one hydrate) and three cocrystals were selected and grouped according to their structure similarities. This set of crystal forms has been investigated in terms of the effects of packing and stacking, intermolecular interactions, geometric lattice parameters and physical properties of guest molecules on the outcome of crystallization experiments and crystal decomposition.

Solution crystallization was mainly used in the preparation of samples suitable for the study of stress-induced transformations of CBZ multicomponent materials. Screening experiments have obtained two new crystal forms that were not reported in literature: CBZ:BZQ and 2CBZ:TFE. It is likely that these new phases were not found in previous studies because the majority of the solvate crystallization experiments are usually performed in pure solvents (or low coformer concentrations, in the case of cocrystals).

The effect of solution concentration and, in the case of needle-like crystals, the solution media were also used to prepare crystals with habit and surface modifications. The aspect ratio of 2CBZ:BZQ, CBZ:2H_2O, CBZ:FORM, CBZ:TFA, CBZ:ACA and CBZ:FA crystals varied according to initial CBZ concentration and/or coformer proportion. In the case of CBZ:2H_2O, however, the results indicate that different dominant surfaces result from different coformer compositions giving rise to crystals with distinct *tracht*. Experiments in alcohol:water have demonstrated that both solvents play a role in controlling crystal shape. The proposed hypothesis is that alcohol and water molecules affect the morphology by two different mechanisms of selective surface adsorption. While the lipophilicity of the alcohol decreases the growth rate of non-hydrogen-bonding crystal faces by modulating the hydrogen bonding character in solution, the water molecules increase the growth of faces in which they are part of the growth unit through hydrogen bonding. Compared to previous reports from the literature, the case of CBZ:2H_2O crystallized in alcohol:water is special because both solvents play different roles in the crystallization outcome. This effect is different than the surface "docking" effect alone.

The crystallization studies of CBZ:2H_2O have illustrated how the solution environment and experimental conditions can affect the particle morphology such that crystals

with different dominant surfaces (*tracht*) could be prepared in laboratory. Considering that the crystals of CBZ:2H_2O are prone to cleavage on the (0k0) plane, these *tracht* variations have shown to be important factors in determining the processability of the sample. In fact, the scale-up from laboratory sized preparations, to pilot-scale batches of CBZ:2H_2O has produced thin crystals which were highly susceptible to fracture. It suggests that variables such as the nature of the material, the equipment used, particle-particle attrition and mechanical stress may have affected the crystallization outcome.

After the crystallization studies, the samples prepared in laboratory were used in the study of dehydration, desolvation and sublimation reactions. It was demonstrated that kinetic variables and experimental conditions significantly influence the product although, in general, the polymorphic outcome follows the structure relation between parent and daughter phases. Deviations from the effect of packing similarities are seen when crystalline seeds are present and/or the lattice collapses, especially in case crystal decomposes via the formation of a liquid phase. It is suggested that the main factors driving the polymorphic outcome of thermal decomposition of CBZ materials are the physical characteristics of the guest molecules and the strength of host-guest interactions in the respective multicomponent crystal form.

Depending on the polymorphic outcome, the product of the physical decomposition presents different surface characteristics. They reflect not only the nature of the newly formed phase, but also provide useful information about the reaction mechanism and the resulting molecular movements. All the crystal forms investigated herein became polycrystalline upon decomposition, although the overall crystal shape was usually maintained. The polycrystalline domains of different materials have shown different sizes and characteristics. The domains on the surface of those crystals correlated to the formation of CBZ polymorph I were characterized as acicular or whisker-like, while the surfaces of the resulting crystals characterized as CBZ polymorph III or IV were smoother and, in general, presented holes and round domains. The holes and the surface of the grains may also align and connect to form “macro-fractures” which propagate quite irregularly throughout the crystal. It was suggested that movements between such grains act as tensile forces that promote lattice collapse at the point where they intersect, leading to the formation of holes and random cracks.

Marked and consistent particle breakage was only observed in CBZ:2H_2O crystals. Although the dihydrate is isostructural to a few other crystal forms, only CBZ:2H_2O crystals are prone to cleavage along crystallographic directions. The structure analysis has shown that sets of equivalent crystallographic planes present geometric differences not only within polytypic structures (2CBZ:BZQ, 2CBZ:OXA and CBZ:2H_2O, compared to CBZ:FORM and 2CBZ:DIOX, and to CBZ:NIT), but also among strictly isostructural materials (2CBZ:BZQ,

compared to 2CBZ:OXA and to CBZ:2H_2O). These findings indicate that the presence of weak planes is not enough to explain the occurrence of particle breakage. It is proposed that the stress caused by molecular movements and the direction of the stress axis in regard to the weak plane play a major role in the cleavage of CBZ crystals. Considering that CBZ is a rigid molecule which usually interacts with other CBZ molecules in strong hydrogen bonded dimers, these pairs of molecules may act as tensile axes which should be considered when analysing the structures.

It is suggested that there is a critical stress amount which can be tolerated by the lattice before cleavage occurs. Below this stress value, molecular migrations may happen as dislocations. Once the stress exceeds this critical value, however, a fracture propagates along the weak plane. In these terms, the present work has shown that CBZ:2H_2O tolerates less stress than other isostructural CBZ crystal forms. It is believed that it is not the characteristics of the CBZ lattice alone that contribute to the formation of cracks in the crystals of CBZ:2H_2O, but its combination to the intermolecular interactions between CBZ and water. The water molecules interact very strongly with the CBZ dimers, which could lead to a substantial stress being produced during molecular movements. Additionally, the stacking of the CBZ molecules in the dihydrate is the strongest seen in the CBZ multicomponent materials analysed, which may also contribute to cleavage along (0k0) other than slip. In the case of the other CBZ materials, however, it is suggested that the critical stress is not overcome, and the dislocation mode is active, rather than the fraction mode.

This hypothesis was only uncovered because the present work has compared the structures not only from their crystal packing and intermolecular interactions, but it has also proposed the analysis of the geometrical characteristics of the slip systems as an alternative to study molecular movements in crystals. This approach makes it possible to deconvolute the contribution of the stress generated during molecular movements in gliding and cleavage elements. It is proposed that these learning messages can be applied to the study of other organic solids, which may contribute to the understanding of particle breakage during drying.

REFERENCES

(1) Desiraju, G. R. A Bond by Any Other Name. *Angew. Chem. Int. Ed. Engl.* **2011**, *50* (1), 52–59.

(2) Bernstein, J. *Polymorphism in Molecular Crystals*, 2nd ed.; Oxford University Press: Oxford, 2013.

(3) Descamps, M.; Willard, J.-F. Some Facets of Molecular Disorder in Crystalline and Amorphous Pharmaceuticals. In *Disordered Pharmaceutical Materials*; Descamps, M., Ed.; Wiley: Weinheim, 2016.

(4) Hosford, W. F. *Mechanical Behaviour of Materials*, 2nd ed.; Cambridge University Press: Cambridge, 2010.

(5) Byrn, S. R.; Pfeiffer, R. R.; Stowell, J. G. *Solid-State Chemistry of Drugs*; Academic Press, New York.: New York, 1999.

(6) Callister, W. D.; Rethwisch, D. G. *Fundamentals of Materials Science and Engineering an Integrated Approach*, 4th ed.; John Wiley & Sons, Inc.: New York, 2012.

(7) Mittemeijer, E. J.; Scardi, P. *Diffraction Analysis of the Microstructure of Materials*; Springer: Berlin, 2004.

(8) Kelly, A. A.; Knowles, K. M. *Crystallography and Crystal Defects*, 2nd ed.; John Wiley & Sons, Inc.: New York, 2012.

(9) Tilley, R. J. D. *Defects in Solids*; Special Topics in Inorganic Chemistry; John Wiley & Sons, Inc.: London, 2008.

(10) Samorjai, G. A.; Li, Y. *Introduction to Surface Chemistry and Catalysis*, 2nd ed.; John Wiley & Sons, Inc., 2010.

(11) Garside, J.; Davey, R. J. *From Molecules to Crystallizers: An Introduction to Crystallization*; Oxford Chemistry Primers: Oxford, 2000.

(12) Dybkov, V. I. *Reaction Diffusion and Solid State Chemical Kinetics*; IPMS Publications: Kyiv, 2002.

(13) Myers, H. P. *Introductory Solid State Physics*, 2nd ed.; Taylor & Francis: London, 1997.

(14) Jones, W.; Eddleston, M. D. Crystal Imperfections in Molecular Crystals: Physical and Chemical Consequences. In *Disordered Pharmaceutical Materials*; Descamps, M., Ed.; Wiley: Weinheim, 2016.

(15) Giacovazzo, C.; Monaco, H. L.; Artioli, G.; Viterbo, D.; Milanesio, M.; Gilli, G.; Gilli, P.; Zanotti, G.; Ferraris, G.; Catti, M. *Fundamentals of Crystallography*, 3rd ed.; International Union of Crystallography Texts on Crystallography; Oxford University Press: Oxford, 2011.

(16) Brittain, H. G. *Polymorphism in Pharmaceutical Solids*; Informa Healthcare: New York, 2009.

(17) Wouters, J.; Quere, L. *Pharmaceutical Salts and Co-Crystals*; The Royal Society of Chemistry: Cambridge, 2012.

(18) Thakuria, R.; Delori, A.; Jones, W.; Lipert, M. P.; Roy, L.; Rodríguez-Hornedo, N. Pharmaceutical Cocrystals and Poorly Soluble Drugs. *Int. J. Pharm.* **2013**, *453* (1), 101–125.

(19) Jones, W. *Organic Molecular Solids: Properties and Applications*; CRC Press: Florida, 1997.

(20) Jones, W.; Rao, C. N. R. *Supramolecular Organization and Materials Design*; Cambridge University Press: Cambridge, 2008.

(21) Vippagunta, S. R.; Brittain, H. G.; Grant, D. J. Crystalline Solids. *Adv. Drug Deliv. Rev.* **2001**, *48* (1), 3–26.

(22) Blagden, N.; de Matas, M.; Gavan, P. T.; York, P. Crystal Engineering of Active Pharmaceutical Ingredients to Improve Solubility and Dissolution Rates. *Adv. Drug Deliv. Rev.* **2007**, *59* (7), 617–630.

(23) Desiraju, G. R. Supramolecular Synthons in Crystal Engineering-A New Organic Synthesis. *Angew. Chem. Int. Ed. Engl.* **1995**, *34* (21), 2311–2327.

(24) Moulton, B.; Zaworotko, M. J. From Molecules to Crystal Engineering : Supramolecular Isomerism and Polymorphism in Network Solids. *Chem. Rev.* **2001**, *101*, 1629–1658.

(25) Fleischman, S. G.; Kuduva, S. S.; McMahon, J. a.; Moulton, B.; Bailey Walsh, R. D.; Rodríguez-Hornedo, N.; Zaworotko, M. J. Crystal Engineering of the Composition of Pharmaceutical Phases: Multiple-Component Crystalline Solids Involving Carbamazepine. *Cryst. Growth Des.* **2003**, *3* (6), 909–919.

(26) Desiraju, G. R.; Vittal, J. J.; Ramanan, A. *Crystal Engineering: A Textbook*; IISc Press: New Jersey, 2011.

(27) Braga, D.; Grepioni, F. *Making Crystals by Design: Methods, Techniques and Applications*; Wiley: Weinheim, 2007.

(28) Desiraju, G. R.; Nangia, A. Use of the Term "Crystal Engineering" in the Regulatory and Patent Literature of Pharmaceutical Solid Forms. Some Comments. *Cryst. Growth Des.* **2016**, *16* (10), 5585–5587.

(29) Braga, D.; Grepioni, F.; Gavezzotti, A.; Bernstein, J. Re: "Crystal Engineering in the Regulatory and Patent Literature of Pharmaceutical Solid Forms." *Cryst. Growth Des.* **2017**, *17* (3), 933–939.

(30) Bučar, D. K. Engineering Molecular Crystals: Backbreaking, yet Gratifying. *Cryst. Growth Des.* **2017**, *17* (6), 2913–2918.

(31) Mishra, M. K.; Ramamurty, U.; Desiraju, G. R. Mechanical Property Design of Molecular Solids. *Curr. Opin. Solid State Mater. Sci.* **2016**, *20* (6), 361–370.

(32) Commins, P.; Desta, I. T.; Karothu, D. P.; Panda, M. K.; Naumov, P. Crystals on the Move: Mechanical Effects in Dynamic Solids. *Chem. Commun.* **2016**, *52* (97), 13941–13954.

(33) Karki, S.; Frisic, T.; Fabian, L.; Laity, P. R.; Day, G. M.; Jones, W. Improving Mechanical Properties of Crystalline Solids by Cocrystal Formation: New Compressible Forms of Paracetamol. *Adv. Mater.* **2009**, *21* (38/"39), 3905–3909.

(34) Ghosh, S.; Mishra, M. K.; Kadambi, S. B.; Ramamurty, U.; Desiraju, G. R. Designing Elastic Organic Crystals: Highly Flexible Polyhalogenated N-Benzylideneanilines. *Angew. Chemie - Int. Ed.* **2015**, *54* (9), 2674–2678.

(35) Reddy, C. M.; Gundakaram, R. C.; Basavoju, S.; Kirchner, M. T.; Padmanabhan, K. A.; Desiraju, G. R. Structural Basis for Bending of Organic Crystals. *Chem. Commun.* **2005**, *1* (31), 3945.

(36) Mohamed, R. M.; Mishra, M. K.; AL-Harbi, L. M.; Al-Ghamdi, M. S.; Ramamurty, U. Anisotropy in the Mechanical Properties of Organic Crystals: Temperature Dependence. *RSC Adv.* **2015**, *5* (79), 64156–64162.

(37) Pulido, A.; Chen, L.; Kaczorowski, T.; Holden, D.; Little, M. A.; Chong, S. Y.; Slater, B. J.; McMahon, D. P.; Bonillo, B.; Stackhouse, C. J.; et al. Functional Materials Discovery Using Energy–structure–function Maps. *Nature* **2017**, *543* (7647), 657–664.

(38) Cruz-Cabeza, A. J.; Reutzel-Edens, S. M.; Bernstein, J. Facts and Fictions about Polymorphism. *Chem.*

Soc. Rev. **2015**, *44* (23), 8619–8635.

(39) Kitaigorodskii, A. I. *Molecular Crystals and Molecules*; Academic Press: New York City, 1973.

(40) Etter, M. C. Hydrogen Bonds as Design Elements in Organic Chemistry. *J. Phys. Chem.* **1991**, *95* (12), 4601–4610.

(41) Davey, R. J.; Dent, G.; Mughal, R. K.; Parveen, S. Concerning the Relationship between Structural and Growth Synthons in Crystal Nucleation: Solution and Crystal Chemistry of Carboxylic Acids as Revealed through IR Spectroscopy. *Cryst. Growth Des.* **2006**, *6* (8), 1788–1796.

(42) Nguyen Thi, Y.; Rademann, K.; Emmerling, F. Direct Evidence of Polyamorphism in Paracetamol. *CrystEngComm* **2015**, *17* (47), 9029–9036.

(43) Belenguer, A. M.; Lampronti, G. I.; Cruz-Cabeza, A. J.; Hunter, C. A.; Sanders, J. K. M. Solvation and Surface Effects on Polymorph Stabilities at the Nanoscale. *Chem. Sci.* **2016**, *72* (11), 171–179.

(44) Arlin, J.-B.; Price, L. S.; Price, S. L.; Florence, A. J. A Strategy for Producing Predicted Polymorphs: Catemeric Carbamazepine Form V. *Chem. Commun. (Camb).* **2011**, *47* (25), 7074–7076.

(45) Cruz-Cabeza, A. J.; Day, G. M.; Motherwell, W. D. S. Amide Pyramidalization in Carbamazepine : A Flexibility Problem in Crystal Structure Prediction ? *Cryst. Growth Des.* **2006**, *5* (10), 1–31.

(46) Cruz-Cabeza, A. J.; Day, G. M.; Motherwell, W. D. S.; Jones, W. Importance of Molecular Shape for the Overall Stability of Hydrogen Bond Motifs in the Crystal Structures of Various Carbamazepine-Type Drug Molecules. *Cryst. Growth Des.* **2007**, *7* (1), 100–107.

(47) Rodriguez-Hornedo, N.; Nehm, S. J.; Seefeldt, K. F.; Pagan-Torres, Y.; Falkiewicz, C. J. Reaction Crystallization of Pharmaceutical Molecular Complexes. *Mol. Pharm.* **2006**, No. 9, 8456–8457.

(48) Rehder, S.; Christensen, N. P. A.; Rantanen, J.; Rades, T.; Leopold, C. S. High-Shear Granulation as a Manufacturing Method for Cocrystal Granules. *Eur. J. Pharm. Biopharm.* **2013**, *85* (3 Pt B), 1019–1030.

(49) Jayasankar, A.; Reddy, L. S.; Bethune, S. J.; Rodríguez-Hornedo, N. The Role of Cocrystal and Solution Chemistry on the Formation and Stability of Cocrystals with Different Stoichiometry. *Cryst. Growth Des.* **2009**, *9* (2), 1–8.

(50) Yu, Z. Q.; Chow, P. S.; Tan, R. B. H. Operating Regions in Cooling Cocrystallization of Caffeine and Glutaric Acid in Acetonitrile. *Cryst. Growth Des.* **2010**, *10* (5), 2382–2387.

(51) Eddleston, M. D.; Patel, B.; Day, G. M.; Jones, W. Cocrystallization by Freeze-Drying: Preparation of Novel Multicomponent Crystal Forms. *Cryst. Growth Des.* **2013**, *13* (10), 4599–4606.

(52) Friščić, T.; Jones, W. Recent Advances in Understanding the Mechanism of Cocrystal Formation via Grinding. *Cryst. Growth Des.* **2009**, *9* (3), 1621–1637.

(53) Friščić, T. Supramolecular Concepts and New Techniques in Mechanochemistry: Cocrystals, Cages, Rotaxanes, Open Metal-Organic Frameworks. *Chem. Soc. Rev.* **2012**, *41* (9), 3493–3510.

(54) Gebauer, D.; Kellermeier, M.; Gale, J. D.; Bergström, L.; Cölfen, H. Pre-Nucleation Clusters as Solute Precursors in Crystallisation. *Chem. Soc. Rev.* **2014**, *43* (7), 2348–2371.

(55) Cacciuto, A.; Auer, S.; Frenkel, D. Onset of Heterogeneous Crystal Nucleation in Colloidal Suspensions. *Nature* **2004**, *428* (6981), 404–406.

(56) Cacciuto, a.; Auer, S.; Frenkel, D. Breakdown of Classical Nucleation Theory near Isostructural Phase Transitions. *Phys. Rev. Lett.* **2004**, *93* (16), 166105.

(57) De Yoreo, J. Crystal Nucleation: More than One Pathway. *Nat. Mater.* **2013**, *12* (4), 284–285.

(58) Myerson, A. S.; Trout, B. L. Chemistry. Nucleation from Solution. *Science* **2013**, *341* (6148), 855–856.

(59) Baumgartner, J.; Dey, A.; Bomans, P. H. H.; Le Coadou, C.; Fratzl, P.; Sommerdijk, N. a J. M.; Faivre, D. Nucleation and Growth of Magnetite from Solution. *Nat. Mater.* **2013**, *12* (4), 310–314.

(60) Vatvani, D.-R. M. Predicting the Morphology of Crystals of Organic Molecules: Assessment and Development of Chemical Informatics and Computational Methods, University of Cambridge, 2014.

(61) Sunagawa, I. *Crystals: Growth, Morphology and Perfection*; Cambridge University Press: Cambridge, 2005.

(62) Clydesdale, G.; Docherty, R. HABIT - a Program for Predicting the Morpholdgy of Molecular Crystals. *Comput. Phys. Commun.* **1991**, *64*, 311–328.

(63) Clydesdale, G.; Roberts, K. J.; Lewtas, K.; Docherty, R. Modelling the Morphology of Molecular Crystals in the Presence of Blocking Tailor-Made Additives. *J. Cryst. Growth* **1994**, *141* (3–4), 443–450.

(64) Hammond, R. B.; Pencheva, K.; Roberts, K. J. A Structural-Kinetic Approach to Model Face-Specific Solution/Crystal Surface Energy Associated with the Crystallization of Acetyl Salicylic Acid from Supersaturated Aqueous/Ethanol Solution. *Cryst. Growth Des.* **2006**, *6* (6), 1324–1334.

(65) Hammond, R. B.; Pencheva, K.; Ramachandran, V.; Roberts, K. J. Application of Grid-Based Molecular Methods for Modeling Solvent-Dependent Crystal Growth Morphology: Aspirin Crystallized from Aqueous Ethanolic Solution. *Cryst. Growth Des.* **2007**, *7* (9), 1571–1574.

(66) Singh, M. R.; Verma, P.; Tung, H. H.; Bordawekar, S.; Ramkrishna, D. Screening Crystal Morphologies from Crystal Structure. *Cryst. Growth Des.* **2013**, *13* (4), 1390–1396.

(67) Singh, M. R.; Ramkrishna, D. A Comprehensive Approach to Predicting Crystal Morphology Distributions with Population Balances. *Cryst. Growth Des.* **2013**, *13* (4), 1397–1411.

(68) Lovette, M. A.; Doherty, M. F. Needle-Shaped Crystals: Causality and Solvent Selection Guidance Based on Periodic Bond Chains. *Cryst. Growth Des.* **2013**, *13* (8), 3341–3352.

(69) Kuvadia, Z. B.; Doherty, M. F. Effect of Structurally Similar Additives on Crystal Habit of Organic Molecular Crystals at Low Supersaturation. *Cryst. Growth Des.* **2013**, *13* (4), 1412–1428.

(70) Dandekar, P.; Kuvadia, Z. B.; Doherty, M. F. Engineering Crystal Morphology. *Annu. Rev. Mater. Res.* **2013**, No. 43, 359–386.

(71) Bordawekar, S.; Kuvadia, Z.; Dandekar, P.; Mukherjee, S.; Doherty, M. Interesting Morphological Behavior of Organic Salt Choline Fenofibrate: Effect of Supersaturation and Polymeric Impurity. *Cryst. Growth Des.* **2014**, *14* (8), 3800–3812.

(72) Camacho, D. M.; Roberts, K. J.; Muller, F.; Thomas, D.; More, I.; Lewtas, K. Morphology & Growth of Methyl Stearate as a Function of Crystallization Environment. *Cryst. Growth Des.* **2017**, *17* (2), 563–575.

(73) Atkins, P.; De Paula, J. *Atkin's Physical Chemistry*, 9th ed.; Oxford University Press: Oxford, 2010.

(74) Solé, R. V. *Phase Transitions*; Princeton University Press: Princeton, 2011.

(75) Akimbekov, Z.; Katsenis, A. D.; Nagabhushana, G. P.; Ayoub, G.; Arhangelskis, M.; Morris, A. J.; Friščić, T.; Navrotsky, A. Experimental and Theoretical Evaluation of the Stability of True MOF Polymorphs Explains Their Mechanochemical Interconversions. *J. Am. Chem. Soc.* **2017**, *139* (23), 7952–7957.

(76) Ostwald, W. Studien Über Die Bildung Und Umwandlung Fester Körper. *Zeitschrift für Phys. Chemie* **1897**, *22U* (1), 289–330.

(77) Cullity, B. D.; Stock, S. R. *Elements of X-Ray Diffraction*, 3rd ed.; Pearson education; Prentice Hall: Michigan, 2001.

(78) Chen, X.; Hua, W.; Huang, Z.; Allen, H. C. Interfacial Water Structure Associated with Phospholipid Membranes Studied by Phase-Sensitive Vibrational Sum Frequency Generation Spectroscopy. *J. Am. Chem. Soc.* **2010**, *132* (32), 11336–11342.

(79) Brittain, H. G. *Physical Characterization of Pharmaceutical Solids*; Drugs and the Pharmaceutical Sciences; Taylor & Francis: New York, 1995.

(80) Eddleston, M. D.; Hejczyk, K. E.; Bithell, E. G.; Day, G. M.; Jones, W. Determination of the Crystal Structure of a New Polymorph of Theophylline. *Chemistry* **2013**, *19* (24), 7883–7888.

(81) Chatterjee, S.; Gadad, S. S.; Kundu, T. K. Atomic Force Microscopy - A Tool to Unveil the Mystery of Biological Systems. *Resonance* **2010**, No. July, 622–642.

(82) Eddleston, M. D.; Hejczyk, K. E.; Bithell, E. G.; Day, G. M.; Jones, W. Polymorph Identification and Crystal Structure Determination by a Combined Crystal Structure Prediction and Transmission Electron Microscopy Approach. *Chemistry* **2013**, *19* (24), 7874–7882.

(83) Chow, E. H. H.; Bučar, D.-K.; Jones, W. New Opportunities in Crystal Engineering--the Role of Atomic Force Microscopy in Studies of Molecular Crystals. *Chem. Commun. (Camb).* **2012**, *48* (74), 9210–9226.

(84) Thakuria, R.; Eddleston, M. D.; Chow, E. H. H.; Lloyd, G. O.; Aldous, B. J.; Krzyzaniak, J. F.; Bond, A. D.; Jones, W. Use of *in Situ* Atomic Force Microscopy to Follow Phase Changes at Crystal Surfaces in Real Time. *Angew. Chem. Int. Ed. Engl.* **2013**, *52* (40), 10541–10544.

(85) Varughese, S.; Kiran, M. S. R. N.; Ramamurty, U.; Desiraju, G. R. Nanoindentation in Crystal Engineering: Quantifying Mechanical Properties of Molecular Crystals. *Angew. Chem. Int. Ed. Engl.* **2013**, *52* (10), 2701–2712.

(86) Zhao, Y.; Cheng, Q.; Qian, M.; Cantrell, J. H. Phase Image Contrast Mechanism in Intermittent Contact Atomic Force Microscopy. *J. Appl. Phys.* **2010**, *108* (9), 094311.

(87) Aulton, M. E.; G., T. K. M. *Aulton's Pharmaceutics - The Design and Manufacture of Medicines*, 4th ed.; Churchill Livingstone.: London.

(88) Qiu, Y.; Chen, Y.; Zhang, G. G. Z.; Liu, L.; Porter, W. *Developing Solid Oral Dosage Forms - Pharmaceutical Theory and Practice*; Academic Press: New York, 2008.

(89) Griesser, U. J. The Importance of Solvates. In *Polymorphism in the Pharmaceutical Industry*; Hilfiker, R., Ed.; Wiley: Weinheim, 2006.

(90) USP. *United States Pharmacopeia*, 30th ed.; United States Pharmacopeia Convention: Rockville, 2007.

(91) Desiraju, G. R. Hydration in Organic Crystals: Prediction from Molecular Structure. *J. Chem. Soc. Chem. Commun.* **1991**, No. 6, 426–428.

(92) Jeffrey, G. A.; Maluszynska, H. The Stereochemistry of the Water Molecules in the Hydrates of Small Biological Molecules. *Acta Crystallogr. B.* **1990**, *46*, 546–549.

(93) Gillon, A. L.; Feeder, N.; Davey, R. J.; Storey, R. Hydration in Molecular Crystals - A Cambridge Structural Database Analysis. *Cryst. Growth Des.* **2003**, *3* (5), 663–673.

(94) Steiner, T.; Saenger, W. Role of C-H···O Hydrogen Bonds in the Coordination of Water Molecules. Analysis of Neutron Diffraction Data. *J. Am. Chem. Soc.* **1993**, *115* (11), 4540–4547.

(95) Infantes, L.; Fábián, L.; Motherwell, W. D. S. Organic Crystal Hydrates: What Are the Important Factors

for Formation. *CrystEngComm* **2007**, *9* (1), 65–71.

(96) Takieddin, K.; Khimyak, Y. Z.; Fábián, L. Prediction of Hydrate and Solvate Formation Using Statistical Models. *Cryst. Growth Des.* **2016**, *16* (1), 70–81.

(97) Galcera, J.; Friščić, T.; Hejczyk, K. E.; Fábián, L.; Clarke, S. M.; Day, G. M.; Molins, E.; Jones, W. Isostructural Organic Binary-Host Frameworks with Tuneable and Diversely Decorated Inclusion Cavities. *CrystEngComm* **2012**, *14* (23), 7898–7906.

(98) Galcera, J.; Friščić, T.; Molins, E.; Jones, W. Isostructurality in Three-Component Crystals Achieved by the Combination of Persistent Hydrogen Bonding Motifs and Solvent Inclusion. *CrystEngComm* **2013**, *15* (7), 1332–1338.

(99) Cinčić, D.; Friščić, T.; Jones, W. Isostructural Materials Achieved by Using Structurally Equivalent Donors and Acceptors in Halogen-Bonded Cocrystals. *Chem. - A Eur. J.* **2008**, *14* (2), 747–753.

(100) Cinčić, D.; Friščić, T.; Jones, W. Structural Equivalence of Br and i Halogen Bonds: A Route to Isostructural Materials with Controllable Properties. *Chem. Mater.* **2008**, *20* (21), 6623–6626.

(101) Ebenezer, S.; Muthiah, P. T.; Butcher, R. J. Design of a Series of Isostructural Co-Crystals with Aminopyrimidines: Isostructurality through Chloro/Methyl Exchange and Studies on Supramolecular Architectures. *Cryst. Growth Des.* **2011**, *11* (8), 3579–3592.

(102) IUCr. Online Dictionary of Crystallography reference.iucr.org/dictionary (accessed Jan 1, 2014).

(103) Galcera, J.; Molins, E. Effect of the Counterion on the Solubility of Isostructural Pharmaceutical Lamotrigine Salts. *Cryst. Growth Des.* **2009**, *9* (1), 327–334.

(104) Csoregh, I.; Hirano, S.; Toyota, S.; Bombicz, P.; Toda, F. Versatility in Stabilization of Crystalline Inclusion Complexes of a Bulky Diol Host by Various Closely Related Acidic and Ester Guests. *CrystEngComm* **2004**, *6* (14), 60–69.

(105) Nassimbeni, L. R.; Su, H.; Weber, E. Polymorphism, Isostructurality and Variability in the Inclusion Chemistry of a Diol Host Compound. *New J. Chem.* **2008**, *32* (10), 1702–1709.

(106) Jones, W.; Thomas, J. M.; Williams, J. O. Electron and Optical Microscopic Studies of a Stress-Induced Phase Transition in l,8-Dichloro-10-Methylanthracene. *Philos. Mag.* **1975**, *32* (1), 1–11.

(107) Mnyukh, Y. V. Laws of Phase Transformation in a Series of Normal Paraffins. *J. Phys. Chem. Solids* **1963**, *24* (5), 631–640.

(108) Mnyukh, Y. V; Kitaigorodskii, A. I.; Asadov, Y. G. A Study of the Polymorphic Transition in Monocrystalline Para-Dichlorobenzene. *Sov. Phys. JETP* **1965**, *21* (1), 12–18.

(109) Mnyukh, Y. *Fundamentals of Solid-State Phase Transitions, Ferromagnetism and Ferroelectricity*, 2nd ed.; DirectScientific Press, 2001.

(110) Amharar, Y.; Petit, S.; Sanselme, M.; Cartigny, Y.; Petit, M. N.; Coquerel, G. Crystal Structures, Dehydration Mechanism, and Chiral Discrimination in the Solid State of a Hydantoin Derivative. *Cryst. Growth Des.* **2011**, *11* (6), 2453–2462.

(111) Braun, D. E.; Gelbrich, T.; Kahlenberg, V.; Tessadri, R.; Wieser, J.; Griesser, U. J. Stability of Solvates and Packing Systematics of Nine Crystal Forms of the Antipsychotic Drug Aripiprazole. *Cryst. Growth Des.* **2009**, *9* (2), 1054–1065.

(112) Minkov, V. S.; Beloborodova, A. A.; Drebushchak, V. A.; Boldyreva, E. V. Furosemide Solvates: Can They Serve as Precursors to Different Polymorphs of Furosemide? *Cryst. Growth Des.* **2014**, *14* (2), 513–522.

(113) Khoo, J. Y.; Shah, U. V.; Schaepertoens, M.; Williams, D. R.; Heng, J. Y. Y. Process-Induced Phase Transformation of Carbamazepine Dihydrate to Its Polymorphic Anhydrates. *Powder Technol.* **2013**, *236*, 114–121.

(114) Petit, S.; Coquerel, G. Mechanism of Several Solid - Solid Transformations between Dihydrated and Anhydrous Copper (II) 8-Hydroxyquinolinates . Proposition for a Unified Model for the Dehydration of Molecular Crystals. *Chem. Mater.* **1996**, *8* (9), 2247–2258.

(115) Kaupp, G. Prediction of Reactivity Is Solid-State Chemistry. In *Making Crystals by Design*; Braga, D., Grepioni, F., Eds.; Wiley: Weinheim, 2007.

(116) Galvey, A. K. The Reactivity of Solids in Thermal Decomposition (Crystolisis) Reactions. In *Reactivity of Solids: Past, Present and Future*; Boldyrev, V., Ed.; Blackwell Science Ltd / Cambridge University Press: Cambridge, 1996.

(117) Boldyreva, E.; Boldyrev, V. *Reactivity of Molecular Solids*, Volume 3.; Reactivity of Molecular Solids; Wiley: Weinheim, 1999.

(118) Wu, L.; Zhang, J.; Watanabe, W. Physical and Chemical Stability of Drug Nanoparticles. *Adv. Drug Deliv. Rev.* **2011**, *63* (6), 456–469.

(119) Perrier, P. R.; Byrn, S. R. Influence of Crystal Packing on the Solid-State Desolvation of Purine and Pyrimidine Hydrates: Loss of Water of Crystallization from Thymine Monohydrate, Cytosine Monohydrate, 5-Nitrouracil Monohydrate, and 2′-Deoxyadenosine Monohydrate. *J. Org. Chem.* **1982**, *47* (24), 4671–4676.

(120) Jones, W. Electron Microscopic Studies of Organic Molecular Crystals, University College of Wales, Aberystwyth, 1974.

(121) Schindler, W. New N-Heterocyclic Compounds. United States Patent Office; Patent 2,948,718, 1960.

(122) BMJ. To-Day's Drugs: Carbamazepine. *Br. Med. J.* **1964**, *2* (5404), 295.

(123) Rang, H. P.; Dale, M. M.; Ritter, J. M.; Flower, R. J. *Rang & Dale's Pharmacology*, 7th ed.; Churchill Livingstone.: London, 2011.

(124) *Remington - The Science and Practice of Pharmacy*, 21st ed.; Beringer, P., DerMarderosian, A., Gelone, S., Gennaro, A. R., Gupta, P. K., Hoover, J. E., Popovich, N. G., Reilly, W. J. J., Hendrikson, R., Eds.; Lippincott Williams & Wilkins: Philadelphia, 2005.

(125) Cartwright, A. C.; Snodin, D. J. Drug Substance - Characterization. In *International Pharmaceutical Product Registration*; Carlwright, A. C., Matthews, B. R., Eds.; CRC Press: New York, 2010.

(126) PBI Carbamazepine Recall of 50 Mil. Tabs. *The Pink Sheet, Pharma Intelligence, Informa PLC*. 1988.

(127) Meyer, M. C.; Straughn, A. B.; Jarvi, E. J.; Wood, G. C.; Pelsor, F. R.; Shah, V. P. The Bioinequivalence of Carbamazepine Tablets with a History of Clinical Failures. *Pharmaceutical Research: An Official Journal of the American Association of Pharmaceutical Scientists*. 1992, pp 1612–1616.

(128) Wang, J. T.; Shiu, G. K.; Ting, O.-C.; Viswanathan, C. T.; Skelly, J. P. Effects of Humidity and Temperature on In Vitro Dissolution of Carbamazepine Tablets. *J. Pharm. Sci.* **1993**, *82* (10), 1002–1005.

(129) Pohlmann, H.; Gulde, C. H.; Jahn, R.; Pfeifer, S. Polymorphie, Teilchengrobe Und Blutspiegelwerte von Carbamazepin. *Pharmazie* **1975**, *30* (11), 709–711.

(130) Laine, E.; Tuominen, V. Formation of Dihydrate from Carbamazepinc Anhydrate in Aqueous Conditions. **1984**, *20*, 307–314.

(131) Kala, H.; Haack, U.; Wenzel, U.; Zessin, G.; Pollandt, P. Phase Transformation of Carbamazepine by the Milling Process. *Pharmazie* **1986**, *41* (11), 777–781.

(132) Kaneniwa, N.; Yamaguchi, T.; Watari, N.; Otsuka, M. Hygroscopicity of Carbamazepine Crystalline Powders. *Yakugaku Zasshi* **1984**, *104* (2), 184–190.

(133) Kala, H.; Haack, U.; Wenzel, U.; Zessin, G.; Pollandt, P. The Crystallography Behavior of Carbamazepine under Compression Pressure. *Pharmazie* **1987**, *42* (8), 524–527.

(134) Krahn, F. U.; Mielck, J. B. Relations between Several Polymorphic Forms and the Dihydrate of Carbamazepine. *Pharm. Acta Helv.* **1987**, *62* (9), 247–254.

(135) Lowes, M. M. J.; Caira, M. R.; Lotter, A. P.; Van der Watt, J. Physicochemical Properties and X-Ray Structural Studies of the Trigonal Polymorph of Carbamazepine. *J. Pharm. Sci.* **1987**, *76* (9), 744–752.

(136) Krahn, F. U.; Mielck, J. B. Effect of Type and Extent of Crystalline Order on Chemical and Physical Stability of Carbamazepine. *Int. J. Pharm.* **1989**, *53* (1), 25–34.

(137) Behme, R. J.; Brooke, D. Heat of Fusion Measurement of a Low Melting Polymorph of Carbamazepine That Undergoes Multiple-Phase Changes during Differential Scanning Calorimetry Analysis. *J. Pharm. Sci.* **1991**, *80* (10), 986–990.

(138) Young, W. W. L.; Suryanarayanan, R. Kinetics of Transition of Anhydrous Carbamazepine to Carbamazepine Dihydrate in Aqueous Suspensions. *J. Pharm. Sci.* **1991**, *80* (5), 496–500.

(139) McMahon, L. E.; Timmins, P.; Williams, a C.; York, P. Characterization of Dihydrates Prepared from Carbamazepine Polymorphs. *J. Pharm. Sci.* **1996**, *85* (10), 1064–1069.

(140) Ceolin, R.; Toscani, S.; Gardette, M. F.; Agafonov, V. N.; Dzyabchenko, a V; Bachet, B. X-Ray Characterization of the Triclinic Polymorph of Carbamazepine. *J. Pharm. Sci.* **1997**, *86* (9), 1062–1065.

(141) Han, J.; Suryanarayanan, R. Applications of Pressure Differential Scanning Calorimetry in the Study of Pharmaceutical Hydrates I, Carbamazepine. *Int. J. Pharmac* **1997**, *157* (2), 209–218.

(142) Han, J.; Suryanarayanan, R. Influence of Environmental Conditions on the Kinetics and Mechanism of Dehydration of Carbamazepine Dihydrate. *Pharm. Dev. Technol.* **1998**, *3* (4), 587–596.

(143) Otsuka, M.; Ofusa, T.; Matsuda, Y. Effect of Environmental Humidity on the Transformation Pathway of Carbamazepine Polymorphic Modifications during Grinding. *Colloids Surfaces B Biointerfaces* **1999**, *13* (5), 263–273.

(144) Li, Y.; Han, J.; Zhang, G. G. Z.; Grant, D. J. W.; Suryanarayanan, R. *In Situ* Dehydration of Carbamazepine Dihydrate: A Novel Technique to Prepare Amorphous Anhydrous Carbamazepine. *Pharm. Dev. Technol.* **2000**, *5* (2), 257–266.

(145) Rustichelli, C.; Gamberini, G.; Ferioli, V.; Gamberini, M. C.; Ficarra, R.; Tommasini, S. Solid-State Study of Polymorphic Drugs: Carbamazepine. *J. Pharm. Biomed. Anal.* **2000**, *23* (1), 41–54.

(146) Edwards, a D.; Shekunov, B. Y.; Forbes, R. T.; Grossmann, J. G.; York, P. Time-Resolved X-Ray Scattering Using Synchrotron Radiation Applied to the Study of a Polymorphic Transition in Carbamazepine. *J. Pharm. Sci.* **2001**, *90* (8), 1106–1114.

(147) Lang, M.; Grzesiak, A. L.; Matzger, A. J. The Use of Polymer Heteronuclei for Crystalline Polymorph Selection. *J. Am. Chem. Soc.* **2002**, *124* (50), 14834–14835.

(148) Lang, M.; Kampf, J. W.; Matzger, A. J. Form IV of Carbamazepine. *J. Pharm. Sci.* **2002**, *91* (4), 1186–1190.

(149) Grzesiak, A. L.; Lang, M.; Kim, K.; Matzger, A. J. Comparison of the Four Anhydrous Polymorphs of

Carbamazepine and the Crystal Structure of Form I. *J. Pharm. Sci.* **2003**, *92* (11), 2260–2271.

(150) Rodríguez-Hornedo, N.; Murphy, D. Surfactant-Facilitated Crystallization of Dihydrate Carbamazepine during Dissolution of Anhydrous Polymorph. *J. Pharm. Sci.* **2004**, *93* (2), 449–460.

(151) Surana, R.; Pyne, A.; Suryanarayanan, R. Solid-Vapor Interactions: Influence of Environmental Conditions on the Dehydration of Carbamazepine Dihydrate. *AAPS PharmSciTech* **2003**, *4* (4), E68.

(152) Brittain, H. G. Fluorescence Studies of the Transformation of Carbamazepine Anhydrate Form III to Its Dihydrate Phase. *J. Pharm. Sci.* **2004**, *93* (2), 375–383.

(153) O'Brien, L. E.; Timmins, P.; Williams, A. C.; York, P. Use of *in Situ* FT-Raman Spectroscopy to Study the Kinetics of the Transformation of Carbamazepine Polymorphs. *J. Pharm. Biomed. Anal.* **2004**, *36* (2), 335–340.

(154) Florence, A. J.; Johnston, A.; Price, S. L.; Nowell, H.; Kennedy, A. R.; Shankland, N. An Automated Parallel Crystallisation Search for Predicted Crystal Structures and Packing Motifs of Carbamazepine. **2006**, *95* (9), 1918–1930.

(155) Tian, F.; Zeitler, J. A.; Strachan, C. J.; Saville, D. J.; Gordon, K. C.; Rades, T. Characterizing the Conversion Kinetics of Carbamazepine Polymorphs to the Dihydrate in Aqueous Suspension Using Raman Spectroscopy. *J. Pharm. Biomed. Anal.* **2006**, *40* (2), 271–280.

(156) Tian, F.; Sandler, N.; Gordon, K. C.; McGoverin, C. M.; Reay, A.; Strachan, C. J.; Saville, D. J.; Rades, T. Visualizing the Conversion of Carbamazepine in Aqueous Suspension with and without the Presence of Excipients: A Single Crystal Study Using SEM and Raman Microscopy. *Eur. J. Pharm. Biopharm.* **2006**, *64* (3), 326–335.

(157) Cruz-Cabeza, A. J.; Day, G. M.; Motherwell, W. D. S.; Jones, W. Solvent Inclusion in Form II Carbamazepine. *Chem. Commun. (Camb).* **2007**, *12* (16), 1600–1602.

(158) Fabbiani, F. P. A.; Byrne, L. T.; McKinnon, J. J.; Spackman, M. A. Solvent Inclusion in the Structural Voids of Form II Carbamazepine: Single-Crystal X-Ray Diffraction, NMR Spectroscopy and Hirshfeld Surface Analysis. *CrystEngComm* **2007**, *9* (9), 728–731.

(159) Getsoian, A.; Lodaya, R. M.; Blackburn, A. C. One-Solvent Polymorph Screen of Carbamazepine. *Int. J. Pharm.* **2008**, *348* (1–2), 3–9.

(160) Liu, W.; Wei, H.; Black, S. An Investigation of the Transformation of Carbamazepine from Anhydrate to Hydrate Using *in Situ* FBRM and PVM An Investigation of the Transformation of Carbamazepine from Anhydrate to Hydrate Using *in Situ* FBRM and PVM. *Org. Process Res. Dev.* **2009**, *13* (3), 494–500.

(161) Qu, H.; Munk, T.; Cornett, C.; Wu, J. X.; Bøtker, J. P.; Christensen, L. P.; Rantanen, J.; Tian, F. Influence of Temperature on Solvent-Mediated Anhydrate-to-Hydrate Transformation Kinetics. *Pharm. Res.* **2011**, *28* (2), 364–373.

(162) Kachrimanis, K.; Griesser, U. J. Dehydration Kinetics and Crystal Water Dynamics of Carbamazepine Dihydrate. *Pharm. Res.* **2012**, *29* (4), 1143–1157.

(163) Khoo, J. Y.; Shah, U. V.; Schaepertoens, M.; Williams, D. R.; Heng, J. Y. Y. Process-Induced Phase Transformation of Carbamazepine Dihydrate to Its Polymorphic Anhydrates. *Powder Technol.* **2013**, *236*, 114–121.

(164) Liu, W.; Wei, H.; Zhao, J.; Black, S.; Sun, C. Investigation into the Cooling Crystallization and Transformations of Carbamazepine Using *in Situ* FBRM and PVM. *Org. Process Res. Dev.* **2013**, *17* (11), 1406–1412.

(165) O'Mahony, M. A.; Seaton, C. C.; Croker, D. M.; Veesler, S.; Rasmuson, Å. C.; Hodnett, B. K. Investigation into the Mechanism of Solution-Mediated Transformation from FI to FIII Carbamazepine:

The Role of Dissolution and the Interaction between Polymorph Surfaces. *Cryst. Growth Des.* **2013**, *13* (5), 1861–1871.

(166) O'Mahony, M.; Seaton, C. C.; Croker, D. M.; Veesler, S.; Rasmuson, Å. C.; Hodnett, B. K. Investigating the Dissolution of the Metastable Triclinic Polymorph of Carbamazepine Using *in Situ* Microscopy. *CrystEngComm* **2014**, *16* (23), 4133–4141.

(167) Parambil, J. V.; Poornachary, S. K.; Tan, R. B. H.; Heng, J. Y. Y. Template-Induced Polymorphic Selectivity: The Effects of Surface Chemistry and Solute Concentration on Carbamazepine Crystallisation. *CrystEngComm* **2014**, *16* (23), 4927–4930.

(168) Parambil, J. V.; Poornachary, S. K.; Hinder, S. J.; Tan, R. B. H.; Heng, J. Y. Y. Establishing Template-Induced Polymorphic Domains for API Crystallisation: The Case of Carbamazepine. *CrystEngComm* **2015**, *17* (33), 6384–6392.

(169) Walshe, N.; Crushell, M.; Karpinska, J.; Erxleben, A.; McArdle, P. Anisotropic Crystal Growth in Flat and Nonflat Systems: The Important Influence of van Der Waals Contact Molecular Stacking on Crystal Growth and Dissolution. *Cryst. Growth Des.* **2015**, *15* (7), 3235–3248.

(170) Guinet, Y.; Paccou, L.; Danède, F.; Willart, J. F.; Derollez, P.; Hédoux, A. Comparison of Amorphous States Prepared by Melt-Quenching and Cryomilling Polymorphs of Carbamazepine. *Int. J. Pharm.* **2016**, *509* (1–2), 305–313.

(171) Jensen, L. G.; Skautrup, F. B.; Müllertz, A.; Abrahamsson, B.; Rades, T.; Priemel, P. A. Amorphous Is Not Always Better—A Dissolution Study on Solid State Forms of Carbamazepine. *Int. J. Pharm.* **2017**, *522* (1–2), 74–79.

(172) Parambil, J. V.; Poornachary, S. K.; Tan, R. B. H.; Heng, J. Y. Y. Influence of Solvent Polarity and Supersaturation on Template-Induced Nucleation of Carbamazepine Crystal Polymorphs. *J. Cryst. Growth* **2017**, *469* (September 2016), 84–90.

(173) Griesser, U. J.; Szelagiewicz, M.; Pitt, C.; Cianferani, S. Vapour Pressure and Heat of Sublimation of Crstal Polymorphs. *J. Therm. Anal. Calorim.* **1999**, *57*, 45–60.

(174) Umeda, T.; Ohnishi, N.; Yokoyama, T.; Kuroda, K.; Kuroda, T.; Tatsumi, E.; Matsuda, Y. Kinetics of the Thermal Transition of Carbamazepine Polymorphic Forms in the Solid State. *Yakugaku Zasshi* **1984**, *104*, 786–792.

(175) Khoo, J. Y.; Williams, D. R.; Heng, J. Y. Y. Dehydration Kinetics of Pharmaceutical Hydrate: Effects of Environmental Conditions and Crystal Forms. *Dry. Technol.* **2010**, *28* (10), 1164–1169.

(176) Cruz-Cabeza, A. J.; Day, G. M.; Jones, W. Predicting Inclusion Behaviour and Framework Structures in Organic Crystals. *Chemistry* **2009**, *15* (47), 13033–13040.

(177) Cruz-Cabeza, A. J.; Day, G. M.; Motherwell, W. D. S.; Jones, W. Prediction and Observation of Isostructurality Induced by Solvent Incorporation in Multicomponent Crystals. *J. Am. Chem. Soc.* **2006**, No. 128, 14466–14467.

(178) Kachrimanis, K.; Griesser, U. J. Dehydration Kinetics and Crystal Water Dynamics of Carbamazepine Dihydrate. *Pharm. Res.* **2012**, *29* (4), 1143–1157.

(179) Rodríguez-Hornedo, N.; Murphy, D. Surfactant-Facilitated Crystallization of Dihydrate Carbamazepine during Dissolution of Anhydrous Polymorph. *J. Pharm. Sci.* **2004**, *93* (2), 449–460.

(180) Harris, R. K.; Ghi, P. Y.; Puschmann, H.; Apperley, D. C.; Griesser, U. J.; Hammond, R. B.; Ma, C.; Roberts, K. J.; Pearce, G. J.; Yates, J. R.; et al. Structural Studies of the Polymorphs of Carbamazepine , Its Dihydrate , and Two Solvates Abstract : *Org. Process Res. Dev.* **2005**, *9* (6), 902–910.

(181) Gelbrich, T.; Hursthouse, M. B. Systematic Investigation of the Relationships between 25 Crystal

Structures Containing the Carbamazepine Molecule or a Close Analogue: A Case Study of the XPac Method. *CrystEngComm* **2006**, *8* (6), 448–460.

(182) Sovago, I.; Gutmann, M. J.; Senn, H. M.; Thomas, L. H.; Wilson, C. C.; Farrugia, L. J. Electron Density, Disorder and Polymorphism: High-Resolution Diffraction Studies of the Highly Polymorphic Neuralgic Drug Carbamazepine. *Acta Crystallogr. Sect. B Struct. Sci. Cryst. Eng. Mater.* **2016**, *72* (1), 39–50.

(183) Childs, S. L.; Wood, P. A.; Rodriguez-Hornedo, N.; Reddy, L. S.; Hardcastle, K. I. Analysis of 50 Crystal Structures Containing Carbamazepine Using the Materials Module of Mercury CSD. *Cryst. Growth Des.* **2009**, *9* (4), 1869–1888.

(184) Monography: Carbamazepine. *Brazilian Pharmacopoeia*; Brazilian Health Surveillence Agency, 2015; p 892.

(185) Macrae, C. F.; Bruno, I. J.; Chisholm, J. a.; Edgington, P. R.; McCabe, P.; Pidcock, E.; Rodriguez-Monge, L.; Taylor, R.; van de Streek, J.; Wood, P. a. Mercury CSD 2.0 – New Features for the Visualization and Investigation of Crystal Structures. *J. Appl. Crystallogr.* **2008**, *41* (2), 466–470.

(186) Wood, P. A.; Olsson, T. S. G.; Cole, J. C.; Cottrell, S. J.; Feeder, N.; Galek, P. T. A.; Groom, C. R.; Pidcock, E. Evaluation of Molecular Crystal Structures Using Full Interaction Maps. *CrystEngComm* **2013**, *15* (1), 65–72.

(187) Gavezzotti, A.; Filippini, G. Geometry of the Intermolecular X-H.Cntdot..Cntdot..Cntdot.Y (X, Y = N, O) Hydrogen Bond and the Calibration of Empirical Hydrogen-Bond Potentials. *J. Phys. Chem.* **1994**, *98* (18), 4831–4837.

(188) Clark, S. J.; Segall, M. D.; Pickard, C. J.; Hasnip, P. J.; Probert, M. J.; Refson, K.; Payne, M. C. First Principles Methods Using CASTEP. *Z. Kryst.* **2005**, *220*, 567–570.

(189) Sheldrick, G. M. SHELXT - Integrated Space-Group and Crystal-Structure Determination. *Acta Crystallogr. Sect. A Found. Crystallogr.* **2015**, *71* (1), 3–8.

(190) Ali, M.; Bonakdar, T.; Ghadiri, M.; Tinke, A. Particle Breakage in a Scirocco Disperser. *Powder Technol.* **2015**, *285*, 138–145.

(191) Bonakdar, T.; Ali, M.; Dogbe, S.; Ghadiri, M.; Tinke, A. A Method for Grindability Testing Using the Scirocco Disperser. *Int. J. Pharm.* **2016**, *501* (1–2), 65–74.

(192) Reboul, J. P.; Cristau, B.; Soyfer, J. C.; Astier, J. P. 5H-Dibenz[b,f]Azepine-5-Carboxamide (Carbamazepine). *Acta Crystallogr. Sect. B Struct. Crystallogr. Cryst. Chem.* **1981**, *B37* (10), 1844–1848.

(193) Cruz-Cabeza, A. J.; Day, G. M.; Jones, W. Structure Prediction, Disorder and Dynamics in a DMSO Solvate of Carbamazepine. *Phys. Chem. Chem. Phys.* **2011**, *13* (28), 12808–12816.

(194) Johnston, A.; Florence, A. J.; Kennedy, A. R. Carbamazepine N,N -Dimethylformamide Solvate. *Acta Crystallogr. Sect. E Struct. Reports Online* **2005**, *61* (5), o1509–o1511.

(195) Johnston, A.; Johnston, B. F.; Kennedy, A. R.; Florence, A. J. Targeted Crystallisation of Novel Carbamazepine Solvates Based on a Retrospective Random Forest Classification. *CrystEngComm* **2008**, *10* (1), 23–25.

(196) Childs, S. L.; Wood, P. A.; Rodriguez-Hornedo, N.; Reddy, L. S.; Hardcastle, K. I. Analysis of 50 Crystal Structures Containing Carbamazepine Using the Materials Module of Mercury. *Cryst. Growth Des.* **2009**, *9* (4), 1869–1888.

(197) Lohani, S.; Zhang, Y.; Chyall, L. J.; Mougin-Andres, P.; Muller, F. X.; Grant, D. J. W. Carbamazepine–2,2,2-Trifluoroethanol (1/1). *Acta Crystallogr. Sect. E Struct. Reports Online* **2005**, *61* (5), o1310–o1312.

(198) Fernandes, P.; Bardin, J.; Johnston, A.; Florence, A. J.; Leech, C. K.; David, W. I. F.; Shankland, K. Carbamazepine Trifluoroacetic Acid Solvate. *Acta Crystallogr. Sect. E Struct. Reports Online* **2007**, *63* (11), o4269–o4269.

(199) Eberlin, A. R.; Eddleston, M. D.; Frampton, C. S. Methanesulfonic Acid Salt Forms of Carbamazepine and 10,11- Dihydrocarbamazepine. *Acta Crystallogr. Sect. C Cryst. Struct. Commun.* **2013**, *69* (11), 1260–1266.

(200) Kuminek, G.; Cao, F.; Bahia de Oliveira da Rocha, A.; Gonçalves Cardoso, S.; Rodríguez-Hornedo, N. Cocrystals to Facilitate Delivery of Poorly Soluble Compounds Beyond-Rule-of-5. *Adv. Drug Deliv. Rev.* **2016**, *101*, 143–166.

(201) Li, Y.; Chow, P. S.; Tan, R. B. H.; Black, S. N. Effect of Water Activity on the Transformation between Hydrate and Anhydrate of Carbamazepine. *Org. Process Res. Dev.* **2008**, *12* (2), 264–270.

(202) Qu, H.; Louhi-Kultanen, M.; Kallas, J. Solubility and Stability of Anhydrate/Hydrate in Solvent Mixtures. *Int. J. Pharm.* **2006**, *321* (1–2), 101–107.

(203) Tung, H. H. Industrial Perspectives of Pharmaceutical Crystallization. *Org. Process Res. Dev.* **2013**, *17* (3), 445–454.

(204) Diwan, M.; Tung, H. H.; Kim, E.; Bordawekar, S. In-Situ Seed Generation with Wet Milling for Pharmaceutical Crystallization. In *AIChE Annual Meeting*; 2010.

(205) Sinha, K. *Carbamazepine Process Development*; Internal Report (AbbVie Inc.), 2016.

(206) Sinha, K. *Carbamazepine Update*; Internal Report (AbbVie Inc.), 2017.

(207) Sousa, E. T.; Da Silva, M. M.; De Andrade, S. J.; Cardoso, M. P.; Silva, L. A.; De Andrade, J. B. Evaluation of Thermal Stability of Quinones by Thermal Analysis Techniques. *Thermochim. Acta* **2012**, *529*, 1–5.

(208) Wobbe, D. E.; Noyes, W. A. Photochemical Studies. IV. The Thermal Decomposition of Anhydrous Oxalic Acid and Its Relation to the Photochemical Decomposition. *J. Am. Chem. Soc.* **1926**, *48* (11), 2856–2868.

(209) Higgins, J.; Zhou, X.; Liu, R.; Huang, T. T.-S. Theoretical Study of Thermal Decomposition Mechanism of Oxalic Acid. *J. Phys. Chem. A* **1997**, *101* (14), 2702–2708.

(210) Debenham, D. F.; Owen, A. J. The Thermal Decomposition of Some Organic Solids. Part II. m-Nitroperoxybenzoic Acid and Related Peroxyacids. *J. Chem. Soc.* **1966**, No. 0, 675–678.

(211) Blake, B. P. G.; Pritchard, H. The Thermal Decomposition of Trif Luoroacetic Acid. *J. Chem. Soc. B* **1967**, *1* (282), 282–286.

(212) Franciscot, J. S. Decomposition Pathways for Trifluoroacetic Acid, CF,C(O)OH. *J. Chem. Soc. Faraday Trans.* **1992**, *88* (24), 3521–3525.

(213) Blake, P. G.; Shraydeh, B. F. The Thermal Decomposition of Fluorinated Esters. *Int. J. Chem. Kinet.* **1981**, *13* (5), 463–471.

(214) Sundberg, R. J.; Sloan, K. B. Acid-Promoted Aromatic Substitution Processes in Photochemical and Thermal Decompositions of Aryl Azides. *J. Org. Chem.* **1973**, *38* (11), 2052–2057.

(215) Canning, P. S. J.; McCrudden, K.; Maskill, H.; Sexton, B. Rates and Mechanisms of the Thermal Solvolytic Decomposition of Arenediazonium Ions. *J. Chem. Soc. Perkin Trans. 2* **1999**, No. 12, 2735–2740.

(216) Perumalla, S. R.; Sun, C. C. Confused HCl: Hydrogen Chloride or Hydrochloric Acid? *Chem. - A Eur. J.*

2012, *18* (21), 6462–6464.

(217) Buist, A. R.; Kennedy, A. R.; Shankland, K.; Shankland, N.; Spillman, M. J. Salt Forms of Amides: Protonation and Polymorphism of Carbamazepine and Cytenamide. *Cryst. Growth Des.* **2013**, *13* (11), 5121–5127.

(218) Riddick, J. A.; Bunger, W. B.; Sakano, T. *Organic Solvents: Physical Properties and Methods of Purification*, 4th ed.; John Wiley & Sons, Inc.: New York, 1986.

(219) Dallinga, L.; Schiller, M.; Gmehling, J. Measurement of Activity Coefficients at Infinite Dilution Using Differential Ebulliometry and Non-Steady-State Gas-Liquid Chromatography. *J. Chem. Eng. Data* **1993**, *38* (1), 147–155.

(220) Park, J. H.; Hussam, A.; Couasnon, P.; Fritz, D.; Carr, P. W.; Tetrahidrofurano, O. Experimental Reexamination of Selected Partition Coefficients from Rohrschneider ' s Data Set. *Society* **1987**, *59* (May), 1970–1976.

(221) Schmidt, T. W. Determination of Infinite Dilution Activity Coefficients (Gamma Infinite) Using Molecular Beams. United States Patent Office (Patent US4214158A), 1980.

(222) The Hansen Solubility Parameters and HSPiP software website www.hansen-solubility.com (accessed Jan 1, 2017).

(223) Grymonpre, W.; Thommes, M. Development of Low-Consuming Miniaturized Screening Methods for Solid Dispersions, Heinrich-Heine University, Dusseldorf, Germany.

(224) McKenzie, J.; Feeder, N.; Hunter, C. A. H-Bond Competition Experiments in Solution and the Solid State. *CrystEngComm* **2016**, *18* (3), 394–397.

(225) Calero, C. S.; Farwer, J.; Gardiner, E. J.; Hunter, C. A.; Mackey, M.; Scuderi, S.; Thompson, S.; Vinter, J. G. Footprinting Molecular Electrostatic Potential Surfaces for Calculation of Solvation Energies. *Phys. Chem. Chem. Phys.* **2013**, *15* (41), 18262–18273.

(226) Petit, S.; Coquerel, G. Contribution to the Understanding of Desolvation Mechanisms: Impact of Crystal Size, Structural Purity and Process. *JEEP – 35th Conf. Phase Equilibria* **2009**, *16*, 1–4.

(227) Petit, S.; Mallet, F.; Petit, M. N.; Coquerel, G. Role of Structural and Macrocrystalline Factors in the Desolvation Behaviour of Cortisone Acetate Solvates. *J. Therm. Anal. Calorim.* **2007**, *90* (1), 39–47.

(228) Fossen, H. *Structural Geology*, 2nd ed.; Cambridge University Press: Cambridge, 2016.

(229) Tse, Y. Y.; McMitchell, S. R. C.; Jackson, T. J.; Jones, I. P.; Genc, A. Line Defects, Planar Defects and Voids in SrTiO3films Grown on MgO by Pulsed Laser and Pulsed Laser Interval Deposition. *Thin Solid Films* **2012**, *520* (9), 3440–3447.

(230) Panda, M. K.; Ghosh, S.; Yasuda, N.; Moriwaki, T.; Mukherjee, G. D.; Reddy, C. M.; Naumov, P. Spatially Resolved Analysis of Short-Range Structure Perturbations in a Plastically Bent Molecular Crystal. *Nat. Chem.* **2015**, *7* (1), 65–72.

APPENDIX 1 – The literature of CBZ polymorphs and CBZ:2H_2O

Table 19 - List of studies developed for CBZ polymorphs and CBZ dihydrate and their relationships (literature data).

Reference	**Paper title**	**Conclusions**
Pohlmann *et al.* (1975)	Polymorphism, particle size and blood level values of carbamazepine	CBZ modifications were prepared (C1, C2 and C3). C1 was prepared from solution crystallization in methanol and acetone; C2 was prepared from solution crystallization in ethyl acetate, benzene and toluene; C3 was prepared from heating C1 and C2, from sublimation (175 ^oC) and from cooling molten CBZ. C1 and C2 convert to C3 from heating at 120 ^oC and 170 ^oC, respectively. C3 melts at 189.5 ^oC.
Kaneniwa *et al.* (1984)	Hygroscopicity of carbamazepine crystalline powders	CBZ Forms I and III transform to CBZ dihydrate upon storage (ambient humidity and 37 ^oC, 2 weeks).
Laine & Tuominen (1984)	Formation of dihydrate from carbamazepinc anhydrate in aqueous conditions	CBZ dihydrate is prepared from CBZ Form III in water.
Umeda *et al.* (1984)	Kinetics of the thermal transition of carbamazepine polymorphic forms in the solid state	CBZ Form III melts at 176 ^oC and concomitantly recrystallizes into CBZ Form I (which melts at 191 ^oC). The transition from CBZ Form III to Form I follows the mechanism of random nucleation and two-dimensional crystal growth (Ea=54.7 kcal mol^{-1}). CBZ Form II converts into CBZ Form I at 131 ^oC (exothermic). The transition of Form II to Form I follows the two-dimensional diffusion (Ea = 31.6 kcal mol^{-1}).
Kala *et al.* (1986)	Phase transformation of carbamazepine by the milling process	CBZ I and II transform to CBZ Form III upon grinding.
Kala *et al.* (1987)	The crystallography behavior of carbamazepine under compression pressure	CBZ I and III are stable under compression. CBZ II transforms to CBZ Form III under compression.
Krahn & Mielck (1987)	Relations between several polymorphic forms and the dihydrate of carbamazepine	The condition of dehydration leads to different CBZ polymorphs. CBZ III is prepared from solvents with high dielectric constants. CBZ Form IV is prepared from CBZ dihydrate in P_2O_5 (under vacuum and 25 ^oC). CBZ Forms I and IV are enantiotropically related.
Lowes *et al.* (1987)	Physicochemical properties and X-ray structural studies of the trigonal polymorph of carbamazepine	CBZ Form I is prepared from solvents with low dielectric constants. CBZ Form II is prepared from tetrahydrofuran solutions. CBZ Form III is prepared from solvents with high dielectric constants.

Reference	Paper title	Conclusions
Krahn *et al.* (1989)	Effect of type and extent of crystalline order on chemical and physical stability of carbamazepine	CBZ Form I (high and low crystalline order) mixed with colloidal silica converted to CBZ Form III under stress conditions (56-72 ºC and 41-71% RH). CBZ Form I with low crystalline order was obtained from dehydration of CBZ dihydrate.
Behme & Brooke (1991)	Heat of fusion measurement of a low melting polymorph of carbamazepine that undergoes multiple-phase changes during differential scanning calorimetry analysis	CBZ Forms I and III are enantiotropically related (T t= 71ºC). Form I melts at 189 ºC. Form III melts at 176 ºC.
Young & Suryanarayanan (1991)	Kinetics of transition of anhydrous carbamazepine to carbamazepine dihydrate in aqueous suspensions.	CBZ dihydrate is prepared from CBZ Form III in water.
McMahon *et al.* (1996)	Characterization of dihydrates prepared from carbamazepine polymorphs.	CBZ Form I is prepared by heating CBZ Form III. CBZ Form I is prepared from CBZ dihydrate under low humidity conditions. CBZ Form I and III are prepared from CBZ dihydrate under high humidity conditions. Under high humidity conditions, the dehydration product is driven by the presence of seeds of CBZ I and III.
Ceolin *et al.* (1997)	X-ray characterization of the triclinic polymorph of carbamazepine.	CBZ Form I is prepared by heating CBZ Form III. CBZ Form I and III are enantiotropically related (Tt = 132 ºC).
Han & Suryanarayanan (1997)	Applications of pressure differential scanning calorimetry in the study of pharmaceutical hydrates. I. Carbamazepine dihydrate.	CBZ Form I is prepared from dehydration of CBZ dihydrate upon heating (ambient pressure). The dehydration showed a first amorphisation step, followed by Form I recrystallization at high temperatures. CBZ Form III is prepared from dehydration of CBZ dihydrate upon heating (high pressure). CBZ Form III appeared first and converted to CBZ I at high temperatures.
Han & Suryanarayanan (1998)	Influence of environmental conditions on the kinetics and mechanism of dehydration of carbamazepine dihydrate.	CBZ amorphous is prepared from the dehydration of CBZ dihydrate in a 2D phase boundary kinetic model, under no water vapour or at water vapour pressures ≤ to 5.1 torr. CBZ crystalline mixtures are prepared from dehydration of CBZ dihydrate in a 3-dimensional nucleation kinetic model, under water pressures ≥ to 12.0 torr.

Reference	Paper title	Conclusions
Griesser *et al.* (1999)	Vapor pressure and heat of sublimation of crystal polymorphs	CBZ Form III to CBZ Form I Tt value ~120 ºC.
Otsuka, Ofusa & Matsuda (1999)	Effect of environmental humidity on the transformation pathway of carbamazepine polymorphic modifications during grinding	CBZ amorphous is prepared from CBZ Form I under low and high humidity conditions. CBZ Form I is prepared from CBZ dihydrate under low and high humidity conditions (first follow an amorphization step). CBZ Form III is prepared by grinding of CBZ dihydrate.
Li *et al.* (2000)	*In situ* dehydration of carbamazepine dihydrate: a novel technique to prepare amorphous anhydrous carbamazepine.	CBZ amorphous is prepared from dehydration of CBZ dihydrate. It is unstable at room temperature and the glass transition occurs at 56 ºC.
Rustichelli *et al.* (2000)	Solid-state study of polymorphic drugs: carbamazepine	CBZ Form I is prepared by heating CBZ III. CBZ Form II is prepared from cooling ethanolic solutions. CBZ Form III is the commercial raw material, generally.
Edwards *et al.* (2001)	Time-resolved X-ray scattering using synchrotron radiation applied to the study of a polymorphic transition in carbamazepine.	CBZ Form I is prepared by heating CBZ III. CBZ Forms I and II are monotropically related (Tt = 120 ºC, exothermic). Thermodynamic stability comparison: CBZ III > CBZ I > CBZ II.
Lang, Grzesiak & Matzger (2002)	The use of polymer heteronuclei for crystalline polymorph selection	CBZ IV is prepared from methanol with polymer.
Lang, Kampf &Matzger (2002)	Form IV of carbamazepine	CBZ IV is prepared from methanol with polymer.
Grzesiak *et al.* (2003)	Comparison of the Four Anhydrous Polymorphs of Carbamazepine and the Crystal Structure of Form I	CBZ Form I is prepared from the melt of CBZ Form III or by heating CBZ Form III above 150 ºC. CBZ Form II is prepared from slow cooling of ethanol solutions (80 ºC to 5 ºC). CBZ Form III is prepared from slow cooling of ethanol solutions (80 ºC to 25 ºC). CBZ Form IV is prepared from slow evaporation of methanol solutions with polymer (HPC). CBZ Forms I and IV are monotropically related. CBZ Forms III and IV are enantiotropically related. Thermodynamic stability comparison: CBZ III > CBZ I > CBZ IV > CBZ II.

Reference	Paper title	Conclusions
Rodriguez-Hornedo &Murphy (2003)	Surfactant-Facilitated Crystallization of Dihydrate Carbamazepine during Dissolution of Anhydrous Polymorph	CBZ dihydrate is prepared from aqueous solutions with sodium lauryl sulfate (SLS) and sodium taurocholate (STC). SLS and STC promoted the crystallisation of CBZ dihydrate. STC changed the morphology of the dihydrate.
Surana, Pyrene & Suryanarayanan (2003)	Solid-Vapor Interactions: Influence of Environmental Conditions on the Dehydration of Carbamazepine Dihydrate	CBZ amorphous is prepared from the dehydration of CBZ dihydrate under 0% RH/25 ºC; the amorphous is stable below 30% RH/25 ºC. CBZ crystalline mixtures (I+III) are directly prepared from dehydration under 4% RH/25 ºC and under ethanol vapour pressures > 6 barr. CBZ crystalline mixtures (I+III) are prepared from dehydration with a previous step of amorphization under ethanol vapour pressures < 4.2 barr. The formation of a CBZ dihydrate intermediate is possible.
Brittain (2004)	Fluorescence Studies of the Transformation of Carbamazepine Anhydrate Form III to its Dihydrate Phase	CBZ dihydrate is prepared from CBZ Form III in water (18-40 ºC).
O'Brien *et al.* (2004)	Use of *in situ* FT-Raman spectroscopy to study the kinetics of the transformation of carbamazepine polymorphs.	CBZ Form I is prepared by heating CBZ Form III.
Cruz-Cabeza *et al.* (2006)	Amide pyramidalization in carbamazepine: a flexibility problem in crystal structure prediction?	Thermodynamic stability comparison: CBZ III = CBZ IV > CBZ I > CBZ II
Florence *et al.* (2006)	An auto- mated parallel crystallisation search for predicted crystal structures and packing motifs of carbamazepine	Thermodynamic stability comparison: CBZ III > CBZ I > CBZ IV > CBZ II
Tian *et al.* (2006)	Characterizing the conversion kinetics of carbamazepine polymorphs to the dihydrate in aqueous suspension using Raman spectroscopy	CBZ dihydrate is prepared from slurry of CBZ Forms I, II and III in water at 24 ºC (same kinetics). Same polymorphs, but with different morphologies, show significant differences in hydration.

Reference	Paper title	Conclusions
Tian *et al.* (2006)	Visualizing the conversion of carbamazepine in aqueous suspension with and without the presence of excipients: A single crystal study using SEM and Raman microscopy	CBZ dihydrate is prepared from CBZ Form III in water. Defects on the surface were more important driving forces than the nature of the crystal faces for the initiation of the hydration. HPC and PVP strongly inhibit the hydration.
Cruz-Cabeza *et al.* (2007)	Importance of molecular shape for the overall stability of hydrogen bond motifs in the crystal structures of various carbamazepine-type drug molecules	Thermodynamic stability comparison: CBZ III = CBZ IV > CBZ I > CBZ II
Cruz-Cabeza *et al.* (2007)	Solvent inclusion in Form II CBZ	CBZ II is prepared from toluene and tridecane solutions
Fabbiani *et al.* (2007)	Solvent inclusion in the structural voids of Form II carbamazepine: single-crystal X-ray diffraction, NMR spectroscopy and Hirshfeld surface analysis	CBZ II is prepared from tetrahydrofuran solutions
Getsoian *et al.* (2007)	One-solvent polymorph screen of carbamazepine	CBZ Form I is prepared from melt of CBZ Form III or from cumene solutions at temperature above 80 ^{o}C (regardless of the level of supersaturation). CBZ Form II is prepared from cooling (to 0 ^{o}C) highly supersaturated ethanolic solutions at temperatures below 60 ^{o}C (supersaturation of twice the solubility of CBZ). CBZ Form III is prepared from cumene solutions at temperatures below 60 ^{o}C (supersaturation of less than twice the solubility of CBZ). CBZ Form IV is prepared by dehydrating CBZ dihydrate obtained from methanolic solution. CBZ Forms I and III are enantiotropically related (Tt=79-82 ^{o}C).
Liu, Wey & Black (2009)	An Investigation of the Transformation of Carbamazepine from Anhydrate to Hydrate Using *in Situ* FBRM and PVM	CBZ dihydrate is prepared from CBZ Form III. Increase of agitation speed, seeds and addition of ethanol in water solutions can accelerate the transformation. High temperature or large size of seeds prolongated the transformation.

Reference	Paper title	Conclusions
Khoo, Williams & Heng (2010)	Dehydration kinetics of pharmaceutical hydrate: effects of environmental conditions and crystal forms	Different CBZ dihydrate samples were prepared from cooling crystallization in organic solvent:water solutions (plates in ethanol:water, needles in methanol:water) and from slurry in water (agglomerated thin particles). The samples were dehydrated upon temperature, vacuum and acetone vapour, resulting in CBZ Form III.
Arlin *et al.* (2011)	A strategy for producing predicted polymorphs: catemeric carbamazepine Form V.	CBZ Form V is prepared from sublimation over dihydrocarbamazepine seeds.
Qu *et al.* (2011)	Influence of temperature on solvent mediated anhydrate-to-hydrate transformation kinetics.	CBZ dihydrate/CBZ Form III transition temperature increases with increasing water fraction in a solvent mixture.
Kachrimanis & Grisser (2012)	Dehydration kinetics and crystal water dynamics of carbamazepine dihydrate.	Amorphous CBZ is prepared from CBZ dihydrate under 0% RH/25 ^{o}C. CBZ Form I is prepared from CBZ dihydrate under 10% RH/25 ^{o}C and above 100 ^{o}C. CBZ crystalline mixtures of I and IV are prepared from CBZ dihydrate under RH > 10%/25 ^{o}C. CBZ crystalline mixtures of I and III are prepared from CBZ dihydrate stored upon 50-100 ^{o}C. CBZ Form IV is prepared from CBZ amorphous in all the experimented conditions.
Khoo *et al.* (2013)	Process-induced phase transformation of carbamazepine dihydrate to its polymorphic anhydrates	CBZ Form I is prepared from CBZ dihydrate under humidity (5-60% RH) and 30-50 ^{o}C. CBZ Form I does not change with storage upon organic vapours (5-90%) and 20-50 ^{o}C. CBZ Form III is prepared from CBZ dihydrate and CBZ II and IV stored upon organic vapours (5-90%) and 20-50 ^{o}C. CBZ Form IV (major component) is prepared from CBZ dihydrate under high pressure and 20-50 ^{o}C.
Liu *et al.* (2013)	Investigation into the Cooling Crystallization and Transformations of Carbamazepine Using *in Situ* FBRM and PVM	CBZ Form III is prepared from CBZ Form II in ethanol solution (solution-mediated transformation). CBZ Form III crystals grow from the surface of Form II.

Reference	Paper title	Conclusions
O'Mahony *et al.* (2013)	Investigation into the mechanism of solution-mediated transformation from FI to FIII carbamazepine: the role of dissolution and the interaction between polymorph surfaces	CBZ Form III is prepared from CBZ Form I in ethanol solution (solution-mediated transformation). The nucleation of CBZ Form III occurs on side faces of the CBZ Form I needle-like crystals parallel to the crystallographic *a* lattice direction
O'Mahony *et al.* (2014)	Investigating the dissolution of the metastable triclinic polymorph of carbamazepine using *in situ* microscopy	CBZ Form III is prepared from CBZ Form I in ethanol solution (solution-mediated transformation). CBZ Form I is preferred in highly concentrated solutions while CBZ Form III is preferred in less concentrated solutions. The authors suggest the reason is due to different surface dissolution mechanisms in different solution concentrations.
Parambil *et al.* (2014)	Template-induced polymorphic selectivity: the effects of surface chemistry and solute concentration on carbamazepine crystallisation	CBZ Form I is prepared in highly concentrated solutions (with differences found according to the use of distinct functionalized glass vials surfaces). CBZ Form III is prepared in highly concentrated solutions (with differences found according to the use of distinct functionalized glass vials surfaces).
Parambil *et al.* (2015)	Establishing template-induced polymorphic domains for API crystallisation: the case of carbamazepine	CBZ Form II has its nucleation promoted over cyano-functionalized templates. CBZ Form III has its nucleation promoted over mercapto- and fluoro-functionalized templates.
Walshe *et al.* (2015)	Anisotropic Crystal Growth in Flat and Nonflat Systems: The Important Influence of van der Waals Contact Molecular Stacking on Crystal Growth and Dissolution	Stacked structures show needle growth along the stacking direction, except if there is hydrogen bonding chain in the stacking direction. The authors analysed different molecules, including CBZ (Form I, II and an orthorhombic Form VI, which they reported as a submitted manuscript). PIXEL analysis has shown that dispersion forces are the largest interaction in the stacking direction.
Guinet *et al.* (2016)	Comparison of amorphous states prepared by melt-quenching and cryomilling polymorphs of carbamazepine	Quench cooling of molten CBZ and cryomilling of CBZ I and III lead to different truly amorphous materials. After non-isothermal crystallisation, the quenched glass converted to CBZ I, the cryomilled from CBZ I resulted in a mixture of CBZ I and IV, and the cryomilled from CBZ III resulted in CBZ III.

Reference	Paper title	Conclusions
Jensen *et al.* (2017)	Amorphous is not always better—A dissolution study on solid state forms of carbamazepine	Pure amorphous CBZ presents a rapid conversion to CBZ dihydrate in dissolution medium. CBZ Form III initially shows high concentration in the media, which decreases later as a result of solution-mediated hydration.
Parambil *et al.* (2017)	Influence of solvent polarity and supersaturation on template-induced nucleation of carbamazepine crystal polymorphs	Functionalized templates can only promote the crystallization of CBZ Form II or CBZ Form I in moderate or low polarity solvents. Highly polar solvents mask the templating effect.

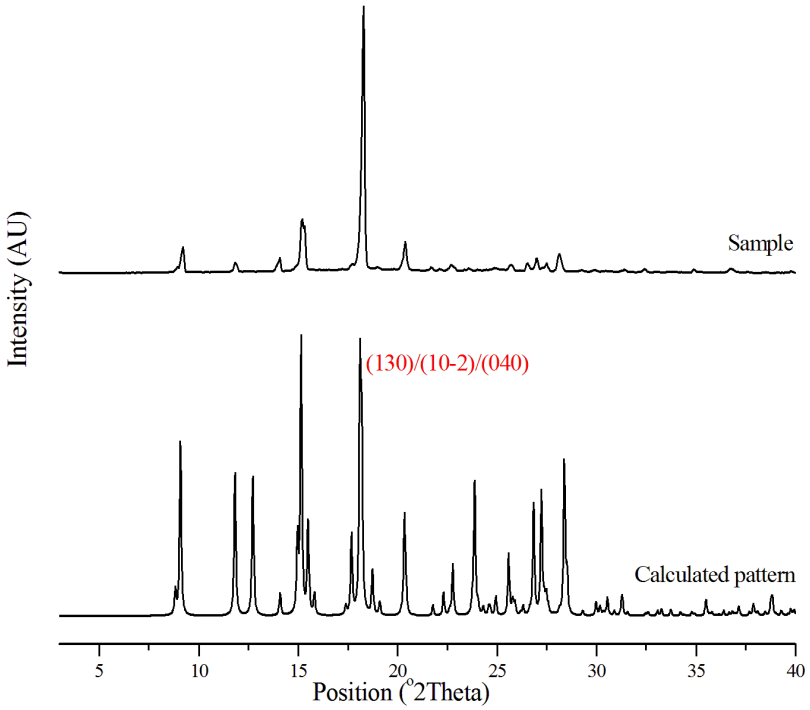

Figure 279 - PXRD patterns illustrating the preferred orientation of CBZ:DMA sample (6xS, 100% DMA) compared to the pattern calculated from KIWBEY. The peak correspondent to the (130)/(10-2)/(040) planes is highlighted in the graph.

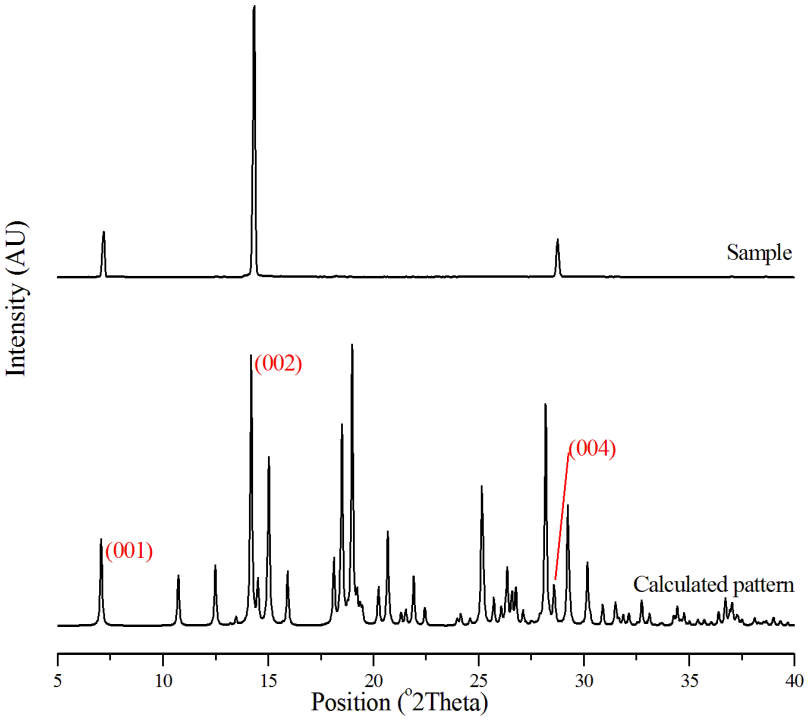

Figure 280 - PXRD patterns illustrating the preferred orientation of CBZ:BZQ sample (6xS, 100% ethanol) compared to the calculated pattern. The peaks correspondent to the (001), (002) and (004) planes are highlighted in the graph.

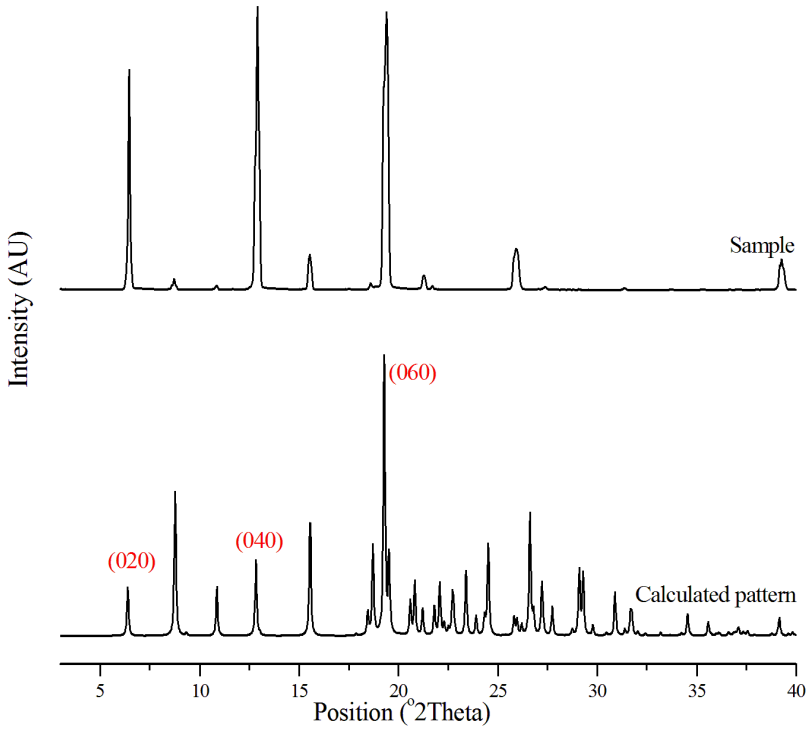

Figure 281 - PXRD patterns illustrating the preferred orientation of 2CBZ:BZQ sample (6xS, 100% ethanol) compared to the pattern calculated from UNEYOB. The peaks correspondent to the (020), (040) and (060) planes are highlighted in the graph.

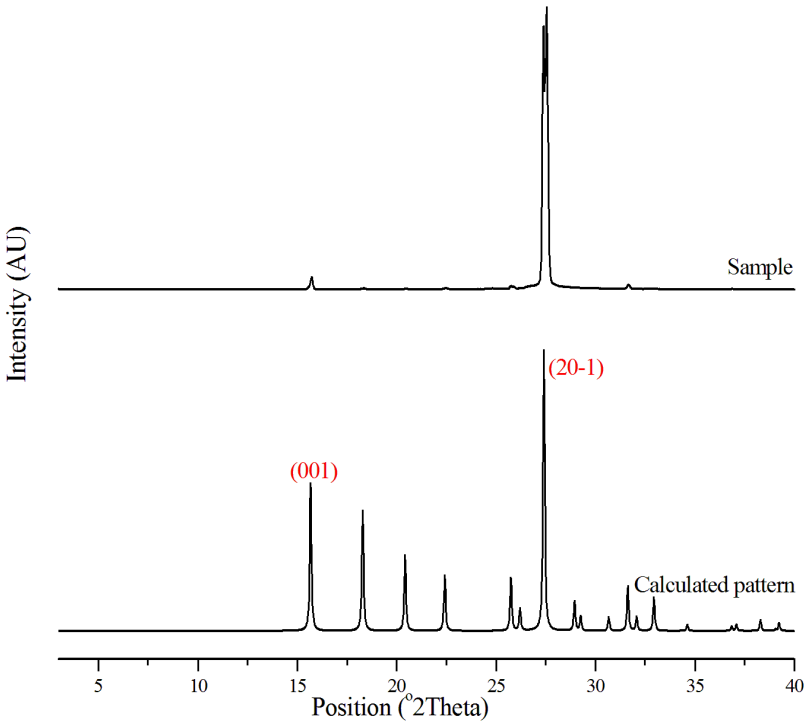

Figure 282 - PXRD patterns illustrating the preferred orientation of BZQ sample (sublimation) compared to the pattern calculated from BNZQUI. The peaks correspondent to the (001) and (20-1) planes are highlighted in the graph.

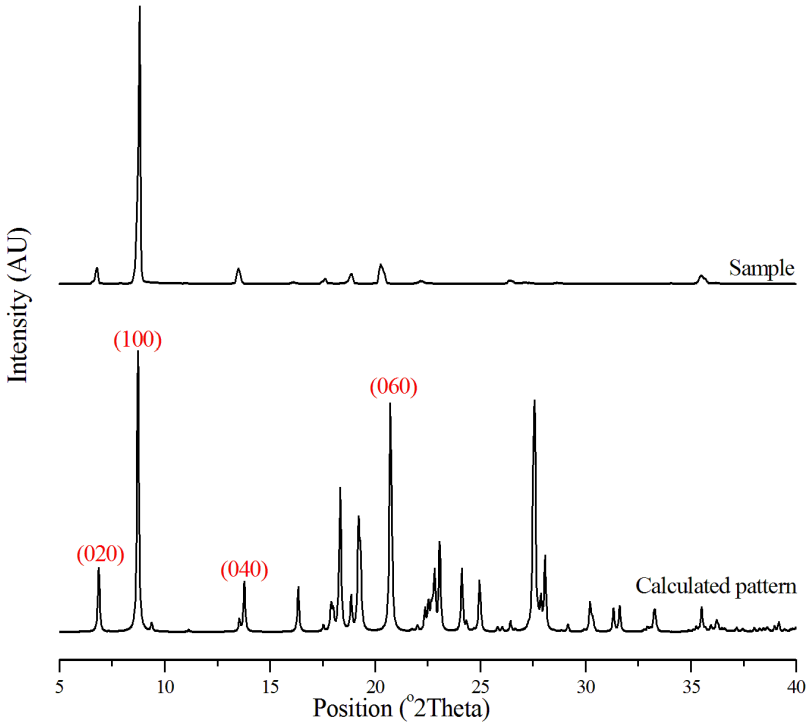

Figure 283 - PXRD patterns illustrating the preferred orientation of 2CBZ:OXA sample (27.0 mg.mL^{-1}, 100% ethyl acetate) compared to the calculated pattern. The peaks correspondent to the (100), (020), (040) and (060) planes are highlighted in the graph.

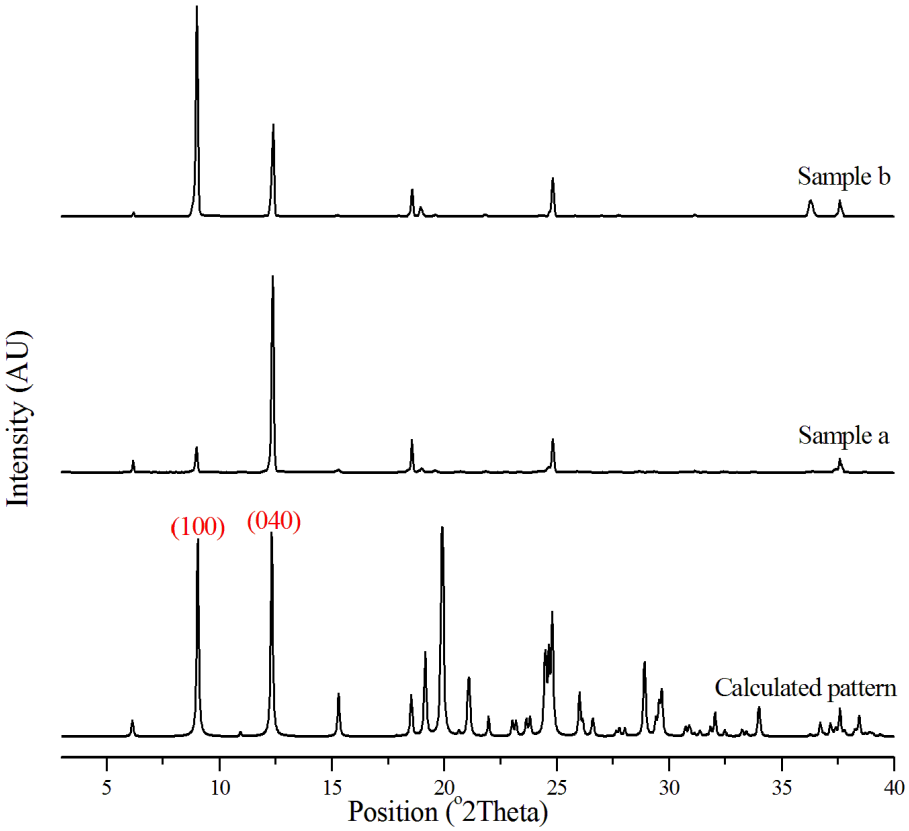

Figure 284 - PXRD patterns illustrating the preferred orientation of CBZ:2H_2O samples compared to the pattern calculated from FEFNOT02. Sample *a* was crystallized in 91 mol% of water in ethanol (6xS), and sample *b* was crystallized in 52 mol% of water (2xS). The peaks correspondent to the (100) and (040) planes are highlighted in the graph.

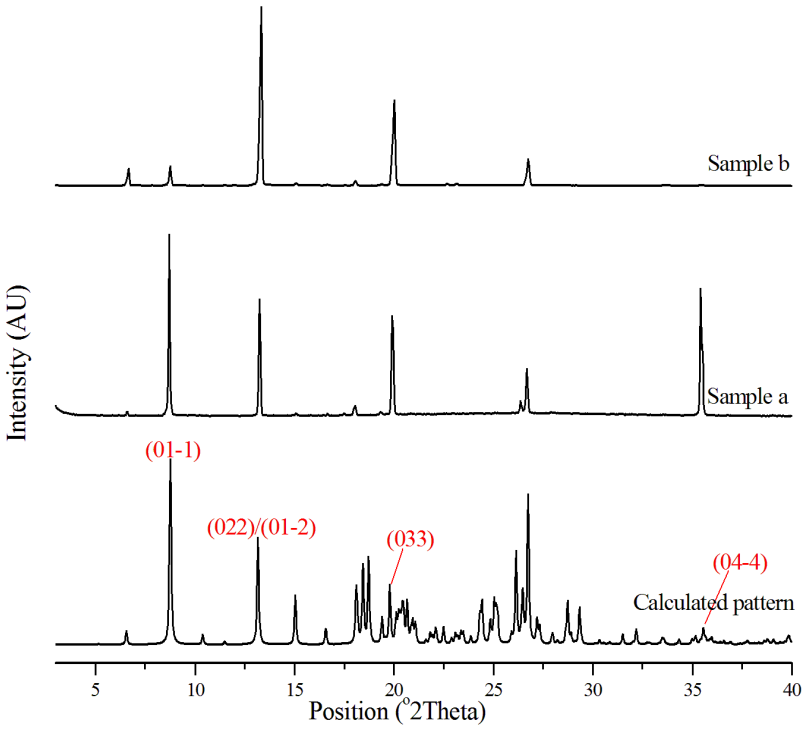

Figure 285 - PXRD patterns illustrating the preferred orientation of CBZ:FORM samples compared to the pattern calculated from UNIBOI. Sample *a* was crystallized in formamide (6xS), and sample *b* was crystallized in 25 mol% of formamide in ethanol (6xS). The peaks correspondent to the (01-1), (022)/(01-2), (033) and (04-4) planes are highlighted in the graph.

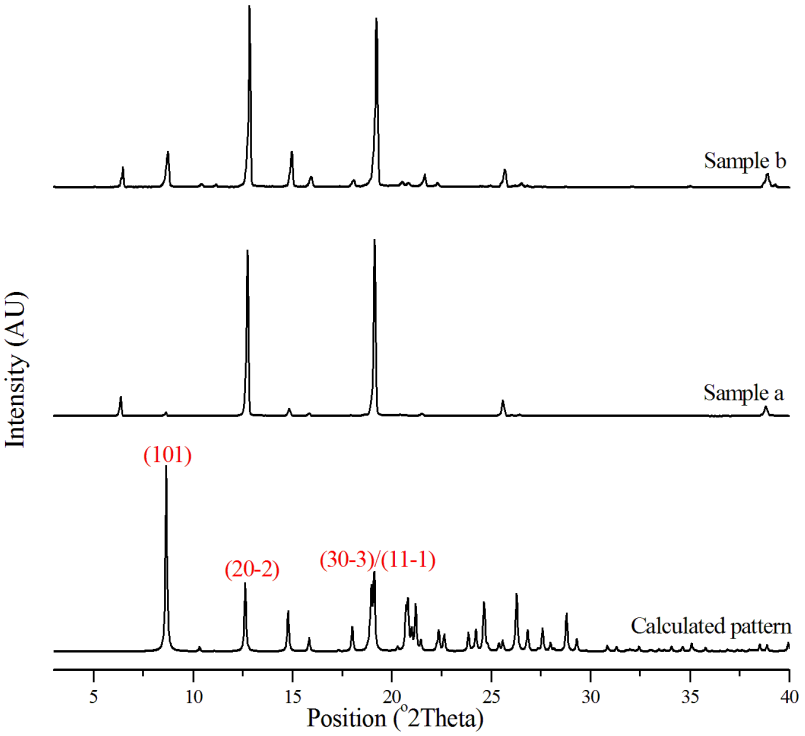

Figure 286 - PXRD patterns illustrating the preferred orientation of 2CBZ:DIOX samples compared to the calculated pattern. Sample *a* was crystallized in 1,4-dioxane (4xS), and sample *b* was crystallized in 25 mol% of 1,4-dioxane in ethanol (4xS). The peaks correspondent to the (101), (20-2) and (30-3)/(11-1) planes are highlighted in the graph.

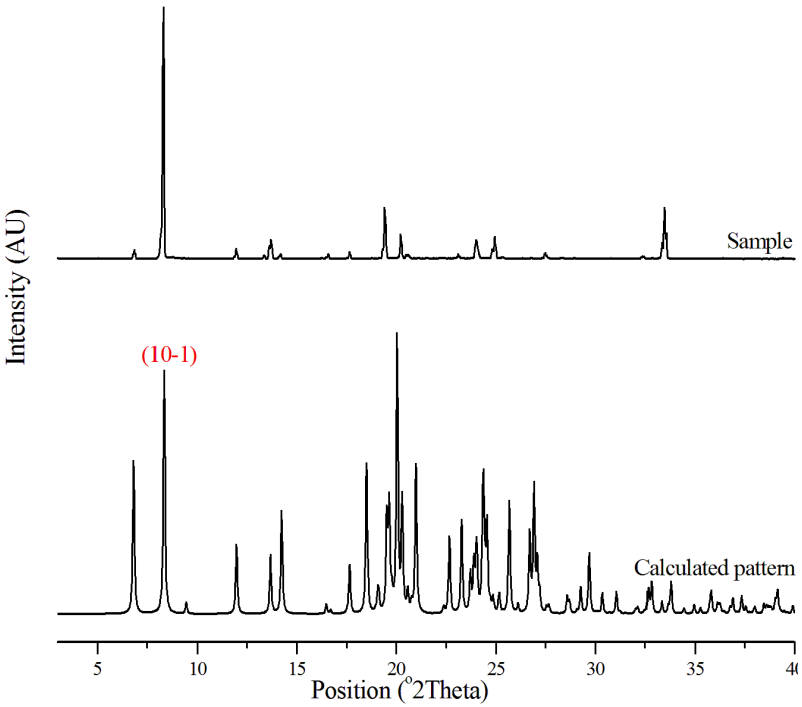

Figure 287 - PXRD patterns illustrating the preferred orientation of CBZ:NIT sample compared to the pattern calculated from KIWBOI. The peak correspondent to the (10-1) plane is highlighted in the graph.

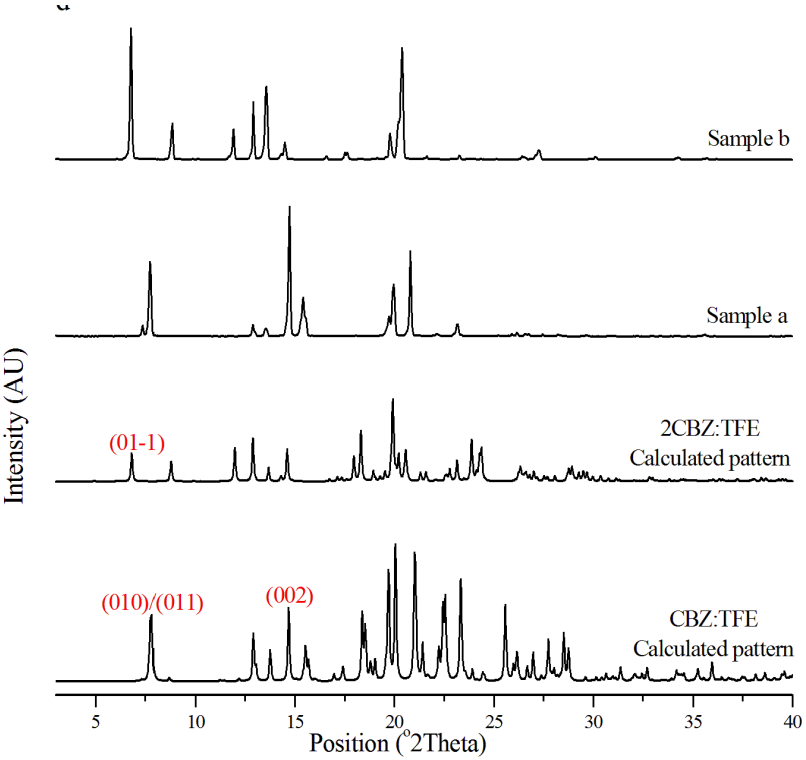

Figure 288 - PXRD patterns illustrating the preferred orientation of CBZ/TFE samples compared to the calculated patterns (CBZ:TFE is the SAPDUJ CSD structure). Sample *a* was crystallized in 2,2,2-trifluoroethanol (4xS), and sample *b* was crystallized in 45 mol% of 2,2,2-trifluoroethanol in ethanol (4xS). The peaks correspondent to the (010)/(011) and (002) planes of CBZ:TFE and (01-1) plane of 2CBZ:TFE are highlighted in the graph.

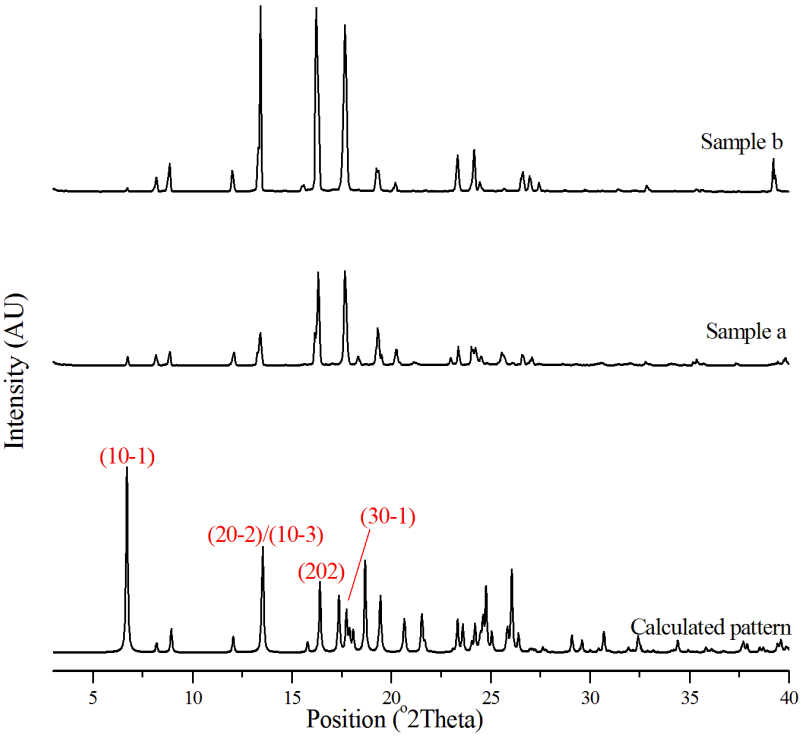

Figure 289 - PXRD patterns illustrating the preferred orientation of CBZ:TFA samples compared to the pattern calculated from GINFOZ. Sample *a* was crystallized in 2,2,2-trifluoroacetic acid (2xS), and sample *b* was crystallized in 43 mol% of 2,2,2-trifluoroacetic acid in ethanol (2xS). The peaks corresponding to the (10-1), (20-2)/(10-3), (202) and (30-1) planes are highlighted in the graph.

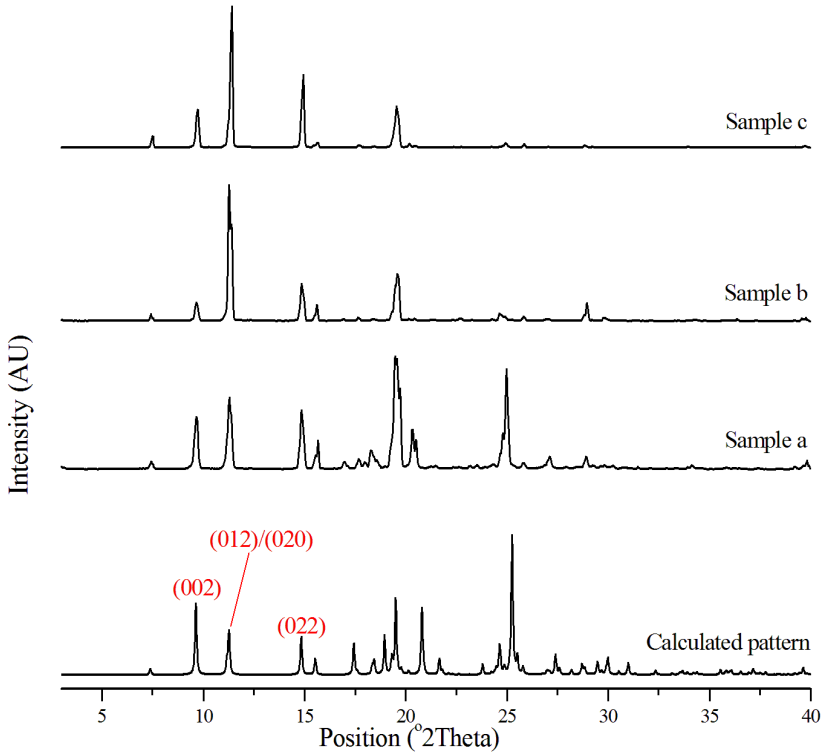

Figure 290 - PXRD patterns illustrating the preferred orientation of CBZ:ACA samples compared to the pattern calculated from UNEZIW. Samples were crystallized in acetic acid (*a*: 2xS; *b*: 4xS; *c*: 6xS). The peaks corresponding to the (002), (012)/(020), and (022) planes are highlighted in the graph.

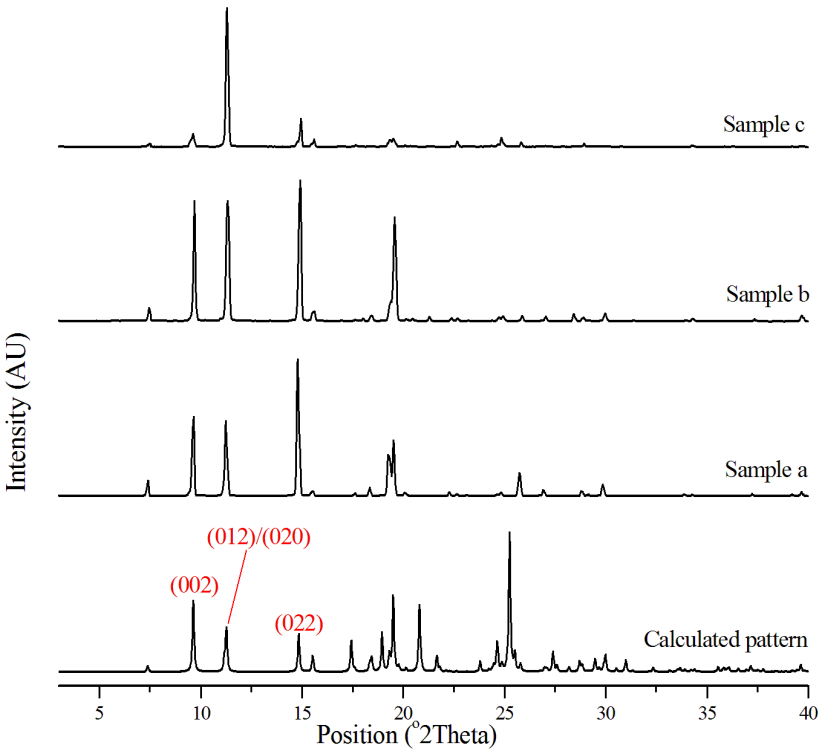

Figure 291 - PXRD patterns illustrating the preferred orientation of CBZ:ACA samples compared to the pattern calculated from UNEZIW. Samples were crystallized in 25 mol% of acetic acid in ethanol (*a*: 2xS; *b*: 4xS; *c*: 6xS). The peaks corresponding to the (002), (012)/(020), and (022) planes are highlighted in the graph.

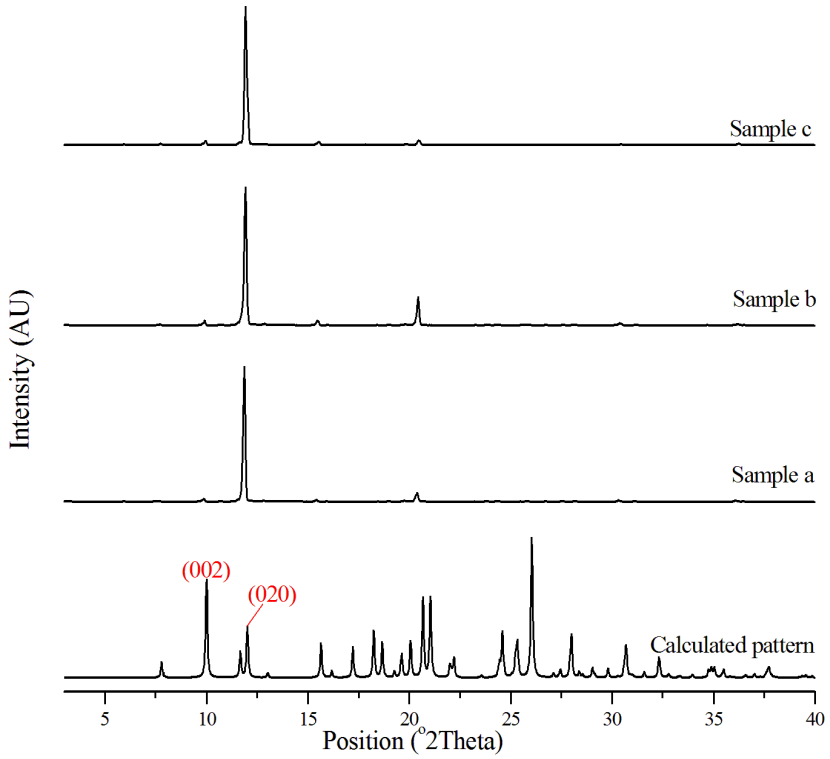

Figure 292 - PXRD patterns illustrating the preferred orientation of CBZ:FA samples compared to the pattern calculated from UNEZOC. Samples were crystallized in formic acid (*a*: 2xS; *b*: 4xS; *c*: 6xS). The peaks corresponding to the (002) and (020) planes are highlighted in the graph.

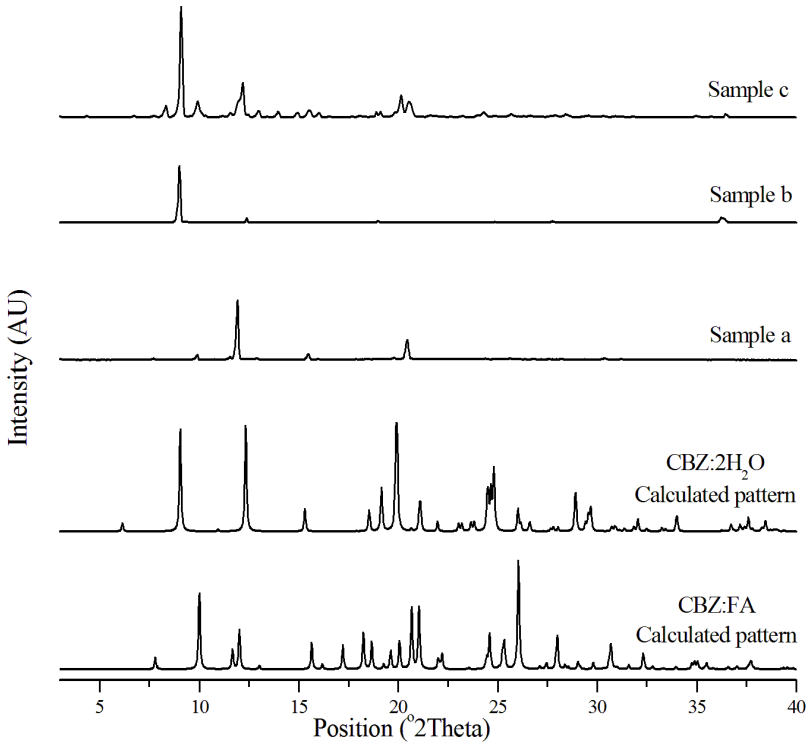

Figure 293 - PXRD patterns illustrating the preferred orientation of CBZ:FA samples compared to the pattern calculated from UNEZOC. Samples were crystallized in 34 mol% of formic acid in ethanol (*a*: 2xS; *b*: 4xS; *c*: 6xS). The calculated pattern of the dihydrate is displayed as some samples were characterized as mixtures of CBZ:FA and $CBZ:2H_2O$.

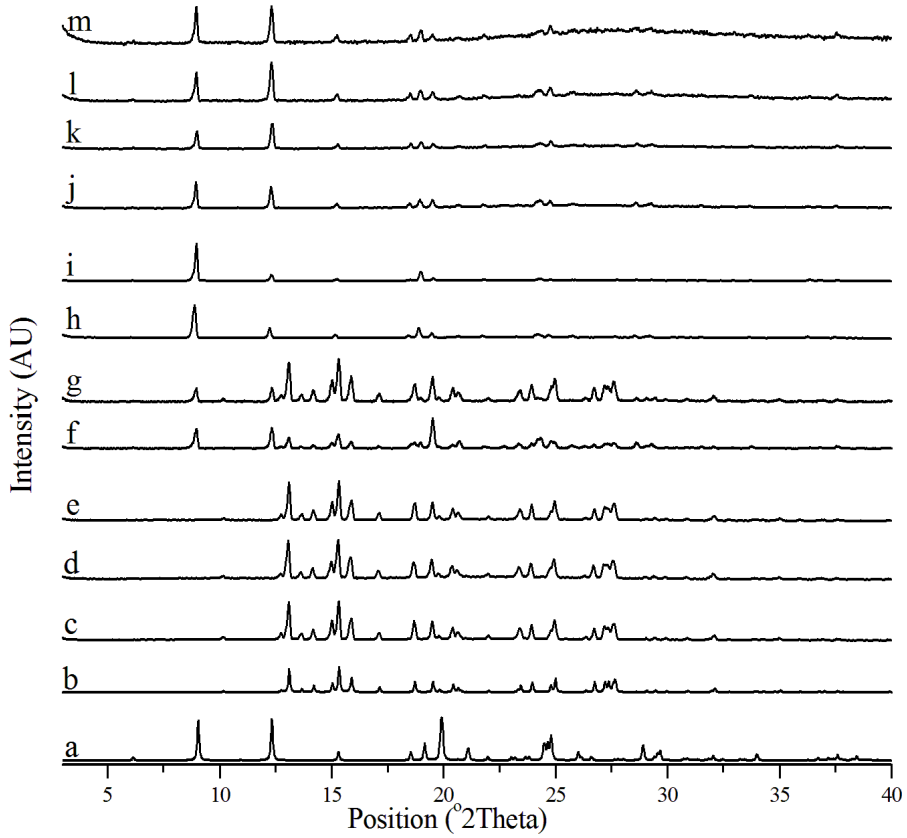

Figure 294 - PXRD patterns showing the results of slurrying of CBZ in ethanol:water. The reference calculated patterns are added for clarification (*a*: CBZ:2H$_2$O from FENOT02; *b*: CBZ Form III from CBMZPN01). The experimental PXRD patterns of slurried materials in different water contents are displayed on the top (*c*: 0%; *d*: 15 mol%; *e*:: 26 mol%; *f:* 30 mol%; *g:* 35 mol%; *h:* 45 mol%; *i*: 68 mol%; *j*: 83 mol%; *k*: 93 mol%; *l*: 97 mol%; *m*: 100%).

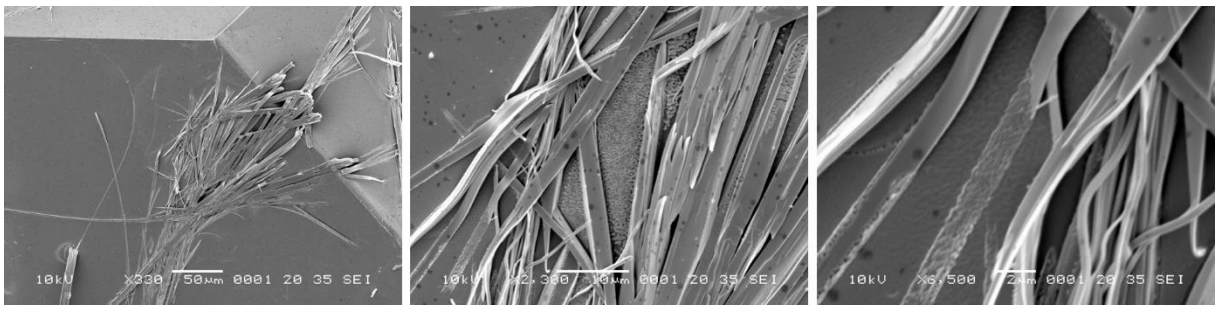

Figure 295 - SEM micrographs showing the growth of needle crystals on CBZ Form III crystals.

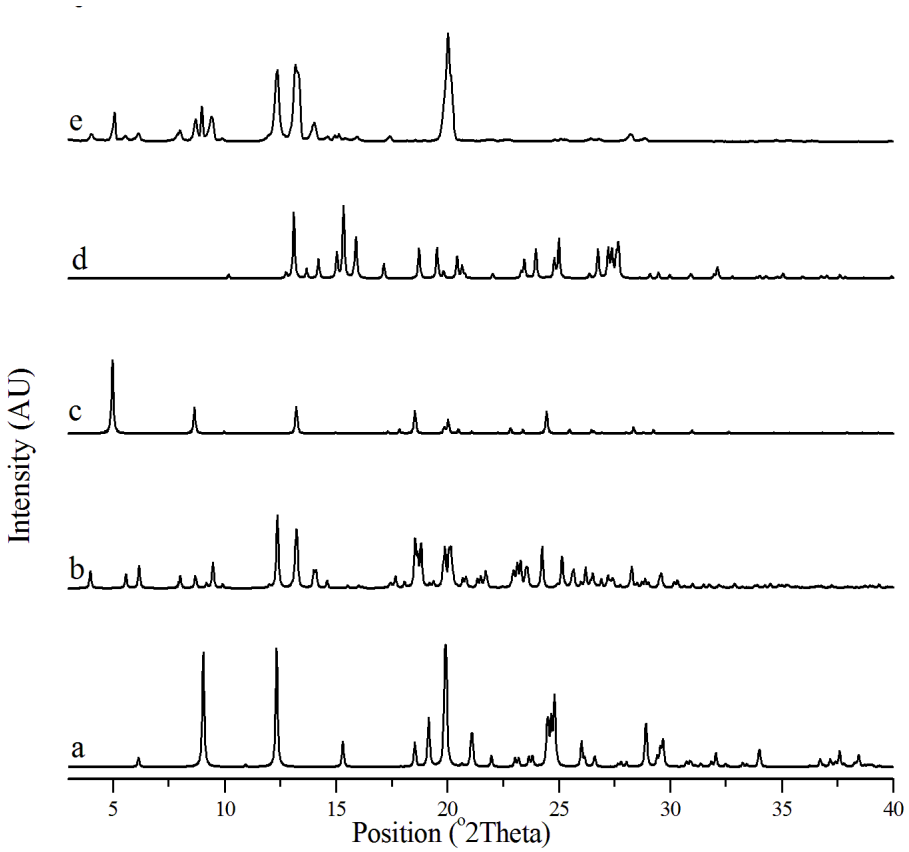

Figure 296 - PXRD patterns characterizing the needles obtained in ethanol:water 74:26 (n:n, 2xS). The *e* indicates the sample, while the other patterns are calculated from references (*a*: CBZ:2H2O from FEFNOT; *b*: CBZ Form I from CBMZPN11; *c*: CBZ Form II from CBMZPN03; *d*: CBZ Form III from CBMZPN 01).

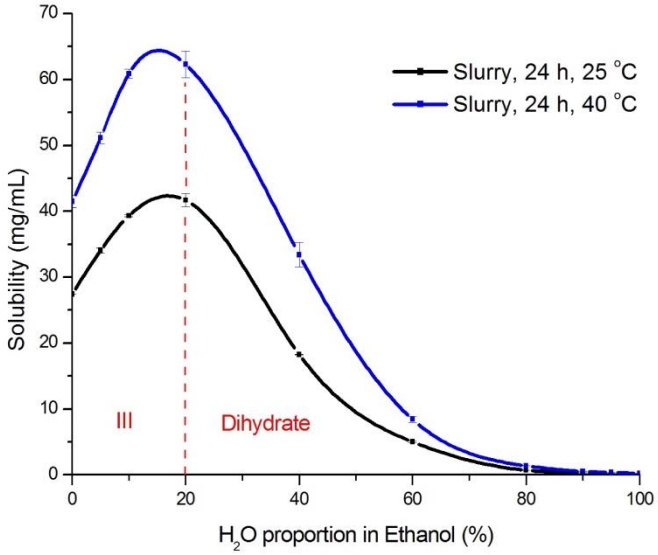

Figure 297 - Equilibrium solubility curves of CBZ in ethanol:water (v:v) at different temperatures. The identification of the solid phases is indicated in the graph.

Table 20 - Nomenclature description of the CBZ:2H_2O samples obtained from different crystallization conditions and methods. The results are summarized on Table 11 and representative micrographs are shown in Figure 298.

C/S[a]	Water proportion (mol%)						
	52%[b]	52%[c]	68%[c]	76%[c]	83%[c]	91%[c]	91%[b]
1.2	A1	A	F	K	P	U	U1[d]
1.4	B1	B	G	L	Q	V	V1
1.7	C1	C	H	M	R	W	W1
2.0	D1	D	I	N	S	X	X1
6.0	-	E	J	O	T	Y	-

[a] Relation of concentration per solubility. This parameter is called "supersaturation degree" in the experiments where the supersaturation at the moment of nucleation was controlled ([b]), or is called "initial concentration" in the other experiments ([c]).
[d] The crystals obtained from crystallization in this experiment were not enough for characterization.

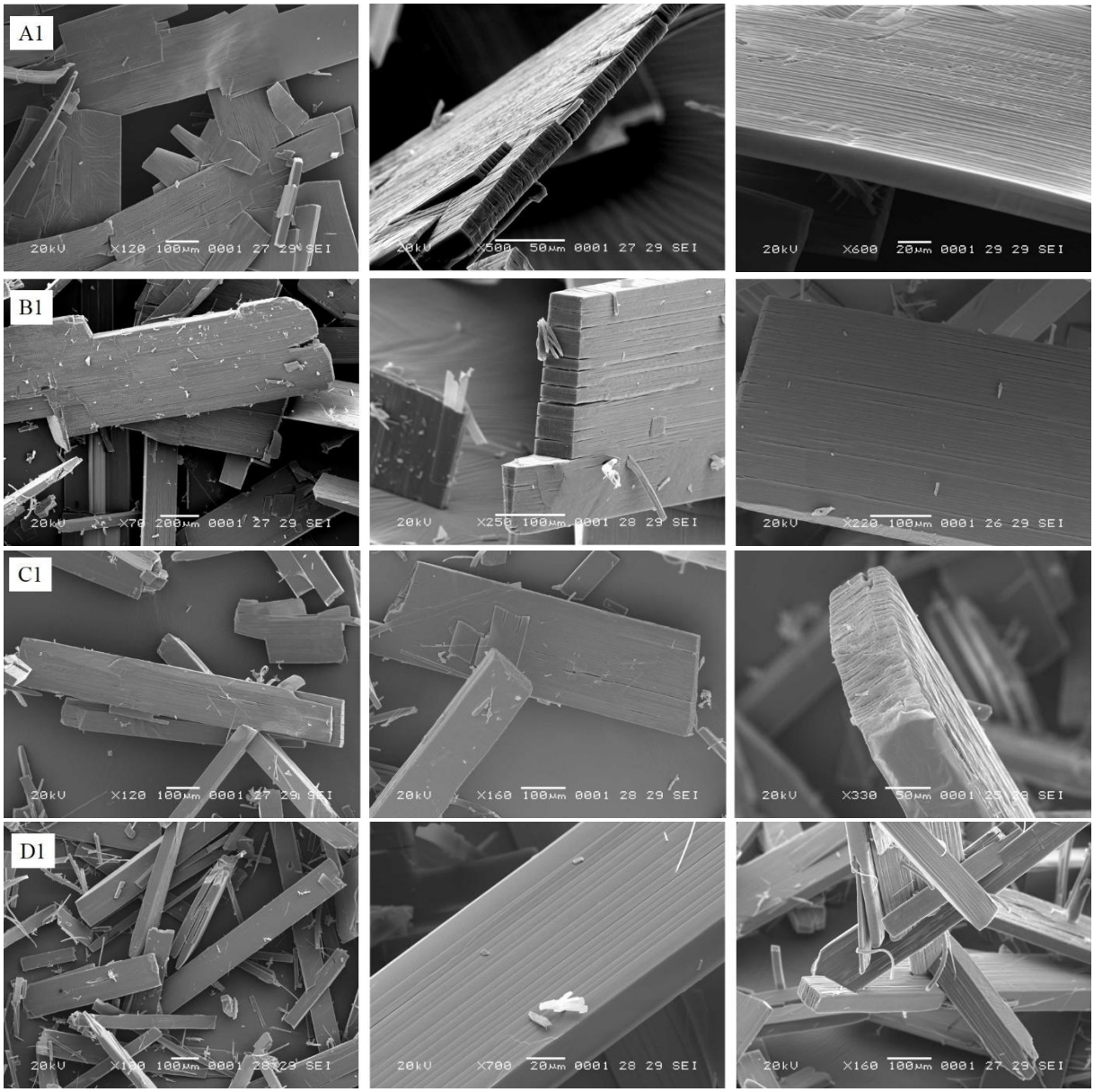

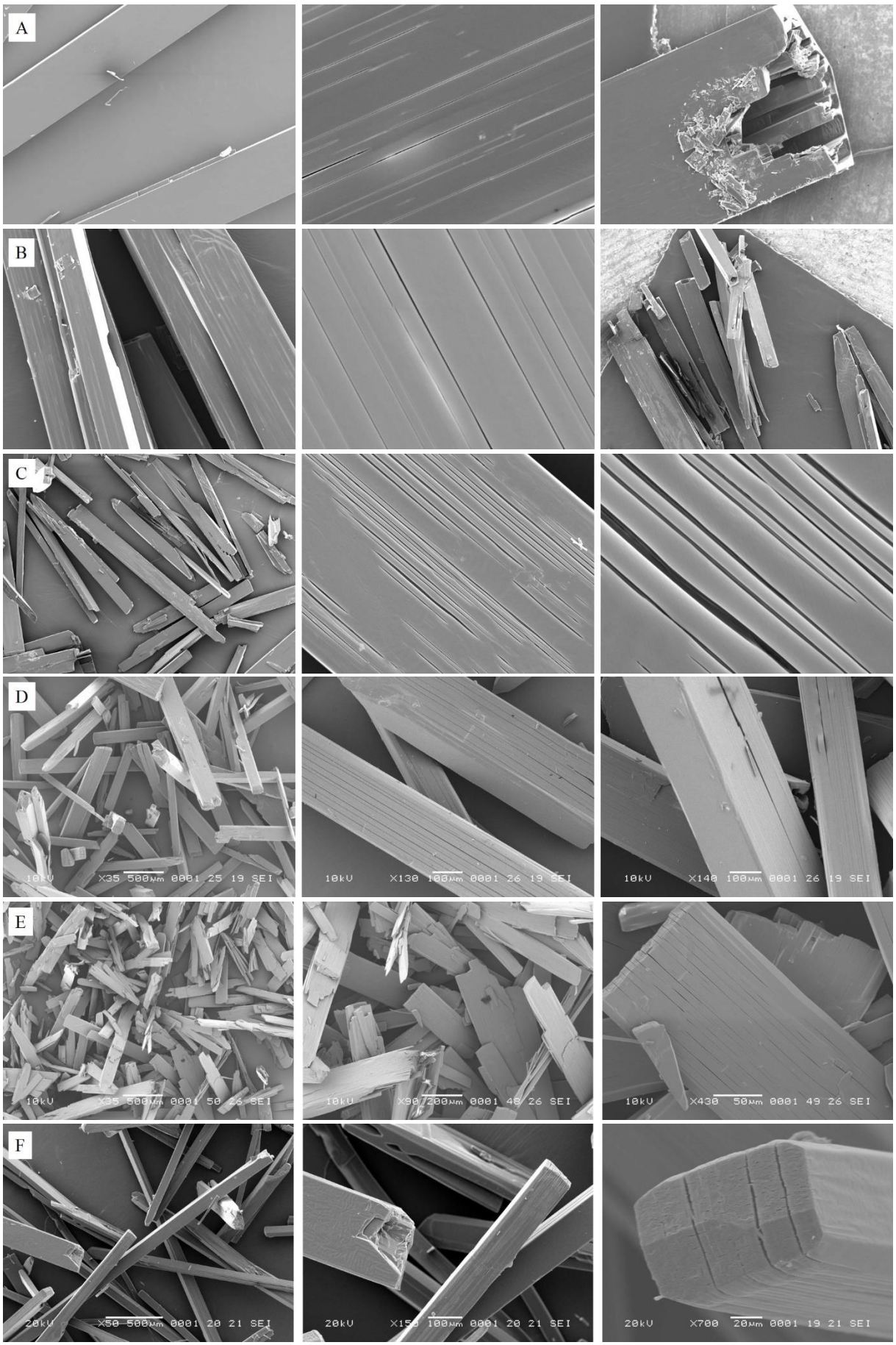
A
B
C
D
10kV X35 500µm 0001 25 19 SEI
10kV X130 100µm 0001 26 19 SEI
10kV X140 100µm 0001 26 19 SEI
E
10kV X35 500µm 0001 50 26 SEI
10kV X90/200µm 0001 48 26 SEI
10kV X430 50µm 0001 49 26 SEI
F
20kV X50 500µm 0001 20 21 SEI
20kV X150 100µm 0001 20 21 SEI
20kV X700 20µm 0001 19 21 SEI

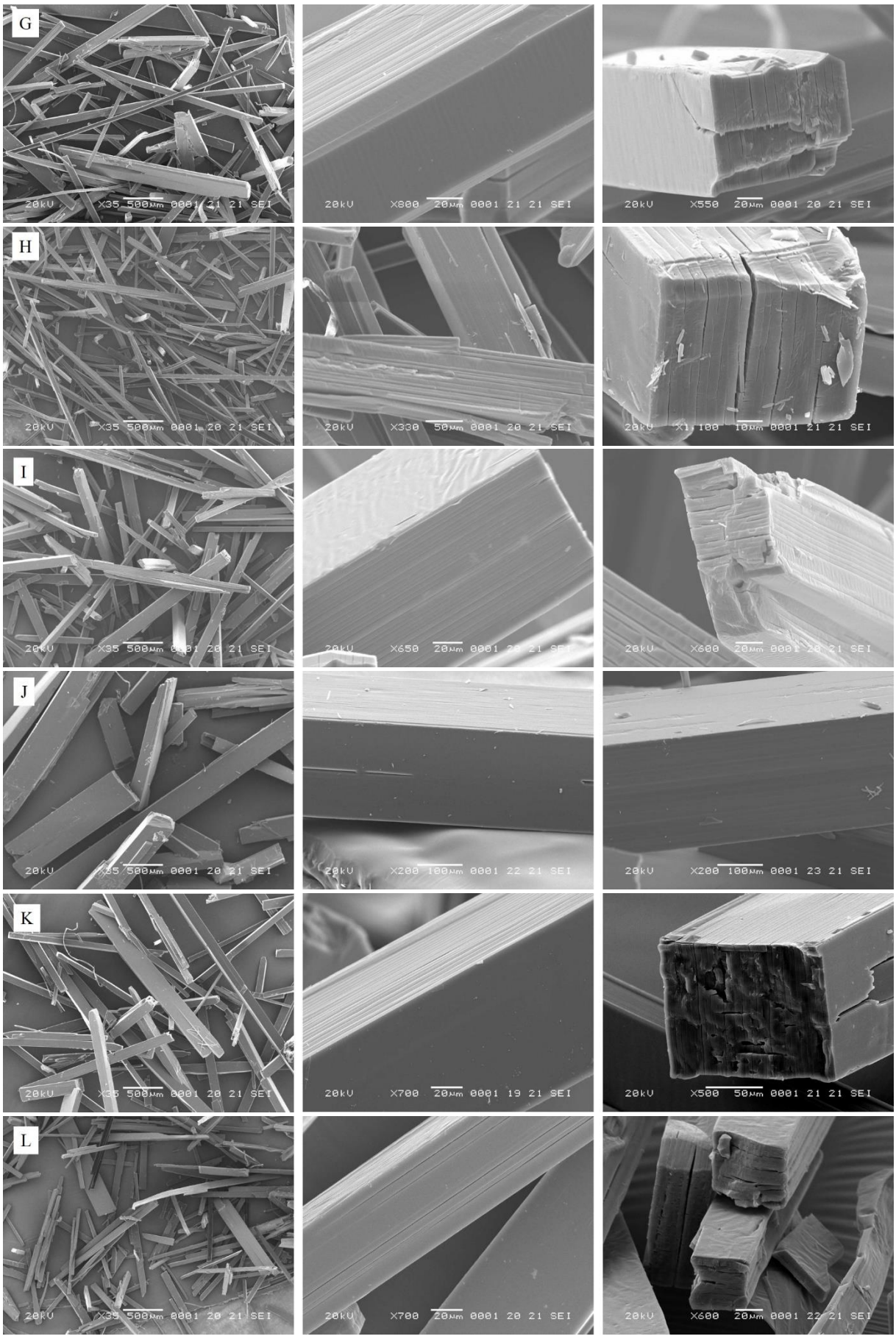
G
20kU X35 500µm 0001 21 21 SEI
20kU X800 20µm 0001 21 21 SEI
20kU X550 20µm 0001 20 21 SEI
H
20kU X35 500µm 0001 20 21 SEI
20kU X330 50µm 0001 20 21 SEI
20kU X1,100 10µm 0001 21 21 SEI
I
20kU X35 500µm 0001 20 21 SEI
20kU X650 20µm 0001 20 21 SEI
20kU X600 20µm 0001 20 21 SEI
J
20kU X35 500µm 0001 20 21 SEI
20kU X200 100µm 0001 22 21 SEI
20kU X200 100µm 0001 23 21 SEI
K
20kU X35 500µm 0001 20 21 SEI
20kU X700 20µm 0001 19 21 SEI
20kU X500 50µm 0001 21 21 SEI
L
20kU X35 500µm 0001 20 21 SEI
20kU X700 20µm 0001 20 21 SEI
20kU X600 20µm 0001 22 21 SEI

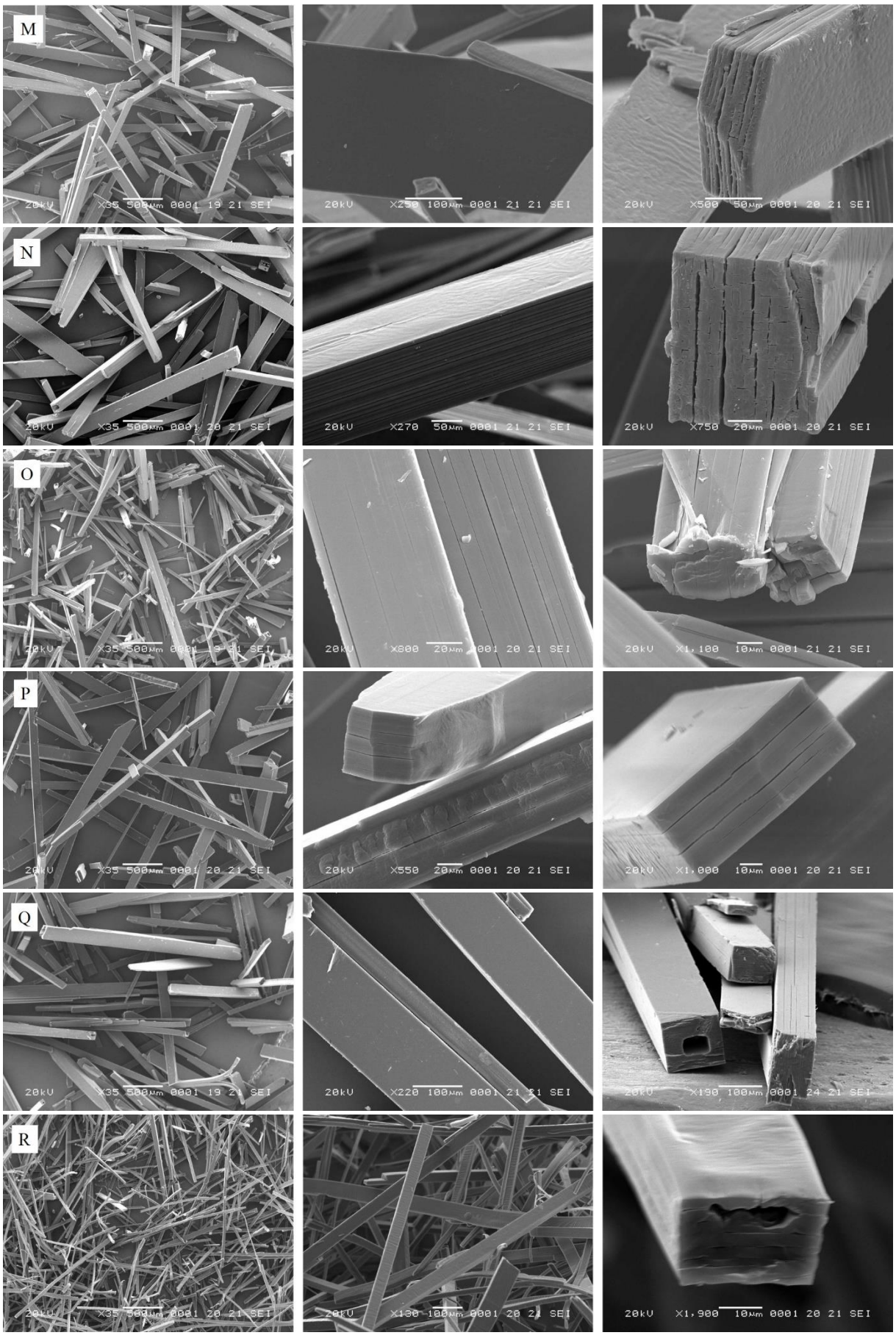
M
20kV X35 500µm 0001 19 21 SEI
20kV X250 100µm 0001 21 21 SEI
20kV X500 50µm 0001 20 21 SEI
N
20kV X35 500µm 0001 20 21 SEI
20kV X270 50µm 0001 21 21 SEI
20kV X750 20µm 0001 20 21 SEI
O
20kV X35 500µm 0001 19 21 SEI
20kV X800 20µm 0001 20 21 SEI
20kV X1,100 10µm 0001 21 21 SEI
P
20kV X35 500µm 0001 20 21 SEI
20kV X550 20µm 0001 20 21 SEI
20kV X1,000 10µm 0001 20 21 SEI
Q
20kV X35 500µm 0001 19 21 SEI
20kV X220 100µm 0001 21 21 SEI
20kV X190 100µm 0001 24 21 SEI
R
20kV X35 500µm 0001 20 21 SEI
20kV X130 100µm 0001 20 21 SEI
20kV X1,900 10µm 0001 20 21 SEI

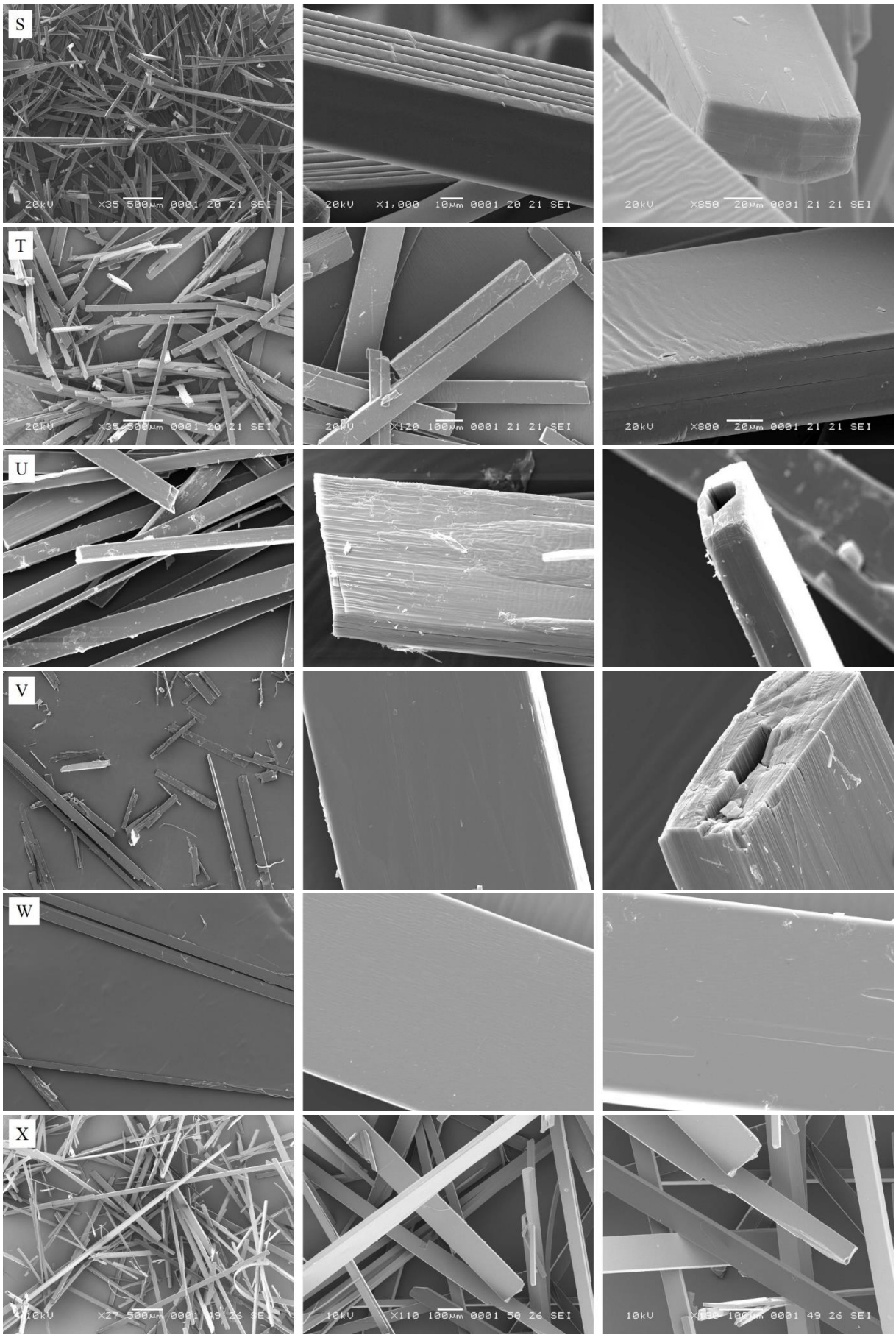
S
20kV X35 500µm 0001 20 21 SEI
20kV X1,000 10µm 0001 20 21 SEI
20kV X850 20µm 0001 21 21 SEI
T
20kV X35 500µm 0001 20 21 SEI
20kV X120 100µm 0001 21 21 SEI
20kV X800 20µm 0001 21 21 SEI
U
V
W
X
10kV X110 100µm 0001 50 26 SEI
10kV 100µm 0001 49 26 SEI

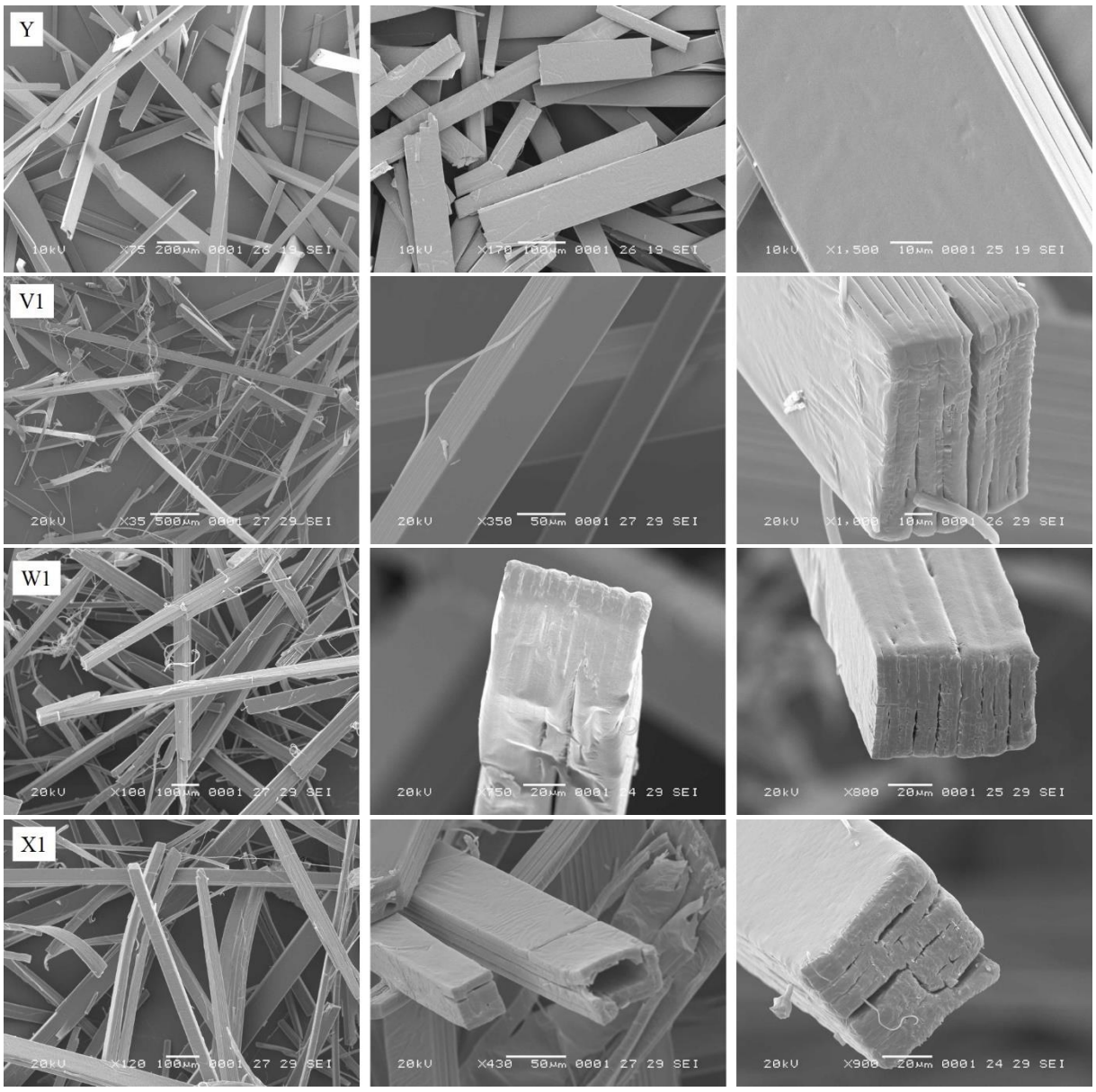

Figure 298 – SEM micrographs representative of the CBZ:2H_2O crystals obtained from different crystallization conditions and methods (different rows represent different samples). The nomenclature of the samples is shown on Table 20 and the summary of the results is described on Table 11.

	Block	Plate	Needle
Aspect Ratio	L≈M≈S	L≈M>S	L>M≈S
M/L	≈1	≈1	≈0
S/L	≈1	≈0	≈0
S/M	≈1	≈0	≈1

Figure 299 - Comparison of aspect ratio values for shapes representative of blocks, plates and needles (reproduced from Vatvani[60] with permission).

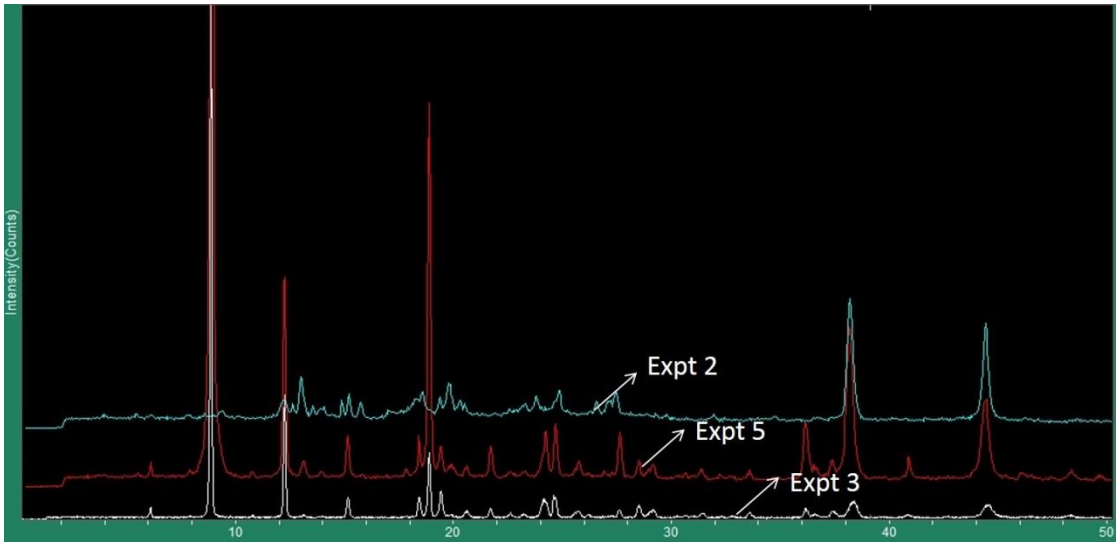

Figure 300 - PXRD patterns of the CBZ:2H_2O samples prepared during the development of the final crystallization method (reproduced from Sinha[205,206] with permission). Experiment 2: reverse addition of anti-solvent with seeding; experiment 3: forward addition of anti-solvent without seeding; experiment 5: forward addition of anti-solvent with seeding.

Table 21 - Observed and calculated compositions of carbamazepine dihydrate crystallized in large scale.

	Calculated (mass %)	Observed (mass %)*	Observed standard deviation
C	66.17	66.16 / 66.16	0.030 / 0.066
H	5.92	5.76 / 6.26	0.085 / 1.014
N	10.29	10.25 / 10.24	0.019 / 0.047
O	17.63	17.84 / 17.34	0.116 / 0.951
H_2O	13.23	13.28 / 13.18	0.007 / 0,021

*The observed CHN composition was determined with elemental analysis while the water content was measured with TGA. The observed O composition was indirectly obtained.

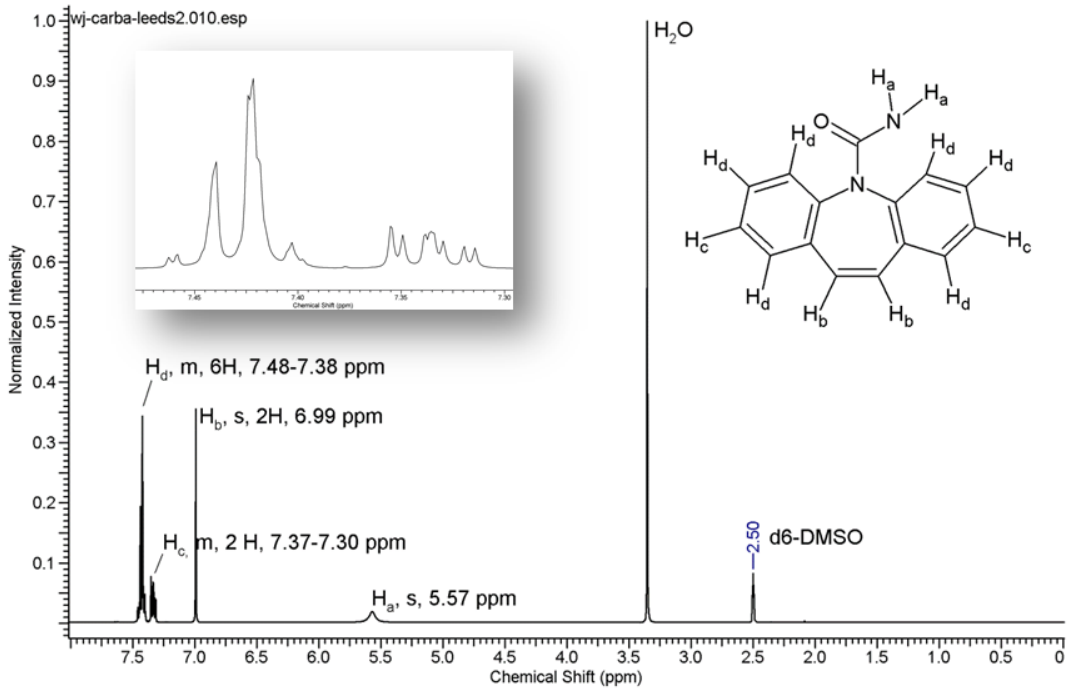

Figure 301 - ^1H spectrum of CBZ dihydrate crystallized in large scale (Solvent: DMSO-d_6). The peaks relative to H_2O and DMSO are indicated.

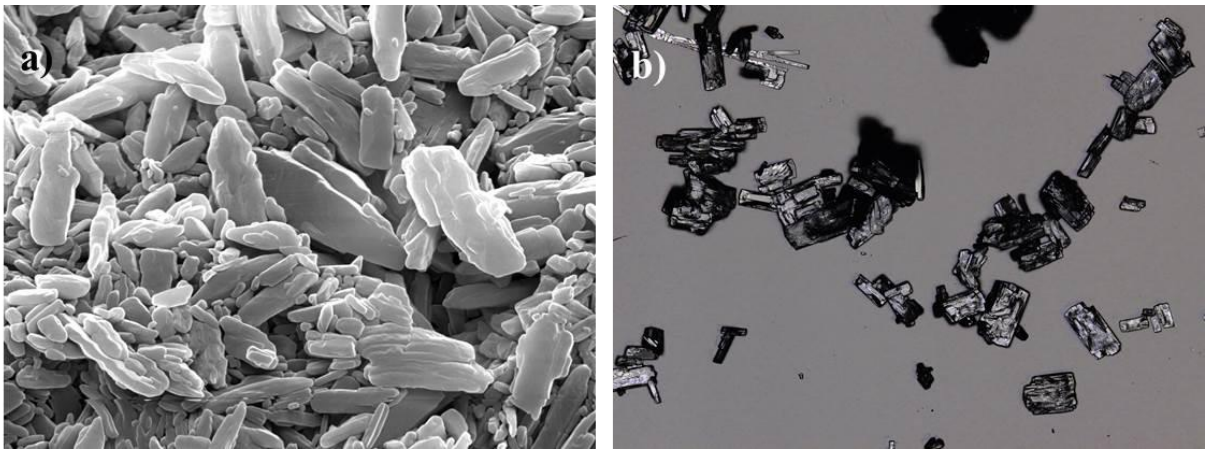

Figure 302 - Micrographs of seeds used in the crystallization of CBZ:$2H_2O$. *a*: SEM of "dry" seeds used in laboratory-scale anti-solvent addition experiments (prepared by slurrying). *b*: confocal laser scanning microscopy of wet milled seeds used in large-scale anti-solvent addition experiments (reproduced from Sinha[205,206] with permission).